SOILS and ROCKS

An International Journal of Geotechnical and Geoenvironmental Engineering

Soils and Rocks publishes papers in English in the broad fields of Geotechnical Engineering, Engineering Geology, and Geoenvironmental Engineering. The Journal is published quarterly in March, June, September and December. The first issue was released in 1978, under the name *Solos e Rochas*, being originally published by the Graduate School of Engineering of the Federal University of Rio de Janeiro. In 1980, the Brazilian Association for Soil Mechanics and Geotechnical Engineering took over the editorial and publishing responsibilities of *Solos e Rochas*, increasing its reach. In 2007, the journal was renamed Soils and Rocks and acquired the status of an international journal, being published jointly by the Brazilian Association for Soil Mechanics and Geotechnical Engineering, by the Portuguese Geotechnical Society, and until 2010 by the Brazilian Association for Engineering Geology and the Environment.

Soils and Rocks

1978,	1 (1, 2)
1979,	1 (3), 2 (1,2)
1980-1983,	3-6 (1, 2, 3)
1984,	7 (single number)
1985-1987,	8-10 (1, 2, 3)
1988-1990,	11-13 (single number)
1991-1992,	14-15 (1, 2)
1993,	16 (1, 2, 3, 4)
1994-2010,	17-33 (1, 2, 3)
2011,	34 (1, 2, 3, 4)
2012-2019,	35-42 (1, 2, 3)
2020,	43 (1, 2, 3, 4)
2021,	44 (1, 2, 3, 4)
2022,	45 (1, 2, 3, 4)
2023,	46 (1, 2, 3

ISSN 1980-9743
ISSN-e 2675-5475 CDU 624.131.1

Soils and Rocks
An International Journal of Geotechnical and Geoenvironmental Engineering
ISSN 1980-9743 ISSN-e 2675-5475

Publication of
ABMS - Brazilian Association for Soil Mechanics and Geotechnical Engineering
SPG - Portuguese Geotechnical Society
Volume 46, N. 3, July-September 2023

Table of Contents

LECTURE

Soils and Rocks

An International Journal of Geotechnical and Geoenvironmental Engineering

www.soilsandrocks.com

ISSN 1980-9743
ISSN-e 2675-5475

The 8th Victor de Mello lecture: role played by viscosity on the undrained behaviour of normally consolidated clays

Ian Schumann Marques Martins[1#]

Lecture

Keywords
Strain-rate effects
Soft clay
Creep
Stress relaxation
Stress-strain-strain-rate relationships

Abstract

Phenomena that do not obey Terzaghi's principle of effective stress (PES) are related to strain rate and time effects. This issue led the author to refer to early articles in soil mechanics, which used to consider the shear resistance of clays as a combination of two components: a frictional and a viscous one. In these articles the viscous component was assigned to the distortion of highly viscous adsorbed water layer in the contact points between grains along the plane where shearing takes place. Assuming the shear resistance of plastic soils comprises frictional and viscous resistance components, a shear stress equation can be added to the PES. It is shown that Mohr's circle of effective stress is the sum of two ellipses: the viscosity and the friction ellipses. The ordinates of the viscosity and the friction ellipses represent the viscous and the frictional components of shear resistance in different planes, respectively. This approach leads to a failure criterion considering strain rate, according to which failure takes place whenever the friction ellipse touches the strength envelope, which is the ϕ'_e sloped straight line passing through the origin, ϕ'_e being the Hvorslev's true angle of friction. By adding such shear stress equation to the PES, a model that explains strain rate and time effects is developed. Predictions of the proposed model are compared to results from tests carried out on San Francisco Bay Mud specimens.

1. Professor Victor de Mello as perceived by the author

Differently from those who have preceded the author towards the honourable task of writing the eighth Victor de Mello Lecture, he belongs to a subsequent generation, the same of his son, his friend Luiz Guilherme de Mello. Our fathers were born in the very year of 1926, with a difference of a month and a half. For this reason, he thinks his way of perceiving Professor Victor F. B. de Mello may be different and more distant from those ways posed by the previous de Mello lecturers. Such a distance should be taken as a measure of the author's respect and admiration since the time he was a student at the Polytechnic School of the Federal University of Rio de Janeiro and trainee at the Geotechnical Laboratory of COPPE/UFRJ at the end of the seventies. The author perceived Professor Victor Froilano Bachmann de Mello as a live legend, as a shining and unreachable sun of knowledge rising from the horizon…

The author has heard about his critical mind several times. In fact, the author has been introduced to his critical way of behaving even before meeting him in person. This happened when the author read the preface of the book *Soil Testing for Engineers* (Lambe, 1951), in which the acknowledgements end with: "*To Dr. Victor F. B. de Mello, a former member of the soil mechanics staff at the Massachusetts Institute of Technology, especial thanks are due for his sharp but constructive criticisms based on a careful study of the manuscript.*" (Lambe, 1951, pp. v-vi).

The practice of criticism is usually taken with reservation among Latins. Many times the Latin spirit takes criticism as a personal attack. Perhaps, for this reason, when practicing criticism, Victor de Mello may often have been misunderstood in the country he chose to live in. The biographical notes posed by Moreira & Décourt (1989) for the *de Mello Volume* suggest that, as regards Victor de Mello, who was born in a family in which education was always taken into high account, the practice of criticism used to be a natural consequence of the act of thinking, with ideas fighting against each other. Criticism as the exercise of ever trying to improve what is being criticized. Criticism in the very analytical meaning of the word. Criticism addressed to opinions and ideas, never to persons.

Perhaps this gift to criticism has even more been developed in the soul of the young man who, having left Goa, an old Portuguese province on the west coast of India, had to triumph by using merit as the main weapon within the competitive environment of the Massachusetts Institute of Technology (MIT), as Christian & Baecher (2015) suggest. If he had not imposed himself, neither would he have become

[#]Corresponding author. E-mail address: ian@coc.ufrj.br
[1]Universidade Federal do Rio de Janeiro, Departamento de Engenharia Civil, Rio de Janeiro, RJ, Brasil.

Submitted on May 18, 2023; Final Acceptance on May 18, 2023; Discussion open until November 30, 2023.

https://doi.org/10.28927/SR.2023.006123

the eventual substitute of Professor Taylor [de Mello, L.G. (2021). Personal communication.] nor would he have deserved the comment made by Moreira & Décourt (1989) in his biographical notes: "*Back at MIT his academic past had left one mark. It has been heard that Taylor often mentioned him as the best student to have gone through the department, and that for a couple of decades the challenge to the new staff was to hear from the older faculty "how de Mello would have handled the problem*" (Moreira & Décourt, 1989, p. xiii). The Italians would say: "*se non è vero è bene trovato*", because vestiges of this admiration appear at Taylor's (1955) acknowledgements in his ultimate report: "*Review of Research on Shearing Strength of Clay*". Part of the acknowledgements says: "*Especially valuable contributions were made by V.F.B. de Mello and R.H.Clough.*" (Taylor, 1955, p. 2). This happened about 6 years after Victor de Mello had left MIT on his way to Brazil, showing that Victor and Don Taylor were still connected.

The author, who was also educated within an environment in which the practice of criticism was always carried out, deeply understood that way of behaving because he apprehended its aims. An illustrative example of Victor de Mello's critical attitude appears in the outline of his potential book (de Mello, 2014), where he presented a list of items which should be reviewed. One of these items is, for instance, the void ratio (e) versus vertical effective stress (σ'_v, log scale) relationship in the one-dimensional compression, which, if represented by a straight line, leads to the mistake of obtaining a void ratio equal to zero (and even negative ones). By the way, the author (Martins, 1983; Martins & Lacerda, 1994) also discussed such subject.

Despite the author had maintained brief contacts with Professor Victor de Mello, usually during conferences and meetings' intervals, he always tried to draw closer to him to listen to the soil mechanics stories he witnessed. These stories, which were always told in a picturesque way and with a special pleasure, were usually "painted" with the colours of his vernacular palette.

Marzionna (2014), a close friend and colleague of his son Luiz Guilherme at the Polytechnic School of the University of São Paulo, managed, in the author's opinion, to capture by the adjectives *passionate*, *unresigned* and *perfectionist* the essence of the man who, even being aware that many things inside his soul were utopian, knew that dreams, although unreachable, have just one purpose in life: to keep everyone walking forward. Nevertheless, according to Burland (2008) his way of saying that was more poetical: "*Choose your love and love your choice*" (Burland, 2008, p. 116). That was what he did throughout his life.

2. Philosophical spirit of this lecture

As regards science, the soul of things is in the fundamentals. The birth of any science is in man's creative ability to observe and imagine how things work. To make science means to explain how things operate in our universe and to establish links between causes and effects, thus following the so-called scientific method. Several texts have been written about the scientific method, but none of them teaches neither how to observe nor how to proceed in order to make ideas spring out concerning a given phenomenon. Such ideas are "creation blows" and nobody knows where they come from… they are the "soul of science".

Costa (2005) quotes the following passage from Lobo Carneiro's study about Galileu's investigation method: "*his scientific investigation method consists in a suitable combination of experiment with mathematics, a deductive logical tool. Considering some experimental facts, a first hypothesis or theory is built in order to interpret them. Certain conclusions are deductively drawn from that theory; then the validity of those conclusions is submitted to experiment, which the last word always correspond to. The hypothesis should be replaced or improved if the tests do not corroborate it. The final verdict is based on the truth criterion, which is always given by the experimental results.*" (Costa, 2005, p. 139).

Philosophically speaking, the first step of that method consists in something that cannot be taught: in the observation of a phenomenon and of ideas concerning why and how that phenomenon occurs. (Where do the ideas come from and how do they spring into our thoughts?) That is a mystery, which is in the birth of all sciences. The idea becomes a working hypothesis regardless of how it has appeared. By means of sequential reasoning or deductive logic, that working hypothesis leads to forecasts regarding the studied phenomenon. If forecasts are confirmed by means of tests whose results are repeated, then the hypothesis becomes a principle, a postulate, an axiom or a law. So to speak, theories that allow predicting phenomena concerning that science are developed based on those laws. Therefore, every science is supported by a principle or a set of principles. The word *principle* is used because it means the beginning of things. As regards soil mechanics, it is not different; it is built upon the Principle of Effective Stress (Terzaghi, 1936).

Being a postulate, a principle cannot be demonstrated. After being accepted as a truth, it is strengthened every time its validity is checked by an experimental result. However, despite a principle may many times have its validity confirmed, the repeatability of experimental results indicating the principle's validity does not turn such repeatability into proof. On the contrary, just one example that does not follow a principle (called a counterexample) is enough to show the validity of that principle is restricted.

Irrespective of a principle having a chance of being of restricted validity (a common thing in science), "to make science" follows no other path than that of the idea that evolves into a working hypothesis, which, after confirming experimental results, reaches the status of a principle. Understanding, examining, reexamining and pondering about what a principle establishes is also a role of science. For this reason, it is necessary to deeply understand the statements of the established principles to correctly apply them but also to adequately check their validity.

If the process of managing to have an idea cannot be taught, perhaps to exercise thinking may be a way of opening the doors of mind to let the ideas come in. [Saramago, R.P. (2021). Personal communication.] reminded that Lobo Carneiro, the creator of the "*Brazilian Test*" (used to measure tensile strength of concrete), of whom the author is also proud of having been a pupil, used to say that, before writing any mathematical equation to describe a phenomenon, "*it is necessary to conceive a mental model explaining how and why the phenomenon occurs, no matter how rudimentary the model can be*". Another important task is to identify the variables on which the studied phenomenon depends and to identify any other already known phenomenon with which an analogy may be established, a parallel may be drawn. We must think about the subject and let ideas flow. [Santa Maria, P.E.L.(2000). Personal communication.] posed to the author the following thought about the matter: "*... so that ideas may arise from our minds, time is necessary to think about them, to appraise them…and thus brain must be "idle" and free from daily tasks, otherwise ideas shall take another way…*".

In these modern times, when lack of time predominates, the profusion of published papers leads to the reflection that much more time has been spent in writing rather than in thinking about things that would be worth writing. In short: producing papers has become more important than producing knowledge. One of the reasons for that can be found in a statement made by Lambe (1981) when he referred to one aspect of the geotechnical engineering history of MIT: "*One outstanding paper can contribute far more than five mediocre papers; unfortunately five mediocre papers can carry more weight in the [university] promotion process than one outstanding paper.*" (Lambe, 1981, p. 56).

Similarly, de Mello's thought "*We professionals beg less rapid novelties, more renewed reviewing of what is already there*" also seems to express his concern about the rapid and abundant way by which most new papers have been written, without taking into consideration a deeper analysis of the subjects. Since Taylor was the sole soil mechanics professor at MIT from the mid thirties up to 1945 (Christian & Baecher, 2015), it is not difficult to imagine how much de Mello and Lambe, both Taylor's pupils at that period, have been influenced by his careful way of thinking, rethinking and understanding the phenomena, mainly as regards the fundamental concepts. Christian & Baecher (2015) realized that part of the cause for the bad treatment dispensed to Taylor by the group led by Terzaghi was related to Taylor's way of being. The following quotation illustrates this point of view: "*Neither MIT nor his Professional colleagues treated Taylor well. The reasons are hard to grasp at this remove, but part of the problem seems to be that he often worked on problems that were supposed to have already been solved and he discovered previously unappreciated complexities. He was a careful and thorough experimentalist, a strength that lay behind many of his successes. He had actually looked at the data and understood mechanics.*" (Christian & Baecher, 2015, p. 16).

The author heard from Professor Victor F. B. de Mello that "*Fundamentals of Soil Mechanics*" could be considered one of the five major books ever written about soil mechanics. The author also shares this opinion. Christian & Baecher (2015) still went further and added: "*Fundamentals of Soil Mechanics remains today a seminal text on soil mechanics and influenced generations of geotechnical engineers. In many ways, it is as contemporary as texts written fifty years later, and it may be as influential to the modern field of soil Mechanics as the books of Terzaghi. The presentation is clear and reflects careful thought.*".

Again, the author not only agrees with the above mentioned comments but also intends to show the ideas presented herein came from Terzaghi (1936) and Terzaghi & Frölich (1936). Those ideas grew up with the special care Taylor (1942, 1948) used to carry out research: observing phenomena, creating a mechanism to explain them, translating them into a mathematical language, solving the equations assumed as representative of the phenomena and comparing their results to the experimental data obtained. Just the same path followed by Galileu.

As the name suggests, "*Fundamentals of Soil Mechanics*" was written with a focus on fundamentals. The author learned from Carneiro & Battista (1975) and studying Taylor (1948) that the soul of science is in the fundamentals. This lecture also concerns fundamentals and was written inspired by de Mello's spirit of thought: "*We professionals beg less rapid novelties, more renewed reviewing of what is already there*" (Jamiolkowski, 2012, p. 117) (or pursuant to the author's perception). That is why the number of references is not so large. After all, the task of reviewing already settled issues in a renewed way requires deeper and more intensive work rather than extensive. That is what the author tried to do.

3. The principle of effective stress (PES)

3.1 PES statement and its fundamental equation

Very usually, the PES is only presented by means of its fundamental equation. However, as the PES has a status of law, besides its fundamental equation, it has a statement that is as important as its equation. Instead of presenting the PES statement just as it was presented by Terzaghi (1936), the PES will be presented split up into two parts, as Atkinson & Bransby (1978) did. This statement "version" uses a more up-to-date terminology and makes the PES statement easier to be understood.

The first part of the PES statement defines the effective stress:

> *The stresses in any point of a section through a mass of soil can be computed from the total principal stresses*

> σ_1, σ_2 *ü* σ_3 *which act at this point. If the voids of the soil are filled with water under a stress u, the total principal stresses consist of two parts. One part u acts in the water and in the solid in every direction with equal intensity. It is called the neutral stress (or the pore pressure). The balance* $\sigma_1' = \sigma_1 - u$, $\sigma_2' = \sigma_2 - u$ *and* $\sigma_3' = \sigma_3 - u$ *represents an excess over the neutral stress u and it has its seat exclusively in the solid phase of the soil. This fraction of the total principal stress will be called the effective principal stress*. (Atkinson & Bransby, 1978, p. 21).

Hence, the fundamental effective stress equation is given by Equation 1.

$$\sigma' = \sigma - u \tag{1}$$

The second part of the PES statement gives the role played by effective stresses on the behaviour of soils:

> *All measurable effects of a change of stress, such as compression, distortion and a change of shearing resistance, are exclusively due to changes in the effective stresses*. (Atkinson & Bransby, 1978, p. 21).

3.2 Role played by effective stresses on the behaviour of soils

Considering the way the PES was stated, the second part only assures that volume change, distortion and a change of shearing resistance are effects caused by a change in the effective stress state. Nevertheless, rigorously speaking, according to the way it was stated, the second part of the PES does not ensure that changes in the effective stress state necessarily cause volume variation, distortion or change of shearing resistance. However, that is the way how soil mechanics interprets and uses the PES. Thus, as far as volume change and distortion are concerned, the second part of the PES might be summarized, without loss of its essence, in the following bidirectional mathematical sentence:

change in effective stress ↔ volume change or distortion

The above mathematical sentence is then interpreted as follows

→ the "going"

Whenever there is a change in the state of effective stress, there will be either a change of volume or distortion (or both).

The connective *or* in the right side of the PES second part sentence makes the sentence true when at least one of the two statements (volume change *or* distortion) is true and false only when both are false.

← the "converse"

Whenever there is a change of volume or distortion (it is enough that one of them occurs) or both, the change(s) was (were) caused by a change in the state of effective stress.

To illustrate the PES meaning according to classical soil mechanics, Atkinson & Bransby (1978) state the three following corollaries:

> *Corollary 1: The engineering behaviour of two soils with the same structure and mineralogy will be the same if they have the same effective stress.*
>
> *Corollary 2: If a soil is loaded or unloaded without any change of volume and without any distortion there will be no change of effective stress.*
>
> *Corollary 3: Soil will expand in volume (and weaken) or compress (and strengthen) if the pore pressure alone is raised or lowered*. (Atkinson & Bransby, 1978, pp. 21-24).

The above-mentioned corollaries are illustrations of how the PES is interpreted and used in classical soil mechanics. Nevertheless, it is possible to present counterexamples which show that these corollaries have no general validity.

As regards corollary 1, one knows that two specimens of the same soil subjected to $\overline{\text{CIU}}$ (isotropically consolidated, undrained) triaxial tests starting from the same state of effective stress, but sheared with different axial strain rates $(\dot{\varepsilon}_a = d\varepsilon_a / dt)$, show different behaviour. This effect was identified a long time ago [see, for instance, Taylor (1948)]. Such effect is illustrated in Figure 1 by $\overline{\text{CIU}}$ test results carried out by Lacerda (1976) on San Francisco Bay Mud samples.

It is possible to present counterexamples which show that the second corollary also has no general validity. In this case, it is enough to observe what happens during an undrained stress relaxation test. As far as this kind of test is concerned, the procedure is almost the same followed during a conventional $\overline{\text{CIU}}$ triaxial test. The specimen is subjected to a constant axial strain rate $(\dot{\varepsilon}_a)$ and led up to a determined deviator stress without necessarily being led to failure. Then, at a given axial strain, the load frame motor is switched off and the specimen behaviour is observed over time. It is the so-called stress relaxation test (or stage).

Provided the soil is saturated, there will be no volume change in a $\overline{\text{CIU}}$ triaxial test during the shearing phase but only distortion. When the load frame motor is switched off, there will be no variation of distortion at all. However, even with no change in volume and distortion, there is a substantial variation of the effective stress state (see Figure 2).

Finally, it is possible to present counterexamples showing that the third corollary does not have general validity. Suppose that a soil specimen has been isotropically consolidated to some stress in the normally consolidated range. If after dissipation of the excess pore pressure drainage is closed and the total stress is kept constant, it is observed that pore pressure increases over time (Figure 3). According to corollary 3, if a soil specimen is kept under a constant isotropic state of total stress and pore pressure increases over time, the effective stress decrease should make the specimen to expand, but this cannot occur since drainage is closed.

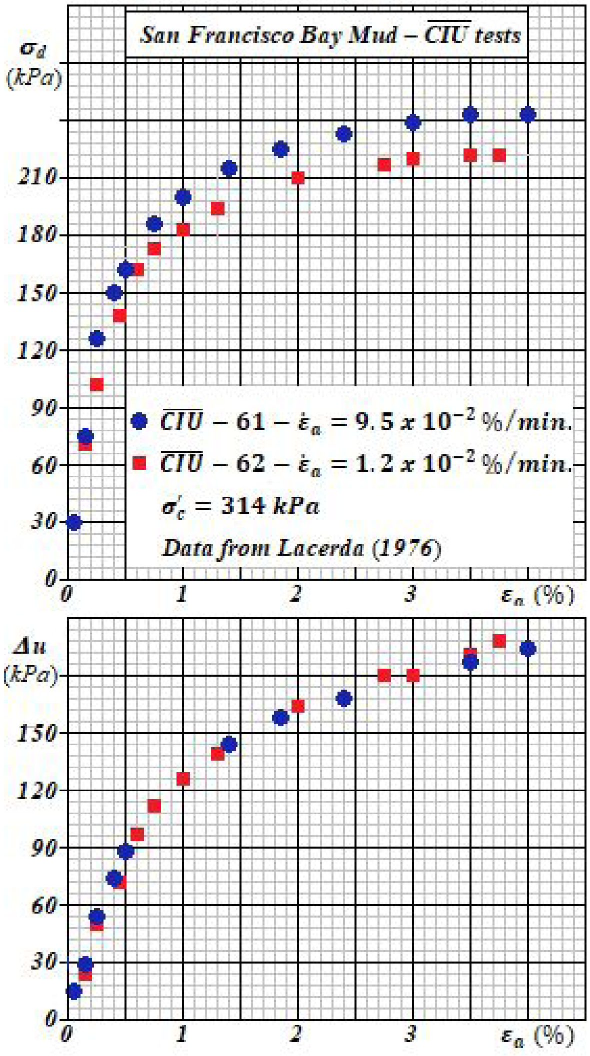

Figure 1. Example of strain rate effect on consolidated-undrained tests [after Lacerda (1976)].

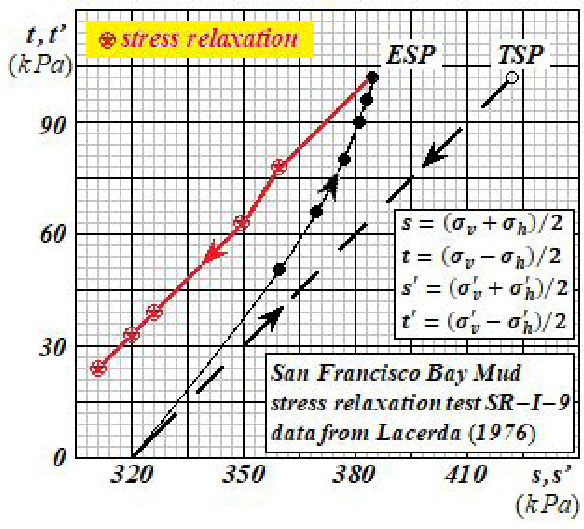

Figure 2. Example of effective stress path (ESP) and total stress path (TSP) during stress relaxation [after Lacerda (1976)].

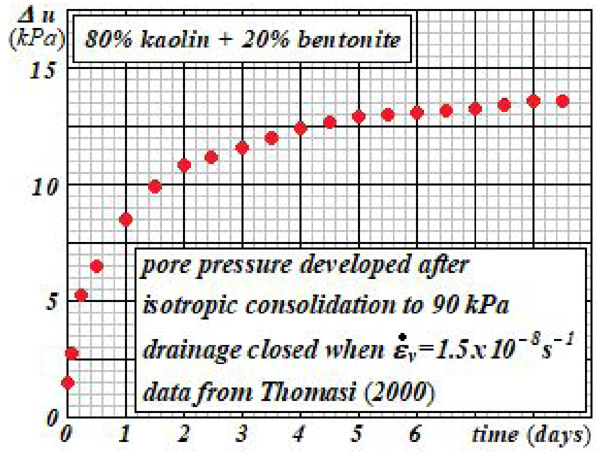

Figure 3. Pore pressure increase after closing drainage after isotropic consolidation (Thomasi, 2000).

The counterexamples relating to the three aforementioned corollaries serve to raise important issues regarding the PES validity. After the advent of critical state soil mechanics, a relevant evolution towards theoretical soil mechanics approach took place, mainly as regards the introduction of plasticity theory concepts. As far as the above-mentioned counterexamples are concerned, time and strain rate effects are present in all of them. Thus, it is natural the attempt to create behavioural models into which concepts that deal with such effects may be introduced. Nevertheless, in view of the theoretical difficulties to deal with phenomena such as creep, stress relaxation and secondary consolidation, the usual approach is to preserve the PES essence and develop tools to tackle one of these specific phenomena, considering each one out of the PES validity domain. A typical example of such an approach is the assumption $C_\alpha / C_c =$constant (Mesri & Godlewski, 1977) to handle secondary consolidation.

Computer-aided numerical analyses have made sophisticated stress-strain-strength models feasible. However, those approaches often become so tricky that the feeling of the physical phenomenon sometimes is lost in the midst of the mathematical approach.

As the main purpose of this paper is to study the causes and effects of strain rate on the undrained behaviour of clays, the focus will be on fundamentals. Thus, one will only study here saturated isotropic normally consolidated clays, without cementation among grains, subjected to undrained axi-symmetric stress states, similar to those found in $\overline{\text{CIU}}$ triaxial tests.

This paper follows a different approach from those usually found. The original PES is extended so that phenomena which escape from its validity domain, such as strain rate effects, undrained creep and stress relaxation, may naturally result from the extended PES version. Concepts that allow such PES extension are already presented in classic texts. Many of these concepts can be found in Terzaghi & Frölich (1936), Terzaghi (1941), Taylor (1942), Taylor (1948), Hvorslev (1960), Bjerrum (1973) and Leroueil et al. (1985), once more illustrating de Mello's thought: "*We professionals beg less rapid novelties, more renewed reviewing of what is already there.*" (Jamiolkowski, 2012, p. 117).

3.3 Strain rate effects on the undrained strength of clays – a brief discussion

The expression *strain rate effects* as used in this article means the effects of speed of shear as defined by Taylor (1948, p. 377). In his own words: "*...all plastic materials exhibit a resistance to shearing strain that varies with the speed at which the shearing strain occurs. The plastic structural resistance to distortion in clays, called herein the plastic resistance, is an example.*".

From now on the acronym $\overline{\text{CIUCL}}$ (consolidated isotropically undrained compression loading) will be used to denote $\overline{\text{CIU}}$ triaxial tests carried out keeping the radial stress σ_r constant and increasing the axial stress σ_a. This is to say that during the undrained shear stage of a $\overline{\text{CIUCL}}$ test, $\aleph_r = {}_2 = {}_3$ and $\sigma_a = \sigma_1$.

The shear strain rate can be defined by Equation 2

$$\dot{\gamma} = d\gamma / dt = d\left(\varepsilon_a - \varepsilon_r\right) / dt \tag{2}$$

where γ is the distortion $\left(\gamma = \varepsilon_a - \varepsilon_r\right)$ and ε_a and ε_r are respectively the axial and radial strains. During the shear stage of a $\overline{\text{CIUCL}}$ test, $\varepsilon_r = \varepsilon_2 = \varepsilon_3$ and $\varepsilon_a = \varepsilon_1$, causing distortions to occur except for horizontal planes.

When ε_a and ε_r are small, volumetric strain $\left(\varepsilon_v\right)$ can be written as $\varepsilon_v = \varepsilon_a + 2\varepsilon_r$. During the shear stage of a $\overline{\text{CIUCL}}$ test $\varepsilon_v = 0$ and $\gamma = \varepsilon_a - \varepsilon_r$. Therefore, $\varepsilon_r = -\varepsilon_a / 2$, $\gamma = {}^3\!/_2\, \varepsilon_a$ and $\dot{\gamma} = {}^3\!/_2\, \dot{\varepsilon}_a$. Thus, $\dot{\gamma}$ can be written as shown in Equation 3.

$$\dot{\gamma} = d\gamma / dt = d\left(\varepsilon_{\ddot{u}} - \varepsilon\ \right) / dt = {}^3\!/_2\, \dot{\varepsilon} \tag{3}$$

According to Equation 3, the shear strain rate $\left(\dot{\gamma}\right)$ effects on $\overline{\text{CIUCL}}$ test results can also be studied by observing axial strain rate $\left(\dot{\varepsilon}_a\right)$ effects. One of these effects is the dependency of the undrained shear strength of clays on the axial strain rate $\left(\dot{\varepsilon}_a\right)$.

In this article the undrained shear strength $\left(S_u\right)$ is defined by

$$S_u = \frac{\left(\sigma'_{af} - \sigma'_{rf}\right)}{2} \tag{4}$$

where σ'_{af} and σ'_{rf} are respectively the axial and radial effective stresses at failure (condition indicated by the use of the subscript *f*).

The strain rate effect on the undrained strength of clays may be illustrated by the results of a $\overline{\text{CIUCL}}$ test carried out in a normally consolidated specimen of Sarapuí II Clay [for a detailed description of this clay, see Danziger et al. (2019)]. Such a test has been carried out using an intact sample and lubricated ends technique so that the specimen could be led to a high axial strain, maintaining the cylindrical format. Different axial strain rates $\left(\dot{\varepsilon}_a\right)$ have been imposed to the specimen during the test. Photos of such specimen taken at the end of the test $\left(\varepsilon_a = 17\%\right)$ are shown in Figure 4.

Figure 5 shows the $\left(\sigma'_a - \sigma'_r\right) / 2 \times \varepsilon_a$ plot for the $\overline{\text{CIUCL}}$ test carried out on the specimen shown in Figure 4. Initially, the specimen was sheared with the strain rate $\dot{\varepsilon}_a = 0.02\ \% / \text{min.}$ up to $\varepsilon_a \cong 10\%$, when failure occurred with Similarly to what has been done for stresses, Equations $S_u \cong 68.5\,\text{kPa}$. Then, the strain rate was increased to 0.2% / min. causing S_u to increase to 76.0 kPa. The strain rate was then reduced to 0.002% / min. obtaining $S_u \cong 62.0$ kPa. Finally, the strain rate was reduced to 0.0002% / min., showing $S_u \cong 56.5\,\text{kPa}$. The deviator stress drops observed in Figure 5 are due to the stress relaxation stages carried out before the strain rate was changed.

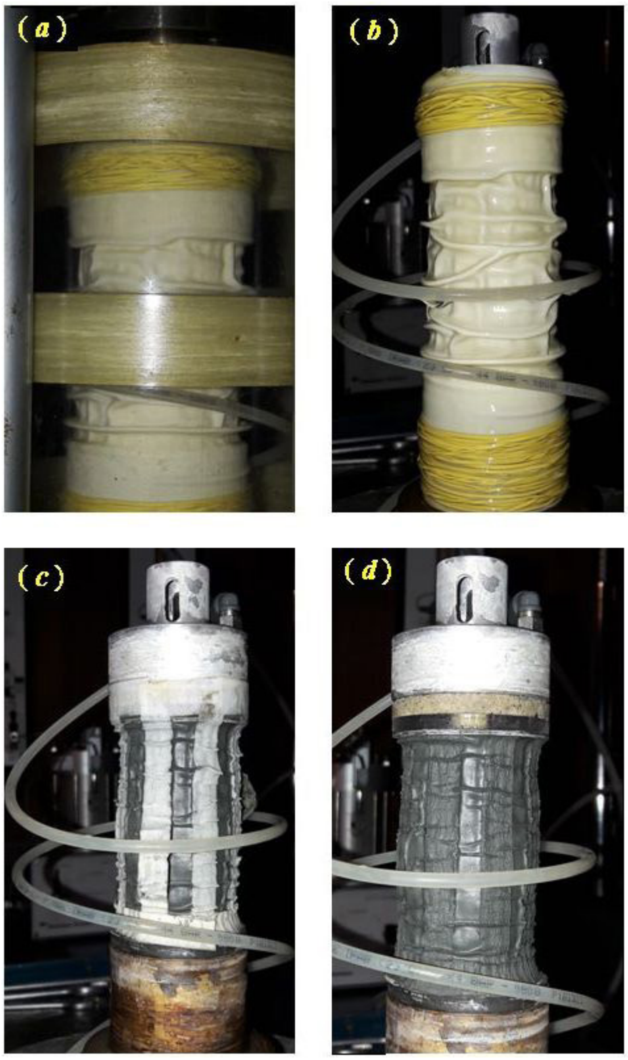

Figure 4. Sarapuí II Clay specimen after a $\overline{\text{CIUCL}}$ test with lubricated ends: (a) Inside the triaxial chamber $\left(\varepsilon_a = 17\%\right)$; (b) Outside the triaxial chamber with the rubber membrane; (c) Without the rubber membrane and with the lateral filter paper; (d) Without the filter paper.

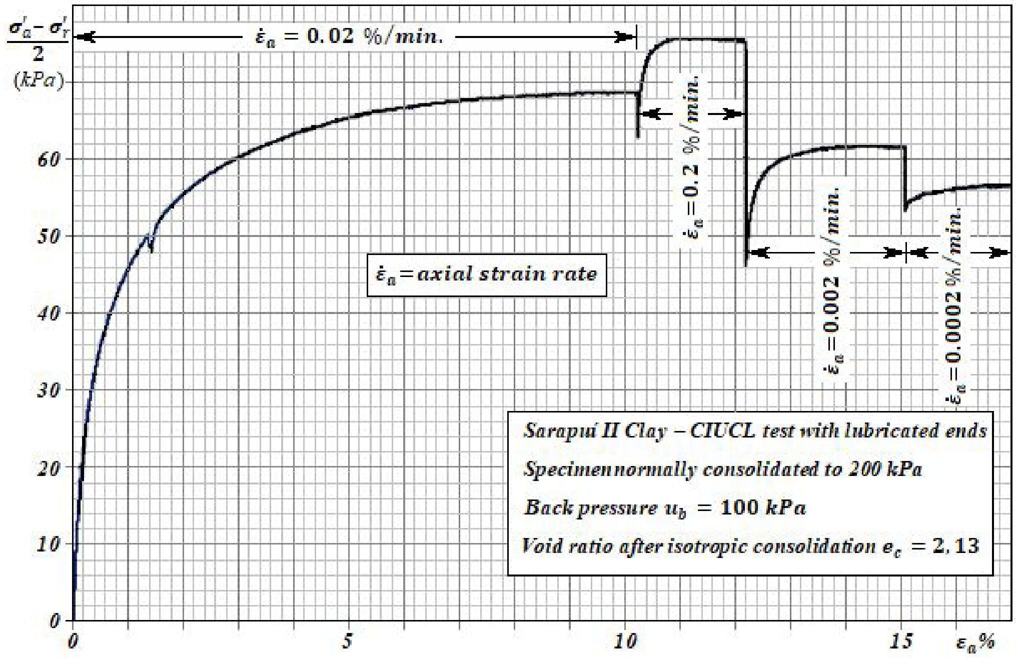

Figure 5. Strain rate effect on the undrained strength of Sarapuí II Clay.

An attempt to estimate the undrained shear strength (S_u) as a function of strain rate is given by Equation 5 [see, for example, Schnaid et al. (2021)].

$$S_u = S_{u,ref}\left[1 + \mu \log \frac{\dot{\gamma}}{\dot{\gamma}_{ref}}\right] \tag{5}$$

where $\dot{\gamma}_{ref}$ is a reference distortion rate, taken as 1%/hour or 0.017%/min. As in a $\overline{\text{CIUCL}}$ test $\dot{\gamma} = \frac{3}{2}\dot{\varepsilon}_a$ (see Equation 3), Equation 5 can be rewritten as:

$$S_u = S_{u,ref}\left[1 + \mu \log \frac{\dot{\varepsilon}_a}{\dot{\varepsilon}_{aref}}\right] \tag{6}$$

being $\dot{\varepsilon}_{aref} = \frac{2}{3}\dot{\gamma}_{ref} \cong 0.01\ \%/\text{min}$.

Figure 6 presents S_u values as a function of $\dot{\varepsilon}_a$ from the test results shown in Figure 5. Using Equation 6 and $S_{u,ref} = 66.5\,\text{kPa}$, corresponding to $\dot{\varepsilon}_{aref} = 0.01\%/\text{min.}$, a $\mu \cong 0.10$ is obtained. The fitted curve is also shown in Figure 6.

Figures similar to Figure 6 were firstly presented by Taylor (1948, p. 378) and afterwards by several authors [as for instance Berre & Bjerrum (1973) and Sheahan et al. (1996)]. Although Equations 5 and 6 provide good fitting curves, one can observe that, in general, the curve $S_u \times \dot{\varepsilon}_a\ (\log scale)$ shows an upward concavity, thereby suggesting that S_u might have a lower bound as $\dot{\varepsilon}_a$ approaches 0.

The dependence of S_u on $\dot{\varepsilon}_a$ leads to the idea of multiple state boundary surfaces, each one corresponding to a given $\dot{\varepsilon}_a$ value. This would mean that for clayey soils the critical state line (CSL) is dependent on $\dot{\varepsilon}_a$. Therefore, the CSL could

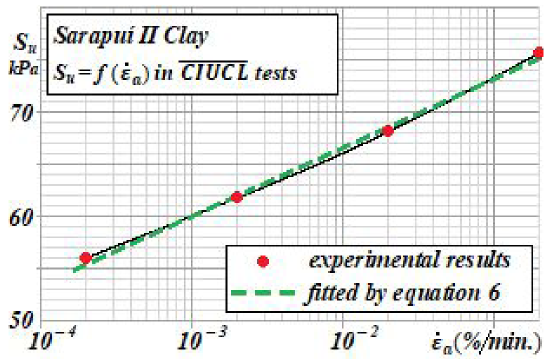

Figure 6. Values of S_u as a function of $\dot{\varepsilon}_a$ for Sarapuí II Clay measured in a $\overline{\text{CIUCL}}$ test.

not be considered a clay property. This idea was qualitatively presented by Leroueil et al. cited by Jamiolkowski et al. (1991) and is reproduced in Figure 7.

As concerns the existence of multiple state boundary surfaces, Figure 7 would also indicate the dependence of the virgin oedometric compression line on the axial strain rate $(\dot{\varepsilon}_a)$. This would be in full accordance with the results of Leroueil et al. (1985), showing that in one-dimensional compression there is a unique relationship between effective vertical stress (σ'_v), vertical strain (ε_a) and axial (vertical) strain rate $(\dot{\varepsilon}_a)$. The following natural question would be what is to happen in this case to the coefficient of earth pressure at rest (K_0). This question, raised by Schmertmann (1983) and discussed by several

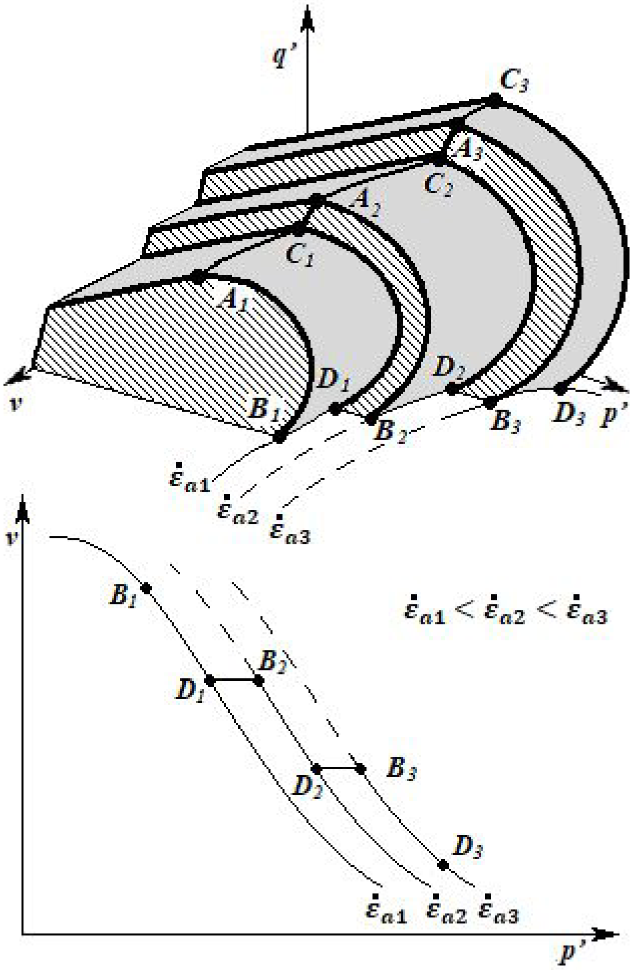

Figure 7. Influence of strain rate $\left(\dot{\varepsilon}_a\right)$ on state boundary surface [adapted from Leroueil et al. cited by Jamiolkowski et al. (1991)].

authors (Lacerda, 1977; Kavazanjian Junior & Mitchell, 1984; Holtz & Jamiolkowski, 1985; Lacerda & Martins, 1985; Leonards, 1985; Kavazanjian Junior & Mitchell, 1985; Mesri & Castro, 1987, 1989), has also remained without a final verdict up to now. Nevertheless, this is a discussion that is beyond the scope of this paper.

According to Bjerrum (1973), who refers to the strain rate effect on the shear strength of clays as "effect of time" (the shorter the time to failure, the greater the strain rate), the referred effect aroused interest from Terzaghi, who discussed it in deep detail in a paper from 1931. According to Bjerrum (1973), the mentioned paper would led Hvorslev to include in his test program the "effect of time" on shear strength of Little Belt plastic remoulded clay.

Henceforth, instead of using the expression "effect of time", it will be used the expression "strain rate effects" since it is an expression which better translates the mechanics of the phenomenon. According to Bjerrum (1973), who was one of the authors that have most deeply studied strain rate effects on the shear strength of clays, there are many evidences which show that strain rate effects are associated with the cohesive component of shear strength, as defined by Hvorslev (1960). Notwithstanding, as discussed by Schofield (1999, 2001) and assumed in critical state soil mechanics, soils do not possess cohesion in the sense used by Coulomb, or rather, they do not resist to effective tensile stresses. How can this impasse be solved? After all, what is cohesion? Do soils have or do not have cohesion? That is what will be discussed in the next section.

4. What is cohesion?

4.1 On the true (Coulomb) cohesion and how the materials fail

> *When I use a word, Humpty Dumpty said in a rather scornful tone, it means just what I choose it to mean – neither more nor less. The question is, said Alice, whether you can make words mean so many different things* (*Lewis Carroll, Through The Looking Glass*).

This seems to be the case of the word cohesion, which in soil mechanics has assumed different meanings, thereby bringing about a lot of confusion [see, for instance, Schofield (1999)]. In order to discuss this subject, it will be necessary to make a brief review of the Mohr failure criterion.

Mohr's failure criterion, for a given material, can be stated as follows: there is a shear stress τ expressed as a function f of the normal stress σ with the following property: if a couple $\left(\sigma,\tau\right)$ which satisfies the function $\tau = f\left(\sigma\right)$ is acting on a plane passing through a point ***P*** of the material, then there will be failure at that point ***P*** along the referred plane.

One of the functions used to express the failure criterion in rocks and natural materials is the so-called Mohr-Coulomb envelope, gathering Mohr criterion and Coulomb law. The Mohr-Coulomb envelope can be written as:

$$\tau_{ff} = c' + \sigma'_{ff}.tan\phi' \qquad (7)$$

where τ_{ff} and σ'_{ff} are respectively the shear stress and the normal effective stress on the failure plane at failure, ϕ' is the *angle of internal friction* and c' is the *cohesion*. Plotting Equation 7, taking into account just the positive values of τ_{ff}, Figure 8 is obtained.

Solid materials such as concrete and rocks have a strength which cannot be assigned to any applied stress state which can be perceived by human eyes. This kind of strength can be described as a consequence of an "*imaginary pressure*", called "*intrinsic pressure*" (Taylor, 1948), denoted by σ_i', which remains from the formation of those materials and which awards a certain tensile strength to those materials. This "*intrinsic pressure*" corresponds to the segment $\overline{\boldsymbol{O'O_P}}$ in Figure 8. This occurs, for example, in the case of an igneous rock that, after being formed by magma cooling, presents this type of strength. Similar thing happens in the formation of a sedimentary rock, when a cementation agent by means of a process called diagenesis gradually links grains of a sedimentary soil. A similar phenomenon happens as regards concrete, when cement connects the aggregates. Cementation makes such materials present a tensile strength (σ_t') when subjected to tensile effective stresses. This type of strength can be quantified by segment $\overline{\boldsymbol{OpC}} = \sigma_i' \ tan\phi'$, as shown in Figure 8. Such strength is denoted by c' and defined as *true cohesion* or *Coulomb cohesion*.

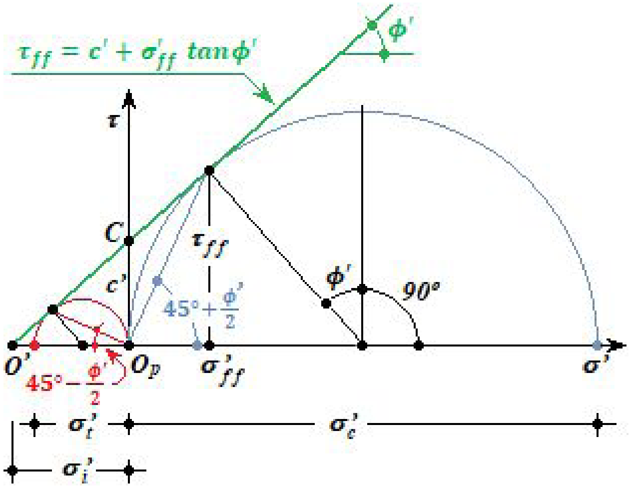

Figure 8. Mohr-Coulomb envelope for soils and rocks.

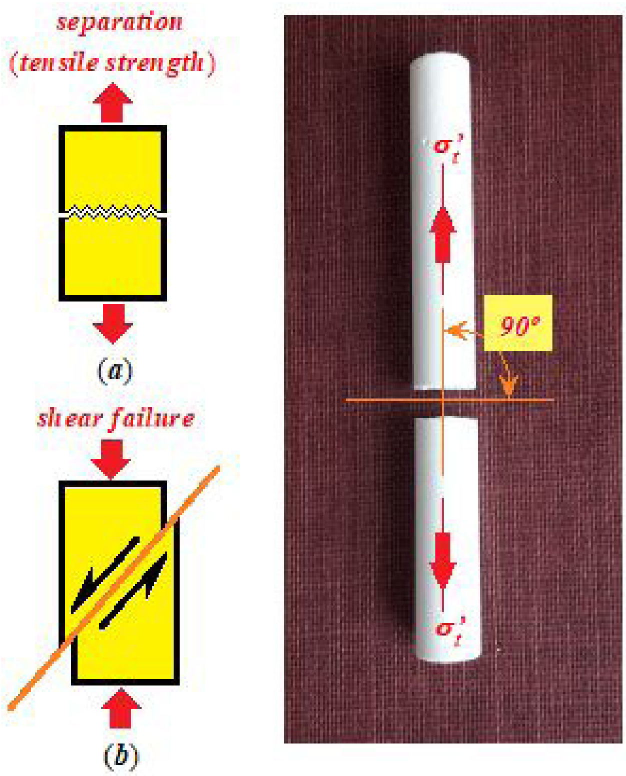

Figure 9. Failure modes: (a) By separation in a tensile test (see the piece of chalk after failure by separation at the right side of Figure 9); (b) By shear during an unconfined compression test.

An alternative way of writing the envelope in Figure 8 would be to introduce the "*intrinsic pressure*", denoted by σ_i', shifting the origin of the graph in Figure 8 to point ***O'***. Thus,

$$\tau_{ff} = c' + \sigma_{ff}' \ tan\phi' = \left(\sigma_i' + \sigma_{ff}'\right) \ tan\phi' \tag{8}$$

According to Figure 8, being $\boldsymbol{O_p}$ the pole of Mohr circles at failure under unconfined compression and simple tension tests, the angles of failure planes in compression and in simple tension would be $45° + \phi'/2$ and $45° - \phi'/2$ respectively (see Figure 8). Nevertheless, in a homogeneous and isotropic material subjected to a simple tension test, failure planes occur orthogonally to the tensile stress direction, as shown in Figure 9. It is the failure by separation. So, there are two failure modes: by shear and by separation [Carneiro, F.L.L.B.(2021). Private communication].

As in the separation failure mode the failure plane is orthogonal to the tensile stress direction, the strength envelope must necessarily be a vertical tangent to the Mohr circle at failure under simple tension at its leftmost point, or rather, at the point of abscissae σ_t', on the left side of the effective stresses axis, as shown in Figure 10a. This kind of strength envelope is illustrated in Figure 10b for a residual soil. In this case, the true cohesion given by *c'* in Figure 10b can be assigned to grain cementation remaining from the mother rock, which have not yet been destroyed by the weathering process in its inexorable march of transforming rocks into soils. A way of evaluating *c'* of a residual soil was used by Rodriguez (2005) carrying out a drained Brazilian Test on a submerged specimen, as shown in Figure 10c.

One can say that weathering, a process by means of which rocks are transformed into residual soils, occurs due to loss of true cohesion (grain cementation) existing in the mother rock. Concerning the inverse process, called diagenesis, in which sedimentary soils suffer a litification process and have their grains cemented, there is a gain in true cohesion. This process is illustrated in Figure 11. The assumption that during weathering/litification the strength envelope suffers a displacement keeping the friction angle ϕ' constant and reducing/increasing the true cohesion is admittedly an oversimplification to better explain the phenomenon.

4.2 Hvorslev's "true cohesion", cohesive soils, plasticity and viscosity

Figure 12 gathers figures from Terzaghi (1938) and Gibson (1953), summing up the results obtained by Hvorslev (1960) as regards a set of drained direct shear tests carried out on saturated remoulded clay specimens.

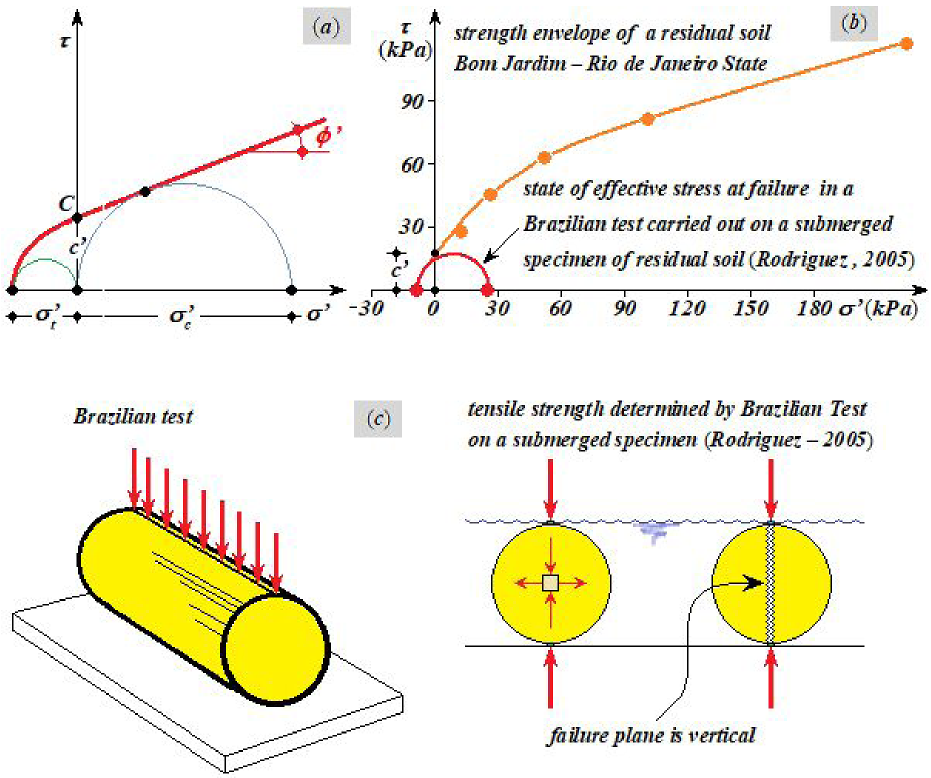

Figura 10. (a) Curved strength envelope showing true cohesion c'; (b) Strength envelope of a residual soil showing true cohesion c' [adapted from Rodriguez (2005)]; (c) Sketch of a Brazilian test carried out on a submerged specimen of residual soil.

In Figure 12, $\boldsymbol{A_0B_0C_0D_0}$ represents the virgin one-dimensional (oedometric) compression line followed by a rebound $\boldsymbol{D_0E_0F_0G_0H_0I_0}$. When the normally consolidated specimens represented by $\boldsymbol{A_0}$, $\boldsymbol{B_0}$, $\boldsymbol{C_0}$ and $\boldsymbol{D_0}$ are subjected to a drained direct shear test, they decrease in volume during shear and fail respectively with the void ratios of points $\boldsymbol{A}$, $\boldsymbol{B}$, $\boldsymbol{C}$ and $\boldsymbol{D}$. At the lower part of Figure 12, it is shown the strength envelope ***OABCD***, corresponding to the normally consolidated condition: a straight line with slope $tan\,\phi'$ passing through the origin. This means that, under the normally consolidated condition, the clay does not have true cohesion in the physical sense given by Coulomb, or rather, it does not have shear strength under effective stress minor than or equal to zero or tensile strength conferred by cementation, as discussed in section 4.1.

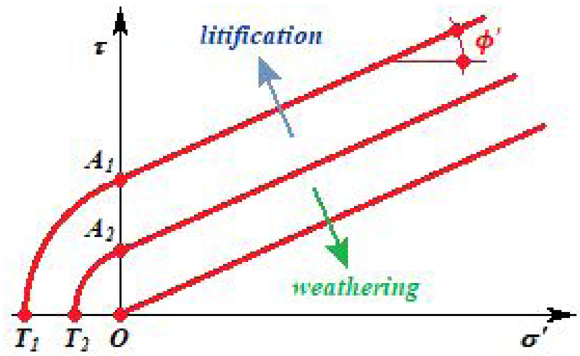

Figure 11. Weathering/litification as a loss/gain in true cohesion of rocks/soils.

When testing the specimens represented by $\boldsymbol{D_0}$, $\boldsymbol{E_0}$, $\boldsymbol{F_0}$, $\boldsymbol{G_0}$ and $\boldsymbol{H_0}$, the last four ones being overconsolidated, the void ratios at failure are given by $\boldsymbol{D}$, $\boldsymbol{E}$, $\boldsymbol{F}$, $\boldsymbol{G}$ and $\boldsymbol{H}$. In the lower part of Figure 12 it is shown the corresponding overconsolidated strength envelope ***DEFGH***. The strength envelope ***DEFGH*** depends upon two variables: the normal effective stress on the failure plane at failure σ'_{ff} (which is equal to σ'_v in a drained direct shear test) and the void ratio at failure. However, Hvorslev (1937) observed that a straight line strength envelope of equation $\tau_{ff} = c_e\left(e\right) + \sigma'_{ff}\,tan\,\phi'_e$ could be drawn provided the specimens had the same void ratio at failure. Hvorslev (1937) also noted that the linear coefficient c_e of these straight lines was a function of the void ratio at failure and that the slope ü ϕ'_e was a constant. One of these straight lines, as shown at the lower part of Figure 12, is the line ***XHB***, whose τ_{ff} axis intercept is $c_e\left(e_1\right)$, associated with the void ratio e_1 at failure. All points of straight line ***XHB*** have the same void ratio at failure equal to e_1. Another straight line, which represents failure of specimens with void ratios at failure equal to e_2, is the straight line ***YFC***, whose τ_{ff} axis intercept is $\boldsymbol{OY} = c_e\left(e_2\right)$. Thus, it is possible to express the shear strength of a clay as:

$$\tau_{ff} = c_e\left(e\right) + \sigma'_{ff}\,tan\,\phi'_e \tag{9}$$

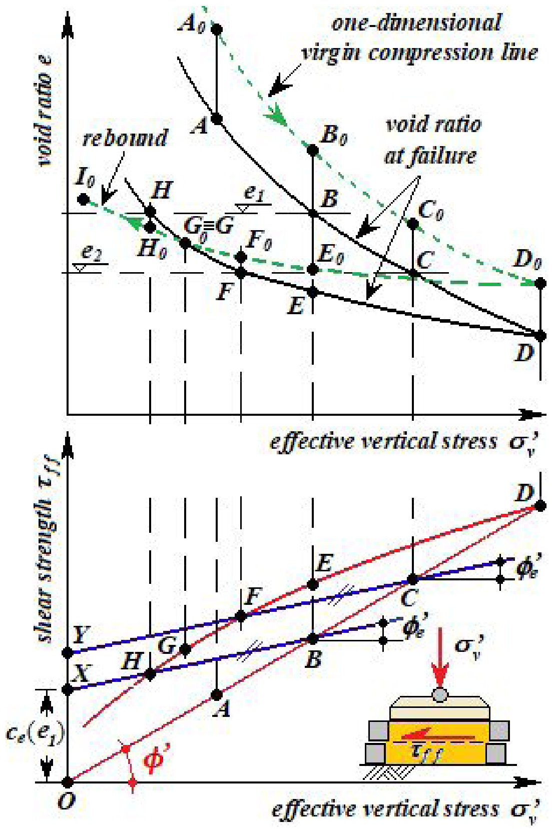

Figure 12. Determination of c_e and ϕ_e' from drained direct shear tests.

In Equation 9, τ_{ff} is the shear stress on the failure plane at failure, c_e is denominated "*effective cohesion*" or "*true cohesion*", a function of the void ratio and soil structure at failure, σ'_{ff} is the effective normal stress on the failure plane at failure, and ϕ_e' is called "*effective angle of internal friction*" or "*true angle of internal friction*".

If the clay is saturated, $e = G \cdot w$, being e the void ratio, G the specific gravity and w the water content. As $G = \text{constant}$ for a given soil, there is a one-to-one correspondence between void ratio and water content. Thus, the parameter c_e can be expressed as a function of either the void ratio or the water content, provided that both correspond to the failure condition.

In order that Equation 9 can be dimensionally homogeneous, $c_e(e)$ must have the physical dimension of a stress. To write $c_e(e)$ expressing it as a stress [see Terzaghi (1938)], the equivalent stress σ_e' has been used. As for direct shear tests, σ_e' is defined as the effective vertical stress, taken on the one-dimensional (oedometric) virgin compression line (see Figure 13), corresponding to the void ratio at failure.

Tests carried out by Hvorslev (1937) on remoulded saturated clay specimens showed that $c_e(e)$ was a linear function of the equivalent stress σ_e' corresponding to the void ratio of the specimen at failure. Thus, $c_e(e)$ can be written as:

$$c_e(e) = K\,\sigma_e' \tag{10}$$

where K is a non-dimensional constant.

Then, the shear strength of a saturated clay would be given by

$$\tau_{ff} = K.\sigma_e' + \sigma'_{ff}\tan\phi_e' \tag{11}$$

Dividing both members of Equation 11 by σ_e', Equation 12 is obtained

$$\tau_{ff} / \sigma_e' = K + \left(\sigma'_{ff} / \sigma_e'\right)\tan\phi_e' \tag{12}$$

According to Terzaghi (1938), if the results of direct shear tests are plotted in a $\left(\sigma'_{ff} / \sigma_e'\right) \times \left(\tau_{ff} / \sigma_e'\right)$ graph, the straight line shown in Figure 14 will be obtained.

As previously told, Terzaghi (1938) and Hvorslev (1937, 1960) called the product $K\,\sigma_e' = c_e(e)$ as "*cohesion*", "*true*

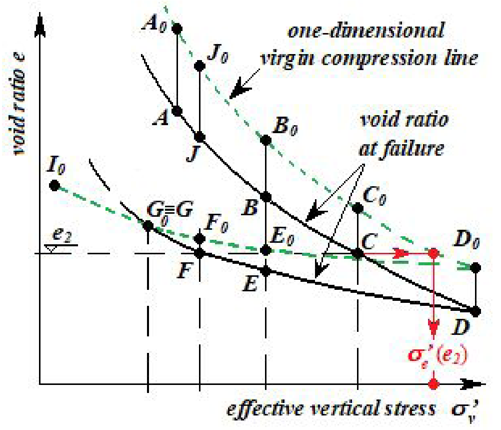

Figure 13. Definition of the equivalent stress σ_e'.

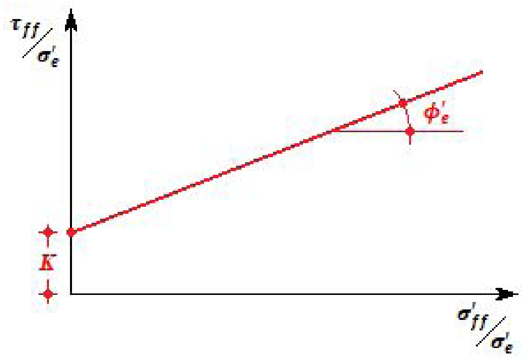

Figure 14. Relationship between normalized shear stress on failure plane at failure $\left(\tau_{ff} / \sigma_e'\right)$ and effective stress on failure plane at failure $\left(\sigma'_{ff} / \sigma_e'\right)$.

cohesion" or "*effective cohesion*" and the product $\sigma'_{ff}\ tan\,\phi'_e$ as "*effective friction component*". Considering what has been discussed, the following question arises: if the clays studied by Hvorslev were remoulded, there would not be cementation among the grains and, therefore, according to the true cohesion concept established by Coulomb [see Schofield (1999, 2001)], as discussed in section 4.1, none of the three terms (cohesion, true cohesion and effective cohesion) would be adequate in this case. Then, what would be the physical meaning of the term $c_e\left(e\right)$ in Equation 9? This is the major discussion posed in this section.

Going ahead on the discussion, all the points on the straight line segment ***HB*** in Figure 12 have the same void ratio e_1 at failure. Therefore, in a $\tau_{ff} \times \sigma'_v$ plot, points ***H*** and ***B*** define a straight line envelope, with slope ü ϕ'_e, for which the Hvorslev "*true cohesion*" is constant and has magnitude equal to ***OX***. Then, along the envelope ***XHB*** there is only variation of the friction component $\sigma'_v\ tan\,\phi'_e$. In a similar way, the points on the straight line segment ***FC*** in Figure 12 have void ratio at failure equal to e_2 $\left(\text{with } e_2 < e_1\right)$. Thus, points ***F*** and ***C*** define another strength envelope, with the same slope $tan\,\phi'_e$, but with a Hvorslev "*true cohesion*" of magnitude ***OY***.

Now, it is worth comparing a strength envelope of the type obtained by Hvorslev (1937) for an overconsolidated clay with the envelope obtained from normally consolidated specimens of the same clay. This is presented in Figure 15.

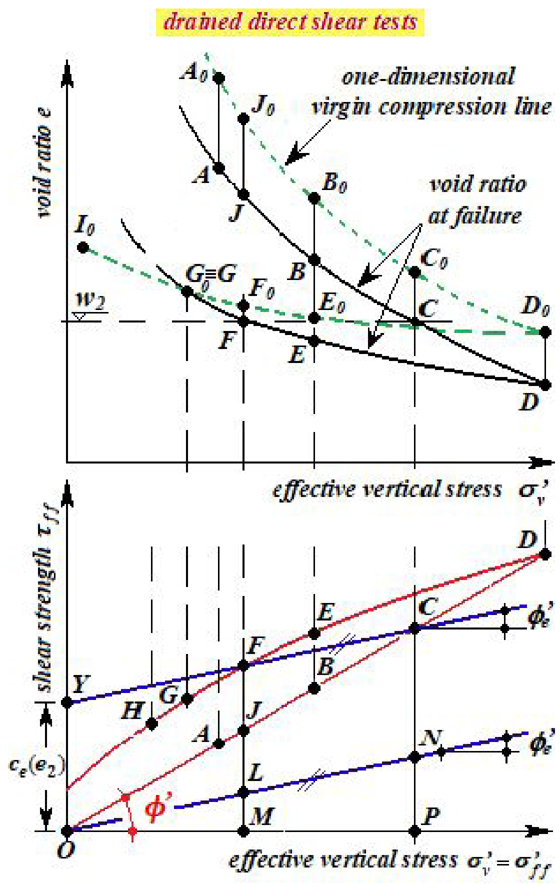

Figure 15. Comparison between Hvorslev (1937) strength envelope for an overconsolidated clay and Mohr-Coulomb strength envelope for the same clay in the normally consolidated condition.

The straight line ***OAJBCD***, at the lower part of Figure 15, is the strength envelope corresponding to the normally consolidated condition, where the shear stress at failure $\tau_{ff} = \sigma'_{ff}\ tan\,\phi'$. On the other hand, the same strength envelope can be written as $\tau_{ff} = c_e\left(e\right) + \sigma'_{ff}\ tan\,\phi'_e$. However, in this case, $c_e\left(e\right)$ varies along the envelope ***OAJBCD*** because the void ratio also varies. The difference between the ordinates of the straight lines ***OAJBCD*** and ***OLN*** is a linear function of σ'_{ff} (or σ'_v), that is:

$$c_e\left(e\right) = \sigma'_{ff}\ \ tan\phi' - \sigma'_{ff}\ \ tan\phi'_e = C.\sigma'_{ff} \tag{13}$$

where C is a constant. This means that the shear strength τ_{ff} of a normally consolidated clay can be written as:

$$\begin{aligned}\tau_{ff} &= \sigma'_{ff}\ tan\,\phi' = c_e\left(e\right) + \sigma'_{ff}\ tan\,\phi'_e = \\ &C.\sigma'_{ff} + \sigma'_{ff}\ tan\,\phi'_e\end{aligned} \tag{14}$$

Dividing Equation 14 by σ'_{ff}, Equation 15 is obtained:

$$tan\,\phi' = C + tan\,\phi'_e \tag{15}$$

Equation 15 reveals that the friction angle ϕ' of a normally consolidated clay is "contamined" by a portion C. In other words, within the shear strength of a normally consolidated clay, which does not have cohesion in the physical sense used by Coulomb, there is a portion C which is not due to friction. Shearing of a normally consolidated clay produces decrease in volume. Being so, C cannot be assigned to the work done to dilate the specimen since, being normally consolidated, the specimen presents a contractile behaviour. Then, once more, a question is asked: which physical phenomenon does the portion $c_e\left(e\right) = C\,\sigma'_{ff}$ come from, since it cannot be attributed neither to cohesion (cementation), as conceived by Coulomb, nor to additional dilating work? After all, what does exist behind the "*effective cohesion*" as inappropriately defined by Hvorslev and Terzaghi? This is the discussion that follows.

What the author believes that exists behind Hvorslev's (1937) "*effective cohesion*" is the "softness" sensation when one rubs between the fingers an amount of clay with a water content between the liquid limit and the plastic limit. It is also the sensation of something "sticky" which is found in clays, because of its *plasticity*. Possibly, owing to such sensation, clays have begun to be improperly called "*cohesive soils*".

According to the author's understanding, the expression "*cohesive soil*" leads to plastic soils. As regards soil mechanics, plastic soils are those soils that present liquid and plastic limits. After all, where does the "sticky" sensation come from when a moist clayey soil is rubbed between the fingers?

A mechanistic picture given by Terzaghi (1941) throws some light on this question.

According to Terzaghi (1941), clay particles are surrounded by an adsorbed water layer. On the clay particles surface, adsorbed water is in the solid state and is strongly adhered to it. As the distance from the particle surface increases, the adsorbed water viscosity decreases. For distances greater than a limiting value, viscous water becomes free water. This means that in a clay the interactions among grains are influenced by the adsorbed water layer that involves them. Since the viscosity of the adsorbed water decreases as the distance from the particle surface increases, it is expected that in a saturated clay the greater the water content (or the void ratio) the smaller the relative displacement resistance between neighbouring particles. In this case, "*true cohesion*" or "*effective cohesion*" to which Hvorslev (1937, 1960) and Terzaghi (1938) refer should be called *viscous resistance*, as explicitly written in a passage by Terzaghi & Frölich (1936). To avoid loss of fidelity, this passage is transcribed below:

> "*Les résultats des expériences entreprises pour trouver la relation entre l'indice des vides et le coefficient de perméabilité des argiles, imposaient déjà il y a quelques années, l'hipothése que chaque particule d'argile est séparée de l'eau interstitielle par une couche séparatrice dont la constitution diffère de celle de l'eau ordinaire. L'épaisseur de cette couche est une fraction d'un micron (1/1000 mm).*
> *A l'intérieur de cette couche séparatrice, la viscosité de l'eau tombe d'une valeur élevée (surface de la particule solide) à sa valeur normale (surface extérieure de la couche séparatrice).*
> *Les avis relatifs aux forces attractives qui provoquent la couche séparatrice sont trés partagés.*
> *La* Figure 7 *représente trois coupes à travers deux particules voisines. A l'intérieur de la zone hachurée, la viscosité augmente beaucoup à mesure que l'on s'approche de la surface solide. Par suite de l'application d'une surcharge, les grains sont serrés les uns contre les autres et les couches d'eau séparatrices entourant les corpuscules solides s'embrassent (*fig. 7a*). Comme à pression constante, la viscosité de l'eau comprise dans la zone hachurée n'augmente au cours du temps qu'avec une vitesse décroissante, un rapprochement plus poussée des elements solides devient de plus en plus difficile et il se passe parfois des années et des dizaines d'années avant que les grains ne se touchent (*fig. 7b*). Dans une couche d'argile qui reste pendant des milliers d'années sous l'influence de son poids propre constant, ce contact devient inévitable. La resistance au glissement des particules n'est pas produite uniquement par la résistance de frottement mais aussi par la viscosité des couches séparatrices, entourant la zone de frottement.*
> *Dans cet état, l'argile doit forcément présenter les propriétés élastiques d'un amas des grains dont les pointes de contact sont reliés rigidement les uns aux autres.*
> *Aprés le glissement (*fig. 7c*), les particules sont de nouveau séparées par une couche de fluide visqueux. La mobilité des particules augmente avec l'épaissseur de cette couche; le coefficient de compressibilité, par contre diminue.*" (Terzaghi & Frölich, 1936, pp. 18-19).

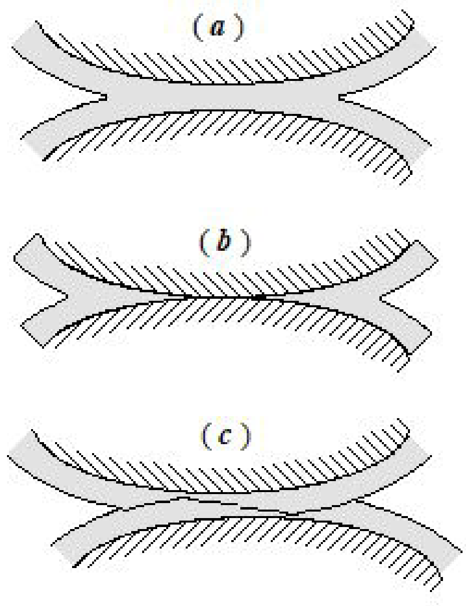

Figure 16. Action of the adsorbed water layer during the relative displacement between two neighbour particles. (a) Clay particles are separated by a thin water layer of high viscosity or (b) Clay particles are in direct touch. (c) Sliding resistance between clay particles is made up of frictionplus viscosity. After relative displacement, clay particles can be separated by a water viscous layer again. [adapted from Terzaghi & Frölich (1936), p.19].

An adaptation of Figures 7a, 7b and 7c as mentioned by Terzaghi & Frölich (1936) in the above quotation is reproduced in this article as Figure 16a, 16b and 16c, as follows:

From the passage transcribed above, it seems clear that the "*cohesion*" to which Terzaghi (1938) refers and the "*effective cohesion*"and "*true cohesion*" referred by Hvorslev (1937, 1960) and Gibson (1953) are all of them from viscous nature. This seems to be Bjerrum's (1973) understanding as well. As a matter of fact, it is the viscous nature of "*cohesion*" which is behind the Bjerrum's (1973) correction factor to be applied to the undrained shear strength $\left(S_u\right)$ measured in the vane test (S_u measured in a vane test is higher because it is obtained with higher shear speed). It is believable that, viewing "*cohesion*" as being of a viscous nature, Bjerrum (1973) proposed the correction factor as a function of the plasticity index. After all, the more plastic the clay the greater its "*cohesion*" (or viscous resistance). Therefore, the higher the plasticity index the higher the influence of viscous resistance on the measured undrained shear strength. What is not appropriate is the use of the expression "*time effect*" to describe the phenomenon. Although Bjerrum (1973) had used the expression "*time effect*", it is clear that, according to his own understanding, the effect in question can be more properly called "*strain rate effect*".

In a re-appraisal of his 1937 work, Hvorslev (1960) highlights three components of shear strength τ_{ff} of a "*cohesive soil*": the effective friction component $\left(\tau_\phi\right)$, the "*effective cohesion*" component $\left(c_e\right)$ and the dilatancy component $\left(\tau_d\right)$. Thus,

$$\tau_{ff} = \tau_\phi + c_e + \tau_d \tag{16}$$

In a normally consolidated clay, which has a contractile behaviour, $\tau_d = 0$. The component τ_ϕ is a function of the effective stress and is expressed by

$$\tau_\phi = \sigma'_{ff} \tan\phi'_e \tag{17}$$

Yet, according to Hvorslev (1960), "*cohesive soils*" (which, due to the confusion created by the term "*cohesive*", the author prefers to call plastic soils) are those which have a strength component c_e. Instead of commenting, it is better to quote how Hvorslev (1960) viewed the c_e component:

> "*Most cohesive soils possess an apparent structural viscosity and their deformations are of visco-elastic character. The corresponding strength component may be called the "viscous component", but factors other than viscosity seem to be involved, and the more inclusive term "rheological component" and the notation c_v are proposed. It will be assumed that c_v forms a part of the effective cohesion component, c_e, because the effective friction component, τ_ϕ, of a remolded clay does not seem to be affected by the increased rate of deformation after failure, provided the soil structure is not changed;see section 8. However, this assumption is in need of further experimental corroboration. The value of* c_v converges on zero with increasing time or decreasing rate of deformation, whereas c_e at the same time approaches an ultimate value, c_u, which may be called the "ultimate cohesion component." By definition, the following relation exists at any given test duration or rate of deformation $c_e = c_u + c_v$".

Hvorslev (1960) still adds the following passage:

> "*For the purpose of definition and experimental determination of the individual components (individual components of shear strength), the basic assumption is made that the cohesion and rheological components are constant when (1) the void ratio or water content of saturated clays is constant, (2) the rate of deformation or test duration is constant, and (3) there is no significant difference in the geometric structure of the clays during a given test series.*" (Hvorslev, 1960, p. 183).

It is worth observing the reference that Hvorslev (1960) made to the strain rate influence. Nevertheless, the approach given to the subject does not explicitly translate the strain rate influence by means of a mathematical expression that quantifies the physical phenomenon. This issue has only become to be coherently approached by Leroueil et al. (1985), showing that, as concerns one-dimensional consolidation, there is a unique relationship among the axial (vertical) strain $\left(\varepsilon_a\right)$, the effective vertical stress $\left({}'_v \right)$ and the axial (vertical) strain rate $\left(\dot{\varepsilon}_a\right)$. However, as far as the author's knowledge

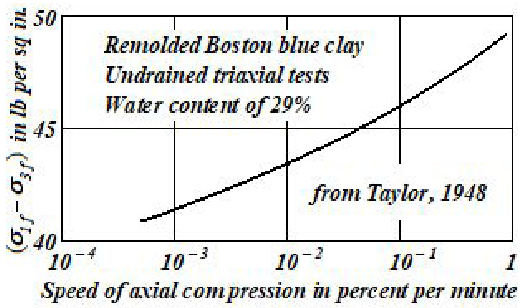

Figure 17. Effect of speed of shear on the compressive strength of clay (Taylor, 1948).

is concerned, Taylor (1948) was the first researcher not only to physically explain the "*effective cohesion*" as being of a viscous origin but also to physically quantify it by means of a mathematical expression.

According to Taylor (1948, pp. 377-378), all viscous materials and all plastic materials exhibit a resistance to shearing strain that varies with the speed at which the shearing strain occurs (see section 3.3). Taylor (1948) called such a kind of resistance in clays as "*plastic resistance*". Figure 17 shows the dependence of the deviator stress at failure $\left(\sigma_{1f} - \sigma_{3f}\right) = \left(\sigma_{af} - \sigma_{rf}\right)$ on the axial strain rate of CIUCL tests. The test results shown in Figure 17 were carried out on remoulded specimens of Boston Blue Clay with the same water content, but subjected to different axial strain rates $\left(\dot{\varepsilon}_a\right)$ (corresponding to different speeds of shear or different shear strain rates).

Also, according to Taylor (1942), experimental results indicated that "*plastic resistance*" under any speed of shear in a given clay with different void ratios is proportional to the effective stress. Assuming that "*plastic resistance*" depends on effective stress and shear strain rate, Taylor (1948) wrote the following equation for the shear strength τ_{ff} of a clay:

$$\tau_{ff} = \left(\sigma'_{ff} + \sigma'_i\right)\left[\tan\phi' + f\left(\partial\varepsilon_s / \partial t\right)\right] \tag{18}$$

where τ_{ff} and σ'_{ff} are, respectively, the shear stress and the effective normal stress on the failure plane at failure, σ'_i is the "*intrinsic pressure*", as defined in section 4.1, ϕ' is the angle of internal friction (to be discussed further again) and $\left(\partial\varepsilon_s / \partial t\right)$ is the shear strain rate on the failure plane. The following passage quoted from Taylor (1948) summarizes the conception of the above-mentioned mechanism. In order to avoid loss of fidelity, it is suitable to quote the referred passage:

> "*The effect of speed of shear on the strength is believed to be caused by the viscous or plastic characteristics of material in the adsorption zones in the vicinity of points of contact or near contact of clay particles. Thus this effect is a colloidal phenomenon, and it is of sufficient importance to justify a detailed discussion.*
> *The following hypothetical explanation of plastic resistance and of time relationships was first presented (*Taylor, 1942*) for one-dimensional compressions, but it may be extended*

to the action of clays in shear. If a drained clay sample is maintained under any given system of constant applied direct and shearing stresses that do not cause failure, it gradually approaches an ultimate shape and an ultimate void ratio at which there is static equilibrium. Ages may be required to reach this state of equilibrium, but when it is reached the applied stresses are equal to static internal resistances and they have values that are free of plastic resistance and all other time effects. During the approach to equilibrium, however, the applied stresses are made up in part of the stresses required to overcome the plastic resistance. The plastic resistance is usually considered to depend mainly on the speed of strain although possibly it depends also on such factors as changes in type or degree of adsorption. As the clay specimen approaches the static case, the strains continuously decrease in speed and the plastic resistance decreases in magnitude; however, the speed becomes almost imperceptibly small when the plastic resistance is still quite large and the strains and the void ratio still have a considerable change to undergo before they reach the static case. Secondary compression, as it occurs in consolidation tests, is a good illustration of this condition. From these concepts it appears that a clay that has reached static equilibrium in nature after the lapse of many centuries and is suddenly subjected to stress increases of relatively small magnitude may be expect immediately to exert a plastic resistance that is equal to the stress increase, and it is possible that the speed of distortion required for the exerting of this amount of plastic resistance may be too small to be noticeable. In such a case the plastic resistance cannot be distinguished from a bond, and the occurrence of bonds of this type is possible both when the shearing stresses are small and when they are relatively large." (Taylor, 1948, pp. 379-380).

From now on the expression "*plastic resistance*" used by Taylor (1948) will be called *viscous resistance*.

5. A possible additional equation for the principle of effective stress (PES)

5.1 The viscosity concept

As the approach of strain rate effects on plastic soils strength is concerned, it is usual to make use of the term viscosity without defining, however, what is understood by soil viscosity. In soil mechanics, the term is generically used without a clear definition (Schnaid et al., 2021). The viscosity concept was introduced by Newton via Newton's law of viscosity: *The tangential stress between neighbouring layers of a fluid in a laminar flow is proportional to the ratio dv/dy with which speed v varies in the transverse direction of flow y* (see Figure 18).

Newton's law of viscosity is written as:

$$\tau = \mu\left(dv/dy\right) \tag{19}$$

which can be written alternatively as:

$$\begin{aligned} \tau &= \mu\frac{dv}{dy} = \mu \lim_{\delta t\to 0}\frac{\delta x}{\delta y.\delta t} = \\ &\mu \lim_{\delta t\to 0}\left(\frac{\delta x}{\delta y}\right)/\,\delta t = \mu\frac{d\gamma}{dt} = \mu\dot{\gamma} \end{aligned} \tag{20}$$

The coefficient μ is called *coefficient of viscosity* or simply *viscosity* and $d\gamma/dt = \dot{\gamma}$ is called distortion rate. Every fluid which obeys Equations 19 or 20 is said to be considered a newtonian fluid.

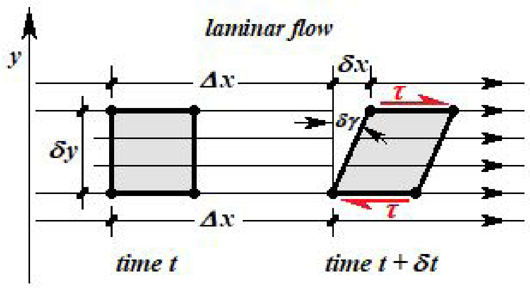

Figure 18. Newton's law of viscosity.

5.2 Shearing of clayey soils – a working hypothesis

The approach presented next is only based on mechanical interactions, which greatly simplify the interaction among clay particles. However, as argued by Bjerrum (1973), in spite of admittedly being an oversimplification, this approach gathers the essential characteristics of the behaviour of plastic soils as far as strain rate effects are concerned.

According to Terzaghi (1941), clay particles are involved by a viscous adsorbed water layer. In the particles surface vicinity, adsorbed water is in a solid state and strongly adhered to grains surface. As the distance from particles surface increases, the adsorbed water viscosity decreases until water becomes free water beyond a certain distance "*d*" (Figure 19). Distance *d* depends on the physico-chemical properties of the minerals of the clay particles and on other substances in the adsorption region.

Also, according to Terzaghi (1941), contacts between grains can occur through solid water (solid to solid contacts) or through viscous water (viscous contacts) and both types of contact transmit effective stresses.

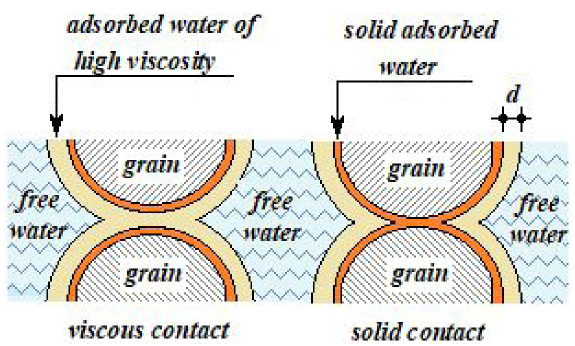

Figure 19. Illustration of adsorbed water and types of contact between clay particles (Terzaghi, 1941).

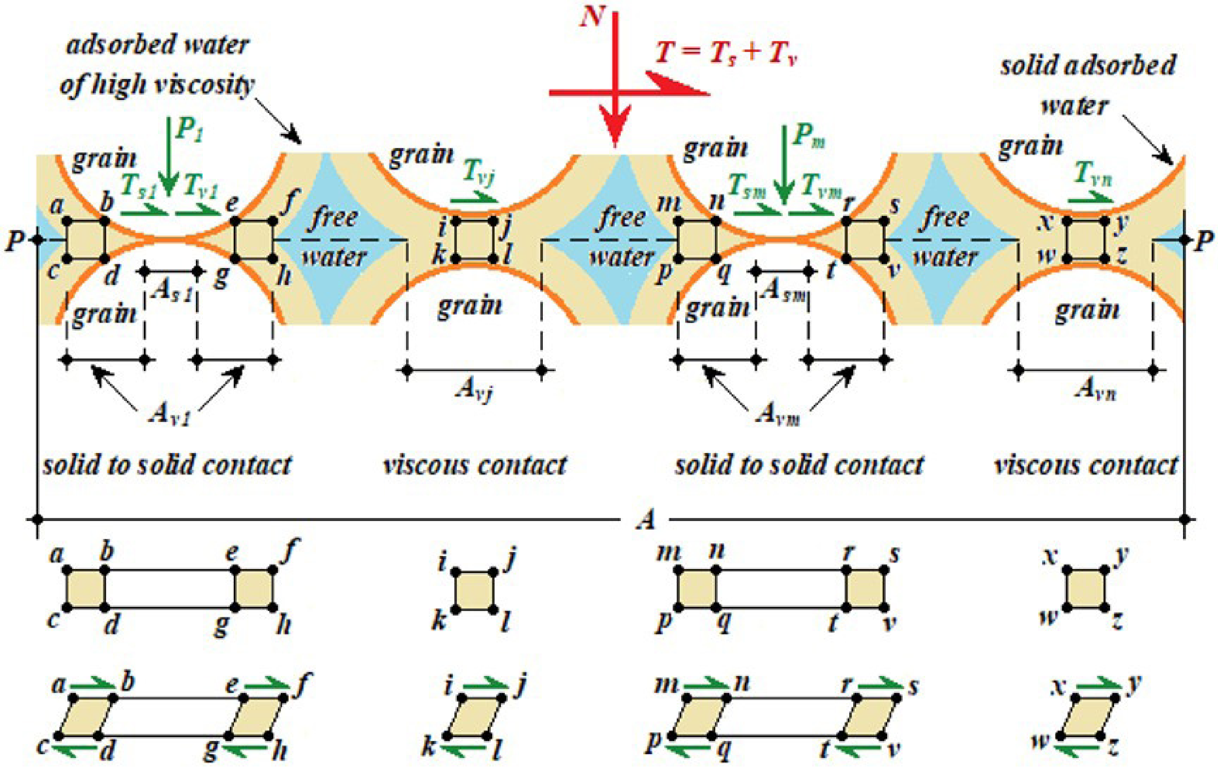

Figure 20. Forces acting on a plane ***P* – *P*** passing through a plastic soil mass.

Starting from the conception of Terzaghi & Frölich (1936) to explain clay shear strength and assuming some additional hypotheses, Martins (1992) obtained the results whose essence is presented as follows.

Considering an imaginary plane ***P* – *P*** passing through a plastic soil mass, it will pass by solid to solid and viscous contacts (Figure 20). Consider now a region of area A ($A = A \times 1u \cdot c$, where $1u \cdot c$ is a unitary length in the normal direction to the plane of Figure 20). Also consider that the normal force N and the tangential force T are acting on the area A.

Assuming that only solid contacts can transmit effective normal stresses, the balance of forces in the normal direction of the plane ***P* – *P*** leads to the PES equation, $\sigma' = \sigma - u$. A more general hypothesis according to which viscous contacts can also transmit effective stresses is being developed but this approach will not be discussed herein.

The tangential force T acting on area A divided by A is by definition the shear stress on the area A along plane ***P* – *P***. Force T can be expressed by the sum of tangential forces, which causes the relative displacement between the particles from the upper side and the lower side of the plane ***P* – *P*** (see Figure 20). According to the mechanism posed by Terzaghi & Frölich (1936), force T consists in summing up the friction resistance component T_s, which exists in solid contacts, and the viscous resistance component T_v, due to the distortion of the adsorbed water.

Suppose there are m solid to solid contacts within the area A in Figure 20. The friction force T_{si} acts at the solid to solid contact of order i as a local reaction to the applied force T. Therefore, the friction resistance component T_s mobilized as a partial reaction to force T can be written as:

$$T_s = \sum_{i=1}^{m} T_{si} = \sum_{i=1}^{m} \xi_i P_i \tan\phi_i' \tag{21}$$

where ϕ_i' is the friction angle of the solid to solid contact of order i and ξ is the degree or percentage of the friction strength mobilized at the solid to solid contact of order i. Thus, Equation 21 provides the mobilized friction resistance component T_s along the plane ***P* – *P***. It is possible to rewrite Equation 21 defining for each solid to solid contact of order i, within the area A, a coefficient ξ_i^* such that $\xi_i \tan\phi_i' = \xi_i^* \tan\phi_e'$, being ϕ_e' the Hvorslev's true angle of friction. Thus, Equation 21 can be rewritten as Equation 22:

$$\sum_{i=1}^{m} \xi_i P_i \tan\phi_i' = \sum_{i=1}^{m} \xi_i^* P_i \tan\phi_e' \tag{22}$$

Finally, denoting by $\bar{\xi}$ the average value of all ξ_i^* values taken over area A, one obtains:

$$T_s = \tan\phi_e' \sum_{i=1}^{m} \xi_i^* P_i = \bar{\xi} \tan\phi_e' \sum_{i=1}^{m} P_i \tag{23}$$

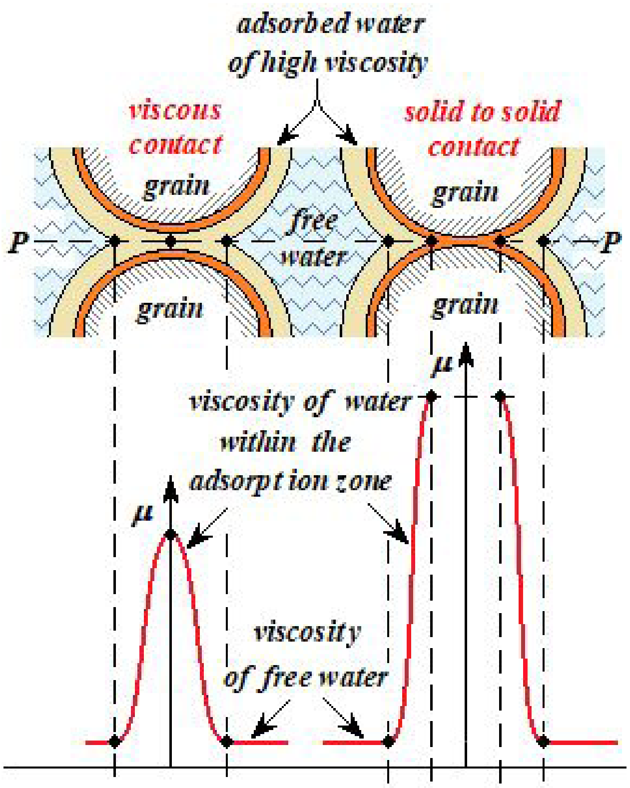

Figure 21. Hypothetical variation of the coefficient of viscosity μ of the adsorbed water along the plane ***P – P*** within the contact zones between clay particles.

Suppose now that the total number of contacts within area A is n. In all contacts, irrespective of their type, there will be viscous resistance. For instance, at the contact between the intermediate couple of grains in Figure 20, viscous resistance comes from the shear strain rate of the adsorbed water element ***ijkl***. Such viscous resistance is also present in the solid to solid contacts. This is illustrated in Figure 20 by the shearing strain of the ring shaped element whose transversal section is ***abcd – efgh***.

The viscous resistance existing in a viscous contact caused by the shear strain rate of an element of section ***ijkl*** or in a solid to solid contact by the shear strain rate of a ring shaped element whose section is ***abcd – efgh*** varies along the contact. This occurs because the viscosity coefficient μ of the adsorbed water at points within the contact zones along the plane ***P – P*** depends on the distances from these points to the particles surface (see Figure 21).

There is also an extremely important issue concerning the behaviour of viscous fluids, as highlighted by Rouse & Howe (1953). As presented in Figure 18, the concept of individual layers or fluid laminae flowing side by side is merely a question of convenience in order to model the phenomenon mathematically. Such a model can lead to the false idea that in a laminar flow fluid laminae can literally slide one over the others producing a kind of mechanical drag measured in terms of the viscous resistance τ, as expressed by Equation 19. In fact, in a submicroscopic scale, viscous resistance results from the interaction of fluid molecules whenever any portion of fluid, no matter how small it is, is subjected to shear strains. A fundamental feature of a viscous fluid is the fact that a slip along a surface between two neighbouring layers of the fluid (inside a fluid mass) or between a viscous fluid and a solid contour cannot occur because this would result in an infinite value for the ratio dv / dy in Equations 19 and 20. Thus, regardless the fluid nature, molecular interactions compel to the condition of identical velocities along both sides of any fluid surface, real or imaginary. For this reason, the velocity of a moving fluid at the surface of contact with a solid contour will be exactly the same as the velocity of the contour itself. If the contour is at rest, the fluid in contact with this contour will also be at rest, irrespective of how great its velocity may be a short distance away. This means that, during shear, relative displacements between soil grains occur without slippage along the surface of contact between viscous adsorbed water and solid grains contours. This also means that during relative displacements, for instance, along the plane ***P – P*** in Figure 20, soil grains are subjected to drag forces due to shear strain of their viscous adsorbed water layers. The resultant of these viscous forces, denoted by T_v, is the viscous component proposed by Terzaghi & Frölich (1936), which, added to the friction resistance component T_s, gives the internal reaction to the applied tangential force T.

As the viscous resistance is present in all n contacts within the area A, irrespective of the type of contacts, T_v can be written as:

$$T_v = \sum_{j=1}^{n} T_{vj} \tag{24}$$

being T_{vj} the local viscous resistance acting at the contact of order j. In its turn, T_{vj} can be written as**:**

$$T_{vj} = \frac{d\gamma_j}{dt} \int \mu dA_{vj} \tag{25}$$

Considering the viscosity of the free water as being negligible if compared to the viscosity of the adsorbed water, the integral in Equation 25 should be taken all over the viscous contact area A_{vj} of contact ***j*** (see Figures 20 and 21), along which μ varies. The term $d\gamma_j / dt$ is the distortion rate of the viscous adsorbed water of the contact of order ***j***, along the plane ***P – P***, in the direction of the tangential force T. Thus, the viscous component T_v acting all over the area A in the direction of T can be written as:

$$T_v = \sum_{j=1}^{n} \frac{d\gamma_j}{dt} \int \mu dA_{vj} \tag{26}$$

Taking $\bar{\mu}_j$ as the average value of μ over the area A_{vj}, $\int \mu dA_{vj}$ can be written as $\bar{\mu}_j A_{vj}$. Thus,

$$T_v = \sum_{j=1}^{n} \bar{\mu}_j A_{vj} \frac{d\gamma_j}{dt} \tag{27}$$

Denoting by $\overline{\overline{\mu}}$ the average value of all $\overline{\mu}_j$ values and taking into account that the distortion γ_{P-P} of a clay along the plane $\boldsymbol{P-P}$ in Figure 20 is the result of the gathered relative displacements of particles from both sides of plane $\boldsymbol{P-P}$, Equation 27 can be rewritten as:

$$T_v = \overline{\overline{\mu}} \frac{d\gamma_{P-P}}{dt} \sum_{j=1}^{n} A_{vj} \tag{28}$$

Summing up the friction resistance component $\left(T_s\right)$ and the viscous resistance component $\left(T_v\right)$ and dividing by the area A, on which the sum $\left(T_s + T_v\right)$ acts, Equation 29 is obtained, as follows.

$$\frac{T}{A} = \frac{T_s + T_v}{A} = \frac{\overline{\xi}\, tan\,\phi'_e \sum_{i=}^{m} P_i}{A} + \frac{\overline{\overline{\mu}} \frac{d\gamma_{P-P}}{dt} \sum_{j=}^{n} A_{vj}}{A} \tag{29}$$

The left hand side of Equation 29 (T / A) is by definition the shear stress τ over area A of the plane $\boldsymbol{P-P}$, as shown in Figure 20. The summation $\sum_{i=1}^{m} P_i / A$ is, by definition, the effective normal stress σ' acting on the area A of the plane $\boldsymbol{P-P}$. The product $\overline{\xi}\, tan\,\phi'_e$ in the first part of the right hand side of Equation 29 is the mobilized degree $\left(\overline{\xi}\right)$ of the friction coefficient $tan\,\phi'_e$. Denoting $\overline{\xi}\, tan\,\phi'_e$ by $tan\,\phi'_{mob}$, the first part of the right hand side of Equation 29 can be written as:

$$\aleph_{\phi}\ \aleph \frac{T_s}{A} \quad \frac{\overline{\xi}\, tan\,\phi'_e \sum_{i=1}^{m} P_i}{A} \quad '\, tan \ {}^{'}_{\ddot{u}} \tag{30}$$

being T_s the mobilized friction resistance, which is a part of the internal reaction to the applied horizontal force T (see Figure 20). As T / A is the shear stress τ acting over the area A, the ratio $T \ / A$, denoted by τ_{ϕ}, is the part of the shear resistance due to friction mobilized on the area A along the plane $\boldsymbol{P-P}$.

In the second part of the right hand side of Equation 29, $\overline{\overline{\mu}}$ is a function of the distance between neighbouring particles and, therefore, of the void ratio (e). However, $\overline{\overline{\mu}}$ is also a function of the relative position according to which clay particles are arranged along the plane $\boldsymbol{P-P}$, that is to say, a function of the structure. Nevertheless, the ratio $\sum_{j=1}^{n} A_{vj} \ / A$ is an exclusive function of the void ratio. Thus, the product $\overline{\overline{\mu}}\left(\sum_{j=1}^{n} A_{vj} \ / A\right)$ can be rewritten as a function $\eta(e)$, being $\eta(e)$ a function of the void ratio and the structure. Thereby, the second part of the right hand side of Equation 29, denoted by τ_{η}, can be rewritten as:

$$\tau_{\eta} = \eta\left(e\right)\left(\frac{d\gamma_{P-P}}{dt}\right) \tag{31}$$

being $\eta(e)$ here defined as the *viscosity of a plastic soil*. Thus, the expression for the shear stress τ_{α} of a plastic soil, at any instant, acting on plane $\boldsymbol{P-P}$ whose normal makes an angle α with the principal direction σ_1, being the soil at failure or not, can be written as:

$$\tau_{\alpha} = \tau_{\phi\alpha} + \tau_{\eta\alpha} = \sigma'_{\alpha}\, tan\,\phi'_{mob\alpha} + \eta\left(e\right)\left(\frac{d\gamma_{\alpha}}{dt}\right) \tag{32}$$

If the simplifying assumptions from which Equation 32 has been derived are accepted as valid, such equation will reveal that, at any moment, the shear stress τ_{α} on a plane whose normal makes an angle α with the direction of σ_1 will be internally resisted by the sum of a friction component $\tau_{\phi\alpha} = \sigma'_{\alpha}\, tan\,\phi'_{mob\alpha}$ and a viscous component $\aleph \ = \ (e)(d \quad / dt)$.

Equation 32 leads to the following immediate consequences:

1. It translates mathematically the mechanism conceived by Terzaghi & Frölich (1936) and by Taylor (1948), as presented in section 4.4, about clay behaviour in shear, where the shear resistance at any instant (and not only at failure) is given by the sum of a friction component $\left(\tau_{\phi\alpha}\right)$ and a viscous component $\left(\tau_{\eta\alpha}\right)$.
2. Part of the shear resistance existing in plastic soils is of a viscous origin. It is worth observing that the viscous component becomes zero when strain rate is zero, which does not correspond to the Coulomb's cohesion concept (Schofield, 1999), but corresponds to the viscous resistance concept introduced by Newton.
3. The viscous component $\left(\tau_{\eta\alpha}\right)$ would correspond to the "*true cohesion*" of Hvorslev (1960), an inappropriate name (in the author's opinion), since according to Hvorslev (1960) himself it would have a viscous feature (see section 4.4) and would be a function of three variables: the void ratio, the strain rate and the clay structure. These three variables are present in Equation 31.
4. Considering that shear stresses are internally resisted by a friction component and a viscous component, an additional equation which refers to shear stresses can be added to the PES. This suggests that Equation 18, presented by Taylor (1948), can be generalized, holding valid at any instant and not only at failure.
5. Equation 32 is also valid outside the soil mechanics domain since, if effective stress σ'_{α} is zero, friction strength will be zero and the resistance to shearing strain will only reside in viscosity, which is a feature of fluids.
6. Finally, Equation 32 explicitly shows the influence of strain rate on the shear strength [see for instance Taylor (1948), Bjerrum (1973), Berre & Bjerrum (1973), Lacerda & Houston (1973), Graham et al. (1983), Sheahan et al. (1996), Tatsuoka et al. (2002), and Aguiar (2014)] and on consolidation (Taylor, 1942; Graham et al., 1983; Leroueil et al., 1985; Andrade, 2014). As previously discussed, being the "*effective cohesion*" or "*true cohesion*", as defined by Terzaghi (1938) and Hvorslev (1937, 1960), of a viscous nature, it is expected that the greater the plasticity of a soil (given by its plasticity index I_p) the greater its viscosity

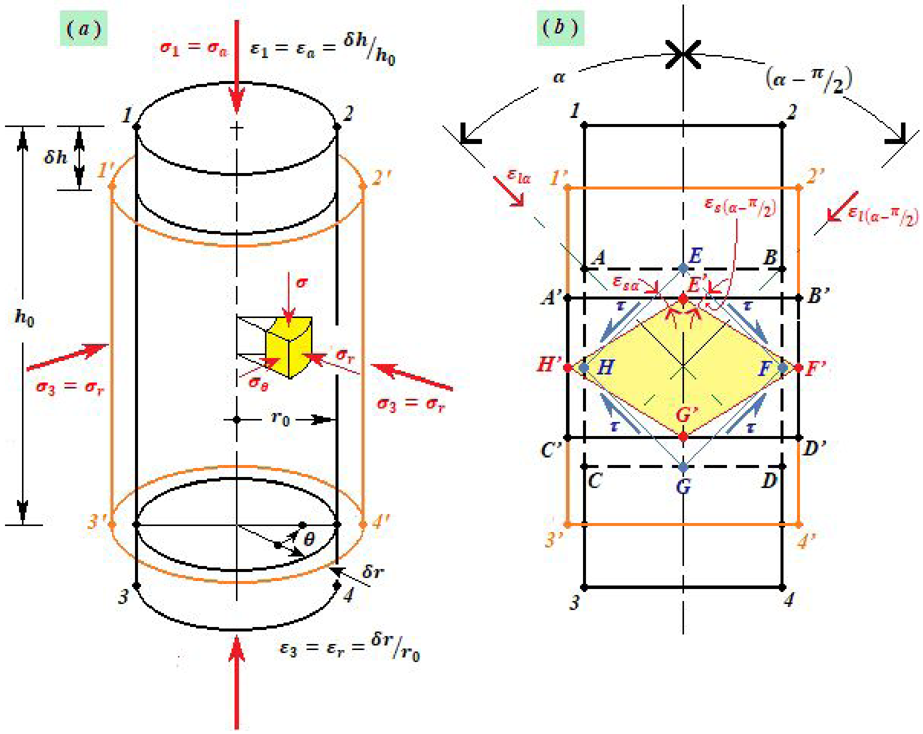

Figure 22. (a) State of stress in a $\overline{\text{CIUCL}}$ test during the undrained shear stage; (b) Corresponding state of strain.

$\eta(e)$. In the author's opinion, this might have been the main reason for Bjerrum (1973) having expressed the influence of strain rate on shear strength of plastic soils as a function of the plasticity index (I_p).

Last but not least, to avoid the confusion created by the inappropriate use of the term "*cohesion*", instead of using the words "*cohesive*" and "*non-cohesive*", it is suggested the use of the words "*plastic*" and "*non-plastic*" soils. By a plastic soil is to be meant a soil on which one can carry out plastic and liquid limit tests.

5.3 Mohr's circle of strain in a $\overline{\text{CIUCL}}$ test

The state of stress found in a $\overline{\text{CIUCL}}$ test is shown in Figure 22a. In this case, $\sigma_1 = \sigma_a$ and, due to the axisymmetry, $\sigma_3 = \sigma_\theta = \sigma_r$. Assuming the soil as isotropic, corresponding to the state of stress of Figure 22a, there is an axisymmetrical state of strain where $\varepsilon_1 = \varepsilon_a$ and $\varepsilon_3 = \varepsilon_2 = \varepsilon_r = \varepsilon_\theta$. In such a case, there will be no shearing strains on horizontal planes.

In a similar way to which has been done for stresses, it can be written:

$$\varepsilon_{l\alpha} = \frac{\varepsilon_1 + \varepsilon_3}{2} + \frac{\varepsilon_1 - \varepsilon_3}{2} \cos 2\alpha \tag{33}$$

and

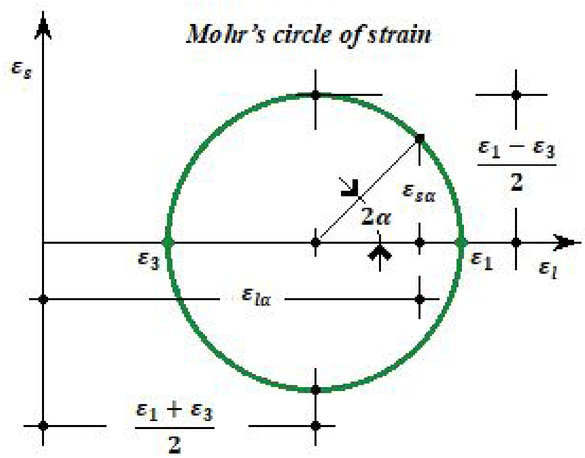

Figure 23. Mohr's circle of strain during the undrained shear stage of a $\overline{\text{CIUCL}}$ test.

$$\varepsilon_s = \frac{\varepsilon_1 - \varepsilon_3}{2} \sin 2\alpha \tag{34}$$

where $\varepsilon_{l\alpha}$ is the normal linear strain (longitudinal strain) of an element of the vertical plane (like ***EFGH*** of Figure 22b) along the direction which makes an angle α with the direction of $\varepsilon_1 = \varepsilon_a$ (α being positive when taken in a counterclockwise sense) and $\varepsilon_{s\alpha}$ the shearing strain (see also Figure 22b).

Similarly to what has been done for stresses, Equations 33 and 34 can be represented on plane $\varepsilon_l \times \varepsilon_s$ (Figure 23) by a circle of radius $\left(\varepsilon_1 - \varepsilon_3\right)/2$ and center of coordinates $\left[\left(\varepsilon_1 + \varepsilon_3\right)/2, 0\right]$. It is the Mohr's circle of strain, shown in Figure 23.

In soil mechanics it is usual to take a normal linear strain as positive when the element suffers a reduction in length (shortening). On the contrary, an elongation is considered negative. In the case of the specimen shown in Figure 22, the axial strain $\varepsilon_a = \varepsilon_1 = -\left(\delta h / h_0\right)$ is positive (because δh is negative) and the radial strain $\varepsilon_r = \varepsilon_3 = -\left(\delta r / r_0\right)$ is negative (because δr is positive).

Being V_f and V_0, respectively, the final and the initial specimen volumes, the volumetric strain, denoted by ε_V, is by definition:

$$\varepsilon_V = \frac{\left(V_0 - V_f\right)}{V_0} \tag{35}$$

In soil mechanics it is usual to consider a compression (decrease of volume) as being positive. Thus, in the case of a triaxial test specimen (see Figure 22), ε_V, defined by Equation 35, is accurately given by:

$$\begin{aligned}\varepsilon_V &= -\frac{\delta h}{h_0} - \frac{2\delta r}{r_0} - \frac{2\delta r \delta h}{r_0 h_0} - \frac{\delta r^2}{r_0^2} - \frac{\delta r^2 \delta h}{r_0^2 h_0} = \\ &\varepsilon_a + 2\varepsilon_r + \varepsilon_r\left[2\varepsilon_a + \varepsilon_r\left(1 + \varepsilon_a\right)\right]\end{aligned} \tag{36}$$

When ε_a and ε_r are small, Equation 36 can be simplified as $\varepsilon_V = \varepsilon_a + 2\varepsilon_r$. During the undrained shear of a saturated specimen in a $\overline{\text{CIUCL}}$ test, there is no volume change, so $\varepsilon_V = 0$. In this case $\varepsilon_r = -\left(\varepsilon_a / 2\right)$ and the specimen is distorted on planes which are not horizontal (see Figure 22b).

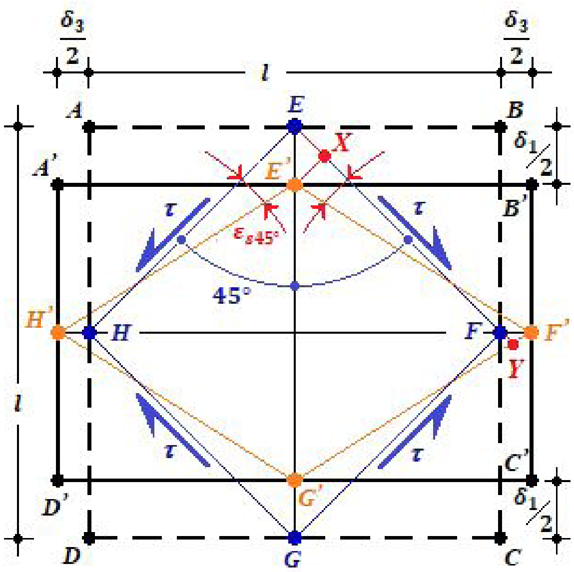

Figure 24. Normal linear strains and shear strains of elements ***ABCD*** and ***EFGH***.

Figure 22b shows the section ***1234*** made by a vertical plane that contains the axis of the specimen of Figure 22a. Consider now the square region ***ABCD*** on the section 1234 before deformation. Taking $\alpha = 45°$ in Figure 22b, the square ***ABCD*** of side l, shown in Figure 24, is deformed into the rectangle ***A'B'C'D'***. In a similar way, the square ***EFGH*** of side $l\sqrt{2}/2$ is deformed into the rhombus ***E'F'G'H'***.

According to Figure 24, $\varepsilon_1 = \varepsilon_a = \delta_1 / l$ and $\varepsilon_3 = \varepsilon_r = -\delta_3 / l = -\delta_1 / 2l$. Thus, $\varepsilon_{l45°}$ can be evaluated as shown in Figure 24.

$$\begin{aligned}\varepsilon_{l45°} &= \frac{\overline{\boldsymbol{EE'}}\cos 45° - \overline{\boldsymbol{FF'}}\cos 45°}{\overline{\boldsymbol{EF}}} = \\ &\frac{\frac{\delta_1}{2}\frac{\sqrt{2}}{2} - \frac{\delta_3}{2}\frac{\sqrt{2}}{2}}{\frac{l\sqrt{2}}{2}} = \frac{\frac{\delta_1}{2} - \frac{\delta_3}{2}}{l} = \frac{\delta_1}{4l} = \frac{\varepsilon_1 + \varepsilon_3}{2}\end{aligned} \tag{37}$$

It should be observed that δ_1 and δ_3 have opposite signs because δ_1 is a contraction and δ_3 an elongation. The expression for $\varepsilon_{l45°}$ given by Equation 37 can also be obtained via Equation 33, that is,

$$\begin{aligned}\varepsilon_{l45°} &= \frac{\varepsilon_1 + \varepsilon_3}{2} + \frac{\varepsilon_1 - \varepsilon_3}{2}\cos 90° = \frac{\varepsilon_1 + \varepsilon_3}{2} = \\ &\frac{\frac{\delta_1}{l} - \frac{\delta_3}{l}}{2} = \frac{1}{2}\left(\frac{\delta_1}{l} - \frac{\delta_1}{2l}\right) = \frac{\delta_1}{4l} = \frac{\varepsilon_1}{4}\end{aligned} \tag{38}$$

The value of $\varepsilon_{s45°}$ can be obtained, via Figure 24, taking the transversal component of the relative displacement between points ***E*** and ***F***, by unit length of the segment ***EF***, that is:

$$\begin{aligned}\varepsilon_{s45°} &= \frac{\overline{\boldsymbol{EE'}}\sin 45° - \left(-\overline{\boldsymbol{FF'}}\sin 45°\right)}{\overline{\boldsymbol{EF}}} = \\ &\frac{\frac{\delta_1}{2}\frac{\sqrt{2}}{2} - \left(-\frac{\delta_3}{2}\frac{\sqrt{2}}{2}\right)}{\frac{l\sqrt{2}}{2}} = \frac{\frac{\delta_1}{2} + \frac{\delta_3}{2}}{l} = \frac{3}{4}\varepsilon_1\end{aligned} \tag{39}$$

The value of Equation 39 can also be obtained using $\alpha = 45°$ in Equation 34, that is:

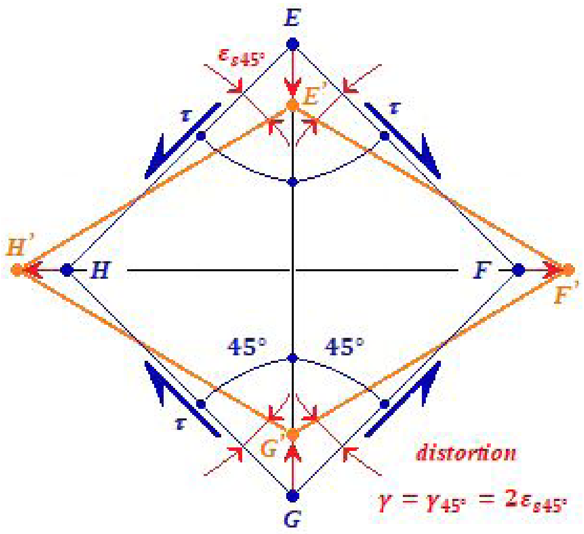

Figure 25. Definition of distortion $= \gamma_{45^\circ} = 2\varepsilon_{s45^\circ}$.

$$\varepsilon_{s45^\circ} = \frac{\varepsilon_1 - \varepsilon_3}{2}\sin 90^\circ = \frac{\frac{\delta_1}{l} - \left(-\frac{\delta_3}{l}\right)}{2} = \frac{\frac{\delta_1}{l} - \left(-\frac{\delta_1}{2l}\right)}{2} = \frac{3}{4}\frac{\delta_1}{l} = \frac{3}{4}\varepsilon_1 \quad (40)$$

Finally, the distortion, denoted by γ_α , is the angular change between two fibres of the vertical plane of Figure 22b, which were originally at right angles one to another and whose normal directions make the angles α and $\left(\alpha - \pi/2\right)$ with the direction of ε_1 (see Figure 22b). Thus, the distortion γ_α can be determined via Equation 34 as $\gamma_\alpha = \varepsilon_{s\alpha} - \varepsilon_{s\left(\alpha - \pi/2\right)}$, that is,

$$\gamma_\alpha = \frac{\left(\varepsilon_1 - \varepsilon_3\right)}{2}\sin 2\alpha - \frac{\left(\varepsilon_1 - \varepsilon_3\right)}{2}\sin 2\left(\alpha - \pi/2\right) = \left(\varepsilon_1 - \varepsilon_3\right)\sin 2\alpha = 2\varepsilon_{s\alpha} \quad (41)$$

The maximum distortion γ_{45°, or simply the distortion γ, is the angular change between two fibres of the vertical plane of Figure 22b, which were originally at right angles one to another and whose normal directions make the angles $+45^\circ$ and -45° with the direction of ε_1 (see Figure 25). This distortion γ, during the undrained shear stage of a $\overline{\text{CIUCL}}$ test, can be obtained using $\alpha = 45^\circ$ in Equation 41 to obtain:

$$\gamma_{45^\circ} = \gamma = \varepsilon_1 - \varepsilon_3 = \frac{3}{2}\varepsilon_1 \quad (42)$$

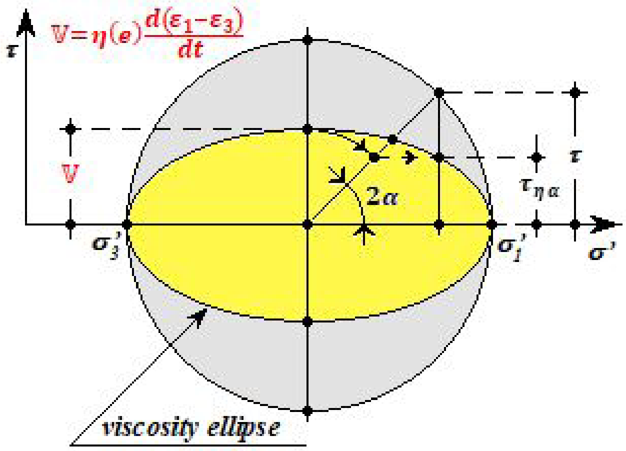

Figure 26. The viscosity ellipse or Taylor's ellipse.

5.4 The Mohr's circle, the viscosity ellipse and the friction ellipse

Considering Equation 31 and assuming $\eta(e)$ does not vary with direction (soil is assumed to be isotropic) and also recalling that distortion γ_α is twice the shear strain $\varepsilon_{s\alpha}$, the viscous component of the shear stress $\tau_{\eta\alpha}$ along a plane whose normal makes an angle α with the σ_1 or ε_1 direction can be written as:

$$\tau_{\eta\alpha} = \eta(e)\left(d\gamma_\alpha\ \text{ü}dt\right) = \eta(e)\left(d\ \ \varepsilon_{s\alpha}\ \ dt\right) = 2\eta(e)\left(d\varepsilon_{s\alpha}/dt\right) \quad (43)$$

Recalling that $\varepsilon_{s\alpha} = \left[\left(\varepsilon_1 - \varepsilon_3\right)/2\right] sin\, 2\alpha$, then

$$\tau_{\eta\alpha} = 2\eta(e)\left(d\varepsilon_{s\alpha}/dt\right) = \eta(e)\left[d\left(\varepsilon_1 - \varepsilon_3\right)/dt\right] sin\, 2\alpha \quad (44)$$

At a given instant of a triaxial compression test, whether it is drained or undrained, provided that accelerations are negligible (so that equilibrium equations can be written), the *state of mobilized viscosity* is given by:

$$\sigma_\alpha' = \frac{\sigma_1' + \sigma_3'}{2} + \frac{\sigma_1' - \sigma_3'}{2} cos\, 2\alpha \quad (45)$$

and

$$\tau_{\eta\alpha} = \eta(e)\frac{d\left(\varepsilon_1 - \varepsilon_3\right)}{dt} sin\, 2\alpha \quad (46)$$

Equations 45 and 46 are the parametric equations of an ellipse whose centre has coordinates $\left[\left(\sigma_1' + \sigma_3'\right)/2, 0\right]$ and whose major and minor axes are respectively $\left(\sigma_1' - \sigma_3'\right)$ and $2\eta(e)d\left(\varepsilon_1 - \varepsilon_3\right)/dt$. This ellipse, as shown in Figure 26, will be called viscosity ellipse or Taylor's ellipse, in honour of Donald Wood Taylor, since, in fact, all these concepts are expressed in several of his writings, though not in detail.

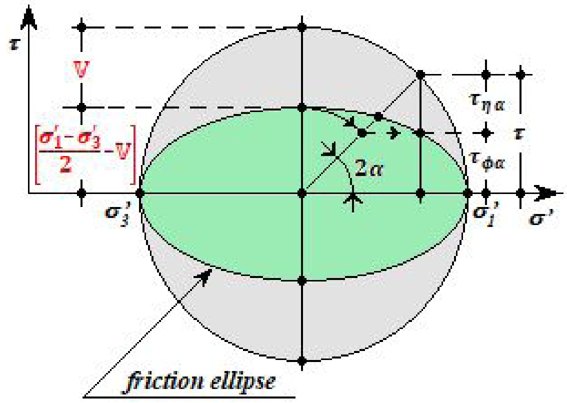

Figure 27. The friction ellipse or Coulomb's ellipse.

From now on, the maximum ordinate of the viscosity ellipse will be denoted by $\mathbb{V}$ and expressed by:

$$\mathbb{V} = \eta(e)\frac{d(\varepsilon_1 - \varepsilon_3)}{dt} = \eta(e)\dot{\gamma} \tag{47}$$

From the above exposed, the friction component of the shear stress $\tau_{\phi\alpha}$, acting on the same plane on which the viscous portion $\tau_{\eta\alpha}$ acts, is given by:

$$\tau_{\phi\alpha} = \tau_\alpha - \tau_{\eta\alpha} = \left[\frac{(\sigma_1' - \sigma_3')}{2} - \mathbb{V}\right] sin 2\alpha \tag{48}$$

Based on Equations 45 and 48, the *state of mobilized friction* is defined. One can observe that Equations 45 and 48 are the equations of another ellipse whose centre has coordinates $\left[(\sigma_1' + \sigma_3')/2, 0\right]$ and whose major and minor axes are, respectively, $(\sigma_1' - \sigma_3')$ and $\left[(\sigma_1' - \sigma_3') - 2\mathbb{V}\right]$. This ellipse, as shown in Figure 27, will be called friction ellipse or Coulomb's ellipse.

It is noteworthy that the Mohr's circle of effective stresses is the result of summing up the viscosity and the friction ellipses. However, the ellipses cannot exist separately since equilibrium conditions are only fulfilled by the Mohr's circle of stress. Thus, the shear stress τ_α, which acts on a plane whose normal makes an angle α with the σ_1 direction, consists of two parts: a friction part $\tau_{\phi\alpha}$ and a viscous part $\tau_{\eta\alpha}$.

5.5 A failure criterion for soils taking into account the strain rate effect

The ideas herein exposed can be generalized for any stress and strain states. Nevertheless, as this text deals with fundamentals, only $\overline{\text{CIUCL}}$ triaxial tests on normally consolidated specimens will be discussed. In this type of test, $\sigma_1' = \sigma_a'$, $\sigma_3' = \sigma_r'$, $\varepsilon_1 = \varepsilon_a$ and $\varepsilon_3 = \varepsilon_r$ (see Figure 22a).

When carrying out a $\overline{\text{CIUCL}}$ triaxial test in a saturated soil, since the water compressibility is negligible, the volumetric strain ε_v is assumed to be zero during the shearing stage. Thus, $\varepsilon_v = \varepsilon_1 + 2\varepsilon_3 = 0$, then $\varepsilon_3 = -\varepsilon_1 / 2$ or $\varepsilon_r = -\varepsilon_a / 2$. So, $\varepsilon_1 - \varepsilon_3 = 3/2(\varepsilon_1) = 3/2(\varepsilon_a)$, and the viscous component of the shear stress $\tau_{\eta\alpha}$ corresponds to:

$$\tau_{\eta\alpha} = \eta(e)\frac{d(\varepsilon_1 - \varepsilon_3)}{dt} sin 2\alpha = \frac{3}{2}\eta(e)\frac{d\varepsilon_a}{dt} sin 2\alpha \tag{49}$$

As in the shear stage of a conventional $\overline{\text{CIUCL}}$ test the axial strain rate $\dot{\varepsilon}_a = d\varepsilon_a / dt$ = constant, Equation 49 reveals that, when a fixed plane is considered, whatever it is, the viscous component $\tau_{\eta\alpha}$ of the shear stress on that plane will remain constant during all test (provided that during shear the soil structure remains approximately constant, so that $\eta(e)$ will keep approximately constant). Thus, according to Equation 49, as soon as the load frame motor is switched on with the strain rate corresponding to $\dot{\varepsilon}_a$, the viscous component will be mobilized immediately (with $\varepsilon_a = 0$), and remaining constant, for each fixed plane, up to the end of shear. Notwithstanding, although the viscous resistance will be fully mobilized immediately and remaining constant along the whole shear, the deviator stress will increase as the specimen strains up to failure. This means that during shear the frictional resistance will be mobilized as the test takes place, contrarily to the viscous resistance mobilization, which occurs instantaneously. The immediate consequences of such mechanism are listed as follows:

1. To mobilize the frictional resistance, it is necessary to strain the specimen and, as it begins to be strained, the deviator stress will begin to increase up to the specimen reaches failure. As during the shear stage of a $\overline{\text{CIUCL}}$ test there are no volume changes, only shear strains occur. Thus, the mobilization of the frictional component is intimately related to shear strains and, therefore, failure will occur when the frictional component is fully mobilized. The conclusion is that shear strains and failure are governed by the mobilization of the frictional component. In the very beginning of shear, there is immediate viscous resistance mobilization, whatever the plane may be. On a fixed plane, viscous resistance will be acting with a value that will be kept constant up to failure (provided that $\dot{\varepsilon}_a$ and soil structure remain the same). As shear strains take place, deviator stress will increase due to the mobilization of the frictional resistance component. When the frictional resistance component is entirely mobilized, failure occurs.
2. As regards specimens with the same void ratio and the same structure, the viscous resistance component at failure, i.e., the viscous part of the undrained shear strength, only depends on the strain rate. Thus, the shear strain rate only affects the shear

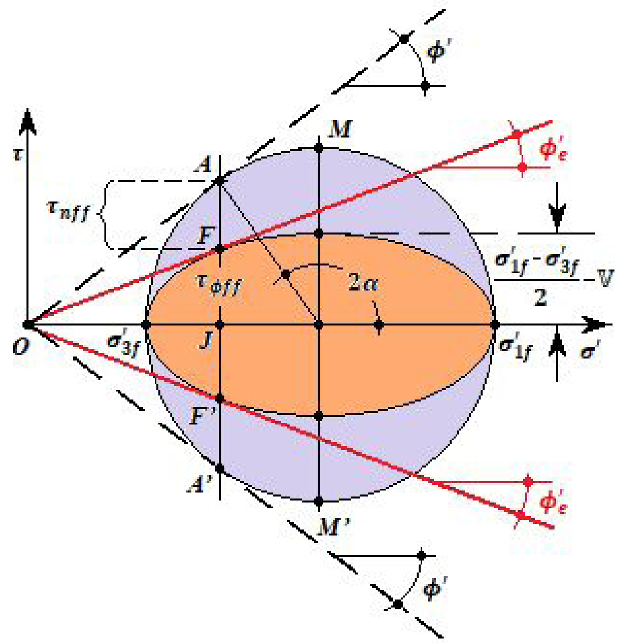

Figure 28. Failure criterion for a normally consolidated clay.

strength value but does not affect strains. This is illustrated by the test results shown in Figure 5 (see also Figure 6). As the field vane test is usually carried out with a higher speed of shear than those observed in real failures in the field, the results of Figures 5 and 6 also explain the need for Bjerrum (1973) having proposed the correction factor to be applied to undrained shear strength results obtained via field vane tests.

3. If failure is commanded by the mobilization of the frictional component of the shear strength and if the frictional part of the shear stress is given by the friction ellipse ordinates, then, if the failure criterion established by Hvorslev (1937) holds valid, failure must occur whenever the friction ellipse touches the strength envelope. Remembering that the approach in this article is limited to the normally consolidated specimens, the strength envelope to be considered is that one which passes through the origin and has slope tan ϕ'_e (see Figure 28).

Denoting by τ_{ff} the shear stress on the failure plane at failure,

$$\tau_{ff} = \tau_{\phi ff} + \tau_{\eta ff} \tag{50}$$

where $\tau_{\phi ff}$ and $\tau_{\eta ff}$ are, respectively, the friction and viscosity parts of the shear stress on the failure plane at failure. As friction is what commands failure, failure occurs according to Mohr-Coulomb-Hvorslev's envelope, which is the straight line that passes through the origin and has slope ü ϕ'_e (see Figure 28). Thus, failure occurs in the maximum obliquity plane, taking into account only the frictional part of the shear stress, given by:

$$tan\,\phi'_{emob} = \left({}^{\tau_{\phi\alpha}}\!/_{\sigma'_\alpha} \right)_{max} \tag{51}$$

Being ϕ'_e the limiting angle of maximum obliquity, $tan\,\phi'_e$ is the maximum value of $tan\,\phi'_{emob}$.

At each moment of a test, $tan\,\phi'_{emob}$ can be obtained by determining $\left(\tau_{\phi\alpha} / \sigma'_\alpha\right)_{max}$. This occurs when

$$\frac{\partial\left(\dfrac{\tau_{\phi\alpha}}{\sigma'_\alpha}\right)}{\partial\alpha} = 0 \tag{52}$$

$$\frac{\partial\left(\dfrac{\tau_{\phi\alpha}}{\sigma'_\alpha}\right)}{\partial\alpha} = \frac{\partial}{\partial\alpha}\left\{ \frac{\left[\dfrac{(\sigma'_1-\sigma'_3)}{2}-\mathbb{V}\right]sin\,2\alpha}{\dfrac{(\sigma'_1+\sigma'_3)}{2}+\dfrac{(\sigma'_1-\sigma'_3)}{2}cos\,2\alpha} \right\} = \tag{53}$$

$$\frac{\partial}{\partial\alpha}\left[\frac{(t'-\mathbb{V})\,sin\,2\alpha}{s'+t'cos\,2\alpha}\right] = 0$$

$$\frac{\partial\left(\dfrac{\tau_{\phi\alpha}}{\sigma'_\alpha}\right)}{\partial\alpha} = \frac{2(t'-\mathbb{V})\cos 2\alpha\,(s'+t'\cos 2\alpha)}{(s'+t'\cos 2\alpha)^2} + \frac{2t'(t'-\mathbb{V})\sin^2 2\alpha}{(s'+t'\cos 2\alpha)^2} = 0 \tag{54}$$

Solving Equation 54, one obtains:

$$cos\,2\alpha = -\frac{t'}{s'} = -\frac{\sigma'_1-\sigma'_3}{\sigma'_1+\sigma'_3} \tag{55}$$

Replacing the result of Equation 55 into Equation 51, one finally obtains:

$$tan\,\phi'_{emob} = \frac{\left(\dfrac{\sigma'_1-\sigma'_3}{2}-\mathbb{V}\right)}{\sqrt{\sigma'_1\sigma'_3}} = \frac{(t'-\mathbb{V})}{\sqrt{s'^2-t'^2}} \tag{56}$$

where

$$s' = \frac{\sigma'_1+\sigma'_3}{2} = \frac{\sigma'_a+\sigma'_r}{2} \tag{57}$$

and

$$t' = \frac{\sigma'_1-\sigma'_3}{2} = \frac{\sigma'_a-\sigma'_r}{2} \tag{58}$$

6. $\overline{\text{CIUCL}}$ tests under the light of the concepts presented in the previous section

6.1 Introduction and summary of the main points of previous section

Although the concepts presented in section 5 can be extended to more general cases, the approach herein presented is restricted to normally consolidated saturated plastic soils subjected to $\overline{\text{CIUCL}}$ tests. Such approach describes and considers the effect of strain rate on clays behaviour based on a mechanical view, via viscosity. Considering the strain rate effect via viscosity greatly simplifies the phenomenon of interaction between clay particles. Nevertheless, this kind of approach captures the essence of the strain rate effects on plastic soils behaviour, making its understanding easier.

The assumptions used in this approach are the following:

1. Soil is seen as a set of grains, each one involved by a highly viscous adsorbed water. The closer the adsorbed water is to the grain surface, the higher its viscosity.
2. Contacts between grains are of two types: solid to solid and viscous (Figures 20 and 21).
3. In a plane passing through a "point" of a soil mass in equilibrium whose normal makes an angle α with the σ_1 direction the effective normal stress σ'_α is written as: $\sigma'_\alpha = \sigma_\alpha - u$, being σ_α the total normal stress and u the pore pressure.
4. Along the tangential direction of the same plane described in (3), the shear stress τ_α consists of two parts: a frictional part $\tau_{\phi\alpha}$ and a viscous part $\tau_{\eta\alpha}$, or rather $\tau_\alpha = \tau_{\phi\alpha} + \tau_{\eta\alpha}$.
5. The viscous part of the shear stress $\tau_{\eta\alpha}$, given by Equation 44, is a function of the void ratio, the soil structure and the distortion rate $\dot{\gamma}$. The friction part $\tau_{\phi\alpha}$, given by Equation 48, is a function of the effective stress σ'_α and the mobilized friction angle ϕ'_{mob} on the plane where σ'_α acts, i.e., $\tau_{\phi\alpha} = \sigma'_\alpha \tan\phi'_{mob\alpha}$ (see Equation 32). It should be reminded here that there is a difference between $\phi'_{mob\alpha}$ and ϕ'_{emob}. For any state of effective stress, $\tan\phi'_{mob\alpha}$ is, by definition, the ratio $\left(\tau_{\phi\alpha} / \sigma'_\alpha\right)$ in a plane given by α, whereas $\tan\phi'_{emob}$ is, for the same state of effective stress, given by $\left(\tau_{\phi\alpha} / \sigma'_\alpha\right)_{max}$ (see Equation 51). When failure is reached, $\phi'_{emob} = \phi'_e$.
6. The ordered pairs $\left(\sigma'_\alpha, \tau_{\eta\alpha}\right)$ define the *state of mobilized viscosity* of a soil, which is represented by the viscosity ellipse or Taylor's ellipse. On the other hand, the pairs $\left(\sigma'_\alpha, \tau_{\phi\alpha}\right)$ define the *state of mobilized friction*, represented by the friction ellipse or Coulomb's ellipse.
7. The two ellipses cannot exist separately since only the stresses given by the Mohr's circle can fulfill equilibrium conditions.
8. In a $\overline{\text{CIUCL}}$ test carried out with $\dot{\varepsilon}_a$ = constant and assuming that there is no significant change in soil structure, $\eta(e)$ = constant. Thus, the viscous part of the shear resistance $\tau_{\eta\alpha}$ is instantaneously mobilized at the beginning of the shear stage, remaining constant on that fixed plane given by α throughout the shear stage.
9. Since the deviator stress increases along the shear stage as ε_a increases, a conclusion to be drawn is that such deviator stress increase should be assigned to the mobilization of frictional resistance.
10. Failure occurs when frictional resistance is fully mobilized. Therefore, failure is ruled by the mobilization of the frictional resistance.
11. Failure occurs when $\tan\phi'_{emob} = \left(\tau_{\phi\alpha} / \sigma'_\alpha\right)_{max} = \tan\phi'_e$, which graphically corresponds to the friction ellipse tangency to the strength envelope, whose slope is $\tan\phi'_e$, being ϕ'_e the Hvorslev's *true angle of friction*.
12. Since there are no volume changes during the shear stage of a $\overline{\text{CIUCL}}$ test, there are only shear strains. Thus, frictional resistance mobilization is closely related to shear strains.
13. The frictional resistance mobilization at any instant of the shear stage of a $\overline{\text{CIUCL}}$ test can be quantified by $\tan\phi'_{emob} = \left(t' - \mathbb{V}\right) / \sqrt{s'^2 - t'^2}$.

6.2 Ideal $\overline{\text{CIUCL}}$ tests

During the shear stage of $\overline{\text{CIUCL}}$ tests it is usual to plot the deviator stress $\left(\sigma'_a - \sigma'_r\right)$ × axial strain $\left(\varepsilon_a\right)$ and developed pore pressure $\left(\Delta u\right)$ × $\left(\varepsilon_a\right)$. As in the shear

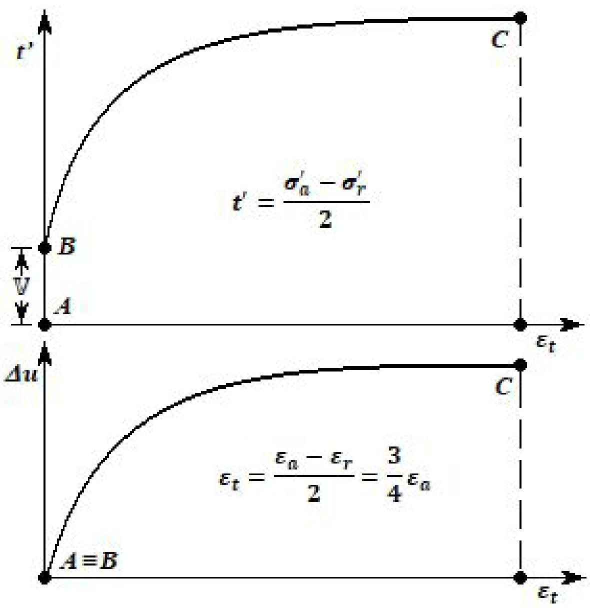

Figure 29. "Viscosity jump"- instantaneous mobilization of viscous resistance in $t' \times \varepsilon_t$ and $\Delta u \times \varepsilon_t$ plots (Martins, 1992).

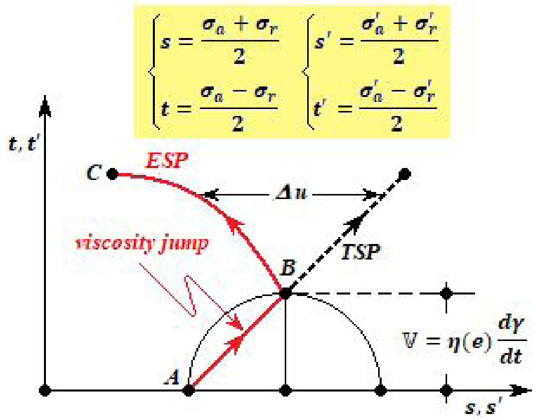

Figure 30. "Viscosity jump"- instantaneous mobilization of viscous resistance in $s' \times t'$ and $s \times t$ plots (Martins, 1992).

stage of a $\overline{\text{CIUCL}}$ test $\varepsilon_r = -\varepsilon_a / 2$, then the shear strain $\varepsilon_{s45°} = (\varepsilon_a - \varepsilon_r)/2 = (3/4)\varepsilon_a$.

Denoting $\varepsilon_{s45°}$ by ε_t, the shear stress associated with ε_t is $\tau_{45°} = (\sigma'_a - \sigma'_r)/2 = t'$. Thus, just as a matter of coherence, graphs $t' \times \varepsilon_t$ and $\Delta u \times \varepsilon_t$ will be plotted. As in $\overline{\text{CIUCL}}$ tests $\varepsilon_t = (3/4)\varepsilon_a$, the use of ε_t instead of ε_a for abscissa of $t' \times \varepsilon_t$ and $\Delta u \times \varepsilon_t$ plots does not alter their shapes.

Figure 29 presents curves $t' \times \varepsilon_t$ and $\Delta u \times \varepsilon_t$ expected for normally consolidated clays in a $\overline{\text{CIUCL}}$ test. This figure shows in the $t' \times \varepsilon_t$ plot an "initial jump" ***AB*** at $\varepsilon_t = 0$. Such "initial jump" or "viscosity jump" corresponds to the instantaneous mobilization of the viscous resistance given by $t' = \mathbb{V} = \eta(e)\dot{\gamma}$. Since the viscous part of the shear resistance is a function of the shear strain rate (and not of the shear strain), when the load frame motor is turned on, the viscous resistance will start to act immediately, when both shear strain (ε_t) and excess pore-pressure (Δu) are still zero. Thereafter, if the shear stage continues running with the same strain rate $\dot{\varepsilon}_t = \dot{\gamma}/2$, this viscous resistance will remain constant for the rest of the test.

The "viscosity jump" appears in both $s' \times t'$ effective stress path (from now on called ESP) and $s \times t$ total stress path (from now on called TSP), as shown in Figure 30. From point ***B*** in Figures 29 and 30, friction resistance begins to be mobilized gradually, pore pressure begins to increase and the specimen begins to undergo shear strains until reaching point ***C***, where all the available friction resistance is mobilized. It is when failure takes place.

In Figure 30, along the "viscosity jump", which goes from ***A*** to ***B*** instantaneously, the ESP and TSP are coincident. This "viscosity jump" causes the ESPs of normally consolidated clays to move to the right afterwards changing their direction moving to the left, as shown in Figure 30. It is important to note that the frictional resistance mobilized at point ***B*** is zero and, therefore, at point ***B*** there is only mobilization of viscous resistance.

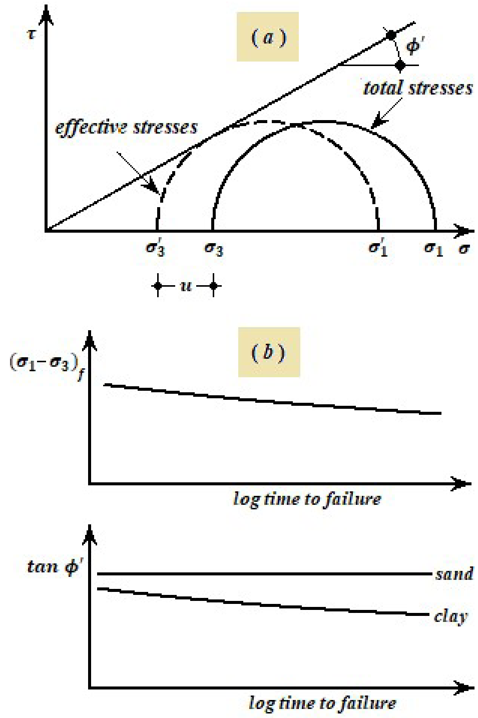

Figure 31. The effect of duration of test on undrained strength [adapted from Bishop & Henkel (1962)]: (a) Mohr circles at failure for a consolidated-undrained test on a normally consolidated clay; (b) Variation in measured strength with time to failure.

This shape of ESPs in $\overline{\text{CIUCL}}$ tests, as shown in Figure 30, seems to have been originally presented by Leroueil et al. cited by Jamiolkowski et al. (1991) and is reproduced in Figure 7. Such a feature suggests that both the critical state line (CSL) and the state boundary surface are not unique but dependent on the strain rate $\dot{\varepsilon}_t = d\varepsilon_t / dt$, or rather one CSL and one state boundary surface exist for each $\dot{\varepsilon}_t$ value. There are several experimental evidences supporting this idea. One of them is found in the following passage from Bishop & Henkel (1962), which refers to strain rate (although the phenomenon has been described as duration of test):

> *[IV] Duration of Test. The duration of test commonly used in the triaxial apparatus and the parameters by which the results are expressed are open to criticism on the grounds that they take no account of the phenomena of creep in soils [for example, Geuze, 1953*].
> *As the criticism is usually based on the results of undrained tests, it is necessary to separate the factors involved. The application of a shear stress to a saturated sample will result, under undrained conditions, in an excess pore pressure. Failure conditions in a consolidated-undrained test on a normally consolidated clay are represented in Figure 1a* (an adaptation is presented in Figure 31a of this article*) by an excess pore pressure u and an effective stress circle tangential to a failure envelope defined by the angle ϕ', c' being zero. If a sample consolidated under the same conditions is tested*

at a much lower rate of testing, it is found that the undrained strength $(\sigma_1 - \sigma_3)$ *is lower and that* ϕ' *has also decreased a little (*Figure 1b*)* (an adaptation is presented in Figure 31b of this article). *The drop in* ϕ' *is negligible for sands but may amount in some clays to about 5% decrease in tan* ϕ' *for each increase of ×10 in the duration of the test*. (Bishop & Henkel, 1962, pp. 30-31).

Taking into account that in a normally consolidated clay failure conditions ind icate that CSL is written as $q'_f = M\ p'_f$, being q'_f the deviator stress at failure ($q'_f = (\sigma'_a - \sigma'_r)_f$) and p'_f the mean effective stress at failure $p'_f = [(\sigma'_a + 2\sigma'_r)/3]_f$, with $M = 6\sin\phi' / (3 - \sin\phi')$, it is clear that if $\tan\phi'$ increases with $\dot{\varepsilon}_a$, M must also increase with $\dot{\varepsilon}_a$, or rather the CSL is dependent on the strain rate $\dot{\varepsilon}_a$. In this case, the CSL cannot be a clay property in the sense of being something intrinsic to the clay, a sense used by Burland (1990) for the word intrinsic. The same fact holds for Roscoe's surface, which would depend on strain rate. These two aspects are illustrated in Figure 7 (Leroueil et al. cited by Jamiolkowski et al., 1991). According to Figure 31, strain rate would not affect sands since they do not present the viscous effects because they do not have plasticity. Evidence that Bjerrum (1973) grasped the essence of the phenomenon mechanism as being of a viscous nature is the fact that he related its importance and magnitude to plasticity (evaluated by the plasticity index I_p).

6.3 A set of ideal $\overline{\text{CIUCL}}$ tests

The advantage of working with the mean effective stress $p' = (\sigma'_a + ü\sigma'_r)$ and the deviator stress $q' = (\sigma'_a - \sigma'_r)$ is their correspondence to the variables ε_v and γ. However, as there is a one-to-one correspondence between the ordered pairs (p', q') and (s', t'), it will make no difference whether one works with the pair (p', q') or with the pair (s', t') to draw stress paths. In this article, it has been preferred to work with the variables s' and t', as a matter of convenience.

Now, one will consider the results of three ideal $\overline{\text{CIUCL}}$ tests carried out on a normally consolidated clay, under isotropic effective stresses p'_e equal to $\sigma'_c, 2\sigma'_c$ and $3\sigma'_c$. The expected $t' \times \varepsilon_t$ and $\Delta u \times \varepsilon_t$ curves are shown in Figure 32: the curves are proportional to p'_e.

The effective stress paths on the $s' \times t'$ plane of these tests are presented in Figure 33 together with their curves $s' \times e$. The ESPs in the upper part of Figure 33 are homothetic with point ***O*** being the centre of homothety. Thus, the generated pore

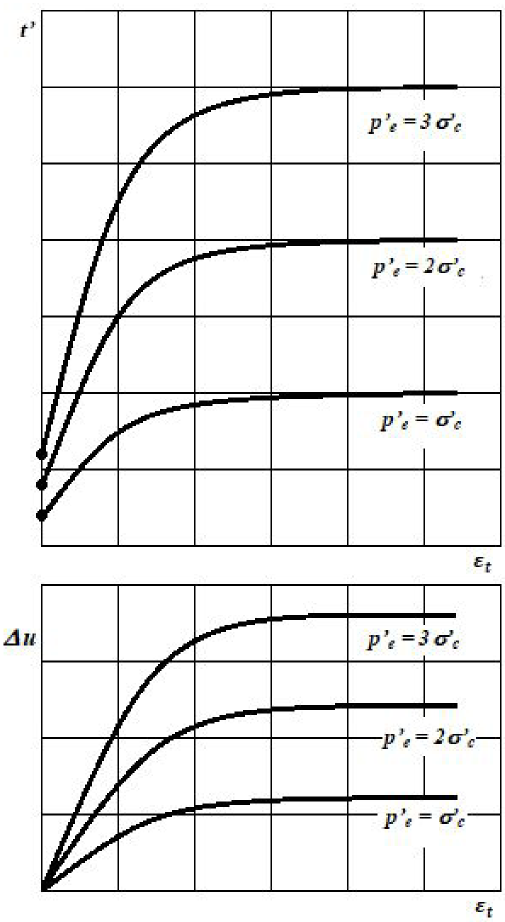

Figure 32. Curves $t' \times \varepsilon_t$ and $\Delta u \times \varepsilon_t$ for a set of ideal $\overline{\text{CIUCL}}$ tests on a normally consolidated clay.

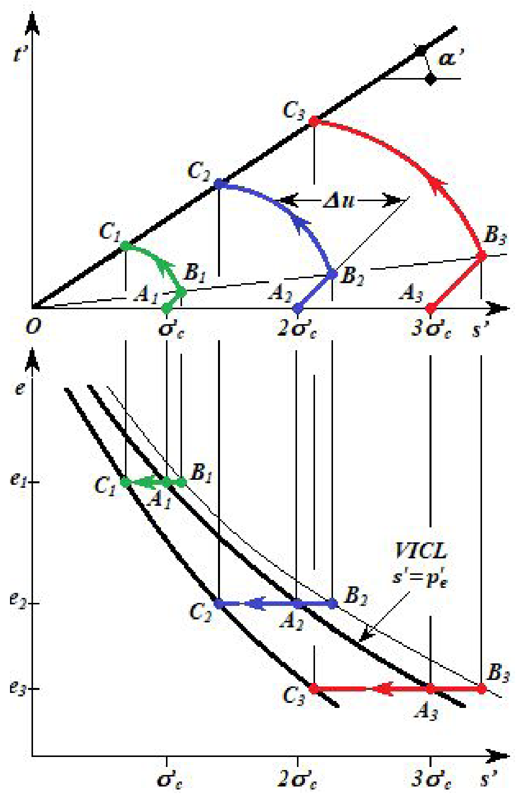

Figure 33. Paths on the $s' \times t'$ and $s' \times e$ planes followed by ideal $\overline{\text{CIUCL}}$ tests carried out on normally consolidated clay specimens under a given shear strain rate $\dot{\varepsilon}_t = \text{constant}$.

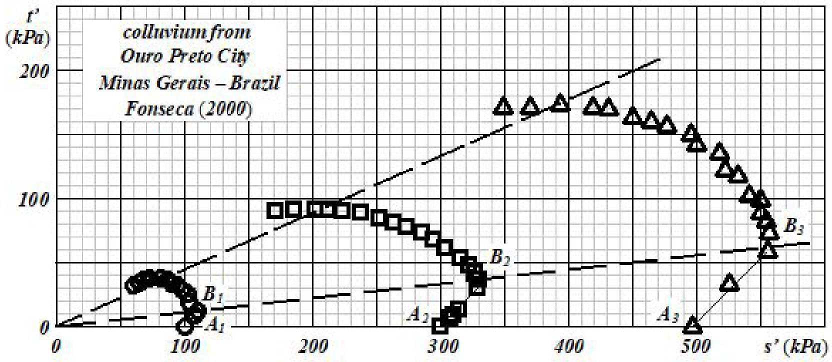

Figure 34. Effective stress paths in $\overline{\text{CIUCL}}$ tests and their respective "viscosity jumps" [adapted from Fonseca (2000)].

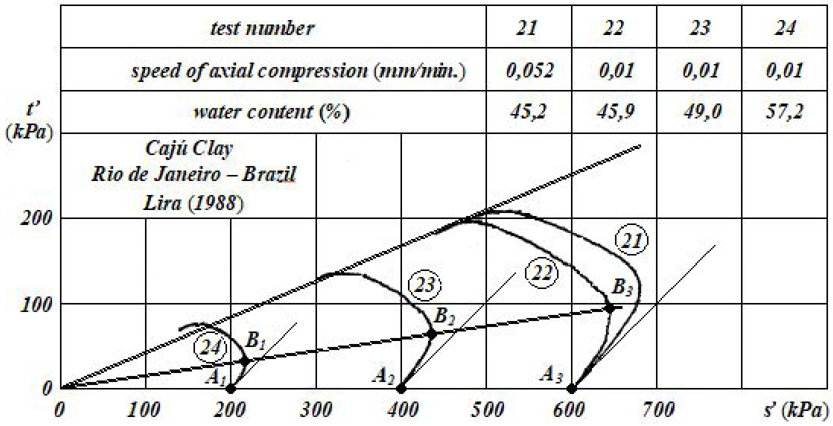

Figure 35. Effective stress paths in $\overline{\text{CIUCL}}$ tests and their respective "viscosity jumps" [adapted from Lira (1988)].

pressures (Δu) also form homothetic geometric figures. The paths followed on the plane $s' \times e$ (lower part of Figure 33) start on the virgin isotropic compression line (VICL), on the floor of the $s' \times t' \times e$ space, and develop on planes for which $e =$ constant. Paths on plane $s' \times e$ start from points $\boldsymbol{A_1}$, $\boldsymbol{A_2}$ and $\boldsymbol{A_3}$ and instantaneously move to the right to points $\boldsymbol{B_1}$, $\boldsymbol{B_2}$ and $\boldsymbol{B_3}$, respectively, forming the viscosity jumps $\boldsymbol{A_1B_1}$, $\boldsymbol{A_2B_2}$ and $\boldsymbol{A_3B_3}$. Along the segments $\boldsymbol{A_1B_1}$, $\boldsymbol{A_2B_2}$ and $\boldsymbol{A_3B_3}$ there is neither shear strain nor pore pressure generation. From points $\boldsymbol{B_1}$, $\boldsymbol{B_2}$ and $\boldsymbol{B_3}$ on, shear strains begin to be developed, the frictional resistance begins to be mobilized and there is pore pressure generation. Specimens fail when points $\boldsymbol{C_1}$, $\boldsymbol{C_2}$ and $\boldsymbol{C_3}$ are reached, on the failure envelope. In the space $p' \times q' \times v$ (where v is the specific volume, $v = 1 + e$), points $\boldsymbol{C_1}$, $\boldsymbol{C_2}$ and $\boldsymbol{C_3}$ are on a critical state line corresponding to the same strain rate $\dot{\varepsilon}_t$ used in the three tests.

According to Equation 47, for a given clay and for a given point (e, p'_e) on the VICL, the "viscosity jump" $\mathbb{V}$ would be proportional to the distortion rate $\dot{\gamma}$. Nevertheless, experimental results have been shown that viscous resistance is not proportional to $\dot{\gamma}$. Thus, it is more correct to rewrite the viscous resistance parameter $\mathbb{V}$ as a non-linear function f of the distortion rate, or rather

$$\mathbb{V} = \eta(e) f(\dot{\gamma}) \tag{59}$$

being f an exclusive function of the distortion rate $(\dot{\gamma})$ and not of the angle α, which indicates the plane considered. Then, for e and $\dot{\gamma}$ as constants, $\mathbb{V} = \eta(e) f(\dot{\gamma})$ is also a constant. Thus, Equation 46 can be rewritten as:

$$\tau_{\eta\alpha} = \eta(e) f\left[\frac{d(\varepsilon_a - \varepsilon_r)}{dt}\right] sin\, 2\alpha = \eta(e) f(\dot{\gamma}) sin\, 2\alpha \tag{60}$$

Thus, in a test where $\dot{\gamma} = \text{constant}$, $f(\dot{\gamma}) = \text{constant}$ and, therefore, both the viscosity ellipse, whose half of minor axis corresponds to $\mathbb{V} = \eta(e) f(\dot{\gamma})$, and the friction ellipse remain valid. The only difference is that the viscous resistance does not follow Newton's law of viscosity, or rather viscous resistance in plastic soils is non-newtonian. Furthermore, Equations 52 to 56 remain valid since derivatives are taken respective to angle α with the aim of determining $tan\, \phi'_{emob}$. Thus, Equation 56 still holds valid.

Regardless of function type, the viscous resistance component $\mathbb{V}$ must have the physical dimension of stress. Experimental data suggest that for normally consolidated clays the "viscosity jump" $\mathbb{V}$ is proportional to the isotropic consolidation stress p'_e, a feature that had already been identified by Taylor (1948, pp. 377-378). Such a feature can be observed for two clays in Figures 34 and 35.

Based on these experimental evidences, it can be written as

$$\mathbb{V} = \eta(e) f(\dot{\gamma}) = C_\eta(\dot{\gamma}) p'_e \tag{61}$$

Thus, viscous resistance $\mathbb{V}$, geometrically identified by the "viscosity jump", can be written as a linear function of p'_e, whose coefficient C_η is a non – linear function of the distortion rate $\dot{\gamma}$ (and also of the soil structure).

The viscosity jumps $\boldsymbol{A_1B_1}$, $\boldsymbol{A_2B_2}$ and $\boldsymbol{A_3B_3}$ in Figures 33 to 35 do not always appear clearly. The author does not know how to explain precisely the reason for that. The author believes that some of the possible reasons are the filter paper and porous stones adjustments, the non-coaxiality between the piston and the specimen axes, the silicone grease when lubricated ends are used, etc. Even when the same equipment, the same soil, the same specimen preparation and the same test procedures are used, sometimes the viscosity jump clearly appears and other times it does not. Although this issue will not be discussed here, it is a practical aspect that deserves more investigation.

7. A model of behaviour for saturated normally consolidated clays taking into account strain rate in $\overline{\text{CIUCL}}$ tests

7.1 Normalization of $s' \times t'$, $t' \times \varepsilon_t$ and $\Delta u \times \varepsilon_t$ curves

This work is supported by experimental evidences and basic hypotheses.

The experimental evidences, which are also considered as hypotheses, are as follows:

1. Normally consolidated, saturated specimens of a given clay consolidated to different isotropic stresses p'_e in $\overline{\text{CIUCL}}$ tests and sheared with the same $\dot{\varepsilon}_t = \dot{\gamma}/2 = \text{constant}$ show geometrically similar curves $t' \times \varepsilon_t$ and $\Delta u \times \varepsilon_t$. They also show homothetic $p' \times q'$ and $s' \times t'$ effective stress paths with origin as the centre of homothety. This is to say: for a fixed strain rate $\dot{\varepsilon}_t$ the clay exhibit normalized behaviour respective to p'_e.
2. For a given strain rate $\dot{\varepsilon}_t$, the ordered triples (p'_f, q'_f, v_f) with subscripts *f* denoting failure define a smooth curve in the (p', q', v) space called the critical state line (CSL) associated with that given strain rate $\dot{\varepsilon}_t$. For each strain rate there is only one corresponding CSL.
3. The projection of a CSL associated with a fixed $\dot{\varepsilon}_t$ on the planes $p' \times q'$ and $s' \times t'$ is a straight line passing through the origin.

The basic hypotheses are the following:

4. Validity of PES equation: $\sigma' = \sigma - u$.
5. At any instant the shear stress τ_α acting on plane whose normal makes an angle α with the direction of σ_1 consists of two parts: a friction part $\tau_{\phi\alpha}$ and a viscous part $\tau_{\eta\alpha}$, or rather $\tau_\alpha = \tau_{\phi\alpha} + \tau_{\eta\alpha}$.
6. The viscous part $\tau_{\eta\alpha}$ is written as $\tau_{\eta\alpha} = \eta(e) f(\dot{\gamma}) sin\, 2\alpha$, being $\eta(e)$ defined as the soil viscosity, a function of void ratio and structure, and $f(\dot{\gamma})$ an exclusive function of distortion rate $\dot{\gamma}$. On the plane whose normal makes 45° with the direction of σ_1, $2\alpha = 90°$ and $\tau_{\eta 45°} = \eta(e) f(d(\varepsilon_1 - \varepsilon_3)/dt) = \eta(e) f(\dot{\gamma}) = \mathbb{V}$.
7. The friction part on a plane whose normal makes an angle α with the direction of σ_1 corresponds to $\tau_{\phi\alpha} = \tau - \tau_{\eta\alpha} = \left[(\sigma'_1 - \sigma'_3)/2 - \mathbb{V}\right] sin\, 2\alpha$.
8. The couples $(\sigma'_\alpha, \tau_{\eta\alpha})$ define the *state of mobilized viscosity* of a soil, which is represented by the viscosity ellipse. The couples $(\sigma'_\alpha, \tau_{\phi\alpha})$ define the *state of mobilized friction*, which is represented by the friction ellipse. The sum of these two ellipses corresponds to the Mohr's circle of effective stress and, therefore, they cannot exist separately since only the stresses given by the Mohr's circle meet equilibrium.
9. As a consequence of hypotheses (5) and (6), during the undrained shear stage of a $\overline{\text{CIUCL}}$ test carried out with $\dot{\varepsilon}_t = \text{constant}$, $\tau_{\eta\alpha}$ is instantaneously mobilized and remains constant up to the end of shear. During the undrained shear of a $\overline{\text{CIUCL}}$ test there is no volume change but only shear strains. Thus, the increase of the deviator stress along the undrained shear is due to the frictional resistance mobilization, which occurs due to the development of shear strains. Therefore, the failure process is ruled by the frictional resistance mobilization. For a given distortion γ, the frictional resistance is fully mobilized and failure occurs. This means that, in a normally consolidated clay, failure occurs when the friction ellipse touches the strength envelope, which is the straight line with slope $tan\, \phi'_e$, as illustrated in Figure 28. In other words, failure occurs when

$$tan\, \phi'_{emob} = \frac{\left(\dfrac{\sigma'_{1f} - \sigma'_{3f}}{2} - \mathbb{V}\right)}{\sqrt{\sigma'_{1f}\sigma'_{3f}}} = \frac{(t'_f - \mathbb{V})}{\sqrt{s'^2_f - t'^2_f}} = tan\, \phi'_e \tag{62}$$

where subscript *f* indicates failure and ϕ_e' is the Hvorslev's "*true angle of internal friction*".

10. Finally, another hypothesis concerning viscous resistance $\mathbb{V}$, which comes from experimental evidences, is that $\mathbb{V}$ is proportional to isotropic consolidation stress p_e'. Thus, $\mathbb{V} = \eta(e) f(\dot{\gamma}) = C_\eta(\dot{\gamma}) p_e'$ (see Equation 61 and Figures 34 and 35), being $C_\eta(\dot{\gamma})$ a non-linear function of distortion rate $\dot{\gamma}$ and of soil structure.

Although this article is limited to normally consolidated clays subjected to CIUCL tests, it is possible to extend the model presented herein to overconsolidated clays. Part of the ten items listed above can be viewed as an extension of Terzaghi's PES and make it possible to consider the influence of strain rate on a failure criterion which gathers concepts from Newton, Mohr, Coulomb, Terzaghi, Hvorslev, Taylor and Bjerrum. Such influence of strain rate occurs by means of Newton's viscosity concept, despite soils viscous resistance does not obey Newton's law of viscosity. In plastic soils the viscous resistance to shear comes from the distortion of viscous adsorbed water whenever two clay particles in contact are moving relative to each other (Terzaghi & Frölich, 1936; Terzaghi, 1941; Taylor, 1942; Taylor, 1948). Such viscous adsorbed water provides clayey soils with plasticity. It is for that reason that Bjerrum (1973) associates strain rate effects with plasticity index. Unfortunately, many times the viscous component of shear resistance is inadequately called "cohesion". As understood by Coulomb and explained by Schofield (1999, 2001), cohesion originates from cementation between grains, like in rocks and saprolites, providing materials with a tensile strength, which is a consequence of true cohesion, as discussed in section 4.1. Therefore, cohesion as defined by Coulomb has a different physical meaning from the "true cohesion" as defined by Hvorslev. Unfortunately, the expression "true cohesion" was used by Hvorslev (1937, 1960) and Terzaghi (1938) improperly, bringing the conceptual confusion raised up by Schofield (1999, 2001). In this article, the strain rate effect on the undrained shear strength is evaluated via viscous resistance originating from the action of adsorbed water on the behaviour of plastic soils.

Back to the geometric similarity in Figure 32 and to the homothety of the ESPs in Figure 33, the curves $t' \times \varepsilon_t$ and $\Delta u \times \varepsilon_t$ and ESPs $s' \times t'$ can be scaled by division by p_e'. Thereby, the normalized curves $(t' / p_e') \times \varepsilon_t$ and $(\Delta u / p_e') \times \varepsilon_t$ and the normalized ESPs $(s' / p_e') \times (t' / p_e')$ in Figure 36 are obtained, provided the strain rate $\dot{\varepsilon}_t$ is the same and kept constant for all tests.

The straight line with slope $tan\,\phi'$ passing through the origin, shown in Figures 15 and 28, is the strength envelope for a normally consolidated clay on the $\tau \times \sigma'$ plane. According to the approach herein developed, such an envelope includes two strength components: the frictional component and the viscous component. Moreover, as stated in experimental evidence (1) of this section, for a fixed strain rate $\dot{\varepsilon}_t$, all ESPs on the $s' \times t'$ plane are homothetic with the origin as the centre of homothety. However, according to hypothesis (9), failure is not determined when the Mohr's circle of effective stresses touches the envelope with slope $tan\,\phi'$, but when the friction ellipse touches the straight line whose slope is $tan\,\phi_e'$, being ϕ_e' the Hvorslev's true angle of internal friction, which is a property of the soil. Thus, the question to be answered is: how can one explain and conciliate the envelope with slope $tan\,\phi'$, which gives the real strength of the soil, and the envelope whose slope is $tan\,\phi_e'$, by which failure is ruled? To answer this question, one must take into account the experimental evidences and basic hypotheses listed in the beginning of this section as well as the following discussion based on Figure 37.

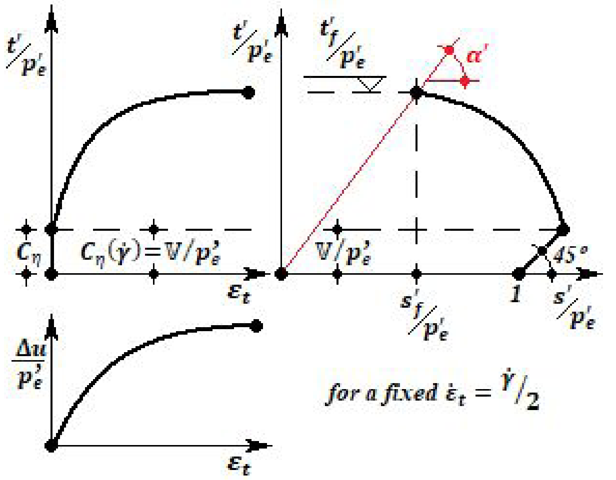

Figure 36. Normalized curves $(t' / p_e') \times \varepsilon_t$ and $(\Delta u / p_e') \times \varepsilon_t$ and normalized ESPs $(s' / p_e') \times (t' / p_e')$ for a fixed strain rate $\dot{\varepsilon}_t$.

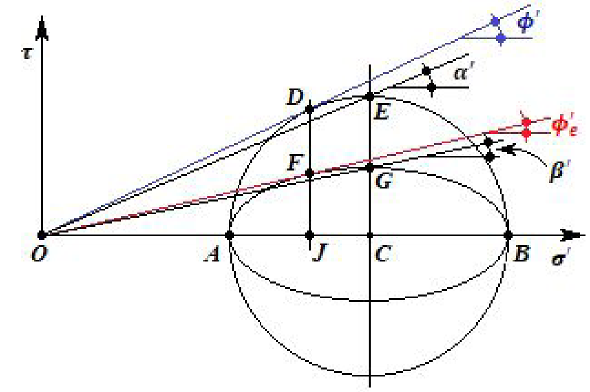

Figure 37. Definition of angles α', β', ϕ' and ϕ_e'.

From Figure 37 it immediately follows that points ***D*** and ***F*** lie on the same vertical straight line since ellipse ***AFGB*** can be obtained from a rotation of Mohr's circle

ADEB around the σ' axis of an angle $\theta = arc\ \cos\left(\boldsymbol{CG / CE}\right)$. Moreover, since normalization respective to p'_e holds valid, Figure 37 could be drawn using for abscissas and ordinates the normalized parameters s' / p'_e and t' / p'_e, respectively. Accordingly, one can go back to Figure 36 and write:

$$t'_f / p'_e = \left(s'_f / p'_e\right) tan\,\alpha' \tag{63}$$

Owing to the homothety of tests results carried out with $\dot{\gamma} = \text{constant}$, one comes to the conclusion that, for a given normally consolidated clay, when $\dot{\gamma}$ is fixed, the s'_f / p'_e and t'_f / p'_e values will automatically be determined, or rather $\left(s'_f / p'_e\right) = f_1\left(\dot{\gamma}\right)$ and $\left(t'_f / p'_e\right) = f_2\left(\dot{\gamma}\right)$, being f_1 and f_2 exclusive functions of $\dot{\gamma}$. Now recalling the hypothesis which assumes that shear stress consists of a frictional component and a viscous component, one can write that at failure

$$t'_f = s'_f\ tan\,\beta' + \mathbb{V} \tag{64}$$

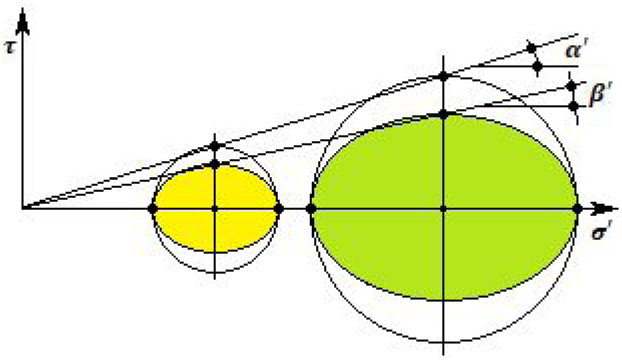

Figure 38. Homothetic (same eccentricity) friction ellipses at failure.

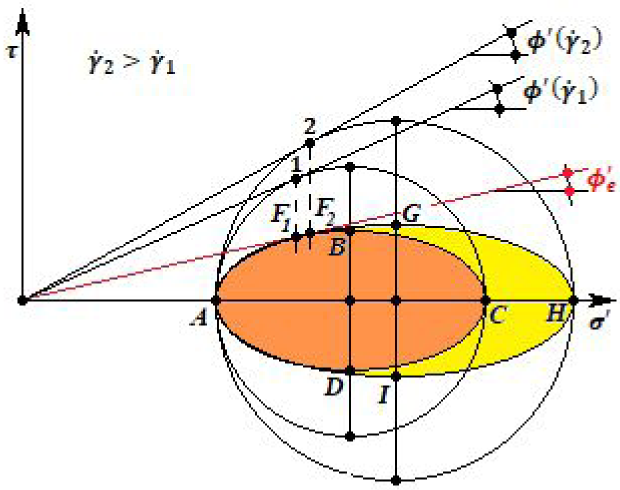

Figure 39. Friction ellipses at failure with different eccentricities, both tangent to the same failure envelope of slope $tan\,\phi'_e$, resulting from $\overline{\text{CIUCL}}$ tests with different distortion rates $\dot{\gamma}$.

Dividing both sides of Equation 64 by p'_e, Equation 65 is obtained as follows:

$$t'_f / p'_e = \left(s'_f / p'_e\right) tan\,\beta' + \mathbb{V} / p'_e \tag{65}$$

However, as $\left(s'_f / p'_e\right) = f_1\left(\dot{\gamma}\right)$, $\left(t'_f / p'_e\right) = f_2\left(\dot{\gamma}\right)$ and, according to Equation 61, $\mathbb{V} / p'_e = C_\eta\left(\dot{\gamma}\right)$, Equation 65 can be rewritten as

$$f_2\left(\dot{\gamma}\right) = f_1\left(\dot{\gamma}\right) tan\,\beta' + C_\eta\left(\dot{\gamma}\right) \tag{66}$$

or

$$tan\,\beta' = \frac{f_2\left(\dot{\gamma}\right) - C_\eta\left(\dot{\gamma}\right)}{f_1\left(\dot{\gamma}\right)} \tag{67}$$

Equation 67 leads to the conclusion that, assuming shear resistance consists of a frictional component and a viscous component, whenever a given normally consolidated clay, sheared with $\dot{\gamma} = \text{constant}$ in a $\overline{\text{CIUCL}}$ test, presents homothetic ESPs, friction ellipses at failure will be homothetic, or rather they will have the same eccentricity, as shown in Figure 38.

When two or more specimens of the same clay are normally consolidated to the same isotropic stress in $\overline{\text{CIUCL}}$ tests, but sheared with different distortion rates, for instance, $\dot{\gamma}_2 > \dot{\gamma}_1$, the friction angle $\phi'\left(\dot{\gamma}_2\right)$ will be greater than the friction angle $\phi'\left(\dot{\gamma}_1\right)$ (see Figure 39). In this case, the friction ellipse at failure ***AGHI*** will present a greater eccentricity than that of the friction ellipse at failure ***ABCD***. The Mohr's circle of effective stresses at failure corresponding to the test carried out with $\dot{\gamma}$ will be larger than that obtained from the test carried out with $\dot{\gamma}_1$. However, both friction ellipses at failure will be tangent to the friction envelope at points $\boldsymbol{F_1}$ and $\boldsymbol{F_2}$. This friction envelope, which is unique for a given normally consolidated clay, is the straight line passing through the origin with slope $tan\,\phi$. Thus, any $\overline{\text{CIUCL}}$ test carried out on the same normally consolidated clay, irrespective of the distortion rate $\dot{\gamma}$ and irrespective of p'_e, will present at failure a friction ellipse which will be tangent to the straight line envelope whose slope is $tan\,\phi'_e$.

7.2 Strain rate effects – additional experimental evidences

In order to quantify the strain rate in the shear stage of a $\overline{\text{CIUCL}}$ test, the variable $\dot{\varepsilon}_t$ will be used from now on. Recalling that as $\varepsilon_t = \left(\varepsilon_a - \varepsilon_r\right)/2$ or $\varepsilon_t = \left(\gamma / 2\right)$ and that during the shear stage of a $\overline{\text{CIUCL}}$ test there is no volume change, one concludes that $\varepsilon_t = \left(3/4\right)\varepsilon_a$, which entails that $\dot{\varepsilon}_t = \left(3/4\right)\dot{\varepsilon}_a$.

Lacerda (1976) carried out a set of $\overline{\text{CIUCL}}$ tests on San Francisco Bay Mud samples, applying different strain rates in the undrained shear phase, during which stress

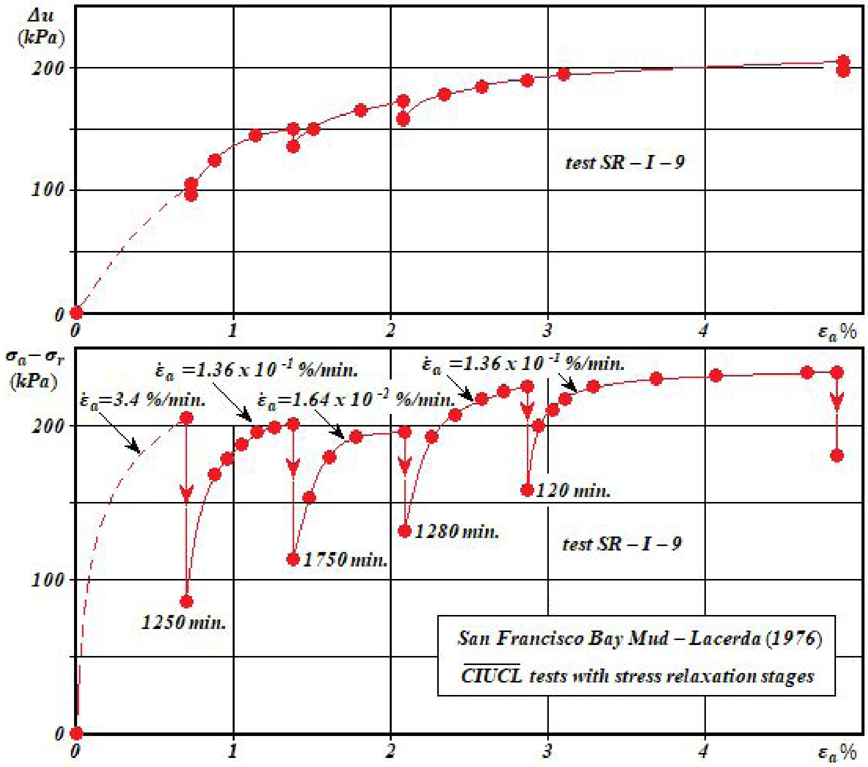

Figure 40. $\overline{\text{CIUCL}}$ test with different strain rates and stress relaxation stages.

relaxation stages were accomplished (see Figure 40). Such stress relaxation stages consist in turning off the load frame motor during the undrained shear phase, for a given time interval, monitoring deviator stress and pore pressure over time.

With the load frame motor turned off, $\dot{\varepsilon}_t$ becomes zero and, therefore, during a stress relaxation stage carried out in the undrained shear phase of a $\overline{\text{CIUCL}}$ test, both volume and shear strains changes are zero. This kind of test, usually called stress relaxation test, would more properly be called $\overline{\text{CIUCL}}$ test with stress relaxation stages. Lacerda (1976) investigated strain rate effects by turning on the load frame motor after the end of the stress relaxation stages at different speeds. A typical result of such a test is shown in Figure 40.

The main features observed by Lacerda (1976), common to all $\overline{\text{CIUCL}}$ tests with stress relaxation stages carried out with different $\dot{\varepsilon}_t$ values on normally consolidated specimens from San Francisco Bay Mud, were the following:

a) The size of $\Delta u \times \varepsilon_t$ curves is proportional to the isotropic stress p'_e to which the specimen was consolidated.

b) For a given isotropic consolidation stress p'_e, the curve $\Delta u \times \varepsilon_t$ is unique, regardless of the shear strain rate $\dot{\varepsilon}_t$.

c) Tests with greater $\dot{\boldsymbol{\varepsilon}}_t$ values present higher $(\sigma_a - \sigma_r)$ values for the same ε_t.

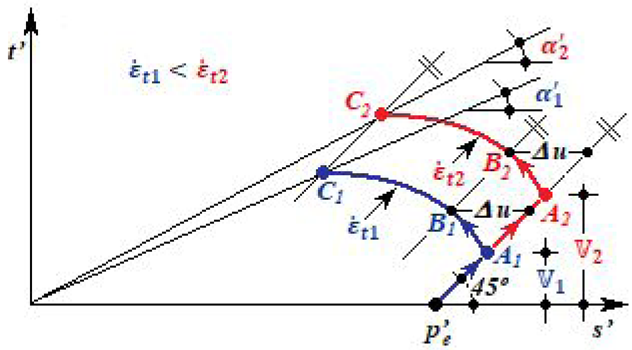

Figure 41. Effective stress paths for $\overline{\text{CIUCL}}$ tests starting out from the same p'_e but corresponding to different strain rates $\dot{\varepsilon}_{t1}$ and $\dot{\varepsilon}_{t2}$ with $\dot{\varepsilon}_{t1} < \dot{\varepsilon}_{t2}$.

d) The pore pressure decrease observed during stress relaxation stages are very small if compared to the deviator stress decrease.

Features b) and d) allow to assume, as an additional hypothesis, that pore pressure does not depend on the shear strain rate $\dot{\varepsilon}_t$, being only dependent on the shear strain ε_t and on the isotropic effective stress p'_e to which the specimen was consolidated. The assumption that pore pressure does

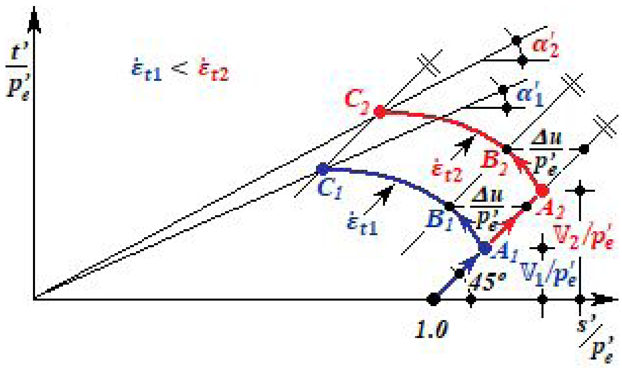

Figure 42. Normalized effective stress paths $\left(s' / p'_e\right) \times \left(t' / p'_e\right)$ for $\overline{\text{CIUCL}}$ tests corresponding to different strain rates $\dot{\varepsilon}_{t1}$ and $\dot{\varepsilon}_{t2}$ with $\dot{\varepsilon}_{t1} < \dot{\varepsilon}_{t2}$.

not depend on $\dot{\varepsilon}_t$ means that pore pressure will remain constant even during a stress relaxation stage, when $\dot{\varepsilon}_t = 0$. This additional assumption, based on such experimental evidences, allows Figure 41 to be drawn.

Figure 41 shows that tests starting from the same isotropic effective stress p'_e, but carried out with different $\dot{\varepsilon}_t$ values, will present, after the viscosity jumps, ESPs which change their directions to the left, until they attain envelopes with different α' values. Nevertheless, as previously explained, all the states of fully mobilized friction are represented by their respective friction ellipses at failure, which are tangent to the same friction strength envelope whose slope is $tan\,\phi'_e$ (see Figure 39).

Taking into account that $tan\,\phi'_{emob} = \left(t' - \mathbb{V}\right) / \sqrt{s'^2 - t'^2}$, it can be concluded that, at points $\boldsymbol{A_1}$ and $\boldsymbol{A_2}$ in Figure 41, $tan\,\phi'_{emob} = 0$. In a similar way, at points $\boldsymbol{C_1}$ and $\boldsymbol{C_2}$, which represent failure, $tan\,\phi'_{emob} = tan\,\phi'_e$. Besides, experimental evidences indicate that, during $\overline{\text{CIUCL}}$ tests on two normally consolidated specimens of the same clay starting from the same p'_e, the following features are observed:

a) Pore pressure Δu does not depend on the shear strain rate $\dot{\varepsilon}_t$.
b) Pore pressure Δu does depend on the strain ε_t.

Thus, it is expected that points like $\boldsymbol{B_1}$ and $\boldsymbol{B_2}$ in Figure 41 have the same values of ε_t, Δu and $tan\phi'_{emob}$, irrespective of the shear strain rate $\dot{\varepsilon}_t$. This working hypothesis, whose validity must be checked experimentally, may be presented in the *complementary principle 1*, as stated below:

Complementary principle 1: All $\overline{\text{CIUCL}}$ tests carried out on a given normally consolidated clay compressed to the same isotropic effective stress p'_e will present, for any fixed shear strain ε_t, the same pore pressure Δu and the same ϕ'_{emob}, provided the points taken from the several ESPs (each ESP corresponding to a different $\dot{\varepsilon}_t$) lie on the same 45º sloped straight line. In other words: points of intersection between a 45º sloped straight line and ESPs corresponding to different shear strain rates $\dot{\varepsilon}_t$ have the same ε_t, Δu and ϕ'_{emob} (see points $\boldsymbol{B_1}$ and $\boldsymbol{B_2}$ in Figure 41).

It should be added that, in $\overline{\text{CIUCL}}$ tests carried out with the same $\dot{\varepsilon}_t$, the curves $t' \times \varepsilon_t$ and $\Delta u \times \varepsilon_t$ and ESPs can be normalized with respect to p'_e. This means that, for $\overline{\text{CIUCL}}$ tests carried out with the same $\dot{\varepsilon}_t$, the curves $t' / p'_e \times \varepsilon_t$, $\Delta u / p'_e \times \varepsilon_t$ and the normalized ESPs in the plane $\left(s' / p'_e\right) \times \left(t' / p'_e\right)$ will also be unique. However, if the pore pressure during $\overline{\text{CIUCL}}$ tests is not affected by the shear strain rate $\dot{\varepsilon}_t$, the curves $\Delta u / p'_e \times \varepsilon_t$ will be unique, irrespective of the $\dot{\varepsilon}_t$ value. Thus, Figure 41 can be redrawn in the $\left(s' / p'_e\right) \times \left(t' / p'_e\right)$ plane and pore pressure can also be normalized with respect to p'_e, as shown in Figure 42.

7.3 Strain rate effects – basic curves

In order to generalize the concepts presented in section 7.2, two $\overline{\text{CIUCL}}$ tests carried out on a normally consolidated clay will now be considered, both starting from the same isotropic effective stress p'_e. In one of these tests $\dot{\varepsilon}_t \neq 0$ whereas in the other $\dot{\varepsilon}_t = 0$. It is obvious that a real $\overline{\text{CIUCL}}$ test cannot be carried out with $\dot{\varepsilon}_t = 0$. However, assuming valid the *complementary principle 1*, the curves $t' \times \varepsilon_t$ and $\Delta u \times \varepsilon_t$ and the ESP on the $s' \times t'$ plane, all corresponding to $\dot{\varepsilon}_t = 0$, can be obtained from the curves $t' \times \varepsilon_t$ and $\Delta u \times \varepsilon_t$ and the ESP on the $s' \times t'$ plane achieved from a test carried out with $\dot{\varepsilon}_t \neq 0$. That is what will be explained next.

The name *basic curves* (denoted by the subscript b in the parameters s' and t' as s'_b and t'_b) will be given to all curves corresponding to $\dot{\varepsilon}_t = 0$. Such basic curves can be drawn from the tests carried out with $\dot{\varepsilon}_t \neq 0$ subtracting the viscous resistance effects.

The main advantage of plotting basic curves is that they are free from viscous effects and, therefore, they are not dependent on the shear strain rate $\dot{\varepsilon}_t$. Thus, such basic curves only give the effects of the frictional resistance.

Figure 43 shows the curves $t' \times \varepsilon_t$ and $\Delta u \times \varepsilon_t$ and the ESP on the $s' \times t'$ plane for a given p'_e and a given $\dot{\varepsilon}_t \neq 0$. The basic curves $t'_b \times \varepsilon_t$ and $\Delta u \times \varepsilon_t$ and the ESP $t'_b \times s'_b$ for the same p'_e and $\dot{\varepsilon}_t = 0$ are also shown in Figure 43. The effective stress path for which $\dot{\varepsilon}_t = 0$ will be called *basic effective stress path* and denoted by bESP.

In Figure 43 the curve $t' \times \varepsilon_t$ and the ESP of the test carried out with $\dot{\varepsilon}_t \neq 0$ show the initial jump $\boldsymbol{AB}$ corresponding to the instantaneous mobilization of the viscous resistance. From point $\boldsymbol{B}$ on, the test carried out with $\dot{\varepsilon}_t \neq 0$ begins to develop shear strains ε_t and pore pressures Δu, with friction mobilization, following the curves $\boldsymbol{BYN}$, until failure is reached at point $\boldsymbol{N}$. The basic curves, corresponding to $\dot{\varepsilon}_t = 0$, do not show the initial jump since for $\dot{\varepsilon}_t = 0$ the viscous

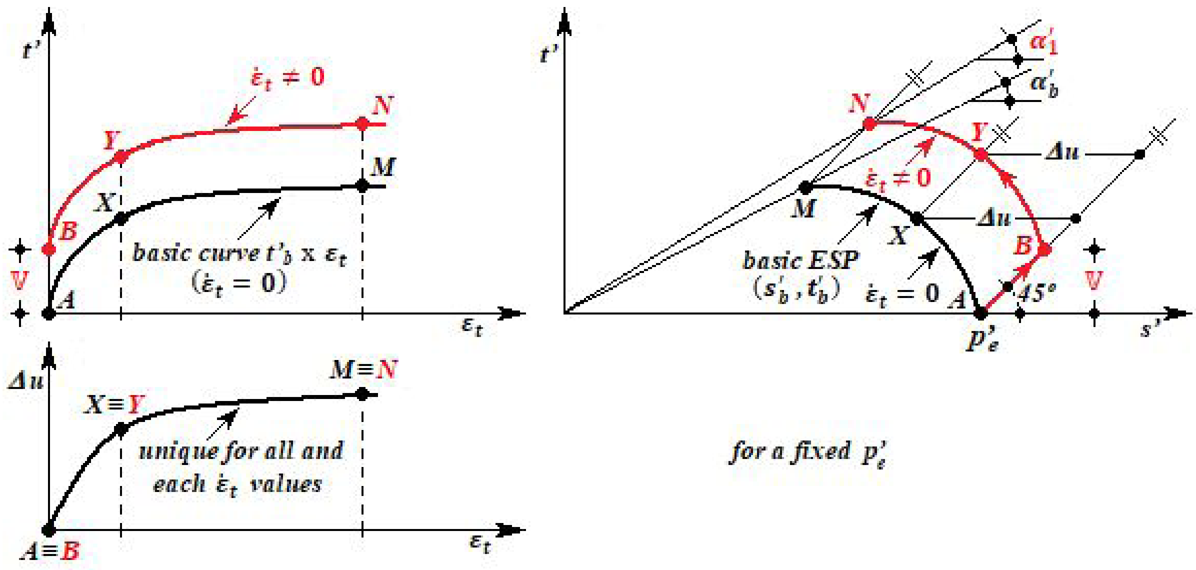

Figure 43. $\overline{\text{CIUCL}}$ tests carried out with a fixed p'_e and $\dot{\varepsilon}_t \neq 0$ and $\dot{\varepsilon}_t = 0$ (basic curves).

resistance vanishes. Thus, when $\dot{\varepsilon}_t = 0$, there is only friction mobilization, which occurs as soil is deformed in shear along the curves ***AXM***.

Another feature which is worth noting in Figure 43 is that for a given p'_e the curve $\Delta u \times \varepsilon_t$ is unique since pore pressure is assumed to be not dependent on $\dot{\varepsilon}_t$. Recalling that this is an assumption based on experimental evidences, as shown in Figure 40.

The relationship between the coordinates of point ***Y*** which lies on the ESP associated with a fixed $\dot{\varepsilon}_t \neq 0$ and the coordinates of point ***X*** which lies on the bESP (associated with $\dot{\varepsilon}_t = 0$), both points lying on the same 45º sloped straight line, can now be derived considering Figure 44.

In Figure 44 the ESP defined by points ***BYN*** corresponds to the shear stage of a $\overline{\text{CIUCL}}$ test carried out with a fixed $\dot{\varepsilon}_t \neq 0$. The coordinates of points ***B***, ***Y*** and ***N*** are $\left(s'(\boldsymbol{B}), t'(\boldsymbol{B})\right)$, $\left(s'(\boldsymbol{Y}), t'(\boldsymbol{Y})\right)$ and $\left(s'(\boldsymbol{N}), t'(\boldsymbol{N})\right)$ respectively. On the other hand, the bESP, corresponding to a $\overline{\text{CIUCL}}$ test carried out with $\dot{\varepsilon}_t = 0$, is the curve defined by points ***A***, ***X*** and ***M***, whose coordinates are, respectively, $\left(s'_b(\boldsymbol{A}), t'_b(\boldsymbol{A})\right)$, $\left(s'_b(\boldsymbol{X}), t'_b(\boldsymbol{X})\right)$ and $\left(s'_b(\boldsymbol{M}), t'_b(\boldsymbol{M})\right)$. According to the *complementary principle 1*, points ***Y*** and ***X*** which lie on the same 45º sloped straight line have the same values of $\tan\phi'_{emob}$, that is:

$$\tan\phi'_{emob}(\boldsymbol{Y}) = \frac{t'(\boldsymbol{Y}) - \mathbb{V}}{\sqrt{\left(s'(\boldsymbol{Y})\right)^2 - \left(t'(\boldsymbol{Y})\right)^2}} = \tag{68}$$
$$\tan\phi'_{emob}(\boldsymbol{X}) = \frac{t'_b(\boldsymbol{X})}{\sqrt{\left(s'_b(\boldsymbol{X})\right)^2 - \left(t'_b(\boldsymbol{X})\right)^2}}$$

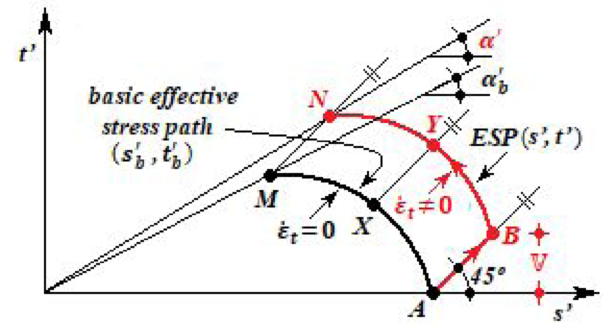

Figure 44. Relationship between coordinates of a point ***Y*** on the ESP for a fixed $^{\cdot} \neq 0$ and coordinates of a corresponding point ***X*** on the bESP (associated with $\dot{\varepsilon}_t = 0$).

Besides,

$$\frac{t'(\boldsymbol{Y}) - t'_b(\boldsymbol{X})}{s'(\boldsymbol{Y}) - s'_b(\boldsymbol{X})} = 1 \tag{69}$$

Particularly, for points ***A*** and ***B***,

$$\tan\phi'_{emob}(\boldsymbol{B}) = \tan\phi'_{emob}(\boldsymbol{A}) = 0 \tag{70}$$

and for points ***N*** and ***M***, corresponding to failure,

$$\tan\phi'_{emob}(\boldsymbol{N}) = \tan\phi'_{emob}(\boldsymbol{M}) = \tan\phi'_e \tag{71}$$

From the coordinates of points ***Y*** that define the ESP of a real $\overline{\text{CIUCL}}$ test carried out with a fixed $\dot{\varepsilon}_t \neq 0$, the coordinates of points ***X*** that define the bESP can be determined (see Figures 44 and 45).

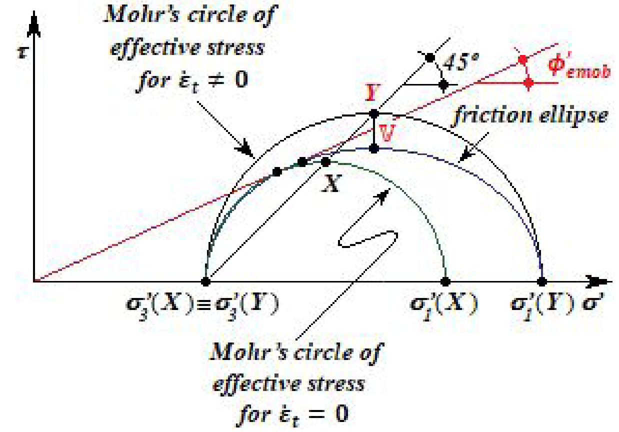

Figure 45. A point ***Y*** on the ESP of a $\overline{\text{CIUCL}}$ test carried out with $\dot{\varepsilon}_t \neq 0$ and its corresponding point ***X*** on the bESP (associated with $\dot{\varepsilon}_t = 0$).

Solving Equations 68 and 69 for t'_b and s'_b, Equations 72 to 75 are obtained:

$$t'_b = tan^2\phi'_{emob}\left(1+csc\,\phi'_{emob}\right)\left(s'-t'\right) \tag{72}$$

or

$$t'_b = \frac{\left(t'-\mathbb{V}\right)^2}{\left(s'+t'\right)}\left[1+\frac{\sqrt{s'^2+\mathbb{V}^2-2\mathbb{V}t'}}{\left(t'-\mathbb{V}\right)}\right] \tag{73}$$

and

$$s'_b = sec^2\phi'_{emob}\left(1+sin\,\phi'_{emob}\right)\left(s'-t'\right) \tag{74}$$

or

$$s'_b = \left(s'-t'\right)+\frac{\left(t'-\mathbb{V}\right)^2}{\left(s'+t'\right)}\left[1+\frac{\sqrt{s'^2+\mathbb{V}^2-2\mathbb{V}t'}}{\left(t'-\mathbb{V}\right)}\right] \tag{75}$$

Conversely, from the coordinates $\left(s'_b, t'_b\right)$ of points ***X*** of a bESP, one can determine the coordinates $\left(s', t'\right)$ of the corresponding points ***Y*** of an ESP of a $\overline{\text{CIUCL}}$ test whose viscous resistance $\mathbb{V}$ is known. This can be done by solving Equations 68 and 69 for s' and t', which gives:

$$s' = \mathbb{V}+\frac{s_b'^2}{\left(s'_b+t'_b\right)}+\frac{t'_b}{\left(s'_b+t'_b\right)}\sqrt{s_b'^2+2\mathbb{V}\left(s'_b+t'_b\right)} \tag{76}$$

and

$$t' = \mathbb{V}+\frac{t_b'^2}{\left(s'_b+t'_b\right)}+\frac{t'_b}{\left(s'_b+t'_b\right)}\sqrt{s_b'^2+2\mathbb{V}\left(s'_b+t'_b\right)} \tag{77}$$

In order to check Equations 76 and 77, one can compute s' and t' for point ***B*** in Figure 44, replacing s'_b and t'_b by $s'_b\left(\boldsymbol{A}\right)$ and $t'_b\left(\boldsymbol{A}\right)$, respectively, in Equations 76 and 77. Since, for point ***A***, $s'_b\left(\boldsymbol{A}\right) = p'_e$ and $t'_b\left(\boldsymbol{A}\right) = 0$, one obtains, for point ***B***, $s'\left(\boldsymbol{B}\right) = \mathbb{V} + p'_e$ and $t'\left(\boldsymbol{B}\right) = \mathbb{V}$. It can also be observed that, when $\mathbb{V} = 0$, $s' = s'_b$ and $t' = t'_b$.

The discussion above leads to the conclusion that, from the results of a $\overline{\text{CIUCL}}$ test carried out on a specimen of a given plastic soil isotropically consolidated to p'_e and sheared with a strain rate $\dot{\varepsilon}_t$ there is a viscous resistance featured by the parameter $\mathbb{V} = C_\eta\left(\dot{\varepsilon}_t\right)p'_e$. With a $\mathbb{V}$ value obtained from a $\overline{\text{CIUCL}}$ test carried out with a given $\dot{\varepsilon}_t \neq 0$ and starting from an isotropic effective stress p'_e, it is possible to draw the corresponding basic curve $t'_b \times \varepsilon_t$ and the bESP (see Figure 43). Thereafter, knowing the function $C_\eta\left(\dot{\varepsilon}_t\right)$ (not discussed in this article), one can predict the curve $t' \times \varepsilon_t$ and the ESP for a $\overline{\text{CIUCL}}$ test starting out from the same p'_e but carried out with any $\dot{\varepsilon}_t$.

7.4 General normalization and basic curves

Consider the ESPs of the four $\overline{\text{CIUCL}}$ tests shown in Figure 46. The test carried out with the strain rate $\dot{\varepsilon}_{t1}$ starts from point ***A*** under the isotropic effective stress p'_{e1} and fails at point ***D*** following the ESP ***ABCD***. Another test carried out with the same strain rate $\dot{\varepsilon}_{t1}$ starts from point ***E*** under the isotropic effective stress p'_{e2} and fails at point ***H*** following the ESP ***EFGH***. A third test carried out with a strain rate $\dot{\varepsilon}_{t2} > \dot{\varepsilon}_{t1}$ also starts from point ***E*** and fails at point ***K*** following the ESP ***EIJK***. Finally, an imaginary fourth test starting from point ***A*** is "carried out" with $\dot{\varepsilon}_t = 0$ and after following the ESP ***AXM*** it fails at point ***M***.

According to the *complementary principle 1*, all points on ESPs starting out from the same p'_e, irrespective of the strain rate $\dot{\varepsilon}_t$ imposed, will show the same shear strain ε_t, the same excess pore pressure Δu and the same ϕ'_{emob} provided they are all on the same 45º sloped straight line. This is the case of points ***X*** and ***C*** and ***G*** and ***J*** in Figure 46. Take, for instance, points ***G*** and ***J*** that are on the same 45º sloped straight line and on the ESPs starting from p'_{e2} (point ***E***) with strain rates $\dot{\varepsilon}_{t1}$ and $\dot{\varepsilon}_{t2}$, respectively. According to the *complementary principle 1*, $\varepsilon_t\left(\boldsymbol{G}\right) = \varepsilon_t\left(\boldsymbol{J}\right)$, $\Delta u\left(\boldsymbol{G}\right) = \Delta u\left(\boldsymbol{J}\right) = \Delta u_2$ and $tan\,\phi'_{emob}\left(\boldsymbol{G}\right) = tan\,\phi'_{emob}\left(\boldsymbol{J}\right)$. Similarly, $\varepsilon_t\left(\boldsymbol{X}\right) = \varepsilon_t\left(\boldsymbol{C}\right)$, $\Delta u\left(\boldsymbol{X}\right) = \Delta u\left(\boldsymbol{C}\right) = \Delta u_1$ and $tan\,\phi'_{emob}\left(\boldsymbol{X}\right) = tan\,\phi'_{emob}\left(\boldsymbol{C}\right)$.

Consider now the ESPs ***ABCD*** and ***EFGH*** in Figure 46, both associated with the same strain rate $\dot{\varepsilon}_{t1}$ but starting from different isotropic effective stresses p'_{e1} and p'_{e2}, respectively. As both ESPs are associated with the same strain rate $\dot{\varepsilon}_{t1}$, they are homothetic by hypothesis. Thus, the following equations hold valid for points ***C*** and ***G***:

$$\frac{s'\left(\boldsymbol{C}\right)}{p'_{e1}} = \frac{s'\left(\boldsymbol{G}\right)}{p'_{e2}} \tag{78}$$

and

$$\frac{t'\left(\boldsymbol{C}\right)}{p'_{e1}} = \frac{t'\left(\boldsymbol{G}\right)}{p'_{e2}} \tag{79}$$

The value of $\tan\phi'_{emob}\left(\boldsymbol{G}\right)$ is given by

$$tan\,\phi'_{emob}\left(\boldsymbol{G}\right) = \frac{t'\left(\boldsymbol{G}\right) - \mathbb{V}_{12}}{\sqrt{\left(s'\left(\boldsymbol{G}\right)\right)^2 - \left(t'\left(\boldsymbol{G}\right)\right)^2}} \tag{80}$$

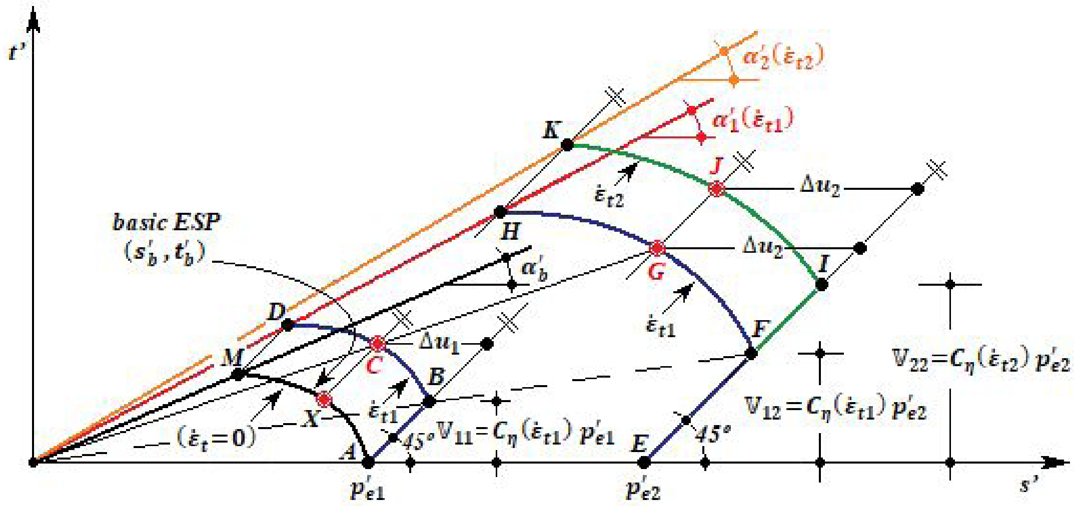

Figure 46. General normalization taking into account different values of p'_e and $\dot{\varepsilon}_t$.

Dividing both numerator and denominator of Equation 80 by p'_{e2}, one obtains:

$$tan\,\phi'_{emob}(\boldsymbol{G}) = \frac{\dfrac{t'(\boldsymbol{G})}{p'_{e2}} - \dfrac{\mathbb{V}_{12}}{p'_{e2}}}{\sqrt{\left(\dfrac{s'(\boldsymbol{G})}{p'_{e2}}\right)^2 - \left(\dfrac{t'(\boldsymbol{G})}{p'_{e2}}\right)^2}} \tag{81}$$

Replacing the values of $s'(\boldsymbol{G})/p'_{e2}$ and $t'(\boldsymbol{G})/p'_{e2}$ in Equation 81 by their respective values given by Equations 78 and 79 and recalling that $(\mathbb{V}_{12}/p'_{e2}) = (\mathbb{V}_{11}/p'_{e1}) = C_\eta(\dot{\varepsilon}_{t1})$, the following equation can be written:

$$tan\,\phi'_{emob}(\boldsymbol{G}) = \frac{\dfrac{t'(\boldsymbol{C})}{p'_{e1}} - \dfrac{\mathbb{V}_{11}}{p'_{e1}}}{\sqrt{\left(\dfrac{s'(\boldsymbol{C})}{p'_{e1}}\right)^2 - \left(\dfrac{t'(\boldsymbol{C})}{p'_{e1}}\right)^2}} \tag{82}$$

Multiplying numerator and denominator of the right hand side of Equation 82 by p'_{e1}, Equation 83 is obtained as shown below:

$$tan\,\phi'_{emob}(\boldsymbol{G}) = \frac{t'(\boldsymbol{C}) - \mathbb{V}_{11}}{\sqrt{\left(s'(\boldsymbol{C})\right)^2 - \left(t'(\boldsymbol{C})\right)^2}} \tag{83}$$

The right hand side of Equation 83 is the expression for $tan\ {}'_{emob}(\boldsymbol{C})$. This leads to the conclusion that $tan\phi'_{emob}(\boldsymbol{G}) = tan\,\phi'_{emob}(\boldsymbol{J}) = tan\,\phi'_{emob}(\boldsymbol{C}) = tan\,\phi'_{emob}(\boldsymbol{X})$.

On the other hand, considering points ***C*** and ***G*** in Figure 46, both belonging to ESPs corresponding to the same strain rate $\dot{\varepsilon}_{t1}$, the following expression can be written:

$$\frac{\Delta u_1}{p'_{e1}} = \frac{\Delta u_2}{p'_{e2}} \tag{84}$$

Since for the same strain rate $\dot{\varepsilon}_{t1}$ the curve $\Delta u / p'_e \times \varepsilon_t$ is assumed to be unique, points ***C*** and ***G*** are assumed to have the same ε_t. On the other hand, it should be noted in Figure 46 that the ratio $(\Delta u_2 / p'_{e2})$ also holds for point ***J***, which belongs to an ESP whose strain rate is $\dot{\varepsilon}_{t2}$. It is worth recalling that points ***G*** and ***J*** belong to different ESPs departing from the same p'_{e2} but corresponding to the strain rates $\dot{\varepsilon}_{t1}$ and $\dot{\varepsilon}_{t2}$, respectively. However, for a fixed p'_e the pore pressure Δu does not depend on the strain rate $\dot{\varepsilon}_t$ (see hypothesis based on experimental evidences shown in section 7.2 – Figure 40). This leads to the conclusion that points ***X***, ***C***, ***G*** and ***J*** have the same values of ε_t, $(\Delta u / p'_e)$ and $tan\,\phi'_{emob}$. This conclusion, which comes from the *complementary principle 1* and the above reasoning, allows to redraw Figure 46 using the normalized parameters s'/p'_e and t'/p'_e for coordinate axes, as shown in Figure 47. Figure 47 shows that, although points ***X***, ***C***, ***G*** and ***J*** belong to distinct normalized ESPs associated with different strain rates $\dot{\varepsilon}_t$, they lie on the same 45º sloped straight line.

The discussion presented above leads to the generalization of the *complementary principle 1*, which can be stated as follows:

Generalized complementary principle 1: During undrained shear of CIUCL tests carried out on normally consolidated clay specimens, points on the plane $(s'/p'_e)\times(t'/p'_e)$ corresponding to the intersections of a given 45º sloped straight line and the several ESPs, each one associated with a different $\dot{\varepsilon}_t$ value, will show, whatever the shear strain rate $\dot{\varepsilon}_t$ is, the same values of ε_t, $(\Delta u / p'_e)$, and $tan\,\phi'_{emob}$ (see Figure 47 – section 7.4).

The *generalized complementary principle 1* leads to three corollaries, namely:

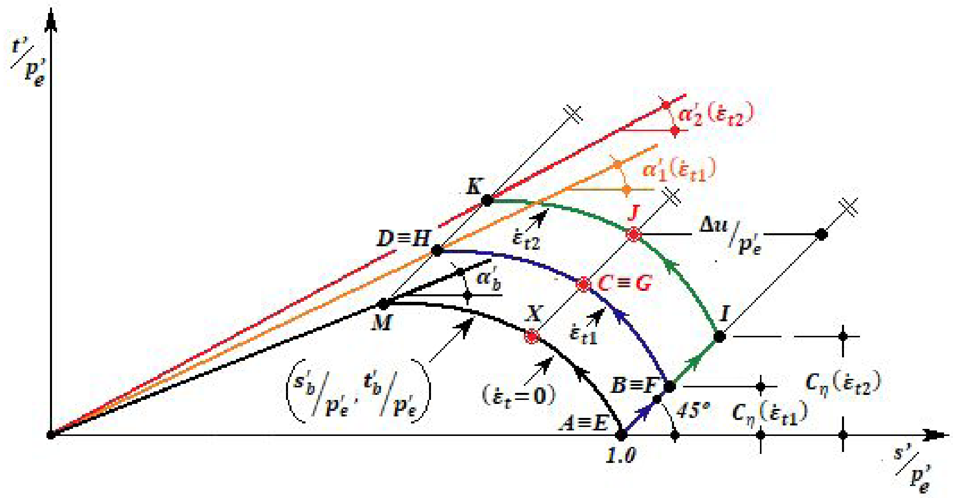

Figure 47. Normalized effective stress paths $s' / p'_e \times t' / p'_e$ for different strain rates $(\dot{\varepsilon}_t)$.

Corollary 1: $\overline{\textbf{\textit{CIUCL}}}$ ***tests carried out on a normally consolidated clay showing homothetic ESPs for any fixed*** $\dot{\varepsilon}_t$ ***and a unique curve*** $\Delta u / p'_e \times \varepsilon_t$***, irrespective of*** $\dot{\varepsilon}_t$***, will show a unique basic curve*** $t'_b / p'_e \times \varepsilon_t$***, whatever*** $\dot{\varepsilon}_t$ ***is.***

Corollary 1 can be demonstrated as follows:

According to the *generalized complementary principle 1* (see Figure 47), $\varepsilon_t(\boldsymbol{X}) = \varepsilon_t(\boldsymbol{C}) = \varepsilon_t(\boldsymbol{G}) = \varepsilon_t(\boldsymbol{J})$ and $\tan\phi'_{emob}(\boldsymbol{X}) = \tan\phi'_{emob}(\boldsymbol{C}) = \tan\phi'_{emob}(\boldsymbol{G}) = \tan\phi'_{emob}(\boldsymbol{J})$. Thus, Equation 83 can be rewritten as

$$\tan\phi'_{emob}(\boldsymbol{X}) = \tan\phi'_{emob}(\boldsymbol{C}) = \tan\phi'_{emob}(\boldsymbol{G}) = \tan\phi'_{emob}(\boldsymbol{J}) = \frac{t'_b(\boldsymbol{X})}{\sqrt{s'^2_b(\boldsymbol{X}) - t'^2_b(\boldsymbol{X})}} \tag{85}$$

Taking into account Figure 46, Equation 72 can be applied to points $\boldsymbol{X}$ and $\boldsymbol{C}$, which are on the same 45º sloped straight line, obtaining Equation 86:

$$t'_b(\boldsymbol{X}) = \tan^2\phi'_{emob}(\boldsymbol{C})\left[1 + \csc\phi'_{emob}(\boldsymbol{C})\right]\left[s'(\boldsymbol{C}) - t'(\boldsymbol{C})\right] \tag{86}$$

Dividing both sides of Equation 86 by p'_{e1}, Equation 87 is obtained:

$$\frac{t'_b(\boldsymbol{X})}{p'_{e1}} = \tan^2\phi'_{emob}(\boldsymbol{C})\left[1 + \csc\phi'_{emob}(\boldsymbol{C})\right]\left[\frac{s'(\boldsymbol{C})}{p'_{e1}} - \frac{t'(\boldsymbol{C})}{p'_{e1}}\right] \tag{87}$$

Besides the fact that $\tan\phi'_{emob}(\boldsymbol{C}) = \tan\phi'_{emob}(\boldsymbol{G})$, $\boldsymbol{C}$ and $\boldsymbol{G}$ are points from tests carried out with the same $\dot{\varepsilon}_t = \dot{\varepsilon}_{t1}$ (see Figure 46) but consolidated to isotropic stresses p'_{e1} and p'_{e2}, respectively. This leads to Equation 88:

$$\frac{s'(\boldsymbol{C})}{p'_{e1}} - \frac{t'(\boldsymbol{C})}{p'_{e1}} = \frac{s'(\boldsymbol{G})}{p'_{e2}} - \frac{t'(\boldsymbol{G})}{p'_{e2}} \tag{88}$$

Replacing $\phi'_{emob}(\boldsymbol{C})$ by $\phi'_{emob}(\boldsymbol{G})$ and $\left[s'(\boldsymbol{C})/p'_{e1} - t'(\boldsymbol{C})/p'_{e1}\right]$ by its equivalent value $\left[s'(\boldsymbol{G})/p'_{e2} - t'(\boldsymbol{G})/p'_{e2}\right]$ in Equation 87, Equation 89 is obtained as follows:

$$\frac{t'_b(\boldsymbol{X})}{p'_{e1}} = \tan^2\phi'_{emob}(\boldsymbol{G})\left[1 + \csc\phi'_{emob}(\boldsymbol{G})\right]\left[\frac{s(\boldsymbol{G})}{p'_{e2}} - \frac{t(\boldsymbol{G})}{p'_{e2}}\right] \tag{89}$$

As points $\boldsymbol{G}$ and $\boldsymbol{J}$ lie on the same 45º sloped straight line (see Figure 46) and on ESPs starting out from the same $p'_e = p'_{e2}$, one can write:

$$\frac{s'(\boldsymbol{G})}{p'_{e2}} - \frac{t'(\boldsymbol{G})}{p'_{e2}} = \frac{s'(\boldsymbol{J})}{p'_{e2}} - \frac{t'(\boldsymbol{J})}{p'_{e2}} \tag{90}$$

As $\phi'_{emob}(\boldsymbol{G}) = \phi'_{emob}(\boldsymbol{J})$, replacing $\phi'_{emob}(\boldsymbol{G})$ by $\phi'_{emob}(\boldsymbol{J})$ and $\left[s'(\boldsymbol{G})/p'_{e2} - t'(\boldsymbol{G})/p'_{e2}\right]$ by its equivalent value $\left[s'(\boldsymbol{J})/p'_{e2} - t'(\boldsymbol{J})/p'_{e2}\right]$ in Equation 89, Equation 91 is obtained:

$$\frac{t'_b(\boldsymbol{X})}{p'_{e1}} = \tan^2\phi'_{emob}(\boldsymbol{J})\left[1 + \csc\phi'_{emob}(\boldsymbol{J})\right]\left[\frac{s'(\boldsymbol{J})}{p'_{e2}} - \frac{t'(\boldsymbol{J})}{p'_{e2}}\right] \tag{91}$$

As points $\boldsymbol{X}$, C, $\boldsymbol{G}$ and $\boldsymbol{J}$ lie on the same 45º sloped straight line in the $(s'/p'_e) \times (t'/p'_e)$ plane, it can be observed from Figure 47 that $\left[s'_b(\boldsymbol{X})/p'_{e1} - t'_b(\boldsymbol{X})/p'_{e1}\right] = \left[s'(\boldsymbol{C})/p'_{e1} - t'(\boldsymbol{C})/p'_{e1}\right] = \left[s'(\boldsymbol{G})/p'_{e2} - t'(\boldsymbol{G})/p'_{e2}\right] = \left[s'(\boldsymbol{J})/p'_{e2} - t'(\boldsymbol{J})/p'_{e2}\right]$. Since point $\boldsymbol{X}$ is a generic point of the normalized basic effective stress path (from now on called bESPn), for which $\dot{\varepsilon}_t = 0$, Equation 91 holds valid for each and every point on the bESPn and can be written according to the generic form of Equation 92:

$$\frac{t'_b}{p'_e} = \tan^2\phi'_{emob}\left(1 + \csc\phi'_{emob}\right)\left[\frac{s'}{p'_e} - \frac{t'}{p'_e}\right] \tag{92}$$

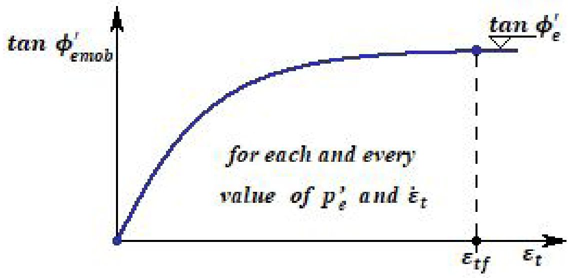

Figure 48. Uniqueness of $tan\,\phi'_{emob} \times \varepsilon_t$ relationship for each and every value of p'_e and $\dot{\varepsilon}_t$.

Finally, it is worth reminding that points ***X***, ***C***, ***G*** and ***J*** have the same shear strain ε_t, which implies a one-to-one correspondence between t'_b / p'_e and ε_t, leading to the conclusion that the basic curve $t'_b / p'_e \times \varepsilon_t$ is unique, as it was to be demonstrated.

Corollary 2: $\overline{CIUCL}$ ***tests carried out on a normally consolidated clay showing homothetic ESPs for any fixed*** $\dot{\varepsilon}_t$ ***and a unique curve*** $\Delta u / p'_e \times \varepsilon_t$, ***irrespective of*** $\dot{\varepsilon}_t$, ***will show a unique normalized basic effective stress path (bESPn)*** $\left(s'_b / p'_e, t'_b / p'_e\right)$, ***whatever*** $\dot{\varepsilon}_t$ ***is.***

Corollary 2 results from the following reasoning:

Starting from Equation 74, which gives the expression for s'_b, and following a similar line of reasoning adopted in the proof of *corollary 1*, it can be shown that a unique curve $s'_b / p'_e \times \varepsilon_t$ exists. Taking the t'_b / p'_e values of the unique $t'_b / p'_e \times \varepsilon_t$ curve, as shown in *corollary 1*, and associating them to the s'_b / p'_e values corresponding to the same ε_t values of the likewise unique $s'_b / p'_e \times \varepsilon_t$ curve, it will also be obtained a unique curve formed by the ordered pairs $(s'_b / p'_e, t'_b / p'_e)$, which is, by definition, the normalized basic effective stress path (bESPn)**.**

Corollary 3: $\overline{CIUCL}$ ***tests carried out on a normally consolidated clay showing homothetic ESPs for any fixed*** $\dot{\varepsilon}_t$ ***and a unique curve*** $\Delta u / p'_e \times \varepsilon_t$, ***irrespective of*** $\dot{\varepsilon}_t$, ***will show a unique curve*** $tan\,\phi'_{emob} \times \varepsilon_t$, ***whatever*** $\dot{\varepsilon}_t$ ***is.***

Corollary 3 can be demonstrated following the reasoning presented below:

Considering corollaries 1 and 2, both curves $t'_b / p'_e \times \varepsilon_t$ and $s'_b / p'_e \times \varepsilon_t$ are unique. This means that one and only one value of shear strain ε_t is associated with each and every ordered pair $\left(s'_b / p'_e, t'_b / p'_e\right)$. However, $tan\,\phi'_{emob}$ can be written in terms of s'_b and t'_b as $tan\phi'_{emob} = t'_b / \sqrt{\left(s'_b\right)^2 - \left(t'_b\right)^2}$. Dividing both numerator and denominator of the right hand side of such expression by p'_e, Equation 93 is obtained:

$$tan\,\phi'_{emob} = \frac{t'_b / p'_e}{\sqrt{\left(s'_b / p'_e\right)^2 - \left(t'_b / p'_e\right)^2}} \tag{93}$$

As t'_b / p'_e and s'_b / p'_e are both exclusive functions of ε_t, thus $tan\ \ '_{emob}$ will also be a sole function of ε_t, which proves corollary 3, as illustrated in Figure 48.

Thus, it can be concluded that curves $t'_b / p'_e \times \varepsilon_t$, $tan\,\phi'_{emob} \times \varepsilon_t$ and the normalized basic effective stress path (bESPn), given by the ordered pairs $\left(s'_b / p'_e, t'_b / p'_e\right)$, are properties of a given normally consolidated plastic soil.

8. Real $\overline{\text{CIUCL}}$ tests

8.1 Introduction

A model of behaviour for saturated normally consolidated clays subjected to $\overline{\text{CIUCL}}$ tests taking into account strain rate $\left(\dot{\varepsilon}_t\right)$ was developed in section 7. Based on the developed model, the main results expected for an ideal plastic soil subjected to $\overline{\text{CIUCL}}$ tests were also presented.

At first, this work was intended to present a testing program consisting of $\overline{\text{CIUCL}}$, undrained creep and stress relaxation tests carried out on samples from a very soft clay deposit close to the city of Rio de Janeiro, called Sarapuí II [see Danziger et al. (2019)]. The main aim would be to check whether the results from such testing program could be predicted by the model presented in section 7. However, the arrival of the pandemic in the beginning of 2020 made such testing program unfeasible. For this reason, the tests herein analyzed are those carried out by Lacerda (1976) on San Francisco Bay Mud samples.

Although the Lacerda's (1976) testing program was not planned to study the behavioural aspects presented in section 7, it is suitable since it is consisted of $\overline{\text{CIUCL}}$, undrained creep and stress relaxation tests, which can be analyzed under the light of the proposed model. Furthermore, San Francisco Bay Mud is a worldwide known and comprehensively studied soil. The main disadvantage of using Lacerda's (1976) tests is that they were carried out when computer-aided data acquisition systems were not available for soil testing. This disadvantage makes it harder to experimentally identify special aspects already discussed such as the "viscosity jump". Nevertheless, the Lacerda's (1976) testing program is useful to check whether its experimental results are in agreement with the main propositions made by the presented model.

8.2 Summary of the model hypotheses and steps to be followed to check their validity

To check the validity of the model, it is necessary to verify if its 11 hypotheses are fulfilled. Among these hypotheses, listed below, the first four come from experimental evidences. The next six are working hypotheses of theoretical nature and the last one is hybrid since it comes from experimental evidences as well as from theoretical considerations.

These hypotheses are the following:

1. Normally consolidated, saturated specimens of a given clay compressed to different isotropic stresses p'_e in $\overline{\text{CIUCL}}$ tests and sheared with the same shear strain rate $\dot{\varepsilon}_t$ show similar curves $t' \times \varepsilon_t$ and $\Delta u \times \varepsilon_t$ and homothetic $p' \times q'$ or $s' \times t'$ effective stress paths with the origin as the centre of homothety. This means that for a fixed strain rate $\dot{\varepsilon}_t$ the clay exhibits normalized behaviour in relation to p'_e.
2. For a given strain rate $\dot{\varepsilon}_t$, the ordered triples $\left(p'_f, q'_f, v_f\right)$, with subscripts f denoting failure, define a smooth curve in the (p', q', v) space called critical state line (CSL) associated with this given shear strain rate $\dot{\varepsilon}_t$. For each shear strain rate $\dot{\varepsilon}_t$, there is only one corresponding CSL.
3. For a fixed $\dot{\varepsilon}_t$, the projection of the CSL on the plane $p' \times q'$ or $s' \times t'$ is a straight line passing through the origin.
4. When $\overline{\text{CIUCL}}$ tests are carried out with the same isotropic effective stress p'_e and different shear strain rates $\dot{\varepsilon}_t$, the deviator stresses are higher the higher the shear strain rate. However, pore pressure values are not affected by shear strain rate. This means that for each $\dot{\varepsilon}_t$ there is just one curve $t' / p'_e \times \varepsilon_t$, but the curve $\Delta u / p'_e \times \varepsilon_t$ is unique regardless of the $\dot{\varepsilon}_t$ value.
5. Validity of Terzaghi's PES equation: $\sigma' = \sigma - u$.
6. The shear stress τ_α acting on a plane whose normal makes an angle α with σ_1 direction consists of two parts: a friction part $\tau_{\phi\alpha}$ and a viscous part $\tau_{\eta\alpha}$, i.e., $\tau_\alpha = \tau_{\phi\alpha} + \tau_{\eta\alpha}$.
7. The viscous part of the shear stress $\tau_{\eta\alpha}$ is written as $\tau_{\eta\alpha} = \eta(e) f(\dot{\gamma}) sin 2\alpha$, being $\eta(e)$ defined as *soil viscosity*, a function of void ratio and of soil structure, and $f(\dot{\gamma})$ an exclusive function of distortion rate $\dot{\gamma}$. On planes whose normal makes 45° with σ_1 direction, $2\alpha = 90°$ and $\tau_{\eta 45°} = \eta(e) f\left(d\left(\varepsilon_1 - \varepsilon_3\right)/dt\right) = \eta(e) f(\dot{\gamma}) = \mathbb{V}$.
8. The friction part of the shear stress acting on a plane whose normal makes an angle α with σ_1 direction corresponds to $\tau_{\phi\alpha} = \tau_\alpha - \tau_{\eta\alpha} = \left[\left(\sigma'_1 - \sigma'_3\right)/2 - \mathbb{V}\right] sin 2\alpha$.
9. The ordered pairs $\left(\sigma'_\alpha, \tau_{\eta\alpha}\right)$ define the *state of mobilized viscosity* of a soil, which is represented by the viscosity ellipse. The ordered pairs $\left(\sigma'_\alpha, \tau_{\phi\alpha}\right)$ define the *state of mobilized friction*, which is represented by the friction ellipse. The sum of these two elipses corresponds to the Mohr's circle of effective stress Thus, the two ellipses cannot exist separately since only the stresses given by the Mohr's circle satisfy equilibrium.
10. As a consequence of hypotheses (6) and (7), during the undrained shear phase of a $\overline{\text{CIUCL}}$ test carried out with ε_t = constant, $\tau_{\eta\alpha}$ is instantaneously mobilized and remains constant up to the end of shear. During the undrained shear phase of a $\overline{\text{CIUCL}}$ test there is no volume change but only shear strains. Thus, the deviator stress increase during the undrained shear is due to friction mobilization, which occurs as shear strains increase. Therefore, failure process is ruled by friction mobilization. For a given distortion γ, friction is fully mobilized and failure occurs. This means that, in a normally consolidated clay, failure will occur when the friction ellipse touches the strength envelope, which is the straight line passing through the origin with slope $tan\,\phi'_e$, as illustrated in Figure 28. In other words, failure will occur when Equation 62 is met.
11. Finally, the last hypothesis assumes the viscous resistance $\mathbb{V} = \eta(e) f(\dot{\gamma}) = C_\eta(\dot{\gamma}) p'_e$. This means that, even though $C_\eta(\dot{\gamma})$ is a non-linear function of distortion rate and of soil structure, for any $\dot{\gamma}$ = constant $\mathbb{V}$ is proportional to p'_e. This hypothesis is a hybrid one because, although it comes from hypotheses (6) and (7), which are of theoretical nature, it also appears as experimental evidence via the "viscosity jumps", as shown in Figures 34 and 35. As $\mathbb{V}$ is proportional to p'_e, this hypothesis is also in agreement with hypothesis (1), which assumes a normalized behaviour in relation to p'_e.

Instead of using distortion γ and distortion rate $\dot{\gamma}$ as they appear in hypotheses (7), (10) and (11), the shear strain ε_t and the shear strain rate $\dot{\varepsilon}_t$ will respectively be used from now on.

The validity of hypotheses (1) to (4) can be directly checked by observing whether or not the plots mentioned in each of them are fulfilled. Hypotheses (6) to (10), of theoretical nature, are concerned with the effects of the viscous adsorbed water on the behaviour of plastic soils. Hypothesis (11), a hybrid one, concerns the "viscosity jump". The "viscosity jump" is a theoretical aspect of the instantaneous mobilization of the viscous resistance. On the other hand, experimental evidences show that the "viscosity jump" is proportional to the effective isotropic stress p'_e, as shown in Figures 34 and 35. The hybrid nature of hypothesis (11) resides in these two aspects.

The eleven hypotheses together with the discussions presented in section 7 lead to the *generalized complementary principle 1*, from which *corollaries 1*, *2* and *3* are consequences. Thus, in order to check whether or not the model holds valid for a given soil, it is enough to check if hypotheses (1) to (4) and (11) as well as the *generalized complementary principle 1* are fulfilled. If so, the other hypotheses will automatically be fulfilled since they are embedded in the *generalized complementary principle 1*. The same will happen to *corollaries 1*, *2* and *3* because they are consequences of the *generalized complementary principle 1*. This will be the

Table 1. Characterization tests results of San Francisco Bay Mud samples (Lacerda, 1976).

Natural water content w (%)	Liquid limit w_L (%)	Plastic limit w_P (%)	Plasticity index I_P (%)	Specific gravity G	Clay fraction % < 2μm	Activity
88 to 93	88 to 90	35 to 44	45 to 55	2.75	60	0.83

Table 2. Lacerda's tests (Lacerda, 1976) analyzed in this article.

Test	Description	Specific volume after isotropic consolidation v	Isotropic compression stress p_e' (kPa)	Shear strain rate $\dot{\varepsilon}_t$ $(\% / \text{min.})$
FP-13	$\overline{\text{CIUCL}}$	3.00	118	0.09
FP-23	$\overline{\text{CIUCL}}$	2.81	158	0.09
FP-32	$\overline{\text{CIUCL}}$	2.98	98.0	0.09
FP-42	$\overline{\text{CIUCL}}$	2.92	137	0.09
SR-I-5	stress relax.	3.11	78.4	1.15
SR-I-8	stress relax.	not informed	78.4	5.5×10^{-4}
SR-I-9	stress relax.	not informed	314	0.10
CR-I-1	undrained creep	3.15	78.4	variable
CR-I-2	undrained creep	3.02	78.4	variable
CR-71-1	undrained creep	2.78	196	variable
CR-I-ST-2	undr. step creep	2.60	314	variable

task to be accomplished in the next sections so as to check if Lacerda's (1976) $\overline{\text{CIUCL}}$ test results follow the predictions of the presented model.

8.3 Testing program carried out on San Francisco Bay Mud by Lacerda (1976)

The soil samples tested by Lacerda (1976) were taken with thin-walled 125 mm-diameter and 300 to 450 mm-long fixed piston samplers. The samples were taken at Hamilton Air Force Base, Marin County, between the 5.20 m and 7.60 m depth.

According to Lacerda's (1976) description, San Francisco Bay Mud "*is a normally consolidated, saturated clay, composed of illite, and chlorite with some montmorillonite, vermiculite and kaolinite. Very thin silty lenses are found along horizontal planes and small broken shells are occasionally present, but the soil as a whole is fairly intact and easily trimmable*" (Lacerda, 1976, p. 262). Characterization tests results are summarized in Table 1.

From the tests carried out by Lacerda (1976) only those which allow the comparison and interpretation of their results under the light of the concepts presented in section 7 were selected. Such tests are identified in the first two columns of Table 2. In the other columns of Table 2, the specific volume (v) after isotropic consolidation, the isotropic effective stress to which the specimen was consolidated (p_e') and the shear strain rate $(\dot{\varepsilon}_t)$ during undrained shear are presented.

The terminology undrained creep test is herein used to denote a test where the specimen is initially consolidated to an isotropic effective stress p_e' followed by an undrained stage during which a constant deviator stress $(\sigma_1 - \sigma_3) = (\sigma_a - \sigma_r)$ is applied, being $\sigma_3 = \sigma_r = p_e' + u_c$ and u_c the back pressure. During the undrained creep stage, shear strains ε_t $(\varepsilon_t = 3/4\,\varepsilon_a)$ and pore pressures Δu are measured over time and strain rates $\dot{\varepsilon}_t$ $(\dot{\varepsilon}_t = 3/4\dot{\varepsilon}_a)$ are also computed over time.

The undrained step creep test is similar to the undrained creep test, except for the fact that during the undrained creep stage the deviator stress $(\sigma_a - \sigma_r)$ is applied in steps, each step lasting for a given time period. At the beginning of a new step, the deviator stress is raised by increasing σ_a, whereas σ_r is kept constant throughout the whole test. During each step, shear strains ε_t and pore pressures Δu are measured over time and strain rates $\dot{\varepsilon}_t$ are computed. Thus, the undrained step creep test can be compared to the conventional $\overline{\text{CIUCL}}$ tests, made with $\dot{\varepsilon}_t$ = constant, provided the points to be compared from both test types have the same $\dot{\varepsilon}_t$ values. An undrained creep test where a single deviator stress value is applied during the whole undrained creep stage can also be compared to a $\overline{\text{CIUCL}}$ test. However, in this case, the comparison is restricted to only the two points having the

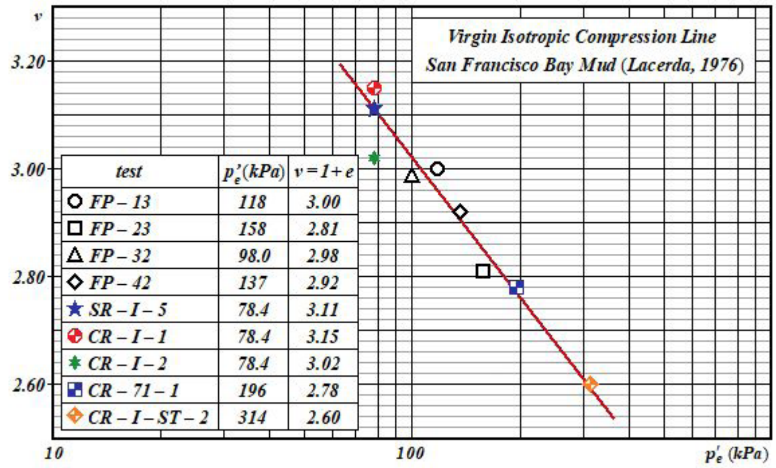

Figure 49. Virgin isotropic compression line – VICL – San Francisco Bay Mud (Lacerda, 1976).

same $\dot{\varepsilon}_t$ values. These questions will become clearer during the presentation of undrained creep tests data in section 8.4.

The name stress relaxation test is herein used to denote a $\overline{\text{CIUCL}}$ test where the undrained shear phase is carried out in consecutive stages of ε_t intervals, along which $\dot{\varepsilon}_t$ = constant. At the end of each interval the load frame motor is switched off, thus making $\dot{\varepsilon}_t = 0$ and starting a stress relaxation phase. Since the drainage is closed and the soil is saturated, during the stress relaxation phase there is neither volume changes nor shear strain changes. Keeping $\sigma_3 = \sigma_r = \left(p'_e + u_c\right)$ constant, deviator stress $\left(\sigma_a - \sigma_r\right)$ and pore pressure Δu are measured over time. After observing stress relaxation over a certain time period, the load frame motor is switched on again with the same or a different strain rate $\dot{\varepsilon}_t$ used during the ε interval which preceded the current stress relaxation phase. This is the case shown in Figure 40, where different shear strain rates $\dot{\varepsilon}_t$ were used between consecutive stress relaxations phases.

From now on, the Lacerda's (1976) tests results are compared to the predictions of the model presented in section 7.

The data concerning the isotropic compression of San Francisco Bay Mud normally consolidated specimens (presented in Table 2) are plotted in Figure 49. The virgin isotropic compression line (VICL) is presented in Figure 49, showing the relationship between specific volume v and isotropic effective stress p'_e obtained by Lacerda (1976) for San Francisco Bay Mud.

Although presented in Figure 49, test CR–I–2 will not be taken into account in the analysis that follows since it presents a specific volume which is considerably distant from the $v \times p'_e$ line. This suggests that such specimen is slightly overconsolidated, with an overconsolidation ratio of 1.3. The undrained shear phases of SR–I–5 test will not also be analysed herein since the shear strain rate $\dot{\varepsilon}_t = 1.15\%/\text{min.}$, applied up to $\varepsilon_a \cong 2.5$ %, is considered too high. Such strain rate has probably not allowed an adequate equalization degree of pore pressure measured at the base of the specimen.

8.4 Checking the model using San Francisco Bay Mud tests results

The eleven hypotheses listed in section 8.2 and the discussions of section 7 have led to the *generalized complementary principle 1*, from which *corollaries 1*, *2* and *3* emerge. Thus, to check whether or not the model holds valid for a given plastic soil, it is enough to verify if the hypotheses (1) to (4) and (11) and the *generalized complementary principle 1* are fulfilled. If so, the remaining hypotheses will automatically be fulfilled since they are embedded in the *generalized complementary principle 1*. Besides, once the validity of the *generalized complementary principle 1* is shown, *corollaries 1*, *2* and *3* will also be automatically fulfilled.

In a few words, to check whether or not San Francisco Bay Mud normally consolidated specimens fulfill the model presented in section 7, the tasks listed and explained at the end of section 8.2 must be carried out. These tasks are:

(i) Validity check of hypotheses (1) to (4), which come from experimental evidences.

(ii) Validity check of hypothesis (11) (from a hybrid nature – experimental + theoretical).

(iii) Validity check of the generalized *complementary principle 1*.

(iv) Validity check of *corollaries 1*, *2* and *3*.

Following the sequential tasks listed above, the first thing to do is to check the validity of hypothesis (1), that is: to verify if normally consolidated, saturated specimens of San Francisco Bay Mud subjected to $\overline{\text{CIUCL}}$ tests carried out with $\dot{\varepsilon}_t$ = constant really present similar $t' \times \varepsilon_t$ and $\Delta u \times \varepsilon_t$ curves and homothetic $s' \times t'$ ESPs with centre of homothety at the origin. If this hypothesis is fulfilled, the normalized

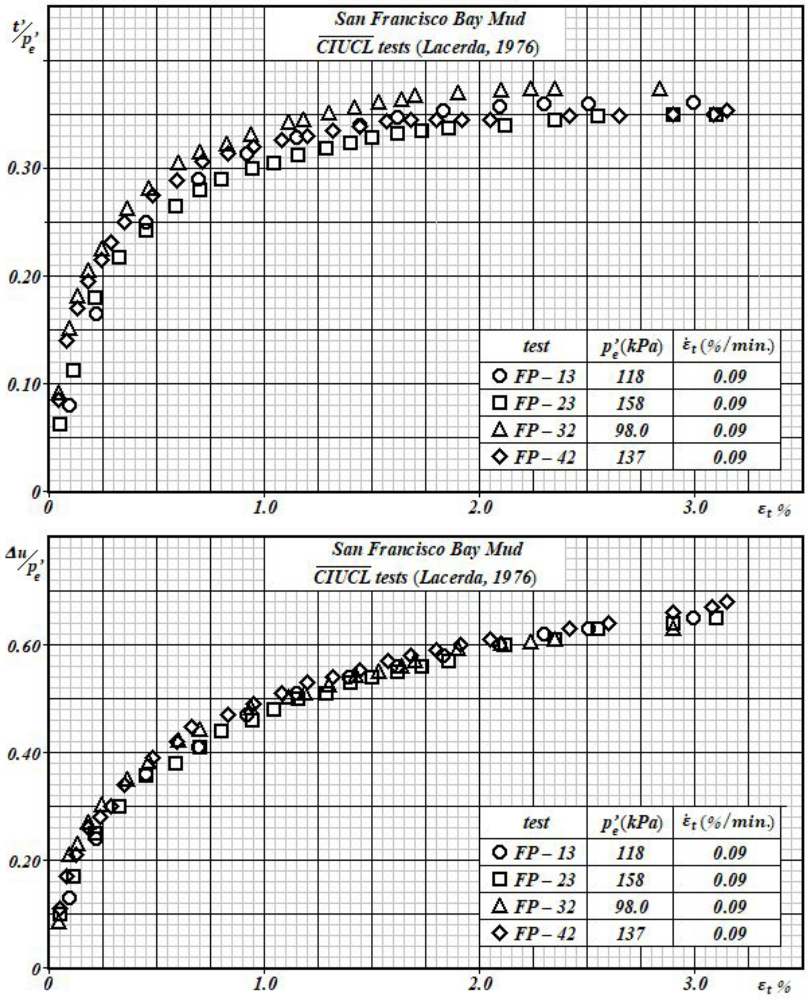

Figure 50. Curves $t' / p'_e \times \varepsilon_t$ and $\Delta u / p'_e \times \varepsilon_t$ for $\overline{\text{CIUCL}}$ tests on San Francisco Bay Mud carried out with $\dot{\varepsilon}_t = 0.09\%/\text{min}$. [data from Lacerda (1976)].

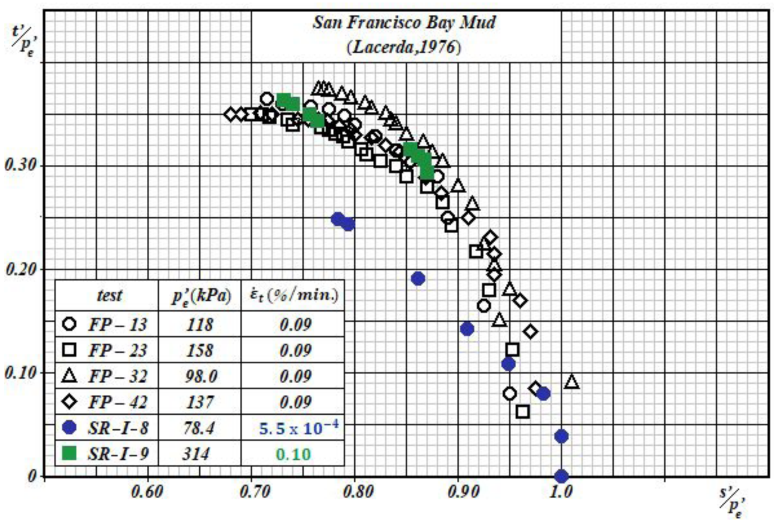

Figure 51. Normalized ESPs $\left(s' / p'_e\right) \times \left(t' / p'_e\right)$ for tests with a fixed strain rate $\dot{\varepsilon}_t$.

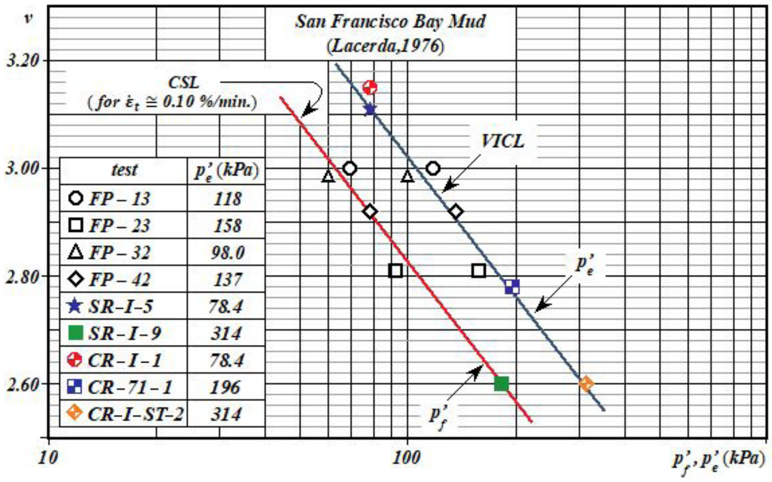

Figure 52. Virgin isotropic compression line (VICL) and critical state line (CSL) for San Francisco Bay Mud corresponding to a strain rate $\dot{\varepsilon}_t \cong 0.10\%/\text{min.}$.

curves $t'/p'_e \times \varepsilon_t$ and $\Delta u/p'_e \times \varepsilon_t$ and the normalized ESP $s'/p'_e \times t'/p'_e$ will be unique for a fixed $\dot{\varepsilon}_t$.

This is the case indeed. Normalized curves $t'/p'_e \times \varepsilon_t$ and $\Delta u/p'_e \times \varepsilon_t$ from $\overline{\text{CIUCL}}$ tests carried out with $\dot{\varepsilon}_t = 0.09\%/\text{min.}$ are shown in Figure 50. The set of curves $t'/p'_e \times \varepsilon_t$ can be fairly represented by a unique curve. The same occurs for the curves $\Delta u/p'_e \times \varepsilon_t$.

The normalized ESPs $s'/p'_e \times t'/p'_e$ of the tests plotted in Figure 50 are plotted in Figure 51, showing that ESPs corresponding to tests carried out with $\dot{\varepsilon}_t = 0.09\%/\text{min.}$ can also be represented by a unique ESP. This means that ESPs corresponding to tests carried out with $\dot{\varepsilon}_t = 0.09\%/\text{min.}$ are homothetic with the origin as the centre of homothety. Some points from test SR–I–9 where the shear strain rate is $\dot{\varepsilon}_t$ $0.10\%/\text{min.}$ are also plotted in Figure 51. $\dot{\varepsilon}_t = 0.10\%/\text{min.}$ is almost the same strain rate of $\dot{\varepsilon}_t = 0.09\%/\text{min.}$ used in tests FP–13, FP–23, FP–32 and FP–42. Although the results shown in Figures 50 and 51 are restricted to $\dot{\varepsilon}_t \cong 0.10\%/\text{min.}$, they show that hypothesis (1) is fulfilled.

Figure 51 also shows the part of the ESP for SR–I–8 test up to the first stress relaxation stage where the shear strain rate applied was $\dot{\varepsilon}_t = 5.5 \times 10^{-4}\%/\text{min.}$. This illustrates that the lower the shear strain rate $\dot{\varepsilon}_t$, the lower the t'/p'_e values of the normalized ESP, which is in agreement with the model presented in section 7.

Hypothesis (2) states that for $\overline{\text{CIUCL}}$ tests carried out with a fixed shear strain rate $\dot{\varepsilon}_t$ the ordered triples $\left(p'_f, q'_f, v_f\right)$ at failure define a smooth curve in the $p' \times q' \times v$ space called critical state line (CSL) associated with that fixed shear strain rate $\dot{\varepsilon}_t$. This means: for a given shear strain rate $\dot{\varepsilon}_t$ there is only one corresponding CSL. This result is illustrated in Figures 52 and 53 for the $\overline{\text{CIUCL}}$ tests carried out with $\dot{\varepsilon}_t \cong 0.10\%/\text{min.}$.

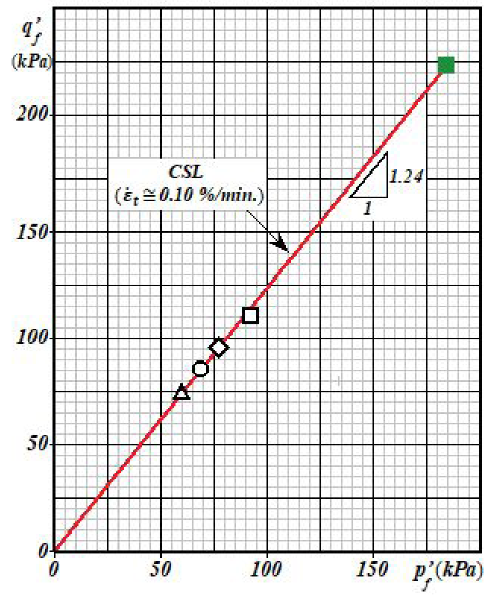

Figure 53. Critical state line for San Francisco Bay Mud corresponding to a strain rate $\dot{\varepsilon}_t \cong 0.10\%/\text{min.}$ [data from Lacerda (1976)].

Figure 53 shows that the projection of the CSL onto the plane $p' \times q'$ (or $s' \times t'$) for the fixed $\dot{\varepsilon}_t \cong 0.10\%/\text{min.}$ is a straight line passing through the origin. Thus, Figure 53 illustrates that hypothesis (3) is also fulfilled by San Francisco Bay Mud.

Based on the results from $\overline{\text{CIUCL}}$ tests carried out with $\dot{\varepsilon}_t \cong 0.10\%/\text{min}$, it is possible to obtain ϕ' for normally consolidated San Francisco Bay Mud corresponding to $\dot{\varepsilon}_t \cong 0.10\%/\text{min.}$. This can be done since M and ϕ' are related to each other by

$$M = 6\sin\phi' / \left(3 - \sin\phi'\right) \tag{94}$$

where $M = q'_f / p'_f$ is the slope of the CSL corresponding to a given $\dot{\varepsilon}_t$ on the plane $p' \times q'$. From Figure 53, one obtains $M = 1.24$, which corresponds to $\phi' \cong 31°$ and to the ordered pair $\left(s'_f / p'_e, t'_f / p'_e\right) = (0,70;0,36)$, assumed as the point representing failure in Figure 51.

Although there is a lack of data to obtain M and ϕ' corresponding to $\dot{\varepsilon}_t$ values different from $\cong 0.10\%/\text{min.}$, the available data corresponding to $\dot{\varepsilon}_t = 5.5\times10^{-4}\%/\text{min.}$ and $\cong 0.7\%/\text{min.}$, suggest that for each shear strain rate there is only one CSL (see also Figure 31 and the discussion associated with it).

Hypothesis (4) must be checked next. This hypothesis assumes that, in CIUCL tests, the higher the shear strain rate applied, the higher the values t'/p'_e in $t'/p'_e \times \varepsilon_t$ curves. On the other hand, hypothesis 4 also assumes that curves $\Delta u / p'_e \times \varepsilon_t$ do not depend on $\dot{\varepsilon}_t$.

Figure 54 shows $t'/p'_e \times \varepsilon_t$ and $\Delta u / p'_e \times \varepsilon_t$ curves corresponding to the undrained shear phases of stress relaxation tests SR–I–8 and SR–I–9. Strain rate effects are mainly observed on $t'/p'_e \times \varepsilon_t$ curves but hardly noted on $\Delta u / p'_e \times \varepsilon_t$, where, regardless the strain rate, experimental results fall within a narrow zone. In Figure 54 it should be noted that $\dot{\varepsilon}_t$ assumes four different orders of magnitude. One can argue that, with $\dot{\varepsilon}_t = 3.4\%/\text{min.}$, the strain rate criterion which should have been used aiming pore pressure equalization along the specimen was not probably fulfilled during the first undrained shear phase of test SR–I–9. Thus, Δu values measured during the first undrained shear phase of test SR–I–9 are probably underestimated. After this observation, it can be concluded from Figure 54 that curves $\Delta u / p'_e \times \varepsilon_t$ can be represented by a unique curve, which means that $\Delta u / p'_e \times \varepsilon_t$ curves can be considered to be independent of the strain rate $\dot{\varepsilon}_t$.

The assumption made in hypothesis (4) considering that strain rate effects are remarkable on $t'/p'_e \times \varepsilon_t$ curves but are practically absent in $\Delta u / p'_e \times \varepsilon_t$ curves is even clearer in Figure 55 obtained by overlapping Figures 50 and 54.

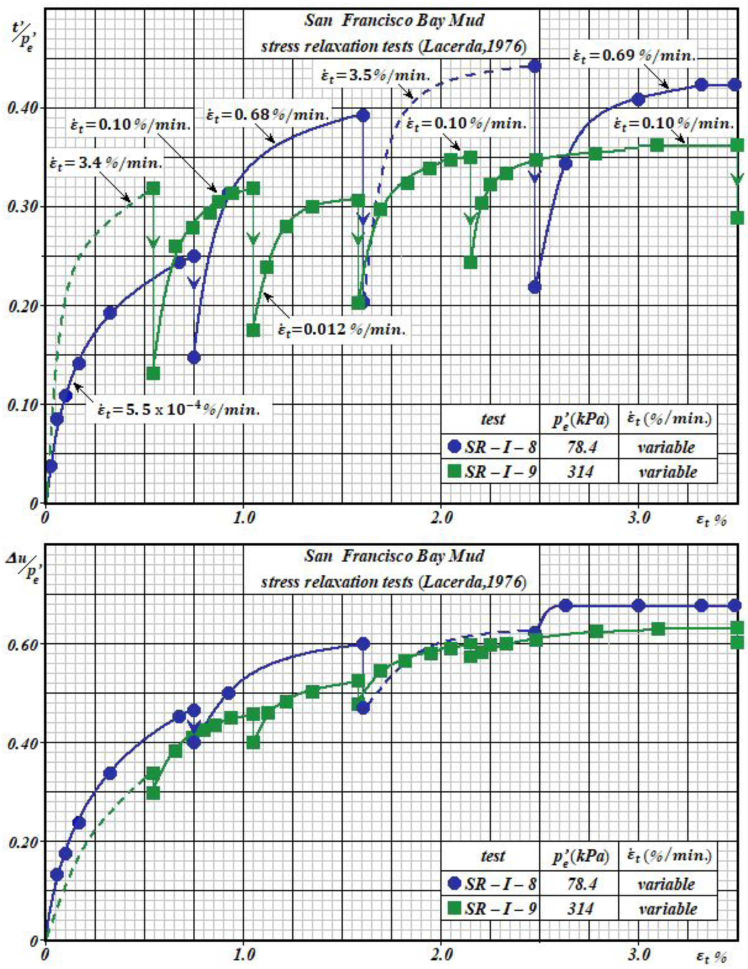

Figure 54. Curves $t'/p'_e \times \varepsilon_t$ and $\Delta u / p'_e \times \varepsilon_t$ for undrained shear phases of stress relaxation tests on San Francisco Bay Mud carried out with different values of $\dot{\varepsilon}_t$.

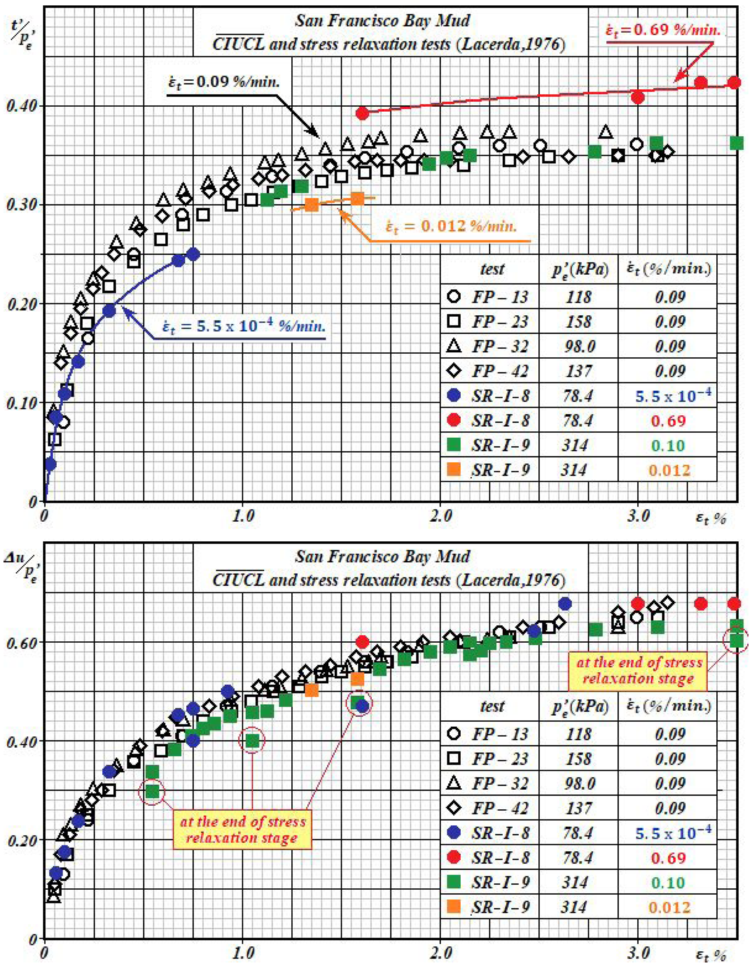

Figure 55. $t' \,/\, p'_e \times \varepsilon_t$ and $\Delta u \,/\, p'_e \times \varepsilon_t$ for $\overline{\text{CIUCL}}$ and stress relaxation tests on San Francisco Bay Mud for several different $\dot{\varepsilon}_t$ values [data from Lacerda (1976)].

After checking the validity of hypotheses (1) to (4), one can now check hypothesis (11), which, being from a hybrid nature, is made up of two parts: one that comes from experimental evidences and the other that comes from theoretical considerations.

According to hypothesis (11), $\mathbb{V} = \eta(e) f(\dot{\gamma}) = C_\eta(\dot{\gamma}) p'_e$ or, recalling that $\dot{\gamma} = 2\dot{\varepsilon}_t$, $\mathbb{V} = C_\eta(\dot{\varepsilon}_t) p'_e$. This means that for a given shear strain rate $\dot{\varepsilon}_t$ the "viscosity jump" is proportional to p'_e, as shown in Figures 34 and 35. Thus, the normalized ESPs $(s' / p'_e) \times (t' / p'_e)$ corresponding to the same $\dot{\varepsilon}_t$ should be represented by a unique ESP beginning with a "viscosity jump" along a 45º sloped straight line, which suddenly changes its direction moving up and to the left, showing an elbow shaped curve like those presented in Figure 47.

Although the normalized ESPs for $\dot{\varepsilon}_t \cong 0.10\% / \text{min.}$ in Figure 51 can be considered as a unique curve, the absence of the "viscosity jump" is noteworthy. Such absence can be possibly assigned to the fact that an automatic data acquisition system was not used, which greatly harms the measurement of *s'*, *t'* and *Δu* corresponding to the beginning of the tests. Another possible explanation for the absence of the "viscosity jump" is the occurrence of bedding errors, which will be not discussed here. One of the signs that some "disturbance" has affected the beginning of $\overline{\text{CIUCL}}$ test data is the fact that points belonging to ESPs associated with $\dot{\varepsilon}_t = 0.09\% / \text{min.}$ fall below points belonging to the ESP associated with $\dot{\varepsilon}_t = 5.5 \times 10^{-4}\% / \text{min.}$, as shown in Figure 51. Thus, one cannot evaluate $C_\eta(\dot{\varepsilon}_t)$ values and, consequently, ϕ'_e value via Figure 51.

In order to obtain $C_\eta(\dot{\varepsilon}_t)$ and ϕ'_e, it will be necessary to make use of the undrained creep tests data. As previously explained, undrained creep tests are carried out by keeping the deviator stress constant, measuring ε_t and Δu over time and evaluating $\dot{\varepsilon}_t$. This way of evaluating $\dot{\varepsilon}_t$ makes its values more reliable, particularly in the early phase of the test when bedding errors are of greater magnitude. Accordingly, the normalized ESPs for the undrained creep tests are shown in Figure 56.

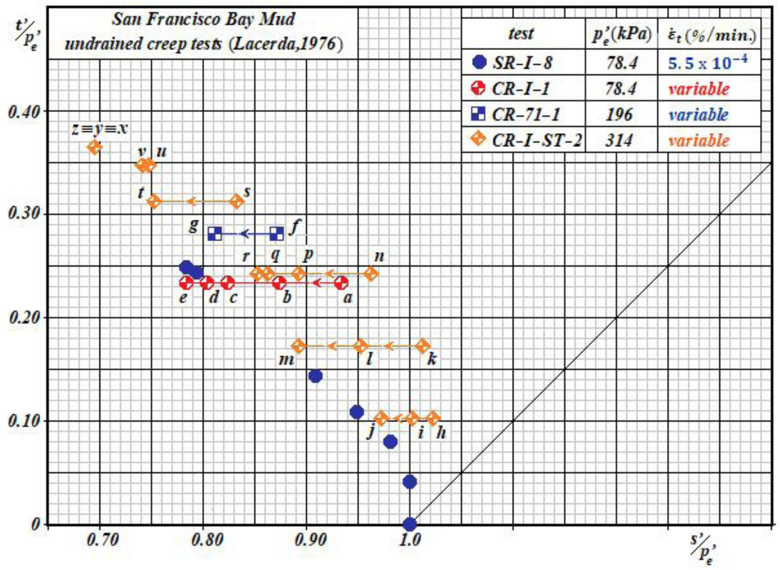

Figure 56. Normalized effective stress paths (ESPs) for undrained creep tests on normally consolidated specimens of San Francisco Bay Mud.

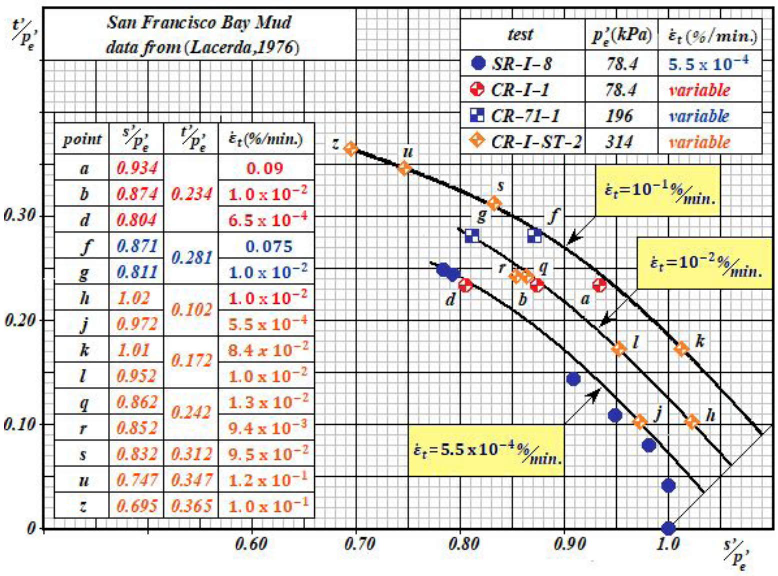

point	s'/p'_e	t'/p'_e	$\dot{\varepsilon}_t$(%/min.)
a	0.934	0.234	0.09
b	0.874		1.0×10^{-2}
d	0.804		6.5×10^{-4}
f	0.871	0.281	0.075
g	0.811		1.0×10^{-2}
h	1.02	0.102	1.0×10^{-2}
j	0.972		5.5×10^{-4}
k	1.01	0.172	8.4×10^{-2}
l	0.952		1.0×10^{-2}
q	0.862	0.242	1.3×10^{-2}
r	0.852		9.4×10^{-3}
s	0.832	0.312	9.5×10^{-2}
u	0.747	0.347	1.2×10^{-1}
z	0.695	0.365	1.0×10^{-1}

Figure 57. Normalized ESPs for 3 different $\dot{\varepsilon}_t$ values determined from undrained creep tests.

As a reference, the normalized ESP of test SR–I–8 carried out with $\dot{\varepsilon}_t = 5.5\times10^{-4}$ % / min. is also shown in Figure 56. Values of ε_t, $\dot{\varepsilon}_t$, t' / p'_e, s' / p'_e and $\Delta u / p'_e$, corresponding to the points shown in Figure 56, are presented in Table 3.

Based on values from Table 3 and on ESPs shown in Figures 51 and 56, ESPs for some selected shear strain rates $\dot{\varepsilon}_t$ can be sketched. ESPs sketches corresponding to $\dot{\varepsilon}_t = 10^{-1}$% / min., $\dot{\varepsilon}_t = 10^{-2}$% / min. and $\dot{\varepsilon}_t = 5.5\times10^{-4}$% / min. are shown in Figure 57.

In Figure 57, each ESP corresponding to a fixed $\dot{\varepsilon}_t$ intersects the normalized total stress path at a point whose ordinate gives the C_η value for that fixed $\dot{\varepsilon}_t$. Thus, from Figure 57 one can estimate the values of C_η for 5.5×10^{-4}% / min., 10^{-2}% / min. and 10^{-1}% / min. as being equal to 0.035, 0.06 and 0.09, respectively. With these C_η values, $\tan\phi'_e$ can be evaluated via Equation 62. Alternatively, $\tan\phi'_e$ can be evaluated using Equation 95, which is Equation 62 written in a normalized way, that is:

Table 3. Summary of undrained creep tests of Figure 56 (Lacerda, 1976).

Point	Test	$\varepsilon_t\,(\%)$	$\dot{\varepsilon}_t\,(\%/\mathrm{min.})$	t'/p'_e	s'/p'_e	$\Delta u/p'_e$
a	CR–I–1	0.29	0.09	0.234	0.934	0.300
b	CR–I–1	0.45	1.0×10^{-2}	0.234	0.874	0.360
c	CR–I–1	0.65	1.0×10^{-3}	0.234	0.824	0.410
d	CR–I–1	0.75	6.5×10^{-4}	0.234	0.804	0.430
e	CR–I–1	0.82	3.4×10^{-4}	0.234	0.784	0.450
f	CR–71–1	0.60	0.075	0.281	0.871	0.410
g	CR–71–1	0.97	$\sim 1.0 \times 10^{-2}$	0.281	0.811	0.470
h	CR–I–ST–2	0.06	1.0×10^{-2}	0.102	1.02	0.080
i	CR–I–ST–2	0.08	1.0×10^{-3}	0.102	1.00	0.100
j	CR–I–ST–2	0.12	5.5×10^{-4}	0.102	0.972	0.130
k	CR–I–ST–2	0.14	8.4×10^{-2}	0.172	1.01	0.160
l	CR–I–ST–2	0.19	1.0×10^{-2}	0.172	0.952	0.220
m	CR–I–ST–2	0.27	1.4×10^{-3}	0.172	0.892	0.270
n	CR–I–ST–2	0.30	3.5×10^{-1}	0.242	0.962	0.280
p	CR–I–ST–2	0.40	5.2×10^{-2}	0.242	0.892	0.350
q	CR–I–ST–2	0.50	1.3×10^{-2}	0.242	0.862	0.380
r	CR–I–ST–2	0.55	9.4×10^{-3}	0.242	0.852	0.390
s	CR–I–ST–2	1.00	9.5×10^{-2}	0.312	0.832	0.48
t	CR–I–ST–2	1.70	1.7×10^{-2}	0.312	0.752	0.560
u	CR–I–ST–2	2.10	1.2×10^{-1}	0.347	0.747	0.600
v	CR–I–ST–2	2.21	9.5×10^{-2}	0.347	0.742	0.610
x	CR–I–ST–2	3.70	2.7×10^{-1}	0.365	0.695	0.670
y	CR–I–ST–2	3.70	$\sim 1.0 \times 10^{-1}$	0.365	0.695	0.670
z	CR–I–ST–2	6.83	$\sim 1.0 \times 10^{-1}$	0.365	0.695	0.670

$$tan\,\phi'_e = \frac{\left(t'_f - \mathbb{V}\right)}{\sqrt{s'^2_f - t'^2_f}} = \frac{\left(t'_f / p'_e - \mathbb{V}/p'_e\right)}{\sqrt{\left(s'_f / p'_e\right)^2 - \left(t'_f / p'_e\right)^2}} = \frac{\left(t'_f / p'_e - C_\eta\left(\dot{\varepsilon}_t\right)\right)}{\sqrt{\left(s'_f / p'_e\right)^2 - \left(t'_f / p'_e\right)^2}} \tag{95}$$

Taking $C_\eta\left(10^{-1}\%/\mathrm{min.}\right) = 0.09$ and the ordered pair $\left(s'_f / p'_e, t'_f / p'_e\right) = \left(0.70, 0.36\right)$ corresponding to stress states at failure in $\overline{\text{CIUCL}}$ tests on normally consolidated specimens of San Francisco Bay Mud carried out with $\dot{\varepsilon}_t = 0.1\%/\mathrm{min.}$ and $0.09\%/\mathrm{min.}$, one obtains:

$$tan\,\phi'_e = \frac{\left(t'_f / p'_e - C_\eta\left(\dot{\varepsilon}_t\right)\right)}{\sqrt{\left(s'_f / p'_e\right)^2 - \left(t'_f / p'_e\right)^2}} = \frac{0.36 - 0.09}{\sqrt{0.70^2 - 0.36^2}} = 0.45 \rightarrow \phi'_e \cong 24° \tag{96}$$

This means that, in the normally consolidated domain, the part of the undrained shear strength of San Francisco Bay Mud which can be assigned to friction can be evaluated using $\phi'_e \cong 24°$, being ϕ'_e the true angle of internal friction, as defined by Hvorslev. This also means that, embedded into the shear strength values of normally consolidated specimens of San Francisco Bay Mud calculated with $\phi' \cong 31°$, there is a part which must be assigned to the viscous resistance.

Back to Figure 51, it is observed that, as already discussed, the ESPs for $\overline{\text{CIUCL}}$ tests FP–13, FP–23, FP–32 and FP–42 seem to be affected by bedding errors, mainly occurring up to the point of coordinates $\left(s'/p'_e, t'/p'_e\right) \cong \left(0.92, 0.25\right)$. The shear strain $\varepsilon_t \cong 0.40$ % is associated with $t'/p'_e = 0.25$ (see Figure 55). Thus, by neglecting the ESPs points concerning FP–13, FP–23, FP–32 and FP–42 tests for which $\varepsilon_t \leq 0.40$ % and overlapping Figures 51 and 57, Figure 58 is obtained.

Figure 58 shows that, making the appropriate "corrections" of the initial parts of the ESPs in Figure 51 and taking into account the undrained creep tests, hypothesis (11) is also fulfilled.

The results of all tests ($\overline{\text{CIUCL}}$, stress relaxation and undrained creep) are presented in Figure 59 to show that normally consolidated San Francisco Bay Mud follows hypotheses (1) to (4) and (11), regardless of the test type.

Going ahead with the task of checking whether or not the model is appropriate to predict the behaviour of normally consolidated San Francisco Bay Mud, now it is necessary to check the validity of the *generalized complementary principle 1*, whose statement is repeated below.

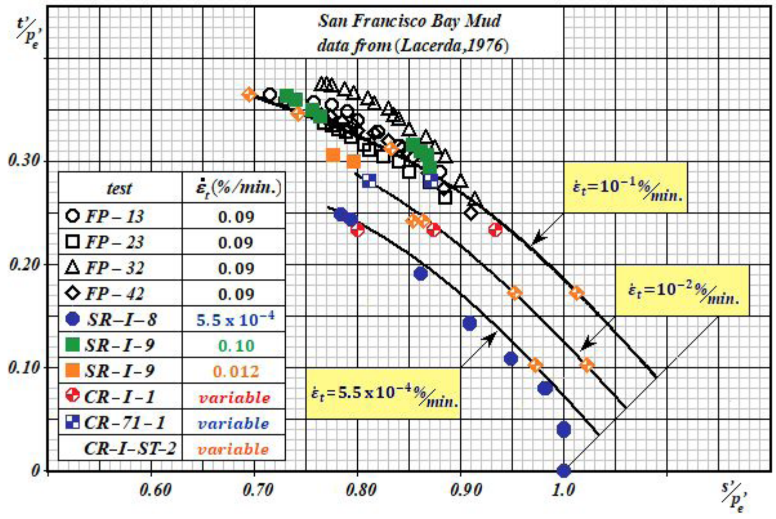

Figure 58. Normalized effective stress paths $\left(s' / p'_e\right) \times \left(t' / p'_e\right)$ for all tests with different strain rates $\left(\dot{\varepsilon}_t\right)$.

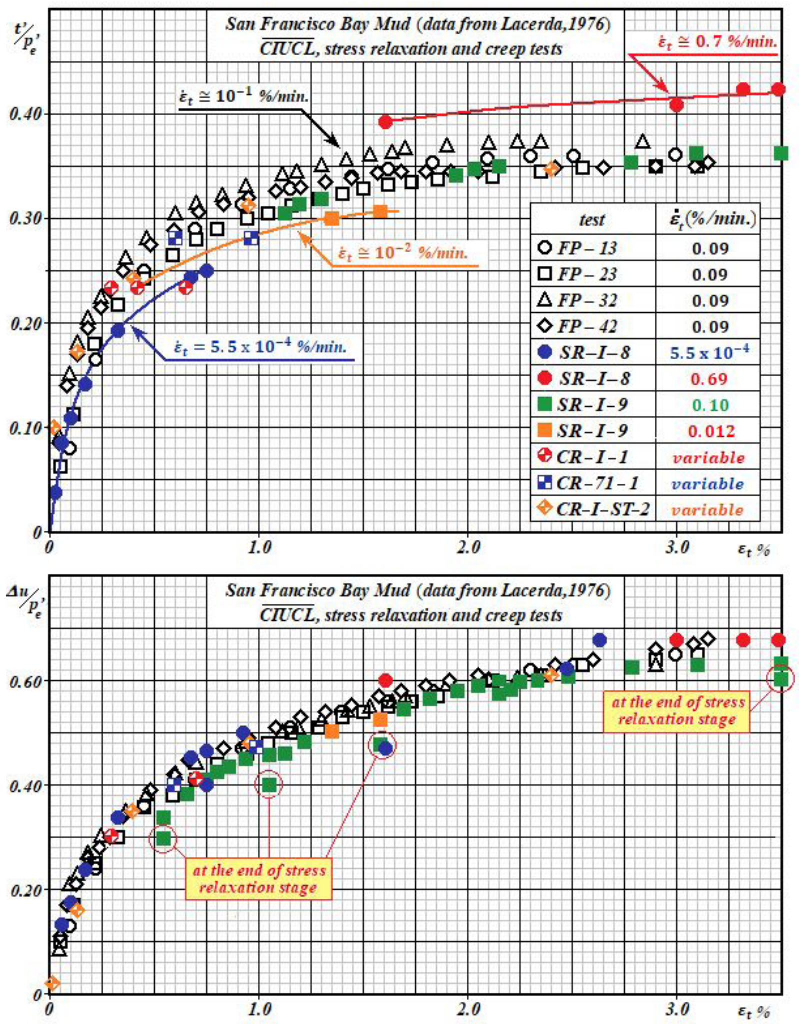

Figure 59. $\left(t' / p'_e\right) \times \varepsilon_t$ and $\left(\Delta u / p'_e\right) \times \varepsilon_t$ curves for $\overline{\text{CIUCL}}$, stress relaxation and undrained creep tests for different strain rates $\dot{\varepsilon}_t$.

Generalized complementary principle 1: During undrained shear of $\overline{CIUCL}$ tests carried out on normally consolidated clay specimens, points on the plane $(s'/p'_e)\times(t'/p'_e)$ corresponding to the intersections of any given 45º sloped straight line and the several ESPs, each one associated with a different $\dot{\varepsilon}_t$ value, will show the same values of ε_t, $(\Delta u/p'_e)$, and $\tan\phi'_{emob}$, whatever the shear strain rate $\dot{\varepsilon}_t$ may be.

The *generalized complementary principle 1* is illustrated in Figure 47, where points ***X***, ***C***, ***G*** and ***J*** all have the same values of ε_t, $(\Delta u/p'_e)$ and $\tan\phi'_{emob}$.

The *generalized complementary principle 1* was stated by induction according to the following reasoning: In Figure 47, points ***A***, ***E***, ***B***, ***F*** and ***I*** lie on the same 45º sloped straight line and all of them have $\varepsilon_t = 0, (\Delta u/p'_e) = 0$ and $\tan\phi'_{emob} = 0$, regardless of the test strain rate $\dot{\varepsilon}_t$. Similarly, points ***M***, ***D***, ***H*** and ***K*** also lie on another 45º sloped straight line and all of them are at failure. Such points are assumed to have the same ε_t and $(\Delta u/p'_e)$ values and, for being at failure, $\tan\phi'_{emob} = \tan\phi'_e$. Thus, it has been assumed by induction that points ***X***, ***C***, ***G*** and ***J***, which lie on a generic 45º sloped straight line, also have the same ε_t, $(\Delta u/p'_e)$ and $\tan\phi'_{emob}$ values.

The validity of the *generalized complementary principle 1* for normally consolidated San Francisco Bay Mud can be checked by observing a summary of the Lacerda's (1976) tests results shown in Table 4, where $\tan\phi'_{emob}$ values were computed by applying the equation $tan\phi'_{emob} = \left[t'/p'_e - C_\eta(\dot{\varepsilon}_t)\right]/\sqrt{(s'/p'_e)^2 - (t'/p'_e)^2}$, obtained from Equation 56 normalized in relation to p'_e. According to the *generalized complementary principle 1*, for each ε_t value there will be only one $(\Delta u/p'_e)$ value and only one $tan\phi'_{emob}$ value, regardless of the shear strain rate $\dot{\varepsilon}_t$. This is what is shown in Table 4, as well as in Figures 59 and 62. Although there is some scattering, considering that soil specimens were trimmed from natural undisturbed samples, it can be concluded that the experimental data are in fair agreement with the *generalized complementary principle 1*.

As already highlighted, by showing that the *generalized complementary principle 1* holds valid, *corollaries 1*, *2* and *3* will be automatically satisfied, as it will be shown next.

Corollary 1, whose statement is repeated below, will be firstly shown to be valid.

Corollary 1: $\overline{CIUCL}$ tests carried out on a normally consolidated clay showing homothetic ESPs for any fixed $\dot{\varepsilon}_t$ and a unique curve $\Delta u/p'_e\times\varepsilon_t$, regardless of $\dot{\varepsilon}_t$, will show a unique basic curve $t'_b/p'_e\times\varepsilon_t$, whatever $\dot{\varepsilon}_t$ is.

In order to show that *corollary 1* holds valid, it is necessary to plot the basic curves $t'_b/p'_e\times\varepsilon_t$. This can be done by dividing both sides of Equation 73 by p'_e to obtain an expression for t'_b/p'_e, which is given by Equation 97 shown below:

$$t'_b/p'_e = \frac{(t'/p'_e - \mathbb{V}/p'_e)^2}{(s'/p'_e + t'/p'_e)}\left[1 + \frac{\sqrt{(s'/p'_e)^2 + (\mathbb{V}/p'_e)^2 - 2\mathbb{V}t'/p'^2_e}}{(t'/p'_e - \mathbb{V}/p'_e)}\right] \quad (97)$$

As $\mathbb{V}/p'_e = C_\eta(\dot{\varepsilon}_t)$, thus Equation 97 can be rewritten as:

$$t'_b/p'_e = \frac{(t'/p'_e - C_\eta(\dot{\varepsilon}_t))^2}{(s'/p'_e + t'/p'_e)}\left\{1 + \frac{\sqrt{(s'/p'_e)^2 + [C_\eta(\dot{\varepsilon}_t)]^2 - 2(t'/p'_e)C_\eta(\dot{\varepsilon}_t)}}{(t'/p'_e - C_\eta(\dot{\varepsilon}_t))}\right\} \quad (98)$$

Alternatively, t'_b/p'_e values can be more simply computed by applying Equation 72, dividing its both sides by p'_e to obtain an expression for t'_b/p'_e, given by Equation 99:

$$t'_b/p'_e = tan^2\phi'_{emob}\left(1 + csc\,\phi'_{emob}\right)\left(s'/p'_e - t'/p'_e\right) \quad (99)$$

Based on Lacerda's (1976) tests results, t'_b/p'_e values can be computed via Equation 98 and the normalized basic curve $t'_b/p'_e\times\dot{\varepsilon}_t$ can be plotted, as presented in Figure 60, which clearly shows the validity of *corollary 1*.

It will be shown next that normally consolidated specimens of San Francisco Bay Mud also fulfill *corollary 2*, whose statement is repeated below:

Corollary 2: $\overline{CIUCL}$ tests carried out on a normally consolidated clay showing homothetic ESPs for any fixed $\dot{\varepsilon}_t$ and a unique curve $\Delta u/p'_e\times\varepsilon_t$, regardless of $\dot{\varepsilon}_t$, will show a unique normalized basic effective stress path $(s'_b/p'_e, t'_b/p'_e)$, whatever $\dot{\varepsilon}_t$ is.

In order to plot the normalized basic effective stress path for normally consolidated San Francisco Bay Mud, the ordered pairs $(s'_b/p'_e, t'_b/p'_e)$ might be obtained. (t'_b/p'_e) can be obtained by Equation 98 or 99. An expression for (s'_b/p'_e) can be obtained by dividing both sides of Equation 75 by p'_e to obtain Equation 100 shown below:

$$\frac{s'_b}{p'_e} = \left(\frac{s'}{p'_e} - \frac{t'}{p'_e}\right) + \frac{\left(\frac{t'}{p'_e} - \frac{\mathbb{V}}{p'_e}\right)^2}{\left(\frac{s'}{p'_e} + \frac{t'}{p'_e}\right)}\left[1 + \frac{\sqrt{\left(\frac{s'}{p'_e}\right)^2 + \left(\frac{\mathbb{V}}{p'_e}\right)^2 - \frac{2\mathbb{V}t'}{p'^2_e}}}{\left(\frac{t'}{p'_e} - \frac{\mathbb{V}}{p'_e}\right)}\right] \quad (100)$$

Replacing $\mathbb{V}/p'_e$ by $C_\eta(\dot{\varepsilon}_t)$ in Equation 100, Equation 101 is obtained:

$$\frac{s'_b}{p'_e} = \left(\frac{s'}{p'_e} - \frac{t'}{p'_e}\right) + \frac{\left(\frac{t'}{p'_e} - C_\eta(\dot{\varepsilon}_t)\right)^2}{\left(\frac{s'}{p'_e} + \frac{t'}{p'_e}\right)}\left[1 + \frac{\sqrt{\frac{s'^2}{p'^2_e} + [C_\eta(\dot{\varepsilon}_t)]^2 - 2\frac{t'}{p'_e}C_\eta(\dot{\varepsilon}_t)}}{\left(\frac{t'}{p'_e} - C_\eta(\dot{\varepsilon}_t)\right)}\right] \quad (101)$$

Still recalling that $s'/p'_e - t'/p'_e = s/p'_e - \Delta u/p'_e - t'/p'_e$ and that $s/p'_e - t'/p'_e = 1$, thus $(s'/p'_e - t'/p'_e) = 1 - \Delta u/p'_e$. Hence, a simple way of determining (s'_b/p'_e) is given by Equation 102

$$\frac{s'_b}{p'_e} = 1 - \frac{\Delta u}{p'_e} + \frac{t'_b}{p'_e} \quad (102)$$

Table 4. Validation checking of the generalized ***complementary principle 1*** for San Francisco Bay Mud [data from Lacerda (1976)].

Test	$\varepsilon_t\,(\%)$	$\dot{\varepsilon}_t\,(\%/\text{min.})$	$t'\ /\ p'_e$	$s'\ /\ p'_e$	$\Delta u\ /\ p'_e$	C_η	$tan\phi'_{emob}$
FP–23	0.13	~1.0 × 10^{-1}	0.123	0.953	0.17	0.09	0.035
FP–32	0.13	~1.0 × 10^{-1}	0.18	0.95	0.23	0.09	0.096
FP–42	0.13	~1.0 × 10^{-1}	0.17	0.960	0.21	0.09	0.075
CR–I–ST–2	0.14	8.4 × 10^{-2}	0.172	1.01	0.16	0.09	0.082
FP–32	0.29	~1.0 × 10^{-1}	0.241	0.920	0.32	0.09	0.170
FP–42	0.29	~1.0 × 10^{-1}	0.231	0.931	0.30	0.09	0.156
CR–I–1	0.29	0.09	0.234	0.934	0.300	0.09	0.159
FP–23	0.35	~1.0 × 10^{-1}	0.217	0.917	0.30	0.09	0.143
FP–32	0.36	~1.0 × 10^{-1}	0.264	0.914	0.35	0.09	0.199
FP–42	0.35	~1.0 × 10^{-1}	0.25	0.91	0.34	0.09	0.183
SR–I–8	0.33	5.5 × 10^{-4}	0.193	0.866	0.33	0.035	0.187
FP–23	0.45	~1.0 × 10^{-1}	0.25	0.89	0.36	0.09	0.187
FP–32	0.46	~1.0 × 10^{-1}	0.28	0.90	0.38	0.09	0.222
CR–I–1	0.45	1.0 × 10^{-2}	0.234	0.874	0.36	0.06	0.207
CR–I–ST–2	0.55	1.0 × 10^{-2}	0.242	0.852	0.39	0.06	0.223
FP–23	0.58	~1.0 × 10^{-1}	0.265	0.885	0.38	0.09	0.207
CR–71–1	0.60	0.075	0.281	0.871	0.41	~0.09	0.232
SR–I–8	0.68	5.5 × 10-4	0.244	0.794	0.45	0.04	0.270
FP–13	0.69	~1.0 × 10^{-1}	0.29	0.88	0.41	0.09	0.241
FP–23	0.70	~1.0 × 10^{-1}	0.28	0.87	0.41	0.09	0.231
FP–32	0.70	~1.0 × 10^{-1}	0.315	0.875	0.44	0.09	0.276
FP–42	0.71	~1.0 × 10^{-1}	0.304	0.854	0.45	0.09	0.268
CR–I–1	0.75	6.5 × 10^{-4}	0.234	0.804	0.43	0.04	0.252
SR–I–8	0.75	5.5 × 10^{-4}	0.247	0.784	0.46	0.035	0.285
FP–23	0.75	~1.0 × 10^{-1}	0.285	0.86	0.43	0.09	0.240
FP–42	0.75	~1.0 × 10^{-1}	0.304	0.851	0.46	0.09	0.269
FP–13	1.0	~1.0 × 10^{-1}	0.319	0.833	0.48	0.09	0.298
FP–23	1.0	~1.0 × 10^{-1}	0.325	0.833	0.47	0.09	0.306
FP–32	1.0	~1.0 × 10^{-1}	0.334	0.846	0.49	0.09	0.314
FP–42	1.0	~1.0 × 10^{-1}	0.322	0.825	0.50	0.09	0.305
SR–I–9	1.0	1.0 × 10^{-1}	0.317	0.863	0.45	0.09	0.283
CR–71–1	0.97	~1.0 × 10^{-2}	0.281	0.811	0.47	0.06	0.290
CR–I–ST–2	1.00	~1.0 × 10^{-1}	0.312	0.832	0.48	0.09	0.288
FP–13	1.15	~1.0 × 10^{-1}	0.328	0.82	0.51	0.09	0.317
FP–23	1.16	~1.0 × 10^{-1}	0.312	0.812	0.50	0.09	0.296
FP–32	1.18	~1.0 × 10^{-1}	0.345	0.835	0.51	0.09	0.335
FP–42	1.20	~1.0 × 10^{-1}	0.33	0.800	0.53	0.09	0.329
FP–13	1.38	~1.0 × 10^{-1}	0.34	0.80	0.54	0.09	0.345
FP–23	1.40	~1.0 × 10^{-1}	0.324	0.794	0.53	0.09	0.323
FP–32	1.42	~1.0 × 10^{-1}	0.356	0.816	0.54	0.09	0.362
FP–42	1.44	~1.0 × 10^{-1}	0.339	0.784	0.56	0.09	0.352
FP–13	1.62	~1.0 × 10^{-1}	0.347	0.79	0.56	0.09	0.362
FP–23	1.62	~1.0 × 10^{-1}	0.332	0.782	0.55	0.09	0.342
FP–32	1.64	~1.0 × 10^{-1}	0.364	0.809	0.56	0.09	0.379
FP–13	1.83	~1.0 × 10^{-1}	0.354	0.774	0.58	0.09	0.384
FP–23	1.86	~1.0 × 10^{-1}	0.336	0.766	0.57	0.09	0.357
FP–42	1.80	~1.0 × 10^{-1}	0.345	0.755	0.59	0.09	0.380
FP–42	2.05	~1.0 × 10^{-1}	0.345	0.735	0.61	0.09	0.393
FP–13	2.08	~1.0 × 10^{-1}	0.357	0.757	0.60	0.09	0.400
FP–23	2.12	~1.0 × 10^{-1}	0.34	0.74	0.60	0.09	0.380
FP–32	2.10	~1.0 × 10^{-1}	0.372	0.772	0.60	0.09	0.417
CR–I–ST–2	2.21	~1.0 × 10^{-1}	0.347	0.742	0.61	0.09	0.392
FP–32	2.24	~1.0 × 10^{-1}	0.375	0.770	0.61	0.09	0.424
FP–13	2.30	~1.0 × 10^{-1}	0.36	0.74	0.62	0.09	0.418
FP–23	2.35	~1.0 × 10^{-1}	0.345	0.735	0.61	0.09	0.393
FP–32	2.35	~1.0 × 10^{-1}	0.375	0.765	0.61	0.09	0.427
FP–42	2.42	~1.0 × 10^{-1}	0.349	0.719	0.63	0.09	0.412
FP–13	2.51	~1.0 × 10^{-1}	0.36	0.73	0.63	0.09	0.425
FP–23	2.55	~1.0 × 10^{-1}	0.347	0.717	0.63	0.09	0.410
FP–32	2.84	~1.0 × 10^{-1}	0.375	0.750	0.63	0.09	0.439
FP–23	2.90	~1.0 × 10^{-1}	0.35	0.710	0.64	0.09	0.421
FP–13	2.98	~1.0 × 10^{-1}	0.365	0.715	0.65	0.09	0.447

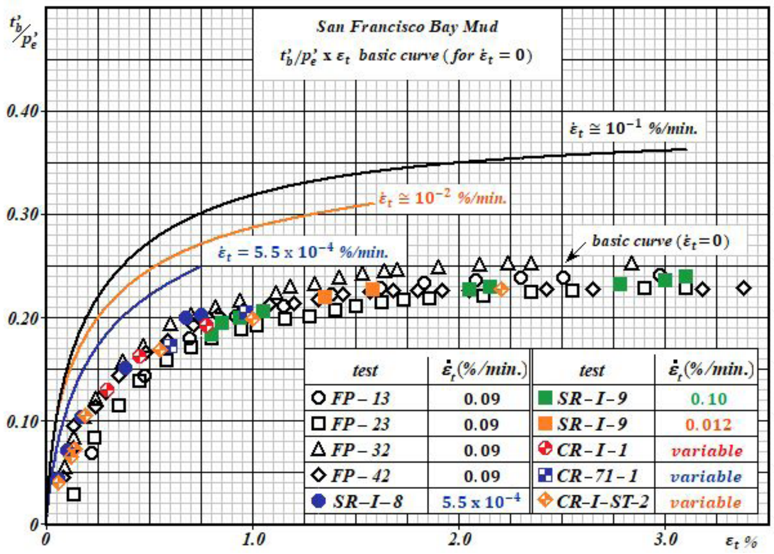

Figure 60. Normalized basic curve $t'_b \,/\, p'_e \times \varepsilon_t$ for normally consolidated specimens of San Francisco Bay Mud [data from Lacerda (1976)].

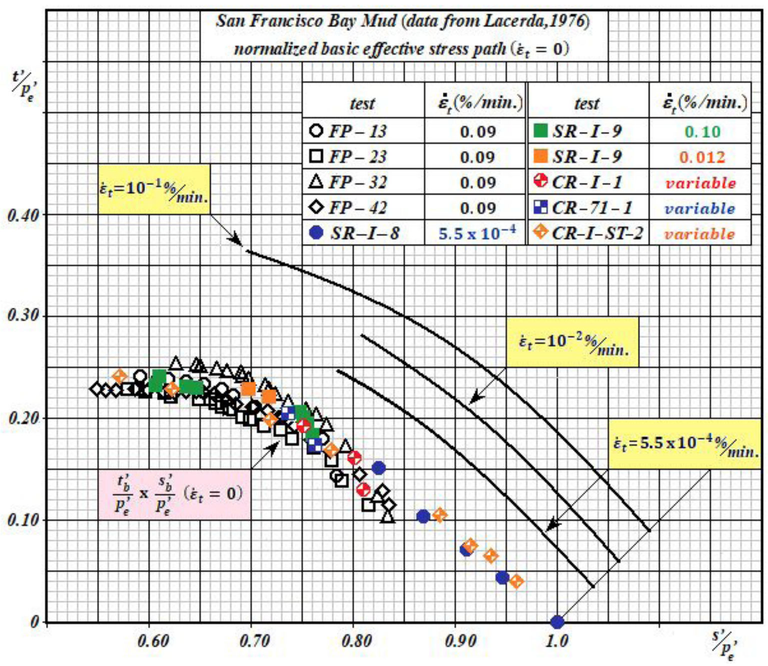

Figure 61. bESPn – normalized basic effective stress path $\left(\dot{\varepsilon}_t = 0\right)$ for normally consolidated San Francisco Bay Mud [data from Lacerda (1976)].

By plotting the ordered pairs $\left(s'_b \,/\, p'_e, t'_b \,/\, p'_e\right)$, one can then obtain the normalized basic effective stress path (bESPn), which is presented in Figure 61. Except for the points corresponding to the beginning of tests FP-13, FP-23, FP-32 and FP-42, which are not plotted in Figure 61 for being suspected of having been affected by bedding errors, as already discussed, all points of the remaining tests can be assumed as lying on a single line. This line is the bESPn (normalized basic effective stress path) for normally consolidated San Francisco Bay Mud. For being associated with the strain rate $\dot{\varepsilon}_t = 0$, the bESPn shown in Figure 61 only represents the mobilization of the frictional part of shear resistance.

An interesting and remarkable aspect which should not escape from observation is that the ESPs shown in Figures 58 and 61 would represent Roscoe Surfaces sections, each one corresponding to a fixed shear strain rate $\dot{\varepsilon}_t$, as suggested by Leroueil et al. cited by Jamiolkowski et al. (1991).

Finally, it will be shown that normally consolidated San Francisco Bay Mud also satisfies *corollary 3*, whose statement is rewritten below.

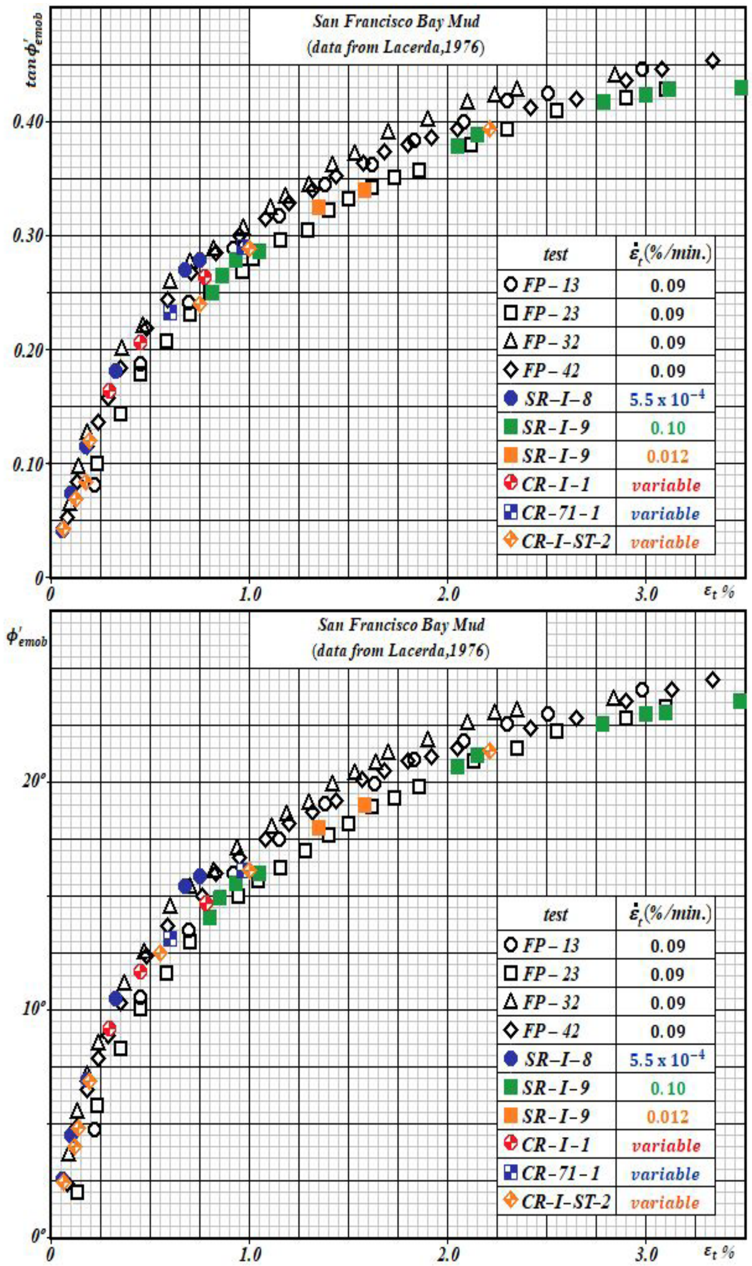

Figure 62. Curves $tan\,\phi'_{emob} \times \varepsilon_t$ and $\phi'_{emob} \times \varepsilon_t$ for normally consolidated San Francisco Bay Mud [data from Lacerda (1976)].

Corollary 3: $\overline{CIUCL}$ ***tests carried out on a normally consolidated clay showing homothetic ESPs for any fixed*** $\dot{\varepsilon}_t$ ***and a unique curve*** $\Delta u\,/\,p'_e \times \varepsilon_t$***, regardless of*** $\dot{\varepsilon}_t$***, will show a unique curve*** $tan\,\phi'_{emob} \times \varepsilon_t$***, whatever*** $\dot{\varepsilon}_t$ ***is.***

Curve $tan\,\phi'_{emob} \times \varepsilon_t$ can be plotted taking s', t' and $\mathbb{V}$ values corresponding to each ε_t value and computing $tan\,\phi'_{emob}$ for each test, via Equation 56, reproduced below.

$$tan\,\phi'_{emob} = \frac{\left(\dfrac{\sigma'_1 - \sigma'_3}{2} - \mathbb{V}\right)}{\sqrt{\sigma'_1\sigma'_3}} = \frac{(t' - \mathbb{V})}{\sqrt{s'^2 - t'^2}} \qquad (56)$$

$tan\,\phi'_{emob}$ values can also be determined rewriting Equation 56 in a normalized way relative to p'_e as

$$tan\,\phi'_{emob} = \frac{\left(\dfrac{t'}{p'_e} - \dfrac{\mathbb{V}}{p'_e}\right)}{\sqrt{\left(\dfrac{s'}{p'_e}\right)^2 - \left(\dfrac{t'}{p'_e}\right)^2}} = \frac{\dfrac{t'}{p'_e} - C_\eta\left(\dot{\varepsilon}_t\right)}{\sqrt{\left(\dfrac{s'}{p'_e}\right)^2 - \left(\dfrac{t'}{p'_e}\right)^2}} \qquad (103)$$

Equation 103 can be potentially applied to each and every point of all tests presented in this article. However, only values of $C_\eta\left(\dot{\varepsilon}_t\right)$ for the shear strain rates $\dot{\varepsilon}_t$ equal to

$5.5\times10^{-4}\%/\min.$, $10^{-2}\%/\min.$ and $10^{-1}\%/\min.$ could be determined, which provided values of C_η equal to 0.035, 0.06 and 0.09, respectively. These values of C_η allowed the curves shown in Figure 62 to be drawn.

It can be observed from Figure 62 that, to fully mobilize the true angle of friction $\left(\phi'_e \cong 24°\right)$ of normally consolidated San Francisco Bay Mud in $\overline{\text{CIUCL}}$ tests type, it is necessary a shear strain at failure $\varepsilon_{tf} \cong 3\%$ corresponding to an axial strain at failure $\varepsilon_{af} \cong 4\%$.

9. Special undrained tests

9.1 Undrained creep tests

Undrained creep is meant in this article as the phenomenon by which a soil specimen is deformed over time when subjected to a constant state of total stress under undrained conditions.

The undrained creep studied in this article will be restricted to those cases where the specimens are of cylindrical shape, subjected to an axysimmetric state of stress, with the axial (vertical) total stress, denoted by σ_a, being the major principal stress and the radial (horizontal) total stress, denoted by σ_r, being the minor principal stress. The study will be also restricted to normally consolidated, saturated plastic clays with no cementation between grains.

To understand the undrained creep under the light of the concepts presented in this article and how it can be related to $\overline{\text{CIUCL}}$ tests, consider Figure 63. This figure shows several $\overline{\text{CIUCL}}$ ESPs, each one corresponding to a different shear strain rate $\dot{\varepsilon}_t$ as, for instance, ESP ***ABCDEFG*** associated with $\dot{\varepsilon}_t = \dot{\varepsilon}_{t1}$. Figure 63 also shows several 45º sloped straight lines, which, according to the *generalized complementary principle 1*, are the loci in which ε_t, $\left(\Delta u / p'_e\right)$ and $\tan\phi'_{emob}$ values are constant. As an example, for the straight line given by ***YFTL***, $\varepsilon_t = \varepsilon_{t4}$, $\Delta u(\boldsymbol{Y}) = \Delta u(\boldsymbol{F}) = \Delta u(\boldsymbol{T}) = \Delta u(\boldsymbol{L})$ and $\tan\phi'_{emob}(\boldsymbol{Y}) = \tan\phi'_{emob}(\boldsymbol{F}) = \tan\phi'_{emob}(\boldsymbol{T}) = \tan\phi'_{emob}(\boldsymbol{L})$.

During the undrained shear phase of a $\overline{\text{CIUCL}}$ test starting from point ***A*** in Figure 63 with a strain rate of $\dot{\varepsilon}_{t3}$, there is an instantaneous jump from point ***A*** to point ***H*** corresponding to the viscous resistance mobilization $\mathbb{V}(\boldsymbol{H})$. At point ***H***, where $\varepsilon_t = 0$, shear strains start taking place and, consequently, frictional resistance begins to be mobilized and pore pressure generated. As soil deforms, the ESP to be followed is ***HIJKLM***. According to *corollary 3*, when point ***M*** is reached, the shear strain $\varepsilon_t = \varepsilon_{tf}$, corresponding to failure, and, therefore, $\phi'_{emob} = \phi'_e$.

Consider now another specimen from the same normally consolidated, saturated clay subjected to the same isotropic effective stress p'_e (point ***A*** in Figure 63). Such specimen will be subjected to an undrained creep test under $t' = t'_{uc}$ (subscript *uc* standing for undrained creep) corresponding to the ordinate of point ***H***, whose value will be kept constant throughout the whole test.

Immediately after applying t'_{uc}, the shear strain at $t = 0^+$ is still $\varepsilon_t = 0$, which means that there is no mobilization of frictional resistance yet, and hence the entire mobilized shear resistance is due to viscosity. Thus, at point ***H***, the shear stress $\tau_{45°} = t'_{uc} = \mathbb{V}(\boldsymbol{H}) = \mathbb{V}(p'_e, \dot{\varepsilon}_{t3})$. At $t = 0^+$, even with $\varepsilon_t = 0$, there is mobilization of viscous resistance, which means that $\dot{\varepsilon}_t \neq 0$ at point ***H***.

Turning on the load frame motor at the beginning of the undrained shear phase of a conventional $\overline{\text{CIUCL}}$ test, making the shear strain rate to be $\dot{}_{t3}$, mobilizes instantaneously the viscous resistance $\mathbb{V}(\boldsymbol{H}) = C_\eta\left(\dot{\varepsilon}_{t3}\right)p'_e$. Conversely, if in an undrained creep test a $t'_{uc} = \mathbb{V}(\boldsymbol{H})$ is applied, the specimen will start to deform with a shear strain rate $\dot{\varepsilon}_t = \dot{\varepsilon}_{t3}$. This is due to the hypothesis that at any instant and on each and every plane given by α the shear stress τ_α is made up of the

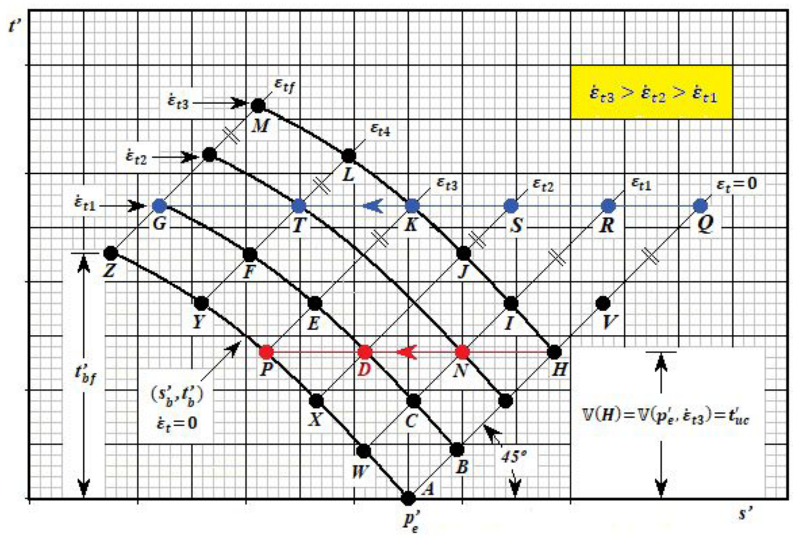

Figure 63. Effective stress paths during undrained creep tests.

sum of two components: the frictional resistance component $\tau_{\phi\alpha}$ and the viscous resistance component $\tau_{\eta\alpha}$. As at point ***H*** the frictional resistance component $\tau_{\phi\alpha} = 0$ (since $\varepsilon_t = 0$), all the shear resistance must exclusively be assigned to the viscous component. Conversely, if the viscous resistance component $\tau_{\eta\alpha}$ 0, which occurs whenever $\dot{\varepsilon}_t = 0$, then the applied shear stress must entirely be resisted by friction.

Based on the above discussion, in the undrained creep test, after applying t'_{uc} as shown in Figure 63, the specimen begins to deform at point ***H*** with a shear strain rate $\dot{\varepsilon}_t = \dot{\varepsilon}_{t3}$ and the ESP to be followed is ***HNDP***. At point ***N***, where $\varepsilon_t = \varepsilon_{t1}$, there is some frictional resistance already mobilized. Considering that $t'_{uc} = \tau_{45°}$ is kept constant, the increasing mobilization of frictional resistance over time causes a decrease of equal magnitude in the mobilized viscous resistance, which in its turn is $\mathbb{V} = \eta(e) f(\dot{\varepsilon}_t)$. As the creep is undrained, $\eta(e) = \text{constant}$. Therefore, if $\mathbb{V}$ decreases over time, so does $f(\dot{\varepsilon}_t)$, making $\dot{\varepsilon}_t$ decreases over time. Moreover, since ε_t increases over time, pore pressure Δu also increases.

It should be noted that, during undrained creep, the effective stress path ***HNDP*** crosses several ESPs from conventional $\overline{\text{CIUCL}}$ tests of decreasing strain rates, each ESP corresponding to a conventional $\overline{\text{CIUCL}}$ test carried out with $\dot{\varepsilon}_t = \text{constant}$.

The process of transference from viscous shear resistance to frictional shear resistance continues until the ESP reaches point ***P*** on the basic ESP (see Figure 63). When point ***P*** is reached, the undrained creep comes to its end because all the viscous resistance will have been transferred to frictional resistance.

This process holds valid for each and every plane given by α. This happens because the diameter of the Mohr's circle of effective stress does not change during undrained creep. Therefore, for a fixed plane α, the shear stress τ_α, which is the sum of the viscous resistance component $(\tau_{\eta\alpha})$ and the frictional resistance component $(\tau_{\phi\alpha})$, is kept constant throughout the whole process.

The previous paragraph also leads to the following discussion: during undrained creep shown in Figure 63 the Mohr's circle of effective stress has a constant diameter equal to $2t'_{uc}$. At point ***H*** one has: $\mathbb{V}(\boldsymbol{H}) = \mathbb{V}(p'_e, \dot{\varepsilon}_{t3}) = \eta(e) f(\dot{\varepsilon}_{t3}) = t'_{uc}$, $\varepsilon_t = 0$, $\dot{\varepsilon}_t = \dot{\varepsilon}_{t3}$, $\Delta u = 0$ and the mobilized frictional resistance is equal to zero, whatever the plane may be. Thus, the viscosity ellipse and the Mohr's circle of effective stress coincide and the friction ellipse collapses into the segment of magnitude $(\sigma'_a - \sigma'_r)$, as shown in Figure 64a.

At point ***N*** in Figures 63 and 64, the shear strain $\varepsilon_t = \varepsilon_{t1}$. Thus, according to *corollary 3*, there is some mobilized frictional resistance. This makes the mobilized viscous resistance $\mathbb{V}(\boldsymbol{N})$ to be lower than $\mathbb{V}(\boldsymbol{H})$. Thus, at point ***N***, $\varepsilon_t = \varepsilon_{t1}$, and $\dot{\varepsilon}_t = \dot{\varepsilon}_{t2} < \dot{\varepsilon}_{t3}$. Therefore, $\mathbb{V}(\boldsymbol{N}) = \eta(e) f(\dot{\varepsilon}_{t2})$ and $\Delta u(\boldsymbol{N}) = \boldsymbol{NH}$. In brief, as undrained creep goes on, the minor axis of the viscosity ellipse decreases, making the minor axis of the friction ellipse increases. This is what is shown in Figure 64b.

At point ***D*** in Figure 63, the shear strain $\varepsilon_t = \varepsilon_{t2}$. The shear strain rate $\dot{\varepsilon}_t = \dot{\varepsilon}_{t1} < \dot{\varepsilon}_{t2}$, $\mathbb{V}(\boldsymbol{D}) = \eta(e) f(\dot{\varepsilon}_{t1}) < \mathbb{V}(\boldsymbol{N})$ and the pore pressure $\Delta u(\boldsymbol{D}) = \boldsymbol{DH}$. At point ***D*** the minor axis of the viscosity ellipse becomes smaller than it was at point ***N***, whereas the minor axis of the friction ellipse at point ***D*** becomes larger than it was at point ***N***, as shown in Figure 64c.

Finally, at point ***P*** in Figure 63, $\varepsilon_t = \varepsilon_{t3}$ and $\dot{\varepsilon}_t = 0$, indicating that all viscous resistance has entirely been transferred to frictional resistance. Thus, at point ***P***, $\mathbb{V}(\boldsymbol{P}) = 0$ and the viscosity ellipse collapses into the segment of magnitude $(\sigma'_a - \sigma'_r)$. On the other hand, the friction ellipse becomes coincident to the Mohr's circle of effective stress as shown in Figure 64d and pore pressure magnitude is given by ***PH*** in Figure 63.

If another undrained creep test was carried out with a t' value corresponding to point ***V*** in Figure 63, the same mechanism of transference from viscous resistance to frictional resistance would take place. In this case, however, the ESP to be followed in Figure 63 would be ***VIEY*** and undrained creep would come to an end at point ***Y*** on the basic bESP. As t'_{uc} in this test would be higher than t'_{uc} corresponding to the test whose ESP is ***HNDP***, the shear strain ε_t at the end of undrained creep would be $\varepsilon_t = \varepsilon_{t4} > \varepsilon_{t3}$. The final excess pore pressure would be higher than that observed in the previous test, being represented by ***YV*** in Figure 63.

It is worth observing that, except for a particular but important feature to be discussed further, undrained creep phenomenon is analogous to isotropic consolidation. During isotropic consolidation, the state of total stress is kept constant and there is an increase in effective stress equal to the dissipation of the excess pore pressure along time. During undrained creep, the state of total stress is also kept constant and there is an increase in the mobilized frictional resistance equal to the decrease in the mobilized viscous resistance along time.

The only feature that makes such analogy not be "perfect" is explained next. This explanation can be made going back to Figure 63 to analyse the undrained creep test carried out with a t'_{uc} value corresponding to the ordinate of point ***Q*** in Figure 63.

The ESP of an undrained creep test starting at point ***Q*** in Figure 63 is ***QRSKTG***. Such an ESP crosses several ESPs of conventional $\overline{\text{CIUCL}}$ tests of decreasing strain rates. Each ESP corresponds to a conventional $\overline{\text{CIUCL}}$ test carried out with a constant $\dot{\varepsilon}_t$. Such ESPs can be viewed as Roscoe's surfaces sections, each one associated with a given $\dot{\varepsilon}_t$. On its way from the right to the left an undrained creep ESP crosses several ESPs of decreasing $\dot{\varepsilon}_t$ values, transferring mobilized viscous resistance to mobilized frictional resistance until reaching point ***G***, whose shear strain is ε_{tf} and whose shear strain rate is $\dot{\varepsilon}_{t1}$. At point ***G***, all the available resistance provided by friction, given by t'_{bf}, has already been fully mobilized.

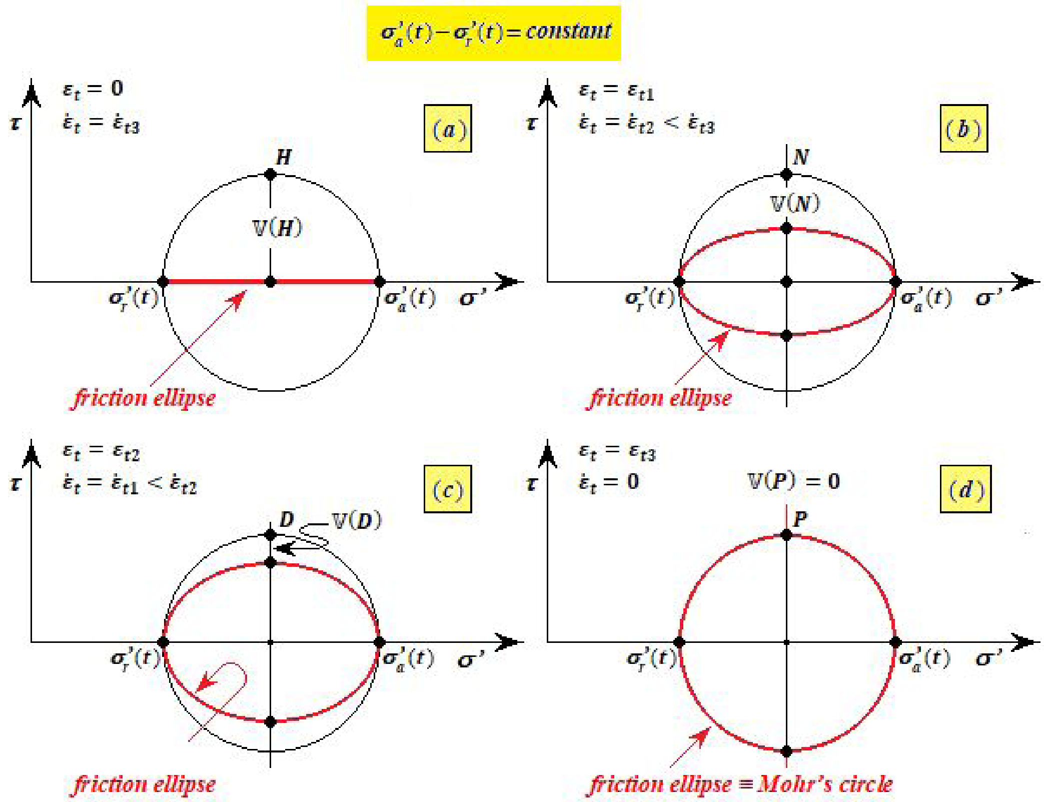

Figure 64. Mohr's circles of effective stress, friction elipses and mobilized states of friction during undrained creep ESP ***HNDP***. (a) At point ***H*** – no friction mobilized (b) Mobilized state of friction at point ***N*** (c) Mobilized state of friction at point ***D*** (d) At point ***P*** – friction fully mobilized.

However, the value of t'_{uc} applied is now $t'(\boldsymbol{Q}) > t'_{bf}$. Thus, in order to meet equilibrium conditions after reaching point ***G***, the specimen needs to make use of an additional resistance corresponding to the difference $t'(\boldsymbol{Q}) - t'_{bf}$. This difference is supplied by the mobilized viscous resistance given at point ***G*** by $\mathbb{V}(\boldsymbol{G}) = \eta(e) f(\dot{\varepsilon}_{t1})$. However, to keep this viscous resistance active so that the equilibrium is satisfied, the specimen must continue to deform with a shear strain rate equal to $\dot{\varepsilon}_{t1}$, that is, shear strains will continue to take place indefinitely with a rate $\dot{\varepsilon}_{t1}$. This is the so-called undrained creep failure.

The undrained creep mechanism described above could be illustrated, without loss of generalization, replacing the axes s' and t' in Figure 63 by the axes s' / p'_e and t' / p'_e and plotting the normalized effective stress paths $(s' / p'_e) \times (t' / p'_e)$. Now, even without not being able to evaluate ε_t and $\dot{\varepsilon}_t$ along time, one can come to some conclusions of remarkable theoretical and practical importance concerning undrained creep. Such conclusions encompass the two cases listed below:

(a) $t'_{uc} / p'_e \leq t'_{bf} / p'_e$

(b) $t'_{uc} / p'_e > t'_{bf} / p'_e$

In case (a), if $(t'_{uc} / p'_e) < (t'_{bf} / p'_e)$, there will be no failure by creep. Shear strain ε_t will approach a definite value over time, shear strain rate will approach zero and creep will come to an end. The ε_t value at which creep will cease can be found entering the basic curve $t'_b / p'_e \times \varepsilon_t$ with the value $t'_b / p'_e = t'_{uc} / p'_e$, thus determining the ε_t value with which t'_{uc} / p'_e is associated.

In case (b), if $(t'_{uc} / p'_e) > (t'_{bf} / p'_e)$, there will be failure by undrained creep in a finite time period, no matter how long it takes. In this case, the higher the ratio (t'_{uc} / p'_e), the shorter the time period to failure (and the higher the strain rate at failure). In this case, failure will occur as soon as $\varepsilon_t = \varepsilon_{tf}$ and the strain rate at failure can be predicted.

Before going on with the study of undrained creep, it is adequate to recall the excerpt from Taylor (1948, pp. 379-380), reproduced at the end of section 4, which reveals his ideas about the action of adsorbed water. Most of these ideas have inspired the author to develop the model presented in this article.

The undrained creep mechanism was also clearly depicted by Bjerrum (1973) in an excerpt of his classic state-of-the-art report, which is reproduced below to avoid loss of fidelity to the original:

"*In general, in a natural clay an applied shear stress will be carried partly as cohesion in the semi-rigid water-film type* *contact points and partly as friction in contact points with mineral contact. However, as demonstrated by Schmertmann and Hall (1961), with time the effect of the interparticle creep will be a tendency to transfer loads from the cohesive to the more rigid and stable frictional contact points with the result that the mobilized cohesion decreases and a correspondingly greater part of the available friction becomes mobilized. As this process will lead to a reduction in shear stress in the cohesive contact points, the result is a reduction in the rate of failure of contact points, and thus in the rate of creep deformation. If the shear stress acting on the clay element is smaller than the available friction, the cohesive contact points will ultimately be relieved and the creep deformations will come to a halt. If the shear stresses exceed the available frictional resistance, the difference will have to be carried by the cohesive-type contact points. The rate of creep will therefore decrease until this condition is reached, and from then on it will remain constant*." (Bjerrum, 1973, p. 125).

With the reproduction of the above excerpts, there is no doubt that both Taylor (1948) and Bjerrum (1973) captured the mechanism the author tried to quantify in this article using the concept of viscous resistance, improperly called cohesion, as already discussed.

After discussing undrained creep and its consequences under the light of the model presented in section 7, one can now check its validity when applied to normally consolidated samples of San Francisco Bay Mud.

9.2 Undrained creep tests on normally consolidated San Francisco Bay Mud specimens

In order to check whether or not the proposed model applies to the undrained creep tests carried out on normally consolidated specimens of San Francisco Bay Mud, the following Lacerda's (1976) undrained creep tests listed in Table 2 are available: CR–I–1, CR–I–2, CR–71–1 and CR–I–ST–2.

According to section 9.1, in order to distinguish among the undrained creep tests listed above those that would fail from those in which creep would cease, one must know the t'_{bf} / p'_e value for normally consolidated San Francisco Bay Mud as well as the t'_{uc} / p'_e value corresponding to each of the undrained creep tests to be analyzed.

Test CR–71–1 was interrupted after about 100 minutes. Therefore, the available data are so scarce that they are not useful. As test CR–I–2 specimen seemed to be slightly overconsolidated (with an $OCR \cong 1.3$), it has been decided not to include its data in the analyses presented in section 8. However, as test CR–I–2 lasted more than 10000 minutes and the specimen failed, it was decided to take it into account in this section due to the data scarcity concerning Lacerda's (1976) undrained creep tests. Due to such scarcity, to better analyze the model's ability in predicting soil behaviour during undrained creep, two additional tests carried out by Lacerda (1976) have been selected. Although these additional tests data are not entirely available in Lacerda's (1976) PhD thesis dissertation, the available data can provide valuable information to be considered in this section. Such additional tests, denoted by S–I–3 and CR–I–5, are both undrained creep tests.

It would also be interesting to analyze the step creep test CR–I–ST–2 carried out in seven steps. However, among these seven steps, only the last one is of interest for this section. So, it was decided to only make a brief comment about the last step of test CR–I–ST–2. The undrained creep tests to be analyzed will then be those whose data are summarized in Table 5.

In order to identify among the tests listed in Table 5 those that would fail and those in which creep would cease, one must compare their t'_{uc} / p'_e values with the t'_{bf} / p'_e value of normally consolidated San Francisco Bay Mud.

Based on Figures 61 and 63 and on what has been discussed in section 9.1, Figure 65 can be drawn showing the normalized ESPs corresponding to $\dot{\varepsilon}_t = 5.5 \times 10^{-4}\% / \text{min.}$, $\dot{\varepsilon}_t = 10^{-2}\% / \text{min.}$ and $\dot{\varepsilon}_t = 10^{-1}\% / \text{min.}$ and the bESPn that corresponds to $\dot{\varepsilon}_t = 0$. Point ***M*** of coordinates $\left(s'_f / p'_e, t'_f / p'_e\right) = (0.70, 0.36)$, shown in Figure 65, corresponds to failure of $\overline{\text{CIUCL}}$ tests carried out with $\dot{\varepsilon}_t = 10^{-1}\% / \text{min.}$. Point ***Z*** coordinates $\left(s'_{bf} / p'_e, t'_{bf} / p'_e\right)$ can easily be computed. Firstly, one determines t'_{bf} / p'_e by entering Equation 99 with $\phi'_{emob} \cong 24°$ and with point ***M*** coordinates (0.70, 0.36) to obtain $t'_{bf} / p'_e = 0.24$. Then, by entering Equation 102 with $t'_{bf} / p'_e = 0.24$ and $\Delta u / p'_e$ corresponding to $\varepsilon_t = \varepsilon_{tf}$, one obtains $s'_{bf} / p'_e = 0.59$. Thus, point ***Z*** coordinates $\left(s'_{bf} / p'_e, t'_{bf} / p'_e\right) = (0.59, 0.24)$ correspond to failure of $\overline{\text{CIUCL}}$ tests "carried out" with $\dot{\varepsilon}_t = 0$. At points ***M*** and ***Z***, $\phi'_{emob} = \phi'_e = 24°$ and, according to *corollary 3*, the shear strain value (ε_t) at both points is the same, corresponding to the shear strain at failure $\varepsilon_t = \varepsilon_{tf} = 3\%$. Besides, points ***M*** and ***Z*** lie on the same 45º sloped straight line. This 45º sloped straight line, defined by points ***M*** and ***Z***, is the locus of all points on the plane $\left(s' / p'_e\right) \times \left(t' / p'_e\right)$ representing failure of San Francisco Bay Mud normally consolidated specimens, subjected to $\overline{\text{CIUCL}}$ tests, irrespective of the shear strain rate $\dot{\varepsilon}_t$ applied during the test.

In order to analyze the tests listed in Table 5 under the light of the model presented in section 7, the t'_{uc} / p'_e value of each undrained creep test must be compared with the t'_{bf} / p'_e value of 0.24.

For test CR–I–1, $t'_{uc} / p'_e = 0.234$. In this case, according to the model, the undrained creep would cease. In order to evaluate the shear strain ε_t at which the creep is expected to cease, one should enter into the basic curve $t'_b / p'_e \times \varepsilon_t$ in Figure 60 with the value $t'_b / p'_e = t'_{uc} / p'_e = 0.234$, thus determining the ε_t value with which t'_{uc} / p'_e is associated. Following this procedure, an $\boldsymbol{\varepsilon_t}$ value from 2% to 3% is found. The $\varepsilon_t \times \dot{\varepsilon}_t$ plot corresponding to test CR–I–1 is shown in Figure 66. Such a test lasted about 20000 minutes, during which the shear strain rate $\dot{\varepsilon}_t$ decreased, reaching $10^{-5}\% / \text{min.}$, after which the test was ended. Such result is in agreement with the model predictions.

In test SR–I–3, $t'_{uc} / p'_e = 0.195$. In this case, since $t'_{uc} / p'_e < t'_{bf} / p'_e = 0.24$, undrained creep should also cease.

By entering into the basic curve $t'_b / p'_e \times \varepsilon_t$ of Figure 60 with the value $t'_b / p'_e = t'_{uc} / p'_e = 0.195$, an $\varepsilon_t \cong 1\%$ is obtained. This is the expected value towards which ε_t should tend along time. The $\varepsilon_t \times \dot{\varepsilon}_t$ plot of test SR–I–3 is shown in Figure 66. Such a figure shows that $\dot{\varepsilon}_t$ decreases all test long. After about 10000 minutes, when $\dot{\varepsilon}_t = 1.4 \times 10^{-5}\% / \text{min.}$ and $\varepsilon_t = 0.87$ %, test SR–I–3 was finished. These results are also in agreement with the model predictions.

In test CR–I–2, $t'_{uc} / p'_e = 0.313$. Since $t'_{uc} / p'_e > t'_{bf} / p'_e = 0.24$, a failure by undrained creep should be expected. By making (by feeling) an extrapolation of the ESP corresponding to $\dot{\varepsilon}_t = 5.5 \times 10^{-4}\% / min.$ shown in Figure 65, one can estimate, for this $\dot{\varepsilon}_t$ value, a $t'_f / p'_e = 0.305$, which is very close to $t'_{uc} / p'_e = 0.313$ corresponding to test CR–I–2. Therefore, it is expected that failure occurs with a shear strain rate $\dot{\varepsilon}_t$ close to $5.5 \times 10^{-4}\% / \text{min.}$. This is indeed the case observing the $\varepsilon_t \times \dot{\varepsilon}_t$ plot for test CR–I–2 in Figure 66. The shear strain rate continuously decreases up to $\varepsilon_t = 3.8\%$, reaching a minimum shear strain rate of $\dot{\varepsilon}_t = 1.5 \times 10^{-4}\% / \text{min.}$. From then on, along 14 days, the specimen was deformed during failure, with a shear strain rate $2 \times 10^{-4}\% / \text{min.} \le \dot{\varepsilon}_t \le 6 \times 10^{-4}\% / \text{min.}$, with an average value of $3.4 \times 10^{-4}\% / \text{min.}$ In spite of making use of an extrapolation of the ESP corresponding to the shear strain rate $\dot{\varepsilon}_t = 5.5 \times 10^{-4}\% / \text{min.}$, the prediction is fairly good and illustrates the validity of the model.

A similar analysis can be carried out for test CR–I–5, whose value of $t'_{uc} / p'_e = 0.351$. Since $t'_{uc} / p'_e > t'_{bf} / p'_e$, a failure by undrained creep is also expected. However, as $t'_{uc} / p'_e \quad 0.351$, the shear strain rate at failure for test CR–I–5 is expected to be higher than that observed for test CR–I–2. By extrapolating (by feeling) the ESP corresponding to an $\dot{\varepsilon}_t = 1.0 \times 10^{-2}\% / min.$ in Figure 65, one can estimate, for this $\dot{\varepsilon}_t$ value, a $t'_f / p'_e \cong 0.33$. The value of $t'_{uc} / p'_e = 0.351$ is only 6% higher than 0.33. This suggests that for test CR–I–5 one can expect a shear strain rate at failure close to $10^{-2}\% / min.$. As shown in Figure 66, the $\varepsilon_t \times \dot{\varepsilon}_t$ plot corresponding to test CR–I–5 shows a decreasing shear strain rate up to $\varepsilon_t = 3.0$ %, when $\dot{\varepsilon}_t$ reaches a minimum value of $1.0 \times 10^{-2}\% / min.$. From then on, strain rate increases with time, probably due to soil structure degradation, but this discussion is beyond the scope of this article.

A similar analysis could also be carried out for the last stage of the test CR–I–ST–2 (step creep test), for which $t'_{uc} / p'_e = 0.365$. In this case, according to Figure 65, failure would take place with a shear strain rate $\dot{\varepsilon}_t = 10^{-1}\% / \text{min.}$, which is ratified by Lacerda's (1976) data.

In summary, regarding undrained creep tests performed on normally consolidated specimens of San Francisco Bay Mud, the presented model is able to make the following predictions:

a) If $t'_{uc} / p'_e < t'_{bf} / p'_e$, undrained creep will cease. The ε_t value at which undrained creep will cease can be found by entering into the basic curve $t'_b / p'_e \times \varepsilon_t$ with the value $t'_b / p'_e = t'_{uc} / p'_e$, thus determining the ε_t value associated with t'_{uc} / p'_e.

b) If $t'_{uc} / p'_e > t'_{bf} / p'_e$, there will be failure by undrained creep as soon as ε_t reaches $\cong 3\%$ (which means that $\phi'_{emob} = \phi'_e$). In these cases, the shear strain rate at failure can be predicted.

Thus, the presented model has shown to be a powerful tool to make predictions concerning the behaviour of normally consolidated specimens of San Francisco Bay Mud when subjected to undrained creep.

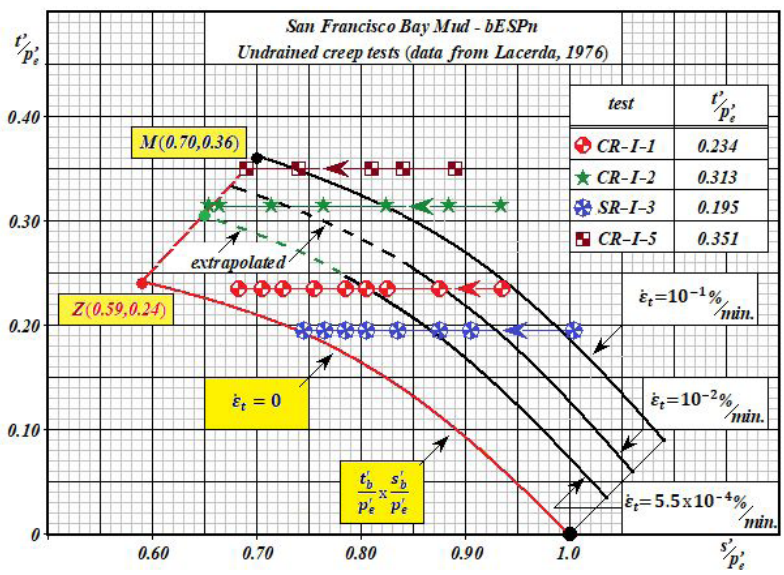

Figure 65. Normalized ESPs corresponding to different $\dot{\varepsilon}_t$ values and the normalized basic effective stress path (bESPn).

Table 5. Undrained creep tests on normally consolidated San Francisco Bay Mud carried out by Lacerda (1976), analyzed in this article.

Test	Stage	p'_e (kPa)	t'_{uc} (kPa)	t'_{uc} / p'_e
CR–I–1	unique	78.4	18.4	0.234
CR–I–2	unique	78.4	24.5	0.313
SR–I–3	unique	78.4	15.3	0.195
CR–I–5	unique	78.4	27.6	0.351

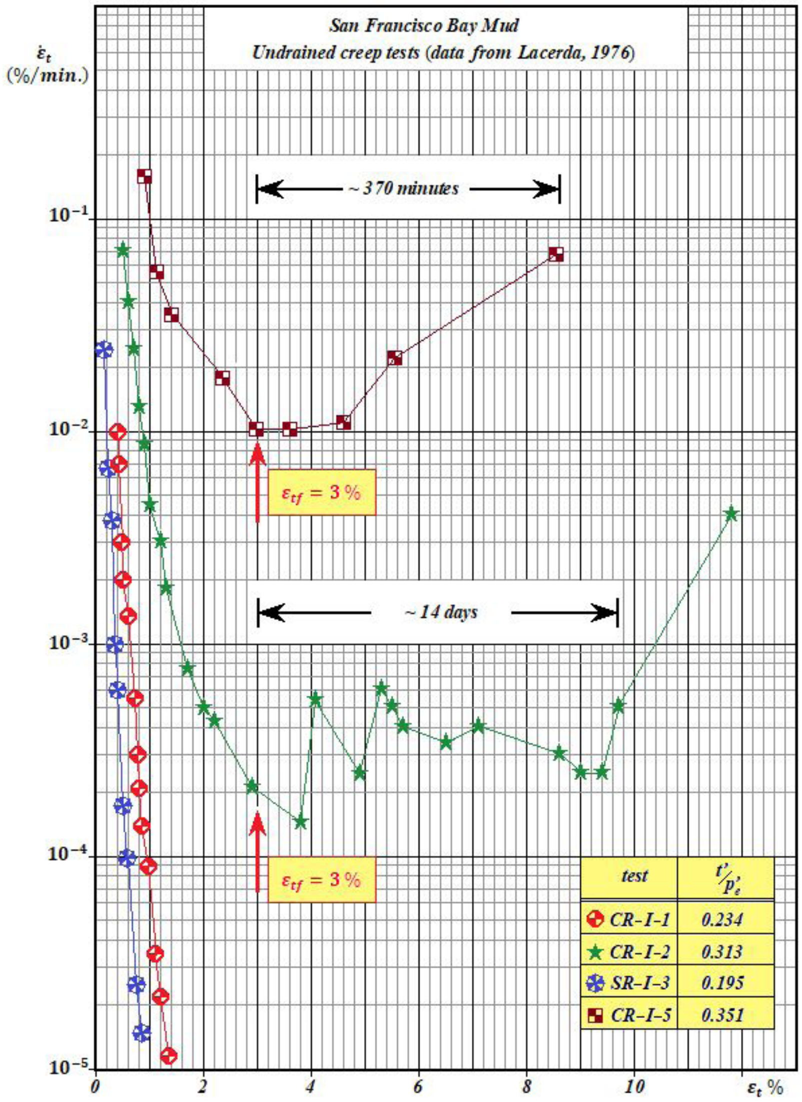

Figure 66. $\varepsilon_t \times \dot{\varepsilon}_t$ plots for undrained creep tests on normally consolidated San Francisco bay Mud specimens [data from Lacerda (1976)].

9.3 Stress relaxation tests

In this article, undrained stress relaxation means the phenomenon in which a soil specimen is kept under a constant state of strain while the state of stress is observed over time.

The undrained stress relaxation tests studied in this article are restricted to those cases where specimens are of cylindrical shape, subjected to an axysimmetric state of stress, the axial (vertical) total stress, denoted by σ_a, being the major principal stress and the radial (horizontal) total stress, denoted by σ_r, the minor principal stress. The study is also restricted to normally consolidated, saturated plastic clays with no cementation between grains.

To understand undrained stress relaxation under the light of the concepts presented in this article and its connection with $\overline{\text{CIUCL}}$ tests, consider Figure 67.

Suppose that a $\overline{\text{CIUCL}}$ test will be carried out with a shear strain rate $\dot{\varepsilon}_t = \dot{\varepsilon}_{t3}$. The ESP to be followed in Figure 67 is ***AHIJKLM***. Initially, there will be a "viscosity jump" ***AH*** and from then on shear strains will become to occur. Failure will take place when the ESP reaches point ***M***.

Suppose now that the $\overline{\text{CIUCL}}$ test previously described will be repeated, except for a detail: at point ***I***, the load frame motor is turned off, starting a stress relaxation stage. From then on, what does the model predict?

Since the soil is saturated and the test is undrained, $\varepsilon_v = 0$. In addition, from the moment the load frame motor is switched off, $\dot{\varepsilon}_t = 0$. Thus, during an undrained stress relaxation stage shear strain does not change with time.

According to the model, since $\dot{\varepsilon}_t = 0$, the viscous resistance will vanish. Besides, since ε_t constant, according to the *generalized complementary principle 1*, Δu and ϕ'_{emob} are expected to have constant values during undrained stress relaxation. As a consequence, the ESP to be followed during undrained stress relaxation is ***IQCW***, a 45º sloped straight line, as shown in Figure 67. Point ***W*** is expected to be the end of the stress relaxation effective stress path ***IQCW***, since at point ***W*** the specimen would already have got rid off all viscous resistance and would become to resist to the remaining shear stress only by friction.

If the load frame motor is turned on during a stress relaxation stage, the viscous resistance will instantaneously be reactivated and the $\overline{\text{CIUCL}}$ test will continue following the ESP associated with the shear strain rate $\dot{\varepsilon}_t$ applied. For instance: suppose that during the stress relaxation ***IQCW*** in Figure 67 the load frame motor is turned on again at point ***C***, with a shear strain rate $\dot{\varepsilon}_t = \dot{\varepsilon}_{t2}$. Thus, there will be an instantaneous jump, represented by ***CQ***, corresponding to the viscous resistance reactivation and the test will continue following the effective stress path ***QRSTV***.

However, if at point ***T*** the load frame motor is turned off again, another stress relaxation stage will start following the effective stress path ***TFY***.

9.4 Stress relaxation tests on normally consolidated San Francisco Bay Mud samples

To illustrate what was discussed in the previous section, three stress relaxation tests carried out by Lacerda (1976) on normally consolidated specimens of San Francisco Bay Mud will be presented. The main features of these tests, denoted by SR–I–5, SR–I–8 and SR–I–9, are summarized in Table 6.

What was presented in section 9.3 for the ESPs can be extended, without loss of generality, to the normalized ESPs $\left(s' / p'_e\right) \times \left(t' / p'_e\right)$. So, it is expected that normalized effective stress paths corresponding to stress relaxation stages are represented in a $\left(s' / p'_e\right) \times \left(t' / p'_e\right)$ plane by 45º sloped straight lines with descending direction.

Four stress relaxation stages have been carried out in each of the three tests listed in Table 6. The normalized ESPs for these stages are shown in Figure 68. These ESPs show that stress relaxation is also in agreement with the proposed model.

The discussions and experimental results presented in this article concerning undrained creep and undrained stress relaxation suggest that Taylor's and Bjerrum's ideas can be gathered in another general principle, which should be tested for other soils and which will be called *generalized complementary principle 2* or Taylor's and Bjerrum's law, whose statement is written below:

Generalized complementary principle 2 or Taylor's – Bjerrum's law

A normally consolidated plastic soil subjected to a given state of stress, in which the shear stresses are resisted partially by frictional resistance and partially by viscous resistance, will tend to get rid off the viscous resistance over time and will try to resist the remaining shear stresses only by friction.

In a clearer and more direct way, the *generalized complementary principle 2* states that a normally consolidated plastic soil under a normalized state of effective stresses given by $(s' / p'_e, t' / p'_e)$ will always move over time towards the normalized basic effective stress path $(s'_b / p'_e\ ,\ t'_b / p'_e)$, which is the Roscoe's surface for $\dot{\varepsilon}_t = 0$.

10. Summary and conclusions

What has been presented and discussed throughout the article can be summarized as listed below:

1. Phenomena that do not obey Terzaghi's principle of effective stress (PES) are related to strain rate and time effects (such as creep and stress relaxation).
2. The usual approach to deal with phenomena which do not obey the PES is to preserve the PES essence and develop tools to tackle each of these particular phenomena as being outside the PES validity domain. The approach followed in this article is different: the original PES is extended to encompass strain rate and time effects in such a way that these effects become natural consequences of the extended PES version. Concepts that allow such PES extension are presented in some classical texts from the beginning of soil mechanics.
3. The word "*cohesion*" has been used in soil mechanics with different meanings, bringing misunderstanding and conceptual confusion. Concerning earth natural materials, the term "cohesion" should be understood as a resistance coming from cementation between soil grains. This "*cohesion*" provides a tensile

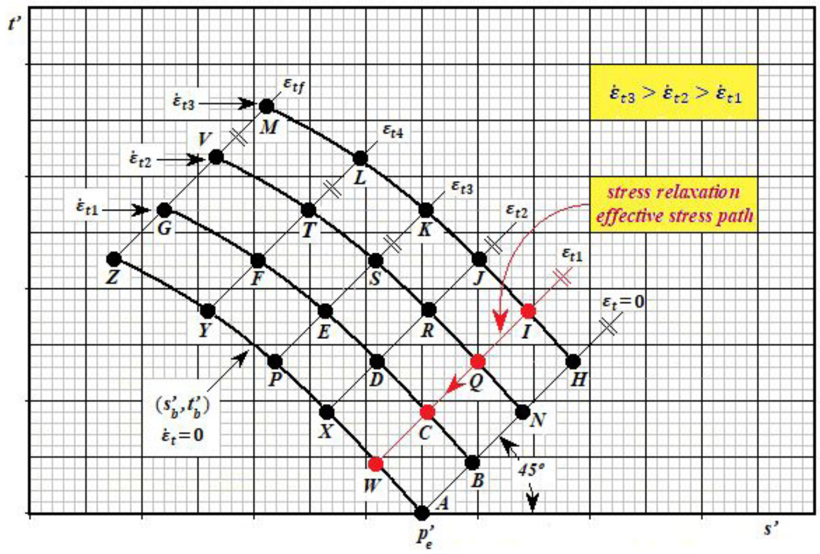

Figure 67. Effective stress paths for $\overline{\text{CIUCL}}$ tests with stress relaxation stages.

Table 6. Summary of data from stress relaxation tests carried out by Lacerda (1976) on normally consolidated specimens of San Francisco Bay Mud.

Test	Stress relaxation stage	s' / p'_e initial value	t' / p'_e initial value	s' / p'_e final value	t' / p'_e final value	Stage duration (minutes)
SR–I–5	1	1.00	0.278	0.850	0.075	3070
$p'_e = 78.4$ (kPa)	2	0.888	0.463	0.700	0.213	1320
	3	0.725	0.388	0.581	0.244	2700
	4	0.568	0.356	0.534	0.234	8370
SR–I–8	1	0.781	0.244	0.751	0.151	4530
$p'_e = 78.4$ (kPa)	2	0.830	0.400	0.741	0.201	1660
	3	0.819	0.444	0.612	0.237	365
	4	0.745	0.425	0.528	0.208	1000
SR–I–9	1	0.979	0.323	0.831	0.128	1250
$p'_e = 314$ (kPa)	2	0.844	0.313	0.775	0.173	1250
	3	0.758	0.303	0.712	0.196	1280
	4	0.764	0.347	0.671	0.249	100

strength under tensile effective stress which makes the difference between rocks and soils.

4. The word "*cohesion*" is also often used to describe a sticky earthy material that is soft to the touch when moistened. Earth materials that show such a feature are also called "*cohesive soils*". To avoid misunderstanding, these materials would more properly be called plastic soils. For the sake of conceptual clearness and objectivity, the expression "*plastic soil*" should be used for all soils that present liquid and plastic limits.
5. When plastic soils are sheared, there is a component of shear resistance that comes from the action (distortion) of the highly viscous adsorbed water layers surrounding particles in contact. The closer the adsorbed water is to the particles surface, the higher its viscosity. Thus, it is expected that the lower the void ratio, the higher the shear resistance component due to the action of the adsorbed water, which is of viscous nature.
6. Hvorslev (1960) showed it is possible to express the shear strength of a clay as: $\tau_{ff} = c_e(e) + \sigma'_{ff} \tan\phi'_e$, where $c_e(e)$ was called "*true cohesion*", a function of void ratio (e), and ϕ a constant, called the true angle of internal friction. Since the soil tested by Hvorslev was a remoulded clay, it could have no cementation. Thus, the Hvorslev's "*true cohesion*" could not have the same nature of Coulomb's "*cohesion*". Hvorslev (1960) assumed that the "*true cohesion*" c_e of a saturated clay depends not only on void ratio but also on strain rate and clay structure.

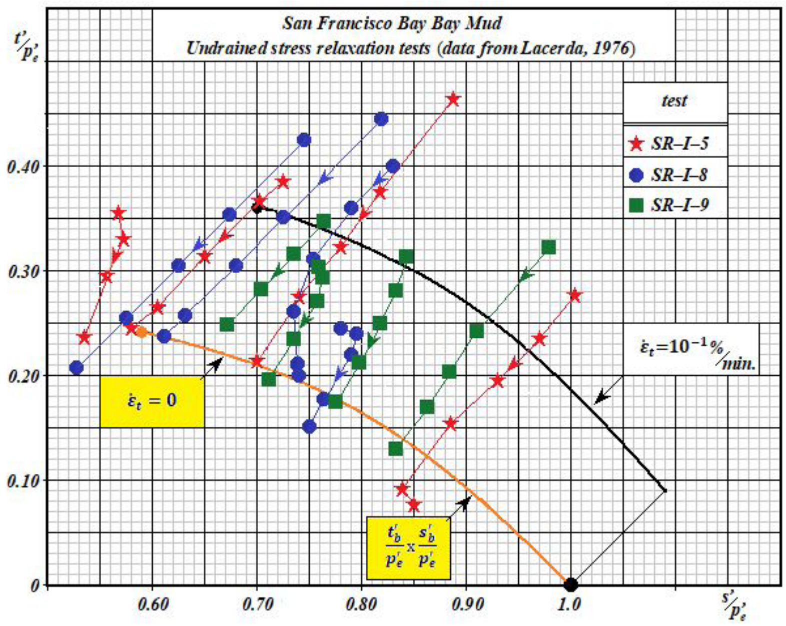

Figure 68. Normalized effective stress paths during stress relaxation stages for normally consolidated specimens of San Francisco Bay Mud [data from Lacerda (1976)].

7. Since normally consolidated, saturated clays have straight line strength envelopes passing through the origin in a $\sigma' \times \tau$ plot, they do not have "*cohesion*" in the sense used by Coulomb but they do have plasticity. In other words: normally consolidated clays do not have "*cohesion*" in the sense used by Coulomb but do have "*true cohesion*" in the sense used by Hvorslev. Furthermore, when normally consolidated specimens of a given clay, with the same void ratio, are subjected to undrained shear, the higher the strain rates, the higher their strengths. These features suggest that Hvorslev's "*true cohesion*" should more properly be called viscous resistance and expressed by the product of the coefficient of viscosity and a function of the shear strain rate.
8. The model presented herein assumes that, in plastic soils, the shear stress τ_α acting on a plane whose normal makes an angle α with the direction of σ_1 is expressed, at any instant, as the sum of a viscous resistance component $\tau_{\eta\alpha}$ and a frictional resistance component $\tau_{\phi\alpha}$, that is, $\tau_\alpha = \tau_{\phi\alpha} + \tau_{\eta\alpha}$.
9. $\tau_{\eta\alpha} = \eta(e) f\left[d(\varepsilon_1 - \varepsilon_3)/dt\right]\sin 2\alpha$, i.e. the viscous resistance component in a plane given by α is a function of the clay structure and of the product of the soil viscosity $\eta(e)$ by a function f of the distortion rate. Therefore, $\tau_{\eta\alpha}$ is similar to Hvorslev's true cohesion c_e (see conclusion 6).
10. Denoting by σ'_α the normal effective stress acting on the plane whose normal makes an angle α with the direction of σ_1, the locus of the ordered pairs $(\sigma'_\alpha, \tau_{\eta\alpha})$ is the viscosity ellipse, whose centre has coordinates $\left[(\sigma'_1 + \sigma'_3)/2, 0\right]$ and whose major and minor axes are respectively $(\sigma'_1 - \sigma'_3)$ and $2\eta(e)d(\varepsilon_1 - \varepsilon_3)/dt = 2\mathbb{V}$.
11. $\tau_{\phi\alpha} = \sigma'_\alpha \tan\phi'_{mob\alpha}$ and thus $\tan\phi'_{mob\alpha} = (\tau_{\phi\alpha}/\sigma'_\alpha)$. The locus of the ordered pairs $(\sigma'_\alpha, \tau_{\phi\alpha})$ is the friction ellipse, whose centre has coordinates $\left[(\sigma'_1 + \sigma'_3)/2, 0\right]$ and whose major and minor axes are respectively $(\sigma'_1 - \sigma'_3)$ and $\left[(\sigma'_1 - \sigma'_3) - 2\mathbb{V}\right]$. (There is a difference between $\tan\phi'_{mob\alpha}$ and $\tan\phi'_{emob}$. For a fixed state of stress, $\tan\phi'_{mob\alpha} = (\tau_{\phi\alpha}/\sigma'_\alpha)$ and $\tan\phi'_{emob}$ is the maximum value of $\tan\phi'_{mob\alpha}$, i.e. maximum obliquity).
12. At any instant $\tan\phi'_{emob}$ can be computed by
$$\tan\phi'_{emob} = \frac{\left(\dfrac{\sigma'_1 - \sigma'_3}{2} - \mathbb{V}\right)}{\sqrt{\sigma'_1 \sigma'_3}} = \frac{(t' - \mathbb{V})}{\sqrt{s'^2 - t'^2}}$$
13. The sum of the viscosity and friction ellipses gives the Mohr's circle of effective stress. The two ellipses cannot exist separately since only the Mohr's circle of stress satisfies equilibrium.
14. Since $\tau_{\eta\alpha} = \eta(e)\dot{\gamma}\sin 2\alpha$, for $\underline{\alpha = 45^\circ}, \tau_{\eta\alpha} = t'$. In the case of an ideal conventional $\overline{\text{CIUCL}}$ test, as soon as the load frame motor is switched on, the viscous resistance is fully mobilized instantaneously. Thus, the ESP shows an immediate "viscosity jump" along a 45º sloped straight line corresponding to a $t' = \mathbb{V}$. From then on, as there is neither volume change nor strain rate change, the viscous resistance remains constant throughout the shear phase. But since t' continues to increase as shear strain ε_t increases, this means the

frictional resistance is mobilized throughout the shear phase, which leads to two remarkable conclusions: frictional resistance mobilization is associated to shear strain development and failure is governed by friction, i.e. when the available frictional resistance is totally mobilized, failure takes place.

15. Since failure is governed by friction mobilization, failure takes place whenever $tan\,\phi'_{emob}$ reaches its maximum available value, which is $tan\,\phi'_e$. Geometrically, this means that failure takes place when the friction ellipse touches the ϕ'_e sloped straight line passing through the origin.
16. To compute the undrained shear strength of a plastic soil, the viscous and frictional resistance components must be summed up. As the viscous resistance component depends on the shear strain rate, the greater the shear strain rate, the higher the viscous resistance component and, therefore, the higher the undrained strength.
17. $\overline{\text{CIUCL}}$ test results have been showing that the viscous resistance $\mathbb{V}$ is not a linear function of $\dot{\gamma}$. Thus, it should be rewritten as $\mathbb{V} = \eta(e) f(\dot{\gamma})$, where f is a non-linear function of $\dot{\gamma}$. On the other hand, for normally consolidated, saturated clays, $\mathbb{V}$ is a linear function of the isotropic consolidation stress p'_e, i.e. $\eta(e) f(\dot{\gamma}) = C_\eta(\dot{\gamma}) p'_e$.
18. In section 7.1 ten hypotheses are listed as the basis for the development of a behavioural model for normally consolidated, saturated clays. Part of these hypotheses comes from experimental evidence and part is working hypotheses of theoretical nature. In section 7.2 it was added another hypothesis that came from experimental evidence, which is: during the undrained shear phase of $\overline{\text{CIUCL}}$ tests starting from the same p'_e, the pore-pressure Δu is the same regardless of the shear strain rate $\dot{\varepsilon}_t$. The set of these eleven hypotheses lead to the *complementary principle 1* which states that *points of intersection between a given 45° sloped straight line and* ESPs *starting from the same* p'_e *and corresponding to different shear strain rates* $\dot{\varepsilon}$ *have the same* ε_t, Δu and ϕ'_{emob}.
19. (s', t') are the coordinates of a point on the ESP of a $\overline{\text{CIUCL}}$ test carried out under a given p'_e and with an $\dot{\varepsilon}_t \neq 0$, whereas (s'_b, t'_b) are the coordinates of a point on the ESP of a idealized $\overline{\text{CIUCL}}$ test carried out under the same p'_e but with $\dot{\varepsilon}_t = 0$. Obviously, it is not possible to carry out a $\overline{\text{CIUCL}}$ test with $\dot{\varepsilon}_t = 0$, whose results would be free from the viscous resistance component. However, based on the *complementary principle 1*, it is possible to derive expressions relating s'_b to s' and t'_b to t', provided they correspond to the same ε_t. Then, for this fixed p'_e, one can plot the basic curves $\Delta u \times \varepsilon_t$, $t'_b \times \varepsilon_t$ and the basic effective stress path (s'_b, t'_b), which are all free from the viscous resistance component.
20. The $t' \times \varepsilon_t$ curves and the ESPs of $\overline{\text{CIUCL}}$ tests carried out with a fixed $\dot{\varepsilon}_t$ but under different values of isotropic consolidation stress p'_e on a given normally consolidated clay are similar. Thus, for a given $\dot{\varepsilon}_t$, there is a unique $(t' / p'_e) \times \varepsilon_t$ curve and a unique ESP on the plane $(s' / p'_e) \times (t' / p'_e)$. Although limited, the experimental evidence presented by Lacerda's (1976) test results show that the $\Delta u \times \varepsilon_t$ curves obtained from CIUCL tests carried out under different values of p'_e are similar, regardless of the $\dot{\varepsilon}_t$ value. Thus, the $(\Delta u / p'_e) \times \varepsilon_t$ plot can be represented by a unique curve regardless of the $\dot{\varepsilon}_t$ value. This means that the complementary principle 1 can be generalized to all p'_e values. Thus, it was renamed as the *generalized complementary principle 1: During undrained shear of* $\overline{\text{CIUCL}}$ *tests carried out on normally consolidated specimens of a given clay, points on the plane* $(s' / p'_e) \times (t' / p'_e)$ *corresponding to the intersections of any given 45° sloped straight line and the several ESPs, each one associated with a different* $\dot{\varepsilon}_t$ *value, will show the same values of* ε_t, $(\Delta u / p'_e)$, *and* $\tan\phi'_{emob}$, *whatever the shear strain rate* $\dot{\varepsilon}_t$ *may be.*
21. The *generalized complementary principle 1* leads to the three corollaries below:
   Corollary 1: $\overline{\text{CIUCL}}$ *tests carried out on a normally consolidated clay showing homothetic* ESPs *for any fixed* $\dot{\varepsilon}_t$ *and a unique curve* $\Delta u / p'_e \times \varepsilon_t$, *regardless of* $\dot{\varepsilon}_t$, *will show a unique basic curve* $t'_b / p'_e \times \varepsilon_t$, *whatever* $\dot{\varepsilon}_t$ *is.*
   Corollary 2: $\overline{\text{CIUCL}}$ *tests carried out on a normally consolidated clay showing homothetic* ESPs *for any fixed* $\dot{\varepsilon}_t$ *and a unique curve* $\Delta u / p'_e \times \varepsilon_t$, *regardless of* $\dot{\varepsilon}_t$, *will show a unique normalized basic effective stress path* $(s'_b / p'_e, t'_b / p'_e)$, *whatever* $\dot{\varepsilon}_t$ *is.*
   Corollary 3: $\overline{\text{CIUCL}}$ *tests carried out on a normally consolidated clay showing homothetic* ESPs *for any fixed* $\dot{\varepsilon}_t$ *and a unique curve* $\Delta u / p'_e \times \varepsilon_t$ *regardless of* $\dot{\varepsilon}_t$, *will show a unique curve* $\tan\phi'_{emob} \times \varepsilon_t$, *whatever* $\dot{\varepsilon}_t$ *is.*
22. The results from $\overline{\text{CIUCL}}$ tests carried out on normally consolidated specimens of San Francisco Bay Mud are in fair agreement with the *generalized complementary principle 1* (see Table 4) as well as with corollaries 1, 2 and 3. Although there is some scattering, considering that soil specimens were trimmed from natural undisturbed samples, it can be concluded that the experimental data follow the proposed model.
23. During undrained creep of a normally consolidated specimen compressed to p'_e, $t' / p'_e = t'_{uc} / p'_e =$ constant, where t'_{uc} corresponds to half of the deviator stress applied. As time goes by, shear strain increases, mobilizing frictional resistance and demobilizing

viscous resistance, which makes the strain rate decreases over time. During the undrained creep process, the ESP crosses successive normalized ESPs of $\overline{\text{CIUCL}}$ tests corresponding to decreasing $\dot{\varepsilon}_t$ values (see Figures 63 and 65). Each of these normalized ESPs of $\overline{\text{CIUCL}}$ tests can be seen as a Roscoe's surface associated with a constant $\dot{\varepsilon}_t$, and the normalized basic effective stress path (bESPn) can be viewed as the Roscoe's surface corresponding to $\dot{\varepsilon}_t = 0$.

Recalling that t'_{bf} / p'_e corresponds to the failure condition for $\varepsilon_t = 0$, two cases may occur:

(a) $t'_{uc} / p'_e \leq t'_{bf} / p'_e$

(b) $t'_{uc} / p'_e > t'_{bf} / p'_e$

In case *(a)*, there will be no failure by undrained creep. Shear strain ε_t will approach a definite value over time, shear strain rate will approach zero and creep will come to an end, at the normalized basic effective stress path (bESPn).

In case *(b)*, there will be failure by undrained creep in a finite time, no matter how long it takes. In this case, the higher the ratio $\left(t'_{uc} / p'_e\right)$, the shorter the time to failure and the higher the strain rate at failure. For normally consolidated San Francisco Bay Mud, $t'_{bf} / p'_e = 0.24$. Since for tests CR–I–1 and SR–I–3 the t'_{uc} / p'_e values were respectively 0.234 and 0.195, both tests belong to case *(a)* and, hence, there would be no undrained creep failure. This is suggested by the results obtained from both tests shown in Figure 66. On the other hand, since for tests CR–I–2 and CR–I–5 the t'_{uc} / p'_e values were respectively 0.313 and 0.351, both tests belong to case *(b)* and, thereby, there was failure by creep, as shown in Figure 66.

Although it has been applied to a few tests, the presented model has shown to be a powerful tool to make predictions concerning the behaviour of normally consolidated specimens of San Francisco Bay Mud when subjected to undrained creep.

24. During an undrained stress relaxation stage, $\varepsilon_v =$, $\dot{\varepsilon}_t = 0$ and thus $\varepsilon_t =$ constant. According to the presented model, since $\dot{\varepsilon}_t = 0$, the viscous resistance must vanish. Since ε_t = constant, according to the generalized complementary principle 1, Δu and ϕ'_{emob} are expected to keep constant values during undrained stress relaxation. Moreover, since the viscous resistance is demobilized (due to $\dot{\varepsilon}_t = 0$) and the mobilized frictional resistance remains constant (due to ε_t = constant), the deviator stress decreases. As a consequence, the ESP to be followed during the undrained stress relaxation is a downward 45º sloped straight line towards the bESPn*,* which would correspond to Roscoe's surface for $\dot{\varepsilon}_t = 0$. When the ESP touches the bESPn, the shear stress is free from its viscous component, the stress relaxation ceases and the remaining shear stress is exclusively of frictional nature.

    The ESPs of the undrained stress relaxation stages carried out by Lacerda (1976), during $\overline{\text{CIUCL}}$ tests on normally consolidated specimens of San Francisco Bay Mud, show that undrained stress relaxation is also in agreement with the proposed model (see Figure 68).

25. The discussion and experimental results presented in this article concerning undrained creep and undrained stress relaxation suggest that Taylor's and Bjerrum's ideas can be gathered into another general principle (which deserves a deeper study) called *generalized complementary principle 2* or *Taylor's and Bjerrum's law*, whose formal statement is presented in section 9.4.

    In a more direct way, the *generalized complementary principle 2* states that a normally consolidated plastic soil under a normalized state of effective stresses given by $(s' / p'_e, t' / p'_e)$ will always move over time towards the normalized basic effective stress path $(s'_b / p'_e\ ,\ t'_b / p'_e)$, which would be the Roscoe's surface for $\dot{\varepsilon}_t = 0$.

Acknowledgements

The author is indebted to Prof. Robson Palhas Saramago for his support in organizing the powerpoint slides, to Dr. Gustavo Santos Domingos for his help in improving the figures in the text, to Prof. Vitor Nascimento Aguiar for his contribution in reading the manuscripts and making valuable suggestions which made the article more readable, to Prof. Luiz Guilherme de Mello for his kindness in sharing with the author interesting aspects of Prof. Victor F. B. de Mello's life, which increased the author's motivation to do his best and to his wife Claudia for her support, patience and love.

Declaration of interest

The author has no conflicts of interest to declare. The author has observed and affirmed the contents of the paper and there is no financial interest to report.

Data availability

All experimental data referring to San Francisco Bay Mud examined in the course of the current study have come from Lacerda's PhD thesis research, the major part of which is available in his PhD thesis dissertation (Lacerda, 1976). Some part of these experimental data has directly been obtained from Lacerda in the form of raw data, which are not available in his PhD thesis dissertation.

List of symbols

bESP Basic effective stress path
bESPn Normalized basic effective stress path
c' Cohesion
c_e Hvorslev's true cohesion
e Void ratio
h_0 Initial height of a triaxial specimen
r_0 Initial radius of triaxial specimen
q'_f Deviator stress at failure
p'_e Isotropic effective stress
p'_f Octahedral stress at failure
s $(\sigma_v + \sigma_h)/2$
s' $(\sigma'_v + \sigma'_h)/2$
s'_b Value of s' when $\dot{\varepsilon}_t = 0$
t $(\sigma_v - \sigma_h)/2$ or time
t' $(\sigma'_v - \sigma'_h)/2$
t'_b Value of t' when $\dot{\varepsilon}_t = 0$
t_{bf} Value of t'_b at failure
t'_{uc} Value of t' during undrained creep
u Pore pressure
v Specific volume ($v = 1 + e$)
w Water content
w_L Liquid limit
w_P Plastic limit
bESP Basic effective stress path
bESPn Normalized basic effective stress path
C_c Compression index
$\overline{\text{CIU}}$ Consolidated isotropically undrained triaxial test
$\overline{\text{CIUCL}}$ Consolidated isotropically undrained compression loading triaxial test
CSL Critical state line
C_α Coefficient of secondary consolidation
ESP Effective stress path
G Specific gravity
I_P Plasticity index
K_0 Coefficient of earth pressure at rest
M Slope of CSL projection on a $p' \times q'$ plane ($M = q'_f / p'_f$)
PES Principle of effective stress
S_u Undrained shear strength
TSP Total stress path
VICL Virgin isotropic compression line
γ Distortion ($\varepsilon_a - \varepsilon_r$)
$\dot{\gamma}$ Distortion rate ($d\gamma / dt$)
ε_a Axial (vertical) strain
ε_1 Major principal strain
ε_3 Minor principal strain
ε_r Radial (horizontal) strain
ε_v Volumetric strain
ε_t Shear strain ($\varepsilon_t = \gamma / 2$)
$\dot{\varepsilon}_t$ Shear strain rate ($\dot{\varepsilon}_t = \dot{\gamma} / 2$)
$\dot{\varepsilon}_a$ Axial (vertical) strain rate $(d\varepsilon_a / dt)$
$\varepsilon_{l\alpha}$ Longitudinal strain of an element on the vertical plane of a triaxial specimen that makes an angle α with the direction of ε_1
$\varepsilon_{s\alpha}$ Shear strain on the vertical plane associated to the angle α
ϕ' Angle of friction
ϕ'_e Hvorslev's true angle of internal friction
$\phi'_{mob\alpha}$ $\tan^{-1}(\tau_{\phi\alpha} / \sigma'_\alpha)$
ϕ'_{emob} $\tan^{-1}(\tau_{\phi\alpha} / \sigma'_\alpha)_{max}$
η Viscosity of a plastic soil
μ Newton's coefficient of viscosity or Bjerrum's vane test correction factor
σ Normal total stress
σ' Normal effective stress
σ_1 Major total principal stress
σ_2 Intermediate total principal stress
σ_3 Minor total principal stress
σ'_1 Major effective principal stress
σ'_2 Intermediate effective principal stress
σ'_3 Minor effective principal stress
σ_a Total axial stress (equal to σ_1 in a $\overline{\text{CIUCL}}$ test)
σ'_e Equivalent stress
σ_v Total vertical stress (equal to σ_1 in a $\overline{\text{CIUCL}}$ test)
σ_r Total radial stress (equal to $\sigma_2 = \sigma_3$ in a $\overline{\text{CIUCL}}$ test)
σ'_a Effective axial stress (equal to σ'_1 in a $\overline{\text{CIUCL}}$ test)
σ'_{af} Effective axial stress at failure
σ'_{ff} Effective stress on failure plane at failure
σ'_i Intrinsic pressure
σ'_{rf} Effective radial stress at failure
σ'_t Tensile effective stress
σ'_v Effective vertical stress (equal to σ'_1 in a $\overline{\text{CIUCL}}$ test)
σ'_r Effective radial stress (equal to $\sigma'_2 = \sigma'_3$ in a $\overline{\text{CIUCL}}$ test)
σ'_α Effective stress on a plane whose normal makes an angle α with the direction of σ_1
τ Shear stress
τ_{ff} Shear stress on failure plane at failure
τ_α Shear stress on a plane whose normal makes an angle α with the direction of σ_1
$\tau_{\eta\alpha}$ Viscous component of τ_α
$\tau_{\phi\alpha}$ Frictional component of τ_α
Δu Excess pore pressure
$\mathbb{V}$ Viscous resistance on a plane whose normal makes 45º with the direction of σ_1

References

Aguiar, V.N. (2014). *Contribution to the study of the stress-stress-strength-time of soft clays* [Doctoral thesis, Federal

University of Rio de Janeiro]. Federal University of Rio de Janeiro's repository (in Portuguese).

Andrade, M.E.A. (2014). *One-dimensional consolidation accounting for viscous resistance to compression* [Doctoral thesis, Federal University of Rio de Janeiro]. Federal University of Rio de Janeiro's repository (in Portuguese).

Atkinson, J.H., & Bransby, P.L. (1978). *The mechanics of soils – an introduction to critical state soil mechanics*. McGraw-Hill Book Company.

Berre, T., & Bjerrum, L. (August 6-11, 1973). Shear strength of normally consolidated clays. In Organizing Comittee of the ICSMFE (Ed.), *Proceedings of 8th International Conference on Soil Mechanics and Foundation Engineering* (Vol. 1, pp. 39-49). Moscow: ICSMFE.

Bishop, A.W., & Henkel, D.J. (1962). *The measurement of soil properties in the triaxial test*. London: Edward Arnold Ltd..

Bjerrum, L. (August 6-11, 1973). Problems of soil mechanics and construction on soft clays – State-of-the-Art report to session IV. In Organizing Comittee of the ICSMFE (Ed.), *Proceedings of 8th International Conference on Soil Mechanics and Foundation Engineering* (Vol. 3, pp. 111-159). Moscow: ICSMFE.

Burland, J.B. (1990). On the compressibility and shear strength of natural clays. *Geotechnique*, 40(3), 329-378. http://dx.doi.org/10.1680/geot.1990.40.3.329.

Burland, J.B. (2008). Reflections on Victor de Mello, Friend, Engineer and Philosopher. *Soils and Rocks,* 31(3), 111-123. https://doi.org/10.28927/sr.313111.

Carneiro, F.L.L.B., & Battista, R.C. (1975). *Mechanics of materials* [Lecture notes]. Retrieved in March-November, 1975, Lecture notes taken by Martins, I.S.M.

Christian, J.T., & Baecher, G.B. (2015). D.W. Taylor and the foundations of modern soil mechanics. *Journal of Geotechnical and Geoenvironmental Engineering*, 141(2), 02514001.

Costa, T. (2005) *Engineering of transparency – life and oeuvre of Lobo Carneiro*. COPPE/UFRJ (in Portuguese).

Danziger, F.A.B., Jannuzzi, G.F., & Martins, I.S.M. (2019). The relationship between sea-level change, soil formation and stress history of a very soft clay deposit. *AIMS Geosciences*, 5(3), 461-479. https://doi.org./10.3934/geosci.2019.3.461.

de Mello, V.F.B. (2014). *Geotechnics of subsoil and of earth and stone used as construction materials: Primordia, questions, updates*. Oficina de Textos. (unfinished book – in Portuguese).

de Mello, L.G. (2021). Personal communication.

Fonseca, A.P. (2000). *Compressibility and shear strength of a gully soil from Ouro Preto-MG* [Master's dissertation, Federal University of Rio de Janeiro]. Federal University of Rio de Janeiro's repository (in Portuguese).

Gibson, R.E. (August 16-27, 1953). Experimental determination of the true cohesion and true angle of internal friction in clays. In Organizing Comittee (Ed.), *Proceedings of the 3rd International Conference on Soil Mechanics and Foundation Engineering* (Vol. 1, pp. 126-130). Zurich.

Graham, J., Crooks, J.H.A., & Bell, A.L. (1983). Time effects on the stress-strain behavior of natural soft clays. *Geotechnique*, 33(3), 327-340. http://dx.doi.org/10.1680/geot.1983.33.3.327.

Holtz, R.D., & Jamiolkowski, M.B. (1985). Discussion of "Time dependence of lateral earth pressure". *Journal of Geotechnical Engineering*, 111(10), 1239-1242. http://dx.doi.org/10.1061/(ASCE)0733-9410(1985)111:10(1239).

Hvorslev, M.J. (1937). Über die festigkeitseigenschaften gestörter bindiger böden. Ingeniörvidenskabelige Skrifter.

Hvorslev, M.J. (June, 1960). Physical components of the shear strength of saturated clays. In American Society of Civil Engineers (Org.), *Research Conference on Shear Strength of Cohesive Soils* (pp. 169-273). Boulder, United States: University of Colorado.

Jamiolkowski, M. (2012). Role of Geophysical Testing in Geotechnical Site Characterization. *Soils and Rocks*, 35(2), 117-137. https://doi.org/10.28927/SR.352117.

Jamiolkowski, M., Leroueil, S., & Lo Presti D.C.F. (1991). Theme lecture: design parameters from theory to practice. In Coastal Development Institute of Technology (Ed.), *Procceedings of the International Conference on Geotechnical Engineering for Coastal Development* (Vol. 91, pp. 877-917). Yokohama: Geo-Coast.

Kavazanjian Junior, E., & Mitchell, J.K. (1984). Time dependence of lateral earth pressure. *Journal of Geotechnical Engineering*, 110(04), 530-533. http://dx.doi.org/10.1061/(ASCE)0733-9410(1984)110:4(530).

Kavazanjian Junior, E., & Mitchell, J.K. (1985). Closure to time dependence of lateral earth pressure. *Journal of Geotechnical Engineering*, 111(10), 1246-1248. http://dx.doi.org/10.1061/(ASCE)0733-9410(1985)111:10(1246).

Lacerda, W.A. (1976). *Stress-relaxation and creep effects on soil deformation* [PhD thesis dissertation]. University of California at Berkeley.

Lacerda, W.A. (1977). Discussion on the evaluation of K_0 during the drained creep in one-dimensional compression tests. In Publications Sub-Committee of the Organizing Comittee Organizing Comittee (Ed.), *Proceedings of the 8th International Conference on Soil Mechanics and Foundation Engineering* (Vol. 3, pp. 347-348). Tokyo.

Lacerda, W.A., & Houston, W.N. (1973). Stress relaxation in soils. In Organizing Committee (Ed.), *8th International Conference on Soil Mechanics and Foundation Engineering* (pp. 221-227). Moscow.

Lacerda, W.A., & Martins, I.S.M. (1985). Discussion of "Time dependence of lateral earth pressure". *Journal of Geotechnical Engineering*, 111(10), 1242-1244. http://dx.doi.org/10.1061/(ASCE)0733-9410(1985)111:10(1242).

Lambe, T.W. (1951). *Soil testing for engineers*. John Wiley & Sons.

Lambe, T.W. (1981). Geotechnical engineering at the Massachusetts Institute of Technology, 1925-1981. In

Massachusetts Institute of Technology (Ed.), *Past, present and future of geotechnical engineering symposium*. (pp. 48-60). Massachusetts Institute of Technology.

Leonards, G.A. (1985) Discussion of "Time dependence of lateral earth pressure". *Journal of Geotechnical Engineering*, 111(10), 1244-1246. https://doi.org/10.1061/(ASCE)0733-9410(1985)111:10(1244).

Leroueil, S., Kabbaj, M., Tavenas, F., & Bouchard, R. (1985). Stress-strain-strain rate relation for the compressibility of sensitive natural clays. *Geotechnique*, 35(2), 159-180. http://dx.doi.org/10.1680/geot.1985.35.2.159.

Lira, E.N.S. (1988). *Automatic data acquisition system for triaxial tests* [Master's dissertation, Federal University of Rio de Janeiro]. Federal University of Rio de Janeiro's repository (in Portuguese).

Martins, I.S.M. (1983). *Sobre uma nova relação índice de vazios tensão em solos* [Master's dissertation, Federal University of Rio de Janeiro]. Federal University of Rio de Janeiro's repository (in Portuguese).

Martins, I.S.M. (1992). *Fundamentals for a model of saturated clay behaviour* [Doctoral thesis, Federal University of Rio de Janeiro]. Federal University of Rio de Janeiro's repository (in Portuguese).

Martins, I.S.M., & Lacerda, W.L. (1994). On the relationship void ratio – vertical effective stress in one-dimensional compression. *Soils & Rocks – Brazilian Journal of Geotechnics. ABMS, V.17, n.3, December, P.155-166. Brazilian Society for Soil Mechanics and Geotechnical Engineering* (in Portuguese).

Marzionna, J.D. (2014). *Foreword to Geotechnics of subsoil and of earth and stone used as construction materials: primordia, questions, updates* ABMS/Oficina de Textos (unfinished book) (in Portuguese).

Mesri, G., & Castro, A. (1987). C_α/C_c concept and K_0 during secondary compression. *Journal of Geotechnical Engineering*, 113(3), 230-247. http://dx.doi.org/10.1061/(ASCE)0733-9410(1987)113:3(230).

Mesri, G., & Castro, A. (1989). Closure to C_α/C_c concept and K_0 during secondary compression. *Journal of Geotechnical Engineering*, 115(2), 273-277. http://dx.doi.org/10.1061/(ASCE)0733-9410(1989)115:2(273).

Mesri, G., & Godlewski, P.M. (1977). Time and stress-compressibility interrelationship : Mesri, G; Godlewski, P M J Geotech Engng Div ASCE, V103, NGT5, 1977, P417–430. *International Journal of Rock Mechanics and Mining Sciences & Geomechanics Abstracts*, 14(4), 60. https://doi.org/10.1016/0148-9062(77)91005-1.

Moreira, J.E., & Décourt, L. (1989). Biographical notes. In V.F.B. De Mello (Ed.), *De Mello volume* (pp. XI-XV). Editora Edgar Blücher Ltda.

Rodriguez, T.T. (2005). *Pourpose of getechnical classification for brazilian colluvium* [Doctoral thesis, Federal University of Rio de Janeiro]. Federal University of Rio de Janeiro's repository (in Portuguese).

Rouse, H., & Howe, J.W. (1953). *Basic mechanics of fluids* (pp. 114-127). John Wiley & Sons.

Santa Maria, P.E.L. (2000). Personal communication.

Saramago, R.P. (2021). Personal communication.

Schmertmann, J.H. (1983). A simple question about consolidation. *Journal of Geotechnical Engineering*, 109(1), 119-122.

Schnaid, F., Martins, I.S.M., Delgado, B.G., & Odebrecht, E. (2021). Strain rates effects in the prediction of geotechnical parameters. *Geotecnia*, 152, 405-434 (in Portuguese). https://doi.org/10.14195/2184-8394_152_12.

Schofield, A.N. (1999). A note on Taylor's interlocking and Terzaghi's "true cohesion" error. *Geotechnical News*, 17(4), 1-6.

Schofield, A.N. (August 27-31, 2001). Re-appraisal of Terzaghi's soil mechanics. In C.S. Desai (Ed.), *Proceedings of the 15th International Conference on Soil Mechanics and Foundation Engineering* (Vol. 1, pp. 2473-2480). Istanbul.

Sheahan, T.C., Ladd, C.C., & Germaine, J.T. (1996). Rate-dependent undrained shear behavior of saturated clay. *Journal of Geotechnical Engineering*, 122(2), 99-108. http://dx.doi.org/10.1061/(ASCE)0733-9410(1996)122:2(99).

Tatsuoka, F., Ishihara, M., Di Benedetto, H., & Kuwano, R. (2002). Time-dependent shear deformation characteristics of geomaterials and their simulation. *Soil and Foundation*, 42(2), 103-129.

Taylor, D.W. (1942). *Research on consolidation of clays*. Massachusetts Institute of Technology/Department of Civil and Sanitary Engineering. Serial 82.

Taylor, D.W. (1948). *Fundamentals of soil mechanics*. John Wiley & Sons.

Taylor, D.W. (1955). *Review of research on shearing strength of clay – 1948 to 1953*. Vicksburg, Mississipi: Waterways Experiment Station.

Terzaghi, K. (1936). The shearing resistance of saturated soil and the angle between the planes of shear. In *Proceedings of the 1st International Conference on Soil Mechanics and Foundation Engineering* (Vol. 1, pp. 54-56). Cambridge, Massachussets: Harvard Printing Office.

Terzaghi, K. (1938). The Coulomb equation for the shear strength of cohesive soils. In *From theory to practice in soil mechanics – selections from the writings of Karl Terzaghi* (pp.174-180). John Wiley & Sons.

Terzaghi, K. (1941). Undisturbed clay samples and undisturbed clays. *Journal of the Boston Society of Civil Engineers*, 28(3), 45-65.

Terzaghi, K., & Frölich, O.K. (1936). *Théorie du tassement des couches argileuses*. Dunod.

Thomasi, L. (2000). *On the existence of a viscous component on the normal effective stress* [Master's dissertation, Federal University of Rio de Janeiro]. Federal University of Rio de Janeiro's repository (in Portuguese).

ARTICLES

Soils and Rocks
An International Journal of Geotechnical and Geoenvironmental Engineering
www.soilsandrocks.com
ISSN 1980-9743
ISSN-e 2675-5475

Estimation of short-term settlements of MSW landfill materials using shear wave velocity

Nagendra Kola[1], Debasis Roy[1#], Debarghya Chakraborty[1]

Article

Keywords
Compaction
Landfill
In-situ
Primary compression ratio
Shear wave velocity
Degradable waste

Abstract

Limited availability of simple yet adequately validated tools for estimating the deformation potential of municipal solid waste (MSW) material poses difficulty in planning and managing landfill operations. Estimation of settlement of MSW landfills has remained a challenge because of heterogeneity and time-varying mechanical behavior of MSW materials and difficulty of extracting representative samples and reconstituting them for laboratory testing. An empirical correlation is proposed here for estimating the short-term settlement of landfill materials. The relationship was developed by calibrating laboratory data from axial (1D) compression and consolidated drained triaxial tests against field-measured shear wave velocities from five landfill sites with varied waste compositions. The correlation was validated against three full scale load tests; one obtained in this research and two reported by others, and a field compaction study from a fourth landfill. Although the proposed correlation was more accurate than an alternative developed earlier, overall it underestimated settlements by about 12%. The proposed relationship could therefore provide a conservative guidance in MSW landfill design and operation.

1. Introduction

Landfill settlement may occur due to both mechanical compression and biological decomposition of the waste material. Typical field settlement data for Municipal Solid Waste (MSW) landfills indicate that settlements result from four physical processes: elastic deformation (Phase I); deformation due to time-rate independent reorientation and repositioning of fibrous, membrane-like, particulate and other MSW constituents under self-weight and other superposed loads (Phase II); deformation due to creep (Phase III); and deformation due to biodegradation, biogas compressibility and gas migration (Grisolia & Napoleoni, 1995). Phase I settlement typically develops over the first few days of fill placement and Phase II settlement develops over the initial 1 to 3 months of fill placement. The volume requirement and operational life of a landfill, for instance, is controlled by maximizing waste compaction during placement (Ham et al., 1978; Fang & Chaney, 2016), i.e., by minimizing the potential of settlements that develop in phases I and II. A reasonable estimate of settlements expected to develop in these phases would therefore be of help in the assessing the volumetric capacity of landfills at their design stages and in the operational management of the landfill operations. An empirical framework for estimating such settlements for a variety of MSW composition is the main focus of this paper. Compaction potential of MSW landfill materials and their primary compression sometimes could be as large as half of its original uncompacted thickness (Zekkos et al., 2016).

2. Differences in laboratory and field deformation behavior of MSW

The primary compression ratio, C'_c, that relates to the compression index, C_c, and initial void ratio, e_0, via $C'_c = C_c/(1+e_0)$ (Durmusoglu et al., 2006), is often used for estimating primary settlement, S_i, employing:

$$S_i = HC'_c \log\left\{\left(\sigma'_v + \Delta\sigma'_v\right)/\sigma'_v\right\} \quad (1)$$

where H is the waste thickness, σ'_v is the initial vertical effective stress and $\Delta\sigma'_v$ is the vertical stress increment that is causing the settlement. Since C'_c relates to the constrained

[#]Corresponding author. E-mail address: debasis@civil.iitkgp.ac.in
[1]IIT Kharagpur, Department of Civil Engineering, Kharagpur, West Bengal, India.

Submitted on December 10, 2021; Final Acceptance on February 6, 2023; Discussion open until: November 3, 2023.
https://doi.org/10.28927/SR.2023.078521

modulus, M, of the waste undergoing settlement such that $M = 2.303\sigma_v' / C_c'$, M can also be used in settlement estimation instead of C_c'.

Characterizing MSW for C_c' (or M) by drilling boreholes or advancing a piezocone or other probes through the waste could be difficult due to the likelihood of premature refusal of the sounding on an impenetrable pocket of construction debris, metal pieces, or stretched plastic waste within the landfill. Such intrusive methods could also open up undesirable pathways for the migration of leachate, contaminants, and landfill gases. The field behavior of MSW depends mostly on its progressive compression and preferential alignment of constituents. So testing of relatively small-sized laboratory specimens prepared by reconstituting the waste materials extracted from drilling may not capture their field deformation behavior. Fibrous or membrane-like materials contained in the waste, for instance, align progressively perpendicular to the direction of compression (Zekkos et al., 2016) making its field deformation behavior stiffer than that inferred from laboratory tests (Bray et al., 2009; Ramaiah & Ramana, 2017). It should be mentioned here that the MSW materials having particle size greater than 20 mm are broadly classified as fibrous or membrane like materials (Bray et al., 2009). In general, they have long main axes and they are slender in nature. These materials show reinforcing effect when they undergo reasonable displacement.

Consequently, laboratory-inferred C_c' has been noted to decrease with the physical size of specimens tested in the laboratory (Hossain & Gabr, 2005). A review of laboratory tests on MSW specimens with similar bulk unit weight, degradable waste content, and moisture content obtained by Wall & Zeiss (1995), Beaven (1999), and Reddy et al. (2009) also indicates that a 10-fold increase in the size of test specimen the average C_c' decreased by about 25%. A similar review by Gabr & Valero (1995), Jang et al. (2010), and Jang (2013) indicates that the average C_c' applicable in the field could be as small as a third of the laboratory-inferred value for MSW materials of similar characteristics. However, since the difference could be to an extent due to rearrangement and reorientation of waste contents developing over time, laboratory-derived C_c' may still provide a reasonable first-order estimate of primary settlements of MSW if a procedure partly based on laboratory tests is validated or calibrated against field observations.

As expected for a deformable material undergoing progressive compression, decomposition and content rearrangement, C_c' decreases with decreasing organic fraction (Hossain et al., 2003; Chen et al., 2009), with increased abundance of incompressible materials (Dixon et al., 2008; Kavazanjian Junior et al., 2013), with increasing depth of burial and age (Landva et al., 2000; Chen et al., 2009) and compaction during placement (von Stockhausen, 2007; Wong, 2009). The influence of moisture content on C_c' is somewhat complicated. Older (and therefore possibly partly decomposed) waste, for instance, has been noted to be more compressible when drier (Vilar & Carvalho, 2004; Durmusoglu et al., 2006), whereas relatively young waste is sometimes more compressible when wetter (Reddy et al., 2009).

3. Database

Laboratory test data from CME Gate and Dharma characterized in this study and Metropolitan Center, Suzhou, Yancheng, Okhla and Ghazipur dumpsites (Table 1) investigated by others were used for developing a C_c'-V_S correlation. The C_c' values were estimated from field stress-strain curves inferred by scaling laboratory deformation responses observed in one dimensional compression and consolidated drained triaxial tests on reconstituted waste materials to reflect the shear stiffness obtained from V_S and Poisson's ratio inferred from field-measured primary and secondary wave velocities (Figure 1). Figure 1 was developed based on the data from the Matasovic & Kavazanjian Junior (1998) and Landva et al. (2000). Details on five other dumps listed in Table 1, IIT-T1, IIT-T2, the Austin Community landfill (Zalachoris, 2010), Valdemingómez landfill (van Elk et al., 2014) and one in Michigan found in Hanson et al. (2010) were used to validate the C_c'-V_S relationship.

4. Landfill characterization and data reduction

CME Gate and Dharma, IIT-T1 and IIT-T2 landfills were characterized for their V_S with MASW employing six geophones placed at 1 m center-to-center spacing and 2 m offset between the source and the geophone nearest to it. The data were analyzed using factored wavelength inversion (Matthews et al., 1996) assuming penetration depth to be a third of the wavelength. The theoretical relationship between

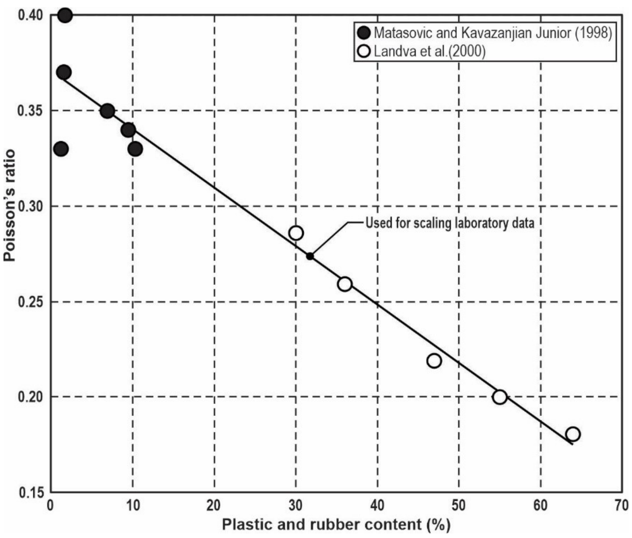

Figure 1. Poisson's ratio for MSW materials inferred from field body wave velocities.

Table 1. MSW data used in this study for correlation development and validation.

Landfill (References)	C'_c, see Note *a*	V_S (m/s), see Note *a*	Waste composition (w/w %)	
			Plastic and rubber	Food, garden, paper/cardboard, textiles, metal, glass, wood, soil-like
CME Gate (this study)	0.250 - 0.310	90 – 110	17.2	−, 15.5, 3.2, −, −, 3.2, 64.1
Dharma (this study)	0.240	70	9.8	−, 3.4, 3.4, −, −, −, 81.6
IIT-T1 (this study)	*0.199 - 0.232*	40 - 150	7.8	−, 2.2, 2.1, 2.4, 3, 1.4, 81.1
IIT-T2 (this study)	*0.200 - 0.251*	60 - 230	19.4	−, 12.1, 0.1, 5.8, 2.3, 1.2, 59.1
Metropolitan Center (Machado et al., 2008; Machado et al., 2002)	0.072	*113*	23.8	36.1, 17.1, 2.6, 2.4, 3.5, 4, 10.5
	0.084	*153*	23.8	36.1, 17.1, 2.6, 2.4, 3.5, 4, 10.5
	0.193	*167*	23.8	36.1, 17.1, 2.6, 2.4, 3.5, 4, 10.5
	0.056	*134*	14	50.2, 5.2, 2.5, 5, 4.1, 5.6, 13.4
	0.125	*143*	14	50.2, 5.2, 2.5, 5, 4.1, 5.6, 13.4
	0.158	*201*	14	50.2, 5.2, 2.5, 5, 4.1, 5.6, 13.4
	0.296	*79*	19	55, 2, 3, 5, 2, 4, 10
	0.498	*95*	19	55, 2, 3, 5, 2, 4, 10
	0.741	*95*	19	55, 2, 3, 5, 2, 4, 10
Suzhou (Zhan et al., 2008)	0.200	*105*	16.6	14.75, 7.07, 0, 1.9, 0, 0, 59.65
Yancheng (Li & Shi, 2016)	0.223	*149*	15.2	53, 11.8, 5.2, 7.5, 4, 5.4, 6
	0.284	*189*	15.2	53, 11.8, 5.2, 7.5, 4, 5.4, 6
Okhla (Ramaiah & Ramana, 2017)	0.141	*77*	1	0, 0, 0.8, 0, 0, 98.2
	0.162	*118*	1	0, 0, 0.8, 0, 0, 98.2
	0.270	*147*	4	0, 0, 6.2, 0, 0, 89.8
	0.102	*213*	4	0, 0, 6.2, 0, 0, 89.8
Ghazipur (Ramaiah & Ramana, 2017)	0.066	*80*	0	0, 0, 0, 0, 0, 100
	0.090	*78*	0	0, 0, 0, 0, 0, 100
	0.154	*175*	0	0, 0, 0, 0, 0, 100
	0.127	*85*	3.3	0, 0, 4.5, 0, 0, 92.2
	0.217	*105*	3.3	0, 0, 4.5, 0, 0, 92.2
	0.413	*141*	3.3	0, 0, 4.5, 0, 0, 92.2
Austin Community (Zalachoris, 2010)	*0.22*	65 – 105	2.0	−, 5.0, −, −, 1.0, 92
Michigan Subtitle D (Hanson et al., 2010)	*0.34*	*49 – 71*	19.0,	25.0, 24.0, 6.0, 7.0, 6.0, 7.0, 6.0,
Valdemingómez (van Elk et al., 2014)	*0.22*	70 – 140	14.0	59, 6.0, −, 4, 8.0, −, 9

Note: *a*. Entries in normal typeface represent parameters representing corrected lab response or direct field measurements. Italicized entries are for C'_c obtained from the correlation developed in this study or V_S from Zekkos et al. (2014).

the velocities of Rayleigh and shear waves for isotropic, linearly elastic materials (Richart et al., 1970) were used to estimate the in-situ shear wave velocity with Poisson's ratio taken from Figure 1. Although there is some scatter in V_S inferred from MASW possibly due to material heterogeneity and consequent Rayleigh wave dispersion multimodality (Kausel et al., 2015; Zhang et al., 2016), their general increase with depth appears to capture the influence of compaction on V_S (Figure 2).

MSW materials from CME Gate and Dharma were subjected to vertical compression testing within a stiff metal cylinder of 600 mm diameter and 440 mm height. The observed deformation responses were corrected to reflect material stiffness inferred from body wave velocity measurements as discussed earlier. C'_c obtained in this manner with the corresponding MASW inferred values of V_S are listed in Table 1. These data were also used in developing the C'_c -V_S correlation proposed below.

5. Correlation for primary compression ratio

Table 1 data indicate that C'_c may relate to V_S (taken in m/s) via the following relationship:

$$C'_c = a \exp\left(-bV_S\right) \tag{2}$$

in which parameters a and b were found to depend on mean normal effective stress, p', and atmospheric pressure, P_a, according to

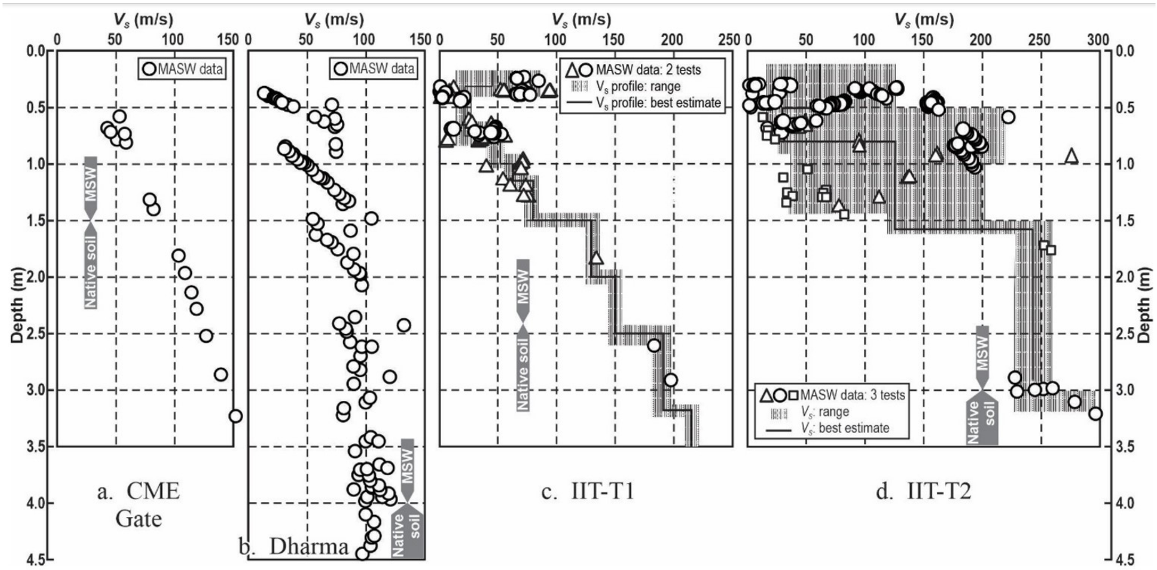

Figure 2. MASW-based shear wave velocity profiles at (a) CME gate landfill; (b) Dharma landfill; (c) IIT-T1; and (d) IIT-T2.

$$a = 2.56399 \times 10^{-1} \left(p'/P_a \right)^{\left(-0.76/\left(p'/P_a\right)\right)}$$
$$b = 8.5541 \times 10^{-3} \left(p'/P_a \right)^{\left(-0.36/\left(p'/P_a\right)\right)} \tag{3}$$

Although Equations 2 and 3 are functionally similar to Zekkos et al. (2014, 2016) correlations, instead of relying on laboratory deformation data, Equations 2 and 3 were developed using laboratory data calibrated for field-measured deformation moduli. Curve export professional 2.7.3 is used to develop these Equations 2 and 3 with $r^2 = 0.99$.

6. Validation

To validate the proposed relationship, field load test was performed at IIT landfill site that has been operating over the last five years as discussed in the following subsection. Measurements from another two field load tests and a compaction trial obtained by others were also used for validation.

6.1 Load test at IIT landfill

Two tanks, T1 and T2, of 1350 mm diameter were placed at the surface of a landfill at two locations with different waste compositions and filled rapidly with water after placement to impose 13.6 kPa surcharge. Waste thicknesses underneath T1 and T2 were 2.4 m and 3 m, respectively, below which saturated, firm to stiff silty clay was found. Over the subsequent 83-day of tank settlement was monitored using a system capable of delivering millimeter level accuracy. Water volume in the tanks were replenished to ensure that the surcharge remained constant over the settlement monitoring period.

The settlement at T1 estimated from Equation 2 using profile of Figure 2c and p' estimated from Zekkos et al. (2014) and Schmertmann et al. (1978) approach exceeded the 83-day observed settlement by about 25 mm (Figure 3a). The corresponding estimate for T2 based on Figure 2d V_S profile, on the other hand, was smaller than the 83-day observation by about 80 mm.

6.2 Load test at Austin community landfill

A 230 mm thick footing of 900 mm diameter was constructed on the surface of the Austin community landfill and footing settlements were recorded with three linear potentiometers placed around the footing that resulted from a series of static vertical loads applied statically with a Vibroseis truck (Zalachoris, 2010). MASW geophones were positioned around the boundary of the footing, and four V_S profiles were obtained with a maximum coefficient of variation of 9.7% with its mean V_S profile. MSW composition and mean V_S values from the field load test location can be found in Table 1. For the mean V_S profile the settlements were estimated from Equation 2 adhering to Schmertmann et al. (1978). The results indicate that the proposed method overestimated the settlement at a 45 kN load by about 14% (Figure 3b).

6.3 Trial compaction at Michigan (subtitle D) landfill

Full-scale field compaction tests were performed over a test cell of about 200 m^2 area at a landfill in Michigan, USA by placing the waste in 500 mm loose lifts and compacting them with 530-kN BOMAG BC 1172RB waste compactor (Hanson et al., 2010). The reported unit weight of waste at placement was 3.3 to 6 kN/m^3. As indicated in Table 1, the corresponding shear wave velocities are expected to range between 49 m/s and 71 m/s (Zekkos et al., 2014). Assuming a tangential contact between the compactor and native ground

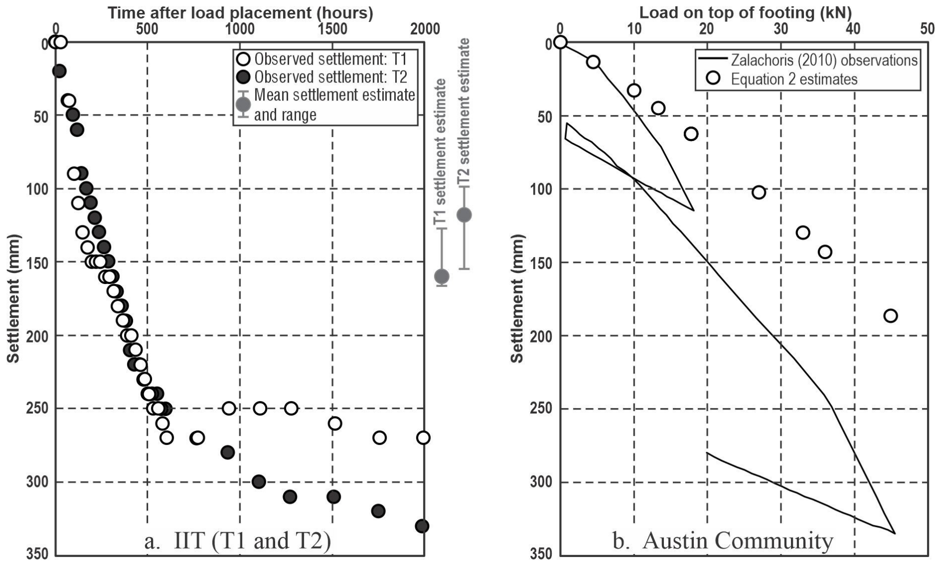

Figure 3. Observed and estimated settlements at (a) IIT –T1 and IIT- T2 landfill; and (b) Austin landfill.

or underlying compacted layer, the compaction is likely to have imposed a $\Delta\sigma_v'$ of about 52 kPa. Assuming an effective stress friction angle of about 30° and zero cohesion for the waste layer at placement (Zekkos et al., 2012), the ultimate bearing capacity that the poorly compacted layer of MSW would have mobilized under compactor wheels would have been about 48 kPa; a value quite close to the estimated stress increment. While the settlement estimate for $\Delta\sigma_v' = 52$ kPa and C_c' from Equation 2 exceeded the corresponding observation in one instance by as much as 73% and was smaller than observation by as much as 28% in another, the majority of observations were in approximate agreement with Equation 2 estimates (Figure 4).

6.4 Valdemingómez landfill load test

A surface surcharge was placed on a 33-m high landfill in Madrid, Spain by placing soil over a rectangular area measuring 39 m in length and 20 m in width (van Elk et al., 2014). Maximum height of the fill was 4 m. Settlements were monitored near the middle of the north and south edges of the fill at various distances from the fill slope toe. MSW composition and mean V_S values inferred from Rayleigh wave measurements for test location are presented in Table 1.

Settlements estimates from Equation 2 were within +9% and −44% of observations with observations by and large exceeding those from Equation 2 marginally (Figure 4).

6.5 Bias and accuracy

Overall, observed short term settlements were found to be larger than Equation 2 estimates by about 12% with the observation clustering within +78% and −42% of estimates (Figure 4). In comparison, the Zekkos et al. (2016) framework underestimated settlements overall by about 63% with observations exceeding the corresponding estimates by between 28% and 330%.

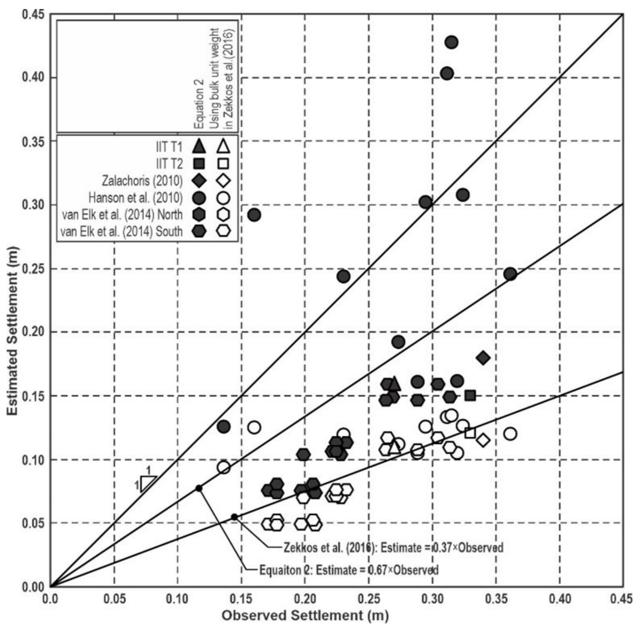

Figure 4. Comparison of settlement estimates with observations.

7. Conclusion

A reliable estimate of short term settlements of MSW materials is an essential input in proper design and operation of MSW landfills. Laboratory testing for obtaining such settlements may not always be feasible due to the difficulty in extracting representative MSW samples and reconstituting them within the small confines of typical laboratory setups.

An empirical procedure has been proposed in this paper for estimating short-term settlements of MSW materials using field-measured shear wave velocity. The relationship was developed by calibrating laboratory deformation test data to reflect field conditions using field-measured primary and secondary wave velocities, calculating the compression ratio from the calibrated deformation response and relating the compression ratio to field-measured shear wave velocities. Data from four MSW landfills characterized in this study and six sites investigated by others were used to develop the correlation. The settlements estimated using the proposed framework were then compared with observations from four full-scale field load tests and a compaction study. Load tests at two locations were conducted in this study and the other three datasets used in this exercise were from published literature. The results indicated that the short-term settlement estimates obtained from the correlations were about 12% less than observations.

The results obtained in this study suggest that short term compaction or deformation potential of MSW landfills could be reasonably estimated from laboratory compression or triaxial test data scaled to reflect the stiffness obtained from field-measured primary and secondary wave velocities. In the absence of laboratory data, the correlation proposed in this study may also provide a reasonable but somewhat conservative option for estimating short term settlements of MSW materials.

Acknowledgements

This work was partly supported by the Ministry of Human Resource Development (MHRD), Government of India under the project Future of Cites initiative.

Declaration of interest

The authors have no conflicts of interest to declare. All co-authors have observed and affirmed the contents of the paper and there is no financial interest to report.

Authors' contributions

Nagendra Kola: data curation, visualization, testing, formal analysis, validation, writing – original draft. Debasis Roy: conceptualization, methodology, supervision, funding acquisition, writing – review & editing. Debarghya Chakraborty: supervision, writing – review & editing, funding acquisition.

Data availability

The datasets produced and analyzed in the course of the present study are available from the corresponding author upon reasonable request.

List of symbols

e_0	initial void ratio
p'	mean normal effective stress
C_c	compression index
C_c'	primary compression ratio
H	waste thickness
M	constrained modulus
P_a	atmospheric pressure
S_i	immediate or short-term settlement
V_S	shear wave velocity
σ_v	initial vertical effective stress
$\Delta\sigma_v'$	vertical stress increment

References

Beaven, R.P. (1999). *The hydrological and geotechnical properties of household waste in relation to sustainable landfilling* [PhD Dissertation, Queen Mary University of London]. Queen Mary University of London's repository.

Bray, J.D., Zekkos, D., Kavazanjian Junior, E., Athanasopoulos, G.A., & Riemer, M.F. (2009). Shear strength of municipal solid waste. *Journal of Geotechnical and Geoenvironmental Engineering*, 135(6), 709-722.

Chen, Y.M., Zhan, T.L.T., Wei, H.Y., & Ke, H. (2009). Aging and compressibility of municipal solid wastes. *Waste Management (New York, N.Y.)*, 29(1), 86-95.

Dixon, N., Langer, L., Reddy, K., Maugeri, M., Tinjum, J., Mahler, C., & Cho, Y. (March 13, 2008). Waste characterization. geotechnical characterization, field measurement and laboratory testing of municipal solid waste (GSP209). In *Proceedings of the International Symposium on Waste Mechanics* (pp. 135-152). New Orleans, Louisiana.

Durmusoglu, E., Sanchez, I.M., & Corapcioglu, M.Y. (2006). Permeability and compression characteristics of municipal solid waste samples. *Environmental Geology*, 50(6), 773-786.

Fang, H.Y., & Chaney, R.C. (2016). *Introduction to environmental geotechnology*. 2nd ed. CRC Press.

Gabr, M.A., & Valero, S.N. (1995). Geotechnical properties of municipal solid waste. *Geotechnical Testing Journal*, 18(2), 241-251.

Grisolia, M., & Napoleoni, Q. (1995). Deformability of waste and settlements of sanitary landfills. In *Proceedings of the World Congress on Waste Management ISWA'95*, Wien.

Ham, R.K., Reinhardt, J.J., & Sevick, G.W. (1978). Density of milled and unprocessed refuse. *Journal of the Environmental Engineering Division*, 104, 109-125.

Hanson, J.L., Yesiller, N., Von Stockhausen, S., & Wong, W.W. (2010). Compaction characteristics of municipal solid waste. *Journal of Geotechnical and Geoenvironmental Engineering*, 136(8), 1095-1102.

Hossain, M., Gabr, M., & Barlaz, M. (2003). Relationship of compressibility parameters to municipal solid waste decomposition. *Journal of Geotechnical and Geoenvironmental Engineering*, 129(12), 1151-1158.

Hossain, M.S., & Gabr, M.A. (2005). Effect of gas and moisture on modelling of bioreactor landfill settlement. *Waste Management (New York, N.Y.)*, 29, 1018-1025.

Jang, Y.S. (2013). Field monitored settlement and other behavior of a multi-stage municipal waste landfill, Korea. *Environmental Earth Sciences*, 69(3), 987-997.

Jang, Y.S., Choi, J.S., & Ryu, H.R. (2010). Management and stability analysis of a seashore waste landfill, Korea. *Environmental Earth Sciences*, 61, 87-92.

Kausel, E., Malischewsky, P., & Barbosa, J.O. (2015). Osculations of spectral lines in a layered medium. *Wave Motion*, 56, 22-42.

Kavazanjian Junior, E., Matasovic, N., & Bachus, R.C. (2013). The 11th peck lecture: predesign geotechnical investigation for the OII superfund site landfill. *Journal of Geotechnical and Geoenvironmental Engineering*, 139(11), 1849-1863.

Landva, A.O., Valsangkar, A.O., & Pelkey, S.G. (2000). Lateral earth pressure at rest and compressibility of municipal solid waste. *Canadian Geotechnical Journal*, 37, 1157-1165.

Li, X., & Shi, J. (2016). Stress-strain behavior and shear strength of municipal solid waste (MSW). *KSCE Journal of Civil Engineering*, 20(5), 1747-1758.

Machado, S.L., Carvalho, M.F., & Vilar, O.M. (2002). Constitutive model for municipal solid waste. *Journal of Geotechnical and Geoenvironmental Engineering*, 128(11), 940-951.

Machado, S.L., Vilar, O.M., & Carvalho, M.F. (2008). Constitutive model for long term municipal solid waste mechanical behavior. *Computers and Geotechnics*, 35, 775-790.

Matasovic, N., & Kavazanjian Junior, E. (1998). Cyclic characterization of OII landfill solid waste. *Journal of Geotechnical and Geoenvironmental Engineering*, 124(3), 197-210.

Matthews, M.C., Hope, V.S., & Clayton, C.R.I. (1996). The use of surface waves in the determination of ground stiffness profiles. *Proceeding of the Institution of Civil Engineers Geotechnical Engineering*, 119(2), 84-95.

Ramaiah, B.J., & Ramana, G.V. (2017). Study of stress-strain and volume change behaviour of emplaced municipal solid waste using large-scale triaxial testing. *Waste Management (New York, N.Y.)*, 63, 366-379.

Reddy, K.R., Hettiarachchi, H., Parakalla, N.S., Gangathulasi, J., & Bogner, J.E. (2009). Geotechnical properties of fresh municipal solid waste at Orchard Hills Landfill, USA. *Waste Management (New York, N.Y.)*, 29(2), 952-959.

Richart, F.E., Woods, R.D., & Hall Junior, J.R. (1970). *Vibrations of soils and foundation*. Prentice-Hall, Inc.

Schmertmann, J.H., Hartman, J.P., & Brown, P.R. (1978). Improved strain influence factor diagrams. Journal of Geotechnical Engineering Division, 104(GT8), 1131-1135.

van Elk, A.G.P., Mañas, L.M.S., & Boscov, M.E.G. (2014). Field survey of compressibility of municipal solid waste. *Soil and Rocks*, 37(1), 85-95.

Vilar, O., & Carvalho, M. (2004). Mechanical properties of municipal solid waste. *Journal of Testing and Evaluation*, 32(6), 1-12.

von Stockhausen, S.A. (2007). *Optimization of waste compaction practices for landfills* [MS thesis, California Polytechnic State University]. California Polytechnic State University's repository.

Wall, D.K., & Zeiss, C. (1995). Municipal landfill biodegradation and settlement. *Journal of Environmental Engineering*, 121(3), 214-224.

Wong, W.W. (2009). *Investigation of the geotechnical properties of municipal solid waste as a function of placement conditions* [MS thesis, California Polytechnic State University]. California Polytechnic State University's repository.

Zalachoris, G. (2010). *Field measurements of linear and nonlinear shear moduli of solid municipal waste using a dynamically loaded surface footing* [MS Thesis, The University of Texas]. The University of Texas's repository.

Zekkos, D., Bray, J.D., & Riemer, M.F. (2012). Drained response of municipal solid waste in large-scale triaxial shear testing. *Waste Management (New York, N.Y.)*, 32, 1873-1885.

Zekkos, D., Fei, X., Grizi, A., & Athanasopoulos, G. (2016). Response of municipal solid waste to mechanical compression. *Journal of Geotechnical and Geoenvironmental Engineering*, 143(3), 1-11.

Zekkos, D., Sahadewa, A., Woods, R., & Stokoe 2nd, K.H. (2014). Development of model for shear wave velocity of municipal solid waste. *Journal of Geotechnical and Geoenvironmental Engineering*, 140(3), 1-14.

Zhan, T.L.T., Chen, Y.M., & Ling, W.A. (2008). Shear strength characteristics of municipal solid waste at the Suzhou landfill, China. *Engineering Geology*, 97(3), 97-111.

Zhang, K., Zhang, B., Liu, J., & Xu, M. (2016). Analysis on the cross of Rayleigh-wave dispersion curves in viscoelastic layered media. *Chinese Journal of Geophysics*, 59(3), 972-980.

Soils and Rocks
An International Journal of Geotechnical and Geoenvironmental Engineering
www.soilsandrocks.com
ISSN 1980-9743
ISSN-e 2675-5475

Brackish water in swelling soil stabilization with lime and sugarcane bagasse ash (SCBA)

Carina Silvani[1#], João Pedro Camelo Guedes[1], Jucimara Cardoso da Silva[2], Eduardo Antonio Guimarães Tenório[2], Renan Carlos de Melo Nascimento[2]

Article

Keywords
Unconfined compressive strength
Chemical stabilization
Tap water saving

Abstract

This research shows that brackish water increases the unconfined compressive strength of swelling soil/sugarcane bagasse ash (SCBA)/lime blends. Therefore, brackish water may substitute tap water in soil stabilization. Sodium chloride (NaCl) has been used in lime-ashes-soil treatments. In northeast Brazil, swelling soils are usual and artesian wells sometimes provide brackish water containing NaCl. Northeast Brazil also has a strong sugar and ethanol industry producing sugarcane bagasse ash (SCBA) as a byproduct. Therefore, brackish water can be used in soil-SCBA-lime stabilization. Hence, this work aims to evaluate the use of brackish water as a substitute for tap water in swelling soil-SCBA-lime blends stabilization. Two series of unconfined compression tests were carried out: one with tap water and the other with brackish water. In each group, the lime content varied from 4% to 8%, and the dry density from 13 kN/m^3 to 15 kN/m^3. All tests were carried out with a swelling soil-SCBA proportion of 75/25 and a water content of 22%. Results have shown that increasing lime content or dry density or using brackish water allowed to increase unconfined compression strength of swelling soil-SCBA-lime blends. The porosity/volumetric content of lime index (η/L_{iv}) was suitable to predict the unconfined compressive strength of swelling soil-SCBA-lime blends, no matter if tap or brackish water was used in the molding process. Thus, brackish can be a feasible substitute for tap water in swelling soil-SCBA-lime stabilization, increasing blends unconfined compression strength, and preserving tap water, a scarce asset in Northeast Brazil.

1. Introduction

Expansive soils undergo volumetric changes by moisture variation. They expand when they are wetted and shrink when dried. (Khazaei & Moayedi, 2017; Pei et al., 2020). Such soils can exert enough pressure to crack floors, pipelines, foundations, and roadways, and usually have low bearing capacity. (Consoli et al., 2010; Taher et al., 2020; Tiwari et al., 2021). This kind of soil is common in several countries such as the United States of America, China, India, and Australia (Phanikumar & Singla, 2016; Pooni et al., 2019; Ito & Azam, 2020). The arid and semi-arid areas, such as northeast Brazil, Canadian Prairies, and the state of Texas-USA, have appropriate environmental factors for expansive soil existence (Puppala et al., 2013; Ferreira et al., 2017; Consoli et al., 2019a).

Chemical stabilization can improve these problematic soils (Mirzababaei et al., 2018). Therefore, some studies have been carried out to stabilize expansive soils with chemical additives, such as cement, blast furnace slag, rice husk ash, recycled ash, and natural fibers (Celik & Nalbantoglu, 2013; Liu et al., 2019; Consoli et al., 2021; Tiwari et al., 2021). However, lime stabilization is widely used in swelling soil improvement (Belchior et al., 2017; Silvani et al., 2020).

Lime can improve soils through the exchange of sodium or potassium cations present in soils for calcium cations. Lime can also react with silica or alumina in the amorphous phase (found in the soil or pozzolanic material) by pozzolanic reaction and produce cementitious material capable of immobilizing soil particles and increasing mechanical strength (Ingles & Metcalf, 1972). Nevertheless, the rate of development of those reactions can be considerably slower, so many materials (e.g., sodium chloride, sodium silicate, and sodium hydroxide) have been studied as reaction catalyzers.

Drake & Haliburton (1972) were the first to analyze sodium chloride (NaCl) use in lime-treated cohesive soils. Recently, several authors (Saldanha et al., 2016; Consoli et al., 2017, 2019b, c; Saldanha et al., 2017) investigated the

[#]Corresponding author. E-mail address: carinasilvani@gmail.com
[1]Universidade Federal do Rio Grande do Sul, Departamento de Engenharia Civil, Porto Alegre, RS, Brasil.
[2]Universidade Federal de Campina Grande, Departamento de Engenharia Civil, Campina Grande, PB, Brasil.

Submitted on September 27, 2022; Final Acceptance on April 1, 2023; Discussion open until November 30, 2023.
https://doi.org/10.28927/SR.2023.010022

addition of NaCl in soil-fly ash-lime blends. These authors found out that the NaCl catalyzed the pozzolanic reaction between lime and fly ash.

In Brazilian Northeast, artesian wells sometimes provide brackish water containing NaCl, unsuitable for human consumption (Lopes, 2004). Therefore, the NaCl in brackish water can act as a potential catalyst in soil-fly ash-lime stabilization, reducing consumption of tap water, a scarce asset in this region.

Although expansive soil areas in Northeast Brazil have a low offer of fly ash, the sugar and alcohol industry produces great amounts of sugarcane bagasse ash (SCBA) as a by-product. Its disposal usually is not appropriate and needs extra attention regarding potassium and heavy metals used in sugarcane's maturation control that can contaminate the soil and the groundwater table (Fernandes Filho et al., 2012; Cordeiro et al., 2019). The use of SCBA as a pozzolanic material has been demonstrated by different authors (i.e., Martirena Hernández et al., 1998; Ganesan et al., 2007; Cordeiro et al., 2009; Alavéz-Ramírez et al., 2012; Zareei et al., 2018).

Consoli et al. (2007) developed the porosity/cement index (η/C_{iv}) to predict unconfined compressive strength (q_u) for a clayey sand soil stabilized with cement. This index is a rational criterion like the water/cement ratio for concretes. Two years later Consoli et al. (2009) used the porosity/lime index (η/L_{iv}) to predict q_u for sandy lean clay stabilized with lime. Silvani et al. (2020) and Consoli et al. (2021) applied this index to predict the swelling behavior of chemical stabilized expansive soil. But there is no research using this index in expansive soil stabilized with brackish water, SCBA, and lime.

Therefore, this research aims to fill this gap in the literature and evaluate the use of brackish water as a substitute for tap water in expansive soil-SCBA-lime blends stabilization and assess the feasibility of this index as an alternative to predict or control q_u of expansive soil/ SCBA/lime blends.

2. Experimental program

The experimental procedure was divided in two parts. The materials were characterized by geotechnical and chemical methods, in the first part. Then, unconfined compressive strength tests (UCS) were carried out to assess the strength of the blends. Two groups of specimens for unconfined compressive strength were done differing only in molding water: the first group was done with tap water and the second group was done with brackish water. Inside each group, amounts of lime were 4%, 6%, and 8% and the dry unit weights were 13, 14, and 15 kN/m^3 with a water content of 22% (w) for the dry mass of swelling soil/SCBA/lime blend. Lime contents were established based on the initial consumption of lime (ICL) proposed by Rogers et al. (1997) and γ_d and w based on the compaction curve using Standard effort according to ASTM D698 (ASTM, 2012) (Figure 1).

2.1 Materials

The expansive soil was collected in Paulista-PE in northeastern Brazil. The soil was classified by USCS (Unified Soil Classification System) as low compressibility plastic clay (CL) (ASTM, 2017a). The SCBA was obtained in Paraiba (PB) state, north-eastern Brazil, from a cachaça (Brazilian drink made from sugarcane) factory and was classified by USCS as low compressibility silt (ML) (ASTM, 2017a). Table 1 presents detailed properties of SCBA and swelling soil. The high value of the soil plastic index is typical in swelling soils.

In addition, Figure 2 and Figure 3 present X-ray diffractograms of soil and SCBA. Swelling soil showed peaks of quartz, muscovite, and smectites (expansive clay mineral). SCBA showed peaks of quartz, aluminum, and calcium, supporting XRF results, and the diffractogram indicates amorphous material.

Calcitic hydrated lime with specific gravity of 2.41 was used as a stabilizer agent (ASTM, 2018a). Distilled water

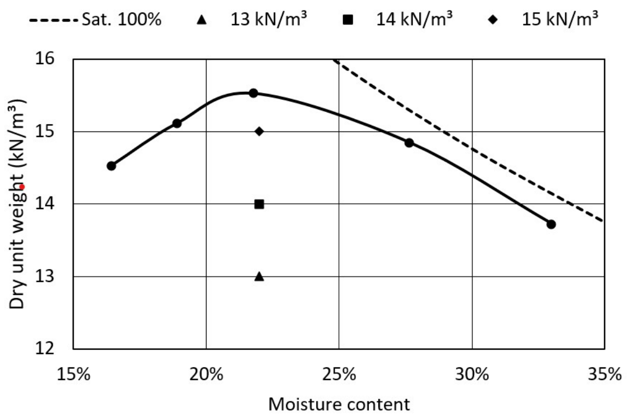

Figure 1. Proctor compaction curve of swelling soil.

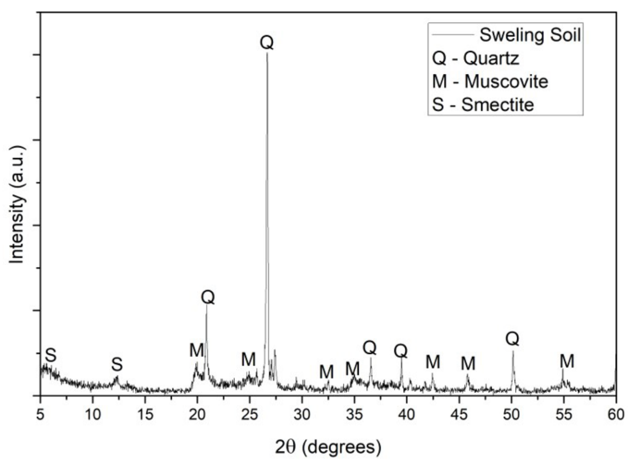

Figure 2. Expansive soil X-ray diffraction.

Table 1. Soil and SCBA characterization.

Properties	Soil	SCBA	Standard
Sand (%)	10.58	29.97	ASTM D6913/2017 (ASTM, 2017b)
Silt (%)	43.96	65.24	
Clay (%)	45.46	4.79	
Liquid limit (%)	49	-	ASTM D4318/2018 (ASTM, 2018b)
Plastic limit (%)	21	-	
Plastic index	28	Non plastic	
Specific gravity	2.65	2.38	ASTM D5550/2014 (ASTM, 2014)
Cation Exchange Capacity (meq/100g)	59.20	18.76	ASTM C837/2019 (ASTM, 2019)
Specific surface area (m^2/g)	462.01	146.41	
SiO_2 (%)	55	53.8	ASTM E1621/2021 (ASTM, 2021)
Al_2O_3 (%)	25	11.4	
CaO (%)	-	12.7	

Table 2. Chemical characterization of tap water and brackish water.

Parameters	Tap clean water	Brackish water	Parameters	Tap water	Brackish water
pH 25 °C	7.1	7.2	Chloride (mg/L)	28	2340
Electric conductivity 25 °C (Ms/cm)	0.238	7.8	Calcium (mg/L)	14	142
Turbidity (UNT)	2.0	1.7	Magnesium (mg/L)	9.2	187
Total hardness (mg$CaCO_3$/L)	73.2	1124	Total alkalinity ($CaCO_3$/L)	36	421
TDS* 103-105 °C (mg/L)	120	5396	Salinity (‰)	0.10	4.2
TDS* 180 °C (mg/L)	118	4792	Bicarbonate (mg/L)	44	421

Note: TDS*: Total dissolved solids.

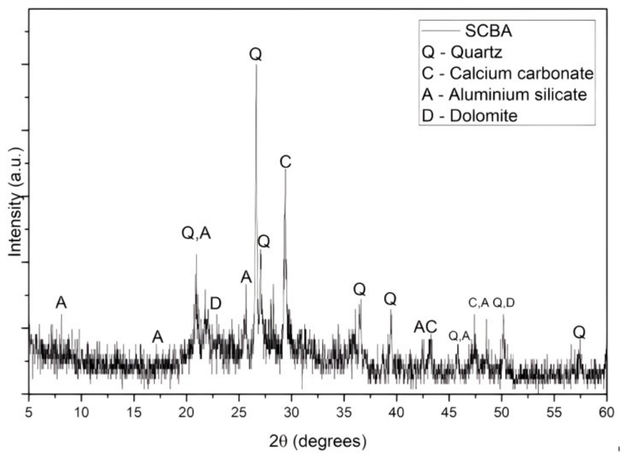

Figure 3. SCBA X-ray diffraction.

was used for the characterization of materials. Tap water from the public supply system and brackish water from an artesian well located in Campina Grande-PB were used for molding specimens. Table 2 presents the results of water characterization tests.

The nº 357 resolution of the Brazilian Environmental National Council (CONAMA) establishes that tap water has salinity lower than 0.5‰ and brackish water salinity can range from 0.5‰ to 30.0‰ (Brasil, 2005). Therefore, the data presented in Table 2 indicates the water from the artesian well is classified as brackish water because of its salinity of 4.2‰, so is inappropriate for human consumption. Tap water has a salinity of 0.10‰.

2.2 Molding and curing of specimens

Cylindrical specimens 50 mm in diameter and 100 mm in height were used. The soil, lime, and SCBA were mixed with water until acquired a homogeneous aspect and statically compacted in 3 layers. Between each layer, the top was scarified. The curing period was fixed at 28 days in a humid room at 23 °C. The specimens were submerged in water for 24 hours to minimize suction (Saldanha & Consoli, 2016) twenty-seven days after the molding, bringing the total curing time to 28 days. The specimens were molded in duplicate.

The cure timing was set to allow pozzolanic reactions to occur. The SCBA content was based on international and Brazilian practices with industrial byproducts (ashes) (Consoli et al., 2001, 2019d).

2.3 Porosity/lime index (η/L_{iv})

The initial porosity (η) can be calculated as the ratio of the volume of voids over the total volume of the specimen (Equation 1). It is a function of dry unit weight (γ_d) of the mixture, lime content (L), soil content (S), SCBA content (SCBA), total volume of the specimen (Vs), and the unit weight of solids of soil (γ_{sS} = 26.5 kN/m^3), SCBA (γ_{sSCBA} = 23.8 kN/m) and lime (γ_{sL} = 24.1 kN/m^3). Volumetric lime content is obtained from Equation 2 considering the volume of lime (lime mass divided by lime specific gravity) and total volume of blends.

$$\eta = 100 - \frac{100\left\{\frac{\frac{\gamma_d Vs}{1+\frac{L}{100}}\left(\frac{S}{100}\right)}{\gamma_{sS}} + \frac{\frac{\gamma_d Vs}{1+\frac{L}{100}}\left(\frac{SCBA}{100}\right)}{\gamma_{sSCBA}} + \frac{\frac{\gamma_d Vs}{1+\frac{L}{100}}\left(\frac{L}{100}\right)}{\gamma_{sL}}\right\}}{Vs} \quad (1)$$

$$L_{iv} = \frac{V_L}{V} = \frac{m_{L/\gamma sL}}{V} \quad (2)$$

2.4 Unconfined compression tests

Unconfined compression tests were carried out with an automated hydraulic press with a displacement rate of 1.14 mm/min.

3. Results

3.1 Lime content effect

Figures 4a and 4b show the relation between lime content and unconfined compressive strength (q_u) for swelling soil/SCBA/Lime molded with tap water and brackish water, respectively. q_u increases linearly when the lime content grows, in both situations, probably because SCBA is rich in amorphous silica and alumina (Figure 2) which allows pozzolanic reactions with lime. In addition, for the same lime content, the higher the dry density, the higher the inclination (slope) of the fitting line. This behavior indicates a bigger unconfined compressive strength growth rate. Especially for specimens with brackish water, the slope and the y-intercept of the fitting lines tend to increase as the dry unit weight also increases. Therefore, the lime effect is greater in more compacted blends as stated by Consoli et al. (2009).

3.2 Porosity effect

The influence of porosity in unconfined compressive strength is shown in Figure 5a for blends molded with tap water and (b) for mixtures done with brackish water. Each curve in Figure 5 is adjusted for specimens molded with the same amount of lime. The unconfined compressive strength decreases when the porosity increases, thus both variables are inversely proportional, no matter if tap or brackish water was used in the molding process. According to Consoli et al. (2007, 2009), when porosity reduces, the contact between lime and soil particles intensifies, improving the cementitious process and, hence, q_u.

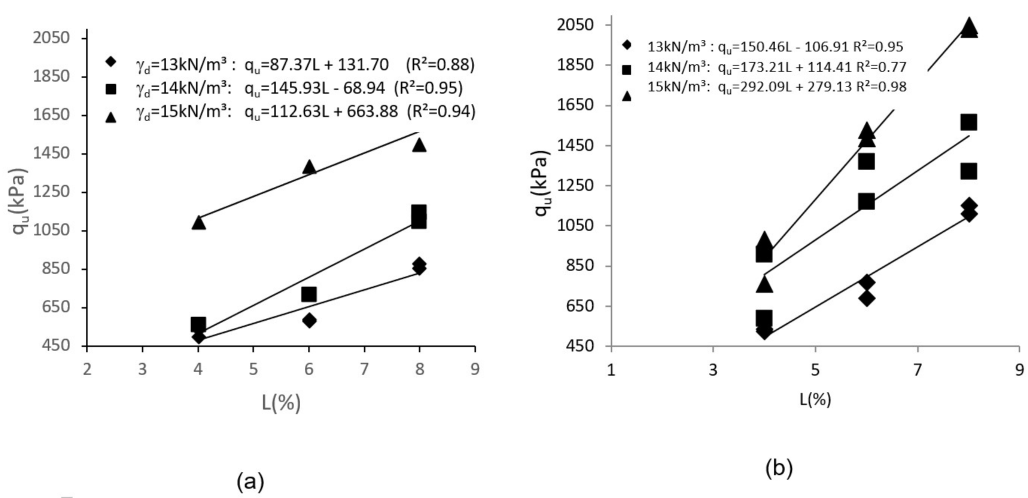

Figure 4. Unconfined compressive strength as a function of lime content of stabilized soil with (a) tap water and (b) brackish water.

3.3 Porosity/lime content index effect

The combination of variable porosity and lime content is presented in Figure 6a for blends done with tap water and (b) for mixtures molded with brackish water. Figure 6 shows that there is no unique relationship between strength and porosity/volumetric lime (η/L_{iv}) content. This behavior was also observed by Tenório (2019) when the author stabilized the same expansive soil using lime only. To obtain a unique dosage curve, it is necessary to make the two variables (η and L_{iv}) compatible setting an exponent (a) on the denominator (L_{iv}). According to Consoli et al. (2007, 2009, 2011) and Consoli & Foppa (2014), this exponent makes it possible to match the different growth rates of q_u with η and L_{iv} and hence, optimize the q_u x η/L_{iv} relation.

Figure 7 shows the relationship between the unconfined compressive strength and $\eta/L_{iv}{}^{a}$ index for stabilized swelling soil with tap water and brackish water with an exponent of 0.26. This same exponent value was used by Silvani et al., (2020) relating the vertical swelling with porosity/lime content (η/L_{iv}), and by Guedes et al. (2022) correlating its q_u with porosity/cement content (η/C_{iv}), for the same soil. The authors found that 0.26 would be the best value to make the parameters and the variation rate compatible to better adjust porosity/cementing agent relation. Diambra et al. (2017) demonstrated through theoretical derivation that the coefficient a is highly dependent on the soil matrix (granular matrix) and is directly related to the external exponent ($3.97 \cong 1/0,26$).

The analysis of Figure 7 indicates that q_u can be forecasted by the η/Liv^a index using a unique dosage curve as occurs with concrete strength while using the water/cement (w/c) ratio. The function to predict q_u with $\eta/L_{iv}{}^{0.26}$ index for blends molded with tap water is presented in Equation 3 and for blends done with brackish water is presented in Equation 4. The coefficient of determination is satisfactory (R^2 >0.85) for both water molding tested. Comparing Equations 3 and 4 can be seen that the only difference between them is the scalar.

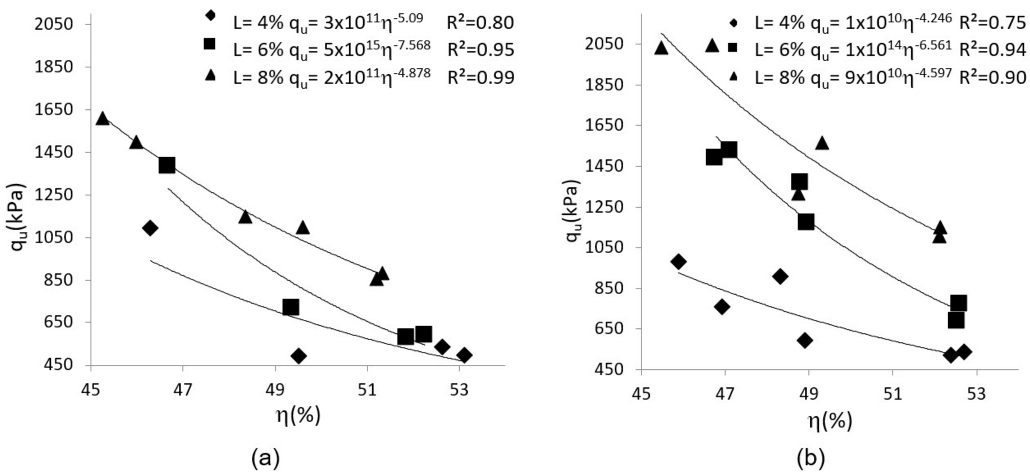

Figure 5. Unconfined compressive strength as a function of porosity of stabilized soil with (a) tap water and (b) brackish water.

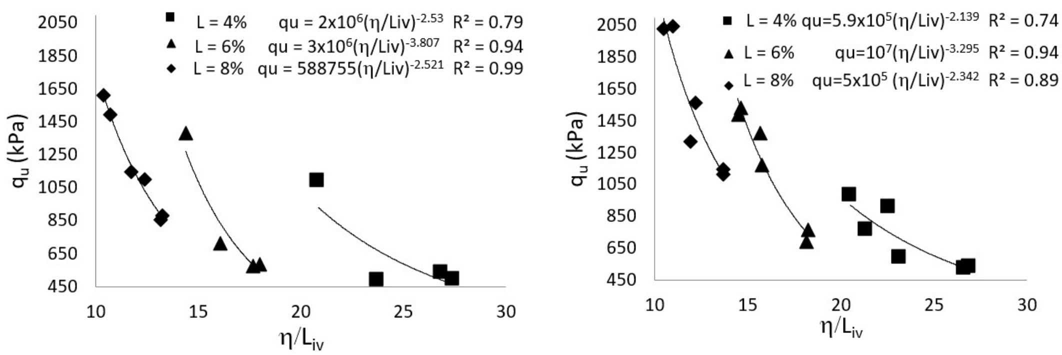

(a) (b)

Figure 6. Unconfined compressive strength as a function of η/Liv index for the stabilized soil with (a) tap water and (b) brackish water.

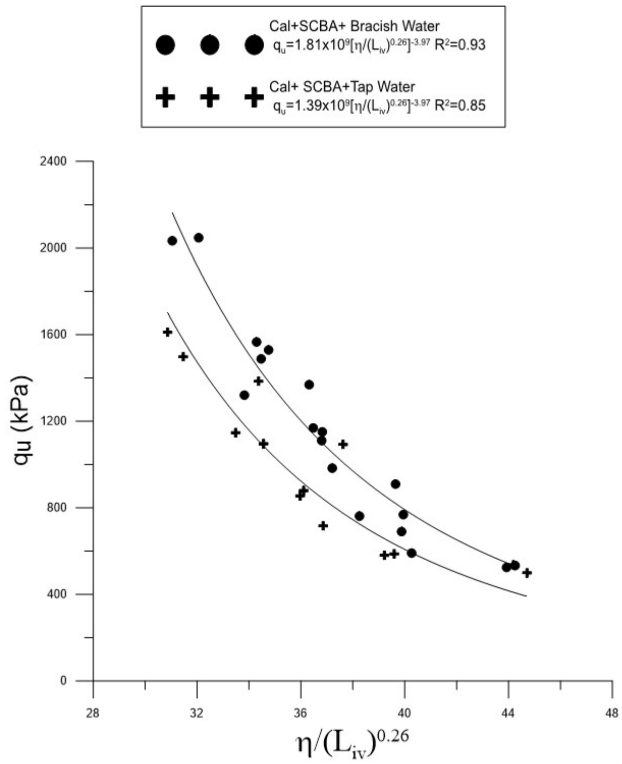

Figure 7. Unconfined compressive strength as a function of η/Liv^a index.

The scalar for mixtures done with brackish water is bigger than the scalar for blends molded with tap water. It shows that blends molded with brackish water have bigger q_u than mixtures done with tap water. The increase in q_u for specimens molded with brackish water came probably from the formation of calcium aluminum chlorohydrate ($Ca_2Al(OH)_6Cl{\bullet}2H_2O$). This mineral is formed due to the reaction of alumina (from SCBA) in conjunction with calcium (from lime) and chlorine (from brackish water) (Talero et al., 2011). Consoli et al. (2019e) studied coal fly ash/lime/NaCl blend and found out the formation of calcium aluminum chlorohydrate, through DRX and thermogravimetric results. SCBA and coal Fly ash are pozzolanic materials with similar compositions.

$$q_u = 1.81 \times 10^9 \left[\frac{\eta}{\left(L_{iv}\right)^{0.26}} \right]^{-3.97} \quad (3)$$

$$q_u = 1.39 \times 10^9 \left[\frac{\eta}{\left(L_{iv}\right)^{0.26}} \right]^{-3.97} \quad (4)$$

4. Conclusions

Based on the findings presented in this research, the following conclusions can be drawn:

- Swelling soil stabilized with lime and SCBA presented unconfined compression strength growth when the lime content was increasing, no matter if tap or brackish water was used in the molding process. This growth is probably due to the soil and SCBA chemical constitution, with high content of amorphous silica and alumina. However, the increase in porosity decays the blend's unconfined compression strength, probably due to the contact between particles reduction;
- The analyzed data showed that the applicability of porosity/Lime content (η/L_{iv}) index, adjusted by an exponent of 0.26 for the studied soil, allowed to forecast the unconfined compressive strength of expansive soil-SCBA-lime blends for both kinds of molding water through a unique dosage curve. However, blends molded with brackish water presented higher unconfined compression strength, probably because of NaCl present in its composition;
- The evaluation of using brackish water in soil stabilization was extremely worthwhile since it can be a feasible substitute for tap water regarding mechanical strength, a scarce asset in the world, especially in Northeast Brazil.

Declaration of interest

The authors have no conflicts of interest to declare. All co-authors have observed and affirmed the contents of the paper and there is no financial interest to report.

Authors' contributions

Carina Silvani: conceptualization, supervision, funding acquisition, project administration, writing – review & editing. João Pedro Camelo Guedes: conceptualization, data curation, methodology, formal analysis, writing – original draft. Jucimara Cardoso da Silva: conceptualization, methodology, formal analysis. Eduardo Antônio Guimarães Tenório: conceptualization, writing – review & editing. Renan Carlos de Melo Nascimento: conceptualization, methodology.

Data availability

The datasets generated and analyzed in the course of the current study are available from the corresponding author upon request.

List of symbols

q_u unconfined compressive strength;
w moisture content;
L_{iv} volumetric lime content;
L amount of lime;

R^2	coefficient of determination;
S	soil content;
SCBA	sugarcane bagasse ash;
Vs	specimen total volume;
γ_d	dry unit weight;
γ_{sS}	unit weight of solids of soil;
γ_{sSCBA}	unit weight of solids of SCBA;
γ_{sL}	unit weight of solids of lime; and
η	porosity
η/C_{iv}	porosity/cement index.
η/L_{iv}	porosity/lime index.

References

ASTM D698. (2012). *Standard test methods for laboratory compaction characteristics of soil using standard effort.* ASTM International, West Conshohocken, PA.

ASTM D5550. (2014). *Standard test method for specific gravity of soil solids by gas pycnometer.* ASTM International, West Conshohocken, PA.

ASTM D2487. (2017a). *Standard practice for classification of soils for engineering purposes (unified soil classification system).* ASTM International, West Conshohocken, PA.

ASTM D6913. (2017b). *Standard test methods for particle-size distribution (gradation) of soils using sieve analysis.* ASTM International, West Conshohocken, PA.

ASTM C977. (2018a). *Standard specification for quicklime and hydrated lime for soil stabilization.* ASTM International, West Conshohocken, PA.

ASTM D431. (2018b). *Standard test method for liquid limit, plastic limit and plasticity index of soils.* ASTM International, West Conshohocken, PA.

ASTM C837. (2019). *Standard test method for methylene blue index of clay.* ASTM International, West Conshohocken, PA.

ASTM E1621. (2021). *Standard guide for elemental analysis by wavelength dispersive x-ray fluorescence spectrometry.* ASTM International, West Conshohocken, PA.

Belchior, I.M.R.M., Casagrande, M.D.T., & Zornberg, J.G. (2017). Swelling behavior evaluation of a lime-treated expansive soil through centrifuge test. *Journal of Materials in Civil Engineering*, 29(12), 04017240. http://dx.doi.org/10.1061/(ASCE)MT.1943-5533.0002090.

Brasil. Conselho Nacional do Meio Ambiente – CONAMA. (March 18, 2005). Resolução nº. 357, de 17 de março de 2005. Dispõe sobre a classificação dos corpos de água e diretrizes ambientais para o seu enquadramento, bem como estabelece as condições e padrões de lançamento de efluentes, e dá outras providências. *Diário Oficial [da] República Federativa do Brasil* (in Portuguese).

Celik, E., & Nalbantoglu, Z. (2013). Effects of ground granulated blastfurnace slag (GGBS) on the swelling properties of lime-stabilized sulfate-bearing soils. *Engineering Geology*, 163, 20-25. http://dx.doi.org/10.1016/j.enggeo.2013.05.016.

Consoli, N.C., & Foppa, D. (2014). Porosity/cement ratio controlling initial bulk modulus and incremental yield stress of an artificially cemented soil cured under stress. *Géotechnique Letters*, 4(1), 22-26. http://dx.doi.org/10.1680/geolett.13.00081.

Consoli, N.C., Prietto, P.D.M., Carraro, J.A.H., & Heineck, K.S. (2001). Behavior of compacted soil-fly ash-carbide lime mixtures. *Journal of Geotechnical and Geoenvironmental Engineering*, 127(9), 774-782. http://dx.doi.org/10.1061/(ASCE)1090-0241(2001)127:9(774).

Consoli, N.C., Foppa, D., Festugato, L., & Heineck, K.S. (2007). Key parameters for strength control of artificially cemented soils. *Journal of Geotechnical and Geoenvironmental Engineering*, 133(2), 197-205. http://dx.doi.org/10.1061/(ASCE)1090-0241(2007)133:2(197).

Consoli, N.C., Lopes Junior, L., Foppa, D., & Heineck, K.S. (2009). Key parameters dictating strength of lime/cement-treated soils. *Proceedings of the Institution of Civil Engineers – Geotechnical Engineering*, 162(2), 111-118. http://dx.doi.org/10.1680/geng.2009.162.2.111.

Consoli, N.C., Cruz, R.C., Floss, M.F., & Festugato, L. (2010). Parameters controlling tensile and compressive strength of artificially cemented sand. *Journal of Geotechnical and Geoenvironmental Engineering*, 136(5), 759-763. http://dx.doi.org/10.1061/(ASCE)GT.1943-5606.0000278.

Consoli, N.C., Dalla Rosa, A., Corte, M.B., Lopes Junior, L., & Consoli, B.S. (2011). Porosity-cement ratio controlling strength of artificially cemented clays. *Journal of Materials in Civil Engineering*, 23(8), 1249-1254. http://dx.doi.org/10.1061/(ASCE)MT.1943-5533.0000283.

Consoli, N.C., Saldanha, R.B., Mallmann, J.E.C., de Paula, T.M., & Hoch, B.Z. (2017). Enhancement of strength of coal fly ash-carbide lime blends through chemical and mechanical activation. *Construction & Building Materials*, 157, 65-74. http://dx.doi.org/10.1016/j.conbuildmat.2017.09.091.

Consoli, N.C., Bittar Marin, E.J., Quiñónez Samaniego, R.A., Scheuermann Filho, H.C., Miranda, T., & Cristelo, N. (2019a). Effect of mellowing and coal fly ash addition on behavior of sulfate-rich dispersive clay after lime stabilization. *Journal of Materials in Civil Engineering*, 31(6), 04019071. http://dx.doi.org/10.1061/(ASCE)MT.1943-5533.0002699.

Consoli, N.C., Godoy, V.B., Rosenbach, C.M.C., & Peccin da Silva, A. (2019b). Effect of sodium chloride and fibre-reinforcement on the durability of sand–coal fly ash–lime mixes subjected to freeze–thaw cycles. *Geotechnical and Geological Engineering*, 37(1), 107-120. http://dx.doi.org/10.1007/s10706-018-0594-8.

Consoli, N.C., Godoy, V.B., Tomasi, L.F., De Paula, T.M., Bortolotto, M.S., & Favretto, F. (2019c). Fibre-reinforced sand-coal fly ash-lime-NaCl blends under severe environmental conditions. *Geosynthetics International*, 26(5), 525. http://dx.doi.org/10.1680/jgein.19.00039.

Consoli, N.C., Marin, E.J.B., Samaniego, R.A.Q., Heineck, K.S., & Johann, A.D.R. (2019d). Use of sustainable binders in soil stabilization. *Journal of Materials in Civil

Engineering, 31(2), 06018023. http://dx.doi.org/10.1061/(ASCE)MT.1943-5533.0002571.

Consoli, N.C., Saldanha, R.B., & Scheurmann Filho, H.C. (2019e). Short-and long-term effect of sodium chloride on strength and durability of coal fly ash stabilized with carbide lime. *Canadian Geotechnical Journal*, 56(12), 1929-1939. http://dx.doi.org/10.1139/cgj-2018-0696.

Consoli, N.C., Festugato, L., Miguel, G.D., & Scheuermann Filho, H.C. (2021). Swelling prediction for green stabilized fiber-reinforced sulfate-rich dispersive soils. *Geosynthetics International*, 28(4), 391-401. http://dx.doi.org/10.1680/jgein.20.00050.

Cordeiro, G.C., Andreão, P.V., & Tavares, L.M. (2019). Pozzolanic properties of ultrafine sugar cane bagasse ash produced by controlled burning. *Heliyon*, 5(10), e02566. http://dx.doi.org/10.1016/j.heliyon.2019.e02566.

Cordeiro, G.C., Toledo Filho, R.D., Tavares, L.M., & Fairbairn, E. (2009). Ultrafine grinding of sugar cane bagasse ash for application as pozzolanic admixture in concrete. *Cement and Concrete Research*, 39(2), 110-115. http://dx.doi.org/10.1016/j.cemconres.2008.11.005.

Diambra, A., Ibraim, E., Peccin, A., Consoli, N.C., & Festugato, L. (2017). Theoretical derivation of artificially cemented granular soil strength. *Journal of Geotechnical and Geoenvironmental Engineering*, 143(5), 04017003. http://dx.doi.org/10.1061/(ASCE)GT.1943-5606.0001646.

Drake, J.A., & Haliburton, T.A. (1972). Accelerated curing of salt-treated and lime- treated cohesive soils. *Highway Research Record*, 381, 10-19.

Fernandes Filho, P., Torres, S.M., Anjos, R.H., & Porto, A. (2012). Solubility of silicate from sugar cane bagasse ash in alkaline solution. *Key Engineering Materials*, 517, 477-483. http://dx.doi.org/10.4028/www.scientific.net/KEM.517.477.

Ferreira, S.R.M., Paiva, S.C., Morais, J.J.O., & Viana, R.B. (2017). Avaliação da expansão de um solo do município de Paulista-PE melhorado com cal. *Matéria*, 22(1), e11930. http://dx.doi.org/10.1590/S1517-707620170005.0266.

Ganesan, K., Rajagopal, K., & Thangavel, K. (2007). Evaluation of bagasse ash as supplementary cementitious material. *Cement and Concrete Composites*, 29(6), 515-524. http://dx.doi.org/10.1016/j.cemconcomp.2007.03.001.

Guedes, J.P.C., Tenório, E.A.G., Silvani, C., & Braz, R.I.F. (2022). Previsão da resistência à compressão simples de um solo expansivo estabilizado com cimento através do índice porosidade/teor volumétrico de cimento. *Princípia*, 59(2), 110-115. http://dx.doi.org/10.18265/1517-0306a2021id5043.

Ingles, O.G., & Metcalf, J.B. (1972). *Soil stabilization: principles and practice* (374 p.). Sidney: Butterworths.

Ito, M., & Azam, S. (2020). Relation between flow through and volumetric changes in natural expansive soils. *Engineering Geology*, 279, 105885. http://dx.doi.org/10.1016/j.enggeo.2020.105885.

Khazaei, J., & Moayedi, H. (2017). Soft expansive soil improvement by eco-friendly waste and quick lime. *Arabian Journal for Science and Engineering*, http://dx.doi.org/10.1007/s13369-017-2590-3.

Liu, Y., Su, Y., Namdar, A., Zhou, G., She, Y., & Yang, Q. (2019). Utilization of cementitious material from residual rice husk ash and lime in stabilization of expansive soil. *Advances in Civil Engineering*, 2019, 1-17. http://dx.doi.org/10.1155/2019/8151087.

Lopes, J.T. (2004). *Dimensionamento e análise de um dessalinizador solar híbrido* [Master's dissertation]. State University of Campinas (in Portuguese).

Martirena Hernández, J., Middendorf, B., Gehrke, M., & Budelmann, H. (1998). Use of wastes of the sugar industry as pozzolana in lime-pozzolana binders: study of the reaction. *Cement and Concrete Research*, 28(11), 1525-1536. http://dx.doi.org/10.1016/S0008-8846(98)00130-6.

Mirzababaei, M., Arulrajah, A., Horpibulsuk, S., Soltani, A., & Khayat, N. (2018). Stabilization of soft clay using short fibers and poly vinyl alcohol. *Geotextiles and Geomembranes*, 46(5), 646-655. http://dx.doi.org/10.1016/j.geotexmem.2018.05.001.

Pei, P., Mei, G., Ni, P., & Zhao, Y. (2020). A protective measure for expansive soil slopes based on moisture content control. *Engineering Geology*, 269, 105527. http://dx.doi.org/10.1016/j.enggeo.2020.105527.

Phanikumar, B.R., & Singla, R. (2016). Swell-consolidation characteristics of fibre-reinforced expansive soils. *Soil and Foundation*, 56(1), 138-143. http://dx.doi.org/10.1016/j.sandf.2016.01.011.

Pooni, J., Giustozzi, F., Robert, D., Setunge, S., & O'Donnell, B. (2019). Durability of enzyme stabilized expansive soil in road pavements subjected to moisture degradation. *Transportation Geotechnics*, 21, 100255. http://dx.doi.org/10.1016/j.trgeo.2019.100255.

Puppala, A.J., Manosuthikij, T., & Chittoori, B.C.S. (2013). Swell and shrinkage characterizations of unsaturated expansive clays from Texas. *Engineering Geology*, 164, 187-194. http://dx.doi.org/10.1016/j.enggeo.2013.07.001.

Alavéz-Ramírez, R., Montes-García, P., Martínez-Reyes, J., Altamirano-Juárez, D.C., & Gochi-Ponce, Y. (2012). The use of sugarcane bagasse ash and lime to improve the durability and mechanical properties of compacted soil blocks. *Construction & Building Materials*, 34, 296-305. http://dx.doi.org/10.1016/j.conbuildmat.2012.02.072.

Rogers, C.D.F., Gledinning, S., & Roff, T.E.J. (1997). Lime modification of clay soils for construction expediency. *Proceedings of the Institution of Civil Engineers - Geotechnical Engineering*, 125(4), 242-249. http://dx.doi.org/10.1680/igeng.1997.29660.

Saldanha, R.B., & Consoli, N.C. (2016). Accelerated mix design of lime stabilized materials. *Journal of Materials in Civil Engineering*, 28(3), 06015012. http://dx.doi.org/10.1061/(ASCE)MT.1943-5533.0001437.

Saldanha, R.B., Mallmann, J.E.C., & Consoli, N.C. (2016). Salts accelerating strength increase of coal fly ash–carbide lime compacted blends. *Géotechnique Letters*, 6(1), 23-27. http://dx.doi.org/10.1680/jgele.15.00111.

Saldanha, R.B., Scheuermann Filho, H.C., Ribeiro, J.L.D., & Consoli, N.C. (2017). Modelling the influence of density, curing time, amounts of lime and sodium chloride on the durability of compacted geopolymers monolithic walls. *Construction & Building Materials*, 136, 65-72. http://dx.doi.org/10.1016/j.conbuildmat.2017.01.023.

Silvani, C., Lucena, L.C., Tenorio, E.A.G., Scheuermann Filho, H.C., & Consoli, N.C. (2020). Key parameter for swelling control of compacted expansive fine-grained soil-lime blends. *Journal of Geotechnical and Geoenvironmental Engineering*, 146(9), 06020012. http://dx.doi.org/10.1061/(ASCE)GT.1943-5606.0002335.

Taher, Z.J.B., Scalia 4th, I.V.J., & Bareither, C.A. (2020). Comparative assessment of expansive soil stabilization by commercially available polymers. *Transportation Geotechnics*, 24, 100387. http://dx.doi.org/10.1016/j.trgeo.2020.100387.

Talero, R., Trusilewicz, L., Delgado, A., Pedrajas, C., Lannegrand, R., Rahhal, V., Mejia, R., & Ramírez, F.A. (2011). Comparative and semi-quantitative XRD analysis of Friedel's salt originating from pozzolan and Portland cement. *Construction & Building Materials*, 25(5), 2370-2380. http://dx.doi.org/10.1016/j.conbuildmat.2010.11.037.

Tenório, E.A.G. (2019). *Controle da expansão dos solos com resíduos de mármore e cal* [Master's dissertation]. Federal University of Campina Grande (in Portuguese).

Tiwari, N., Satyam, N., & Puppala, A.J. (2021). Strength and durability assessment of expansive soil stabilized with recycled ash and natural fibers. *Transportation Geotechnics*, 29, 100556. http://dx.doi.org/10.1016/j.trgeo.2021.100556.

Zareei, S.A., Ameri, F., & Bahrami, N. (2018). Microstructure, strength, and durability of eco-friendly concretes containing sugarcane bagasse ash. *Construction & Building Materials*, 184, 258-268. http://dx.doi.org/10.1016/j.conbuildmat.2018.06.153.

Soils and Rocks
An International Journal of Geotechnical and Geoenvironmental Engineering
www.soilsandrocks.com
ISSN 1980-9743
ISSN-e 2675-5475

Dehydrating subsurface clayey soils using plastic electrodes: a simple, fast, and yet reliable technique

Ronald Beyner Mejia Sanchez[1], José Tavares Araruna Júnior[2#], Roberto Ribeiro de Avillez[3], Hongtao Wang[4], Shuguang Liu[5]

Article

Keywords
Electrokinetic
Plastic electrodes
Marine soil
Soil improvement

Abstract
The electrokinetic process seems to be interesting to the earthwork portion on the construction of buildings, and transportation projects since this simple, fast, yet reliable technique could expedite dehydrating of soil and reduce delays in the construction schedule. This paper examined the technical feasibility and a brief cost analysis of using plastic electrodes for electrokinetically dehydrating clayey soils with high moisture content were also carried out. The results from the experimental program carried out on a marine clayey soil with copper and plastic electrodes showed a great deal of soil improvement since positive changes in undrained shear strength occur due to the free water dehydration process induced by electro-osmosis and to the adsorbed water dehydration process induced by electromigration. It was also observed that values of the undrained shear strength remained stable at the final stages of the electrokinetic process indicating a permanent soil improvement. Finally, it was noticed that dehydrating could be achieved at lower costs by employing plastic electrodes.

1. Introduction

Water has always been the largest obstacle in terms of constructability and time efficiency for as long as mankind has been building on natural soils (Zhuang, 2021; Rao et al., 2021; Indraratna et al., 2019; Zhang et al., 2019). In Brazil and other tropical countries, where extended periods of wet weather usually prevail, surface soils become wet or saturated through infiltration and adsorption of water to clay minerals (Ngo et al., 2021; Mahmoud et al., 2010). As a consequence, higher porewater levels reduce soil strength, increase soil compressibility, and hinder soil ability to be compacted (Zhang & Hu, 2019; Ammami et al., 2020; Babu et al., 2020; Martin et al., 2019; Wang et al., 2021). The excessive water moisture in soil delays the earthwork as current construction equipment cannot operate in such conditions and may cause the project to become off schedule and create an undue hardship for contractors (Lamont-Black et al., 2012; Rittirong et al., 2008). On most construction projects, time constraints preclude relying on nature. To satisfy construction plans and specifications, foundation soils must meet certain levels of strength and compressibility, and to attain such characteristics, a dehydrating technique is necessary to meet design specifications.

It is generally believed that clayey soils have very weak drainage characteristic (Peng et al., 2015). To overcome this challenge, in recent decades different processes have been proposed, such as mechanical-electrical drainage, mechanical-electroacoustic drainage, mechanical-thermal drainage, among others (Mahmoud et al., 2010). However, the complexity, cost, and energy consumption of these methods prevented their implementation in construction projects. Among the most promissory techniques is the electrokinetic process, which is based on the properties of the electrical charges inherent in the particles that make up clayey soils (Zhang et al., 2019). In this process, the electric field is applied to the soil mass, taking the negatively charged constituents toward the anode and the elements positively charged toward the cathode. Several authors, including Bourgès-Gastaud et al. (2015), argue that the versatility of the process is due to the possibility of removing interstitial water that usually cannot be removed by conventional mechanical processes.

The electrokinetic mechanism involves the phenomenon of electro-osmosis, electromigration, and electrophoresis. In a porous medium, electro-osmosis is defined as the net water flow from the positive electrode towards the negative electrode, when an electrical voltage gradient is applied. Electromigration is defined as the transport of the ions in

#Corresponding author. E-mail address: araruna@puc-rio.br
[1]Pontifícia Universidade Católica do Rio de Janeiro, Instituto Tecgraf de Desenvolvimento de Software Técnico-Científico, Rio de Janeiro, RJ, Brasil.
[2]Pontifícia Universidade Católica do Rio de Janeiro, Departamento de Engenharia Civil e Ambiental, Rio de Janeiro, RJ, Brasil.
[3]Pontifícia Universidade Católica do Rio de Janeiro, Departamento de Engenharia Química e Ciência dos Materiais, Rio de Janeiro, RJ, Brasil.
[4]Tongji University, College of Environmental Science and Engineering, Shanghai, P.R. China.
[5]Tongji University, Department of Hydraulic Engineering, Shanghai, P.R.China.

Submitted on September 3, 2021; Final Acceptance on February 6, 2023; Discussion open until November 30, 2023.
https://doi.org/10.28927/SR.2023.074721

solution in the interstitial fluid in the soil matrix towards the opposite charge electrode when the electric field is applied (Cameselle & Gouveia, 2018). The phenomenon of ionic migration or electromigration depends on the size and charge of the ions, as well as the intensity of the applied electric field in accordance with Cameselle (2015). Finally, electrophoresis is the transport of charged particles of colloidal size or contaminants in the soil under the influence of an electric field (Virkutyte et al., 2002). According to Cameselle & Gouveia (2018), its magnitude is insignificant in soil systems with low hydraulic conductivity when compared with electroosmosis and electromigration.

In electrokinetic, the selection of the material and the arrangement of the spatial distribution of the electrodes have a great influence on the process efficiency. Chemical reactions, heat resistance capacity, and cost are the main considerations to be taken into account when it comes to the selection of the type of material for electrodes. From the studies reported in the literature, there is no consistent conclusion about which electrode can achieve the best efficiency of the electrokinetic process since experiments in different soil types can lead to different or even contradictory conclusions (Zhou et al., 2015). Moreover, the generation of gases due to electrolysis causes oxidation of metal electrodes generating a reduction in the efficiency of the electrical conduction, and increasing the costs of the process. For the reasons mentioned above, it is interesting to consider corrosion-resistant and economically viable materials for electrokinetic applications for construction purposes (Bourgès-Gastaud et al., 2015).

In this sense, the electrokinetic process seems to be interesting to the earthwork portion on the construction of commercial, industrial and residential buildings, and transportation projects since this simple, fast, yet reliable technique could expedite dehydrating of soil and decrease delays in the construction schedule. This paper examined the technical and economic feasibility of using plastic electrodes for electrokinetically dehydrating clayey soils with high moisture content, and a brief cost analysis was also carried out.

2. Materials and methods

A soft clayey soil of marine origin obtained at a construction site from the Metropolitan Center in the west zone of the city of Rio de Janeiro was used in the experimental program. The disturbed soil sample was collected from the bucket of an excavator at a depth of approximately 6 meters, stored in 1 m^3 big bags, and transported to the Geotechnical Laboratory where it was later stored in the humid chamber. This material was subjected to geotechnical and mineralogical characterization, and its chemical composition was determined. The geotechnical characterization comprised the determination of moisture content (ASTM, 1998), particle density (ASTM, 2009), Atterberg limits (ASTM, 2017a), and organic matter content (ASTM, 2020b). The soil grain distribution curve was determined following the procedures established in ASTM D7928 (ASTM, 2017c). Its chemical composition was determined using the inductively coupled plasma mass spectroscopy (ICP-MS) technique as detailed in ASTM D1976 (ASTM, 2020a). The procedure used the Agilent spectrometer, model 7500CX. The mineralogical characterization of the clayey soil was performed by the X-ray diffraction technique (ASTM, 2007; Burnett, 1995; Moore, 1970). Two samples were analyzed: the first sample constitutes the natural clayey soil and the second sample is a fraction of this soil that passed through sieve #40 (i.e., 0.42mm).

Dehydrating tests were carried out using a plastic water tank with 100L volumetric capacity as observed in Figure 1. Changes in the pH of the effluent during tests were monitored with an AKSO digital pH meter model AK90 which has calibration in three points and automatic temperature compensation. The electrical current intensity was monitored with a MULTILASER digital multimeter model AU325 that has a range of 200 μA up to 10A operating in direct current mode. The electric field was induced using a Minipa MPC3030 DC source that provides a maximum potential difference of 30V, which allowed the application of a potential gradient of 1.5 V/cm. For the tests with the voltage of 150 V DC, a DC source was used that generates a maximum potential difference of 220 V DC, developed by the Laboratory of Conversion and Electrical Machines of PUC-Rio. The use of this electrical source allowed the application of a voltage gradient of 7.5 V/cm maintaining the same geometric configuration.

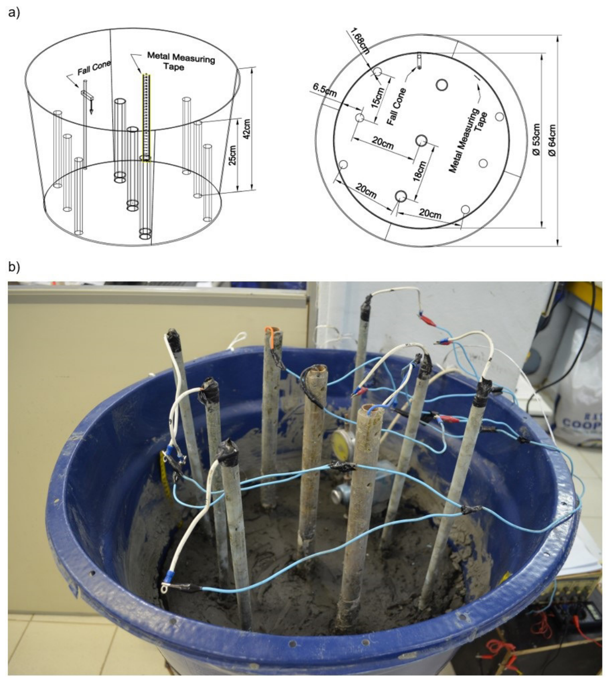

Figure 1. Electrokinetic test device: (a) general arrangement; and (b) test layout.

Remolded samples were obtained by drying the natural soil in an oven for 24 h at a temperature of 60 °C. After the drying process, 29.6 Kg of soil were weighed, and tap water with an electrical conductivity of 127.8 µS/cm and a pH of 7.6 was then added until a moisture content equivalent to 1.25 times the soil liquid limit was observed. The authors decided to use tap water in order to enhance the repeatability of the sample fabric even though, as stated by Jardine et al. (1984), it is preferably that the chemistry of the water be similar to that of the pore water in the clayey soil in order to preserve its natural state (i.e., structure). Tap water chemical composition was determined using the ICP-MS technique as detailed in ASTM D1976 (ASTM, 2020a) for inorganic constituents and ion chromatography for anionic constituents using the procedure described in ASTM D4327 (ASTM, 2017b). The sample was then mixed for 30 minutes in an orbital mixer until the soil reached a soft soil consistency. The assembly of the test consisted of positioning the electrodes in the previously designated locations for each type of spatial configuration in the water tank described in Figure 1.

Cathodes were wrapped by #40 Whatman filter paper to prevent the intrusion of soil particles through their drainage holes. During tests, the volume drained from the effluent was measured using Pyrex graduated cylinders with a volumetric capacity of 1,000 mL with a 10 mL resolution, and the soil settlement was measured by two metal measuring tapes fixed at opposite sides of the tank inner wall with a 1 mm resolution. Drainage was measured at regular intervals of 6 hours, and soil settlement was measured at regular intervals of 24 hours. Although tests were carried out in a temperature-controlled environment, the relative humidity and ambient temperature values were determined with an HTC DIGITAL equipment model BFHTC-1 at pre-established time intervals of 24 hours.

An electrokinetic soil dehydration testing program was performed using two gradient potentials. In the first batch, a 1.5 V/cm potential gradient was applied in three tests with plastic electrodes developed by Mejia (2018) to assess repeatability. Plastic electrodes consist of a composite comprised of brass filaments embedded in a BB2004 epoxy resin and a 3154BB hardener. An additional test was carried out applying the same potential gradient with copper electrodes to assess electrolysis-induced corrosion and to appraise the efficacy of the plastic electrodes. The effect of electrolysis was measured by determining the weight loss of anodes using an analytical scale TOLEDO Prix AS with 0.01 g resolution. The second batch comprised two tests employing a 7.5 V/cm potential gradient to assess plastic and copper electrodes efficiency.

Soil strength was evaluated using the fall cone apparatus using a Wykeham Farrance apparatus following the procedures described in BS1377-2 (BS, 1990). The device was adapted within the plastic tank and measurements were carried out at regular intervals. To assess fall cone tests results unconsolidated undrained triaxial tests were performed with samples collected after the completion of the dehydrating process following the procedures described in ASTM D2850 (ASTM, 2015).

Power consumption was measured during each test and the dehydrating cost was calculated assuming the electricity rate of 0.035 US$/kW.h charged by the local distributor in November 2018.

3. Results and discussion

The grain size distribution curve of the clayey soil is shown in Figure 2 and its index properties are described in Table 1. Based on the aforementioned results it was possible to classify the soil according to the Unified Soil Classification System (ASTM, 2000) as MH-OH. Table 2 presents the chemical composition of the tap water and the marine soil.

The concentration of the tap water anionic constituents was well bellow to those commonly found in sea water (i.e., fluoride 0.44 mg/L; chloride 16.1 mg/L; bromide <0.05 mg/L; nitrate 17.9 mg/L; phosphate <0.05 mg/L, and sulphate 22.7 mg/L). It is clear that the use of tap water changed the original structure of the marine soil but since the experimental program was carried out in a different environment, it seems that the adopted strategy did not play an important role in the examination between plastic and copper dehydrating performance.

The mineral characterization of the soil sample indicates the presence of calcite, quartz, and kaolinite, as can be seen in Figure 3. The X-ray diffractogram indicates that the sample is a mixture of clay minerals that make up the amorphous

Table 1. Values of index properties.

Property	Value
Natural moisture content	132%
Particle density	2.61
Plastic limit	32%
Liquid limit	55%
Organic matter content	7.4%

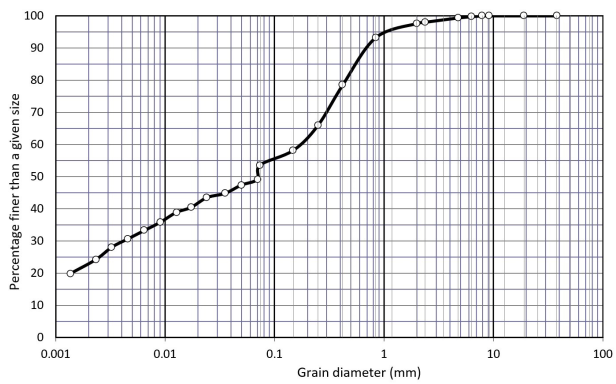

Figure 2. Grain size distribution curve.

Table 2. Chemical Composition.

Parameter	Tap Water Concentration (mg/L)	Soil Concentration (mg/kg)
Al	n.a.	720
V	<0.01	0.564
Cr	<0.001	0.515
Mn	0.002	3.88
Fe	0.033	480
Ni	<0.002	0.182
Cu	0.004	0.143
Zn	0.11	0.818
Cd	<0.001	0.0034
Ba	0.024	1.01
Pb	<0.01	0.191

n.a. – not available.

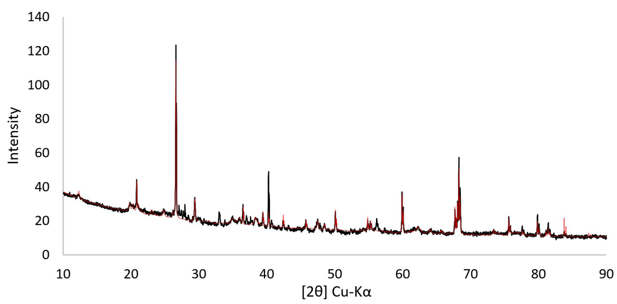

Figure 3. X-ray diffractogram of the sample under study.

part and minerals that represent the crystalline phase of the sample under study.

Soil dehydrating during the electrokinetic process as a function of time is presented in the sequence of photographs shown in Figure 4 for tests with a voltage gradient of 1.5V/cm and, in Figure 5, for the tests with a voltage gradient of 7.5 V/cm. One can observe the variation in soil consistency due to dehydration since the electroosmotic phenomenon generates a water flow from the regions near the cathode towards the regions of the anode where the water is drained. The soil mass near the cathodes shows a greater increase in soil solids compared to the soil mass close to the anode since the water molecules from the double layer move preferentially towards the anode (Mahalleh et al., 2021; Vocciante et al., 2016; Menon et al., 2019; Martin et al., 2019).

The volume drained and soil settlement as a function of time are shown in Figures 6 and Figure 7 respectively. The dehydrating process is faster when copper anodes are used since they possess a higher electrical conductivity (i.e., the measured electrical conductivity of plastic electrodes is 5.64 x10^3 $\Omega^{-1}m^{-1}$ and the measured electrical conductivity of copper electrodes is 6.0x10^7 $\Omega^{-1}m^{-1}$). When the voltage gradient of 1.5 V/cm was applied, soil settlements in the test that used copper anodes were higher compared to the tests that employed plastic anodes. This behavior also leads to higher drainage due to the higher electrical conductivity of copper electrodes. On the other hand, when the voltage gradient of 7.5 V/cm was applied, higher settlement values were observed

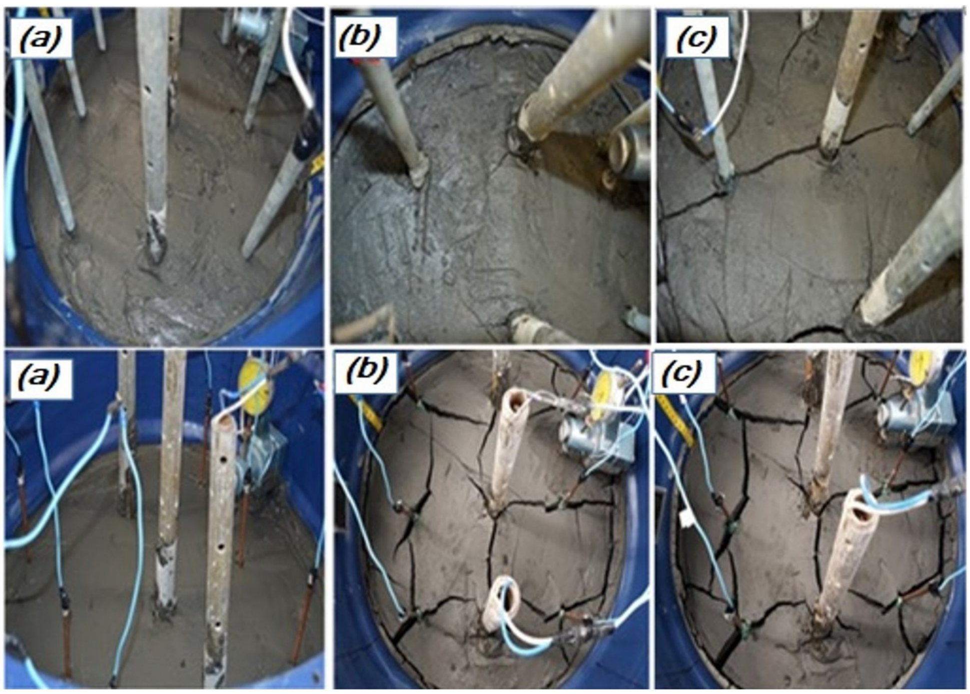

Figure 4. Sequence of photographs for test with voltage gradient of 1. 5 Volts/cm: First row with plastic anodes in which: (a) 1 hour; (b) 6 days; and (c) 10 days. Second row with copper anodes, where: (a) 1 hour; (b) 4 days; and (c) 6 days.

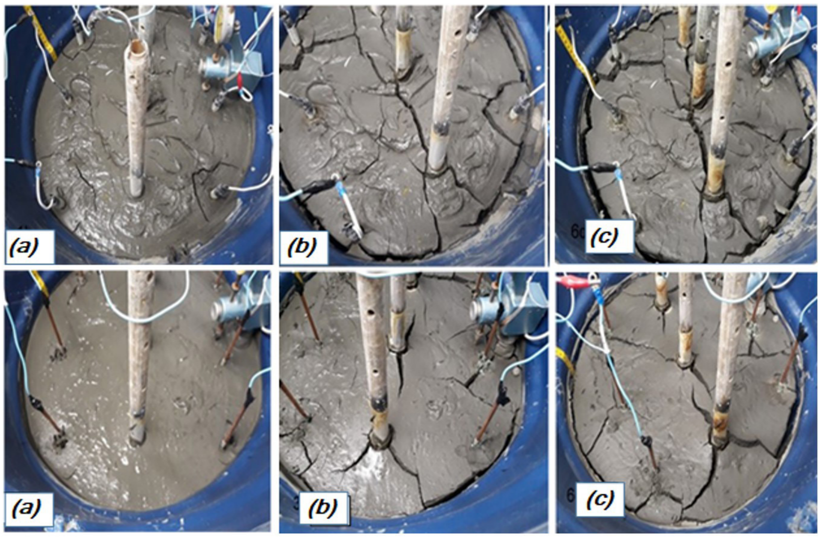

Figure 5. Sequence of photographs for tests with voltage gradient of 7.5 volts/cm: First row with plastic anodes. Second row with copper anodes, in which: (a) 1 hour; (b) 3 days; and (c) 6 days.

in the initial moments of the tests. However, the settlement rate decreased considerably with time in tests that employed copper anodes since the increase in the voltage gradient caused a rise in the magnitude of electrolysis in the vicinity of the anodes, which, in turn, generated greater corrosion that prevented the drainage process. This phenomenon had already been reported in the literature by Zhou et al. (2015), who called it anode passivation. It was also observed that plastic anodes were little affected by electrolysis.

The intensity of the electric current induced by the voltage gradients is shown in Figure 8. It can be observed that plastic electrodes induce lower current when compared to copper electrodes despite the magnitude of the applied voltage gradient. This difference has a great influence on the dehydrating process because a higher electrical current intensity induces large changes in moisture content in the soil mass as can be seen in Figure 8. However, the use of copper electrodes increases energy consumption, and also reduces electro-osmotic efficiency as Figure 9 shows. The electro-osmotic efficiency relates the electrical current induced during the tests with the drained volume and length of the test (Jones et al., 2011), as follows:

$$k_i = \frac{I}{\frac{\Delta V}{\Delta t}} \tag{1}$$

where k_i is the electro-osmotic efficiency, I is the electrical current applied, ΔV is the drained volume, and Δt is the time interval in which the drained volume reading was recorded.

It was observed that electro-osmotic efficiency is higher in the initial stages of tests. As the electrokinetic process takes place hydraulic fracturing occurs, as shown in Figure 5 and Figure 6, and electro-osmotic efficiency is reduced (Zhang & Hu, 2019; Hu et al., 2016). Also, it should be noticed that electrolysis reactions in the vicinity of the anodes are very severe when copper electrodes are used impacting electro-osmotic efficiency (Lockhart, 1983; Turer & Genc, 2005).

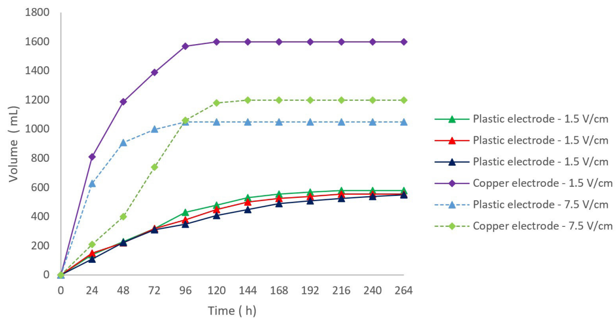

Figure 6. Drained volume as a function of time.

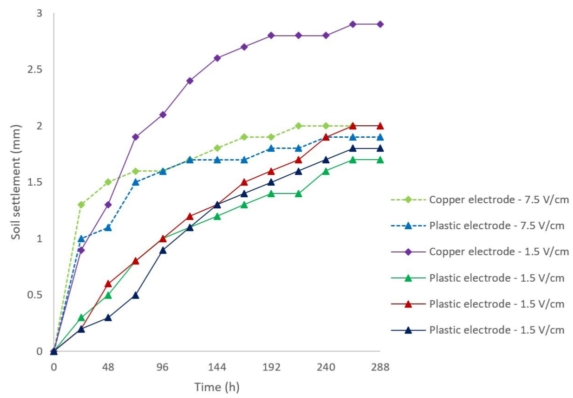

Figure 7. Soil settlement as a function of time.

It was also noticed a sudden increase in electro-osmotic efficiency at 96 hours concerning copper electrodes could be attributed to the corrosion of the anodes induced by electrolysis.

$$Cu + H_2O \rightarrow CuO + 2H^+ + 2e^- \quad (2)$$

$$2H_2O \rightarrow O_2 + 4H^+ + 4e^- \quad (3)$$

In these tests, the rise in electro-osmotic efficiency might be related to anode corrosion and the subsequent transport of metallic ions that increases the electrical conductivity of the media (Gregolec et al., 2005; Wu & Hu, 2014; Acar & Alshawabkeh, 1993). As process takes place, electro-osmotic efficiency sharply reduces as electrolysis induced corrosion occurs. This observation agrees with results from different authors (Mahmoud et al., 2010; Zhou et al., 2015; Karim, 2014). Corrosion was assessed by measuring changes in the mass of plastic and copper electrodes shown in Figure 10 before and after each test.

Figures 11 and 12 show the mass loss of plastic and copper anodes. It can be observed that plastic anodes have virtually no mass loss. On the other hand, it was also verified that the life of the copper anodes is greatly reduced since they are affected more severely by electrolysis-induced corrosion. The induced electric current during the electrokinetic process causes chemical oxidation and reduction reactions in the electrodes. The loss of electrons from the copper anodes generates their oxidation, which can lead to the loss of their mass. The mass loss is proportional to the oxidation process

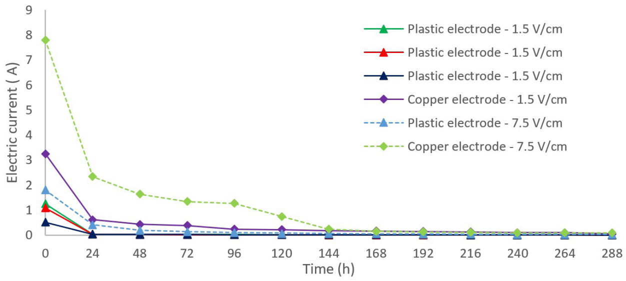

Figure 8. Intensity of electrical current induced during the electrokinetic process.

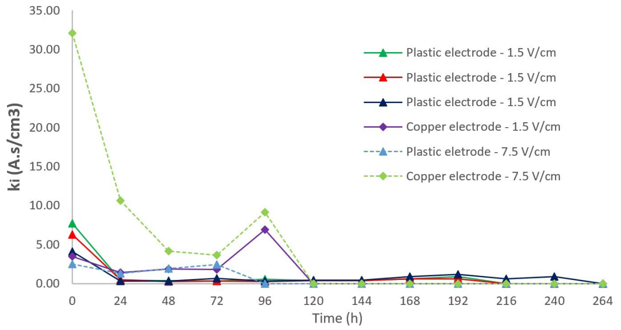

Figure 9. Electro-osmotic efficiency.

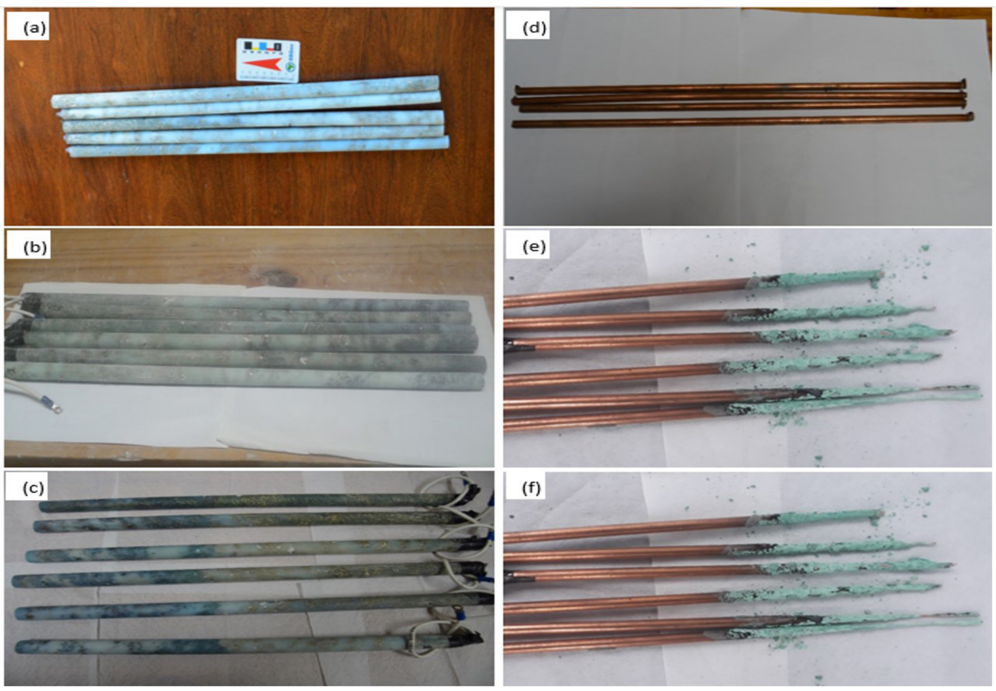

Figure 10. Electrodes: (a) original plastic anodes; (b) plastic anodes after tests with voltage gradient of 1.5 V/cm; (c) plastic anodes after tests with voltage gradient of 7.5 V/cm; (d) copper anodes; (e) copper anodes after tests with voltage gradient of 1.5 V/cm; (f) copper anodes after tests with voltage gradient of 7.5 V/cm.

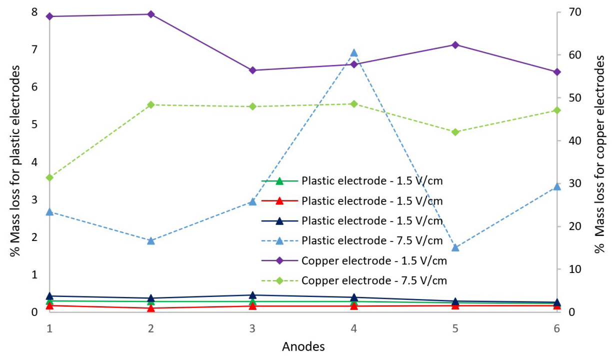

Figure 11. Anode mass loss. Plastic electrode on the main axis and a copper electrode on the secondary axis.

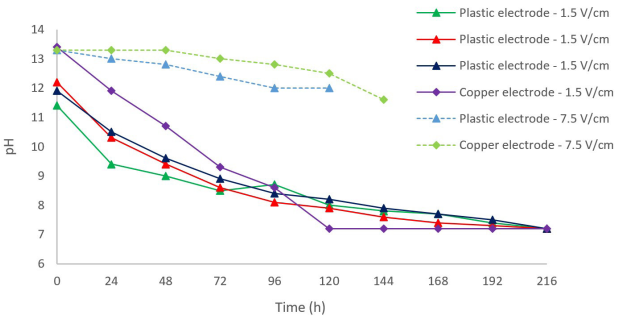

Figure 12. Changes in the pH values.

and since its magnitude could be related to the induced current intensity it is expected that tests performed with a greater electrical gradient cause a rise in percentage mass loss.

Electrolysis also induces changes in the pH of the soil mass. The oxidation of the water molecule in the anodes generates an acid front, and the reduction of water in the cathodes generates a basic front, as suggested by several authors (i.e., Estabragh et al., 2014; Azhar et al., 2017; Cameselle et al., 2013; Cameselle, 2015). Due to these processes, the pH of the porous medium in the vicinity of the anode usually decreases and the pH of the porous medium in the vicinity of the cathode generally increases. It is generally believed that changes in pH depend on the intensity of the current applied to the soil (Fardin et al., 2021; Chien et al., 2010; Hu et al., 2019; Cameselle & Reddy, 2012). The acid front generated in the anode will advance through the soil mass towards the cathodes due to the migration of ions and the phenomenon of electro-osmosis (Saichek & Reddy, 2003; Tuan et al., 2012). As the acid front advances through the soil mass towards the cathode, decreasing pH values of the effluent are observed, as shown in Figure 12.

It is verified, in the initial moments, that the pH values of the effluent present high values due to the generation of OH^- by the reaction of hydrolysis of water in the vicinity of the cathodes caused by electrolysis (Reddy & Saichek, 2004; Martin et al., 2019; Zhou et al., 2015). As the acid front advances from the regions close to the anode towards the cathode, there is a reduction in the pH values of the effluent, since H^+ is more mobile (Cameselle & Gouveia, 2018; Ghobadi et al., 2020; Wu et al., 2016). The results of the tests using a voltage gradient of 1.5 V/cm suggest that the reduction seems to be proportional to the intensity of the electrolysis reactions. The authors observed changes in pH values of the effluent depending on the intensity of the generated current. One can observe from the data displayed in Figure 8 that the magnitude of the generated electric current during the initial stages of the tests is directly proportional to the applied voltage gradient. As the process takes place, the authors observed similar values of either current magnitude and pH in tests with different voltage gradients.

The authors also point out that pH values did not undergo significant variation after 114 h of tests, indicating that the acid front arrived in the cathode generating a polarization of the medium preventing the development of the electro-osmotic flow that generates movement of fluid from one region to another (Virkutyte et al., 2002; Alaydi, 2016; Li & Li, 2000). It is also observed that there were no great changes in pH values of the effluent in tests where a voltage gradient of 7.5 V/cm was applied. The authors believe that the use of a gradient of such magnitude generated a rapid displacement of the acid front and induced a rapid polarization of the medium (Dukhin & Mishchuk, 1993; Mishchuk, 2010).

The electrokinetic process induces soil improvement (Hunter et al., 2021; Peng et al., 2015; Ammami et al., 2020; Babu et al., 2020). A fall cone apparatus was assembled in the plastic tank to assess the change in the undrained shear strength of the clayey soil. Hansbo (1957) proposed to determine the undrained shear strength, s_u, from the cone penetration amount d of soil by the fall cone, as follows:

$$s_u = K\frac{W}{d^2} \tag{4}$$

where W is the cone weight, m is the cone mass (g), g is the gravitational acceleration and K is the cone factor. According to the BS standard BS 1377-2 (BS, 1990), the conical tip has a standardized weight, size and angle (i.e., 80 g, 35 mm and 30°) and the sinking time is 5s. In these conditions, the cone factor (K) is equal to 1.0. Test results are presented in Figure 13.

Test results indicate that changes in undrained shear strength occur due to the free water dehydration process induced by electro-osmosis, and to the adsorbed water dehydration process induced by electromigration (Abdullah & Al-Abadi, 2010; Acar & Alshawabkeh, 1993; Gregolec et al., 2005). It was also observed that values of the undrained shear strength remained stable at the final stages of the electrokinetic process indicating a permanent soil improvement. This phenomenon had already been described in the literature by several authors, including (Casagrande, 1948, 1949, 1952, 1983; Bjerrum et al., 1967; Gray, 1970; Gray & Mitchell,

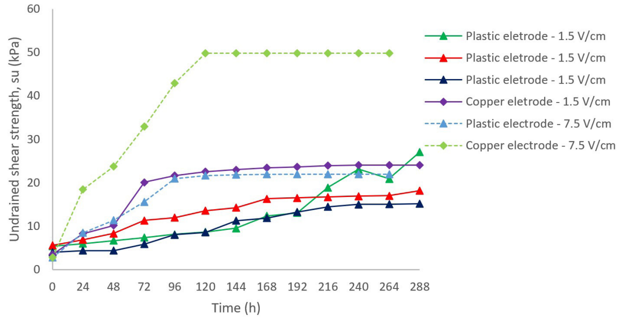

Figure 13. Changes in the undrained shear strength during tests.

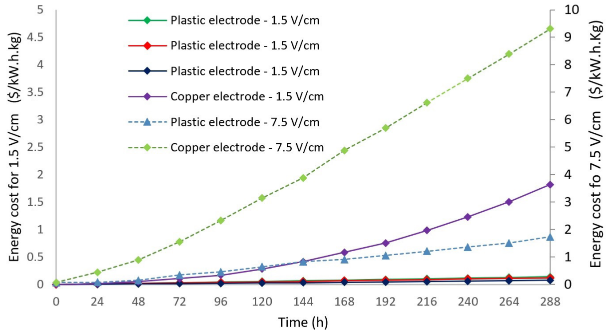

Figure 14. Costs associated to power consumption during tests.

1967, 1969; Lo & Ho, 1991; Lo et al., 1991; Micic et al., 2001). Unconsolidated undrained triaxial tests performed on samples collected just after the end of each test resulted in similar values, i.e., 50 KPa for 7.5 V/cm tests and 17 KPa for 1.5 V/cm tests, validating the results obtained from fall cone tests.

Figure 14 shows the costs associated with power consumption during tests. The primary vertical axis describes power consumption for tests where plastic electrodes were used and the secondary vertical axis describes power consumption for tests where copper electrodes were used. It should be noticed that dehydrating could be achieved at lower costs by employing plastic electrodes.

Plastic electrodes are also much cheaper. Plastic electrodes used in this study cost US$ 6.75 / each whereas copper electrodes with the same dimensions cost US$19.98/each.

4. Conclusions

A laboratory program was carried out aimed at assessing the efficacy of dehydrating subsurface clayey using plastic electrodes. A marine soil, classified according to the Unified Soil Classification System as MH-OH, composed of calcite, quartz, and kaolinite, and with a high concentration of Al, Fe, Mn and Ba, was used in the experimental program.

Tests were carried out on remolded soil samples using plastics and copper electrodes. Remolded samples were obtained using tap water instead of marine water, which significantly affects the electric conductivity of the medium. However, since the manuscript has focused on dehydrating efficacy using plastic and copper electrodes, a minor effect is expected in this regard. It was found that the dehydrating process is faster and more efficient when copper anodes were used since they possess a higher electrical conductivity despite the magnitude of the applied voltage gradient. However, the use of copper electrodes increases energy consumption, and also reduces electro-osmotic efficiency. It was observed that electro-osmotic efficiency is higher in the initial stages of tests, and as the electrokinetic process takes place hydraulic fracturing occurs and electro-osmotic efficiency is reduced. Also, it was noticed that electrolysis reactions in the vicinity of the anodes are very severe when copper alloys are used impacting electro-osmotic efficiency and reducing its life. On the other hand, it was observed that plastic anodes were less affected by electrolysis and have virtually no mass loss. Tests also indicate that pH changes in the soil mass seem to be proportional to the intensity of the electrolysis reactions. It was noticed that this effect is more severe at the early stages of the test.

The electrokinetic process induced positive changes in undrained shear strength due to the free water dehydration process induced by electro-osmosis and the adsorbed water dehydration process induced by electromigration. It was also observed that values of the undrained shear strength remained stable at the final stages of the electrokinetic process indicating a permanent soil improvement.

Finally, it was noticed that dehydrating could be achieved at lower costs by employing plastic electrodes. Hence, dehydrating subsurface clayey soils using plastic electrodes seems to be interesting to the earthwork portion on the construction of commercial, industrial and residential buildings, and transportation projects.

Acknowledgements

This study was financed in part by the Coordenação de Aperfeiçoamento de Pessoal de Nível Superior – Brasil (CAPES) and was made possible by the support of DAAD to the EXCEED SWINDON project.

Declaration of interest

The authors declare that they have no known competing financial interests or personal relationships that could have appeared to influence the work reported in this paper.

Authors' contributions

Ronald Beyner Mejia Sanchez: data curation, writing – original draft. José Tavares Araruna Júnior: supervision, funding acquisition, conceptualization, writing – review &

editing. Roberto Ribeiro de Avillez: writing – review & editing. Hongtao Wang: Writing – review & editing. Shuguang Liu: Writing – review & editing.

Data availability

All data, models, and code generated or used during the study appear in the submitted article.

References

Abdullah, W.S., & Al-Abadi, A.M. (2010). Cationic-electrokinetic improvement of an expansive soil. *Applied Clay Science*, 47(3-4), 343-350. http://dx.doi.org/10.1016/j.clay.2009.11.046.

Acar, Y.B., & Alshawabkeh, A.N. (1993). Principles of electrokinetic remediation. *Environmental Science & Technology*, 27(13), 2638-2647. http://dx.doi.org/10.1021/es00049a002.

Alaydi, K. (2016). *The application of electroosmosis in clay improvement: a laboratory investigation of electrokinetics use on clay* [Master's dissertation]. Chalmers University of Technology.

Ammami, M.T., Song, Y., Benamar, A., Portet-Koltalo, F., & Wang, H. (2020). Electro-dewatering of dredged sediments by combined effects of mechanical and electrical processes: influence of operating conditions. *Electrochimica Acta*, 353, 136462. http://dx.doi.org/10.1016/j.electacta.2020.136462.

ASTM 4318. (2017a). *Standard test methods for liquid limit, plastic limit, and plasticity index of soils* (pp. 1-20). ASTM International, West Conshohocken, PA. http://dx.doi.org/10.1520/D4318-17E01.

ASTM D1976. (2020a). *Standard test method for elements in water by inductively-coupled plasma atomic emission spectroscopy.* ASTM International, West Conshohocken, PA. http://dx.doi.org/10.1520/D1976-20.

ASTM D2216. (1998). *Standard test method for laboratory determination of water (moisture) content of soil and rock by mass* (pp. 1-5). ASTM International, West Conshohocken, PA. http://dx.doi.org/10.1520/D2216-19.

ASTM D2487. (2000). *Standard practice for classification of soils for engineering purposes (unified soil classification system)* (pp. 249-260). ASTM International, West Conshohocken, PA. https://doi.org/doi.org/10.1520/D2487-17E01.

ASTM D2850. (2015). *Standard test method for unconsolidated-undrained triaxial compression test on cohesive soils* (pp. 1-6). ASTM International, West Conshohocken, PA. https://doi.org/10.1520/D2850-15.2.

ASTM D2974. (2020b). *Standard test methods for determining the water (moisture) content, ash content, and organic material of peat and other organic soils* (pp. 1-4). ASTM International, West Conshohocken, PA. https://doi.org/10.1520/D2974-20E01.2.

ASTM D422. (2007). *Standard test method for particle-size analysis of soils (Reapproved)* (pp. 1-8). ASTM International, West Conshohocken, PA. https://doi.org/10.1520/D0422-63R07E02.2.

ASTM D4327. (2017b). *Standard test method for anions in water by suppressed ion chromatography* (pp. 1-13). ASTM International, West Conshohocken, PA. http://dx.doi.org/10.1520/D4327-17.

ASTM D7263. (2009). *Standard test methods for laboratory determination of density (unit weight) of soil specimens* (pp. 1-7). ASTM International, West Conshohocken, PA. https://doi.org/10.1520/D7263-21.1.2.

ASTM D7928. (2017c). *Standard test method for particle-size distribution (gradation) of fine-grained soils using the sedimentation (hydrometer) analysis* (pp. 1-25). ASTM International, West Conshohocken, PA. http://dx.doi.org/10.1520/D7928-17.

Azhar, A.T.S., Azim, M.A.M., Syakeera, N.N., Jefferson, I.F., & Rogers, C.D.F. (2017). Application of Electrokinetic Stabilisation (EKS) method for soft soil: a review. *IOP Conference Series. Materials Science and Engineering*, 226(1), 012075. http://dx.doi.org/10.1088/1757-899X/226/1/012075.

Babu, S., Thirumalai, R., Naveen Nayak, V., & Gobinath, S. (2020). Experimental investigation on expansive soils using electro kinetic geosynthetics (EKG) under cyclic loading. *Materials Today: Proceedings*, http://dx.doi.org/10.1016/j.matpr.2020.06.349.

Bjerrum, L., Moum, J., & Eide, O. (1967). Application of electro-osmosis to a foundation problem in a Norwegian Quick Clay. *Geotechnique*, 17(3), 214-235. http://dx.doi.org/10.1680/geot.1967.17.3.214.

Bourgès-Gastaud, S., Stoltz, G., Dolez, P., Blond, E., & Touze-Foltz, N. (2015). Laboratory device to characterize electrokinetic geocomposites for fluid fine tailings. *Canadian Geotechnical Journal*, 52(4), 505-514. http://dx.doi.org/10.1139/cgj-2014-0031.

BS 1377-2. (1990). *Methods of test for soils for civil engineering purposes: classification tests.* London.

Burnett, A.D. (1995). Quantitative X-ray diffraction technique for analyzing sedimentary rocks and soils. *Journal of Testing and Evaluation*, 23(2), 111-118. http://dx.doi.org/10.1520/JTE10902J.

Cameselle, C. (2015). Enhancement of electro-osmotic flow during the electrokinetic treatment of a contaminated soil. *Electrochimica Acta*, 181, 31-38. http://dx.doi.org/10.1016/j.electacta.2015.02.191.

Cameselle, C., & Gouveia, S. (2018). Advances in electrokinetic remediation for the removal of organic contaminants in soils. *Current Opinion in Electrochemistry*, 11, 41-47. http://dx.doi.org/10.1016/j.coelec.2018.07.005.

Cameselle, C., & Reddy, K.R. (2012). Development and enhancement of electro-osmotic flow for the removal of contaminants from soils. *Electrochimica Acta*, 86, 10-22. http://dx.doi.org/10.1016/j.electacta.2012.06.121.

Cameselle, C., Chirakkara, R.A., Krishna, R., & Reddy, K.R. (2013). Electrokinetic-enhanced phytoremediation of soils:

status and opportunities. *Chemosphere*, 93(4), 626-636. http://dx.doi.org/10.1016/j.chemosphere.2013.06.029.

Casagrande, L. (1948). Electro-osmosis. In *Proceedings of the 2nd International Conference on Soil Mechanics and Foundation Engineering* (Vol. 1, pp. 218-223). Netherlands.

Casagrande, L. (1949). Electro-osmosis in soils. *Géotechnique*, 1(3), 159-177. https://doi.org/10.1680/geot.1949.1.3.159.

Casagrande, L. (1952). Electro-osmotic stabilization of soils. *Journal of the Boston Society of Civil Engineers*, 39, 51-83.

Casagrande, L. (1983). Stabilization of soils by means of electro-osmosis - state-of-the-art. *Journal of Boston Society of Civil Engineers*, 69(2), 255-302.

Chien, S.C., Ou, C.Y., & Lee, Y.C. (2010). A novel electroosmotic chemical treatment technique for soil improvement. *Applied Clay Science*, 50(4), 481-492. http://dx.doi.org/10.1016/j.clay.2010.09.014.

Dukhin, S.S., & Mishchuk, N.A. (1993). Intensification of electrodialysis based on electroosmosis of the second kind. *Journal of Membrane Science*, 79(2-3), 199-210. http://dx.doi.org/10.1016/0376-7388(93)85116-E.

Estabragh, A.R., Naseh, M., & Javadi, A.A. (2014). Improvement of clay soil by electro-osmosis technique. *Applied Clay Science*, 95, 32-36. http://dx.doi.org/10.1016/j.clay.2014.03.019.

Fardin, A.B., Jamshidi-Zanjani, A., & Darban, A.K. (2021). Application of enhanced electrokinetic remediation by coupling surfactants for kerosene-contaminated soils: effect of ionic and nonionic surfactants. *Journal of Environmental Management*, 277, 111422. http://dx.doi.org/10.1016/j.jenvman.2020.111422.

Ghobadi, R., Altaee, A., Zhou, J.L., McLean, P., & Yadav, S. (2020). Copper removal from contaminated soil through electrokinetic process with reactive filter media. *Chemosphere*, 252, 126607. http://dx.doi.org/10.1016/j.chemosphere.2020.126607.

Gray, D.H. (1970). Electrochemical hardening of clay soils. *Geotechnique*, 20(1), 81-93. http://dx.doi.org/10.1680/geot.1970.20.1.81.

Gray, D.H., & Mitchell, J.K. (1967). Fundamental aspects of electro-osmosis in soils. *Journal of the Soil Mechanics and Foundations Division*, 93(6), 209-236. http://dx.doi.org/10.1061/JSFEAQ.0001053.

Gray, D.H., & Mitchell, J.K. (1969). Fundamental aspects of electro-osmosis in soils: closure discussion. *Journal of the Soil Mechanics and Foundations Division*, 95(SM3), 875-879. http://dx.doi.org/10.1061/JSFEAQ.0001289.

Gregolec, G., Roehl, K.E., & Czurda, K. (2005). Electrokinetic techniques. *Trace Metals and Other Contaminants in the Environment*, 7, 183-209. http://dx.doi.org/10.1016/S0927-5215(05)80012-8.

Hansbo, S. (1957). A new approach to the determination of the shear strength of clay by the fall-cone test. *Swedish Geotechnical Institute Proceedings*, 14, 1-59.

Hu, L., Wu, H., Ren, Y., & Wen, Q. (2016). Experimental study on soft soils improvement by the deep electro-osmotic consolidation technique. In *Geo-Chicago 2016* (pp. 235-244). Reston: American Society of Civil Engineers. http://dx.doi.org/10.1061/9780784480168.024.

Hu, L., Zhang, L., & Wu, H. (2019). Experimental study of the effects of soil pH and ionic species on the electro-osmotic consolidation of kaolin. *Journal of Hazardous Materials*, 368, 885-893. http://dx.doi.org/10.1016/j.jhazmat.2018.09.015.

Hunter, C., Mohamedelhassan, E., & Sadhu, A. (2021). Monitoring the strength properties of electrokinetically treated soil by bender elements to determine the treatment period. *Soil and Foundation*, 61(3), 675-691. http://dx.doi.org/10.1016/j.sandf.2021.02.005.

Indraratna, B., Rujikiatkamjorn, C., Baral, P., & Ameratunga, J. (2019). Performance of marine clay stabilised with vacuum pressure: based on Queensland experience. *Journal of Rock Mechanics and Geotechnical Engineering*, 11(3), 598-611. http://dx.doi.org/10.1016/j.jrmge.2018.11.002.

Jardine, R.J., Symes, M.J., & Burland, J.B. (1984). The measurement of soil stiffness in the triaxial apparatus. *Geotechnique*, 34(3), 323-340.

Jones, C.J.F.P., Lamont-Black, J., & Glendinning, S. (2011). Electrokinetic geosynthetics in hydraulic applications. *Geotextiles and Geomembranes*, 29(4), 381-390. http://dx.doi.org/10.1016/j.geotexmem.2010.11.011.

Karim, M.A. (2014). Electrokinetics and soil decontamination: concepts and overview. *Journal of Electrochemical Science and Engineering*, 4(4), http://dx.doi.org/10.5599/jese.2014.0054.

Lamont-Black, J., Hall, J.A., Glendinning, S., White, C.P., & Jones, C.J.F.P. (2012). Stabilization of a railway embankment using electrokinetic geosynthetics. *Geological Society Engineering Geology Special Publication*, 26(1), 125-139. http://dx.doi.org/10.1144/EGSP26.15.

Li, R., & Li, L.Y. (2000). Enhancement of electrokinetic extraction from lead-spiked soils. *Journal of Environmental Engineering*, 126(9), 849-857. http://dx.doi.org/10.1061/(ASCE)0733-9372(2000)126:9(849).

Lo, K.Y., & Ho, K.S. (1991). The effects of electroosmotic field treatment on the soil properties of a soft sensitive clay. *Canadian Geotechnical Journal*, 28(6), 763-770. http://dx.doi.org/10.1139/t91-093.

Lo, K.Y., Ho, K.S., & Inculet, I.I. (1991). Field test of electroosmotic strengthening of soft sensitive clay. *Canadian Geotechnical Journal*, 28(1), 74-83. http://dx.doi.org/10.1139/t91-008.

Lockhart, N.C. (1983). Electroosmotic dewatering of clays, III. Influence of clay type, exchangeable cations, and electrode materials. *Colloids and Surfaces*, 6(3), 253-269. http://dx.doi.org/10.1016/0166-6622(83)80017-1.

Mahalleh, H.A.M., Siavoshnia, M., & Yazdi, M. (2021). Effects of electro-osmosis on the properties of high plasticity clay soil: chemical and geotechnical investigations. *Journal of Electroanalytical Chemistry*, 880, 114890. http://dx.doi.org/10.1016/j.jelechem.2020.114890.

Mahmoud, A., Olivier, J., Vaxelaire, J., & Hoadley, A.F.A. (2010). Electrical field: a historical review of its application and contributions in wastewater sludge dewatering. *Water Research*, 44(8), 2381-2407. http://dx.doi.org/10.1016/j.watres.2010.01.033.

Martin, L., Alizadeh, V., & Meegoda, J. (2019). Electro-osmosis treatment techniques and their effect on dewatering of soils, sediments, and sludge: a review. *Soil and Foundation*, 59(2), 407-418. http://dx.doi.org/10.1016/j.sandf.2018.12.015.

Mejia, R.B. (2018). *Desenvolvimento de eletrodos de polímeros de baixo custo para aplicações geotécnicas* [Doctoral thesis]. Pontifical Catholic University of Rio de Janeiro.

Menon, A., Mashyamombe, T.R., Kaygen, E., Nasiri, M.S.M., & Stojceska, V. (2019). Electro-osmosis dewatering as an energy efficient technique for drying food materials. *Energy Procedia*, 161(0), 123-132. http://dx.doi.org/10.1016/j.egypro.2019.02.069.

Micic, S., Shang, J.Q., Lo, K.Y., Lee, Y.N., & Lee, S.W. (2001). Electrokinetic strengthening of a marine sediment using intermittent current. *Canadian Geotechnical Journal*, 38(2), 287-302. http://dx.doi.org/10.1139/t00-098.

Mishchuk, N.A. (2010). Concentration polarization of interface and non-linear electrokinetic phenomena. *Advances in Colloid and Interface Science*, 160(1-2), 16-39. http://dx.doi.org/10.1016/j.cis.2010.07.001.

Moore, C.A. (1970). *Suggested method for applications of X-ray diffraction of clay structural analysis to the understanding of the engineering behavior of soil* (5th ed., pp. 291-300). West Conshohocken: ASTM International. http://dx.doi.org/10.1520/STP38520S.

Ngo, D.H., Horpibulsuk, S., Suddeepong, A., Samingthong, W., Udomchai, A., Doncommul, P., Arulrajah, A., & Bo, M.W. (2021). Full scale consolidation test on ultra-soft soil improved by prefabricated vertical drains in MAE MOH mine, Thailand. *Geotextiles and Geomembranes*, 49(1), 72-80. http://dx.doi.org/10.1016/j.geotexmem.2020.09.005.

Peng, J., Ye, H., & Alshawabkeh, A.N. (2015). Soil improvement by electroosmotic grouting of saline solutions with vacuum drainage at the cathode. *Applied Clay Science*, 114, 53-60. http://dx.doi.org/10.1016/j.clay.2015.05.012.

Rao, B., Pang, H., Fan, F., Zhang, J., Xu, P., Qiu, S., Wu, X., Lu, X., Zhu, J., Wang, G., & Su, J. (2021). Pore-scale model and dewatering performance of municipal sludge by ultrahigh pressurized electro-dewatering with constant voltage gradient. *Water Research*, 189, 116611. http://dx.doi.org/10.1016/j.watres.2020.116611.

Reddy, K.R., & Saichek, R.E. (2004). Enhanced electrokinetic removal of phenanthrene from clay soil by periodic electric potential application. *Journal of Environmental Science and Health. Part A, Toxic/Hazardous Substances & Environmental Engineering*, 39(5), 1189-1212. http://dx.doi.org/10.1081/ESE-120030326.

Rittirong, A., Douglas, R.S., Shang, J.Q., & Lee, E.C. (2008). Electrokinetic improvement of soft clay using electrical vertical drains. *Geosynthetics International*, 15(5), 369-381. http://dx.doi.org/10.1680/gein.2008.15.5.369.

Saichek, R.E., & Reddy, K.R. (2003). Effect of pH control at the anode for the electrokinetic removal of phenanthrene from kaolin soil. *Chemosphere*, 51(4), 273-287. http://dx.doi.org/10.1016/S0045-6535(02)00849-4.

Tuan, P.A., Mika, S., & Pirjo, I. (2012). Sewage sludge electro-dewatering treatment: a review. *Drying Technology*, 30(7), 691-706. http://dx.doi.org/10.1080/07373937.2012.654874.

Turer, D., & Genc, A. (2005). Assessing effect of electrode configuration on the efficiency of electrokinetic remediation by sequential extraction analysis. *Journal of Hazardous Materials*, 119(1-3), 167-174. http://dx.doi.org/10.1016/j.jhazmat.2004.12.003.

Virkutyte, J., Sillanpää, M., & Latostenmaa, P. (2002). Electrokinetic soil remediation: critical overview. *The Science of the Total Environment*, 289(1-3), 97-121. http://dx.doi.org/10.1016/S0048-9697(01)01027-0.

Vocciante, M., Caretta, A., Bua, L., Bagatin, R., & Ferro, S. (2016). Enhancements in ElectroKinetic Remediation Technology: environmental assessment in comparison with other configurations and consolidated solutions. *Chemical Engineering Journal*, 289, 123-134. http://dx.doi.org/10.1016/j.cej.2015.12.065.

Wang, L., Shen, C., Liu, S., Alonso, E., & Huang, P. (2021). A hydro-mechanical coupled solution for electro-osmotic consolidation in unsaturated soils considering the decrease in effective voltage with time. *Computers and Geotechnics*, 133, 104050. http://dx.doi.org/10.1016/j.compgeo.2021.104050.

Wu, H., & Hu, L. (2014). Microfabric change of electro-osmotic stabilized bentonite. *Applied Clay Science*, 101, 503-509. http://dx.doi.org/10.1016/j.clay.2014.09.014.

Wu, J., Zhang, J., & Xiao, C. (2016). Focus on factors affecting pH, flow of Cr and transformation between Cr(VI) and Cr(III) in the soil with different electrolytes. *Electrochimica Acta*, 211, 652-662. http://dx.doi.org/10.1016/j.electacta.2016.06.048.

Zhang, H., Rigamonti, L., Visigalli, S., Turolla, A., Gronchi, P., & Canziani, R. (2019). Environmental and economic assessment of electro-dewatering application to sewage sludge: a case study of an Italian wastewater treatment plant. *Journal of Cleaner Production*, 210, 1180-1192. http://dx.doi.org/10.1016/j.jclepro.2018.11.044.

Zhang, L., & Hu, L. (2019). Laboratory tests of electro-osmotic consolidation combined with vacuum preloading on kaolinite using electrokinetic geosynthetics. *Geotextiles and Geomembranes*, 47(2), 166-176. http://dx.doi.org/10.1016/j.geotexmem.2018.12.010.

Zhou, J., Tao, Y.L., Xu, C.J., Gong, X.N., & Hu, P.C. (2015). Electro-osmotic strengthening of silts based on selected electrode materials. *Soil and Foundation*, 55(5), 1171-1180. http://dx.doi.org/10.1016/j.sandf.2015.09.017.

Zhuang, Y. (2021). Large scale soft ground consolidation using electrokinetic geosynthetics. *Geotextiles and Geomembranes*, 49(3), 757-770. http://dx.doi.org/10.1016/j.geotexmem.2020.12.006.

Soils and Rocks
An International Journal of Geotechnical and Geoenvironmental Engineering
www.soilsandrocks.com
ISSN 1980-9743
ISSN-e 2675-5475

Analysis of the creep and dilatant behavior of a salt cavern in long-term using Brazilian geotechnical properties

Renathielly Fernanda da Silva Brunetta[1#], Alessander C. M. Kormann[1], José Eduardo Gubaua[2], Jucélio Tomás Pereira[2]

Article

Keywords
Solution mining
Evaporitic rocks
Abaqus
Salt cavern abandonment
Finite element method
Nonlinear model

Abstract
The geomechanical behavior of a salt rock cavern was studied using Brazilian geotechnical properties. To design the finite element model, it was necessary to implement, using Fortran language, a constitutive model representing the creep behavior, since the model used is not native to the program. The constitutive model implemented was the Multiple Deformation Mechanism Model. This model was chosen for being a robust model that represents the primary and secondary phases of creep and presents good agreement with the Brazilian salt rocks. The analyzes considered a period of 50 years after the mine closure and five internal pressures acting in the analyzed cave. The pressures considered correspond to 40%, 50%, 60%, 70% and 80% of the vertical stress at the top of the mine. The creep and dilation behaviors were analyzed, and the creep deformations obtained in the simulations was acceptable in relation to the failure criterion adopted in this paper. However, only the design of experiment that considered the two biggest internal pressure resulted in a permissible micro-crack ratio value.

1. Introduction

Due to the products in its chain, chlorine and caustic soda are very relevant for society. Examples include polyvinyl chloride (PVC), agrochemicals, products for water and sewage treatment, pharmaceutical inputs, and lubricants (Jörissen, 2014).

Chlorine-soda is obtained by the electrolysis of a solution of rock salt (halite) in water. One of the rock salt mining techniques is dissolution extraction using recovery wells. The wells must reach the depth of saline material that can reach thousands of meters below the earth's surface. Afterwards, water is injected by these wells and when it comes into contact with rock salt, it dissolves the rock. Thus, it is possible to extract the brine used to obtain chlorine-soda. Curi (2017) presents a more detailed explanation about the extraction process.

Inevitably, at some point, the chlorine-soda extraction ceases. The most common technique of abandonment is to fill the cavern with brine and seal the well permanently. Thus, the pressure applied by the brine maintains the structural integrity of the cavern (Crotogino & Kepplinger, 2006). However, failures in the well seal, leakage through micro-cracks in the walls of the cave, tectonic movements, and other factors, can cause loss of internal pressure in the cavern. Recent researches have been studied the possibility of using abandoned caverns for the storage of hydrocarbons (Thoraval et al., 2015; Wei et al., 2016a, b; Zhang et al., 2020a, b).

The study of cave abandonment involves three important aspects. The first aspect is the experimental characterization of the saline material. The second aspect is in-situ tests to investigate mine geometry. The third aspect is the applying constitutive models to simulate the material behavior. These models can predict the time-dependent behavior of the material (Thoraval et al., 2015).

Some evaporitic rocks, especially halite, have a very particular behavior. The material suffers permanent deformations under constant loads and/or high temperatures. These deformations change throughout time. This time-dependent behavior is known as creep (Costa, 1984). In the case of caverns, built on salt rocks, the material that surrounds the cavern flows into the cavern. This causes mass movement that reduces the cavern volume. As consequence, the mass movement can cause lowering of the terrain surface (subsidence). Subsidences and instabilities in salt-caverns regions are old geotechnical problems and found in several countries (Bell et al., 2000; Autin, 2002; Whyatt & Varley,

[#]Corresponding author. E-mail address: renathielly@hotmail.com
[1]Universidade Federal do Paraná, Departamento de Construção Civil, Curitiba, PR, Brasil.
[2]Universidade Federal do Paraná, Laboratório de Mecânica dos Sólidos Computacional, Curitiba, PR, Brasil.

Submitted on June 23, 2022; Final Acceptance on March 19, 2023; Discussion open until December 30, 2023.
https://doi.org/10.28927/SR.2023.006722

2008; Yerro et al., 2014; Wang et al., 2018; Vassileva et al., 2021).

Creep occurs in three stages. The primary creep is where the strain rate decreases. The secondary creep follows the primary phase, with a constant strain rate. Finally, the tertiary phase. Literature does not characterize this phase well. But, in this phase, there may be an acceleration of the strain rate followed by the material rupture (Poiate Junior, 2012).

The dilatancy behavior of the saline rock is very important. A high level of stress can cause the generation of micro-cracks (Firme et al., 2019). Two domains define the salt rocks behavior. The first domain is compression. Here, the micro-cracks heal and guarantee the material impermeability. The second domain is dilatancy. The salt rock enters this domain when the active deviatoric stress exceeds the limit deviatoric stress. In this case, the expansion of the material can increase the permeability of the material (due to the occurrence of micro-cracks) and even cause damage (Van Sambeek et al., 1993).

Both dilatancy and creep behaviors can cause instabilities in abandoned caverns. This can lead to instabilities on the ground surface, such as subsidence. Although it is difficult to control the variables of a mine-abandonment project, due to its depth (it can be thousands of meters), maintaining an adequate internal pressure can help to avoid geotechnical instability. Therefore, the objective of this paper is to analyze the influence of internal pressure on the creep and dilation behavior of a rock salt mine with a geometry similar to those existing in the chlorine-soda mining fields in Brazil.

2. Constitutive modeling of rock salt

The constitutive relation applied to describe the rock salt behavior follows the Multiple Deformation Mechanism developed by Munson & Dawson (1979). The Multiple Deformation Mechanism allows simulating the creep behavior of rock salt under deviatoric stress. This model simulates transient (primary) and steady-state (secondary) creep phases. Different factors such as stress state, temperature, and material chemical composition, influence dislocations in salt rock (Firme et al., 2016). The Multiple Deformation Mechanism model uses three mechanisms to determine the steady-state phase creep: dislocation climb, undefined mechanism, and dislocation glid. The sum of them quantifies the secondary creep rate.

The dislocation climb can be described as a mechanism of thermal activation that depends on the stress intensity. This mechanism has a meaningful significance at high temperatures (approximately 50 °C). The high deformation energy generated during the dislocations leads to plastic deformation and hardening. The climb mechanism allows the movement of the dislocations (Firme et al., 2016).

An Arrhenius expression determines the contribution of dislocation climb on steady-state creep rate $\left(\dot{\varepsilon}_{DC}\right)$ as:

$$\dot{\varepsilon}_{DC} = A_1 \left(\frac{\sigma_{eq}}{G}\right)^{n_1} exp^{\left(\frac{-Q_1}{R\,T}\right)} \tag{1}$$

In rocks, such as halite, the contribution of the dislocation climb is considerable when the temperature is above 40% of the melting temperature of the material. The second mechanism is known as undefined mechanism and its rate ($\dot{\varepsilon}_{UM}$) is determined using an Arrhenius expression as the one used to determine the dislocation climb, defined as:

$$\dot{\varepsilon}_{UM} = A_2 \left(\frac{\sigma_{eq}}{G}\right)^{n_2} exp^{\left(\frac{-Q_2}{R\,T}\right)} \tag{2}$$

The third mechanism used is the dislocation glide $\left(DGL\right)$. It is a slow creep mechanism and arises from displacements in the material crystal lattice. This mechanism occurs at any stress level unbalanced by deviatoric stress. Shear stress also can influence the occurrence of this mechanism. Consequently, there is plastic strain and material hardening. The rate of this mechanism $\left(\dot{\varepsilon}_{DG}\right)$ is computed as:

$$\dot{\varepsilon}_{DG} = \left|H\left(\sigma_{eq} - \sigma_0\right)\right| \times \left(B_1 exp^{\left(\frac{-Q_1}{R\,T}\right)} + B_2 exp^{\left(\frac{-Q_2}{R\,T}\right)}\right) \times senh\left(\frac{q\left(\sigma_{eq} - \sigma_0\right)}{G}\right) . \tag{3}$$

In this equation, $\left|H\left(\sigma_{eq} - \sigma_0\right)\right|$ is a Heaviside step function with argument $\left(\sigma_{eq} - \sigma_0\right)$. This argument limits the occurrence of DGL for a deviatoric (or equivalent) stress higher than the reference stress value of the mechanism $\left(\sigma_0\right)$.

The primary creep was determined by performing a retro analysis with the secondary creep rate. Thus, it is possible to estimate a limit strain during the transient creep $\left(\varepsilon_t^*\right)$ as:

$$\varepsilon_t^* = K_0 \exp^{cT} \left(\frac{\sigma_{eq}}{G}\right)^m \tag{4}$$

From $\left(\varepsilon_t^*\right)$ it is possible to determine the function F as:

$$F = \begin{cases} exp\left[\Delta\left(-\frac{\varsigma}{\varepsilon_t^*}\right)^2\right] & if \quad \varsigma < \varepsilon_t^* \\ 1 & if \quad \varsigma = \varepsilon_t^* \\ exp\left[-\delta\left(-\frac{\varsigma}{\varepsilon_t^*}\right)^2\right] & if \quad \varsigma > \varepsilon_t^* \end{cases} \tag{5}$$

In this equation, ς is an internal isotropic hardening variable subject to an evolutionary rate $\left(\dot{\varsigma}\right)$ defined as:

$$\dot{\varsigma} = \left(F - 1\right)\dot{\varepsilon}_{SS} \tag{6}$$

The value of $\dot{\varepsilon}_{SS}$ is obtained by the summetion of the three micromechanical creep mechanisms presented in Equations 1, 2, and 3.

The hardening $\left(\Delta\right)$ and softening $\left(\delta\right)$ parameters are computed using:

$$\Delta = \alpha_h + \beta_h \log\left(\frac{\sigma_{eq}}{G}\right) \tag{7}$$

and

$$\delta = \alpha_s + \beta_s \log\left(\frac{\sigma_{eq}}{G}\right) \tag{8}$$

respectively.

Finally, the total creep rate $\left(\dot{\varepsilon}\right)$ is determine, including the primary and secondary creeps, by using:

$$\dot{\varepsilon} = F\dot{\varepsilon}_{SS} \tag{9}$$

After integrating $\dot{\varepsilon}$, it is possible determine the total creep strain $\left(\varepsilon\right)$ as:

$$\varepsilon\left(t\right) = \int_0^t (F\dot{\varepsilon}_{SS})dt \tag{10}$$

2.1 Validation

The Multiple Deformation Mechanism model is very effective to simulate the salt rock behavior. Munson (1979) presents accurate results for simulations involving experimental and field situations. Thus, this paper does not prove the model efficiency, which is very used and established. The purpose of validation is to verify that the model implementation using the Fortran language was performed correctly. This implementation is necessary as this model is not native to the software.

Three triaxial creep tests was simulated to validate the implementation. During the validation simulation the samples was kept under confining stress of 10 MPa and deviatoric stress of 10, 14, and 17 MPa. Poiate Junior et al. (2006) presented the test with deviatoric stress of 10 MPa, while Costa et al. (2005) presented the other tests.

All tests simulated was performed using cylindrical body tests of 88.9 mm (3.5 inches) diameter and 177.8 mm (7.0 inches) length. The aspect ratio of 2 for 1 follows the recommendation of the International Society for Rock Mechanics. During the test, the temperature was controlled and kept at 86 °C.

Figure 1 presents both experimental and numerical results obtained for the samples. Table 1 presents the parameters used to perform the numerical simulations. Firme et al. (2016). calibrated the parameters using tests of Sergipe-Alagoas-Brazil basin. Adequated agreement was observed between numerical and experimental results.

To characterize the elastic phase of the material was adopted the values presented by Poiate Junior (2012).

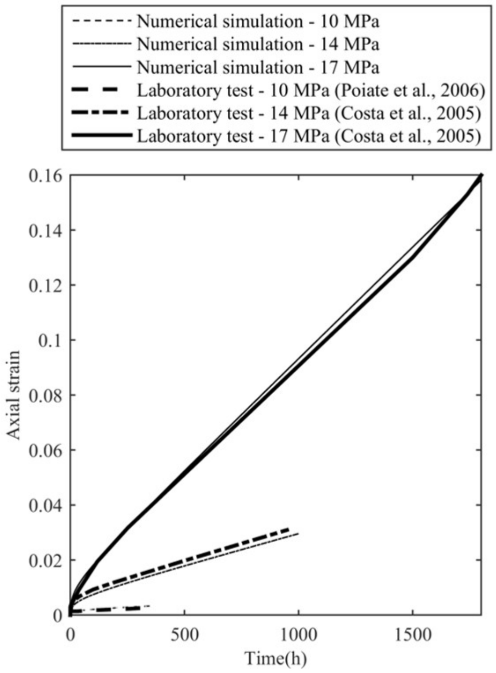

Figure 1. Comparison between numerical results and experimental results of triaxial tests on halite.

Table 1. Parameters used to characterize the creep behavior of the rock salt.

Parameter	Unit	Value
A_1	s^{-1}	1.638×10^{27}
Q_1	kJ/mol	1.045×10^5
n_1	-	7.2
B_1	s^{-1}	9.981×10^6
A_2	s^{-1}	1.924×10^6
Q_2	kJ/mol	4.18×10^4
n_2	-	3.2
B_2	s^{-1}	4.976×10^{-2}
σ_0	MPa	20.57
q	-	9.335×10^3
R	J $(mol.K)^{-1}$	8.3143
m	-	3.0
K_0	-	7.750×10^4
c	K^{-1}	0.009198
α	-	-17.37
θ	-	-7.738
δ	-	0.58

The author used 20.4 GPa and 21.29 kN/m^3 to describe the Halite's dynamic elastic modulus, and unit specific weight. Finally, we used the dynamic Poisson's ratio equal to 0.36 as presented by Costa et al. (2005).

3. Stratigraphy and typical geometry

The geometries of chlorine-soda mines are very variable due to their construction techniques and the material characteristics. The cavern studied in this paper has geometry and dimensions similar to existing mines in northeastern Brazil (CPRM, 2019). Figure 2 shows the geometry of the mine studied and its dimensions obtained by sonar measurement.

The stratigraphy used is based on the characteristics of the Sergipe-Alagoas sedimentary basin, also located in northeastern Brazil. In this basement, the rock salt stratum starts at approximately 900 m of depth and the overburden is composed mainly of shale and sandstone, and there may be the presence of other sedimentary rocks.

In this paper, it was considered the most recent geometry obtained by sonar measurement performed in 2018. However, the geometry was simplified by replacing the original format by an ellipse, with height and radius similar to the original geometry. Figure 3 shows the simplified geometry.

The simulation, despite being based on data of parameters and geometry of Brazilian mines, is not representative of any specific case, it is a hypothetical situation that aims to analyze the behavior for conditions similar to that simulated.

Simplifications are common in studies of underground salt caverns (Goulart et al., 2020; Li et al., 2021). They bring the advantage of avoiding the action of stress concentrators due to the corners. Another important point is the quality of the mesh used to discretize the model. A simpler geometry avoids the use of a greater number of elements in regions with sharp corners, for example. Furthermore, discretization can be performed with more robust elements. This provides an improvement in determining the variables involved in the simulation.

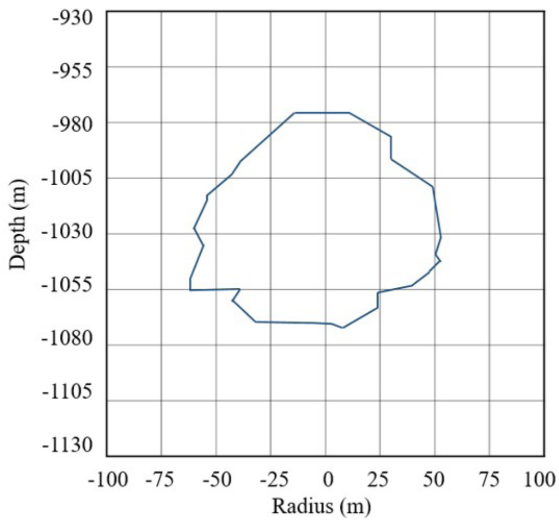

Figure 2. Shape and dimensions of cavern obtained by the sonar survey in 2018 (CPRM, 2019).

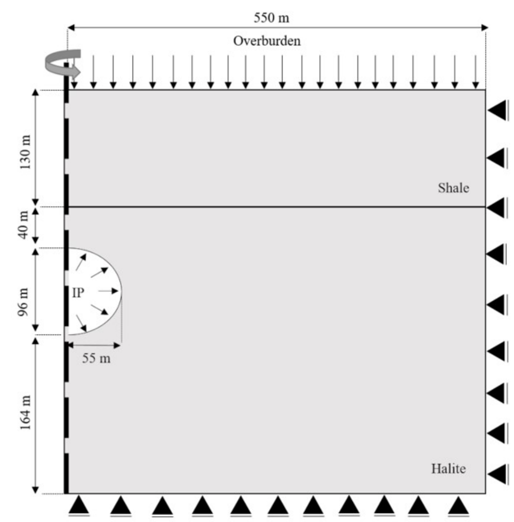

Figure 3. Geometry used for representing the cavern.

4. Geomechanical model, boundary, and initial conditions

Figure 3 presents the model used for performing the simulations. At the top of the model was applied a 19.03 MPa pressure, which characterizes the overburden. This pressure represents the sediments above the shale layer. The height of the mine is 96 m and the approximate radius is 55 m. Figure 3 also presents the others measurements of the model.

The finite element model was built using the commercial software Abaqus. An axisymmetric model represented the saline environment. It was used CAX4R elements (4-node bilinear axisymmetric quadrilateral, reduced integration) to discretize the model.

Two materials composed the model: halite and shale (Figure 3). We applied the elastoplastic model proposed by Mohr-Coulomb to the shale's behavior. It was considered the elastic modulus, Poisson's ratio, friction angle, cohesion and the specific weight equal to 18.97 GPa, 0.15, 22°, 4.8 MPa and 24.00 kN/m³ (Costa et al., 2015). The geothermal gradients, i.e., the temperature rate of geotechnical materials, suggested by Costa et al. (2012) were used. The temperature is higher the greater the depth, these authors suggest 10ºC/km for saline material and 30ºC/km for the sedimentary rocks that constitute the overburden.

Figure 4a presents the mesh discretization around the cavern and the five points of interest (A, B, C, D, e E). These points were used to perform some analysis presented in section 4. Figure 4b presents the mesh and boundary conditions. The thick black line indicates the axis of revolution to build the model. Figure 4b represents a 90-degree revolution of Figure 3. However, the software understands the model as a complete 360-degree revolution. The blue and gray portions represent shale and halite.

On the right side, the horizontal displacement was constrained. This restriction represents the continuity of the layer and allows the vertical movement. Vertical displacements were constrained at the model bottom.

The simulation was performed in three steps. In the first step, the geostatic stresses are generated, and the excavation of the mine is carried out. The coefficient of earth pressure at rest of overburden was considered 0.25 and for salt rock was considered 1, cause your creep behavior. The excavation is carried out instantly with the complete removal of the material. The second step is the instantaneous elastic behavior of the material. Finally, the third step if visco-elasto-plastic behavior using the Multiple Deformation Mechanism model concerning a period of 50 years.

Given the fact that some units of the constitutive model use seconds as a time unit, the simulations were performed considering seconds as the time unit. The time for data processing of each simulation is directly linked to the internal pressure considered. Higher internal pressures are more stable conditions. So, they are more agile, while smaller internal pressures need more time to be completed. The simulations performed in this research took between 10 and 30 minutes using an Intel Core I7 computer with 8GB of RAM.

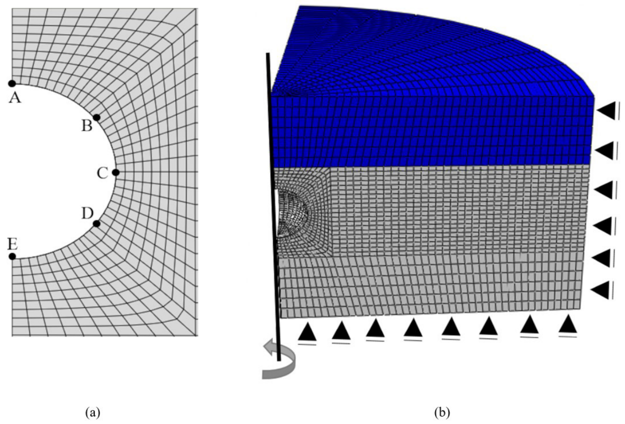

Figure 4. Axisymmetric model and finite element mesh discretization: (a) detail of the analysis points; (b) partial revolution of the analysis plane.

Table 2. Design of experiments.

Internal pressure (MPa)	Symbol
9.19	IP40
11.49	IP50
13.79	IP60
16.09	IP70
18.38	IP80

5. Numerical experiments and stability criteria

Five simulations were performed by considering different internal pressures applied on the cavern (Table 2). The values of the internal pressures are a percentage of the effective vertical tension at the top of the cavern. Those values ranging from 40% to 80% of the value of the effective vertical tension.

The analyzed internal pressures were based on literature to choose, which indicates values between 30% and 85% of the effective vertical stress at the top of the cavern. Pressures less than 30% cause instability in the caverns. While pressures greater than 85% can generate tensile stress. Salt rocks do not resist this type of effort (Bérest et al., 2020; Costa et al., 2015; Yuan et al., 2021). Stability criteria considered both the creep and dilatation behaviors.

5.1 Creep criterion

The creep behavior causes a decrease in the volume of salt caverns. Thus, the creep criterion relates to the cavern volume loss. The largest shrinkage volume limit was defined as 10% of the initial cavern volume throughout the analysis (50 years). This is a value often used in salt cavern stability analyses (Yuan et al., 2021).

5.2 Dilatancy criterion

In this research, the tertiary (accelerated) stage of creep was not considered. However, an expansion criterion monitored the damage in the salt rock. Salt rocks in situ are usually impermeable. But, when an increase in deformation happens, there is a rise in permeability of the rock due to damage (Van Sambeek et al., 1993; Firme et al., 2016). Ratigan's criterion (Van Sambeek et al., 1993) was used, since this criterion is widely used to model the Brazilian halite (Costa et al., 2015; Firme et al., 2016; Firme et al., 2019). This criterion considers the mean stress $\left(\sigma_m\right)$ of each point to estimate a critical deviatoric stress $\left(\sigma_{d,cr}\right)$ for that point by following equation:

$$\sigma_{d,cr} = \left(a\sigma_m\right)\sqrt{3} \tag{11}$$

in which a receives the value of 0.81.
Damage will occur if the ratio between the deviatoric $\left(\sigma_d\right)$ effective stress and the critical deviatoric stress $\left(\sigma_{d,cr}\right)$ is greater than the critical value indicated by the criterion. This value corresponds to 0.8, i.e., the ratio between the acting deviatoric effective stress and critical deviatoric stress is the micro-crack ratio $\left(MC\right)$ defined as:

$$MC = \frac{\sigma_d}{\sigma_{d,cr}} \tag{12}$$

The deviatoric effective stress $\left(\sigma_d\right)$ considered in this paper is the equivalent von Mises stress $\left(\sigma_d = \sqrt{3J_2}\right)$ that can be described from the second invariant of the deviatoric stress tensors $\left(J_2\right)$.

6. Results

6.1 Salt cavern convergence

As highlighted above, the creep behavior is responsible for the convergence of salt caverns. That is, the volume of shrinkage of the cavern. The strain at each point of the model depends on the acting deviatoric stress (von Mises equivalent stress), as shown in Equations 1, 2, and 3. Thus, the shrinkage volume is dependent on the von Mises equivalent stress.

The Figure 5 shows the von Mises equivalent stress for IP40. One can observe that the cap rock causes a stress arching effect. This relieves the stresses in the saline material. Thus, cap rock is very important for cavern simulations. Zhang et al. (2020a) also verified the importance of the surrounding rocks.

Figure 6 shows the equivalent creep strains for all internal pressures presented in Table 2. The point C was presented the highest level of strain among five points.

Figure 7 shows the wall equivalent strain rate at point C for all analyzed internal pressures. It was analyzed this point because it is at the region with the highest strain. Costa et al. (2015) indicates an admissible creep rate in steady-state regime equal to 0.5×10^{-06} per hour. One can note that the strain rates (per hour) are between 10^{-07} and 10^{-10} at the end of analysis. Instantly the creep strain rate has values greater than the admissible value for all internal pressures. However, in a small portion of time, the creep rate becomes higher than the admissible value. Afterwards, one can observe the deceleration phase of the strain rate until reaching the steady-state. There is an unstable condition for the IP80. However, the creep rate presents the smallest values at the end of simulation.

Figure 8 shows the wall equivalent strain at point C. In the numerical analysis performed, the maximum strain was 0.038 for IP40. The simulations did not reach the maximum value allowable considered equal to 0.100 (Costa et al., 2015). This indicates that shrinkage caused by salt creep is not meaningful even for IP40, which presents an increasing behavior during the simulation.

Figure 9 shows the percentage of volume shrinkage over time. None of the numerical experiments reached the maximum shrinkage volume of 10% of the initial volume.

Figure 10 presents the numerical results of displacements norm resulting from creep strain. Clearly, displacements decreased when the internal pressure increases.

A large displacement increase was noted when the internal pressure was reduced from 80% to 70% of the in situ vertical stress on the mine roof. Bérest et al. (2020) performed several studies on the internal pressure of salt caverns. They indicate that the adequate pressure is between 80 and 85% of the in situ vertical stress on the mine roof. However, it is not always possible to ensure this pressurization, due to several factors such as reactivation of geological faults, cracks due to the low tensile strength of the saline material or, even, due to leakage due to the filling of the well.

6.2 Dilatant behavior

Figure 11 presents the micro-cracking (MC) ratio obtained for each internal pressure considered. One observes that the regions close to points B and C provide the necessary condition for initiation the micro cracks.

At the end of the 50 years analyzed by finite element modeling, the micro-crack ratio was acceptable only for IP70 and IP80. Figure 12 shows the micro-cracking ratio values, considering 50 years of analysis, for point C for all simulated internal pressures.

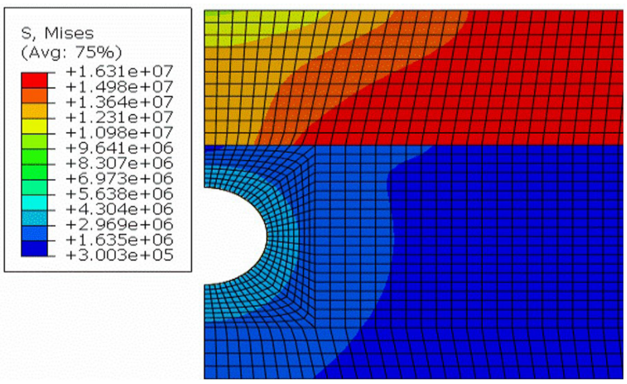

Figure 5. Von Mises equivalent stress regarding the IP40.

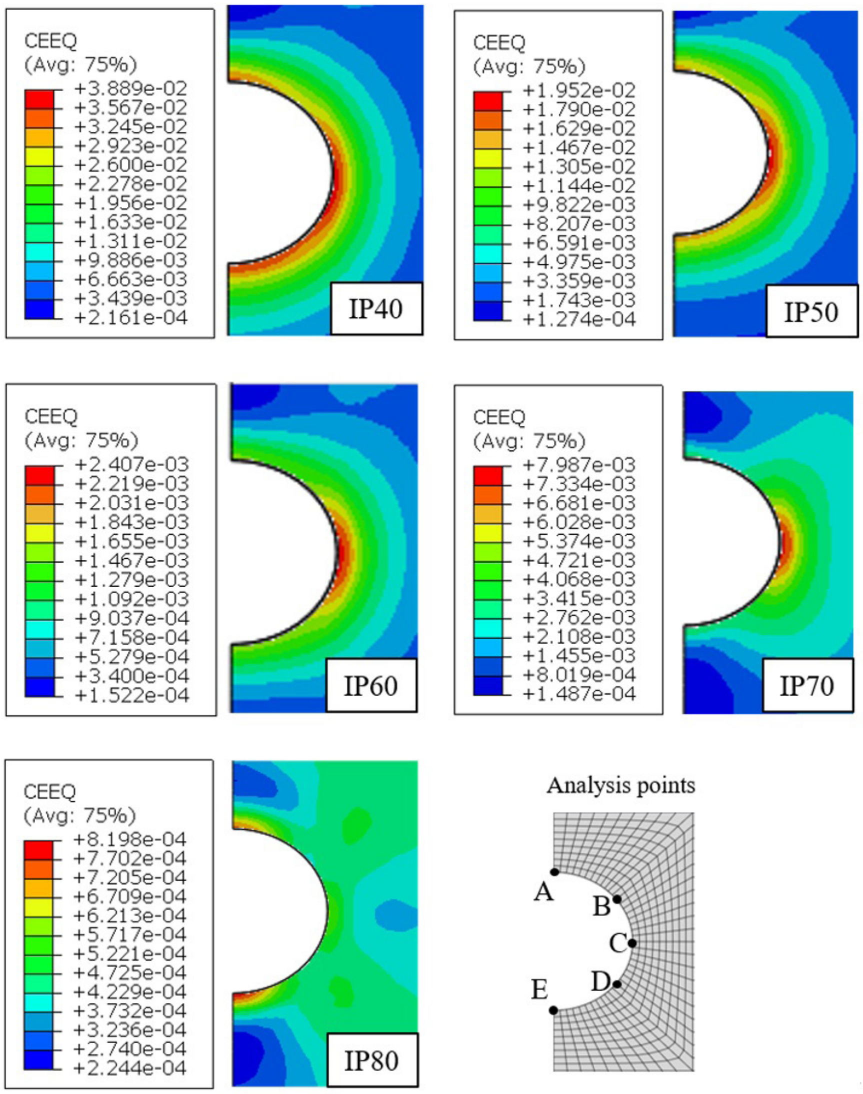

Figure 6. Equivalent creep strains (CEEQ) around the cavern for the internal pressures studied.

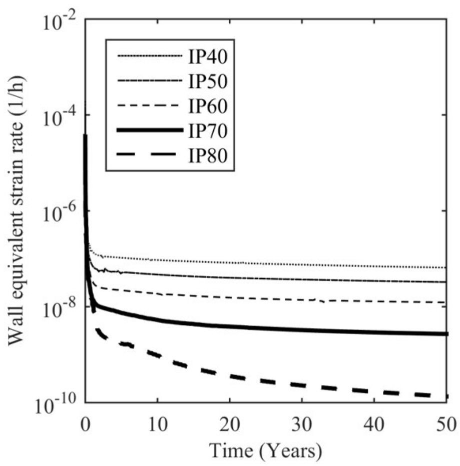

Figure 7. Wall equivalent strain rate at point C.

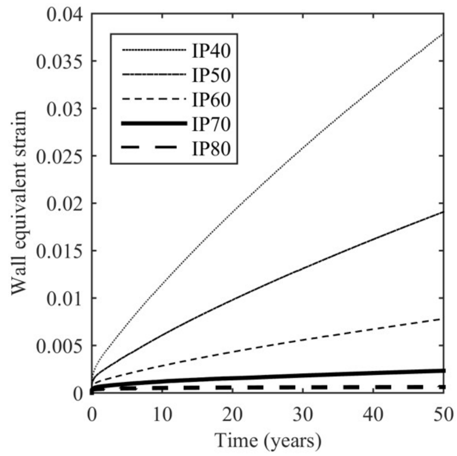

Figure 8. Wall equivalent strain at point C.

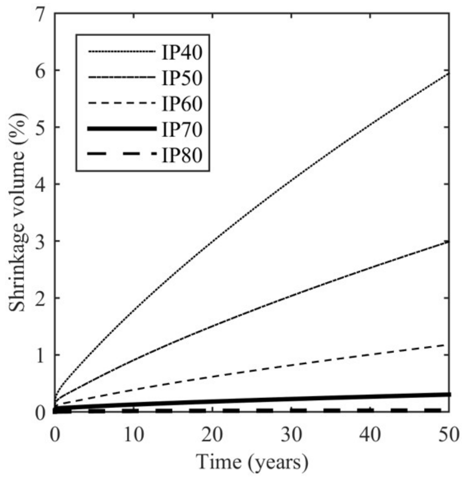

Figure 9. Percentage of volume shrinkage over time.

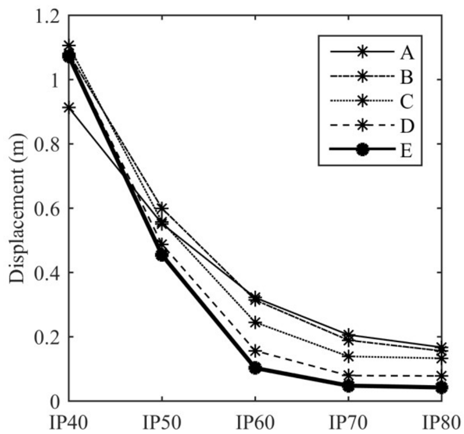

Figure 10. Magnitude of displacements at the analyzed points.

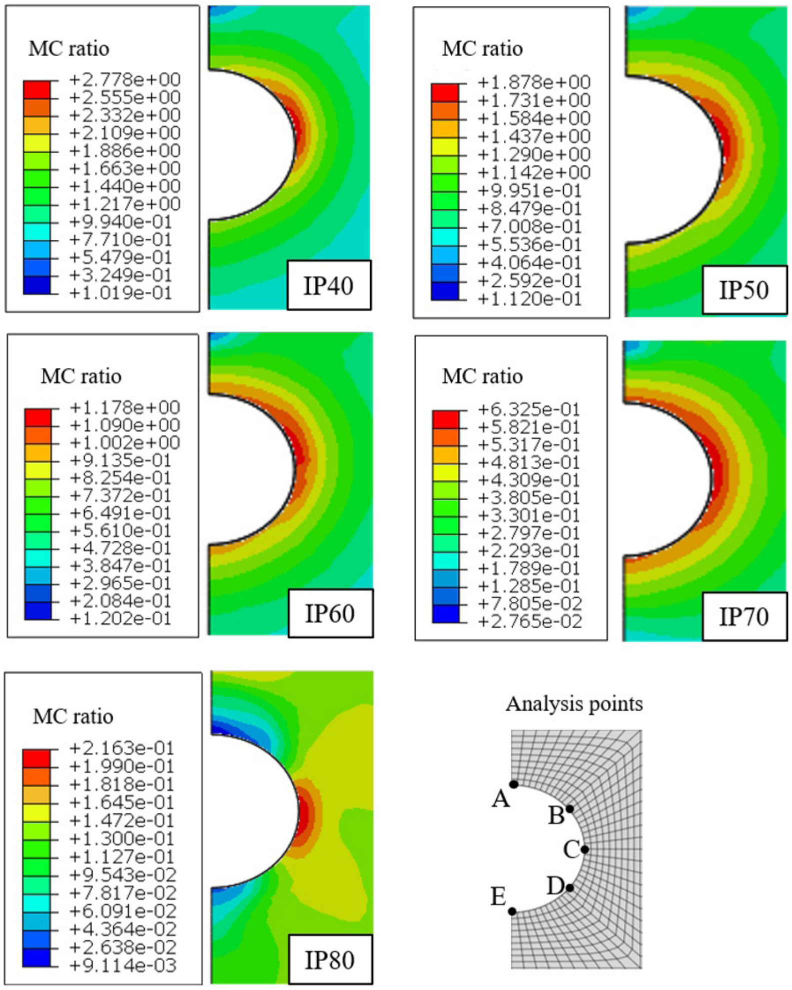

Figure 11. Micro-cracking ratio (MC) around the cavern for the internal pressures studied.

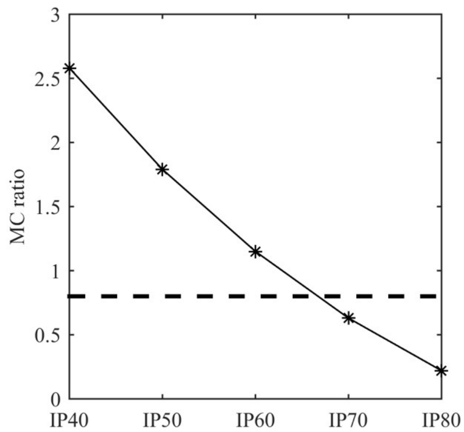

Figure 12. MC ratio at point C after 50 years of analysis. Dashed line represents the dilatancy criterion critical value.

7. Conclusions

The high level of stress due to the creep phenomenon in salt rocks can cause the failure of abandoned caverns. In this sense, the knowledge of this complex behavior is fundamental. The use of Multiple Deformation Mechanism model combined with a suitable dilatation criterion allows modeling the primary creep, the steady-state creep and damage of a salt cavern. Thus, one can perform numerical studies by considering the modifications of the cavern's geometry or the internal pressure.

Simulations was carried out, using the finite element method, to analyze the behavior of caverns located in saline environments. Creep and dilation were investigated. Despite the occurrence of displacements with high magnitude (greater than 1 m), the creep deformation for all analyzed internal pressure was considered acceptable, as the shrinkage volume was smaller than the maximum allowable shrinkage volume. Another important aspect simulated was the micro-crack ratio. It was considered as an acceptable the value of 0.8. Values greater than this indicate the occurrence of micro-cracks in the cavern walls. This paper indicates that only the IP70 and IP80 condition provided acceptable results.

Several research have been carried out in order to analyze the behavior of salt-rock caverns, but there are difficulties in representing the behavior of this material over time. It is necessary to emphasize that the combination of a model that simulates primary and secondary creep with a damage criterion, as done in this research, is one of the most robust ways of analyzing rock salt behavior over time. Finally, the integrated analysis between creep and dilatant behavior was considered an important tool for reliability analysis, as it allows an accurate analysis of the behavior of rock salts. Future research should focus on analyzing the variability of geotechnical parameters to also provide a probabilistic approach.

Acknowledgements

The authors are grateful to the Post-Degree in Civil Construction Engineering from Federal University of Paraná (PPGECC-UFPR) and to the Araucária Foundation for enabling such a study. This work was carried out with the support of Coordination of Improvement of Personnel of Higher Education - Brazil (CAPES) - Code of Financing 001. J. T. Pereira acknowledges the financial support from National Council for Scientific and Technological Development (CNPq/Brazil).

Declaration of interest

The authors have no conflicts of interest to declare. All co-authors have observed and affirmed the contents of the paper and there is no financial interest to report.

Authors' contributions

Renathielly Fernanda da Silva Brunetta: conceptualization, data curation, visualization, writing – original draft. Alessander C. M. Kormann: formal analysis, funding acquisition, investigation, methodology, project administration, resources, software. José Eduardo Gubaua: conceptualization, data curation, methodology, supervision, validation, writing – original draft. Jucélio Tomás Pereira: supervision, validation, writing – review & editing.

Data availability

The datasets generated and analyzed during the current study are available from the corresponding author upon request.

List of symbols

c	theoretical material's constants
m	theoretical material's constants
n_1	stress power of the Dislocation Climb Mechanism
n_2	stress power of the undefined mechanism
q	stress parameter
A_1	structure factor of the Dislocation Climb Mechanism
A_2	structure factor of the undefined mechanism
B_1	structure factor of the Dislocation Glide Mechanism
B_2	structure factor of the Dislocation Glide Mechanism
G	elastic shear modulus
H	heaviside step function
K_0	transient parameter
Q_1	thermal activation energy of the Dislocation Climb Mechanism
Q_2	thermal activation energy of the undefined mechanism
R	universal gas constant
T	temperature
α_h	internal isotropic hardening variable
α_s	internal isotropic softening variable
β_h	internal isotropic hardening variable
β_s	internal isotropic softening variable
Δ	hardening parameter
δ	softening parameter
$\dot{\varepsilon}_{DC}$	Dislocation Climb strain rate
$\dot{\varepsilon}_{DG}$	Dislocation Glide strain rate
$\dot{\varepsilon}_{SS}$	steady-state strain rate
ε_t^*	limit strain during the transient creep
$\dot{\varepsilon}_{UM}$	undefined mechanism strain rate
σ_0	reference stress value of the mechanism
σ_{eq}	von Mises equivalent stress

References

Autin, W.J. (2002). Landscape evolution of the Five Islands of south Louisiana: scientific policy and salt dome utilization and management. *Geomorphology*, 47, 227-244. http://dx.doi.org/10.1016/S0169-555X(02)00086-7.

Bell, F.G., Stacey, T.R., & Genske, D.D. (2000). Mining subsidence and its effect in the environment: some differing examples. *Environmental Geology*, 40, 135-152. http://dx.doi.org/10.1007/s002540000140.

Bérest, P., Brouard, B., Karimi-Jafari, M., & Réveillère, A. (2020). Maximum admissible pressure in salt caverns used for brine production and hydrocarbon storage. *Oil & Gas Science and Technology*, 75, 1-15. http://dx.doi.org/10.2516/ogst/2020068.

Costa, A.M. (1984). *An application of computational methods and rock mechanics principles in the design and analysis of mining excavations* [Doctoral thesis, Pontifical Catholic University of Rio de Janeiro]. Pontifical Catholic University of Rio de Janeiro's repository (in Portuguese).

Costa, A.M., Amaral, C.S., & Poiate Junior, E. (2015). Hydrocarbon production and storage using offshore underground salt caverns. In L. Roberts, K. Mellegard & F. Hansen (Eds.), *Mechanical behaviour of salt VIII* (pp. 211-220). Boca Raton: CRC Press. https://doi.org/10.1201/b18393-28.

Costa, A.M., Amaral, C.S., Poiate Junior, E., Pereira, A.M.B., Martha, L.F., Gattass, M., & Roehl, D. (October 16-21, 2012). Underground storage of natural gas and CO_2 in salt caverns in deep and ultra-deep water offshore Brazil. In Q. Qian & Y. Zhou (Eds.), Proceedings of the 12th ISRM International Congress on Rock Mechanics (pp. 1659-1664). Boca Raton, USA: CRC Press.

Costa, A.M., Poiate Junior, E., Falcão, J.L., & Coelho, L.F.M. (February 23-25, 2005). Triaxial creep tests in salt applied in drilling through thick salt layers in campos Basin-Brazil. In *SPE/IADC Drill Conference* (pp. 1009-1017). Red Hook, USA: Curran Associates, Inc. https://doi.org/10.2523/92629-MS.

CPRM. (2019). *Estudo sobre a instabilide do terreno nos bairros Pinheiro, Mutange e Bebedouro, Maceió (AL). Geofísica – gravimetria* (Vol. II). Brasília: CPRM. Retrieved in June 23, 2022, from https://rigeo.cprm.gov.br/jspui/bitstream/doc/21134/9/volumeII_j.pdf (in Portuguese).

Crotogino, F., & Kepplinger, J. (2006). *Cavern well abandonment techniques guidelines manual*. Hannover: SMRI.

Curi, A. (2017). *Lavra de minas*. São Paulo: Oficina de Textos (in Portuguese).

Firme, P.A.L.P., Roehl, D., & Romanel, C. (2016). An assessment of the creep behaviour of Brazilian salt rocks using the multi-mechanism deformation model. *Acta Geotechnica*, 11, 1445-1463. http://dx.doi.org/10.1007/s11440-016-0451-y.

Firme, P.A.L.P., Roehl, D., & Romanel, C. (2019). Salt caverns history and geomechanics towards future natural gas strategic storage in Brazil. *Journal of Natural Gas Science and Engineering*, 72, 103006. http://dx.doi.org/10.1016/j.jngse.2019.103006.

Goulart, M.B.R., Costa, P.V.M., Costa, A.M., Miranda, A.C.O., Mendes, A.B., & Ebecken, N.F.F. (2020). Technology readiness assessment of ultra-deep Salt caverns for carbon capture and storage in Brazil. *International Journal of Greenhouse Gas Control*, 99, 103083. http://dx.doi.org/10.1016/j.ijggc.2020.103083.

Jörissen, J. (2014). Chlorine and caustic technology, overview and traditional processes. In G. Kreysa, K.-I. Ota & R. F. Savinell (Eds.), *Encyclopedia of applied electrochemistry* (pp. 194-200). New York: Springer. https://doi.org/10.1007/978-1-4419-6996-5_297.

Li, P., Li, Y., Shi, X., Zhao, K., Liu, X., & Ma, H. (2021). Prediction method for calculating the porosity of insoluble sediments for salt cavern gas storage applications. *Energy*, 221, 119815. http://dx.doi.org/10.1016/j.energy.2021.119815.

Munson, D.E. (1979). *Preliminary deformation-mechanism map for salt (with application to WIPP)*. Albuquerque: Sandia Laboratories. Report nº SAND-79-0076. https://doi.org/10.2172/6499296.

Munson, D.E., & Dawson, P.R. (1979). *Constitutive model for the low temperature creep of salt (with application to WIPP)*. Albuquerque: Sandia Laboratories. Report nº SAND-79-1853. https://doi.org/10.2172/5729479.

Poiate Junior, E. (2012). *Rock mechanics and computational mechanics for the design of oil wells in salt zones* [Doctoral thesis, Pontifical Catholic University of Rio de Janeiro]. Pontifical Catholic University of Rio de Janeiro's repository (in Portuguese). https://doi.org/10.17771/PUCRio.acad.34904.

Poiate Junior, E., Costa, A.M., & Falcao, J.L. (February 21-23, 2006). Well design for drilling through thick evaporite layers in Santos Basin - Brazil. In *SPE/IADC Drill Conference* (pp. 1081-1096). Red Hook, USA: Curran Associates, Inc. https://doi.org/10.2523/99161-ms.

Thoraval, A., Lahaie, F., Brouard, B., & Berest, P. (2015). A generic model for predicting long-term behavior of storage salt caverns after their abandonment as an aid to risk assessment. *International Journal of Rock Mechanics and Mining Sciences*, 77, 44-59. http://dx.doi.org/10.1016/j.ijrmms.2014.10.014.

Van Sambeek, L.L., Ratigan, J.L., & Hansen, F.D. (1993). Dilatancy of rock salt in laboratory tests. *International Journal of Rock Mechanics and Mining Sciences*, 30, 735-738. http://dx.doi.org/10.1016/0148-9062(93)90015-6.

Vassileva, M., Al-Halbouni, D., Motagh, M., Walter, T.R., Dahm, T., & Wetzel, H.U. (2021). A decade-long silent ground subsidence hazard culminating in a metropolitan disaster in Maceió, Brazil. *Scientific Reports*, 11, 7704. https://doi.org/10.1038/s41598-021-87033-0.

Wang, T., Yang, C., Chen, J., & Daemen, J.J.K. (2018). Geomechanical investigation of roof failure of China's first gas storage salt cavern. *Engineering Geology*, 243, 59-69. http://dx.doi.org/10.1016/j.enggeo.2018.06.013.

Wei, L., Jie, C., Deyi, J., Xilin, S., Yinping, L., & Daemen, J.J.K. (2016a). Tightness and suitability evaluation of abandoned salt caverns served as hydrocarbon energies storage under adverse geological conditions (AGC). *Applied Energy*, 178, 703-720. https://doi.org/10.1016/j.apenergy.2016.06.086.

Wei, L., Yinping, L., Chunhe, Y., Deyi, J., Daemen, J.J.K., & Jie, C. (2016b). A new method of surface subsidence prediction for natural gas storage cavern in bedded rock salts. *Environmental Earth Sciences*, 75, 800. http://dx.doi.org/10.1007/s12665-016-5611-8.

Whyatt, J., & Varley, F. (July 29-31, 2008). Catastrophic failures of underground evaporite mines. In S. S. Peng, C. Mark, G. L. Finfinger, S. C. Tadolini, A. W. Khair, K. A. Heasley & Y. Luo (Eds.), *27th International Conference on Ground Control Mining* (pp. 113-122). Morgantown, USA: West Virginia University.

Yerro, A., Corominas, J., Monells, D., & Mallorquí, J.J. (2014). Analysis of the evolution of ground movements in a low densely urban area by means of DInSAR technique. *Engineering Geology*, 170(20), 52-65. https://doi.org/10.1016/j.enggeo.12.002.

Yuan, G., Wan, J., Li, J., Li, G., Xia, Y., & Ban, F. (2021). Stability analysis of a typical two-well-horizontal saddle-shaped salt cavern. *Journal of Energy Storage*, 40, 102763. http://dx.doi.org/10.1016/j.est.2021.102763.

Zhang, G., Wang, Z., Liu, J., Li, Y., Cui, Z., Zhang, H., Wang, L., & Sui, L. (2020a). Stability of the bedded key roof above abandoned horizontal salt cavern used for underground gas storage. *Bulletin of Engineering Geology and the Environment*, 79, 4205-4219. http://dx.doi.org/10.1007/s10064-020-01830-x.

Zhang, N., Shi, X., Zhang, Y., & Shan, P. (2020b). Tightness analysis of underground natural gas and oil storage caverns with limit pillar widths in bedded rock salt. *IEEE Acces*, 8, 12130-12145. http://dx.doi.org/10.1109/ACCESS.2020.2966006.

Soils and Rocks
An International Journal of Geotechnical and Geoenvironmental Engineering
www.soilsandrocks.com
ISSN 1980-9743
ISSN-e 2675-5475

Lateritic soil deformability regarding the variation of compaction energy in the construction of pavement subgrade

Paula Taiane Pascoal[1#], Amanda Vielmo Sagrilo[1], Magnos Baroni[1], Luciano Pivoto Specht[1], Deiv idi da Silva Pereira[1]

Article

Keywords
Subgrade soil
Undisturbed samples
Resilient modulus
Permanent deformation
Repeated load triaxial tests

Abstract
The performance of the subgrade towards the main deterioration mechanisms must be considered in the pavement structure design. Thus, this paper discusses the resilient modulus and permanent deformation evaluation of a pedological horizon of a Brazilian lateritic soil deposit, comparing samples compacted in the laboratory at the three compaction energies (standard, intermediate and modified) and undisturbed samples. Physical, chemical, and mechanical characterization tests were conducted. The cyclic tests were performed in repeated load triaxial tests and according to the current Brazilian standards. Five mathematical models widely used were employed to verify the resilient modulus behavior of the sample conditions, in which the Compound and Universal models showed the best correlations. For permanent deformation, the model was used, which well-expressed the plastic behavior of the analyzed conditions. Although all cases appeared to attend the shakedown criteria, some samples did not reach the deformation rate required by the standard. As the compaction energy was increased, the resilient modulus increased, and the permanent deformation decreased. Therefore, there is a substantial modification of the material behavior by increasing the compaction.

1. Introduction

Pavement consists of a system of elastic layers with finite thicknesses, composed of varied materials intended to distribute stresses vertically and horizontally until it reaches the subgrade, which receives a portion of the stresses. Pavements must present satisfactory performance even with the appearance and accumulation of defects during the service life, which are related to loss of serviceability and bearing capacity (Yoder & Witczak, 1975; Balbo, 2007; Papagiannakis & Massad, 2008; Medina & Motta, 2015).

The proper design of a pavement by the mechanistic-empirical methodology relates the selection of materials and their thicknesses to assure that, with the repeated passage of vehicles, does not occur excessive fatigue cracking of the surface does not occur (resilient deformation) and ensure that the effects of permanent deformation associated with rutting are minimized (Cerni et al., 2012; Erlingsson et al., 2017; Nazzal et al., 2020).

For paving structures, soils go through the compaction process, which consists of reducing their void content by the action of a mechanical force, increasing shear strength and stability, and reducing deformability, permeability, and erodibility (Lambe & Whitman, 1969; Van Impe, 1989; Crispim et al., 2011; Kodikara et al., 2018). In the case of tropical soils, their performance in the field is influenced by the genesis, degree of weathering, morphological characteristics, mineralogical and chemical composition, among others. The use of these soils is feasible to pavements (Guimarães et al., 2018; Lima et al., 2020; Pascoal et al., 2021; Coutinho & Sousa, 2021).

The performance of the subgrade regarding the main pavements' deterioration mechanisms should be considered when designing by the Brazilian mechanistic-empirical design guide (Brazilian Pavement Design Method – Medina). Thus, it is necessary to obtain resilient parameters and permanent deformation, in addition to physical and chemical characterization tests, considering the peculiarities of tropical soils (Medina & Preussler, 1980; Nogami & Villibor, 1995; Camapum de Carvalho et al., 2015; Freitas et al., 2020).

Resilience is the ability of a material to not keep deformations after loads cease. The resilient parameters of soil can be obtained from the resilient modulus (*RM*) test and from the models and mathematical equations. The non-linear behavior of soils is associated with several factors, such as: soil nature and grain size composition, physical state, loading condition, histcory and state of stresses, number of repetitions of deviator stress, degree of saturation, density and

[#]Corresponding author. E-mail address: ptpascoal@hotmail.com
[1]Universidade Federal de Santa Maria, Departamento de Transportes, Santa Maria, RS, Brasil.

Submitted on September 26, 2022; Final Acceptance on May 18, 2023; Discussion open until November 30, 2023.
https://doi.org/10.28927/SR.2023.009922

moisture of compaction, compaction method, among others (Hicks & Monismith, 1971; Bayomi & Al-Sanad, 1993; Li & Selig, 1994; Guimarães et al., 2001; Ceratti et al., 2004; Buttanaporamakul et al., 2014; Soliman & Shalaby, 2013; Biswal et al., 2016; Razouki & Ibrahim, 2017; Rahman & Gassman, 2017; Bhuvaneshwari et al., 2019; Jibon et al., 2020; Tamrakar & Nazarian, 2021; Byun & Kim, 2022).

Permanent deformations (PD) are small non-recoverable deformations accumulated by the pavement throughout its service life caused by external loads cyclically applied. The PD parameters can be obtained following DNIT 179 standards (DNIT, 2018b), supported by the model proposed by Guimarães (2009). Generally, the factors that influence the permanent deformation of soils are related to stress, loading, physical state and material type (Bayomi & Al-Sanad, 1993; Núñez et al., 2011; Salour & Erlingsson, 2015; Lima et al., 2019a, b; Zago et al., 2021; Zhang et al., 2020; Ackah et al., 2020; Silva et al., 2021).

Permanent deformation has two distinct behaviors. The deformation can increase until the material's rupture, or it can increase until an equilibrium state is reached and then the increase ceases. When the permanent deformation stabilizes and the material presents only an elastic behavior, a phenomenon called shakedown occurs (Dawson & Wellner, 1999; Werkmeister et al., 2001). This investigation is important to identify if the pavement will present progressive accumulation of plastic deformation, leading to stabilization, rupture or collapse. Quian et al. (2016) emphasize that the shakedown theory is an effective way to predict the material behavior and estimate the number of loading cycles that the material can be subjected to, without excessive rutting or rupture.

This research aims to evaluate the resilient behavior, the permanent deformation and the occurrence of shakedown of tropical lateritic soil from a deposit located in Cruz Alta, state of Rio Grande do Sul (Brazil). The material was compacted in the laboratory at standard, intermediate and modified compaction energies, and comparing it with undisturbed samples, extracted from the top layer of the embankment, employed in the field at intermediate energy.

The characterization of field compaction and the comparison with laboratory compaction energies is extremely relevant, since the compaction energy is correlated to deformations by modifying the interaction between the particles, resulting in increased density of the material, improving strength and deformability. To prove this, analysis of a pavement structure with the application of different compaction conditions will be presented, using the Brazilian mechanistic-empirical design guide (MeDiNa).

2. Lateritic soil from the northwest region of the state of Rio Grande do Sul

The soil object of this research was used in road subgrade and has tropical origin and lateritic behavior. It was extracted from a soil deposit in the municipality of Cruz Alta, northwest of the state of Rio Grande do Sul, Brazil (Figure 1a), at the margins of RS-342 highway, and was used to compose the pavement subgrade. In terms of pedological and geological aspects, the studied area presents dark red latosols of medium clayey texture and quite deep, resulting from the weathering process at the upper portions of the Paraná Basin basalt effusion, Serra Geral formation (Lemos, 1973).

The soil used in the laboratory tests was collected in the pedological horizon B, the same material used in the road embankment, as shown in Figure 1b. The undisturbed

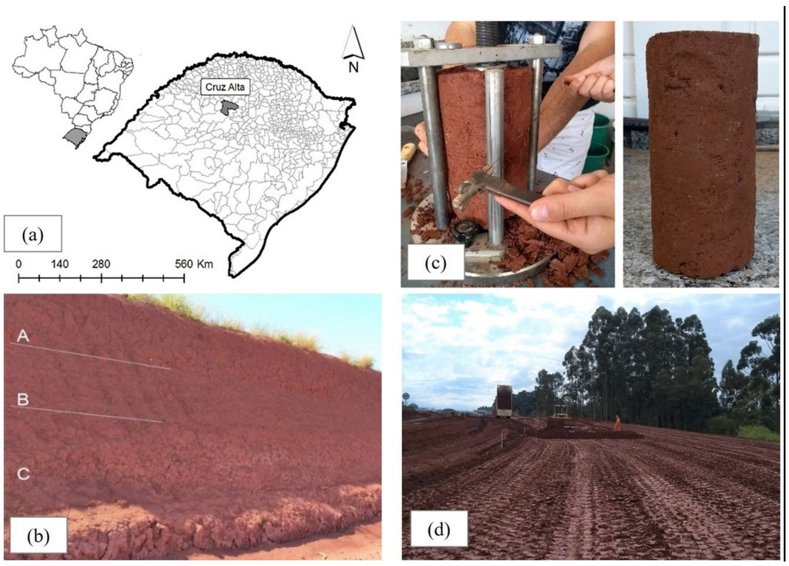

Figure 1. (a) Location of the municipality of Cruz Alta, State of Rio Grande do Sul, Brazil; (b) deposit in the margins of RS-342; (c) undisturbed sample after measures reduction process before testing; (d) road subgrade in the construction process.

samples were extracted in the top layer of the embankment (TL) and compacted in the field at intermediate energy. The extraction of the undisturbed samples from the top layer of the embankment was performed by driving cylindrical steel samplers with 150 mm diameter and 300 mm height. The procedure of extraction and reduction of the dimensions can be consulted in Pascoal et al. (2021). In Figure 1c, it is possible to observe an undisturbed sample sculpted in the dimensions ready to be tested. This procedure occurred to avoid any alteration in the structure of the specimen due to the contact between soil and sampler. Figure 1d demonstrates the road embankment in the construction phase.

In the laboratory, the soil was physically characterized by traditional Soil Mechanics tests, following the Brazilian standards (ABNT, 2016b; ABNT, 2016c; ABNT, 2016d; ABNT, 2016a). Table 1 shows the average values of the physical and chemical characterization and classification of the soil. Regarding the granulometry, about 67% of the soil particles are smaller than 0.06 mm, which means, silt and clay fractions. According to the MCT classification (DNER, 1996), the soil has clayey lateritic behavior (LG'), presenting characteristics such as high bearing capacity, low expansion, and permeability, which can provide excellent behavior for application in pavement subgrade. The comparison between MCT classification and traditional classifications of AASHTO and USCS highlights the importance of the classification methodology for tropical soils, since, according to traditional classifications, the soil under study would exhibit poor behavior towards pavement structures.

Still referring to Table 1, the presence of iron hydroxide and aluminum hydroxide, evidenced by the X-Ray Fluorescence test, is consistent with the MCT classification and the physical characteristics of soils with lateritic behavior. Also, according to the chemical analysis, the soil presented low organic matter in its composition and cation exchange capacity (CEC) lower than 6, characterizing it as clay of low activity. The presence of aluminum, higher clay content and CEC indicate the presence of the mineral kaolinite (Camapum de Carvalho et al., 2015).

As shown in Table 1, note that as the compaction energy is increased, the optimum moisture content (OMC) is reduced and there is an increase in the value of maximum dry density (MDD) of the soil. As for the undisturbed samples, the OMC and MDD values were obtained from the bulk density test using the cutting cylinder method, performed when the samples were collected. All details of the experimental tests can be consulted in Pascoal et al. (2021).

3. Methodology

The experimental program of this investigation was divided into five stages: a collection of disturbed and undisturbed samples; physical, chemical, and mechanical characterization tests; triaxial tests of repeated loads for *RM* and PD, with an analysis of five models to investigate the resilient behavior and with the model by Guimarães (2009) to obtain the permanent deformation parameters; investigation of shakedown based on the model developed by Dawson & Wellner (1999); and finally, analysis of a pavement structure with the application of different compaction conditions, using the Brazilian mechanistic-empirical design guide (MeDiNa).

Repeated load triaxial tests (RLT) were performed on samples with 100 mm diameter and 200 mm height. The equipment used for the RL and PD tests was the triaxial repeated load equipment, which has the purpose of reproducing in the laboratory the cyclic loading conditions of traffic loads on the pavement structure. The elastic deformations are measured by two Linear Variable Differential Transformer (LVDT) transducers, allowing readings up to 5 mm and used

Table 1. Physical and chemical characterization of Cruz Alta's soil.

Physical characterization		Chemical analysis and Classifications	
Liquid Limit, w_L (%)	55	MCT - Brazilian Classification	LG'
Plastic Limit, w_P (%)	44	AASHTO Classification	A-7-6
Plasticity Index, *PI* (%)	11	USCS Classification	MH
Specific Weight, γ (kN/m^3)	27.8	CEC	1.8
% coarse sand (0.6-2.0mm)	0	Basic cations Ca/K/Mg (Cmol$_c$dm^3)	0.3/0.02/0.4
% medium sand (0.2-0.6mm)	8	Saturation - Al/bases (%)	55.6/9.2
% fine sand (0.06-0.2mm)	25	Organic matter (%)	0.2
% silt (2μm-0.06mm)	26	pH	5.8
% clay (%< 2μm)	41	EDXRF - Most frequent chemical components	Fe2O3/SiO2/ Al2O3/TiO2
Compaction tests			
Energy / Condition		MDD (kg/m^3)	OMC (%)
Standard Energy (SE)		1550	28.90
Intermediate Energy (IE)		1625	25.60
Modified Energy (ME)		1652	22.60
Undisturbed Samples (TL)		1645	21.52

Note: Results of granulometry refer only to analysis with dispersant.

inside the triaxial chamber, supported under a top cap that receives the action of the deviator stress through a load cell and a piston. To study the plastic deformation, the equipment has a Rectilinear Displacement Transducer (RDT) that enables readings up to 25 mm.

Thus, the disturbed samples of horizon B were compacted at standard, intermediate, and modified energies, while the undisturbed samples of TL, compacted in the field at intermediate energy, had their dimensions reduced to the required size. The criterion for considering the sample moldings valid was the maximum variation of ± 0.5% about the OMC, as established by DNIT 134 and DNIT 179 standards (DNIT, 2018a; DNIT, 2018b). These standards do not determine an acceptable variation for MDD, thus the limit of ± 1.0% was adopted.

The stiffness of the compacted soil samples at the three energies and the undisturbed samples were evaluated by testing the resilient modulus (DNIT, 2018a). Thus, after the conditioning phase 12 pairs of deviator and confining stresses were applied, according to the standard. The test was performed in triplicate for each of the four specimen conditions, at a repeated load application frequency of 1 Hz with a 0.1 second load pulse and 0.9 seconds of rest.

The plastic deformation and subsequent obtaining of permanent deformation parameters were considered the precepts of the DNIT (2018b). After the conditioning procedure, each specimen was subjected to at least 150,000 cycles of a pair of confining and deviator stresses at a frequency of 2 Hz. Testing was performed at the following stress conditions (confining × deviator): 0.04 × 0.04 MPa, 0.04 × 0.12 MPa, 0.08 × 0.08 MPa, 0.08 × 0.24 MPa, 0.12 × 0.24 MPa e 0.12 × 0.36 MPa (Lima et al., 2019a).

Table 2 shows the mathematical models for obtaining the resilient parameters that were considered for analyzing the results, as well as the Guimarães' model used to acquire the permanent deformation parameters (Guimarães et al., 2018; Lima et al., 2020). The criterion used to evaluate the models was the best fit of the coefficient of determination (R^2).

Non-linear multiple analysis were performed using the method of minimizing the sum of squares of residuals, using the software Statistica v.10. Although there are other models for permanent deformation in the literature (Barksdale, 1972; Monismith et al., 1975; Tseng & Lytton, 1989), it was decided to use only the model of Guimarães (2009), since the current Brazilian regulations take into account the use of this model, besides it presents good correlations to the characterization and peculiarities of tropical soils (Guimarães et al., 2018; Lima et al., 2019b; Lima et al., 2020; Lima et al., 2021; Zago et al., 2021).

Then, the occurrence of shakedown was identified based on the model developed by Dawson & Wellner (1999). The results of permanent deformation were analyzed to relate the accumulated vertical permanent deformation to the rate of increase of deformation at each load cycle, following the classification of levels A (shakedown), B (plastic creep), C (incremental collapse) or AB (significant initial deformations and accommodation in the sequence).

With the parameters from the Guimarães' model and considering the compound model for resilient modulus, simulations of a typical road pavement structure were performed using the MeDiNa v 1.1.5.0 program. For this, the following conditions were considered:

- Medium traffic (*N*: $5x10^6$) e heavy traffic ($1x10^7$) (Ceratti et al., 2015);
- Primary Arterial System - maximum of 30% of cracked area and 10 mm of permanent deformation to the end of pavement life;
- Standard road axis of 8.2 tf, tire pressure 0.56 MPa;
- Project period of 10 years, average growth rate of 3.0%.

The structure considered in the analysis is composed of 5 cm asphalt concrete pavement (MeDiNa default, Class 2, RM: 6743 MPa) and of 15 cm granular material of base (MeDiNa default, RM: 381 MPa) and subgrade with variable conditions, considering the four conditions evaluated in this research.

Table 2. Models were used to obtain the resilient parameters and permanent deformation.

Properties	Models	Equation
Resilient Modulus	Confining Stress (Biarez, 1962)	$RM = k_1.\sigma_3^{k_2}$
	Stress Invariant	$RM = k_1.\theta^{k_2}$
	Deviator Stress (Svenson, 1980)	$RM = k_1.\sigma_d^{k_2}$
	Compound (Pezo et al., 1992)	$RM = k_1.\sigma_3^{k_2}.\sigma_d^{k_3}$
	Universal (AASHTO, 2004)	$RM = k_1.\rho_a\left(\theta / \rho a\right)^{k_2}.\left(\tau_{oct} / \rho a + 1\right)^{k_3}$
Permanent Deformation	Guimarães (2009)	$\varepsilon_{p(\%)} = \psi_1\left(\sigma_3 / \rho a\right)^{\psi_2}.\left(\sigma_d / \rho a\right)^{\psi_3}.N^{\psi_4}$

Where: *RM*: resilient modulus; σ_3: confining stress; σ_d: deviator stress; θ: principal stress; τ_{oct}: octahedral stress; ρ_a: atmospheric pressure; k_1, k_2 and k_3: resilient parameters experimentally determined; ε_p (%): plastic specific deformation; ψ_1, ψ_2, ψ_3, ψ_4,,,: parameters experimentally determined; *N*: number of load application cycles.

4. Results

4.1 Resilient modulus

The resilient modulus results were analysed by five *RM* prediction models. For this, multiple non-linear regression of the results for each test condition was performed. Each sample tested results in 12 values of resilient modulus, one for each pair of stresses. Since the test was conducted in triplicate, there are 36 values of *RM* for each sample condition. Table 3 shows the average resilient parameters of this set of 36 resilient modulus values for each sample condition.

The models that best represented the four groups of samples were the Universal (AASHTO, 2004) and the Compound (Pezo et al., 1992), both models that consider the confining and deviator stresses act on the samples. Regarding the Compound model, as the deviator stress increases, the *RM* decreases; The opposite happens for the confining stress, which, when increased, increases the *RM* value. The Biarez (1962) and Stress Invariant models showed similar behavior, because for low energies, they did not show good correlations, while for modified energy, the R^2 values were high. Svenson's model (1980) was found to be unsatisfactory for all sample conditions. Figure 2 shows the modelling of the resilient modulus for the four test conditions for confining stress and for deviator stress.

The increase in *RM* as a function of compaction energy is evident, as shown in Figure 3, which presents results of average, minimum and maximum *RM* for the Compound model. Considering the average resilient modulus, a 60.2% gain of RM was observed for samples compacted at intermediate energy compared to those compacted at standard energy.

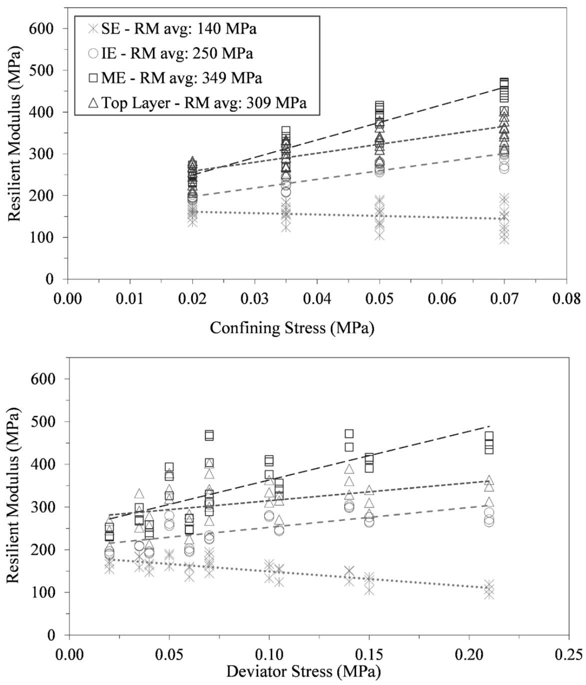

Figure 2. Comparison between deviator stress and confining stress for the four resilient modulus conditions.

Table 3. Resilient parameters for five mathematical models.

Condition	Model	k_1	k_2	k_3	R^2	*RM* avg (MPa)
Standard Energy	Confining Stress	109.76	-0.08	-	0.05	140
	Stress Invariant	122.03	-0.14	-	0.20	153
	Deviator Stress	102.98	-0.15	-	0.41	153
	Compound	144.30	0.18	-0.24	0.55	153
	Universal	391.49	0.28	-1.45	0.74	138
Intermediate Energy	Confining Stress	751.38	0.34	-	0.90	250
	Stress Invariant	397.98	0.30	-	0.80	247
	Deviator Stress	387.90	0.17	-	0.48	247
	Compound	739.20	0.34	0.00	0.90	247
	Universal	727.29	0.53	-0.69	0.93	247
Modified Energy	Confining Stress	1724.20	0.50	-	0.91	349
	Stress Invariant	721.03	0.46	-	0.89	349
	Deviator Stress	729.83	0.29	-	0.62	349
	Compound	1640.16	0.43	0.08	0.93	348
	Universal	1185.26	0.65	-0.55	0.94	349
Undisturbed Samples - TL	Confining Stress	775.59	0.29	-	0.68	309
	Stress Invariant	454.16	0.24	-	0.55	309
	Deviator Stress	433.04	0.13	-	0.28	309
	Compound	792.87	0.32	-0.03	0.69	309
	Universal	875.11	0.48	-0.76	0.72	309

With the addition of standard to modified compaction, the resilience gain became 127%. If the intermediate and modified energy are compared, an increase of 41.8% is noted. The set of undisturbed samples TL, compacted in the field at intermediate energy, presented results above expectations, since their *RM* were higher than the samples molded at intermediate energy in the laboratory, thus they were close to those obtained by the modified energy. The material was compacted at a lower than OMC, evidencing the suction effect. In summary, increasing the compaction energy reduces the voids content of the samples, increasing the *RM*, this typical behavior can result in less deformable pavements, contributing to reducing stresses in the upper layers.

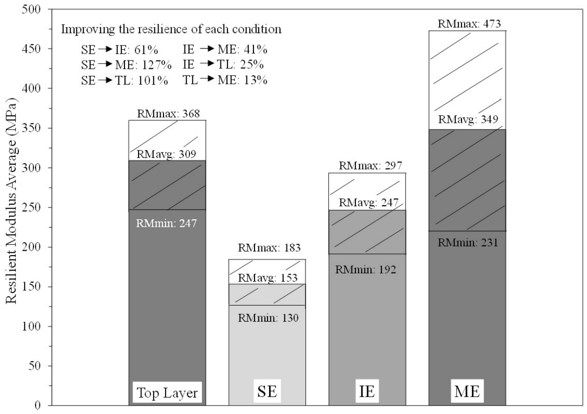

Figure 3. Resilience improvement as the compaction energy increases from average *RM*.

4.2 Permanent deformation

The permanent deformation tests were conducted for the three compaction energies and for the undisturbed samples. In Figure 4 it is possible to observe the permanent deformation accumulated versus the number of cycles of load application (150,000 cycles) for the four sample conditions. It is clear that as the stresses increased, the deformations also increased and, as the number of cycles go up, the deformations tend to stabilize. Higher stresses are generally the result of pavements with low thickness where traffic stresses are closer to the subgrade.

As expected, in all cases, the largest deformation occurred for the largest pair of stresses (σ_3: 120 and σ_d: 360 kPa), due to the magnitude and to the fact that the higher the ratio σ_1/σ_3, the larger the deformations. As the deviator stress is raised,

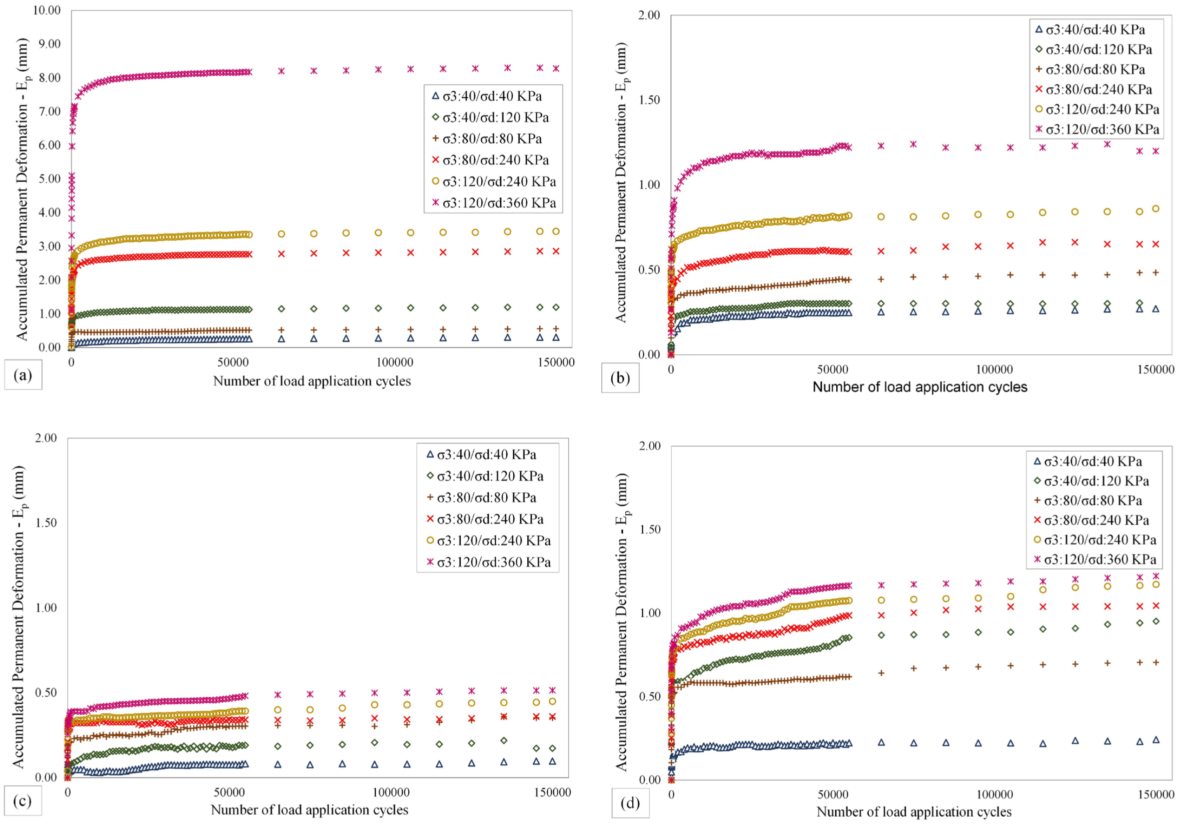

Figure 4. Accumulated permanent deformation of (a) standard energy, (b) intermediate energy, (c) modified energy and (d) undisturbed from top layer.

the permanent deformation is increased. As cycles increase, the rate of PD addition decreases. The final deformation of the specimen subjected to the highest pair of stresses was: 0.83 cm at standard energy, 0.12 cm at intermediate energy, 0.05 cm at modified energy, and 0.13 cm in the TL (compacted in the field at intermediate energy). Unlike the *RM* result, in this case, regarding accumulated deformations, the undisturbed samples behaved similarly to the samples molded in the laboratory at intermediate energy, reinforcing the need to investigate the stiffness and resistance to plastic stress separately.

In Figure 4, a similar behavior is observed in all test conditions, where the samples show a tendency to the accommodation of permanent deformation, fitting in Type I or Type II, according to the considerations of the DNIT 179 standard (2018b). Type I and II refer to materials that tend to stabilize PD with a number of loading cycles. The difference between them is that Type II presents a high value of cumulative permanent displacement before accommodation. Guimarães et al. (2001) explains that the rate of change of PD can be null with increasing cycles of loading or tends to decrease greatly when the material is close to accommodation.

After a certain number of cycles of load application, the deformations tend to become constant, presenting small variations. To investigate this phenomenon, Figure 5 shows the total deformation portion for each specimen at 1,000, 10,000, 50,000, 100,000, and 150,000 cycles of repeated loading.

Regarding the samples compacted at standard energy, except for the sample submitted to the lowest pair of stresses, at the end of the initial 1,000 cycles, the specimen had already deformed 75% to 85% of its final deformation. By the time it reached 10,000 cycles of repeated loading, the accumulated permanent deformation was already approaching 90%. A similar fact occurred for the specimens compacted at intermediate energy, which at 1,000 cycles of PD testing reached 67% to

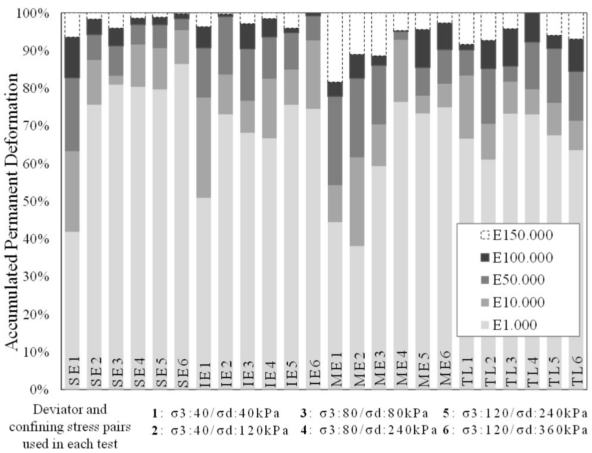

Figure 5. Part of accumulated permanent deformation as cycles increase.

76% of total accumulated deformation, and upon reaching 50,000 cycles, the samples showed more than 90% to total sample deformation.

For the samples compacted at the modified energy, if compared to the other energies, the PD rate associated with the initial PD of the samples was lower, which occurred due to the high compaction energy applied to these specimens. However, when reaching 50,000 cycles, the set of modified samples presented from 78% to 95% of the total deformation of each sample. The deformations in the initial cycles of this set of samples were smaller than the others, given the higher stiffness.

The undisturbed samples from the TL showed similar behavior to the samples compacted in the laboratory at intermediate energy. At the end of 50,000 cycles, they had already deformed 85% to 92% of the total PD. In summary, it is concluded that the undisturbed samples have behavior similar to the samples compacted in the laboratory at intermediate energy towards permanent deformation.

The data from the sets of each compaction energy and undisturbed samples were submitted to non-linear regression in order to obtain the parameters of the model by Guimarães (2009), presented in Table 2. Table 4 summarizes the parameters obtained considering the value of ρ_a equal to 0.1 MPa, considering all permanent deformations with their respective pairs of stress and load repetition cycles. The values of the coefficients of determination show that the model is adequate for the deformability of the materials under study.

With the permanent deformation values and the load application cycles, it was possible to obtain the permanent deformation variation rate and plot the graphs to analyze the occurrence of shakedown conditions in the soil, as presented in Figure 6. The material can be considered in shakedown state if the increase rate of PD reaches the order of 10^{-7}x10^{-3} meters per load application cycle.

Although all cases appeared to go into shakedown, most samples did not reach the PD rate required by the DNIT 179 standard (2018b). Possibly, with the application of a higher number of load repetition cycles, all samples would reach the rate of 10^{-7}x10^{-3} meters per cycle. However, it is not considered necessary to apply a higher number of cycles, since about 90% of the total deformation occurred in the 50,000 cycles, as shown in Figure 6.

Except for a sample of standard energy, which was subjected to the highest pair of stresses, all samples subjected to the PD test showed behavior A indicating that this layer would not contribute to the subsidence in the pavement layer (Dawson & Wellner, 1999). The sample considered as an exception fits the AB behavior (Guimarães, 2009), which encompasses materials that present significant initial deformations, followed by plastic accommodation.

It is evident that with the increase of the compaction energy, there is a substantial modification of the material's behavior when subjected to cyclic loading, and this resource can be applied more often to optimize pavement designs,

Table 4. Parameters of permanent deformation by the Guimarães model (2009).

Condition	Ψ_1	Ψ_2	Ψ_3	Ψ_4	R^2
Standard Energy	0.089	0.225	2.161	0.095	0.97
Intermediate Energy	0.083	0.699	0.517	0.103	0.93
Modified Energy	0.064	0.663	0.027	0.078	0.89
Undisturbed sample - TL	0.115	-0.042	0.516	0.092	0.87

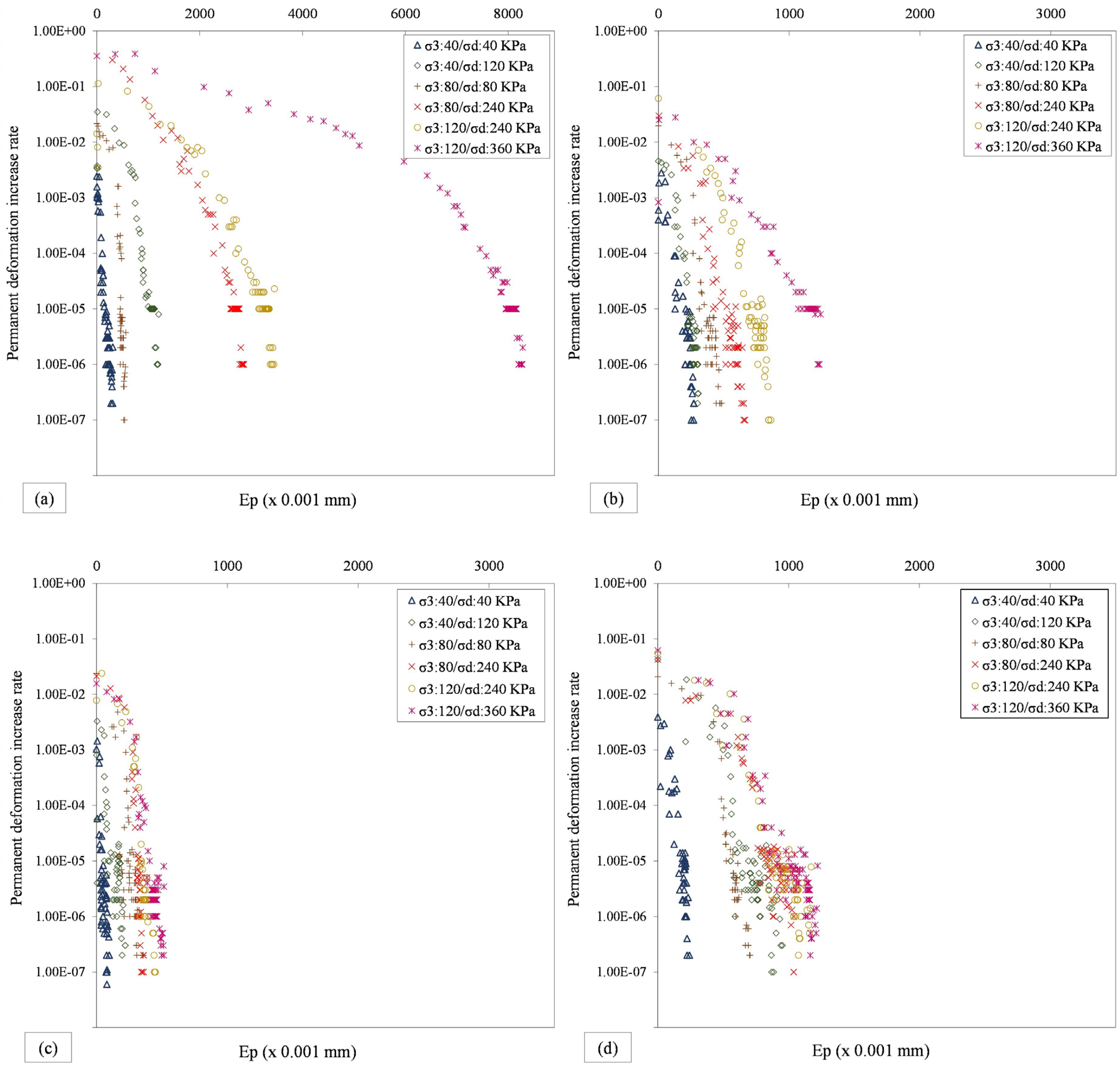

Figure 6. Shakedown occurrence research according to Dawson & Wellner (1999) of the (a) standard energy, (b) intermediate energy, (c) modified energy and (d) undisturbed of top layer.

if field compaction limitations and financial aspects are observed, which deserve specific studies.

4.3 Analysis with de Brazilian pavement design method

When analysed the application of different compaction energies of the subgrade, when dealing with cracked area, the thicknesses of the asphalt concrete pavement and granular base were fixed, to demonstrate the performance of soil conditions over the period of 10 years. The cracked area decreases as the compaction energy increases, regardless of the number of stresses on the structure (Figure 7). The rutting caused by permanent deformations decreases considerably with increasing compaction energy. Within the rutting value is encompassed the behavior of the subgrade and the granular material used in the base.

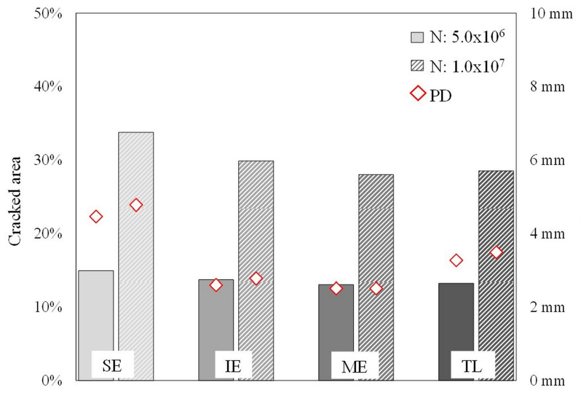

Figure 7. Comparison of four structural performance in the face of permanent deformation (rutting) and fatigue (cracked area) submitted to two *N*.

By increasing the compaction from SE to ME, the rutting throughout the design period, decreases about 43% and 48% of the permanent deformation for N of $5.0\text{x}10^6$ and $1.0\text{x}10^7$, respectively. The evaluation of the undisturbed TL samples shows that the analysed condition is similar to the conditions reproduced in the laboratory.

By AASHTO classification, this fine-grained soil would present poor to poor behavior. However, the feasibility of its use, regardless of the compaction energy, was proven from this analysis, corroborating the performance prediction previously obtained by the MCT classification.

5. Final considerations

This investigation aimed to perform the elastic and plastic characterization of a tropical and lateritic soil deposit, compacted at the three energies, and to compare these with the results of undisturbed samples from the top layer of an embankment compacted with soil from the same deposit. The comparison with undeformed samples to evaluate if what was reproduced in the laboratory is really representative of the field, in view of the importance of investigating the deformability and characterization of soils at the new Brazilian mechanistic-empirical design guide. The main conclusions were:

- According to the MCT classification, the deposit presents clayey soil with lateritic behavior (LG'). Thus, this material can be considered good for application in pavement structures, since it is well executed. Regarding the chemical characterization from the X-ray fluorescence test and chemical analysis, it was found that there is a predominance of silicon dioxide, iron oxide and aluminum oxide, which corroborates the results of the MCT classification.
- The moisture content of the undisturbed samples, compacted at the intermediate energy in the field, was close to the optimum moisture content obtained in the laboratory at the modified energy, while the maximum dry density has a value similar to the intermediate energy.
- Regarding the resilient behavior of the soils, the Compound and Universal models presented the best correlations. The increase of the *RM* with the elevation of the compaction energy was relevant. The resilient behavior of the samples compacted in the field at intermediate energy was close to the samples compacted at modified energy.
- Compaction energy is correlated with deformation. As the energy is increased from standard to intermediate or modified energy, there is a gain in the value of *RM* and a reduction in PD. With this increase in energy, the confining stress begins to influence the behavior of the soil more, something that does not occur when compacted at standard energy.
- Regarding permanent deformation, it was found that the analyzed materials tend to accommodate PD, fitting into Type I or Type II. The model of Guimarães (2009) proved to be appropriate to the deformability of the materials in question, showing good correlations. When the occurrence of shakedown was evaluated, it was found that although all cases appeared to enter plastic accommodation, some samples did not reach the PD rate required by Brazilian standards. Thus, the samples presented behavior A almost in their total, indicating that there will be no significant contributions by the soil to surface rutting.
- It is evident that increasing the energy modifies the behavior of the material, and this resource can be applied more often in pavement projects, provided that field compaction limitations and the financial aspects are observed, which deserve specific studies. The simulations by MeDiNa for two different *N* proved the effectiveness of varying the compaction energy, in relation to the performance, especially, of rutting.

Acknowledgements

The authors are grateful to the ANP/PETROBRAS, *Conselho Nacional de Desenvolvimento Científico e Tecnológico* (CNPq), and *Universidade Federal de Santa Maria* for their support and the reviewers for their valuable contributions.

Declaration of interest

The authors have no conflicts of interest to declare. All co-authors have observed and affirmed the contents of the paper and there is no financial interest to report.

Authors' contributions

Paula Taiane Pascoal: conceptualization, data curation, visualization, methodology, and experimental procedures, writing – original draft, review & editing. Amanda Vielmo Sagrilo: validation, experimental procedures, writing – review & editing, validation, methodology, and experimental procedures writing – review & editing. Magnos Baroni: supervision, validation, writing – review & editing. Luciano Pivoto Specht: supervision, funding acquisition, project administration, writing – review. Deividi da Silva Pereira: funding acquisition, project administration, writing – review.

Data availability

Data is available upon request to the corresponding author.

List of symbols

k_1, k_2, k_3	resilient parameters experimentally determined
N	number of loading cycles
PD	permanent deformation
R^2	coefficient of determination
RM	resilient modulus
RLT	repeated load tests
ε_p	specific permanent deformation
θ	principal stress
ρ_a	atmospheric pressure
σ_3	confining stress
σ_d	deviator stress
σ_d / σ_3	stress ratio
τ_{oct}	octahedral stress
ψ_n	permanent deformation parameters experimentally determined

References

AASHTO NCHRP 1-37A. (2004). *Guide for mechanistic-empirical design of new and rehabilitated pavement structures - final report*. AASHTO - American Association of State Highway and Transportation Officials, Washington, DC.

ABNT NBR 6459. (2016a). *Solo - determinação do limite de liquidez*. ABNT - Associação Brasileira de Normas Técnicas, Rio de Janeiro, RJ (in Portuguese).

ABNT NBR 6548. (2016b). *Grãos de pedregulho retidos na peneira de abertura 4,8mm - determinação da massa específica, da massa específica aparente e da absorção de água*. ABNT - Associação Brasileira de Normas Técnicas, Rio de Janeiro, RJ (in Portuguese).

ABNT NBR 7180. (2016c). *Determinação do limite de plasticidade*. ABNT - Associação Brasileira de Normas Técnicas, Rio de Janeiro, RJ (in Portuguese).

ABNT NBR 7181. (2016d). *Solo - análise granulométrica*. ABNT - Associação Brasileira de Normas Técnicas, Rio de Janeiro, RJ (in Portuguese).

Ackah, F.S., Zhuoochen, N., & Huaiping, F. (2020). Effect of wetting and drying on the resilient modulus and permanent strain of a sandy clay by RLTT. *International Journal of Pavement Research and Technology*, 14, 336-377. http://dx.doi.org/10.1007/s42947-020-0067-3.

Balbo, J.T. (2007). *Pavimentação asfáltica: materiais, projetos e restauração*. São Paulo: Oficina de Textos (in Portuguese).

Buttanaporamakul, P., Rout, R.K., Puppala, A., & Pedarla, A. (February 23-26, 2014). Resilient behaviors of compacted and unsaturated subgrade materials. In American Society of Civil Engineers (Org.), *Geo-Congress 2014: Geo-characterization and Modeling for Sustainability* (pp. 1396-1405). Reston, VA, United States: American Society of Civil Engineers.

Barksdale, R.D. (September 11-15, 1972). Laboratory evaluation of rutting in base course materials. In National Academies of Sciences, Engineering, and Medicine (Org.), *Third International Conference on the Structural Design of Asphalt Pavements* (pp. 161-174). Washington, D.C., United States: National Academies of Sciences, Engineering, and Medicine.

Bayomi, F.M., & Al-Sanad, H.A. (1993). Deformation characteristics of subgrade soils in Kuwait. *Transportation Research Record*, 1406, 77-87.

Bhuvaneshwari, S., Robinson, R.G., & Gandhi, S.R. (2019). Resilient modulus of lime treated expansive soil. *Geotechnical and Geological Engineering*, 37, 305-315. http://dx.doi.org/10.1007/s10706-018-0610-z.

Biarez, J. (1962). *Contribution a l'étude des proprietes mecaniques des sols et des materiaux pulverents* [Doctoral thesis]. École Centrale Paris.

Biswal, D.R., Sahoo, U.C., & Dash, S.R. (2016). Characterization of granular lateritic soils as pavement material. *Transportation Geotechnics*, 6, 108-122. http://dx.doi.org/10.1016/j.trgeo.2015.10.005.

Byun, Y.H., & Kim, D.J. (2022). In-situ modulus detector for subgrade characterization. *The International Journal of Pavement Engineering*, 23(2), 297-307. http://dx.doi.org/10.1080/10298436.2020.1743291.

Camapum de Carvalho, J., Rezende, L.R., Cardoso, F.B.F., Lucena, L.C.F.L., Guimarães, R.C., & Valencia, Y.G. (2015). Tropical soils for highway construction: peculiarities and considerations. *Transportation Geotechnics*, 5, 3-19. http://dx.doi.org/10.1016/j.trgeo.2015.10.004.

Ceratti, J.A., Bernucci, L.B., & Soares, J.B. (2015). *Utilização de ligantes asfálticos em serviços de pavimentação*. Rio de Janeiro: Abeda (in Portuguese).

Ceratti, J.A., Gehling, W.Y.Y., & Núnez, W.P. (2004). Seasonal variations of a subgrade soil resilient modulus in Southern Brazil. *Transportation Research Record*, 1871, 165-173. http://dx.doi.org/10.3141/1874-18.

Cerni, G., Cardone, F., Virgili, A., & Camilli, S. (2012). Characterization of permanent deformation behaviour of unbound granular materials under repeated triaxial loading. *Construction & Building Materials*, 28, 79-89. http://dx.doi.org/10.1016/j.conbuildmat.2011.07.066.

Coutinho, R.Q., & Sousa, M.A.S. (2021). Analysis of the applicability of USCS, TRB and MCT classification systems to the tropical soils of Pernambuco, Brazil, for use in road paving. In E. Tutumluer, S. Nazarian, I. Al-Qadi & I.I.A. Qamhia (Eds.), *Advances in transportation geotechnics IV: proceedings of the 4th International Conference on Transportation Geotechnics volume 1* (pp. 373-385). Cham: Springer. https://doi.org/10.1007/978-3-030-77230-7_29.

Crispim, F.A., Lima, D.C., Shaefer, C.E.G.R., Silva, C.H.C., Carvalho, C.C.B., Barbosa, P.S.A., & Brandão, E.H. (2011). The influence of laboratory compaction methods on soil structure: mechanical and micromorphological analysis. *Soils and Rocks*, 34, 91-98.

Dawson, A.R., & Wellner, F. (1999). *Plastic behavior of granular materials. Report ARC project 933. Reference PRG 99014*. Nottingham: University of Nottingham.

DNER CLA 259. (1996). *Classificação de solos tropicais para finalidades rodoviárias utilizando corpos-de-prova compactados em equipamento miniatura*. DNER - Departamento Nacional de Estradas de Rodagem, Brasília, DF (in Portuguese).

DNIT 134. (2018a). *Pavimentação - solos - determinação do modulo de resiliência - método do ensaio*. DNIT - Departamento Nacional de Infraestrutura de Transportes, Brasília, DF (in Portuguese).

DNIT 179. (2018b). *Pavimentação - solos - determinação da deformação permanente - instrução do ensaio*. DNIT - Departamento Nacional de Infraestrutura de Transportes, Brasília, DF (in Portuguese).

Erlingsson, S., Rahman, S., & Farhad, S. (2017). Characteristic of unbound granular materials and subgrades based on multistage RLT testing. *Transportation Geotechnics*, 13, 28-42. http://dx.doi.org/10.1016/j.trgeo.2017.08.009.

Freitas, J.B., Rezende, L.R., & Gitirana Junior, G.F.N. (2020). Prediction of the resilient modulus of two tropical subgrade soils considering unsaturated conditions. *Engineering Geology*, 270, 105580. http://dx.doi.org/10.1016/j.enggeo.2020.105580.

Guimarães, A.C.R. (2009). *Um método mecanístico-empírico para a previsão da deformação permanente em solos tropicais constituintes de pavimentos* [Doctoral thesis, Federal University of Rio de Janeiro]. Universidade Federal do Rio de Janeiro (in Portuguese).

Guimarães, A.C.R., Motta, L.M.G., & Castro, C.D. (2018). Permanent deformation parameters of fine - grained tropical soils. *Road Materials and Pavement Design*, 20(7), 1664-1681. http://dx.doi.org/10.1080/14680629.2018.1473283.

Guimarães, A.C.R., Motta, L.M.G., & Medina, J. (2001). Estudo de deformação permanente em solo típico de subleito de rodovia brasileira. In ABPv (Ed.), *33ª Reunião Anual de Pavimentação* (pp. 336-354). Florianópolis: Editora ABPv. (in Portuguese).

Hicks, R.G., & Monismith, C.L. (1971). Factors influencing the resilient properties of granular materials. *Transportation Research Board*, 345, 15-31. Retrieved in May 18, 2023, from http://onlinepubs.trb.org/Onlinepubs/hrr/1971/345/345-002.pdf

Jibon, M., Mishra, D., & Kassem, E. (2020). Laboratory characterization of fine-grained soils for pavement ME design implementation in Idaho. *Transportation Geotechnics*, 25, 100395. http://dx.doi.org/10.1016/j.trgeo.2020.100395.

Kodikara, J., Islam, T., & Sountharajah, A. (2018). Review of soil compaction: history and recent developments. *Transportation Geotechnics*, 17, 24-34. http://dx.doi.org/10.1016/j.trgeo.2018.09.006.

Lambe, T.W., & Whitman, R.V. (1969). *Soil mechanics*. New York: John Wiley.

Lemos, R.C. (1973). *Levantamento de reconhecimento dos solos do Rio Grande do Sul*. Rio de Janeiro: Embrapa (in Portuguese).

Li, D., & Selig, E. (1994). Resilient modulus for fine-grained subgrade soil. *Journal of Geotechnical Engineering*, 120, 939-957. http://dx.doi.org/10.1061/(ASCE)0733-9410(1994)120:6(939).

Lima, C.D.A., Motta, L.M.G., & Aragão, F.T.S. (2019a). Análise das tensões aplicadas nos ensaios de deformação permanente de solos e britas para o dimensionamento mecanístico-empírico de pavimentos. In Associação Nacional de Pesquisa e Ensino em Transportes (Org.), *33º Congresso de Pesquisa e Ensino em Transportes da ANPET* (pp. 1222-1233). Rio de Janeiro, Brazil: ANPET (in Portuguese).

Lima, C.D.A., Motta, L.M.G., & Aragão, F.T.S. (2019b). Effects of compaction moisture content on permanent deformation of soils subjected to repeated triaxial load tests. *Transportation Research Record*, 2673(2), 466-476. https://doi.org/10.1177/0361198118825124.

Lima, C.D.A., Motta, L.M.G., & Aragão, F.T.S. (2021). A permanent deformation predictive model for fine tropical soils considering the effects of the compaction moisture content on material selection. *Transportation Geotechnics*, 28, 100534. http://dx.doi.org/10.1016/j.trgeo.2021.100534.

Lima, C.D.A., Motta, L.M.G., Aragão, F.T.S., & Guimarães, A.C.R. (2020). Mechanical characterization of fine-grained lateritic soils for mechanistic-empirical flexible pavement design. *Journal of Testing and Evaluation*, 48(1), 1-17. http://dx.doi.org/10.1520/JTE20180890.

Medina, J., & Motta, L.M.G. (2015). *Mecânica dos pavimentos*. Rio de Janeiro: Editora Interciência (638 p.) (in Portuguese).

Medina, J., & Preussler, E.S. (1980). Características resilientes de solos em estudos de pavimentos. *Solos e Rochas*, 3, 3-26 (in Portuguese).

Monismith, C.L., Ogawa, N., & Freeme, C.R. (1975). Permanent deformation characteristics of subgrade soils due to repeated loading. *Transportation Research Record*, 537, 1-17.

Nazzal, M.D., Mohammad, L.N., & Austin, A. (2020). Evaluating laboratory tests for use in specifications for unbound base course materials. *Journal of Materials in Civil Engineering*, 32(4), 1-8. http://dx.doi.org/10.1061/(ASCE)MT.1943-5533.0003042.

Nogami, J.S., & Villibor, D.F. (1995). *Pavimentação de baixo custo com solos lateríticos*. São Paulo: Villibor.

Núñez, W.P., Ceratti, J.A.P., Bressani, L.A., Pinheiro, R.J.B., Peraça, V., & Nogueira, M.L. (2011). Rational approach to the evaluation of soils for low-volume roads. *Transportation Research Record*, 2205, 73-78. http://dx.doi.org/10.3141/2205-10.

Papagiannakis, A.T.E., & Massad, E.A. (2008). *Pavement design and materials*. Hoboken: John Wiley & Sons.

Pascoal, P.T., Sagrilo, A.V., Baroni, M., Specht, L.P., & Pereira, D.S. (2021). Evaluation of the influence of compaction energy on the resilient behavior of lateritic soil in the field and laboratory. *Soils and Rocks*, 44(4), 1-14. http://dx.doi.org/10.28927/SR.2021.071321.

Pezo, R.F., Carlos, G., Hudson, W.R., & Stokoe II, K.H. (1992). *Development of reliable resilient modulus test for subgrade and non-granular subbase materials for use in routine pavement design*. Retrieved in May 18, 2023, from https://trid.trb.org/view/369153

Quian, J., Wang, Y., Lin, Z., Liu, Y., & Su, T. (2016). Dynamic shakedown analysis of flexible pavement under traffic moving loading. *Procedia Engineering*, 143, 1293-1300.

Rahman, M.M., & Gassman, S.L. (2017). Effect of resilient modulus of undisturbed subgrade soils on pavement rutting. *International Journal of Geotechnical Engineering*, 13, 152-161. http://dx.doi.org/10.1080/19386362.2017.1328773.

Razouki, S.S., & Ibrahim, A.N. (2017). Improving the resilient modulus of a gypsum sand roadbed soil by increased compaction. *The International Journal of Pavement Engineering*, 20(4), 432-438. http://dx.doi.org/10.1080/10298436.2017.1309190.

Salour, F., & Erlingsson, S. (2015). Permanent deformation characteristics of silty sand subgrades from multistage RLT tests. *International Journal of Pavement*, 18, 236-246. http://dx.doi.org/10.1080/10298436.2015.1065991.

Silva, M.D., Ribeiro, M.M.P., Furlan, A.P., & Fabbri, G.T.P. (2021). Effect of compaction water content and stress ratio on permanent deformation of a subgrade lateritic soil. *Transportation Geotechnics*, 26, 100443. http://dx.doi.org/10.1016/j.trgeo.2020.100443.

Soliman, H., & Shalaby, A. (2013). Characterising the elastic behaviour of fine-grained subgrade soils under traffic loading. *International Journal of Pavement*, 15, 698-707. http://dx.doi.org/10.1080/10298436.2013.857773.

Svenson, M. (1980). *Ensaios triaxiais dinâmicos de solos argilosos* [Master's dissertation]. Universidade Federal do Rio de Janeiro (in Portuguese).

Tamrakar, P., & Nazarian, S. (2021). Moisture effects on moduli of pavement bases. *The International Journal of Pavement Engineering*, 22(11), 1410-1422. http://dx.doi.org/10.1080/10298436.2019.1696460.

Tseng, K.H., & Lytton, R.L. (1989). Prediction of permanent deformation in flexible pavement materials. In H.G. Schreuders & C.R. Marek (Eds.), *Implication of aggregates in the design, construction and performance of flexible pavements* (pp. 154-172). Philadelphia: American Society for Testing and Materials.

Van Impe, W.F.V. (1989). *Soil improvement techniques and their evolution*. Rotterdam: A. A. Balkema.

Werkmeister, S., Dawson, A.R., & Wellner, F. (2001). Permanent deformation behavior of granular materials and the shakedown concept. *Transportation Research Record*, 1757, 75-81. http://dx.doi.org/10.3141/1757-09.

Yoder, E.J., & Witczak, M.W. (1975). *Principles of pavement design*. New York: John Wiley & Sons Inc.

Zago, J.P., Pinheiro, R.J.B., Baroni, M., Specht, L.P., Delongui, L., & Sagrilo, A.V. (2021). Study of the permanent deformation of three soils employed in highway subgrades in the municipality of Santa Maria-RS, Brazil. *International Journal of Pavement Research and Technology*, 14, 729-739. http://dx.doi.org/10.1007/s42947-020-0129-6.

Zhang, J., Peng, J., Zhang, A., & Li, J. (2020). Prediction of permanent deformation for subgrade soils under traffic loading in Southern China. *International Journal of Pavement*, 23, 673-682. http://dx.doi.org/10.1080/10298436.2020.17652449.

Soils and Rocks
An International Journal of Geotechnical and Geoenvironmental Engineering
www.soilsandrocks.com
ISSN 1980-9743
ISSN-e 2675-5475

Technical feasibility analysis of using phosphogypsum, bentonite and lateritic soil mixtures in hydraulic barriers

Yago Isaias da Silva Borges[1], Bismarck Chaussê de Oliveira[2], Maria Eugênia Gimenez Boscov[1], Márcia Maria dos Anjos Mascarenha[2#]

Article

Keywords
Di-hydrated phosphogypsum
Liner
Hydromechanical performance
Compatibility

Abstract

Every year, millions of tons of phosphogypsum, a by-product of the fertilizer industry, are produced worldwide. As just a small part of this amount is reused, this study analyzed a new alternative to reuse this material in geotechnical works, in mixtures with lateritic soil and bentonite for the construction of liners for sanitary landfills. Four compositions were tested: 100% soil, 10% phosphogypsum + 90% soil, 10% phosphogypsum + 3% bentonite + 87% soil and 10% phosphogypsum + 6% bentonite + 84% soil. X-ray diffraction and scanning electron microscopy were used to analyze the mineralogy, while the hydromechanical performance was evaluated through compaction, hydraulic conductivity, and unconfined compressive tests. Modified free swell tests and modified Atterberg limits were used to test compatibility with NaCl, NaOH and ethanol. A solubilization test was carried out to investigate the presence of inorganic contaminants in the phosphogypsum. The addition of phosphogypsum increased the optimum water content in the compaction curves, did not change the hydraulic conductivity and decreased the unconfined compressive strength of the mixtures. The addition of bentonite increased the optimum water content, reduced the hydraulic conductivity, and increased the unconfined compressive strength. The possibility of dissolution of gypsite (main component of phosphogypsum), the problems that may arise from the interaction with chemical products, and the risk of manganese release in the subsoil lead to the conclusion that phosphogypsum is not suitable to be used in liners. However, soil-bentonite-phosphogypsum mixtures were considered eligible materials to be used in impermeable layers of other geotechnical works.

1. Introduction

Phosphate rocks are an important source of raw materials for the fertilizer industry, which consumes about 71% of these mined rocks in the world (IAEA, 2013). In this process, represented by the idealized chemical reaction presented in Equation 1 (Hull & Burnett 1996), the phosphate rock ($Ca_{10}F_2(PO_4)_6$) reacts with sulfuric acid (H_2SO_4) to form two products: the phosphoric acid (H_3PO_4) and the hydrofluoric acid (HF), and one by-product, the phosphogypsum ($CaSO_4.nH_2O$).

$$Ca_{10}F_2(PO_4)_6 + 10\ H_2SO_4 + 10\ nH_2O \rightarrow 6\ H_3PO_4 + 2\ HF + 10\ CaSO_4.nH_2O \tag{1}$$

In Equation 1, n may be 0, 0.5, or 2, depending on the industrial process employed. In the wet process, n is equal to 2, resulting in the di-hydrated form of phosphogypsum ($CaSO_4.2H_2O$), a material similar to gypsite, except for the presence of impurities, such as fluorides, phosphates, organic matter, heavy metals (Mascarenha et al. 2018), and radionuclides of uranium and thorium (Nisti et al. 2015).

This process generates about 2.5 tons of phosphogypsum per ton of phosphate rock (Pérez-Moreno et al. 2018) resulting in a global production of 200 million tons of this by-product per year (Saadaoui et al. 2017). In Brazil, 5 million tons of phosphate rock exploited per year (Brazil, 2019) generate about 10 million tons of phosphogypsum. It is estimated that only 15% of the global production of phosphogypsum is reused – mainly in agriculture – while 85% is disposed in stockpiles and water bodies, representing a potential risk of environmental contamination (IAEA, 2013; Rashad, 2017).

To reduce this volume of stocked material, several studies have been carried out aiming at reuse, such as addition in cements, mortars, concretes, and bricks (Rashad, 2017). In geotechnical engineering, phosphogypsum has been used, especially, for road construction (Rezende et al., 2016;

[#]Corresponding author. E-mail address: marciamascarenha@ufg.br
[1]Universidade de São Paulo, Escola de Engenharia, São Paulo, SP, Brasil.
[2]Universidade Federal de Goiás, Escola de Engenharia Civil e Ambiental, Goiânia, GO, Brasil.

Submitted on September 14, 2022; Final Acceptance on May 18, 2023; Discussion open until November 30, 2023.
https://doi.org/10.28927/SR.2023.009622

Silva et al., 2019; Amrani et al., 2020; Li et al., 2020) and backfilling (Dang et al., 2013; Li et al., 2017; Chen et al., 2017; Jiang et al., 2018). However, there is a lack of studies regarding its use in environmental geotechnical works, such as hydraulic barriers.

A key point to ensure security and efficiency of a geotechnical work is a good characterization of materials, including their hydromechanical and geochemical properties. When using wastes and by-products, it is furthermore necessary to guarantee that these materials will not be a source of environmental contamination. In this context, this paper presents a geoenvironmental characterization of soil mixtures containing phosphogypsum and bentonite in order to analyze their technical feasibility as geomaterials for hydraulic barriers.

2. Materials

The di-hydrated phosphogypsum (P) was collected at a plant located in the state of Goiás (Midwest Brazil) which generates 720,000 tons of this by-product per year, most of which stored in piles (Rezende et al., 2016). Its chemical composition (Table 1) shows a predominance of sulfur oxides (which form sulfates) and calcium oxide. There are also lower levels of iron, titanium and aluminum oxides and phosphate. This material was classified as non-hazardous and non-inert (Rezende et al., 2016) according to Brazilian regulations (ABNT, 2004).

The lateritic soil (S) from Aparecida de Goiânia, Goiás, was collected at a depth of 0.4 m. This soil is mainly composed of quartz, gibbsite, hematite, and kaolinite (Rezende et al., 2016). It is classified as low plasticity silt (ML) according to the Unified Soil Classification System (ASTM, 2017) and as sandy lateritic soil according to the Brazilian Compacted Tropical Miniature Classification System (MCT) (Villibor & Nogami, 2009). Mixtures of this soil with phosphogypsum have already been investigated in previous studies (Rezende et al., 2016; Mascarenha et al., 2018; Ribeiro et al., 2018; Silva et al., 2019).

Since the predominant fraction of the soil is sand (Table 2), sodic bentonite was added to the soil-phosphogypsum mixtures because of its well-known ability to reduce hydraulic conductivity (Amadi & Eberemu, 2012; Amadi & Osinubi, 2017; De La Morena et al., 2018). The bentonite (B) used in this study was commercially available and produced in north-eastern Brazil.

Table 1. Chemical composition of phosphogypsum.

Oxide	Percentage
Silicon dioxide (SiO_2)	1.8
Titanium dioxide (TiO_2)	0.2
Aluminum oxide (Al_2O_3)	0.3
Iron oxide (Fe_2O_3)	0.5
Calcium oxide (CaO)	33.6
Phosphorus oxide (P_2O_5)	0.8
Sulfur oxide (SO_3)	42.7
Loss on ignition	20.1

The mixtures were prepared with 10% phosphogypsum in dry weight, the maximum content that can be added to this lateritic soil without impairing its hydromechanical performance, according to Mascarenha et al. (2018). Contents of 3% and 6% of bentonite in dry weight were added to the mixtures SPB3 and SPB6, respectively. These contents are expected to reduce the hydraulic conductivity coefficients of the mixtures to values close to or lower than 1×10^{-9} m/s (Morandini & Leite, 2012; Ribeiro et al., 2018).

The composition of the mixtures, their Atterberg limits and grain size distribution are presented in Table 2.

3. Methods

3.1. Thermal analysis of phosphogypsum

A preliminary thermal analysis was performed to determine the ideal temperature to measure the moisture content of phosphogypsum. Excessive heat can cause di-hydrated phosphogypsum to lose microstructural water, transforming it into hemi-hydrated phosphogypsum, a material with different properties (Rezende et al., 2016).

Phosphogypsum samples were oven dried until mass constancy at two different temperatures (70 ºC and 90 ºC), based on previous studies (Rezende et al., 2016). X-ray diffraction tests (XRD) showed that the sample dried at 70 ˚C was basically composed of gypsite (di-hydrated phosphogypsum) and quartz, while the sample dried at 90 ˚C contained more than 74% basanite (hemi-hydrated phosphogypsum) and only 8.54% gypsite (Table 3). Hence, 70 ºC was the temperature chosen to determine moisture of samples containing phosphogypsum.

Ribeiro et al. (2018) observed that the required temperature to achieve mass constancy for sodium bentonites is 130 ºC, while temperatures ranging from 105 °C to 110 °C are recommended to measure the moisture content of soils (ABNT, 2016). Since each material has an ideal temperature for determining the moisture content, the moisture content of the mixtures was obtained by mathematical correlations.

For that, soil and bentonite were moisturized with different water contents and oven dried at temperatures of 70 ºC, 110 ºC and 130 ºC. Linear correlations were then determined, as presented in Figure 1(a) for soil and 1(b) for bentonite.

The moisture of samples dried at 70 ºC was corrected according to these correlations and to the bentonite and phosphogypsum contents in each mixture. Although phosphogypsum and bentonite have greater affinity for water molecules than soil, water was assumed to be proportionally distributed among these three materials.

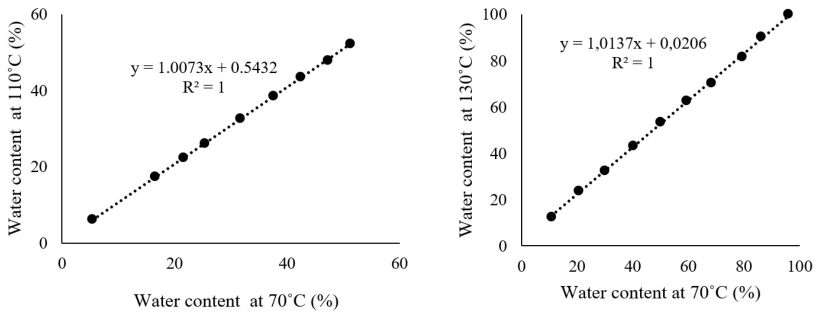

(a) (b)

Figure 1. Mathematical correlation: (a) soil; (b) bentonite.

Table 2. Geotechnical characterization of the mixtures of soil, bentonite and phosphogypsum.

Item	Mixture					
	S	P	B	SP	SPB3	SPB6
Soil (%)	100	-	-	90	87	84
Phosphogypsum (%)	-	100	-	10	10	10
Bentonite (%)	-	-	100	-	3	6
Specific gravity (g/cm^3)	2.64	2.36	2.71	2.59	2.59	2.58
Liquid limit (%)	37	-	47	36	40	44
Plastic limit (%)	27	-	48	27	23	24
Plasticity Index (%)	10	Non plastic	422	9	17	20
Grain size distribution[1]						
Gravel (%)	0.1	0.0	0.0	0.1	0.1	0.1
Sand (%)	56.6	26.6	8.0	51.6	52.5	42.0
Silt (%)	29.2	65.4	83.0	33.9	37.8	44.8
Clay (%)	14.0	8.0	9.0	14.4	9.6	13.1

[1]Terminology according to ABNT (1995). The percentages of gravel, sand, silt, and clay in all mixtures were obtained from the granulometric distribution curves. Sodium hexametaphosphate was used as a dispersant agent for the sedimentation test.

3.2. Compaction tests

Compaction tests were carried out according to the Brazilian MCT methodology (DNER, 1994; Villibor & Nogami, 2009). Specimens were compacted in a miniature MCV apparatus inside a cylindrical mold of 130 mm height and 50 mm diameter, following procedure A, described by DNER (1994) for the normal energy compaction. In this procedure, the material to be compacted, which must pass through the sieve with a 2.0 mm opening, is distributed in two layers. In each layer, five blows of a 2,270 g hammer are applied, with a falling height of 305 mm. The specimen is considered suitable when its final height (after compaction) is 50±1 mm.

This methodology was chosen to decrease the time necessary to saturate samples for the hydraulic conductivity tests, since the specimens are smaller (≈ 50 x 50 mm) than those obtained by conventional compaction tests.

Compaction curves were not obtained for samples P (100% phosphogypsum) and B (100% bentonite), once the interest of this study was focused on the mixtures with soil.

Table 3. Phosphogypsum mineralogy obtained from XRD analysis.

Mineral	Percentage (%)	
	70°C	90°C
Basanite	<DL	74.08
Anidrite	<DL	14.79
Gypsite	93.37	8.54
Ettringite	<DL	<DL
Quartz	2.27	2.42
Gibbsite	<DL	<DL
Hematite	<DL	<DL
Portlandite	<DL	<DL

Note: <DL: value below the detection limit.

3.3. Hydraulic conductivity tests

Hydraulic conductivity tests were performed in rigid wall permeameters, using the same cylinders of the compaction tests. To avoid preferential leakage along the wall (Shackelford et al., 2000; Chapuis, 2012), the specimens were compacted directly inside the permeameters (with an inner diameter of 50 mm, 25 times greater than the maximum diameter of soil particles, i.e., 2 mm). Similar approaches were used by Razakamantsoa & Djeran-Maigre (2016) and De Camillis et al. (2016).

Specimens were compacted at the optimum water content (w_{op}) and maximum apparent dry weight (γ_{dmax}), presented in Table 4, and were saturated by backpressure. A hydraulic gradient of 10 m/m (≈ 0.5 m of water column) was applied. The hydraulic conductivities were calculated according to ASTM D5856–15 (ASTM, 2015), as the average value of four measurements that showed a pattern of stability.

3.4. Unconfined compressive tests

Specimens with 5 cm diameter and 10 cm height were compacted at w_{op} and γ_{dmax} (Table 4) following the procedures described in Section 3.2, doubling the mass of material and the number of layers. Compacted specimens were wrapped in plastic film and kept in a closed box for 28 days, the ideal curing time verified in previous studies with phosphogypsum-lateritic soil mixtures (Rezende et al., 2016; Silva et al., 2019). The failure process followed the prescriptions of ABNT (1992) and ASTM (2016).

3.5. Compatibility tests

The term compatibility refers to the ability of a material to maintain its properties after contact with chemicals (Shackelford, 1994; Farnezi & Leite, 2007). In this study, compatibility was analyzed through modified free swell tests and modified Atterberg Limits. In both cases, the following solutions were used: sodium chloride (NaCl, 0.125 mol/L), sodium hydroxide (NaOH, 0.001 mol/L) and ethanol (1 mol/L). Similar solutions were used by Morandini & Leite (2012) to simulate saline, alkaline and organic miscible liquids that might be in contact with the mixtures in geotechnical works.

The modified free swell tests were performed as suggested by Sivapullaih et al. (1987): 10 g in dry mas of the material, passing through a sieve of an opening size of 0.42 mm, are poured into a 100 cm^3 graduated jar, which is then filled with the liquid of interest. The initial volume of the solids and the volume after 24 hours are registered, and the swelling potential is calculated by (2):

$$SI = \left(V - V_i\right) / V_i \tag{2}$$

Where *SI* is the modified free swelling index, V is the volume after 24 hours swelling and V_i the initial volume of solids.

The modified Atterberg limits were determined following the standard method (ASTM, 2000) with water and the aforementioned solutions. The effect of the solutions on the plastic properties of the mixtures was analyzed using the plastic incompatibility index (*PIC*), as proposed by Farnezi & Leite (2007):

$$PIC = \left(\left(PI_s - PI_w\right) / PI_w\right) \times 100 \tag{3}$$

Where PI_s is the plasticity index with the solution and PI_w is the plasticity index with water.

3.6. Microstructural analysis

Scanning electron microscopy (SEM) was used to analyze possible changes in the microstructure of the specimens used in the hydraulic conductivity and unconfined compressive tests. The samples were air dried and covered with a thin layer of gold (via sputtering). Images were obtained using a high vacuum technique in a scanning electron microscope (model Jeol 6610), in the Multiuser laboratory of high-resolution microscopy (LabMic) of Federal University of Goias.

3.7. Solubilization tests

Due to the possible presence of impurities in the phosphogypsum, such as heavy metals, solubilization tests were performed to analyze the risks of environmental contamination.

For these tests, solubilized extracts were obtained from the samples S and SP, following the Brazilian standard NBR 10006 (ABNT, 2004): a suspension of 250 g in dry weight and 1000 mL of distilled water was prepared and kept at rest for seven days. The suspension was mixed by a rotational mixer for five minutes before and after the rest period, and then the solution was filtered using a 0.45 µm pore size membrane.

The solubilized extract was analyzed to measure the concentration of inorganic chemical species, and the values were compared with reference values available in Brazilian environmental standards (CONAMA, 2008).

4. Results and discussion

4.1. Compaction tests

Compaction curves are presented in Figure 2. Values of γ_{dmax}, w_{op} and void ratio (*e*) are shown in Table 4.

Table 4. γ_{dmax}, w_{op}, and e of samples S, SP, SPB3 and SPB6.

Sample	γ_{dmax} (kN/m^3)	w_{op} (%)	*e*
S	14.7	25.3	0.79
SP	14.6	26.1	0.77
SPB3	14.6	26.3	0.77
SPB6	14.7	26.1	0.76

The w_{op} of the mixtures was higher than that of the soil because the addition of phosphogypsum and bentonite increased the percentage of fines (Table 2) resulting in a greater specific surface, so that more water is needed in the hydration process (Eberemu et al., 2013; Eberemu, 2013; Osinubi et al., 2015).

Addition of phosphogypsum has been reported to cause flocculation in soils, due to the replacement of adsorbed ions by calcium, creating a more porous structure and, therefore, reducing γ_{dmax} (Rezende et al., 2016; Mascarenha et al., 2018). In this study, flocculation does not seem to be an important phenomenon, since γ_{dmax} and void ratios of soil and mixtures containing phosphogypsum are alike. The low percentage of phosphogypsum in the mixtures (10%) was probably not enough to cause an expressive flocculation process.

4.2. Hydraulic conductivity tests

The hydraulic conductivity of the samples, at a temperature of 20 ºC (k_{20}), are presented in Table 5. A ratio (KRC) between the k_{20} of soil and the k_{20} of the mixtures was calculated, as proposed by Morandini & Leite (2015).

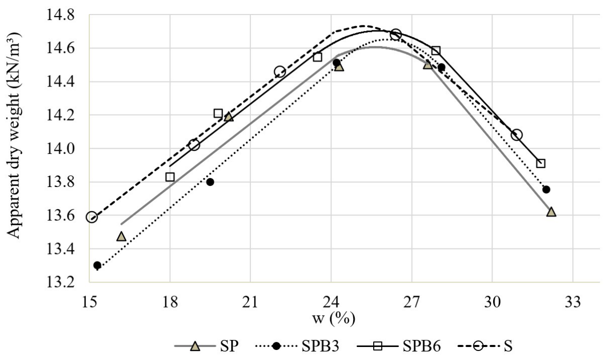

Figure 2. Compaction curves of samples S, SP, SPB3, and SPB6.

Sample SP presented a KRC of 0.97, which indicates that the addition of phosphogypsum practically did not affect the hydraulic conductivity of the soil. On the other hand, for a bentonite content of 3% (SPB3) k_{20} decreased by approximately one order of magnitude (KRC=14.5). Morandini & Leite (2015) also observed similar results for hydraulic conductivity tests carried out with Brazilian lateritic-bentonite soil mixtures in flexible wall permeameters: for an effective confining stress of 80 kPa, an addition of 3% bentonite produced values of KCR ranging from 11.4 to 18.9, while a 6% addition produced KCR values ranging from 65.3 to 76.4.

Bentonite is mainly composed of montmorillonite. During the hydration process, montmorillonite has a great potential to adsorb water molecules and hydrated ions, due to its large specific surface and negative net charge (Shackelford et al. 2000). These water molecules and cations are essentially immobile and occupy most of the pores, forming irregular flow channels. Thus, although the void ratio is similar for all samples, the pores of samples containing bentonite are partially filled by a gel formed around soil particles (Amadi, 2013).

A comparison between the porous aspects of the soil and a mixture of soil with bentonite is provided in Figures 3(a) and 3(b). A more detailed explanation of the swelling and hydration processes of bentonites can be found in Liu (2013), Yu et al. (2018), and Jadda & Bag (2020).

Table 5. Hydraulic conductivity at 20˚C.

Sample	k_{20} (m/s)	KRC
S	$3.4x10^{-8}$	1.0
SP	$3.5x10^{-8}$	0.97
SPB3	$2.3x10^{-9}$	14.5
SPB6	$4.7x10^{-10}$	72.3

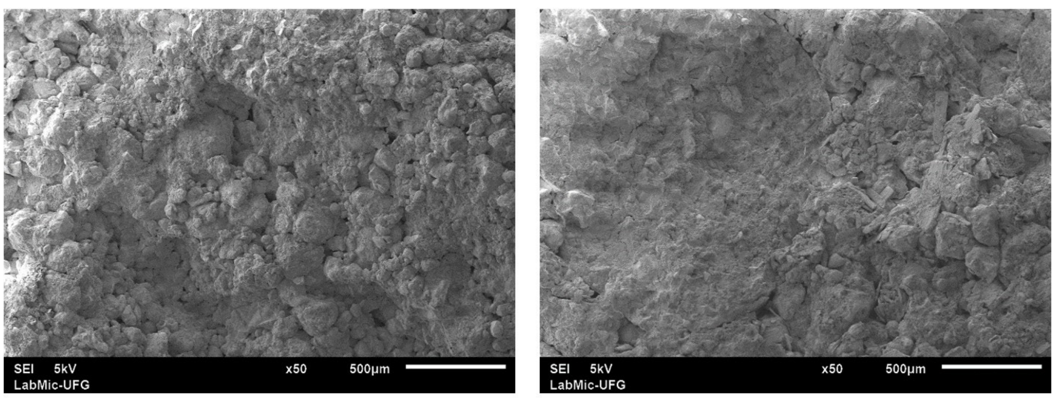

(a)

(b)

Figure 3. Comparison between the porous aspects of the soil (a) and a mixture of the soil with bentonite (b).

4.3. Unconfined compressive tests

The results of the unconfined compressive tests are presented in Table 6.

The addition of phosphogypsum decreased the unconfined compressive strength (UCS) of the compacted soil, a result expected for the addition of a non-cohesive material. Moreover, di-hydrated phosphogypsum is mainly composed of gypsite, a mineral that has a tabular structure, with particles in the form of large and thin plates (Mascarenha et al., 2018) (Figure 4). This geometry favors the breakage of phosphogypsum particles, further decreasing the UCS. Rezende et al. (2016) also reported a decrease in UCS with the addition of phosphogypsum to soil mixtures such as those analyzed in this study.

Sample SPB6 showed higher UCS than sample SPB3, which in turn was higher than SP, indicating that the addition of bentonite improved the UCS of the mixtures. During the process of adsorption of water molecules and hydrated ions, bentonite promotes an attraction between soil particles, increasing the contact area (Ahmed, 2015), plasticity and cohesion (Malizia & Shakoor, 2018), which may explain the increase in UCS values.

Neither phosphogypsum nor bentonite altered the strain at failure, which was around 3% for the soil and for the mixtures. Mascarenha et al. (2018) analyzed the compressibility (in one-dimensional consolidation tests) of a mixture composed of 90% lateritic soil and 10% phosphogypsum, with the same materials used in this study, and reported a strain of about 2% for an effective vertical stress of 200 kPa.

Table 6. Results of unconfined compressive tests.

Sample	UCS (kPa)	Strain at failure (%)
S	304	2.8
SP	207	2.8
SPB3	272	2.9
SPB6	362	2.9

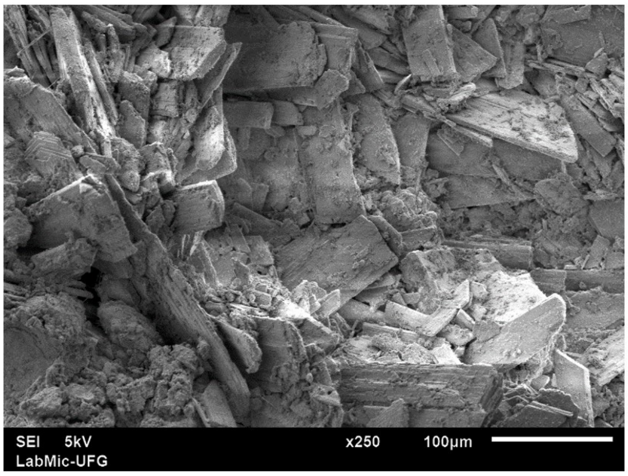

Figure 4. Phosphogypsum plates in sample SP.

4.4. Compatibility tests

The results of the modified free swell tests are presented in Figure 5. For comparison, the values of SI obtained in the tests carried out with NaCl, NaOH and ethanol (SI_s) were divided by the values of SI with distilled water (SI_w). Values higher than one mean that swelling was higher in contact with solutions than with water.

Figure 5 shows that the swelling potential of the mixtures was mainly affected by the solution containing NaOH. This alkaline medium (pH 11) favors the development of negative surface charges on the minerals present in the mixtures. Because of electrostatic repulsion, particles tend to move as far away from each other as possible, increasing swelling.

Liquids with dielectric constants lower than water can also affect the swelling of minerals, shrinking their electrical double layer (Shackelford et al., 2000). In this case, the mineral will present less swelling than in water, as observed in tests carried out with ethanol. No significant variations were observed in the tests performed with NaCl.

The influence of these solutions on the plastic properties of the mixtures can be seen in Figure 6, where the results of

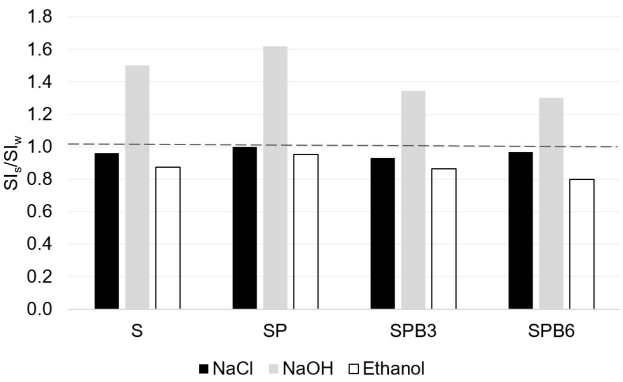

Figure 5. Modified free swell indexes.

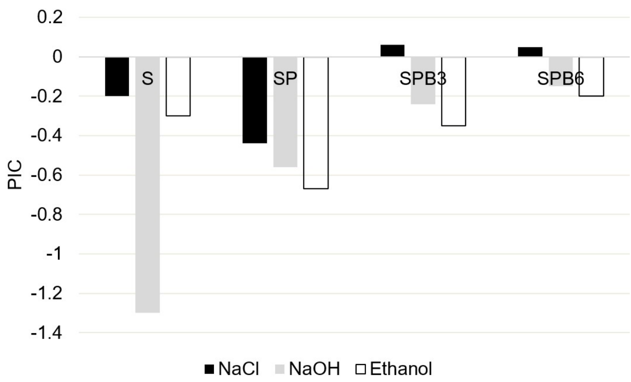

Figure 6. Plastic Incompatibility Indexes (PIC).

the modified Atterberg limits in terms of plastic incompatibility indexes (*PIC*) are presented. Negative values indicate that the solutions used in the tests decreased the plasticity of the mixtures, except for samples SPB3 and SPB6 in contact with NaCl, which showed a small increase in plasticity.

Although it is not possible to establish a direct comparison between the results presented in Figure 5 and 6, they clearly show that the chemical composition of the liquids can affect the geotechnical properties of the analyzed materials. In practical terms, it means the possibility of unexpected geotechnical problems, including swelling, heaving, shrinkage and collapse, for example.

4.5. Solubilization tests

The results of the chemical analysis of the inorganic groundwater contamination parameters are shown in Table 7.

The concentrations of iron and manganese in sample SP exceed the limits of the Brazilian technical standard for inert solid waste (ABNT, 2004), 0.3 mg/L and 0.1 mg/L, respectively. However, these metals are not considered for hazardousness, and SP can be classified as a non-inert and non-hazardous material. These concentrations also exceeded acceptable limits prescribed by Brazilian regulations for water use (CONAMA, 2008) and United States Environmental Protection Agency prescriptions for drinking water (USEPA, 2009).

The excess of iron can be attributed to the soil, where this metal is abundant in form of oxides and hydroxides, like goethite and hematite, for example (Villibor & Nogami, 2009; Osinubi et al., 2015). Since sample S did not present excess of manganese, this metal can be related to phosphogypsum. These patterns were also observed by Mascarenha et al. (2018) in chemical analysis of water percolated through compacted specimens of soil-phosphogypsum mixtures, from the same sources and in the same proportions as those used in this study.

The emission of radionuclides by phosphogypsum is another environmental concern, but many phosphogypsum samples collected in different plants in Brazil were classified as non-hazardous from a radiological point of view (Nisti et al. 2015; Rezende et al., 2016; Campos et al., 2017; Silva et al., 2019). In addition, Brazilian legislation requires the measurement of the emission of radionuclides

Table 7. Chemical analysis for inorganic parameters.

Parameter	Limit for human consumption (mg/L)[1]	Results (mg/L)		
		Background	S	SP
Antimony	0.005	<0.005	0.005	<0.005
Arsenic	0.010	<0.005	0.010	0.010
Barium	0.700	<0.003	0.096	0.116
Beryllium	0.004	<0.0004	<0.0004	<0.0004
Boron	0.500	0.0640	0.0700	0.0850
Cadmium	0.005	<0.001	<0.001	<0.001
Lead	0.010	<0.005	0.0100	0.0100
Cyanide	0.070	<0.001	<0.001	<0.001
Cobalt	-	<0.003	<0.003	<0.003
Copper	2.000	0.0920	0.0940	0.1120
Chromium (III)	0.050	<0.100	<0.100	<0.100
Chromium (IV)	0.050	<0.100	<0.100	<0.100
Lithium	-	0.0100	0.0100	0.0110
Manganese	0.100	0.0110	0.0230	1.1140
Mercury	0.001	<0.0002	<0.0002	<0.0002
Molybdenum	0.070	<0.0070	<0.0070	<0.0070
Nickel	0.020	<0.0070	<0.0070	<0.0070
Silver	0.100	<0.0050	<0.0050	0.0070
Selenium	0.010	<0.0100	<0.0100	<0.0100
Uranium	0.015	<0.0100	<0.0100	<0.0100
Vanadium	0.050	<0.0300	<0.0300	<0.0300
Zinc	5.000	<0.0200	0.0400	0.0900
Aluminum	0.200	<0.0200	<0.0200	<0.0200
Chlorides	250.0	10.800	30.100	32.500
Iron	0.300	<0.0100	4.920	1.380
Fluorides	1.500	<0.100	<0.100	<0.100
Total dissolved solids	1000.0	3.000	31.000	954.000

[1] After CONAMA (2008).

of Ra^{226} and Ra^{228} and prohibits samples containing more than 1,000 Bq/kg of these radionuclides from leaving the plant for commercial purposes (CNEN, 2007). Therefore, the risk of radiological contamination is very low.

5. Conclusion

This study was motivated by the attempt to find a new alternative to reuse phosphogypsum, i.e., as a soil additive in geotechnical works. The chemical and mineralogical analysis demonstrated that this material is mainly composed of gypsite, a di-hydrated calcium sulphate whose crystals have the shape of tabular plates.

The addition of phosphogypsum to the soil increased the optimum water content at standard compaction energy, but almost did not affect the maximum apparent dry weight and the void ratio of the compacted specimens. This was reflected in the hydraulic conductivity tests by the similar hydraulic conductivities obtained for the soil and for the sample containing soil and phosphogypsum. Conversely, a reduction in the unconfined compressive strength was observed and attributed to this by-product being non cohesive and to its microstructure characteristics.

The samples containing phosphogypsum and bentonite presented a better hydromechanical performance than that composed only by soil. The unconfined compressive strength of about 300 kPa is a value acceptable for several small and medium-sized geotechnical works, while hydraulic conductivities in the range of 10^{-9} – 10^{-10} m/s meet the requirements of materials used in hydraulic barriers of sanitary landfills.

Regarding environmental aspects, there are some problems in the reutilization of this by-product: possibility of dissolution of gypsite, additional problems that may arise from the interaction with chemical products, and the risk of manganese release in the subsoil.

Although these aspects lead to the conclusion that phosphogypsum is not a suitable material to be used in hydraulic barriers, the soil-bentonite-phosphogypsum mixtures could be considered eligible materials for impermeable layers in geotechnical works, provided that the surface loads are greater than the swelling pressure of these mixtures and the environmental impact of manganese release in the subsoil is evaluated.

Acknowledgements

The authors are thankful for the funds provided by Brazilian Research Agencies (CNPq, process 408756/2016-0 and CAPES, Finance code 001) and CMOC International Brazil to support this study, as well as the partner laboratories in the Federal University of Goias and in the University of Brasilia.

Declaration of interest

The authors have no conflicts of interest to declare. All co-authors have observed and affirmed the contents of the paper and there is no financial interest to report.

Authors' contributions

Yago Isaias da Silva Borges: writing – original draft, methodology, investigation, formal analysis. Bismarck Chaussê de Oliveira: methodology, investigation, formal analysis, writing – review & editing. Maria Eugênia Gimenez Boscov: formal analysis, writing – review & editing, Márcia Maria dos Anjos Mascarenha: methodology, formal analysis, writing – review & editing, supervision, funding acquisition, project administration.

Data availability

The datasets of this current study are available from the corresponding author on request.

List of symbols

e	void ratio
k_{20}	hydraulic conductivity coefficient at 20 °C
n	number of water molecule
B	bentonite
$Ca_{10}F_2(PO_4)_6$	phosphate rock
$CaSO_4.nH_2O$	phosphogypsum
CL	low plasticity clay
HF	hydrofluoric acid
H_2O	water
H_2SO_4	sulfuric acid
H_3PO_4	phosphoric acid
KRC	ratio between the k of natural soil and the k of the mixtures
LabMic	Multiuser laboratory of high-resolution microscopy
MCT	Brazilian Miniature Compacted Tropical
NaCl	sodium chloride
NaOH	sodium hydroxide
PIC	plastic incompatibility indexes
PI_s	plasticity index with the solution
PI_w	plasticity index with water.
S	lateritic soil
SI	modified free swelling index
SP	soil - phosphogypsum
SEM	Scanning electron microscopy
SI	modified free swelling index
UCS	Unconfined compressive strength
V	volume after swelling
Vs	volume of solids
XRD	X-ray diffraction tests
w_{op}	optimum water content
γ_{dmax}	maximum apparent dry weight

References

ABNT NBR 1004 (2004). *Solid wastes Classification*. ABNT - Associação Brasileira de Normas Técnicas, Rio de Janeiro, RJ. (in Portuguese).

ABNT NBR 6457 (2016) *Soil samples – Preparation for characterization and compaction tests*. ABNT - Associação Brasileira de Normas Técnicas, Rio de Janeiro, RJ. (in Portuguese).

ABNT NBR 6502 (1995). *Rocks and soils. Terminology*. ABNT - Associação Brasileira de Normas Técnicas, Rio de Janeiro, RJ. (in Portuguese).

ABNT NBR12770 (1992). *Cohesive soil – Determination of unconfined compression strength*. ABNT - Associação Brasileira de Normas Técnicas, Rio de Janeiro, RJ. (in Portuguese).

Ahmed, A. (2015). Compressive strength and microstructure of soft clay soil stabilized with recycled basanite. *Applied Clay Science*, 104, 27-35. http://dx.doi.org/10.1016/j.clay.2014.11.031.

Amadi, A.A. (2013). Swelling characteristics of compacted lateritic soil-bentonite mixtures subjected to municipal waste leachate contamination. *Environmental Earth Sciences*, 70, 2437-2442.

Amadi, A.A., & Eberemu, A.O. (2012). Delineation of compaction criteria for acceptable hydraulic conductivity of lateritic soil-bentonite mixtures designed as landfill liners. *Environmental Earth Sciences*, 67, 999-1006.

Amadi, A.A., & Osinubi, K.J. (2017). Transport parameters of lead (Pb) ions migrating through saturated lateritic soil-bentonite column. *International Journal of Geotechnical Engineering*, 12(3), 302-308.

Amrani, M., Taha, Y., Kchikach, A., Benzaazoua, M., & Hakkou, R. (2020). Phosphogypsum recycling: new horizons for a more sustainable road material application. *Journal of Building Engineering*, 30, 101267.

ASTM D4318 – 00. (2000) Standard test method for liquid limit, plastic limit and plasticity index of soils. ASTM International, West Conshohocken, USA.

ASTM D2166 – 16. (2016) *Standard test method for unconfined compressive strength for cohesive soils*. ASTM International, West Conshohocken, USA.

ASTM D5856 – 15. (2015) *Standard test method for measurement of hydraulic conductivity of porous material using a rigid-wall, compaction-mold permeameter*. ASTM International, West Conshohocken, USA.

ASTM D2487. (2017). *Standard Practice for Classification of Soils for Engineering Purposes (Unified Soil Classification System)*. ASTM International, West Conshohocken, USA.

Brazil. (2019). *Mineral sector bulletin*. Ministry of Mines and Energy. (2nd issue, 28 p.).

Campos, M.P., Costa, L.J.P., & Nisti, M.B. (2017). Phosphogypsum recycling in the building material industry: assessment of the radon exhalation. *Journal of Environmental Radioactivity*, 144, 120-126. http://dx.doi.org/10.1016/j.jenvrad.2017.04.002.

Chapuis, R.P. (2012). Predicting the hydraulic saturated conductivity of soils: a review. *Bulletin of Engineering Geology and the Environment*, 71, 401-434.

Chen, Q., Zhang, Q., Fourie, A., & Xin, C. (2017). Utilization of phosphogypsum and phosphate tailings for cemented paste backfill. *Journal of Environmental Management*, 201, 19-27.

Comissão Nacional de Energia Nuclear – CNEN. (2007). Portaria DRS N. 9 de 28 de maio de 2013. *Diário Oficial [da] República Federativa do Brasil.* (In Portuguese).

Conselho Nacional do Meio Ambiente – CONAMA . (2008). Resolução 397 de 3 de Abril de 2008. *Diário Oficial [da] República Federativa do Brasil.* (In Portuguese).

Dang, W.G., Liu, Z., He, X., & Liu, Q. (2013). Ixture ratio of phosphogypsum in backfilling. *Mining Technology*, 122(1), 1-7.

De Camillis, M., Di Emidio, G., Bezuijen, A., & Verástegui-Flores, R.D. (2016). Hydraulic conductivity and swelling ability of a polymer modified bentonite subjected to wetedry cycles in seawater. *Geotextiles and Geomembranes*, 44, 739-747.

De La Morena, G., Asensio, L., & Navarro, V. (2018). Intra-aggregate water content and void ratio model for MX-80 bentonites. *Engineering Geology*, 246, 131-138. http://dx.doi.org/10.1016/j.enggeo.2018.09.028.

Departamento Nacional de Estradas de Rodagem – DNER. (1994). *ME-228: Soils, compaction in miniature apparatus*. Departamento Nacional de Estradas de Rodagem. (In Portuguese).

Eberemu, A.O. (2013). Evaluation of bagasse ash treated lateritic soil as potential barrier material in waste containment application. *Acta Geotechnica*, 8, 407-421.

Eberemu, A.O., Amadi, A.A., & Osinubi, K.J. (2013). The use of compacted tropical treated with rice husk as a suitable hydraulic barrier material in waste containment applications. *Waste and Biomass Valorization*, 4, 309-323.

Farnezi, M.K., & Leite, A.L. (2007). Lateritic soil and bentonite mixtures assessment for liner usage purpose. *Soil and Rocks*, 30(2), 103-112.

Hull, C.D., & Burnett, W.C. (1996). Radiochemistry of Florida phosphogypsum. *Journal of Environmental Radioactivity*, 32(3), 213-238.

International Atomic Energy Agency – IAEA. (2013). Radiation protect and management of norm residues in the phosphate industry. In International Atomic Energy Agency (Ed.), *Safety Reports Series*. IAEA. (Vol. 78).

Jadda, K., & Bag, R. (2020). Variation of swelling pressure, consolidation characteristics and hydraulic conductivity of two Indian bentonites due to electrolyte concentration. *Engineering Geology*, 272(105637), 1-14.

Jiang, G., Wu, A., Wang, Y., & Lan, W. (2018). Low cost and high efficiency utilization of hemihydrate phosphogypsum:

used as binder to prepare filling material. *Construction & Building Materials*, 167, 263-270.

Li, B., Sha, W., & Zhen, Y. (2020). An effective recycling direction of water-based drilling cuttings and phosphogypsum co-processing in road cushion layer. *Environmental Sciences and Pollution Resources*, 27, 17420-17424.

Li, X., Du, J., Gao, L., He, S., Gan, L., Sun, C., & Shi, Y. (2017). Immobilization of phosphogypsum for cemented paste backfill and its environmental effects. *Journal of Cleaner Production*, 156, 137-146.

Liu, L. (2013). Prediction of swelling process in different types of bentonites in dilute solutions. *Colloids and Surfaces. A, Physicochemical and Engineering Aspects*, 434, 303-318.

Malizia, J.P., & Shakoor, A. (2018). Effect of water content and density on strength and deformation behavior of clay soils. *Engineering Geology*, 244, 125-131. http://dx.doi.org/10.1016/j.enggeo.2018.07.028.

Mascarenha, M.M.A., Cordão Neto, M.P., Matos, T.H.C., Chagas, J.V.R., & Rezende, L.R. (2018). Effects of the addition of phosphogypsum on the characterization and mechanical behavior of lateritic clay. *Soil and Rocks*, 4, 157-170.

Morandini, T.L.C., & Leite, A.L. (2012). Characterization, hydraulic conductivity and compatibility of mixtures of tropical soil and bentonite mixtures for barrier usage purpose. *Soils and Rocks*, 35(3), 267-278.

Morandini, T.L.C., & Leite, A.L. (2015). Characterization and hydraulic conductivity of tropical soils and bentonite mixtures for CCL purposes. *Engineering Geology*, 196, 251-267. http://dx.doi.org/10.1016/j.enggeo.2015.07.011.

Nisti, M.B., Saueia, C.R., Malheiro, R.H., Groppo, G.H., & Mazzilli, B.P. (2015). Lixiviation of natural radionuclides and heavy metals in tropical soils amended with phosphogypsum. *Journal of Environmental Radioactivity*, 144, 120-126. http://dx.doi.org/10.1016/j.jenvrad.2015.03.013.

Osinubi, K.J., Moses, G., & Liman, A.S. (2015). The influence of compactive effort on compacted lateritic soil treated with cement kiln dust as hydraulic barrier material. *Journal of Geotechnical Geological Engineering*, 33, 523-535.

Pérez-Moreno, S.M., Gázquez, M.J., Pérez-Lopez, R., Vioque, I., & Bolívar, J.P. (2018). Assessment of natural radionuclides mobility in a phosphogypsum disposal area. *Chemosphere*, 211, 775-783.

Rashad, A.M. (2017). Phosphogypsum as a construction material. *Journal of Cleaner Production*, 166, 732-743. http://dx.doi.org/10.1016/j.jclepro.2017.08.049.

Razakamanantsoa, A.R., & Djeran-Maigre, I. (2016). Long term chemo-hydro-mechanical behavior of compacted soil bentonite polymer complex submitted to synthetic leachate. *Waste Management*, 53, 92-104.

Rezende, L.R., Curado, T.S., Silva, M.V., Mascarenha, M.M., Metogo, D.A.N., Cordão Neto, M.P., & Bernucci, L.L.B. (2016). Laboratory study of phosphogypsum, stabilizers, and tropical soil mixtures. *Journal of Materials in Civil Engineering*, 29(1), 1-16.

Ribeiro, M.E.S., Mascarenha, M.M.A., & Santos, T.L. (2018). Estudo de viabilidade técnica do fosfogesso hemidratado para aplicação em sistemas de cobertura de aterros sanitários. *Revista Eletrônica de Engenharia Civil*, 14(2), 263-277. http://dx.doi.org/10.5216/reec.v14i2.51458. [In Portuguese]

Saadaoui, E., Ghazel, N., Romdhane, C.B., & Massoudi, N. (2017). Phosphogypsum: potential uses and problems - a review. *International Journal of Environmental Studies*, 74(4): 558-567.

Shackelford, C.D. (1994). Waste-soil interactions that alter hydraulic conductivity hydraulic conductivity and waste contaminant transport in soil. ASTM International.

Shackelford, C.D., Benson, C.H., Katsumi, T., Edil, T.B., & Lin, L. (2000). Evaluating the hydraulic conductivity of GCLs permeated with non-standard liquids. *Geotextiles and Geomembranes*, 18, 133-161.

Silva, M.V., Rezende, L.R., Mascarenha, M.M.A., & Oliveira, R.B. (2019). Phosphogypsum, tropical soil and cement for asphalt pavements under wet and dry environmental conditions. *Resources, Conservation and Recycling*, 144, 123-136. http://dx.doi.org/10.1016/j.resconrec.2019.01.029.

Sivapullaih, P.V., Sitharam, T.G., & Rao, K.S.S. (1987). Modified free swell index for clays. *Geotechnical Testing Journal*, 10(2), 80-85.

United States Environmental Protection Agency – USEPA. (2009). N*ational primary drinking water regulation*. USEPA.

Villibor, D.F., & Nogami, J.S. (2009) *Pavimentos econômicos: tecnologia e uso dos solos finos lateríticos.* Arte e Ciencia. (In Portuguese).

Yu, H., Sun, D., & Gao, Y. (2018). Effect of NaCl on swelling characteristics of bentonites with different diffuse double layers. *Applied Magnetic Resonance*, 49, 725-737.

Soils and Rocks

An International Journal of Geotechnical and Geoenvironmental Engineering

www.soilsandrocks.com

ISSN 1980-9743
ISSN-e 2675-5475

Design of agglomerates using Weibull distribution to simulate crushable particles in the discrete element method

Bruna Mota Mendes Silva Tedesco[1#], Manoel Porfirio Cordão Neto[1], Márcio Muniz de Farias[1], Alessandro Tarantino[2]

Article

Keywords
Agglomerate
Discrete element method
Crushable sand
Particle tensile strength
Weibull distribution

Abstract

This paper focuses on the use of the agglomerate technique to simulate crushable particles in the Discrete Element Method. A novel approach is proposed to design a Weibullian agglomerate by mimicking flaws within the crushable particle. The particle is designed with a constant number of sub-spheres in contrast to the approach widely used in the literature. However, the adhesion bonds between sub-spheres within the particle are selected randomly from a normal distribution. The normal distribution is designed to generate negative adhesion values, which are replaced by zero adhesion to mimic flaws within the particle. It is shown that the particle designed in this fashion exhibits a tensile strength that follows the Weibull probability function. This includes the effect of particle size that is remarkably captured quantitatively. Finally, a simple method is proposed to derive the parameters of the adhesion normal distribution from the Weibull parameters determined experimentally on single particle diametral compression tests.

1. Introduction

Particle crushing, or particle breakage, is a critical aspect of the mechanical response of granular materials. Silica sand undergoes crushing when subjected to high isotropic and deviatoric stresses as occurs, for example, around driven piles. Particle crushing significantly affects shaft and tip resistance of the pile in the short and long term (creep) (Leung et al., 1996; Klotz & Coop, 2001; Yang et al., 2010). Carbonate sand undergoes crushing even at low stresses and this affects its compression and shear response (Coop, 1990; Coop et al., 2004; Tarantino & Hyde, 2005). Particle crushing under low isotropic and deviatoric stresses occurs, for example, below shallow footings (Dijkstra et al., 2013).

Many aspects of the behavior of crushable granular materials can be adequately investigated by the Discrete Element Method (DEM). DEM allows the observation of their response at the scale of the particles and the investigation of the relation between small scale phenomena and macroscopic behavior.

There are two main traditional numerical techniques used to simulate particle crushing with the DEM. The first one consists in replacing the original particle by smaller ones when a stress limit is reached (Ciantia et al., 2016; Hanely et al., 2015; Clearly & Sinnott, 2015). The main advantage of the replacement technique is a relatively small computational cost, since the number of particles only increases when breakage occurs. But this comes at the cost of representativeness as the method considers breakage to occur always in the same manner and in one single stage, whereas variations are observed in nature. Other important disadvantage of this approach consists in its inability of ensuring a mass conservation after the breakage process.

The second technique consists in representing particles as agglomerates, i.e. a group of sub-spheres "glued" to each other by adhesion forces. When the force between these sub-spheres exceeds the adhesion force, the contact is irreversibly broken. Thus, crushing results in fragmentation due to the separation of sub-spheres. The main advantage of the agglomerate technique is the better representativeness of crushing processes. For example, it allows fragmentation of the particle to occur before the particle eventually crushes. In addition, particle shape can be better reproduced, which is not the case in the replacement technique even when polyhedrons or super quadrics particles are used. However, computational costs may be a restraining factor to the use of this method. The 'agglomerate' technique is explored further in this paper.

The design of the agglomerate is a critical aspect in DEM modelling of crushable materials and several approaches have been proposed in the literature. The agglomerate design includes the number of sub-spheres used to build the particle,

[#]Corresponding author. E-mail address: bmotams@gmail.com
[1]Universidade de Brasília, Departamento de Engenharia Civil e Ambiental, Brasília, DF, Brasil.
[2]University of Strathclyde, Department of Civil and Environmental Engineering, Glasgow, United Kingdom.

Submitted on May 10, 2022; Final Acceptance on April 27, 2023; Discussion open until November 30, 2023.
https://doi.org/10.28927/SR.2023.004922

the adhesion forces used to bond the sub-spheres, the approach used to simulate flaws within the particle, and the criteria used to validate the agglomerate design and calibrate the 'bonding' parameters.

Wang & Arson (2016) and Afshar et al. (2017) designed agglomerates by assuming that bonds between sub-spheres within a given agglomerate have the same strength and validated the agglomerate design and bonding parameters against single particle crushing tests in diametral compression. The limitation of this approach is that the variability of the tensile strength observed experimentally on particles of similar size sampled from the same batch is not taken into account.

Indeed, tensile strength of equally sized particles of same provenance shows variability and, as a result, tensile strength of individual grains is acknowledged to be a stochastic variable (Brzesowsky et al., 2011). The variability is attributed to flaws within the particles, which vary randomly from one particle to another. According to Weibull (1951), Weibull's distribution generally captures satisfactorily the variability of the grain tensile strength since it is developed on the assumption that the resistance of a structure is determined by its weakest link or component (Brzesowsky et al., 2011).

To simulate the variability of particle tensile strength, flaws need to be introduced randomly within the DEM agglomerate. A popular approach consists in generating flaws by omitting a percentage of sub-spheres during the particle construction as first adopted by Robertson (2000). This approach has been pursued by several authors since the random omission of sub-spheres within the agglomerate allows reproducing a Weibull distribution of survival probability (McDowell & Harierche, 2002; Lim & McDowell, 2007; Bolton et al., 2008; Wang & Yan, 2013; Cheng et al., 2003; McDowell & Bolton, 1998).

While the omission of sub-spheres is successful in generating a Weibullian agglomerate, its capability to capture particle size effects is more controversial. McDowell & Harierche (2002) had to remove an excessive number of sub-spheres to reproduce quantitatively size effects observed experimentally. However, this made it difficult to get diametral fast fracture on these agglomerates during single particle crushing tests because the agglomerates were too porous and crumbled. Later on, Lim & McDowell (2007) observed that the coordination number is the key to reproduce size effect correctly. It was found that a minimum of around 500 sub-spheres was necessary to give an approximately constant coordination number and the correct size effect. However, this poses problems when testing an assembly of agglomerates due to the large number of sub-spheres required to represent correctly the agglomerate. More in general, the design of the agglomerate based on sub-sphere removal to simulate flaws appears to be based on trials and errors and no rigorous approaches have been proposed so far to 'design' the percentage of sub-spheres to be removed.

This paper presents an alternative approach to design Weibullian agglomerates. These are designed with the same number of sub-spheres. However, the adhesion forces between sub-spheres within an agglomerate are not taken constant but are assumed to vary according to a normal distribution. Different agglomerates are then characterised by different randomly distributed adhesion forces that, however, are sampled from the same probabilistic distribution. Two key aspects are addressed in the paper to validate this new approach, i) the capability to generate a Weibulllian distribution of tensile strength including size effects and ii) the development of an objective criterion to infer the parameters of the normal distribution from experimental data on single particle crushing test.

2. Background

Tensile strength of single grains can be measured indirectly by the diametral compression test, where single particles are placed between two rigid plates and subjected to uniaxial compression until breakage (McDowell & Bolton, 1998). Tensile strength is generally found to vary according to the Weibull distribution. The probability of survival of a particle with volume $_0$ is represented by the following equation:

$$P_s\left(V_0\right) = \exp\left[-\left(\frac{\sigma}{\sigma_0}\right)^m\right] \tag{1}$$

where σ_0 is the stress value at which 37% of the particles with volume V_0 survives and the exponent m is the Weibull modulus, which is a measure of the variability of the tensile strength (m decreases as tensile strength variability increases).

As the crushing of grains is initiated by the propagation of pre-existent flaws under tensile stress, particle tensile strength is dependent on the number of flaws, and ultimately on its size, as probability of finding a flaw increases with size (Brzesowsky et al., 2011). Hence, small particles are stronger than the larger ones, and this effect of particle dimensions can be understood as a direct consequence of the tensile strength statistical distribution (McDowell & Bolton, 1998).

Weibull (1951) accounts for particle size through the relation between the particle diameter d and a reference diameter d_0, as stated in the following equation:

$$P_s\left(d\right) = \exp\left[-\left(\frac{d}{d_0}\right)^3\left(\frac{\sigma}{\sigma_0}\right)^m\right] \tag{2}$$

Equation 2 can be re-written as follows

$$P_s\left(d\right) = \exp\left[-\left(\frac{\sigma}{\sigma_0^*}\right)^m\right] \tag{3}$$

$$\sigma_0^* = \sigma_0\left(\frac{d}{d_0}\right)^{-\frac{3}{m}} \tag{4}$$

where σ_0^* is the size-dependent tensile strength associated with 37% survival probability.

Equation 2 makes implicitly two strong assumptions. The Weibull modulus *m* is independent of the grain size and the size effect is only controlled by the Weibull modulus *m* via the exponent 3/*m*, which can be determined in principle by testing a single grain size. These two assumptions have relatively wide experimental evidence including quartz sand (Nakata et al., 1999), Quiou calcareous sand (McDowell & Amon, 2000), Leighton Buzzard silica sand (McDowell, 2002), and Chongqing sandstone gravel (Xiao et al., 2018).

3. Methodology

3.1 Particle design

A 0.6 mm diameter virtual particle of Dogs Bay sand (Tarantino & Hyde, 2005) was designed with the agglomerate technique. One particle consists of spheres glued to each other by adhesion forces as illustrated in Figure 1. As the particle is compressed, forces between the spheres increase; when a limit is reached, adhesion is lost to represent fragmentation or total crushing of the particle.

To introduce flaws in the particles, adhesion between spheres was assumed to have a normal distribution with initial mean of 500 kPa and standard deviation of 700 kPa. These values allow the existence of negative adhesion as shown in Figure 2. Such values were replaced by zero since negative values do not hold any physical meaning. These zero values allow mimicking flaws within the particle. A methodology is latter explained to choose the most appropriate values for the average normal strength and its standard deviation.

Two adhesion values are attributed to each contact, a normal and a tangential component. These are attributed independently, i.e. one component can be randomly assigned a value equal to zero whereas the other one can be assigned randomly a value different from zero. The contacts fall apart when both the tangential and normal adhesion are exceeded.

Normal and tangential stiffness, k_n and k_t respectively, between sub-spheres were defined according to the standard values calculated by YADE, a Discrete Element Method open-source code (Šmilauer et al., 2015). The normal stiffness k_n is related to fictitious Young's modulus of the particles' material, E_i, and the distance between the centre of the particle and the contact point, proportional to r_i, according to the expression:

$$k_n = \frac{E_1 2r_1 E_2 2r_2}{E_1 2r_1 + E_2 2r_2} \quad (5)$$

The value assumed to E_i was 100 MPa.

The tangential stiffness is determined as a given fraction of computed k_n (Šmilauer et al., 2015).

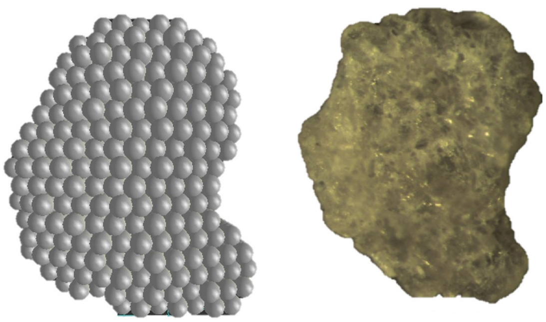

Figure 1. Dogs-bay sand particle: (a) virtual, (b) real.

3.2 Virtual diametral compression test

Diametral compression tests were simulated with YADE. The particle was placed on a plane while a platen on the other side compressed the particle. The simulation scheme is illustrated in Figure 3. An example of typical force-displacement curves is shown in Figure 4 for particles of 0.6 mm diameter assembled with 500 sub-spheres of 0.030 mm diameter. All the curves in Figure 4 were obtained from the same agglomerate, i.e., same shape and same number of spheres. The difference between the results happens because each one of the agglomerates have a unique bond distribution

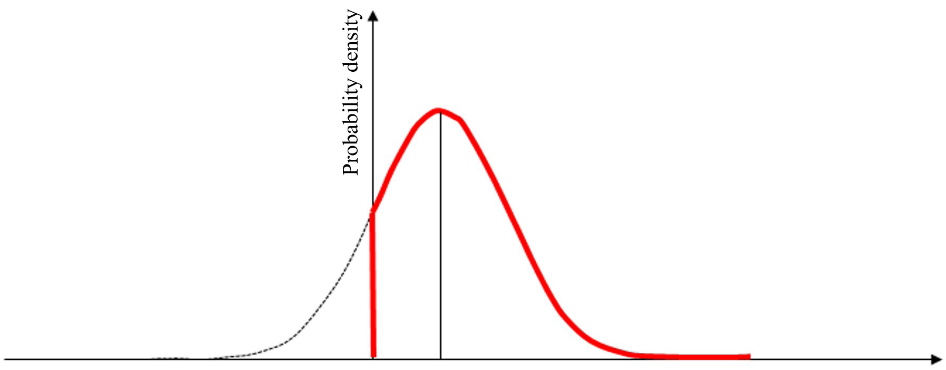

Figure 2. Normal distribution of adhesion forces between spheres.

between its spheres resulting in different resistances. It can be observed that a peak is well defined, and this peak force was taken to characterize the particle tensile strength.

The contact between the platens and the particle sub-spheres in contact with the basal plane and the platen were assumed to be frictionless and the basal plane and the platens were assumed to be infinitely stiff.

Two different contact models were used to reach the simulation desired behavior. The first one is related with the interaction between the platens and the particle. The "FrictMat_FrictMat_FrictPhys" contact model adopting friction as zero simulating a frictionless and cohesionless interaction. The other contact model used is related to the interactions between the bonded spheres inside the agglomerate. "CohFrictMat_CohFrictMat_CohFrictPhys" was used to simulate these cohesive interactions.

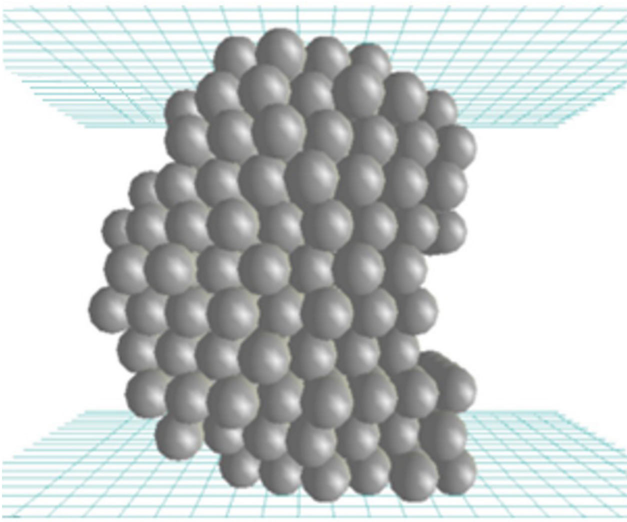

Figure 3. Virtual diametral compression test on crushable particle.

3.3 Representativeness of the tensile strength sample

Since particle tensile strength is defined in probabilistic terms, it is important to define an adequate size of the sample required to represent the tensile strength population. McDowell (2001) suggested that the number of tests should be between 10% and 15% of the real population, depending on the standard deviation of the tensile strength.

The population of analyses required to characterize Weibull's probability was defined with the Monte Carlo Method, which is adequate for problems with random variables. This method was selected because of the randomness generated by the normal distribution of adhesion forces, since a new configuration of adhesion forces (sampled from the same probabilistic distribution) is generated in each test.

The methodology consisted in simulating initially 100 compression tests. Then, additional sets of 50 tests were executed. For each cumulative set of tests, the probabilistic distribution of the survival probability $P_s(d)$ of the particle of size d was drawn in Figure 5. It was observed that the survival probability stabilized for a number of tests ≥ 300, which is then assumed to be the minimum number of virtual crushing tests to be carried out to return a statistical representative sample of tensile strength.

3.4 Effect of the number of sub-spheres

The number of sub-spheres forming the particle introduces potentially a scale effect that was also investigated. Particles formed with 500, 1000, 2000, and 3000 sub-spheres were tested in diametral compression as illustrated in Figure 6. The minimum number of sub-spheres was selected based on Lim & McDowell (2007), who established a minimum of 500 sub-spheres to capture size-effects according to Weibull distribution. A number of 600 compression tests were simulated

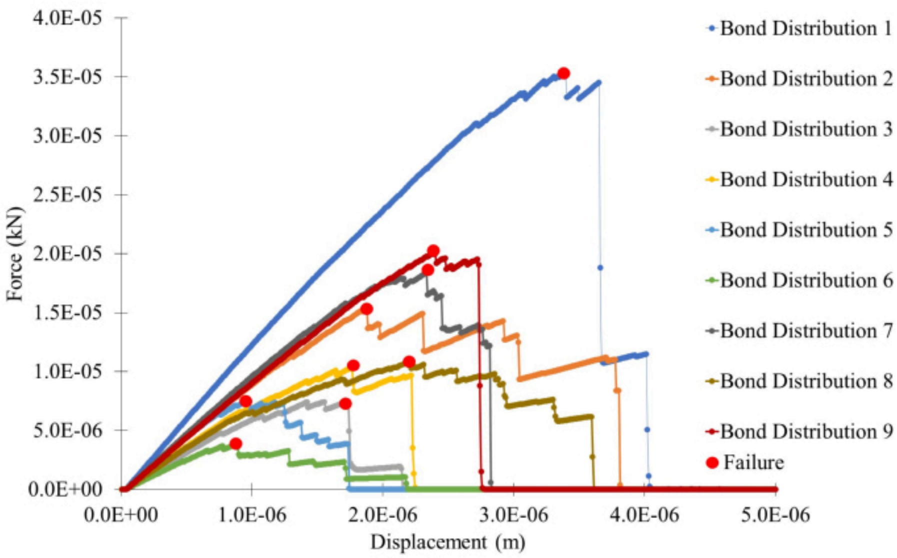

Figure 4. Typical force versus displacement plot for 0.6 mm particle (500 sub-spheres 0.030 mm diameter).

on each particle to characterize their statistical distribution of survival probability. As shown in Figure 7, the number of sub-spheres does not essentially affect the distribution of survival probability. Only the distribution associated with 2000 sub-spheres deviates slightly from the other three distributions but there is not a trend as the number of sub-spheres is increased.

3.5 Effect of platen velocity

To test the effect of platen velocity, the same particle 0.6 mm diameter was compressed at the velocities of 0.01, 0.1, and 1 mm/s. The results of these tests in terms of distribution of survival probability are shown in Figure 8 and show that the platen velocity does not influence the diametral compression test results. A velocity of 0.1 mm/s was adopted for all the tests presented on the following.

4. Results

4.1 Survival probability of particle of given size

Figure 9 shows the particle survival distribution data for particles of same size (0.6 mm) and formed with a different

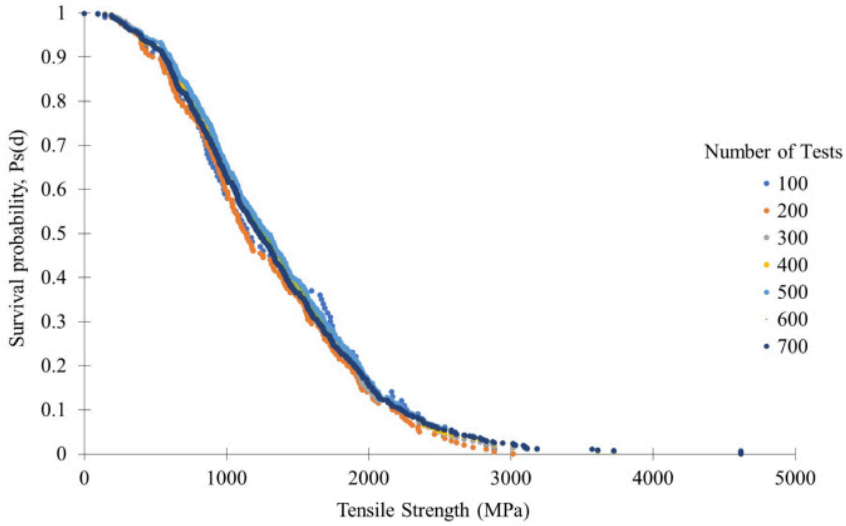

Figure 5. Effect of number of tests on the statistical distribution of survival probability $P_s(d)$.

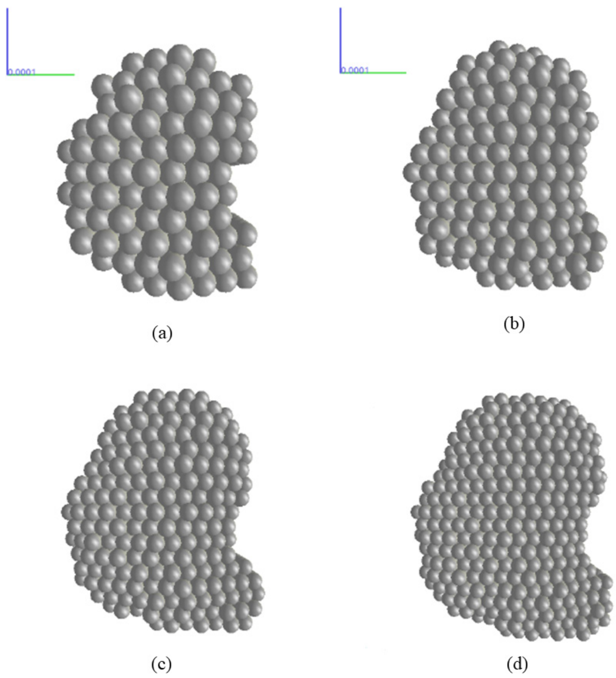

Figure 6. Particles 0.6 mm diameter tested in diametral compression: (a) 500 sub-spheres 0.030 mm diameter, (b) 1000 sub-spheres 0.025 mm diameter, (c) 2000 sub-spheres 0.020 mm diameter, (d) 3000 sub-spheres 0.017 mm diameter.

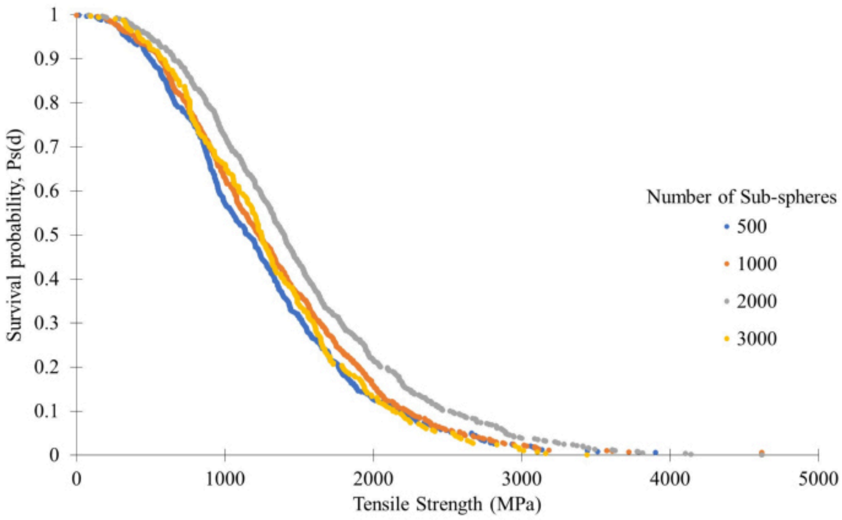

Figure 7. Statistical distribution of survival probability 0.6 mm particles generated using 500, 1000, 2000, and 3000 sub-spheres respectively (based on 600 crushing tests for each particle).

number of sub-spheres (500, 1000 and 2000 respectively) fitted by the Weibull function given by Equation 2. The data for each particle in Figure 9 were generated by 600 virtual diametral compression tests. The excellent fitting clearly shows that the approach put forward in this paper based on random adhesion between sub-spheres is successful in generating a Weibullian survival distribution, which is consistent with experimental data from single particle crushing tests.

Figure 10 shows the evolution of the Weibull modulus m and the 37% survival tensile strength σ_0 with the number of virtual diametral tests used to generate the tensile strength data. The Weibull parameters tend to stabilize for a relatively large number of tests as discussed in a previous section. It is also worth noticing that number of sub-spheres used to generate the 0.6 mm particle (500, 1000, and 2000) has a negligible effect on the Weibull parameters. It was concluded that any of number of sub-spheres in this range could be adopted successfully to represent a Weibullian particle. This finding is used in the next section where the effect of particle size is investigated.

4.2 Particle size effect

Weibull (1951) introduced the effect of particle size in his equations to account for the higher probability of crushing of larger particles. It should therefore be demonstrated that the agglomerate design approach put forward in this paper is capable of capturing qualitatively and quantitatively the influence of the size of the compressed particle.

Studies on size effects were performed by testing particles of 0.48, 0.60 and 0.72 mm diameter constructed by using 500, 1000, and 1700 sub-spheres respectively, as shown in Figure 11. The size of the sub-spheres was maintained the same in each particle and equal to 0.025 mm.

Each particle was compressed 600 times to derive a Weibull probability distribution. The survival probability distribution for these three particles is shown in Figure 12. It can be inferred that the particle size effect is captured correctly. The distribution of the largest particle is shifted to the right, indicating that the largest particle is more susceptible to crushing.

It is interesting to plot the evolution of the Weibull modulus *m* with the number of tests for the three particles as shown in Figure 13. When the number of tests becomes sufficiently large, the Weibull modulus *m* is found to be essentially independent of the particle size. This is a feature required to the agglomerate in accordance with experimental results as discussed in Section 2.

Figure 14 shows the 37% survival tensile strength σ_0* plotted against the particle size *d*. The slope of the curve *log d- log* σ_0* is equal to 1.40, which equals the ratio ~ 3/*m* = 1.4 as derived from Figure 13. The approach based on the normal distribution of adhesion (Figure 2) therefore proves capable of capturing quantitatively the effect of particle size according to the Weibull theory (Equations 2 and 4).

5. Calibration of bonding parameters

After attesting the validity of the approach proposed to design agglomerates, it is useful to discuss how the parameters of the normal distribution of the adhesion forces, namely the Average *Av* the Standard Deviation *SD* can be calibrated to match the behaviour of real particles in diametral compression observed experimentally.

Figure 15 shows the effect of standard deviation to average ratio *SD/Av* on the Weibull modulus *m* and the 37% survival tensile strength σ_0 for a given average *Av*. It can be observed that the ratio *SD/Av* controls both the parameters m and σ_0 of the Weibull distribution.

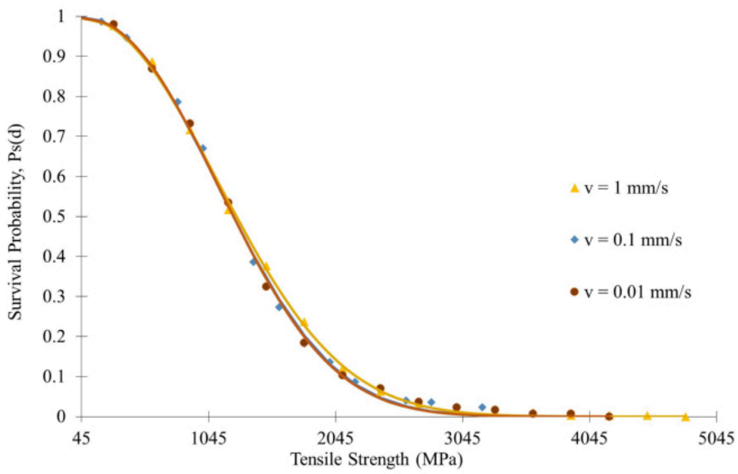

Figure 8. Effect of platen velocity.

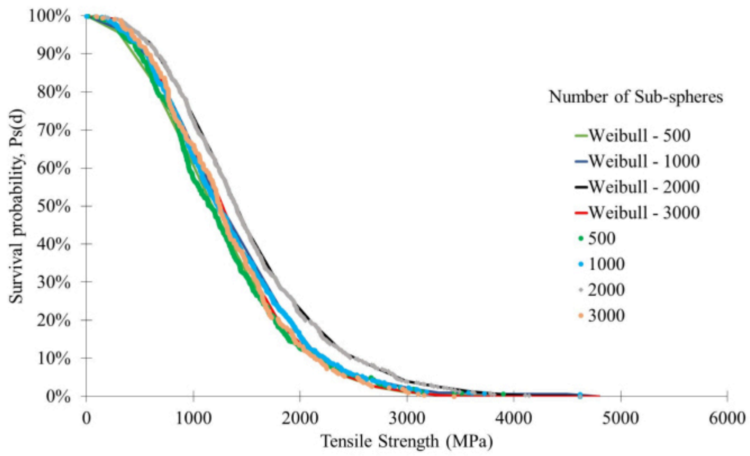

Figure 9. Survival statistical distribution for particle 0.6 mm size fitted with Weibull probability function.

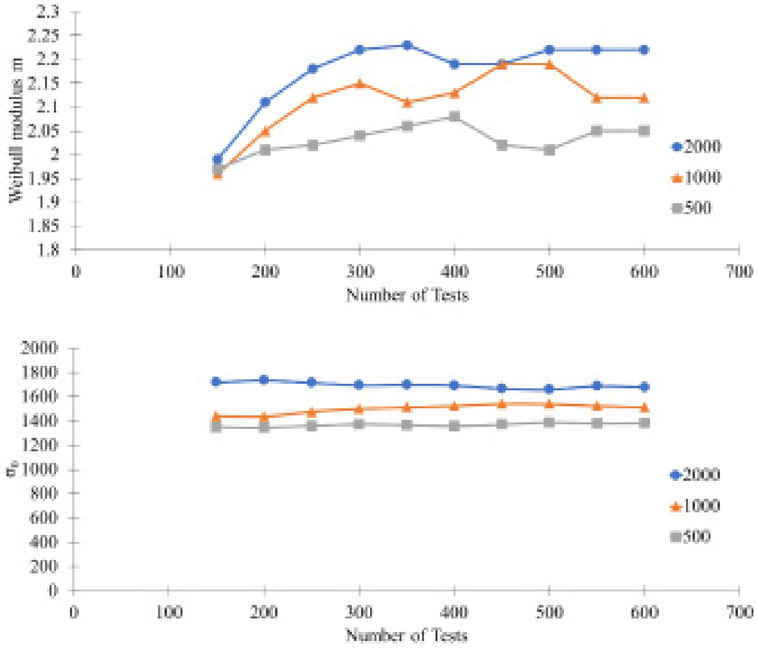

Figure 10. Stabilization of m and σ0 for particles 0.6 mm size made of 500, 1000, 2000, and 3000 sub-spheres.

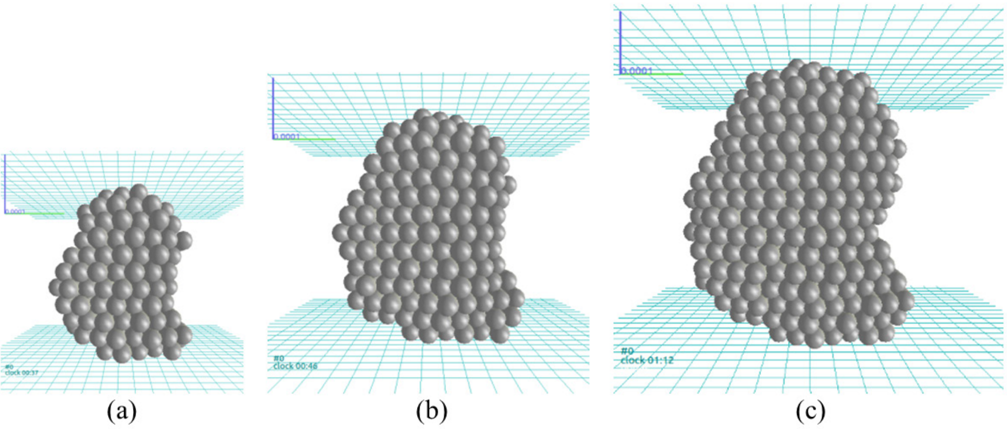

Figure 11. Particles tested on the size effects studies: (a) d = 0.48 mm and 500 sub-spheres, (b) d = 0.60 mm and 1000 sub-spheres, (c) d = 0.72 mm and 1800 sub-spheres (size of sub-sphere equal to 0.025 mm).

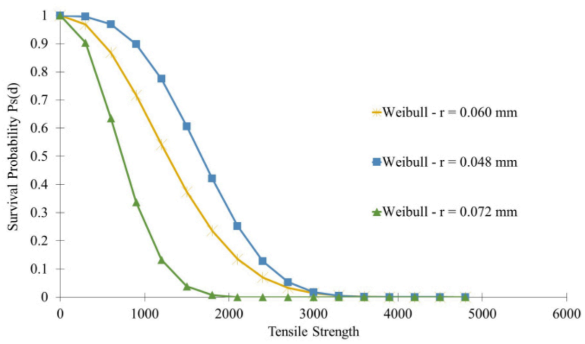

Figure 12. Statistical distribution of survival probability for particles having 0.48, 0.60, and 0.72 mm diameter fitted with the Weibull probability function.

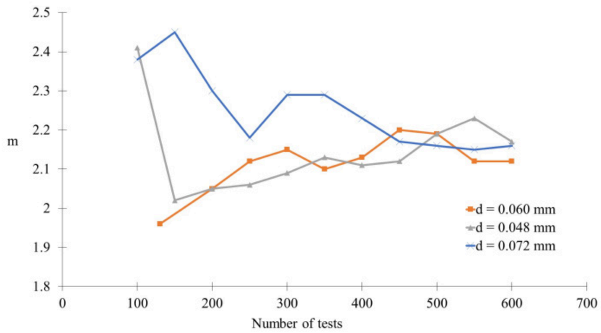

Figure 13. Effect of particle size on Weibull modulus *m*.

Figure 16 shows the effect of average *Av* on the Weibull modulus *m* and the 37% survival tensile strength σ_0 for a given ratio *SD/Av*. In this case, the average *Av* seems to have essentially no effect on the Weibull modulus *m* but only on the 37% survival tensile strength σ_0. This can be used

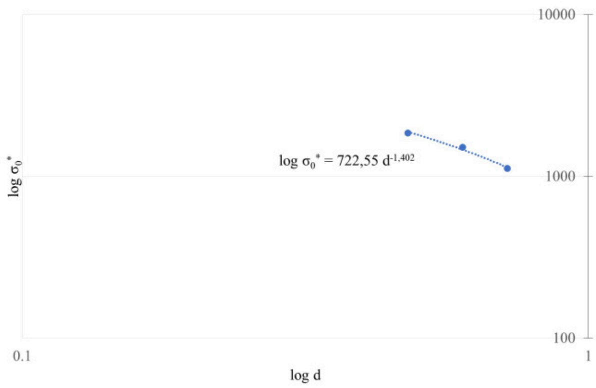

Figure 14. Effect of particle size on 37% survival tensile strength σ_0*.

advantageously to calibrate the parameters *Av* and *SD/Av* of the normal distribution of the adhesion forces.

Let us assume in this example that the diametral compression tests on crushable grains return m = 3.2 and σ_0 = 2900 kPa. A value of *Av* = 500 kPa is initially tentatively selected and the dependency of *m* and σ_0 upon the ratio *SD/Av* is explored numerically as shown in Figure 15. Figure 15a shows that m = 3.2 is associated with value of *SD/Av* = 1, which is value selected for the normal distribution of adhesion forces. For this ratio *SD/Av* = 1, the dependency of *m* and σ_0 upon the average is explored numerically in Figure 16. Figure 16b shows that σ_0 = 2900 kPa is associated with *Av* = 700 kPa, which is the value eventually selected for the normal distribution of adhesion forces.

Because *m* and σ_0 are not controlled independently by *SD/Av* and *Av*, this new value of *Av* = 700 kPa returns a value of m = 3.5 as shown in Figure 16b that is slightly different from the target one initially inputted in Figure 15a. However, this difference is not significant and can be deemed acceptable for most practical applications. If not, the iteration can be started again by considering *Av* = 700 kPa rather than *Av* = 500 kPa in Figure 15.

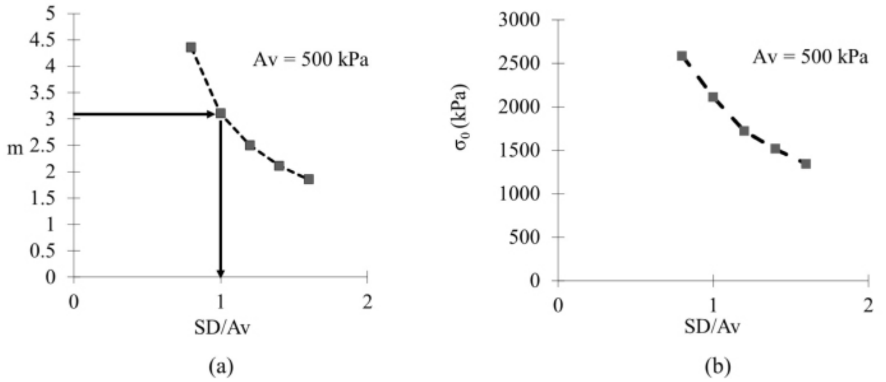

Figure 15. Effect of standard deviation to average ratio *SD/Av* on (a) Weibull modulus m and (b) 37% survival tensile strength σ_0.

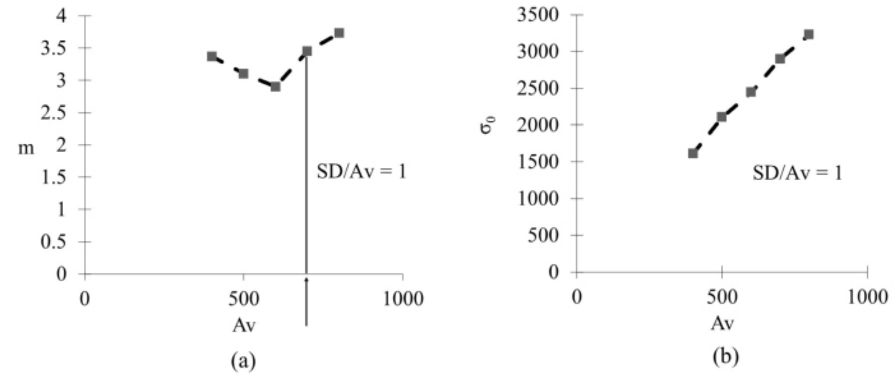

Figure 16. Effect of average *Av* on (a) Weibull modulus m and (b) 37% survival tensile strength σ_0.

6. Conclusion

This paper has presented an approach to design crushable particles in the Discrete Element Method. The particle is designed with a given number of sub-spheres, and the adhesion bonds between sub-spheres are selected randomly from a normal distribution. The normal distribution is designed to generate negative adhesion values, which are then replaced by zero adhesion to mimic flaws within the particle.

The effects of number of tests, platen velocity, and number of sub-spheres composing the particle have been preliminary investigated to make sure that numerical results were not biased by the numerical setting. Numerical results have shown that the tensile strength of particle of given size follows the Weibull distribution and that the dependency of the 37% survival tensile strength on particle size is also consistent with the Weibull distribution. It is worthy noticing that all tests were carried out for only one agglomerate shape, positioned in one direction.

The approach proposed in the paper is therefore capable of producing a Weibullian agglomerate in a simple and robust fashion. Finally, a simple method is proposed to derive the parameters of the adhesion normal distribution from the Weibull parameters determined experimentally on single particle diametral compression tests.

Declaration of interest

The authors have no conflicts of interest to declare. All co-authors have observed and affirmed the contents of the paper and there is no financial interest to report.

Authors' contributions

Bruna Mota Mendes Silva Tedesco: conceptualization, data curation, methodology, resources, software, writing – original draft. Manoel Porfirio Cordão-Neto: conceptualization, methodology, supervision, validation, project administration. Márcio Muniz de Farias: supervision, validation. Alessandro Tarantino: supervision, validation, writing – review & editing.

Data availability

The data generated on this study are not public but may be available from the corresponding author on reasonable request.

List of symbols

d	diameter
d_0	reference diameter

k_n	normal stiffness
k_t	tangential stiffness
m	Weibull's modulus
r_i	particle's radius
A_v	normal distribution average
DEM	descrete element method
E_i	fictitious Young's modulus of the particles' material
P_s	probability if survival of a particle
SD	normal distribution standard deviation
V_0	particle's volume
σ_0	stress value at which 37% of the particles survives
σ_0*	size-dependent tensile strength associated with 37% survival probability

References

Afshar, T., Disfani, M.M., Arulrajah, A., Narsilio, G.A., & Eman, S. (2017). Impact of particle shape on breakage of recycled construction and demolition aggregates. *Powder Technology*, 308, 1-12. http://dx.doi.org/10.1016/j.powtec.2016.11.043.

Bolton, M.D., Nakata, Y., & Cheng, Y.P. (2008). Micro- and macro-mechanical behaviour of DEM crushable materials. *Geotechnique*, 58(6), 471-480. http://dx.doi.org/10.1680/geot.2008.58.6.471.

Brzesowsky, R.H., Spiers, C.J., Peach, C.J., & Hang, S.J.T. (2011). Failure behaviour of single sand grains: theory versus experiment. *Journal of Geophysical Research*, 116(B6), 1-13. http://dx.doi.org/10.1029/2010JB008120.

Cheng, Y.P., Nakata, Y., & Bolton, M.D. (2003). Discrete element simulation of crushable soil. *Geotechnique*, 53(7), 633-641. http://dx.doi.org/10.1680/geot.2003.53.7.633.

Ciantia, M.O., Arroyo, M., Calvetii, F., & Gens, A. (2016). A numerical investigation of the incremental behavior of crushable granular soils. *International Journal for Numerical and Analytical Methods in Geomechanics*, 40(13), 1773-1798. http://dx.doi.org/10.1002/nag.2503.

Clearly, P.W., & Sinnott, M.D. (2015). Simulation of particle flows and breakage in crushers using DEM. *Minerals Engineering*, 74, 178-197.

Coop, M.R. (1990). The mechanics of uncemented carbonate sands. *Geotechnique*, 40(4), 607-626. http://dx.doi.org/10.1680/geot.1990.40.4.607.

Coop, M.R., Sorensen, K.K., Freitas, T.B., & Georgoutsos, G. (2004). Particle breakage during shearing of a carbonate sand. *Geotechnique*, 54(3), 157-163. http://dx.doi.org/10.1680/geot.2004.54.3.157.

Dijkstra, J., Gaudin, C., & White, D.J. (2013). Comparison of failure modes below footings on carbonate and silica sands. *International Journal of Physical Modelling in Geotechnics*, 13(1), 1-12. http://dx.doi.org/10.1680/ijpmg.12.00004.

Hanely, K.J., O'Sullivan, C., & Huang, X. (2015). Particle-scale mechanics of sand crushing in compression and shearing using DEM. *Soil and Foundation*, 55(5), 1100-1112. http://dx.doi.org/10.1016/j.sandf.2015.09.011.

Klotz, E.U., & Coop, M.R. (2001). An investigation of the effect of soil state on the capacity of driven piles in sands. *Geotechnique*, 51(9), 733-751. http://dx.doi.org/10.1680/geot.2001.51.9.733.

Leung, C.F., Lee, F.H., & Yet, N.S. (1996). The role of particle breakage in pile creep in sand. *Canadian Geotechnical Journal*, 33(6), 888-898. http://dx.doi.org/10.1139/t96-119.

Lim, W.L., & McDowell, G.R. (2007). The importance of coordination number in using agglomerates to simulate crushable particles in the discrete element method. *Geotechnique*, 57(8), 701-705. http://dx.doi.org/10.1680/geot.2007.57.8.701.

McDowell, G.R. (2001). Statistics of soil particle strength. *Geotechnique*, 51(10), 897-900. http://dx.doi.org/10.1680/geot.2001.51.10.897.

McDowell, G.R. (2002). On the yielding and plastic compression of sand. *Soil and Foundation*, 42(1), 139-145. http://dx.doi.org/10.3208/sandf.42.1139.

McDowell, G.R., & Amon, A. (2000). The application of Weibull statistics to the fracture of soil particles. *Soil and Foundation*, 40(5), 133-141. http://dx.doi.org/10.3208/sandf.40.5_133.

McDowell, G.R., & Bolton, M.D. (1998). On the micromechanics of crushable aggregates. *Geotechnique*, 48(5), 667-679. http://dx.doi.org/10.1680/geot.1998.48.5.667.

McDowell, G.R., & Harierche, O. (2002). Discrete element modelling of soil particle fracture. *Geotechnique*, 52(2), 131-135. http://dx.doi.org/10.1680/geot.2002.52.2.131.

Nakata, Y., Hyde, A.F.L., Hyodo, M., & Murata, H. (1999). A probabilistic approach to sand particle crushing in the triaxial test. *Geotechnique*, 49(5), 567-583. http://dx.doi.org/10.1680/geot.1999.49.5.567.

Robertson, D. (2000). *Computer simulations of crushable aggregates* [Doctoral thesis]. University of Cambridge.

Šmilauer, V., Catalano, E., Chareyre, B., Dorofeenko, S., Duriez, J., Dyck, N., & Yuan, C. (2015). *Yade documentation* (2nd ed.). The Yade Project. https://doi.org/10.5281/zenodo.34073.

Tarantino, A., & Hyde, A.F.L. (2005). An experimental investigation of work dissipation in crushable materials. *Geotechnique*, 55(8), 575-584. http://dx.doi.org/10.1680/geot.2005.55.8.575.

Wang, J., & Yan, H. (2013). On the role of particle breakage in the shear failure behaviour of granular soils by DEM. *International Journal for Numerical and Analytical Methods in Geomechanics*, 37(8), 832-854. http://dx.doi.org/10.1002/nag.1124.

Wang, P., & Arson, C. (2016). DEM of shielding and size effects during single particle crushing. *Computers and Geotechnics*, 78, 227-236. http://dx.doi.org/10.1016/j.compgeo.2016.04.003.

Weibull, W. (1951). A statistical distribution function of wide applicability. *Journal of Applied Mechanics*, 18(3), 293-297. http://dx.doi.org/10.1115/1.4010337.

Xiao, Y., Meng, M., Daouadji, A., Chen, Q., Wu, Z., & Jiang, X. (2018). Effects of particle size on crushing and deformation behaviors of rockfill materials. *Geoscience Frontiers*, 11(2), 375-388. http://dx.doi.org/10.1016/j.gsf.2018.10.010.

Yang, Z.X., Jardine, R.J., Zhu, B.T., Foray, P., & Tsuha, C.H.C. (2010). Sand grain crushing and interface shearing during displacement pile installation in sand. *Geotechnique*, 60(6), 469-482. http://dx.doi.org/10.1680/geot.2010.60.6.469.

Soils and Rocks
An International Journal of Geotechnical and Geoenvironmental Engineering
www.soilsandrocks.com
ISSN 1980-9743
ISSN-e 2675-5475

Contribution to resilient and permanent deformation investigation of unbound granular materials with different geological origins from Rio Grande do Sul, Brazil

Amanda Vielmo Sagrilo[1#], Paula Taiane Pascoal[1], Magnos Baroni[1], Ana Helena Back[2], Rinaldo José Barbosa Pinheiro[1], Luciano Pivoto Specht[1], Antônio Carlos Rodrigues Guimarães[3]

Article

Keywords
Deformability
Pavement
Shakedown theory
Granular base course
Lithological origins

Abstract

This article evaluates the resilient modulus and permanent deformation of granular materials of different lithological origins widely used as a pavements base layer in south Brazil. For this, a single particle size distribution was determined for the materials that were subjected to physical, chemical, mechanical characterizations, especially resilient modulus and permanent deformation by repeated load triaxial tests. It was noticed that the denser materials had a higher resilient modulus generated by increase in the sample's stiffness. For permanent deformation this tendency has not been maintained for all materials. Therefore, the granulation and structure of the materials can influence long-term tests. The Guimarães' model has proven to be adequate for the sample evaluation. For the shakedown research, samples showed accommodation and creep shakedown. The samples that presented accommodation had an increase in the resilient modulus after permanent deformation, while those that presented creep increased or decreased resilient modulus according to the material origin.

1. Introduction

Granular materials, used as a base layer for flexible pavements, influence the structure performance as a whole. In this layer, when the material receives and supports the stresses of traffic, successively returning to its original state throughout its service life, it is said that this material has a high resilient modulus (RM), preventing the formation of fatigue cracks on the pavement surface. Concomitantly, part of the deformations caused by traffic action are accumulated, called permanent deformations (PD) which, added to the deformations of other layers, are manifested on the pavement surface as rutting (Huang, 2004; Cerni et al., 2012; Erlingsson et al., 2017).

Shakedown theory is used to characterize soils and unbound granular materials employed in pavements (Werkmeister et al., 2001; Werkmeister, 2003; Werkmeister, 2006; Wang & Yu, 2013; Gu et al., 2017; Alnedawi et al., 2019a; Nazzal et al., 2020). According to the theory, the unbound granular materials (UGM) can present three different ranges: range A or plastic shakedown, after a finite number of cicles, the acumulation of permanent deformations reaches a constant; range B or creep shakedown, the permanent strain rate decreases after a number of cycles, but the resilient strains are not constant and the stiffness decrease; range C or incremental colapse, the permanent deformation increases with the cycles. The UGMs can fail by shear or overstressing.

The main parameters that affect the elastic and plastic deformability of granular layers are the active stresses, the reorientation of the main stresses, the history of stresses, number, duration and frequency of loads, degree of compaction, moisture content, particle size distribution, maximum size of aggregates, fines content, type of aggregate and particle shape (Collins & Boulbibane, 2000; Lekarp et al., 2000; Lekarp & Isacsson, 2001; Song & Ooi, 2010; Xiao et al., 2019; Soliman & Shalaby, 2015). Among these factors, for the present study, the lithological origin of the aggregates that compound the granular material is emphasized.

[#]Corresponding author. E-mail address: amandavs94@gmail.com
[1]Universidade Federal de Santa Maria, Departamento de Transportes, Santa Maria, RS, Brasil.
[2]Faculdade Dom Alberto, Santa Cruz do Sul, RS, Brasil.
[3]Instituto Militar de Engenharia, Seção de Ensino de Engenharia de Fortificação e Construção, Rio de Janeiro, RJ, Brasil.

Submitted on September 22, 2022; Final Acceptance on May 18, 2023; Discussion open until November 30, 2023.

https://doi.org/10.28927/SR.2023.009822

According to Xiao et al., (2019), Ba et al. (2015), Alnedawi et al. (2019b) and Alnedawi et al. (2021), granular materials composed of different lithological origins show different deformability behavior, even when the granulometric curve is similar among them. Lima et al. (2017) have analyzed two quarries of the same lithological origin and for the same granulometric curve obtained similar results in terms of resilience and permanent deformation. Nazzal et al. (2020) have conducted RM and PD tests of granular granite, sandstone and limestone materials. The mixtures' granulometric curves were similar, although the behavior in terms of resilience, permanent deformation and shakedown are considerably different.

In this paper, for the tests of the resilient modulus (DNIT, 2018a) and permanent deformation (DNIT, 2018b), repeated load triaxial (RLT) test has been used. Among the mathematical models employed for the RM behavior the following models stand out: model k-σ_3, dependent on the confining stress (Biarez, 1962), model k-σ_d as a function of the deviator stress (Svenson, 1980), model k-θ, addressed by Seed et al. (1967), Compound model proposed by Pezo et al. (1992), and Universal model that had been presented by AASHTO (2004), in addition to the models by Witczak (Rada & Witczak,1981) and Witczak & Uzan (1988). In the analysis of permanent deformation, the Guimarães' model (Guimarães, 2009; Guimarães et al., 2018), has been used, which proved to be adequate to the particularities of soils and tropical materials (Nogami & Villibor, 1991; Medina & Motta, 2015; Carvalho et al., 2015; Lima et al., 2020; Pascoal et al., 2021).

The objective of this study is to evaluate the resilient and permanent deformation behavior of three unbound granular materials from different lithological origins. The characterization of the materials that compose the UGM and the results of tests and mathematical modeling of RM and PD and shakedown research are presented. The relevance of this study is related to the extensive use of granular bases regionally, due the abundance and variability of rock masses in the territory of the state of Rio Grande do Sul. Therefore, these materials should be characterized in terms of deformability. Besides, this study contributes to the database of the Brazilian M-E Design Method (MeDiNa), which is being implemented.

2. Materials and methods

2.1 Materials

To evaluate the influence of the lithological origin on the resilient behavior, permanent deformation and shakedown of the base course layer, three different types of mineral aggregates were selected. It is noteworthy that such materials came from different geomorphological provinces, including practically all lithological formations in the state of Rio Grande do Sul, Brazil. For this purpose, São Juvenal quarry and Della Pasqua quarry, named respectively as SJ and DPA, are originated from the Planalto Meridional Province, the geographical coordinates (UTM; Universal Transverse Mercator coordinate system) of which are, respectively: 22J – 251945.40 m W 6826112.10 m S and 22J – 228402.58 m W 6724545.40 m S. In contrast, the third material, originated from SBS Engenharia quarry, called SBS, is located in the Escudo Sul-Rio-Grandense Province under coordinates 22J – 357488.45 m W 6483361.81 m S. Figure 1 shows the unbound granular material analyzed in this study.

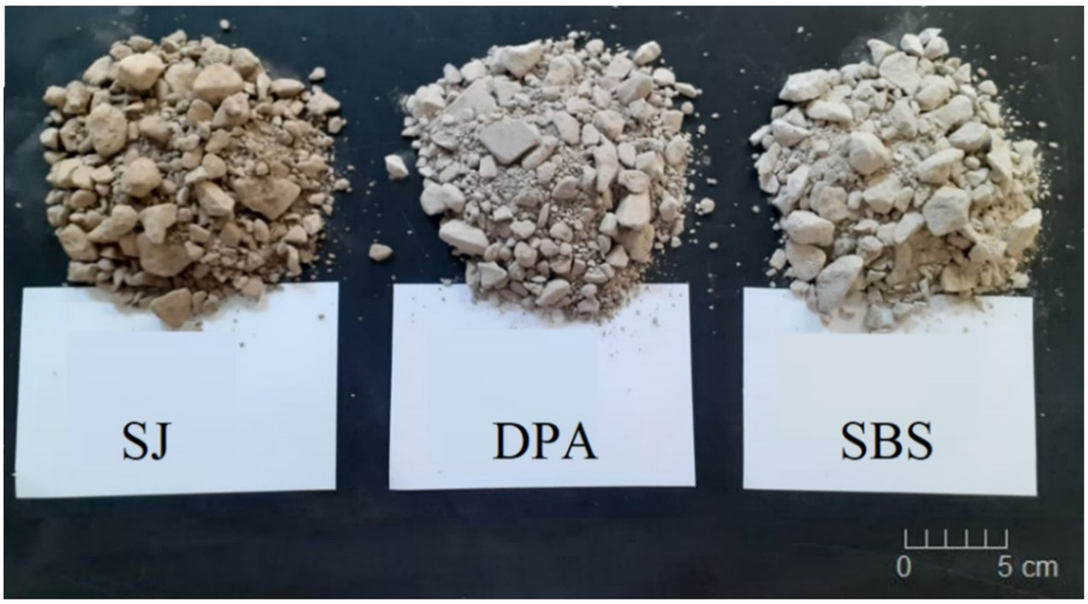

Figure 1. General aspect of the unbound granular material from different lithologies analyzed in this work.

The petrographic thin section slides provided the microscopic description of the textural, structural and mineralogical characteristics of the rocks, in addition to the physical and mechanical characterization tests. Table 1 presents the mineralogical composition, rock description and the physical and mechanical indexes.

Based on Table 1, aggregates mechanical performance is consistent with their different types of formation, since SJ and DPA are defined as volcanic igneous rocks, with aphanitic texture, and SBS as plutonic igneous rock, with phaneritic texture. Although plutonic igneous rocks have satisfactory mechanical resistance due to the relative homogeneity of rock bodies in addition to the mineralogical composition that holds minerals of high hardness, the high granulation of their minerals promotes points of weakness in the rock, increasing the occurrence of micro fractures and consequently decreasing the material mechanical strength (Curtis Neto et al., 2018; Back et al., 2021; Adomaki et al., 2021). This fact justifies the superior mechanical performance of SJ and DPA, since they have aphanitic texture and/or fine granulation, thus presenting better distributions of mechanical efforts.

The presence of large percentages of alkali feldspar corroborates to the high abrasive loss of SBS, which contains minerals of high hardness (e.g., feldspar: 6 and quartz: 7) with the rocky matrix and show low tenacity due to the granulation. Similarly, the presence of foliation also influences the SBS mechanical performance since it adds horizontal weakness planes that tend to generate a higher percentage of lamellar aggregates in the crushing process and these particles tend to break in the compaction process (Wojahn et al., 2021). In addition to the abrasive loss, there is high loss due to impact and crushing.

Regarding the high percentage of olivine in the SJ rock, it appears that such mineral does not have a dominant influence on the basaltic rock. Although it presents tendencies to alterability, still exhibits excellent results in laboratory tests of mechanical performance and soundness, showing a relatively healthy behavior.

Table 1. Mineralogical composition and rock characterization.

	SJ	DPA	SBS
Essential minerals	40% Plagioclase 30% Clinopyroxene 20% Olivine 10% Oxides	35% Feldspar 32% Quartz 25% Pyroxene 8% Opaque	45% K-Feldspar 20% Quartz 20% Biotite 15% Plagioclase
Secondary minerals	Biotite Oxides	Opaque	Mafics Oxides
Carbonate minerals	Absent	Absent	Absent
Deleterious minerals	Oxides	Absent	Mafics Oxides
Structure	Massive	Massive	Foliated
Texture	Aphanitic	Very thin porphyritic inequigranular aphanitic	Inequigranular phaneritic
Rock Type (DNER, 1994a)	Basalt	Rhyodacite	Syenogranite
Rock acidity nature	Basic	Acidic	Acidic
Petrographic thin section slides under polarized light (scale: 100 pixels)	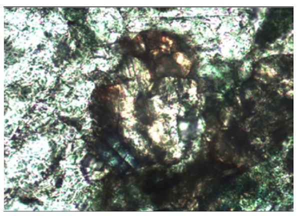	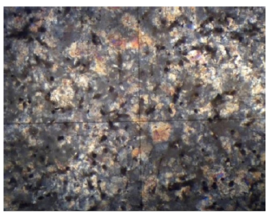	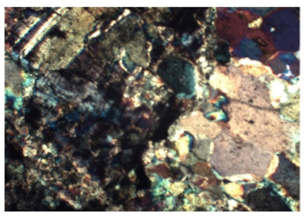
Specific Gravity (g/cm^3) (DNER, 1997a)	2.87	2.5	2.61
Water Absorption (%) (DNER, 1997a)	1.19	2.19	0.69
Sodium sulphate soundness (%) (DNER, 1994b)	5.62 – C 5.70 – F	0.66 – C 5.61 – F	1.72 – C 8.98 – F
"LA" Abrasion (%) (DNER, 1998a)	12.56	10.05	26.39
Impact value (%) (DNER, 1999)	8.44	4.66	18.70
Crushing value (%) (DNER, 1997b)	13.73	13.17	26.38

Where: C: coarse aggregate; F: fine aggregate.

2.2 Experimental program

The granulometric curve adopted for the evaluated UGM is in accordance with a highway road standard (DNER, 1998b). The material from the aforementioned rock deposits went through separation, sieving and mixing procedures in order to obtain the specified UGM. A single granulometric curve was used for the three unbound granular materials, which was included within the limits of the most used specifications for the granular base layers of Brazil's southern region by the federal highway agencies (range C) (DNIT, 2006) and state highway agencies (maximum size 3/4") (DAER, 1991). Figure 2 shows the selected particle size distribution.

The samples were subjected to the compaction test to determine the maximum dry density (MDD) and

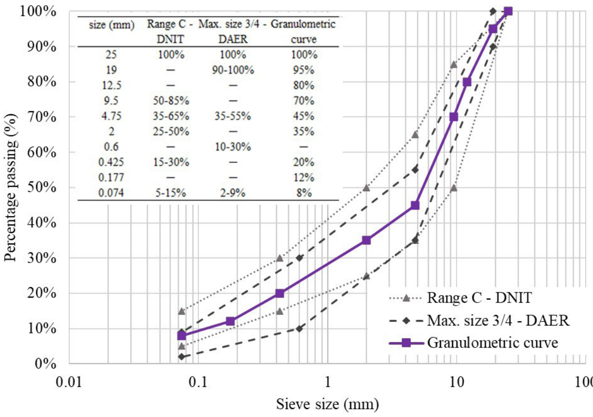

Figure 2. Granulometric curve.

the optimum moisture content (OMC). The compaction process follows the procedures described in the standards of resilient modulus (DNIT, 2018a) and permanent deformation (DNIT, 2018b), similar to the technical procedures adopted by American Association of State Highway and Transportation Officials (AASHTO, 2004), Australia (AGPT, 2006) and the European Union (BSI, 2004). For this, a three-part cylindrical steel mold with dimensions of 200 mm in height and 100 mm in diameter was used. The compaction energy used was equivalent to that of the modified energy. Samples were considered valid for RM and PD tests if the variation was not superior than ± 1% in relation to the MDD and OMC.

The repeated load triaxial equipment used is located in the Department of Transportation from *Universidade Federal de Santa Maria* (UFSM). In the RM test, firstly 1,500 cycles are applied for conditioning the sample; then the test proposes the application of a 100 load cycles for each of 18 pairs of confining stress and deviator stress (DNIT, 2018a). The test was performed in triplicate and with a loading frequency of 1 Hz. Figure 3 presents a sample of UGM compacted in the conditions mentioned above, being positioned in the equipment for a subsequent RLT test.

After the resilient modulus test, the test data were adjusted to mathematical models that were representative of the paving materials mechanical behavior. The mathematical models that can describe the behavior of granular materials regarding resilience, pointed out in the technical literature and cited in this study, are in Table 2. For multiple nonlinear analysis, we used the software Statistica v.10.0.228.2, for linear analysis we used the software Microsoft Office Excel 2013.

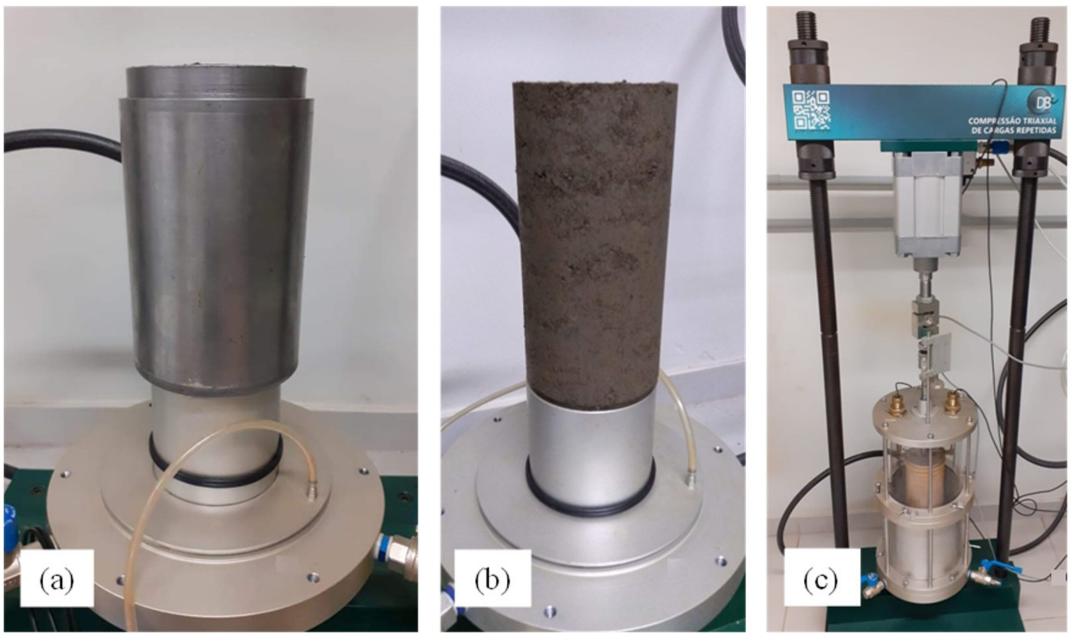

Figure 3. UGM sample being positioned on equipment (a, b) and viewed from the equipment set (c).

In order to evaluate the plasticization to which the granular materials are subjected, the permanent deformation tests were carried out (DNIT, 2018b). Again, the RLT was used to obtain the experimental data. In this test, 100 conditioning cycles are applied for conditioning phase with the 30×30 kPa stresses pair. It is followed by the application of 150,000 charging cycles of each stress pair. For this study, the test protocol was performed according to Lima et al. (2019), with six samples and application of the following single stage stresses (confining versus deviator): 40×40 kPa, 40×120 kPa, 80×80 kPa, 80×240 kPa, 120×240 kPa and 120×360 kPa.

Among the models for predicting permanent deformation of granular materials, the models of Barksdale (1972), Monismith et al. (1975), Uzan (1985) and Tseng & Lytton (1989) stand out. However, for the coherent characterization of tropical materials and their particularities, the model that seems more adequate is the Guimarães' model (Guimarães et al., 2018; Lima et al., 2020), a model used in this research and addressed in Brazilian regulations (Equation 8). The parameters ψ_1, ψ_2, ψ_3 and ψ_4 were obtained by software Statistica v.10.0.228.2. The parameters of the Guimarães' model are essential to characterize and understand the deformability of soils and unbound granular materials, mainly due de advance of the Brazilian M-E Design Method (MeDiNa).

$$\varepsilon_p\left(\%\right)=\psi_1\left(\frac{\sigma_3}{\rho_a}\right)^{\psi_2}\left(\frac{\sigma_d}{\rho_a}\right)^{\psi_3}N^{\psi_4} \tag{8}$$

Where: $\varepsilon_p\left(\%\right)$: specific permanent deformation; ψ_1, ψ_2, ψ_3 *and* ψ_4: regression parameters; σ : confining stress; σ_d : deviator stress; ρ_a : atmospheric pressure; N: number of loading cycles.

3. Results and analysis

The results are presented in four distinct topics, in the following order: results of sample compaction; resilient modulus, permanent deformation and the relationship between void ratio and deformability.

3.1 Compaction

The results from the compaction tests in this study are shown in Figure 4. SJ basalt granular material reached higher densities, due the high specific gravity of the basalt aggregates. The DPA rhyodacite showed the highest OMC and lowest density among all samples. According to Paiva (2017), this rock presents devitrification of the rock matrix, which is replaced by clay minerals, thus increasing porosity and absorption, justifying the high optimum moisture content.

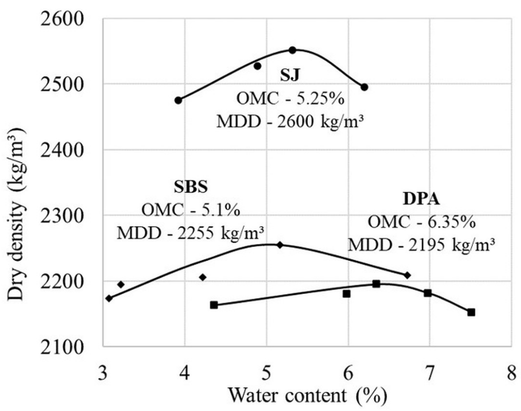

Figure 4. Sample compaction curve.

Table 2. Mathematical models of RM prediction.

Models	Equation	
Model k-σ_3 (Biarez, 1962)	$RM = k_1.{\sigma_3}^{k_2}$	(1)
Model k-σ_d (Svenson, 1980)	$RM = k_1.{\sigma_d}^{k_2}$	(2)
Model k- θ (Seed et al., 1967)	$RM = k_1.\theta^{k_2}$	(3)
Compound model (Pezo et al., 1992)	$RM = k_1.{\sigma_3}^{k_2}.{\sigma_d}^{k_3}$	(4)
Universal model (AASHTO, 2004)	$RM = k_1 \cdot \rho_a\left(\frac{\theta}{\rho a}\right)^{k_2} \cdot \left(\frac{\tau_{oct}}{\rho a}+1\right)^{k_3}$	(5)
Witczak's model (Rada & Witczak, 1981)	$RM = k_1 \cdot \left(\frac{\theta}{\rho a}\right)^{k_2} \cdot \left(\frac{\sigma_d}{\rho a}\right)^{k_3}$	(6)
Witczak's and Uzan's model (Witczak & Uzan, 1988)	$RM = k_1 \cdot \rho_a\left(\frac{\theta}{\rho a}\right)^{k_2} \cdot \left(\frac{\tau_{oct}}{\rho a}\right)^{k_3}$	(7)

Where: RM : resilient modulus; $_3$: confining stress; σ_d : deviator stress; θ: first stress invariant ($\theta = \sigma_1 + 2\sigma_3 = \sigma_d + 3\sigma_3$) ; τ_{oct} : octahedral shear stress; ρ_a: atmospheric pressure; k_1, k_2 and k_3: regression parameters.

The SBS syenogranite, on the other hand, has the lowest OMC among the mixtures due to its lower absorption, as mentioned in Table 1.

3.2 Resilient modulus

In order to evaluate the stiffness properties of the UGMs samples, after the repeated load triaxial tests the laboratory results were analyzed and submitted to mathematical modeling by means of models k-σ_3, k-σ_d, k-θ, Compound, Universal, Witczak and Witczak and Uzan. The regression parameters are presented in Table 3 with the values of the coefficient of determination (R^2) and the value of the linear resilient modulus, that is, the average of the RM values obtained for each stress pair after performing the mathematical modeling.

The model k-σ_3 presents high R^2, evidencing the strong relationship between the resilient modulus and the confining stress for granular materials; while the model k-σ_d, usually more appropriate to represent soils behavior, presents low R^2. Based on Table 3, the mathematical models that consider both stresses, confining and deviator, are more representative of the material behavior; in this case are mentioned the models Compound, Universal and Witczak, Witczak and Uzan. The first two of which, for SJ basalt, are exemplified in Figure 5.

Table 3. Parameters of mathematical modeling of RM.

		SJ	DPA	SBS
Model k- $_3$ $RM = k_1.\sigma_3^{k_2}$	k_1	2046	1828	2048
	k_2	0.703	0.772	0.768
	R^2	0.930	0.946	0.959
	RM avg (MPa)	304	227	257
Model k-σ_d $RM = k_1.\sigma_d^{k_2}$	k_1	916.96	742.88	826.64
	k_2	0.533	0.578	0.571
	R^2	0.793	0.784	0.781
	RM avg (MPa)	300	223	252
Model k-θ $RM = k_1.\theta^{k_2}$	k_1	656.4	520.9	585.8
	k_2	0.690	0.755	0.784
	R^2	0.955	0.960	0.968
	RM avg (MPa)	305	228	249
Compound model $RM = k_1.\sigma_3^{k_2}.\sigma_d^{k_3}$	k_1	2256.46	1983.87	1896.11
	k_2	0.589	0.665	0.612
	k_3	0.196	0.18	0.164
	R^2	0.977	0.981	0.982
	RM avg (MPa)	306	229	258
Universal model $RM = k_1 \cdot {}_a\left(\frac{}{\rho a}\right)^{k_2}\cdot\left(\frac{_{oct}}{\rho a}+1\right)^{k_3}$	k_1	1206.47	829.12	1029.97
	k_2	0.863	0.985	0.915
	k_3	-0.213	-0.358	-0.355
	R^2	0.973	0.977	0.980
	RM avg (MPa)	306	228	258
Witczak's model $RM = k_1.\left(\frac{\theta}{\rho a}\right)^{k_2}.\left(\frac{\sigma_d}{\rho a}\right)^{k_3}$	k_1	103.18	67.18	84.43
	k_2	0.928	1.045	0.962
	k_3	-0.145	-0.202	-0.188
	R^2	0.977	0.979	0.982
	RM avg (MPa)	306	227	258
Witczak's and Uzan's model $RM = k_1.\rho_a\left(\frac{\theta}{\rho a}\right)^{k_2}.\left(\frac{\tau_{oct}}{\rho a}\right)^{k_3}$	k_1	925.11	576.79	732.61
	k_2	0.928	1.045	0.962
	k_3	-0.141	-0.203	-0.188
	R^2	0.977	0.979	0.982
	RM avg (MPa)	306	227	258

For the Compound model, coefficient k_2 referring to the confining stress action has higher impact on the RM value to the detriment of coefficient k_3 related to the deviator stress. However, the fact that the coefficient k_3 has a positive value indicates that, by increasing the deviator stress, an increase in the resilient modulus occurs. The Compound model is the most discussed in this study since it is currently used in the Brazilian M-E Design Method (MeDiNa) for characterization related to the stiffness of subgrade soils and granular materials (Guimarães & Motta, 2016; Freitas et al., 2020; Lima et al., 2020; Sagrilo, 2020; Pascoal et al., 2021; Zago et al., 2021; Pascoal et al., 2023).

The analysis of the Universal model indicates that the increase of the first stress invariant collaborate to the RM of the material, by the positive value of k_2. On the other hand, the coefficient k_3 presented a negative value due to the increase in the octahedrical shear stress, causing a lower RM value. This is similar to the Witczak's and Uzan's model, in which coefficients k_2 and k_3 are related to the same stresses as the Universal model. The model by Witczak also demonstrate that the increase of first stress invariant reflects in a higher RM, due to the positive value of k_2 for all materials; although the increase of the deviator stress does not strongly affect the RM, due to the negative and low value of k_3.

3.3 Permanent deformation

In order to understand the behavior of the granular material subjected to damage by permanent deformation, the UGM of different lithologies were submitted to the RLT test of long duration. Subsequently, the shakedown analysis was carried out according to Werkmeister (2003), the Guimarães' model was implemented to the mixtures and loss or gain of stiffness of the samples was verified after the stress history of the PD test.

Figures 6, 7 and 8 show the graphs representing the permanent deformation tests of UGM SJ, DPA and SBS, respectively. The graphs at the left (a) show the accumulated PD versus number of cycles, so the increase rate of the curve gives evidence of stabilization or not of these deformations; the right graph line shows the behavior of the permanent deformation increase rate over the accumulation of deformations.

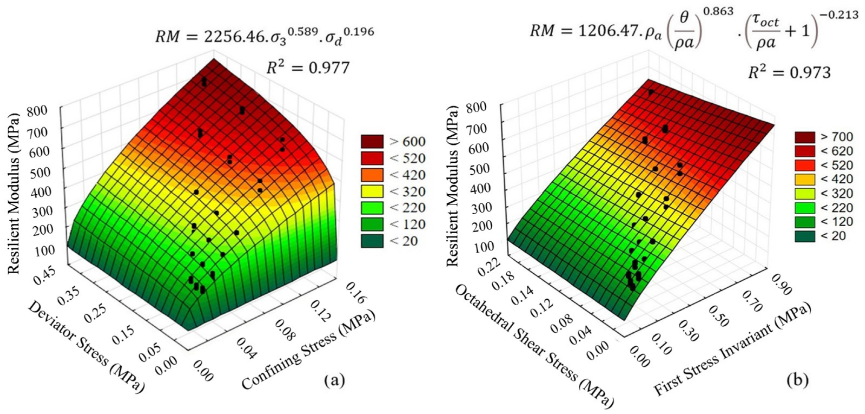

Figure 5. Examples of the statistical fitting – Compound (a) and Universal (b) Models for SJ.

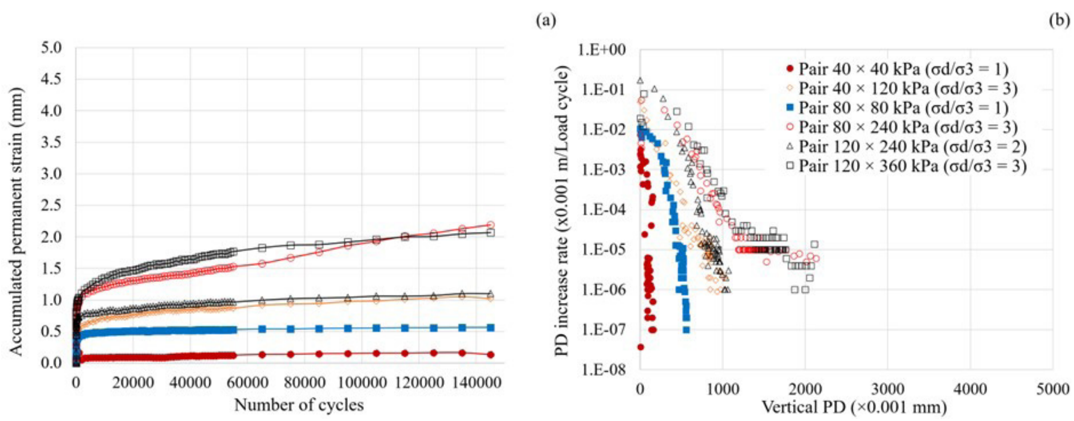

Figure 6. Permanent deformation test results – SJ: accumulated PD (a) and PD increase rate (b).

For SJ basalt the highest permanent deformations recorded were observed in tests whose stress pairs are 120×360 kPa and 80×240 kPa, confining versus deviator, respectively, reaching values close to 2.3 mm at the end of the tests (Figure 6a). The pair 120×240 kPa presented considerably smaller deformations than the pairs 120×360 kPa and 80×240 kPa. The smallest deformations were found in the 40×40 kPa e 80×80 kPa tests. This behavior indicates that the permanent deformations magnitude is related to the ratio among σ_d / σ_3 in a directly proportional relation. Similar results were pointed out by Lekarp et al. (2000), Lima et al. (2017) and Delongui et al. (2018).

Observing the increase rate graph in PD by the cumulative vertical deformation of the SJ it can be seen that only tests whose stress ratio σ_d / σ_3 is equal to one entered shakedown (i.e., type A behavior) according to the parameters of Dawson & Wellner (1999) and Werkmeister (2003) with the permanent deformation increase rate in 10^{-7}x10^{-3} meters per load application cycle in 150000 cycles. Those tests are presented in the Figure 6b with filled markers. The other pairs presented creep shakedown, i.e., behavior B. Projecting the PD values with the Guimarães' model, the pair 40×120 kPa would reach the rate of 10^{-7}x10^{-3} meters per load application cycle in 155000 cycles, while the same would happen to the pair 120×240 kPa at 185000 cycles.

For the DPA rhyodacite the deformation results were similar to that observed with basalt, in relation to the pairs that deformed more or less, as well as the value of higher accumulated deformation, close to 2.5 mm (Figure 7a). The 40×40 kPa pair reached the accommodation – behavior A, as it possible to see in Figure 7b; the same happened to the pair 80×80 kPa by the projection of the Guimarães' model for this material, reaching 10^{-7}x10^{-3} meters per load application cycle. The other pairs present behavior B.

Syenogranite, an aggregate with a different texture from the others, presented considerably higher plastic deformability than the other analyzed materials. The highest deformation observed was approximately 5 mm, although the densities obtained in the compaction test were close to that for the rhyodacite (Figure 8a). This behavior seems to be related to this rock's inferior mechanical performance in relation to the others with respect to the laboratory tests of mechanical characterization, as previously shown in Table 1.

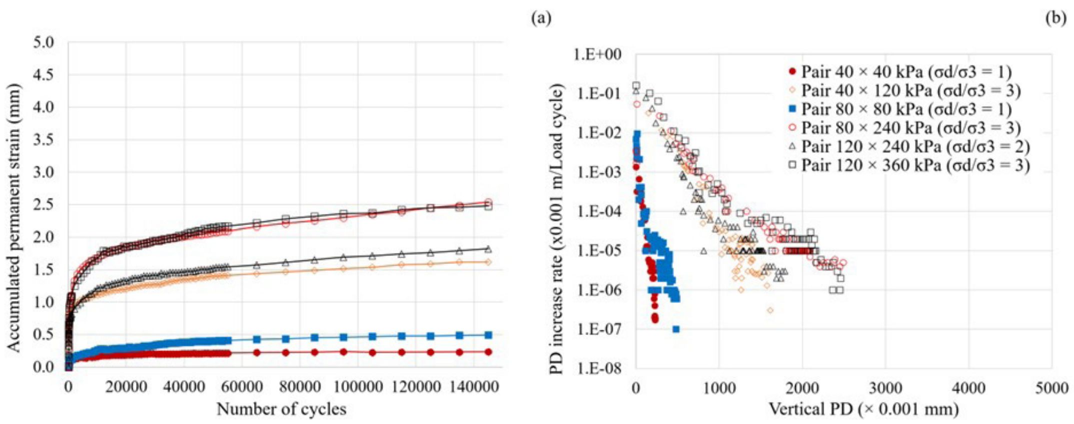

Figure 7. Permanent deformation test results – DPA: accumulated PD (a) and PD increase rate (b).

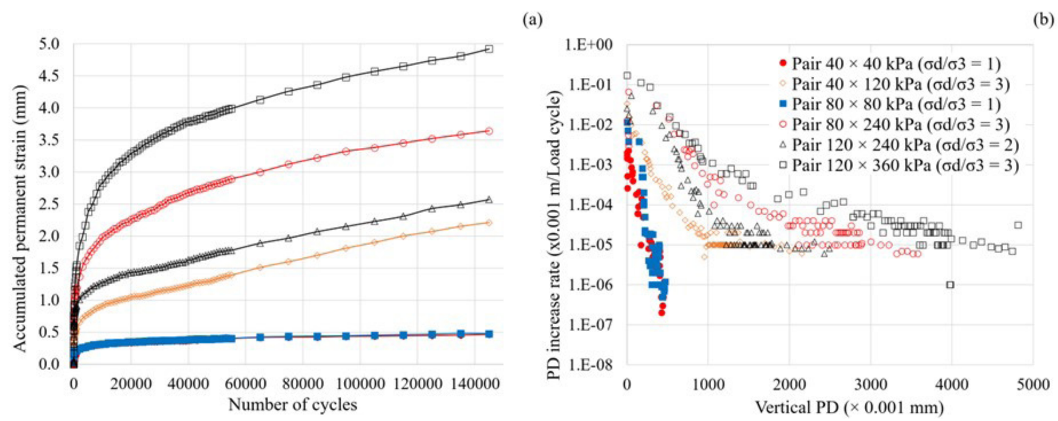

Figure 8. Permanent deformation test results – SBS: accumulated PD (a) and PD increase rate (b).

The stress pairs that showed a tendency to shakedown with the highest number of cycles are the pairs with σ_d / σ_3 is equal to one - 40×40 kPa and 80×80 kPa (Figure 8b). Other pairs present type B behavior.

The materials were, by multiple nonlinear regression analysis, mathematically characterized as to their PD by the Guimarães' model. The parameters obtained for the specific permanent deformation are in Table 4. From the parameters and the coefficient of determination, it is evident that the Guimarães' model is representative of the deformability of the materials under study; also noticeable is the strong impact of the deviator stress in the PD, represented by the high values of ψ_3 , a trend already observed in Figures 6, 7 and 8 by relations σ_d / σ_3 .

The stiffness gain of samples submitted to stress history was evaluated by the resilient modulus test after the permanent deformation test. It was possible to compare the average RM value after the test for each stress pair and the value obtained for the conventional RM test. The average RM for Compound Model after each PD test is shown in Figure 9 in a bar format, while the horizontal line represents the conventional RM test. In addition, in the center of each bar, is it shown the shakedown behavior of each sample, in this case, A or B.

It is possible to infer that there is a relationship among the lithological type, resilient behavior and shakedown. For basalt, after the PD test, all samples show a relative loss of stiffness in relation to the conventional RM, a result similar to that obtained by Guimarães (2009) for other basaltic material; it is also clear that this loss is not proportionally evidenced among all pairs. For those whose behavior towards shakedown pointed to behavior B, the loss was more significant. For rhyodacite, only the pairs that demonstrated accommodation of the particles had the stiffness increase of the samples with the history of stresses; the other pairs lost stiffness, as expressive as the higher the deformations undergone. Finally, for the syenogranite all samples gained stiffness after the long-term PD test, with the exception of the last pair. Close results were obtained by Lima et al. (2017) and Norback (2018) for UGM of similar origin. It is also noticed that the pairs that had behavior A towards the shakedown had an increase in RM which was more significant than the others. For all the materials, according to Figure 9, as the deviator stress increases for the same confining stress, the resilient modulus of the material decreases, in accordance to shakedown theory. A deeper investigation must be conducted in order to verify any relationship between this decrease and the type of aggregate.

3.4 Void ratio and deformability

Based on physical indexes and compaction parameters, it was observed a relation between the samples void ratio and its RM. This behavior seems to be dependent on the lithological origin of the UGM. Figure 10 exhibits the results of average RM for Compound model and void ratio; the filled markers represent the RM after PD and the not filled markers denote the conventional RM test.

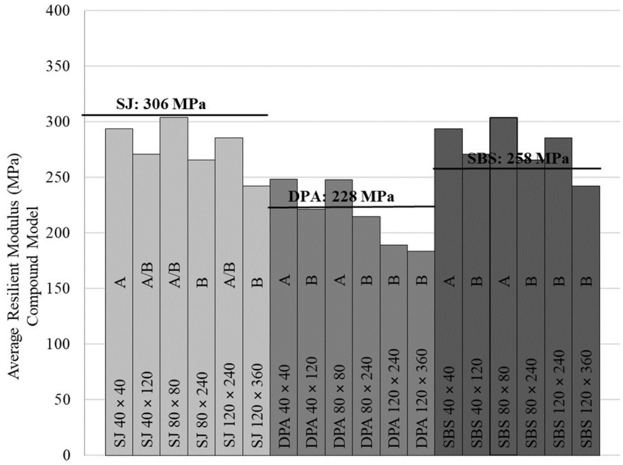

Figure 9. Relationship between conventional RM and after PD – SJ, DPA and SBS.

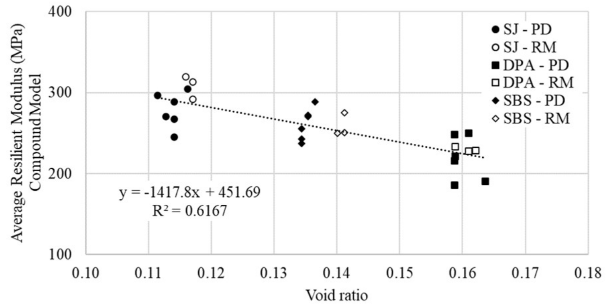

Figure 10. Void ratio vs average RM for SJ, DPA, SBS granular materials.

Table 4. Parameters of permanent deformation from the Guimarães' model (Guimarães, 2009).

		SJ	DPA	SBS
Guimarães' model (Guimarães, 2009)	ψ_1	0.048	0.040	0.019
	ψ_2	-0.622	-0.892	-0.908
	ψ_3	1.188	1.311	1.816
	ψ_4	0.138	0.169	0.226
	R^2	0.938	0.967	0.989

Basalt SJ presented the highest modulus, followed by SBS syenogranite and DPA rhyodacite, opposed to the void ratio achieved in the compaction. Based on this work, materials with different properties - such as abrasion, shape, texture and crushing process, even with the same particle size distribution, followed a trendline that suggest that void ratio may be a key parameter to predict RM.

Currently, we are researching the relation between stress state and physical indexes and the densification, gain of stiffness and loss of void volume during the PD test. This research topic is still in progress and is not fully developed, so we limited the contribution in the present manuscript for this initial analysis.

4. Final considerations

This research aimed, by means of laboratory tests and mathematical modeling, to understand the deformability, especially resilient modulus and permanent deformation, of unbound granular materials. For this purpose, the granulometric curve was kept constant with the basalt, rhyodacite and syenogranite, materials representative of the Brazilian state of Rio Grande do Sul.

The stiffness of the materials, expressed by the resilient modulus, was tested and mathematically represented by models k-σ_3, k-σ_d, k-θ, Compound, Universal, Witczak and Witczak and Uzan. The models that demonstrated the best fitting were those that consider the action of the confining and deviator stresses. In accordance to the literature, granular materials are mostly confining stress dependent; which was stated in this research as well.

The performance of the three UGMs regarding to RM and PD were different. For damage by permanent deformation, the trend found for the RM was not maintained. Syenogranite, for example, presented the worst behavior in view of permanent deformation, even though showed an intermediate RM. This effect may be related to the greater granulation of the minerals of the SBS rock in addition to the foliated structure, which starts to show poor mechanical behavior (see results for LA abrasion, impact value and crushing value). These mechanical characteristics result in the breaking of the particles promoted by the zones of weaknesses among the minerals, promoting a thinner granulometric curve, liable to high permanent deformations.

The Guimarães' model proved to be adequate to represent the PD of the materials under study, showing a high coefficient of determination. Some pairs seemed to show accommodation after 150000 cycles, and the model made it possible to predict the number of cycles needed. Furthermore, this study described a relationship between the conventional RM and after the PD test, lithological origin and shakedown.

Also, this study showed a relevant relation between the void ratio of the compacted UGM and its resilient modulus. The void ratio is affected by aggregate shape, texture, rock crushing processes and compaction parameters; this could be, with deeper investigation, a key parameter to predict RM.

Acknowledgements

The authors would like to thank ANP/Petrobras, Conselho Nacional de Desenvolvimento Científico e Tecnológico (CNPq), Coordenação de Aperfeiçoamento de Pessoal de Nível Superior (CAPES) for their financial support and the reviewers of Soils and Rocks for their valuable contributions.

Declaration of interest

The authors have no conflicts of interest to declare. All co-authors have observed and affirmed the contents of the paper and there is no financial interest to report.

Authors' contributions

Amanda Vielmo Sagrilo: conceptualization, data curation, visualization, methodology and experimental procedures, writing – original draft, review & editing. Paula Taiane Pascoal: validation, methodology and experimental procedures, writing – review & editing. Magnos Baroni: supervision, validation, writing – review & editing. Ana Helena Back: validation, methodology and experimental procedures, writing – review & editing. Rinaldo José Barbosa Pinheiro: supervision, validation, writing – review. Luciano Pivoto Specht: supervision, funding acquisition, project administration, writing – review. Antônio Carlos Rodrigues Guimarães: supervision, validation, writing – review.

Data availability

The datasets produced and analyzed in the course of the present study are available from the corresponding author upon reasonable request.

List of symbols

k_1, k_2, k_3	resilient parameters experimentally determined
DPA	granular material from Della Pasqua quarry
N	number of loading cycles
PD	permanent deformation
R^2	coefficient of determination
RLT	repeated load triaxial
RM	resilient modulus
SBS	granular material from SBS Engenharia quarry
SJ	granular material from São Juvenal quarry
UFSM	Universidade Federal de Santa Maria
UGM	unbound granular material
UTM	Universal Transverse Mercator coordinate system
ε_p	specific permanent deformation
θ	principal stress
ρ_a	atmospheric pressure

σ_3	confining stress
σ_d	deviator stress
σ_d / σ_3	stress ratio
τ_{oct}	octahedral stress
$\psi_1,\psi_2,\psi_3,\psi_4$	permanent deformation parameters experimentally determined

References

AASHTO NCHRP 1-37A. (2004). *Guide for mechanistic-empirical design of new and rehabilitated pavement structure - Final report*. Transportation Research Board, Washington, DC.

Adomaki, S., Engelsen, C.J., Thorstensen, R.J., & Barbieri, D.M. (2021). Review of the relationship between aggregates geology and Los Angeles and micro-Deval tests. *Bulletin of Engineering Geology and the Environment*, 80, 1963-1980. http://dx.doi.org/10.1007/s10064-020-02097-y.

AGPT T053. (2006). *Determination of permanent deformation and resilient modulus characteristics of unbound granular materials under drained conditions*. Austroads, Sydney.

Alnedawi, A., Klafe, B., Ullah, S., & Kerr, W. (2021). Investigation of non-standard unbound granular materials under cyclic loads: experimental and regression analyses. *The International Journal of Pavement Engineering*, 23(9), 2998-3010. http://dx.doi.org/10.1080/10298436.2021.1877291.

Alnedawi, A., Nepal, K.P., & Al-Ameri, R. (2019a). New shakedown criterion and permanent deformation properties of unbound granular materials. *Journal of Modern Transportation*, 27(2), 108-119. http://dx.doi.org/10.1007/s40534-019-0185-2.

Alnedawi, A., Nepal, K.P., & Al-Ameri, R. (2019b). Permanent deformation prediction model of unbound granular materials for flexible pavement design. *Transportation Infrastructure Geotechnology*, 6, 39-55. http://dx.doi.org/10.1007/s40515-018-00068-1.

Ba, M., Tinjum, J.M., & Fall, M. (2015). Prediction of permanent deformation model parameters of unbound base course aggregates under repeated loading. *Road Materials and Pavement Design*, 16(4), 854-869. http://dx.doi.org/10.1080/14680629.2015.1063534.

Back, A.H., Ceccato, H.D., Pinheiro, R.J.B., Nummer, A.V., & Sagrilo, A.V. (2021). Avaliação do comportamento característico de rochas vulcânicas da formação Serra Geral e sua implementação em obras rodoviárias. *Geociências*, 40, 1125-1136. http://dx.doi.org/10.5016/geociencias.v40i04.15845.

Barksdale, R.D. (1972). Laboratory evaluation of rutting in base course materials. In *Proceedings of the 3rd International Conference on the Structural Design of Asphalt Pavements* (pp. 161-174). Ann Arbor: University of Michigan.

Biarez, J. (1962). *Contribution a l'étude des proprietes mecaniques des sols et des materiaux pulverents* [Doctoral thesis]. Faculté des Sciences Grenoble.

BSI EN 13286-7. (2004). *Unbound and hydraulically bound mixtures - part 7: cyclic load triaxial test for unbound mixtures*. British Standards Institution, London.

Carvalho, J.C., Rezende, L.R., Cardoso, F.B.F., Lucena, L.C.F.L., Guimarães, R.C., & Valencia, Y.G. (2015). Tropical soils for highway construction: peculiarities and considerations. *Transportation Geotechnics*, 5, 3-19. http://dx.doi.org/10.1016/j.trgeo.2015.10.004.

Cerni, G., Cardone, F., Virgili, A., & Camilli, S. (2012). Characterisation of permanent deformation behavior of unbound granular materials under repeated triaxial loading. *Construction & Building Materials*, 28, 79-87. http://dx.doi.org/10.1016/j.conbuildmat.2011.07.066.

Collins, I.F., & Boulbibane, M. (2000). Geomechanical analysis of unbound pavements based on shakedown theory. *Journal of Geotechnical and Geoenvironmental Engineering*, 126(1), 50-59. http://dx.doi.org/10.1061/(ASCE)1090-0241(2000)126:1(50).

Curtis Neto, J.A., Ribeiro, R.P., Watashi, D.B., Paraguassu, A.B., Santos, R.S., & Xavier, G.C. (August-September, 28-01, 2018). Comparação estatística entre ensaios mecânicos de agregados pétreos. In *8º Simpósio Brasileiro de Mecânica das Rochas*, Salvador, Brazil (in Portuguese).

DAER ES-P 08/91. (1991). *Base granular*. DAER – Departamento Autônomo de Estradas de Rodagem, Porto Alegre, RS (in Portuguese).

Dawson, A.R., & Wellner, F. (1999). *Plastic behavior of granular materials. Report ARC project 933. Reference PRG 99014*. University of Nottingham.

Delongui, L., Matuella, M., Núñez, W.P., Fedrigo, W., Silva Filho, L.C.P., & Ceratti, J.A.P. (2018). Construction and demolition waste parameters for rational pavement design. *Construction & Building Materials*, 168, 105-112. http://dx.doi.org/10.1016/j.conbuildmat.2018.02.086.

DNER 006. (1994a). *Materiais rochosos usados em rodovias – análise petrográfica – instrução de ensaio DNER 006*. DNER - Departamento Nacional de Infraestrutura de Transportes, Rio de Janeiro, RJ (in Portuguese).

DNER 195. (1997a). *Agregado – determinação da absorção e da densidade do agregado graúdo – método de ensaio DNER 195*. DNER - Departamento Nacional de Infraestrutura de Transportes, Rio de Janeiro, RJ (in Portuguese).

DNER 197. (1997b). *Agregado graúdo – determinação da resistência do esmagamento – método de ensaio DNER 197*. DNER - Departamento Nacional de Infraestrutura de Transportes, Rio de Janeiro, RJ (in Portuguese).

DNER 35. (1998a). *Agregado graúdo – ensaio de abrasão "Los Angeles" – método de ensaio DNER 35*. DNER - Departamento Nacional de Infraestrutura de Transportes, Rio de Janeiro, RJ (in Portuguese).

DNER 399. (1999). *Agregados - determinação da perda ao choque no aparelho Treton - método de ensaio DNER 399*. DNER - Departamento Nacional de Infraestrutura de Transportes, Rio de Janeiro, RJ (in Portuguese).

DNER 83. (1998b). *Agregado – análise granulométrica - método de ensaio DNER 83*. DNER - Departamento Nacional de Infraestrutura de Transportes, Rio de Janeiro, RJ (in Portuguese).

DNER 89. (1994b). *Avaliação da durabilidade pelo emprego de soluções de sulfato de sódio ou de magnésio – método de ensaio DNER 89*. DNER - Departamento Nacional de Infraestrutura de Transportes, Rio de Janeiro, RJ (in Portuguese).

DNIT 134. (2018a). *Pavimentação – solos – determinação do modulo de resiliência – método de ensaio DNIT 134*. DNIT - Departamento Nacional de Infraestrutura de Transportes, Rio de Janeiro, RJ (in Portuguese).

DNIT 179. (2018b). *Pavimentação - solos - determinação da deformação permanente – instrução de ensaio DNIT 179*. DNIT - Departamento Nacional de Infraestrutura de Transportes, Rio de Janeiro, RJ (in Portuguese).

DNIT. (2006). *Manual de pavimentação*. DNIT - Departamento Nacional de Infraestrutura de Transportes, Rio de Janeiro, RJ (in Portuguese).

Erlingsson, S., Rahman, S., & Salour, F. (2017). Characteristics of unbound granular materials and subgrades based on multi stage RLT testing. *Transportation Geotechnics*, 13, 28-42. http://dx.doi.org/10.1016/j.trgeo.2017.08.009.

Freitas, J.B., Rezende, L.R., & Gitirana Junior, G.F.N. (2020). Prediction of the resilient modulus of two tropical subgrade soils considering unsaturated conditions. *Engineering Geology*, 270, 105580. http://dx.doi.org/10.1016/j.enggeo.2020.105580.

Gu, F., Zhang, Y., Luo, X., Sahin, H., & Lytton, R.L. (2017). Characterization and prediction of permanent deformation properties of unbound granular materials for Pavement ME Design. *Construction & Building Materials*, 155, 584-592. http://dx.doi.org/10.1016/j.conbuildmat.2017.08.116.

Guimarães, A.C.R. (2009). *Um método mecanístico - empírico para a previsão da deformação permanente em solos tropicais constituintes de pavimentos* [Doctoral thesis, Federal University of Rio de Janeiro]. Federal University of Rio de Janeiro's repository (in Portuguese). Retrieved in May 18, 2023, from http://www.coc.ufrj.br/pt/teses-de-doutorado/153-2009/1199-antonio-carlos-rodrigues-guimaraes

Guimarães, A.C.R., & Motta, L.M.G. (2016). Mechanical behavior of basaltic rocks from Serra Geral Formation used as road material in Santa Catarina State, Brazil. *Soils and Rocks*, 39(2), 203-210. http://dx.doi.org/10.28927/SR.392203.

Guimarães, A.C.R., Motta, L.M.G., & Castro, C.D. (2018). Permanent deformation parameters of fine - grained tropical soils. *Road Materials and Pavement Design*, 20(7), 1664-1681. http://dx.doi.org/10.1080/14680629.2018.1473283.

Huang, Y.H. (2004). *Pavement analysis and design*. Editora Prentice Hall.

Lekarp, F., & Isacsson, U. (2001). The effects of grading scale on repeated load triaxial test results. *The International Journal of Pavement Engineering*, 2(2), 85-101. http://dx.doi.org/10.1080/10298430108901719.

Lekarp, F., Isacsson, U., & Dawson, A. (2000). State of the art II: permanent strain response of unbound aggregates. *Journal of Transportation Engineering*, 126(1), 76-83. http://dx.doi.org/10.1061/(ASCE)0733-947X(2000)126:1(76).

Lima, C.D.A., Motta, L.M.G., & Aragão, F.T.S. (November 10-14, 2019). Análise das tensões aplicadas nos ensaios de deformação permanente de solos e britas para o dimensionamento mecanístico-empírico de pavimentos. In Associação Nacional de Pesquisa e Ensino em Transportes (Org.), *33º Congresso de Pesquisa e Ensino em Transportes da ANPET* (pp. 1222-1233). Rio de Janeiro: ANPET (in Portuguese).

Lima, C.D.A., Motta, L.M.G., & Guimarães, A.C.R. (2017). Estudo da deformação permanente de britas granito-gnaisse para uso em base e sub-base de pavimentos. *Revista Transportes*, 25, 41-52. http://dx.doi.org/10.14295/transportes.v25i2.1262.

Lima, C.D.A., Motta, L.M.G., Aragão, F.T.S., & Guimarães, A.C.R. (2020). Mechanical characterization of fine-grained lateritic soils for mechanistic-empirical flexible pavement design. *Journal of Testing and Evaluation*, 48(1), 1-17. http://dx.doi.org/10.1520/JTE20180890.

Medina, J., & Motta, L.M.G. (2015). *Mecânica dos pavimentos*. Editora Interciência (in Portuguese).

Monismith, C.L., Ogawa, N., & Freeme, C.R. (January 13-17, 1975). Permanent deformation characteristics of subgrade soils due to repeated loading. In *54º Annual Meeting of TRB*, Washington, United States of America.

Nazzal, M.D., Mohammad, L.N., & Austin, A. (2020). Evaluating laboratory tests for use in specifications for unbound base course materials. *Journal of Materials in Civil Engineering*, 32(4), 1-8. http://dx.doi.org/10.1061/(ASCE)MT.1943-5533.0003042.

Nogami, J.S., & Villibor, D.F. (1991). Use of lateritic fine-grained soils in road pavement base courses. *Geotechnical and Geological Engineering*, 9, 167-182. http://dx.doi.org/10.1007/BF00881739.

Norback, C. (2018). *Caracterização do módulo de resiliência e da deformação permanente de três solos e misturas solo-brita* [Master's dissertation, Federal University of Rio de Janeiro]. Federal University of Rio de Janeiro's repository (in Portuguese). Retrieved in May 18, 2023, from https://pantheon.ufrj.br/handle/11422/13425

Paiva, P.S. (2017). *Caracterização e avaliação das propriedades geomecânicas para uso em pavimentação de agregados de rochas vulcânicas da porção central do Rio Grande do Sul* [Master's dissertation, Federal University of Santa Maria]. Federal University of Santa Maria's repository (in Portuguese). Retrieved in May 18, 2023, from https://repositorio.ufsm.br/handle/1/14728

Pascoal, P.T., Sagrilo, A.V., Baroni, M., Specht, L.P., & Pereira, D.S. (2021). Evaluation of the influence of compaction energy on the resilient behavior of lateritic soil in the field and laboratory. *Soils and Rocks*, 44(4), e2021071321. http://dx.doi.org/10.28927/SR.2021.071321.

Pascoal, P.T., Sagrilo, A.V., Baroni, M., Specht, L.P., & Pereira, D.S. (2023). Lateritic soil deformability regarding the variation of compaction energy in the construction of pavement subgrade. *Soils and Rocks*, 46(3), e2023009922. https://doi.org/10.28927/SR.2023.009922.

Pezo, R.F., Carlos, G., Hudson, W.R., & Stokoe II, K.H. (1992). *Development of reliable resilient modulus test for subgrade and non-granular subbase materials for use in routine pavement design*. Retrieved in May 18, 2023, from https://trid.trb.org/view/369153

Rada, G., & Witczak, M.W. (1981). Comprehensive evaluation of laboratory resilient moduli results for granular materials. *Transportation Research Record: Journal of the Transportation Research Board*, (810), 23-33. Retrieved in May 18, 2023, from http://onlinepubs.trb.org/Onlinepubs/trr/1981/810/810-004.pdf

Sagrilo, A.V. (2020). *Estudo de deformabilidade e empacotamento de britas com diferentes origens litológicas do estado do Rio Grande do Sul* [Master's dissertation, Federal University of Santa Maria]. Federal University of Santa Maria's repository (in Portuguese). Retrieved in May 18, 2023, from https://repositorio.ufsm.br/handle/1/22211

Seed, H.B., Mitry, F. G., Monismith, C. L., Chan, C. K. (1967). *Prediction of flexible pavement deflections from laboratory repeated load tests*. National Cooperative Highway Research Program. Report No. 35.

Soliman, H., & Shalaby, A. (2015). Permanent deformation behavior of unbound granular base materials with varying moisture and fines content. *Transportation Geotechnics*, 37(4), 1-12. http://dx.doi.org/10.1016/j.trgeo.2015.06.001.

Song, Y., & Ooi, P.S.K. (2010). Interpretation of shakedown limit from multistage permanent deformation test. *Transportation Research Record: Journal of the Transportation Research Board*, (2167), 72-82. http://dx.doi.org/10.3141/2167-08.

Svenson, M. (1980). *Ensaios triaxiais dinâmicos de solos argilosos* [Master's dissertation, Federal University of Rio de Janeiro]. Federal University of Rio de Janeiro's repository (in Portuguese). Retrieved in May 18, 2023, from https://pantheon.ufrj.br/bitstream/11422/3001/1/152894.pdf

Tseng, K.H., & Lytton, R.L. (1989). *Prediction of permanent deformation in flexible pavement materials. Implication of aggregates in the design, construction and performance of flexible pavements* (pp. 154-172). American Society for Testing and Materials.

Uzan, J. (1985). Characterization of granular material. *Transportation Research Record*, 1022, 52-59. Retrieved in May 18, 2023, from https://onlinepubs.trb.org/Onlinepubs/trr/1985/1022/1022-007.pdf

Wang, J., & Yu, H.S. (2013). Shakedown analysis for design of flexible pavements under moving loads. *Road Materials and Pavement Design*, 14(3), 703-722. http://dx.doi.org/10.1080/14680629.2013.814318.

Werkmeister, S. (2003). *Permanent deformation behavior under granular materials in pavement constructions* [Doctoral thesis]. Dresden University of Technology.

Werkmeister, S. (June 6-8, 2006). Shakedown analysis of unbound granular materials using accelerated pavement test results from New Zealand's CAPTIF facility. In B. Huang, R. Meier, J. Prozzi & E. Tutumluer (Eds.), *Pavements Mechanics and Performance: Proceedings of Sessions of GeoShanghai* (pp. 220-228). Reston, United States of America: ASCE. https://doi.org/10.1061/40866(198)28.

Werkmeister, S., Dawson, A.R., & Wellner, F. (2001). Permanent deformation behavior of granular materials and the shakedown concept. *Transportation Research Record: Journal of the Transportation Research Board*, (1757), 75-81. http://dx.doi.org/10.3141/1757-09.

Witczak, M.W., & Uzan, J. (1988). *The universal airport pavement design system. Report I of V: granular material characterization*. University of Maryland.

Wojahn, R.E., Clemente, I.M., Back, A.H., Nummer, A.V., & Pinheiro, R.J.B. (2021). Avaliação das propriedades tecnológicas de agregados de composição granítica oriundos de duas jazidas do estado do Rio Grande do Sul. *Anuário do Instituto de Geociências*, 44(36308), 1-12. http://dx.doi.org/10.11137/1982-3908_2021_44_36308.

Xiao, Y., Tutumluer, E., & Mishra, D. (2019). Performance evaluations of unbound aggregate permanent deformation models for various aggregate physical properties. *Transportation Research Record: Journal of the Transportation Research Board*, 2525(1), 20-30. http://dx.doi.org/10.3141/2525-03.

Zago, J.P., Pinheiro, R.J.B., Baroni, M., Specht, L.P., Delongui, L., & Sagrilo, A.V. (2021). Study of the permanent deformation of three soils employed in highway subgrades in the municipality of Santa Maria-RS, Brazil. *International Journal of Pavement Research and Technology*, 14, 729-739. http://dx.doi.org/10.1007/s42947-020-0129-6.

Soils and Rocks
An International Journal of Geotechnical and Geoenvironmental Engineering
www.soilsandrocks.com
ISSN 1980-9743
ISSN-e 2675-5475

Ballast with siderurgic aggregates: variation analysis of the shape parameters of particles submitted to triaxial tests through 3D scanner

Maelckson Bruno Barros Gomes[1#], Antônio Carlos Rodrigues Guimarães[2], Filipe Almeida Corrêa do Nascimento[2], Juliana Tanabe Assad dos Santos[1]

Article

Keywords
Elipsoidness ratio
Rail ballast material
Railway pavement
3D scan
Repeat load triaxial test

Abstract

Across countries, associations and institutions publish technical standards for railway ballast, however it is observed that those norms have differences when compared to each other. Each one of them has its particularity, varying according to the stone materials available in their countries, axle load and climate. In that sense, it is still a challenge to establish specific guidelines for the properties of the ballast layer. Recently, several techniques for acquisition, image analysis and particle scanning have been developed, either in 2D or in 3D. Those techniques vary from the use of pachymeter to the use of sophisticated scanners. This research seeks to evaluate, through laboratory tests, the evolution of the particle shape parameters through 3D scanning and the level of degradation of the steel slag when subjected to stresses close to those experienced in freight transport railways. Based on the performed tests and the obtained results, the authors recommend for a railway pavement subjected to a load of 32.5 t/axle and composed of steel aggregates used as ballast, a granulometric distribution with uniformity coefficient $1.5 \leq Cu \leq 1.6$ (AREMA n. 4) and particles with: $0.625 \leq$ Elongation ≤ 0.999, $0.567 \leq$ Flatness ≤ 0.995, $0.475 \leq$ Aspect ≤ 0.969 and $0.825 \leq$ Ellipsoidness ≤ 0.957. These specifications enable a good performance of the ballast layer. In addition, the results found contribute to the understanding of siderurgic aggregate behavior under cyclic loading conditions.

1. Introduction

Over the past decades, there have been numerous researches aiming a better understanding of railway pavements, as well as the performance of their layer materials. The accurate understanding of this subject makes it possible to predict, locate and correct pathologies, avoiding accelerated deterioration and premature failures that may even lead to the interruption of railroad operation (Indraratna & Ngo, 2018).

Rail ballast is the pavement component with the highest weight and volume. It can be found in different granulometries, generally composed of medium and large particles. This layer material usually consists of crushed rocks that vary according to the region where the railway is located. The main used lithologies are: limestone, gneiss, basalt, quartzite, granite, rhyolite, dolomite, etc (Selig & Waters, 1994; Raymond & Diyaljee, 1994).

In this context, and aiming the reuse of materials, steel slag has been widely studied, particularly in geotechnical works and in transport infrastructure. Steel slag is a by-product resulting from the steel manufacturing process. It has been observed that, after adequate processing, chemical and environmental stabilization, this material can be an excellent alternative to natural aggregates especially when it can be found close to the pavement to be built (Fernandes, 2010; Delgado et al., 2019; Chamling et al., 2020; Guimarães et al., 2021; Indraratna et al, 2022;).

In 2020, 622 kg of waste/co-products were generated per ton of steel produced in Brazil, of which approximately 25% resulted in steel slag. That means 155 kg of steel slag for each ton of steel produced (Brazilian Steel Institute, 2020). According to the Worldsteel Association (2022), around 31 million tons of steel were produced in Brazil that year. Therefore, approximately 19.3 million of waste/co-products and 4.8 million tons of steel slag were generated in 2020. This high availability associated with the current increase in demand for rail network expansion show a window of opportunity to combine economic growth with sustainability.

[#]Corresponding author. E-mail address: bruno.gomes@ime.eb.br
[1]Instituto Militar de Engenharia, Programa de Pós-graduação em Engenharia de Transportes, Rio de Janeiro, RJ, Brasil.
[2]Instituto Militar de Engenharia, Departamento de Engenharia Civil, Rio de Janeiro, RJ, Brasil.

Submitted on June 9, 2022; Final Acceptance on June 12, 2023; Discussion open until November 30, 2023.

https://doi.org/10.28927/SR.2023.006122

Numerous associations and institutions in different countries publish technical standards guiding the use of materials in the ballast layer. It is observed that the technical standards for railway ballast have differences when compared to each other. Each one of them has its particularity, varying according to the stone materials available in their countries, axle load and climate.

For example, the Brazilian standard for rail ballast NBR 5564/2011 (ABNT, 2021) was limited to tests to be carried out with particles or a set of particles, but not mentioning their lithologies. On the other hand, the same standard republished in October 2021, brings the limits to be observed according to the lithology, however, it does not mention the steel aggregates, which can be seen in the American standard.

It is still difficult to establish strict constitutive standards and models for the properties of the ballast layer (Fortunato, 2005). However, it is known that the layer behavior is essentially conditioned by its mechanical (strength and deformability) and hydraulic (permeability) characteristics.

Thus, it is desirable that these values remain relatively constant throughout the passage of railway compositions and the lifetime of the track. Nevertheless, the stability of this rate is hampered by the gradual increase in long-term stiffness of the material when cyclically loaded. This phenomenon can be intensified if the particles used in the layer have a propensity to produce fines when subjected to the imposed forces.

Although there is still no consensus on the standards to be followed in the world, with regard to the execution of the ballast layer, the parameters that define its behavior are:

- the characteristics of the individual particles: size, shape, texture, angularity, lithology, weathering level, mineralogical composition, durability, hardness, specific weight and toughness;
- the characteristics of the particles set: granulometric curve, void ratio, thickness of the ballast layer and degree of saturation; and
- loading characteristics: main stress, confining pressure, the ratio between the main stress and the confining pressure, stress history, current stress state, number of cycles, frequency and amplitude.

While the properties of individual particles interfere in their degradation under cyclic traffic loading, deformation is also influenced by magnitude, frequency, stress ratio and the number of load cycles (Indraratna et al., 2011; Sun et al., 2014a, 2016).

Therefore, this research seeks to evaluate, through laboratory tests, the evolution of the particle shape parameters through 3D scanning and the level of degradation of the steel slag when subjected to stresses close to those experienced in freight transport railways. The results found contribute to the understanding of steel aggregate behavior under cyclic loading conditions.

1.1 Triaxial tests

The elastic-plastic behavior of the material used in railway ballast is traditionally investigated through laboratory tests, either to obtain its resilient modulus or to predict its plastic deformation under a certain number of cycles. For laboratory studies of railway ballasts, the greatest difficulty found is to reproduce a ballast layer with its real granulometry, with some particles with dimensions equal to or greater than 63.5 mm, preventing the use of triaxial equipment of traditional dimensions (100 x 200 mm and 150 x 300 mm).

In order to overcome this problem, several authors have been using two alternatives: scaling the granulometric curve and large-scale triaxial equipment. Alabbasi & Hussein (2019) presents a summary of the dimensions of the specimen compatible with triaxial equipment and the relation between the diameter of the specimen and the maximum diameter of the particles (D/d_{max}) established. It is observed that both the size of the specimens and the relation D/d_{max} are not a consensus among the different authors.

In Brazil, the national standard for determining permanent deformation, DNIT 179/2018 (DNIT, 2018) guides that in case of granular material, the ratio between the maximum particle diameter and the specimen diameter must be 1:4. Furthermore, if the sample shows material retained in the 1” sieve but completely passing through the 1.1/2” sieve, a cylinder with a 150 mm diameter and 300 mm height must be used. Therefore, these were the ratio and the sample used in this research.

When testing a granular material with a high number of cyclic loadings, one of the most important parameters is the development and accommodation of the plastic deformations. This phenomenon is described by the shakedown theory, proposed for paving materials analysis by Werkmeister et al. (2001). Figure 1 illustrates typical responses of soils and granular aggregates subjected to cyclic loading.

During stage A, known as plastic shakedown, the material accumulates plasticity during several load applications, until deformations increment is practically zero, which results in a final behavior considered purely elastic. During stage B, called plastic creep, high levels of plastic deformation rate, which the material shows in the first load cycles, decrease rapidly until they reach a relatively low and approximate constant value.

The transition from stage A to stage B is normally related to a rapid increase in resilient deformations. For higher stress states, the material behavior goes to stage C, called incremental collapse, where successive increases in plasticization occur. In this case, the rate of plastic deformation either decreases very slowly, or does not decrease at all. It also can lead to rupture.

Werkmeister et al. (2001) suggests that the best way to investigate the occurrence of shakedown is to plot the permanent deformation curves according to the criterion expressed by Dawson and Wellner model (Dawson & Wellner,

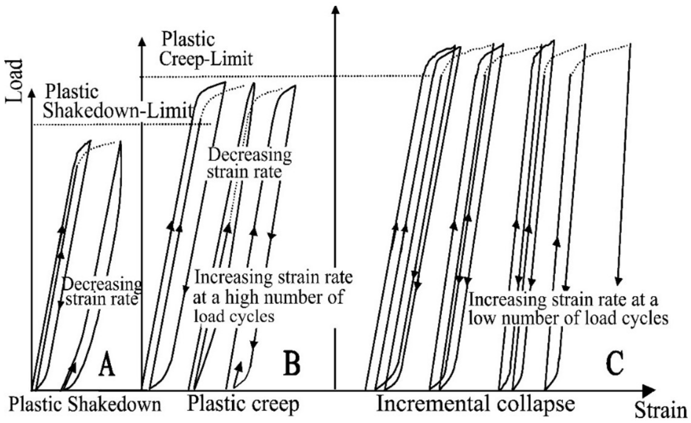

Figure 1. Typical responses of soils and granular aggregates subjected to cyclic loading (Werkmeister et al. (2001).

1999). These authors found that materials with adequate long-term behavior tend to stabilize permanent deformations when their rate of increase at each load application cycle was of the order of 10^{-7} mm/load cycle.

During repeated load tests, it is possible to measure the material resilient modulus (*RM*) through ratio between σ_d and ε_r (where σ_d is the difference between maximum and minimum stresses, and ε_r is the recoverable axial strain during triaxial cyclic load) under the same cyclic stress state. Guimarães (2009) observes that, for stages A and B, the resilient deformation is relatively constant throughout the load application cycles, and its magnitude varies according to the type of material and the state of stress applied. However, for stage C, if the material begins to show granulometric evolution (considerable morphological changes of the particles), a drop in *RM* will be evidenced, which should stabilize again for the new granulometric distribution, however, at a new level of magnitude.

1.2 Particle scanning

Recently, several techniques for acquisition, image analysis and particle scanning have been developed, either in 2D or in 3D. Each one of them with its own particularity, ranging from the use of pachymeter to the use of sophisticated scanners. Three particle analysis scales are traditionally established: shape, angularity and texture (Figure 2). Shape is a larger scale feature; texture is a microscopic feature and angularity is an intermediate scale feature.

Regarding the shape, which is the focus of this research, most quantifications are based on the measurement of the longest (*L*), shortest (*S*) and intermediate (*I*) orthogonal dimensions, being commonly combined two by two: elongation (*I/L*), flattening (*S/I*) and aspect ratio (*S/L*). The elongation and flattening parameters vary between 0 and 1 and seek to demonstrate how close the particles are to being planar, columnar, spherical or planar-columnar, according to the classification proposed by Zingg (1935). After the Zingg

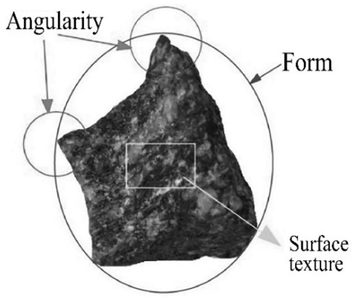

Figure 2. Shape characteristics of a ballast particle (Guo et al., 2019).

diagram, many researchers proposed new diagrams and modifications to the existing ones (Graham & Gadsden, 2019), such as proposed by Blott & Pye (2008).

3D analysis provides a more realistic analysis of the particle, considering the possible distortions that a 2D or 2.5D analysis can generate. In addition, the correct assessment of particle degradation can be compromised if the particles break instead of only being polished by abrasion (Fonseca et al., 2012; Guo et al., 2019).

Considering this, (Sun et al., 2014a) proposed an alternative to quantify the shape of particles with 3D scanning called "ellipsesity". This factor represents how closely the analyzed particle approaches the shape of an ellipsoid and it is defined as the division of the surface area of an ellipsoid of the same volume as the particle, and the actual surface area of the particle. The factor varies between 0 and 1, meaning that the closer the ellipses of the particle is to 1, the more it resembles an ellipsoid of prolate revolution, which is an ellipsoid that has a larger radius (*a*) and two equal radii ($b = c < a$), smaller.

According to Table 1, the parameters established to obtain the ellipsoidness ratio are:

The ellipsoid surface area is twice the area generated by rotating the first-quadrant portion of the ellipse (Equation 1) about the x-axis, resulting in Equation 2, which entails in

Table 1. Ellipsoidness ratio parameters (Gomes et al., 2022).

Equation	Where
$a=\dfrac{L}{2}$	a = Ellipsoid largest radius; and L = Longest particle length (Figure 3a).
$b=c=\sqrt{\dfrac{3V}{2\pi L}}$	b = c<a for a prolate ellipsoid (Figure 3c); b and c = Equal and smaller radii of the ellipsoid; and V = Particle volume.
$S_e=2\pi\left\{b^2+a^2.\dfrac{\arccos\left(\frac{b}{a}\right)}{\tan\left[\arccos\left(\frac{b}{a}\right)\right]}\right\}$	Se = Ellipsoid surface area with the same volume as the particle.
$E=\dfrac{S_e}{S_o}$	E = Ellipsoidness; So = Particle surface area

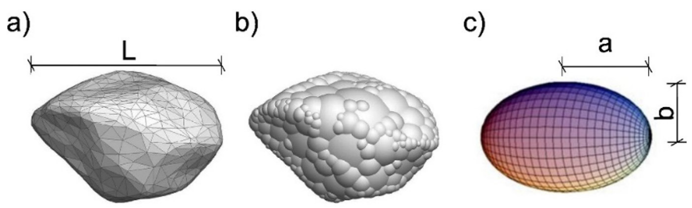

Figure 3. (a) Simulated ballast particle: Scanned surface of a real ballast particle, (b) corresponding virtual particle made of spheres and (c) ellipsoid with the same volume as the ballast particle. Adapted from: Bono et al. (2020).

Equation 3 and after numerical development, generates Equation 4. More details on the development of the ellipsoidness ratio can be seen in Gomes et al. (2022).

$$\frac{x^2}{a^2}+\frac{y^2}{b^2}=1,\ a > b \tag{1}$$

$$s_e=2\int_0^a 2\pi y\sqrt{1+\left(\frac{dy}{dx}\right)^2}\,dx \tag{2}$$

$$1+\left(\frac{dy}{dx}\right)^2=\frac{a^4+b^2x^2-a^2x^2}{a^4-a^2x^2} \tag{3}$$

$$s_e=2\pi\left\{b^2+a^2\,\frac{\arccos\left(\frac{b}{a}\right)}{\tan\left[\arccos\left(\frac{b}{a}\right)\right]}\right\} \tag{4}$$

1.3 Particles degradation

The understanding of the way particles generates fines, how their morphological characteristics change and the impact on layers deformation has shown to be relevant. It assists the development of increasingly sophisticated numerical models to describe particles set behavior under stress.

Some authors have focused on describing the contact mechanism and the way in which contact degradation occurs. Among them are Bono et al. (2020) and Ngo & Indraratna (2020), who modeled particles to a discrete element model through 3D scanning of real particles (Figure 3a and 3b) in order to increase modelling accuracy.

Although the contact between irregular particles and their interactions when subjected to cyclic stress is still complex, the way particle degradation occurs can be grouped into the following types (Wang et al., 2019; Lees & Kennedy, 1975; Guo et al., 2019): abrasion (surface polishing), fracture (particle breakage generating two or more new smaller particles), friction (sharp edges removal) and chipping (removal of chips from particles).

The occurrence of the events of particle degradation is related to particles size, applied stresses and granulometry. Indraratna et al. (2018) showed, however, that most of the ballast degradation is not related to particles splitting, but mainly to edges breaking.

Regarding the evolution of particle shape parameters before and after laboratory tests, Paixão & Fortunato (2021) investigated the performance of a steel slag submitted to the Micro-Deval test and morphological parameters evolution through a low-cost photogrammetry method and compared to a granite result. It was concluded that the morphological alterations of the slag were smaller and more uniform, despite the fact that the two materials presented similar Micro-Deval abrasion coefficients.

Also, through the Micro-Deval test, Quintanilla et al. (2019) used an X-ray tomography device and identified that in the first revolutions of the test there is a tendency to break the sharp and more angular edges of the particles. Consequently, there is an increase in the contact area at the end of these edges wear. However, it was concluded that the test is not able to change the general shape of the grains, being limited to the surface polishing.

Indraratna et al. (2016) used a 3D laser scanner to obtain the morphological parameters of particles. The materials were molded into cylindrical specimens and subjected to dynamical triaxial tests at frequencies of 20 Hz and 30 Hz. A rise in the ellipsoidness ratio (E) and in the flatness ratio was observed after the tests were carried out. The particles became progressively rounded and regular while the frequency of load application was being increased. In view of the executed tests, a range for the ellipsoidness ratio of the evaluated particles was proposed, with the purpose of attenuating degradation and deformation under high cyclic loading frequencies.

In triaxial tests performed on stony materials, in addition to the deformations quantified through *LVDT*s (Linear Variable Differential Transformer), it is necessary to evaluate particles degradation. Some approaches have been developed in the last few decades, and can be categorized into two main types: particle breaking single-grading indices and global-grading indices (Xiao et al., 2021).

The Bg proposed by Marsal (1967) is the particle breaking single-grading indices most used by researchers of railway ballast while BBI (Indraratna et al., 2005), B (Einav, 2007) and Br (Hardin, 1985) are the commonly used particle breaking global-grading indices.

Single-grading indices do not usually represent the breakage of all different sizes particles. On the other hand, global-grading indices are established by assuming the potential breakage of all particles (Xiao et al., 2021).

2. Material properties and performed tests

2.1 Materials

The material used in this research was a steel slag from the Ternium S.A. steel mill located in the state of Rio de Janeiro, Brazil. The slag was chemically and environmentally inert when it was made available for the development of the studies. Characterization tests were carried out (determination of the particles shape, apparent specific mass, apparent porosity, water absorption, resistance to weathering, mass loss by Los Angeles abrasion and resistance to shock through the Treton equipment) following the Brazilian guidelines, according to standard NBR 5564:2021 (ABNT, 2021) that establishes requirements and test methods for railway ballast.

The results were compared with those found by Delgado (2019), with the limits established in Manual for Railway Engineering of AREMA (2015), standard for steel aggregate, and with the Brazilian standard, ABNT (2021), for other lithologies. Regarding shape, non-cubic particles, apparent specific mass, wear resistance and shock resistance, the slag met the limits to be observed, according to the Table 2.

2.2 Particle scanning proceedings

To investigate the particles morphological parameters variation when submitted to repeated loads triaxial tests, it was delimited the sampling effort of 54 particles. They were selected following AREMA n. 4 particle size distribution (Figure 4), resulting in 18 particles per specimen (6 per sieve interval), randomly selected.

The equipment used to digitize the particles was the portable scanner GO!SCAN 3D from CREAFORM, from the robotics laboratory of the Military Institute of Engineering with linear and volumetric accuracy up to 0.10 mm and 0.30 mm/m

Table 2. Aggregate's properties

Parameter	Value	ABNT (2021) limit	AREMA (2015) limit	Delgado (2019)
		Other lithologies	Steel Slag	Steel Slag
Average particle shape	cubic	cubic	cubic	cubic
Non-cubic particles	7%	<15%	<5%	7%
Apparent specific mass	3.153 kg/m^3	>2.500 kg/m^3	>2.900 kg/m^3	3.200 kg/m^3
Water absorption	3.9%	<2.0%	<2.0%	1.7%
Apparent porosity	11.0%	<2.0%	-	-
Wear resistance (Los Angeles abrasion)	10.6%	<30%	<30%	23%
Shock resistance (Treton toughness index)	5.2%	<25%	-	-
Powdery material	0.1%	<1%	<1%	0%
Clay clods	0.0%	<0.50%	<0.50%	-
Unit mass limit in loose state	1585 kg/m^3	>1250 kg/m^3	-	-

respectively, and resolution up to 0.50 mm. The object digitization was executed through VXScan software and meshes were treated with the VXModel software. Reflective targets were placed on the table used in the digitization in order to better capture light beams emitted by the scanner.

Before being submitted to digitalization, the particles were identified following a pre-defined pattern after performing permanent deformation test. In that way, they were painted in different colors, according to the granulometry, and numbered from 1 to 6, as specified in Table 3 and Figure 5.

Each particle was scanned 3 times (turning each particle 90°) in order to establish common mesh intervals between successive scans and join the meshes to form the definitive particle. The VXModel allows to fit each particle into a cube, in order to obtain its largest, smallest and intermediate dimensions (Figure 5b).

In addition, it allows the extraction of the surface area as well as the particle volume. The values got from scans were used to obtain the classification according to the Zingg diagram, and to investigate the modifications imposed on the particles by the cyclic tests, as suggested by Indraratna et al. (2016).

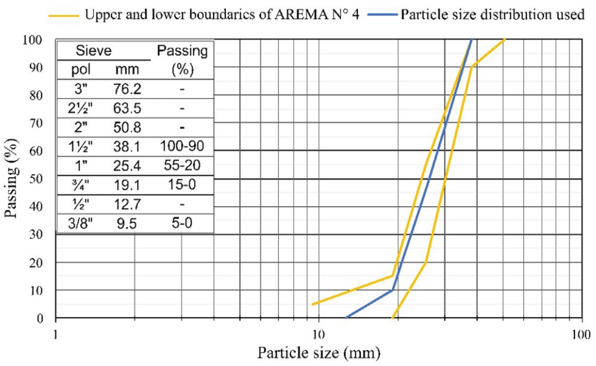

Figure 4. AREMA n. 4 particle size distribution.

2.3 Repeated load triaxial tests

Permanent deformation analysis was carried out through the Repeated Load Triaxial Test (RLTT) results that were executed in a triaxial apparatus similar to that presented in Figure 6. In this test, a state of stress is applied repeatedly to assess the material response to a given number of loading cycles.

Three specimens of around 150 mm of diameter and 300 mm of height were used. The samples were subjected to 250,000 load cycles with cyclic axial loads (σ1) on the top at a frequency of 2 Hz and static axisymmetric loads (σ3).

The specimens were molded by vibration in four layers with a granulometric distribution according to AREMA n. 4 (Figure 4). It was performed the regularization of the top of the specimens (Figure 7b) with paster before submitting

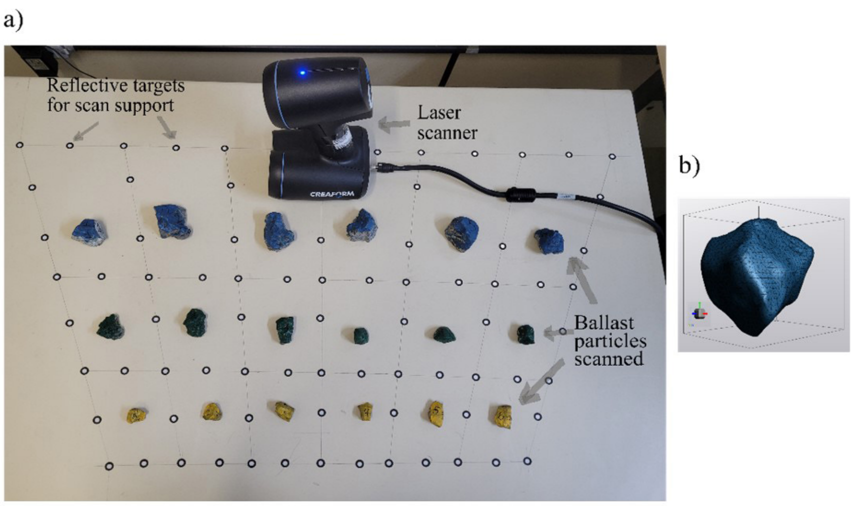

Figure 5. (a) Scanning proceedings: Painted particles and reflective targets in place and (b) an example of a scanned particle fitted into a cube.

Table 3. Identifying particles.

Color	Sieve interval	Particle identification
Blue	Particles passing through the 1.1/2” sieve and retained in the sieve 1”	A1, A2, A3, A4, A5 and A6
Green	Particles passing through the 1” sieve and retained in the 3/4” sieve	B1, B2, B3, B4, B5 and B6
Yellow	Particles passing through the 3/4” sieve and retained in the 1/2” sieve	C1, C2, C3, C4, C5 and C6

them through the triaxial apparatus. More details about this procedure can be found on Gomes (2022). As a result of this procedure, the void index (*e*) and uniformity coefficient (*Cu*) used were similar to the values found by other authors who performed large-scale triaxial tests, such as Lackenby et al. (2007) and Indraratna et al. (2016).

Scanned particles constituted the two intermediate specimen layers (Figure 7a). The objective of this method is to mitigate possible distortions if they were placed on the top, which is immediately in contact with the place of load application, or at the bottom, where it might not faithfully reproduce the transition between the ballast and subballast layer.

The stress state applied on the test was a main stress of 350 kPa with a confining pressure of 70 kPa and a 280 kPa deviator stress. This state of tension is commonly observed in heavy haul railways and was conducted by Delgado et al. (2021) in a steel aggregate with similar characteristics to this research. This stress state, conducted at a 2 Hz frequency, reproduces a train formed by GBT-type gondola wagons with a 1.60 m gauge and a 32.5 t/axle load operating at an average speed of 80 km/h.

The conditioning phase was performed with the same stress state of the permanent deformation test, in which the first 500 cycles were considered to simulate the tamping process performed in the execution of railway pavements. This process was adopted at the Soil Laboratory of the Military Engineering Institute (Figure 7c).

After the conditioning phase, the system coupled to the equipment automatically collects data referring to: cycle number, plastic deformation, elastic deformation, plastic displacement, elastic displacement, accumulated elastic displacement and final height of the specimen.

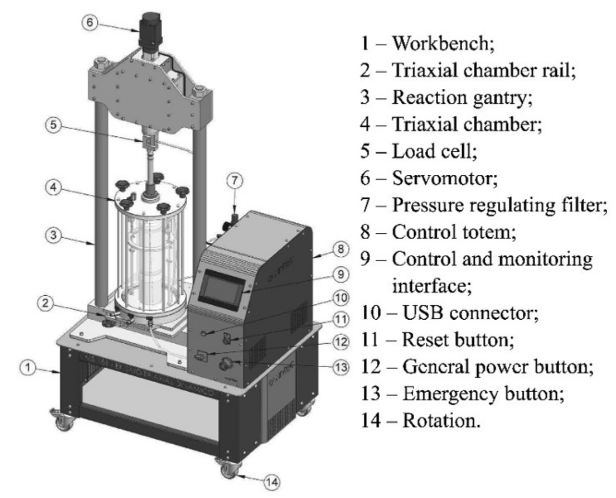

Figure 6. Triaxial apparatus.

3. Analysis and results

3.1 Permanent deformation and particles breakage

Table 4 present the ballast breakage rates obtained during the permanent deformation tests (CP-01, CP-02 e CP-03). From the evaluation of the other parameters of the material, such as void index (*e*) and uniformity coefficient (*Cu*), it was considered that the procedure used for specimens molding proved to be satisfactory.

It is observed that all three specimens had type A behavior (plastic shakedown). The level observed in Figure 8 indicates an almost null plastic deformations increase and a purely elastic response to cyclic loading.

The studies performed allowed the verification of the magnitude of plastic deformations of less than 1.5 mm. Furthermore, the permanent deformations of specimens CP-02 and CP-03 starting from cycle number 150,000 onwards remained practically collinear. The resilient module in the initial cycles were similar, around 400 MPa, indicating a

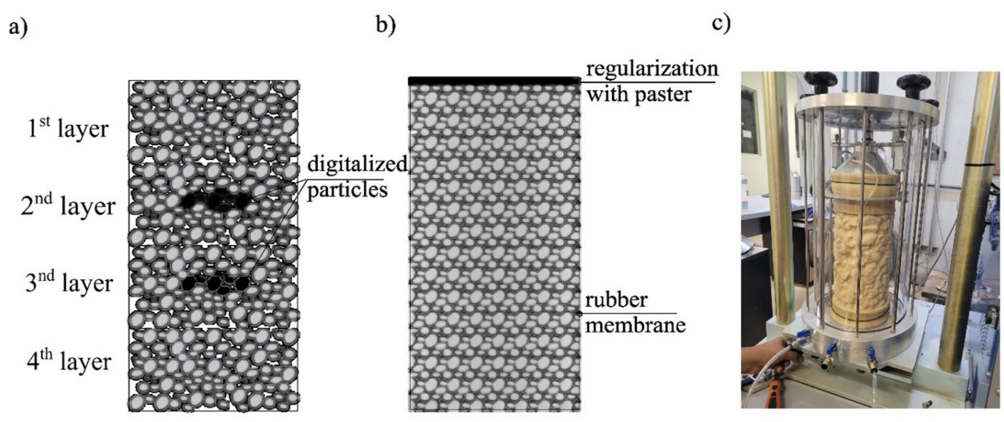

Figure 7. (a) Scanned particles positioned in layers, (b) specimen after conditioning and top regularization with paster and (c) specimen in triaxial chamber.

Table 4. Ballast breakage rates obtained.

Specimen	*e*	*Cu*	σ_1 (kPa)	σ_3 (kPa)	σ_d (kPa)	σ_1/σ_3	*Bg* (Marsal, 1967)	*Br* (Hardin, 1985)	*BBI* (Indraratna et al., 2005)	*B* (Einav, 2007)
CP-01	0.81	1.50	350	70	280	5	0.031	0.008	0.030	0.015
CP-02	0.74	1.59	350	70	280	5	0.016	0.009	0.036	0.017
CP-03	0.84	1.51	350	70	280	5	0.020	0.012	0.044	0.021

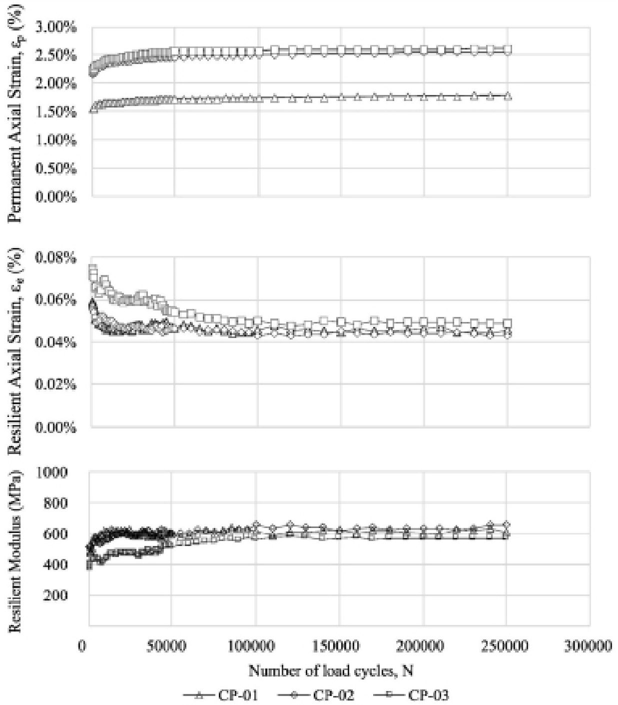

Figure 8. Mechanical parameters: permanent axial strain (ε_r), resilient axial strain (ε_p) and resilient modulus (RM) according to number of load cycles.

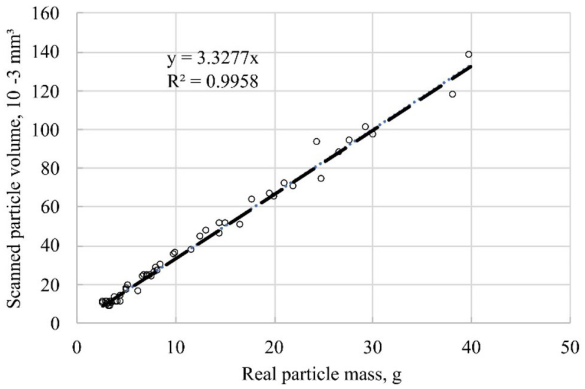

Figure 9. Relation between real particle mass and its corresponding scanned volume.

probable repeatability of the procedure imposed in specimens' preparation for the laboratory tests and constancy of the intrinsic parameters of the material.

The breakage potentials vary according to the granulometric distribution. Well-graded grading curves have a low breaking potential compared to uniform grading curves if *Br* or *BBI* are to be used. Therefore, the use of different indices must be done with caution to obtain the degradation values of the analyzed granulometric curves.

On the other hand, there is a similar behavior of the *B, Br* and *BBI* indices. The *Bg* index was similar to the other indices only in CP-02 and CP-03. This difference in behavior is reported by Indraratna et al. (2016) who found a different behavior pattern for *Bg* index when the uniformity coefficient and maximum particle diameter varied in triaxial tests.

3.2 Particle size and shape variation

From the digitization of the 54 particles (18 per specimen) it was possible to obtain morphological parameters, with an accuracy of 0.01mm, of particles with d_{max}=37.5 mm (1.1/2”). In Figure 9 it is possible to verify the scan adherence to the actual particle digitization, since the angular coefficient (3.327) of the linear trend line found was similar to the specific mass of the material 3153.0 kg/m^3, after the conversion of the measurement unit.

Through the Zingg diagram it was possible to observe the before and after of the particle's classification. All particles were classified as cuboid which is the recommended shape for a particle that composes ballast layer.

Figure 10 presents graphs with the Zingg diagram classification obtained before and after the permanent deformation tests. Table 5 allows evaluating the variation of the ratios of elongation, flatness, aspect and ellipsoidness of the eighteen known particles in each of the three specimens.

In relation to the ellipsoidness, for the evaluated particles, a minimum value of 0.825 and a maximum value of 0.957 were obtained (Figure 11). It was also not possible to observe a parameter modification pattern regarding to specimen dimensions.

It is noted that with a considerable sampling effort, in tests conducted with tensions, uniformity coefficients, void index and very similar aggregates, the modifications obtained by the particles were variable. This is an indication that the evolution of morphological parameters is still difficult to describe and are related to more intrinsic and extrinsic factors.

Indraratna et al. (2016) observed an increase in the rates of elongation, flatness, aspect and ellipsoidness in a basalt. It was evaluated that the particles suffered surface abrasion or

Table 5. Shape characteristics of scanned particles.

Specimen	Particle	Elongation ratio (*I/L*)		Flatness ratio (*S/I*)		Aspect ratio (*S/L*)		Ellipsoidness	
		before	after	before	after	before	after	before	after
CP-01	A1	0.850	0.794	0.833	0.985	0.708	0.782	0.860	0.866
	A2	0.818	0.932	0.796	0.566	0.651	0.527	0.840	0.843
	A3	0.888	0.961	0.895	0.784	0.795	0.753	0.860	0.860
	A4	0.908	0.884	0.801	0.855	0.727	0.756	0.857	0.874
	A5	0.939	0.828	0.881	0.930	0.827	0.769	0.865	0.873
	A6	0.972	0.859	0.809	0.928	0.787	0.797	0.873	0.877
	B1	0.814	0.956	0.741	0.755	0.603	0.722	0.846	0.836
	B2	0.705	0.743	0.674	0.860	0.475	0.639	0.886	0.870
	B3	0.886	0.847	0.915	0.963	0.810	0.816	0.908	0.926
	B4	0.834	0.991	0.953	0.942	0.795	0.934	0.929	0.929
	B5	0.653	0.703	0.950	0.995	0.621	0.699	0.888	0.883
	B6	0.892	0.876	0.928	0.973	0.827	0.852	0.880	0.888
	C1	0.912	0.963	0.866	0.817	0.789	0.787	0.949	0.957
	C2	0.789	0.788	0.951	0.920	0.750	0.725	0.867	0.868
	C3	0.814	0.870	0.832	0.848	0.677	0.738	0.875	0.908
	C4	0.903	0.898	0.915	0.914	0.826	0.821	0.904	0.907
	C5	0.910	0.821	0.862	0.852	0.784	0.700	0.902	0.918
	C6	0.943	0.880	0.702	0.746	0.662	0.657	0.838	0.876
CP-02	A1	0.994	0.839	0.923	0.778	0.923	0.778	0.827	0.842
	A2	0.880	0.972	0.841	0.791	0.841	0.791	0.877	0.880
	A3	0.706	0.848	0.670	0.750	0.670	0.750	0.888	0.872
	A4	0.969	0.915	0.921	0.856	0.921	0.856	0.888	0.903
	A5	0.835	0.958	0.796	0.902	0.796	0.902	0.906	0.904
	A6	0.927	0.874	0.902	0.806	0.902	0.806	0.874	0.868
	B1	0.886	0.758	0.866	0.671	0.866	0.671	0.909	0.925
	B2	0.852	0.726	0.653	0.586	0.653	0.586	0.849	0.855
	B3	0.720	0.922	0.718	0.795	0.718	0.795	0.850	0.837
	B4	0.784	0.901	0.720	0.743	0.720	0.743	0.849	0.841
	B5	0.625	0.789	0.567	0.719	0.567	0.719	0.889	0.857
	B6	0.918	0.696	0.849	0.613	0.849	0.613	0.890	0.919
	C1	0.829	0.769	0.650	0.702	0.650	0.702	0.900	0.901
	C2	0.748	0.805	0.733	0.734	0.733	0.734	0.925	0.935
	C3	0.941	0.992	0.898	0.969	0.898	0.969	0.874	0.877
	C4	0.879	0.886	0.862	0.822	0.862	0.822	0.947	0.939
	C5	0.863	0.981	0.774	0.770	0.774	0.770	0.894	0.895
	C6	0.920	0.717	0.697	0.624	0.697	0.624	0.877	0.927
CP-03	A1	0.925	0.867	0.712	0.723	0.712	0.723	0.847	0.845
	A2	0.884	0.825	0.608	0.751	0.608	0.751	0.860	0.872
	A3	0.941	0.990	0.925	0.904	0.925	0.904	0.842	0.835
	A4	0.874	0.957	0.841	0.912	0.841	0.912	0.880	0.888
	A5	0.799	0.882	0.697	0.661	0.697	0.661	0.825	0.828
	A6	0.999	0.901	0.827	0.852	0.827	0.852	0.890	0.910
	B1	0.859	0.684	0.680	0.667	0.680	0.667	0.881	0.894
	B2	0.762	0.778	0.661	0.712	0.661	0.712	0.875	0.872
	B3	0.860	0.681	0.771	0.639	0.771	0.639	0.875	0.859
	B4	0.842	0.800	0.758	0.739	0.758	0.739	0.886	0.903
	B5	0.935	0.845	0.750	0.801	0.750	0.801	0.854	0.849
	B6	0.973	0.873	0.868	0.858	0.868	0.858	0.898	0.913
	C1	0.727	0.711	0.628	0.634	0.628	0.634	0.879	0.893
	C2	0.793	0.898	0.791	0.785	0.791	0.785	0.896	0.884
	C3	0.835	0.826	0.650	0.647	0.650	0.647	0.946	0.946
	C4	0.858	0.871	0.847	0.811	0.847	0.811	0.878	0.861
	C5	0.922	0.972	0.743	0.942	0.743	0.942	0.890	0.894
	C6	0.802	0.808	0.708	0.713	0.708	0.713	0.897	0.895

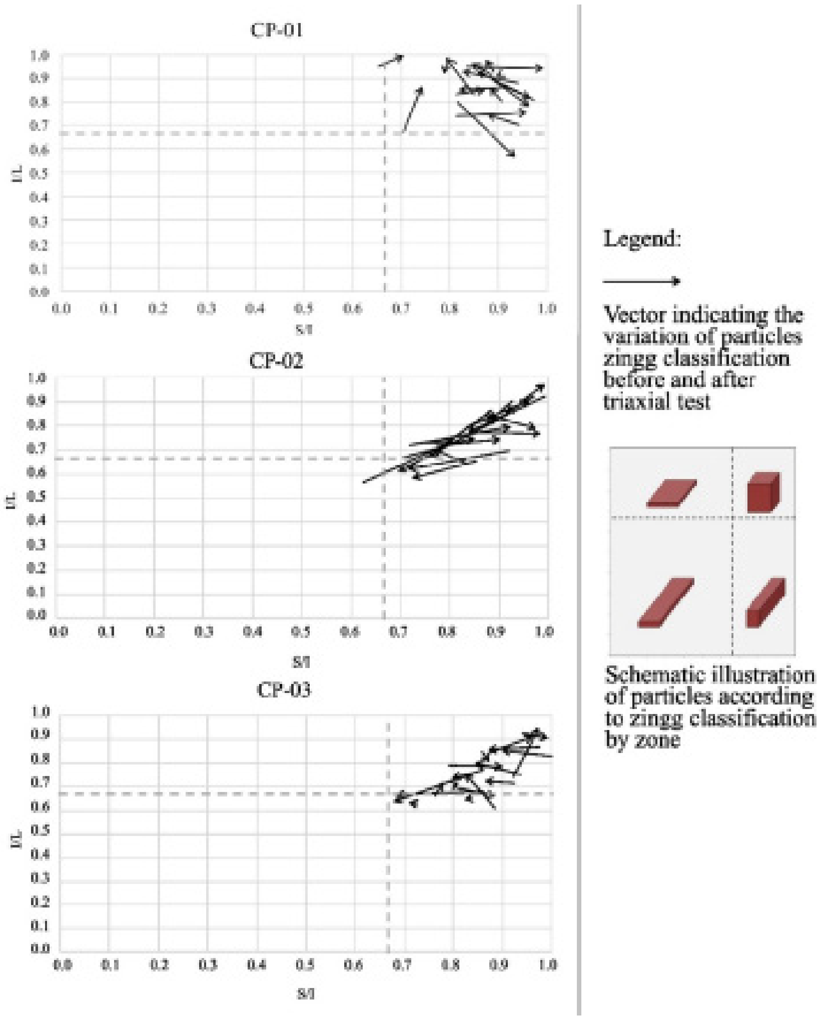

Figure 10. Evolution of particles shapes parameters submitted to triaxial test.

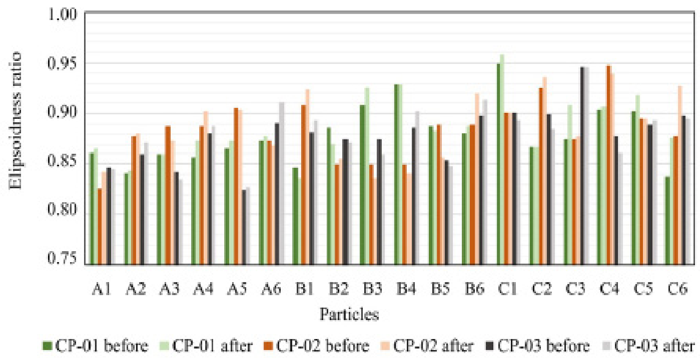

Figure 11. Elipsoidness ratio variation of particles.

chipping with a tendency to become closer to a cube. However, it is noteworthy that the digitized particles of the present research, despite not having presented a pattern of evolution of the morphological parameters, were already predominantly cubic before the tests and remained that way after the tests.

According to Indraratna et al. (2018), for a ballast to have good mechanical performance, it is recommended that the ellipsoidness ratio of the particles be in a range of 0.375 to 0.376. This interval should probably be revised, or, at least, not generalized to all cases, according to the results found here. This can contribute to the selection of materials for the ballast layer in a more assertive way.

4. Conclusions

The rail ballast behavior under high tensions imposed by heavy loads is an investigation that interests many researchers. Its correct understanding can inhibit possible degradations that may compromise the integrity of the railway pavement in service during the project lifetime.

In this work, a method of scanning the particles through a portable 3D scanner was presented. This study proved to be promising in view of the current scientific interest in computationally simulating physical phenomena (Alabbasi & Hussein, 2021).

Digitization made it possible to classify the particles based on the dimensions obtained with an accuracy of 0.01mm. However, it was not possible to observe a trend of shape parameters evolution for the steel aggregate.

For this reason, further triaxial testing is recommended. This methodology, along with the box test, is composed of tests that describe the behavior of the in-situ layer more faithfully than the Los Angeles and Micro-Deval abrasion tests.

The steel aggregate showed low plastic deformations for the imposed stress state. The values were similar to those found by Delgado et al. (2021), who conducted tests with the same stress state of this research in a steel aggregate in Portugal.

The breakage indices obtained were similar to those found by other authors (Sun et al., 2014b; Indraratna et al., 2016; Delgado et al., 2021; Sun & Zheng, 2017). After the tests, ruptured particles were not identified (i.e. particles giving rise to two or more new particles), but only surface polishing and breaking of sharp corners, which is an indication that the particles have a high crushing resistance.

Finally, based on the performed tests and the obtained results, the authors recommend for a railway pavement subjected to a load of 32.5 t/axle and composed of steel aggregates used as ballast, a granulometric distribution with $1.5 \leq Cu \leq 1.6$ (AREMA n. 4) and particles with: $0.625 \leq$ Elongation ≤ 0.999, $0.567 \leq$ Flatness ≤ 0.995, $0.475 \leq$ Aspect ≤ 0.969 and $0.825 \leq$ Ellipsoidness ≤ 0.957. Therefore, a good behavior of the material regarding permanent deformations and draining characteristics is expected, considering the low level of fines generated after 250,000 loading cycles.

This recommendation of values for the ellipsoidness ratio disagrees with what was recommended by Indraratna et al. (2016, 2018), which suggests a very small range, ranging from $0.375 \leq$ ellipsoidness ≤ 0.376. Although Indraratna et al. (2016) have recommended this range of ellipsoidness ratio based on high frequency tests, it is believed that this value should be reviewed or, at least, not applied to all scenarios of: loading, frequency, lithology and particle size distribution.

Acknowledgements

The authors are thankful for the Instituto Militar de Engenharia (IME), for the support given by Ciro Azevedo Junior on the laboratory tests conducted in this research and for Tamires Albarelli on the assistance on the text translation.

Declaration of interest

The authors declare that they have no known competing financial interests or personal relationships that could have appeared to influence the work reported in this paper.

Authors' contributions

Maelckson Bruno Barros Gomes: writing- original draft preparation, data curation, methodology, investigation. Antônio Carlos Rodrigues Guimarães: validation, supervision. Filipe Almeida Corrêa do Nascimento: visualization, supervision. Juliana Tanabe Assad dos Santos: writing - review & editing.

Data availability

The raw and processed data required to reproduce these findings are available to download from: https://drive.google.com/drive/folders/1OAWW1uoztAX0n5uYj-WXrcJMXuV4-md9?usp=sharing

List of symbols

a	Major axis
b, c	Minor radii
e	Void index
B	Breakage index proposed by Einav (2007)
BBI	Ballast breakage index proposed by Indraratna et al. (2005)
Bg	Breakage index proposed by Marsal (1967)
Br	Breakage index proposed by Hardin (1985)
Cu	Uniformity coefficient
D	Specimens diameter
D_{10}	Particle diameters defining 10% finer from the grain-size distribution curve
D_{60}	Particle diameters defining 60% finer from the grain-size distribution curve
d_{max}	Maximum diameter of particles
E	*E*llipsoidness ratio
I	Intermediate dimension
L	Longest dimension
PD	Permanent Deformation
RM	Resilient Modulus
S_o	Real surface
S_e	Surface area of an ellipsoid having the same volume as the scanned particle
S	Shortest dimension

V	Volume of the scanned particle
V_v	Volume of voids
V_s	Volume of solids
ε_r	Elastic strain
σ_d	Deviator stress
σ_1	Maximum major stress
$\sigma_{1max,cyclic}$	Maximum cyclic major stress
σ_3	Minimum major stress or confining pressure

References

ABNT NBR 5564. (2021). *Railroad - rail ballast - requirements and test method*. ABNT - Associação Brasileira de Normas Técnicas, Rio de Janeiro, RJ (in Portuguese).

Alabbasi, Y., & Hussein, M. (2019). Large-scale triaxial and box testing on railroad ballast: a review. *SN Applied Sciences*, 1, 1592. https://doi.org/10.1007/s42452-019-1459-3.

Alabbasi, Y., & Hussein, M. (2021). Geomechanical modelling of railroad ballast: a review. *Archives of Computational Methods in Engineering*, 28, 815-839. http://dx.doi.org/10.1007/s11831-019-09390-4.

American Railway Engineering Maintenance-of-way Association - AREMA. (2015). *Manual for railway engineering* (Vol. 1-4). AREMA.

Blott, S.J., & Pye, K. (2008). Particle shape: a review and new methods of characterization and classification. *Sedimentology*, 55, 31-63. http://dx.doi.org/10.1111/j.1365-3091.2007.00892.x.

Bono, J., Li, H., & McDowell, G. (2020). A new abrasive wear model for railway ballast. *Soil and Foundation*, 60(3), http://dx.doi.org/10.1016/j.sandf.2020.05.001.

Brazilian Steel Institute. (2020). *Three foundations of sustainable development*. Retrieved in April 2, 2022, from https://www.acobrasil.org.br/relatoriodesustentabilidade/#ambiental

Chamling, K., Haldar, S., & Patra, S. (2020). Physico-chemical and mechanical characterization of steel slag as Railway Ballast. *Indian Geotech J*, 50(2), 267-275. http://dx.doi.org/10.1007/s40098-020-00421-7.

Dawson, A.R., & Wellner, F. (1999). *Plastic behaviour of granular materials* (Final Report ARC Project, 933). Department of Civil Engineering, University of Nottingham.

Delgado, B., Da Fonseca, A., Fortunato, E., & Motta, L. (2019). *Aproveitamento de escórias de aciaria em infraestruturas de transportes - estudos e aplicações em Portugal e no Brasil*. Retrieved in April 14, 2022, from http://repositorio.lnec.pt:8080/jspui/handle/123456789/1012121

Delgado, B.G. (2019). *Geomechanics of an inert steel aggregate as an alternative material for heavy haul railway ballast* [Doctoral thesis, Faculty of Engineering]. University of Porto (in Portuguese).Retrieved in April 14, 2022, from https://hdl.handle.net/10216/125559

Delgado, B.G., Fonseca, A.V., Fortunato, E., Paixão, A., & Alves, R. (2021). Geomechanical assessment of an inert steel slag aggregate as an alternative ballast material for heavy haul rail tracks. *Construction & Building Materials*, 279, http://dx.doi.org/10.1016/j.conbuildmat.2021.122438.

DNIT 179/2018–IE. (2018). *Paving – Soils – Determination of Permanent Deformation – Test Instruction*. DNIT - Departamento Nacional de Infraestrutura de Transportes. Rio de Janeiro, RJ. (in Portuguese).

Einav, I. (2007). Breakage mechanics—Part I: theory. *Journal of the Mechanics and Physics of Solids*, 55(6), 1274-1297. http://dx.doi.org/10.1016/j.jmps.2006.11.003.

Fernandes, D.P. (2010). *Study of chemical, geo-mechanical and environmental stabilization of LD steel slag for application as railway ballast material on signalized roads* [Master thesis]. Ouro Preto Federal University. (in Portuguese). Retrieved in April 2, 2022, from http://www.repositorio.ufop.br/bitstream/123456789/2325/1/DISSERTA%c3%87%c3%83O_EstudoEstabiliza%c3%a7%c3%a3oQu%c3%admica.pdf

Fonseca, J., O'Sullivan, C., Coop, M.R., & Lee, P. (2012). Non-invasive characterization of particle morphology of natural sands. *Soil and Foundation*, 52, 712-722. http://dx.doi.org/10.1016/j.sandf.2012.07.011.

Fortunato, E. (2005). *Renewal of railway platforms: studies on load capacity* [Doctoral dissertation, LNEC/Engineering College] Porto University (in Portuguese). Retrieved in April 14, 2022, from https://hdl.handle.net/10216/11441

Gomes, M., Guimarães, A., & Nascimento, F. (2022). Revisão do cálculo do parâmetro para quantificar tridimensionalmente a morfologia das partículas de lastro: a elipsoidade. In *Anais Eletrônicos do 36º Congresso de Pesquisa e Ensino em Transportes*. Fortaleza, Ceará. (in Portuguese). Retrieved in December 21, 2022, from https://proceedings.science/anpet-2022/trabalhos/revisao-do-calculo-do-parametro-para-quantificar-tridimensionalmente-a-morfologi?lang=pt-br#

Gomes, M.B.B. (2022). *Análise da deformabilidade do lastro ferroviário de agregado siderúrgico utilizando ensaios triaxiais de cargas repetidas* [Master Thesis, Transportation Engineering]. Military Institute of Engineering. (in Portuguese). http://dx.doi.org/10.13140/RG.2.2.12223.59048.

Graham, D.J., & Gadsden, R.J. (2019). New statistical methods for the comparison and characterization of particle shape. *Earth Surface Processes and Landforms*, 44, 2396-2407. http://dx.doi.org/10.1002/esp.4669.

Guimarães, A.C.R. (2009). *An empirical mechanistic method for the prediction of permanent deformation in tropical soils constituent of pavements* [Doctor thesis, Civil Engineering Program]. Federal University of Rio de Janeiro (in Portuguese). Retrieved in April 2, 2022, from http://www.coc.ufrj.br/pt/teses-de-doutorado/153-2009/1199-antonio-carlos-rodrigues-guimaraes

Guimarães, A.C.R., Costa, K.Á., Reis, M.M., Santana, C.S.A., & Castro, C.D. (2021). Study of controlled leaching process of steel slag in soxhlet extractor aiming employment in pavements. *Transportation Geotechnics*, 27, http://dx.doi.org/10.1016/j.trgeo.2020.100485.

Guo, Y., Markine, V.L., Zhang, X., Qiang, W., & Jing, G. (2019). Image analysis for morphology. rheology and degradation study of railway ballast. *Transportation Geotechnics*, 18, 173-211. http://dx.doi.org/10.1016/j.trgeo.2018.12.001.

Hardin, B. O. (1985). Crushing of soil particles. *Journal of Geotechnical Engineering*, 111(10), 1177-1192. https://doi.org/10.1061/(ASCE)0733-9410(1985)111:10(1177).

Indraratna, B., & Ngo, T. (2018). *Ballast railroad design: smart-uow approach*. CRC Press. https://doi.org/10.1201/9780429504242.

Indraratna, B., Lackenby, J., & Christie, D. (2005). Effect of confining pressure on the degradation of ballast under cyclic loading. *Geotechnique*, 55(4), 325-328. http://dx.doi.org/10.1680/geot.2005.55.4.325.

Indraratna, B., Ngo, N.T., Nimbalkar, S., & Rujikiatkamjorn, C. (2018). Two decades of advancement in process simulation testing of ballast strength, deformation, and degradation. In T.D. Stark, R.H. Swan & R. Szecsy (Eds.), *Railroad ballast testing and properties* (pp. 11-38). West Conshohocken, United States: ASTM International. http://dx.doi.org/10.1520/STP160520170029.

Indraratna, B., Qi, Y., Tawk, M.H.A., Rujikiatkamjorn, C., & Navaratnarajah, S.K. (2022). Advances in ground improvement using waste materials for transportation infrastructure. *Proceedings of the Institution of Civil Engineers: Ground Improvement*, 175(1), 3-22. http://dx.doi.org/10.1680/jgrim.20.00007.

Indraratna, B., Salim, W., & Rujikiatkamjorn, C. (2011). *Advanced rail geotechnology – ballasted track*. CRC Press. https://doi.org/10.1201/b10861.

Indraratna, B., Sun, Y., & Nimbalkar, S. (2016). Laboratory assessment of the role of particle size distribution on the deformation and degradation of ballast under cyclic loading. *Journal of Geotechnical and Geoenvironmental Engineering*, 142(7), http://dx.doi.org/10.1061/(ASCE)GT.1943-5606.0001463.

Lackenby, J., Indraratna, B., McDowell, G., & Christie, D. (2007). Effect of confining pressure on ballast degradation and deformation under cyclic triaxial loading. *Géotechnique*, 57(6), 527-536. https://doi.org/10.1680/geot.2007.57.6.527.

Lees, G., & Kennedy, C.K. (1975). Quality, shape and degradation of aggregates. *Quarterly Journal of Engineering Geology and Hydrogeology*, 8(3), 193-209. http://dx.doi.org/10.1144/GSL.QJEG.1975.008.03.03.

Marsal, R.J. (1967). Large scale testing of rockfill materials. *Journal of the Soil Mechanics and Foundations Division*, 93(2), 27-43. http://dx.doi.org/10.1061/JSFEAQ.0000958.

Ngo, T., & Indraratna, B. (2020). Analysis of deformation and degradation of fouled ballast: experimental testing and DEM modeling. *International Journal of Geomechanics*, 20, 06020020. http://dx.doi.org/10.1061/(ASCE)GM.1943-5622.0001783.

Paixão, A., & Fortunato, E. (2021). Abrasion evolution of steel furnace slag aggregate for railway ballast: 3D morphology analysis of scanned particles by close-range photogrammetry. *Construction & Building Materials*, 267, http://dx.doi.org/10.1016/j.conbuildmat.2020.121225.

Quintanilla, I.D., Combe, G., Emeriault, F., Voivret, C., & Ferellec, J. (2019). X-ray CT analysis of the evolution of ballast grain morphology along a Micro-Deval test: key role of the asperity scale. *Granular Matter*, 21, http://dx.doi.org/10.1007/s10035-019-0881-y.

Raymond, G. P., & Diyaljee, V. A., (1994). Railroad ballast sizing and grading. *Journal of the Geotechnical Engineering Divison*, 105(5), 676-681. https://doi.org/10.1061/AJGEB6.0000803.

Selig, E.T., & Waters, J.M. (1994). *Track geotechnology and substructure management*. Thomas Telford. https://doi.org/10.1680/tgasm.20139.0007.

Sun, Y., Indraratna, B., & Nimbalkar, S. (2014a). Three-dimensional characterisation of particle size and shape for ballast. *Géotechnique Letters*, 4(3), 197-202. http://dx.doi.org/10.1680/geolett.14.00036.

Sun, Q.D., Indraratna, B., & Nimbalkar, S. (2014b). Effect of cyclic loading frequency on the permanent deformation and degradation of railway ballast. *Geotechnique*, 64(9), 746-751. http://dx.doi.org/10.1680/geot.14.T.015.

Sun, Q.D., Indraratna, B., & Nimbalkar, S. (2016). The deformation and degradation mechanisms of railway ballast under high frequency cyclic loading. *Journal of Geotechnical and Geoenvironmental Engineering*, 142(1). 04012056. https://doi.org/10.1061/(ASCE)GT.1943-5606.0001.

Sun, Y., & Zheng, C. (2017). Breakage and shape analysis of ballast aggregates with different size distributions. *Particuology*, 35, 84-92. http://dx.doi.org/10.1016/j.partic.2017.02.004.

Wang, Y., Shao, S., & Wang, Z. (2019). Effect of particle breakage and shape on the mechanical behaviors of granular materials. *Advances in Civil Engineering*, 2019, 1-15. http://dx.doi.org/10.1155/2019/7248427.

Werkmeister, S., Dawson, A.R., & Wellner, F. (2001). Permanent deformation behavior of granular materials and the shakedown concept. *Transportation Research Record: Journal of the Transportation Research Board*, 1757(1), 75-81. http://dx.doi.org/10.3141/1757-09.

Worldsteel Association. (2022). *Global crude steel output decreases by 0.9% in 2020*. Retrieved in April 7, 2022, from https://worldsteel.org/media-centre/press-releases/2021/global-crude-steel-output-decreases-by-0-9-in-2020/

Xiao, Y., Wang, C., Wu, H., & Desai, C.S. (2021). New simple breakage index for crushable granular soils. *International Journal of Geomechanics*, 21(8), 04021136. http://dx.doi.org/10.1061/(ASCE)GM.1943-5622.0002091.

Zingg, T. (1935). Beitrag zur schotteranalyse. *Schweizerische Mineralogische und Petrographische Mitteilungen*, 15, 39-140. http://dx.doi.org/10.3929/ethz-a-000103455.

Soils and Rocks
An International Journal of Geotechnical and Geoenvironmental Engineering
www.soilsandrocks.com
ISSN 1980-9743
ISSN-e 2675-5475

Influence of the filling process on the behaviour of geotextile tubes

Michael Andrey Vargas Barrantes[1#], Luís Fernando Martins Ribeiro[1], Ennio Marques Palmeira[1]

Article

Keywords
Geotextile tube
Dewatering
Nonwoven geotextile

Abstract

Geotextile tubes can be used to dewater materials such as sludge, sediments or residues aiming at reducing their moisture contents to acceptable levels. The tube filling process can be carried out using one or several filling stages, and the number of stages can influence the tube behaviour in terms of dewatering rate, final shape and geotextile strains, for instance. In this research, laboratory tests were carried out on nonwoven geotextile tubes for the dewatering of a fine-grained material using different numbers of filling stages. The behaviour of the tube was monitored by instrumentation to assess tube geometry, pore pressures, total stresses at the tube base, geotextile strains and retention capacity. Evaluations of the accuracy of some available methods for the prediction of tube behaviour were also made. The results obtained showed that the increase in the number of filling stages resulted in larger final tube height, volume, geotextile strains as well as larger diameters of the soil particles that piped through the geotextile. Predictions of tube behaviour by available methods showed varying degrees of accuracy depending on the tube parameter considered.

1. Introduction

Geosynthetics have been used for various functions in geotechnical and environmental engineering projects, such as soil reinforcement, drainage, filtration and as barriers, for instance. Among the reasons why geosynthetic have gained considerable acceptance over the years are: easy transportation to working sites, quick installation, repeatable properties and savings in the use of natural construction materials. These characteristics can yield to significant cost savings compared to traditional geotechnical alternatives and provide environmentally friendly engineering solutions.

The increase in industrial activities causes large amounts of waste to be generated with large percentages of fines, varying contents of liquid and, not seldom, contaminant substances. This creates difficulties for the disposal of these materials, and alternative management techniques must be necessary (Moo-Young et al., 2002; Muthukumaran & Ilamparuthi. 2006; Bourgès-Gastaud et al., 2014). The technique of using geotextile tubes has been considered an efficient and economical solution for moisture content reduction and safer disposal of wastes (Maurer et al., 2012). To better understand the dewatering behaviour of geotextile tubes, several laboratory studies have been carried out over the last decades (Moo-Young et al., 2002; Moo-Young & Tucker, 2002; Koerner & Koerner, 2006; Muthukumaran & Ilamparuthi, 2006; Lawson, 2008; Liao & Bathia, 2008; Satyamurthy & Bhatia, 2009; Cantré & Saathoff, 2011).

Several works in the literature have reported the use of geotextile tubes for a series of purposes such as drying sludge or sewage material in wastewater treatment plants, rehabilitation of slopes, protection of coastal areas by means of breakwaters, slope buttresses and protection dikes, among others (Leshchinsky et al.,1996; Plaut & Suherman, 1998; Koh et al., 2020, Pilarczyk, 2000; Koerner & Koerner, 2006; Lawson, 2008; Yan and Chu, 2010; Yee et al., 2012; Yee & Lawson, 2012).

A specific problem faced in the field of engineering is how to efficiently dispose sludge with high water-content such as dredged sediment, industrial waste, wastewater treatment sludge, and mining tailings (Bourgès-Gastaud et al., 2014). In addition, the use of geotextile tubes for the dewatering of tailings in mining plants has increased in acceptance because of drainage efficiency and lower investments and maintenance costs (Assinder et al., 2016; Newman et al., 2004; Li et al., 2016; Wilke et al., 2015). Results presented by Yang et al, (2019) show that the application of geotextile tubes in tailings storage structures represent a good alternative for fine tailings disposal.

The typical process of dewatering with geotextile tubes consists of several stages of filling and dewatering (Yee & Lawson, 2012). During the filling stage, the sludge material

[#]Corresponding author. E-mail address: ma12vargas@gmail.com.
[1]Universidade de Brasília, Departamento de Engenharia Civil e Ambiental, Brasília, DF, Brasil.

Submitted on October 11, 2022; Final Acceptance on March 19, 2023; Discussion open until November 30, 2023.

https://doi.org/10.28927/SR.2023.010522

is pumped into the tube under turbulent conditions followed by the outflow of the liquid, with sedimentation of particles in the lower part of the tube. The filling and dewatering stages are then repeated up to the maximum operational capacity of the system. Despite the success in use of geotextile tubes, some uncertainties remain regarding important design and construction issues.

Some studies (Lawson, 2008; Yee & Lawson, 2012, Wilke & Cantré, 2016, Ratnayesuraj & Bhatia 2018, Kim & Dinoy, 2021) admit tube filling and dewatering processes in a single or multiple stages. The number of stages can influence pore pressure generation (Zhang et al., 2022), strains and tensile forces in the geotextile (Plaut & Filz, 2008, Kim et al., 2020) as well as limiting the accuracy of predictions of tube behaviour from theoretical solutions.

This paper presents and discusses results of large-scale laboratory tests to investigate the influence of varying numbers of filling stages on geotextile tube behaviour considering the development of pore pressures and total stresses in the filling material, as well as the strains in the geotextile. For this purpose, tubes were filled with slurry in a single stage and in three stages. The results obtained in the experiments are presented and discussed in the following items.

2. Experimental

2.1 Materials

The infill material used in the experimental program consisted of a mixture of a lateritic silty clay and water in the form of a slurry with a concentration (in mass) of solids of 50%. The grain size analysis of the soil carried out using a laser beam grain size analyzer (Microtrac) revealed values of D_{85} (diameter for which 85% of the remaining particle diameters are smaller than that value, Table 1) of 0.063 mm and 0.259 mm in tests with and without dispersing agent, respectively, D_{50} of 0.027 mm and 0.120 mm, D_{10} of 0.0036 mm and 0.040 mm, liquid limit of 37% and plastic limit of 28%. The predominant soil mineral is gibbsite, an in its natural state the soil fabric presents macropores and many aggregates (Burgos, 2016). Table 1 presents the main geotechnical properties of the soil used in the test.

A nonwoven, needle-punched, geotextile made of polyester continuous filaments was used. The mass per unit area of the geotextile is equal to 200 g/m^2 and its filtration opening size is equal to 0.115 mm. The geotextile tubes had a length of 1 m and a diameter of 0.8 m. The main geotextile properties are summarized in Table 2.

2.2 Equipment

A channel (6 m long x 1.5 m high; 1 m wide) was used in the experiments. A section at one of the extremities of the channel was used for the mixing of the soil with water. The rest of the channel length was used to construct the geotextile tubes (Figure 1). The sides of the channel are transparent to allow the view of the deformed shape of the tube during the test. Two layers of lubricated plastic were applied to the channel walls to minimize friction between the geotextile and the glass. Soil was continuously and uniformly mixed with water to form a slurry with a unit weight of 13.5 kN/m^3 using of a 3000 watts power pump prior to the inflow of the slurry in the tube. The geotextile tubes were cylindrical, with a diameter of 0.8 m and a length of 1 m. The geotextile tube rested on a rigid platform at the bottom of the channel.

The tube was instrumented with electric total stress cells and pore pressure transducers installed at its base, as shown in Figure 2. A standpipe connected to the tube base was also installed. The deformation of the tube was measured at several points along its perimeter by monitoring the deformed shape of a square meshes (20 mm wide) printed along the surface of the tube in its central region (Figure 2).

The tests started with the preparation of the soil slurry with a concentration (in mass) of solids of approximately

Table 1. Soil Properties.

Proprieties	Values
D_{10} (mm)[1]	0.040/0.0036[2]
D_{50} (mm)	0.120/0.027
D_{85} (mm)	0.259/0.063
Coefficient of uniformity	3.7/8.4
% smaller than 0.075 mm	29/87
Liquid Limit (%)*	37
Plastic Limit (%)*	28
Plasticity Index (%)*	9
SUCS Classification	CL
AASHTO Classification	A-4
MCT Classification	LA-LA'

[1] D_n = diameter of the particle for which n% of the remaining particles are smaller. [2] Values on the left are from tests without the use of dispersing agent and values on the right with the use of dispersing agent.
***Source:** Burgos (2016).

Table 2. Geosynthetics properties.

Propriety	Values
Polymer [1]	PET
M_A (g/m^2)	200*
t_{GT} (mm)	2.2*
O_{95} (mm)[2]	0.115
J_5 (kN/m)[3,6]	11.5
'T_{max} (kN/m)[4,6]	9.8
ε_{max} (%)[5,6]	83-100

[1] PET= polyester; M_A = mass per unit area (ASTM D5261); t_{GT} = nominal thickness (ASTM D 5261). [2] O_{95} = filtration opening size (ASTM D6767). [3] J5 = secant tensile stiffness at 5% strain. [4] *Tmax* = tensile strength. [5] εmax = maximum tensile strain. [6] Wide-strip tensile tests as per ASTM D4595. * Data provided by the manufacturer.

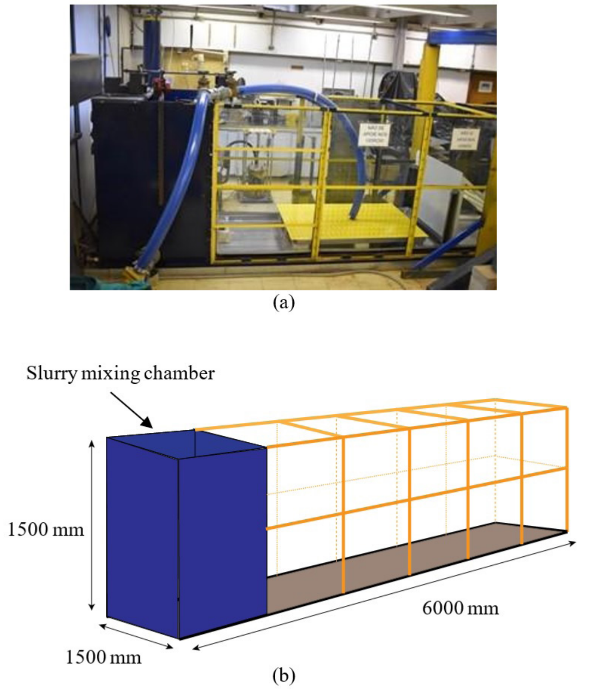

Figure 1. View and dimensions of the equipment (a) View of the mixing and test sections; (b) Dimensions of the channel.

50%. The process of mixing and filling was carried out by means of a dredge pump. The injection flow rate of the mixture inside the geotextile tubes was equal to 0.75 l/s. The tubes were filled with a single filling step or with three filling steps. The filling stage lasted until the tubes reached an initial height of 450 mm.

After the end of the tests, the soil particles that piped through the geotextile were collected for grain size analysis. A laser beam particle analyzer (Microtrac) was used for the measurement of the diameters of the piped particles.

3. Results

3.1 Volume reduction and change in dewatering rate

Figure 3 shows the volume of water drained from the tubes over 4 weeks for the two tests performed, which are identified by the codes GT-1FS (single filling stage) and GT-3FS (three filling stages). Stabilization of the readings at the end of the second, third and fourth week in the test GT-3FS can be noted. For the case of the GT-1FS test, the same stabilization of drained water volume can be observed after 13 days after filling. The use of three filling stages led

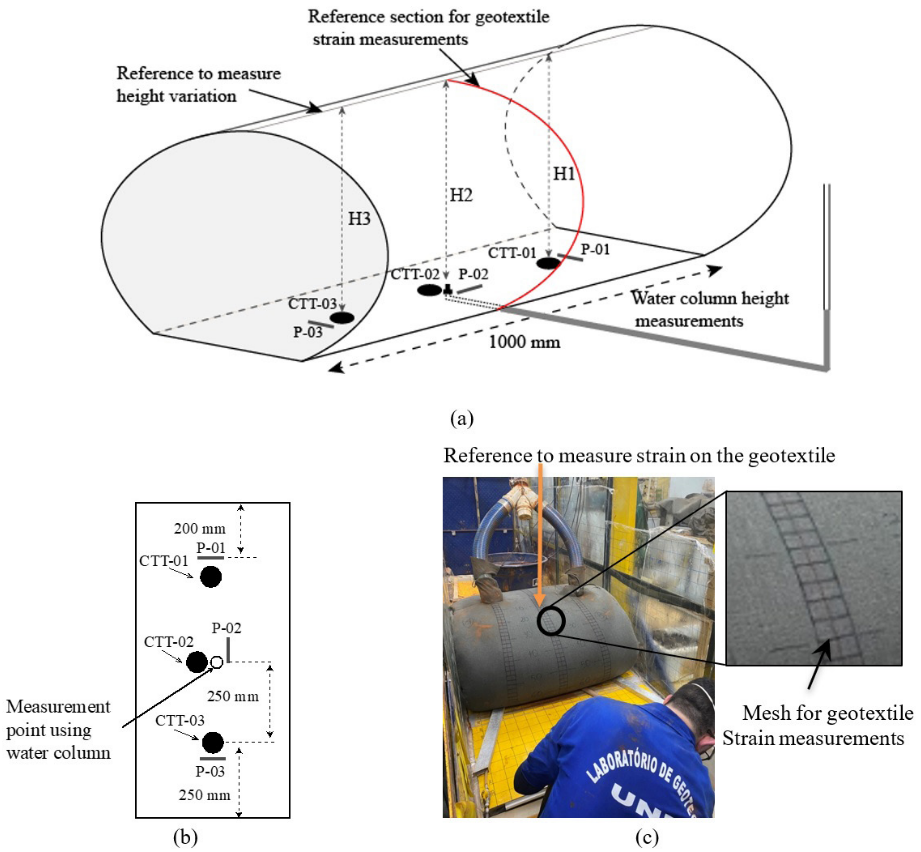

Figure 2. Instrumentation of the tube (a) Location of pressure cells and pore pressure transducers; (b) Location of the instruments at the base of the geotextile tube; (c) Square mesh printed along the surface of the tube for geotextile strain measurements.

to a volume of drained water 29% higher compared to the test with a single filling stage.

The tube height variation with time was recorded throughout the test and is depicted in Figure 4. It can be noted that the magnitude of the tube height increases at the beginning of each filling stage decreased in test GT-3FS. According to Yee & Lawson (2012), as the number of draining stages increases, the volume of solids and flakes deposited in the tube also increases, thus decreasing the variation in height between each filling stage. A similar behaviour of the two tests can be observed in the first two weeks, with just a slight difference in height at the end of the second week when compared with test GT-3FS. The formation of layers of sedimented material at the bottom of the tube occurs more quickly after the filling process, associated with a greater output of free water (Figure 3). A transition from a process dominated by dewatering to another dominated by consolidation takes place, as described by Lawson (2008).

The volume of slurry injected in the tube was measured for each filling stage. Figure 5 presents the variation of the tube total volume with time during tests GT-1FS and GT-3FS. The change in contained slurry volume within the geotextile tube and the change in concentration of solids are interrelated (Lawson, 2008). For a single filling-dewatering cycle, the expected increase in solids concentration can be determined for a given reduction in contained slurry volume from (Lawson, 2008):

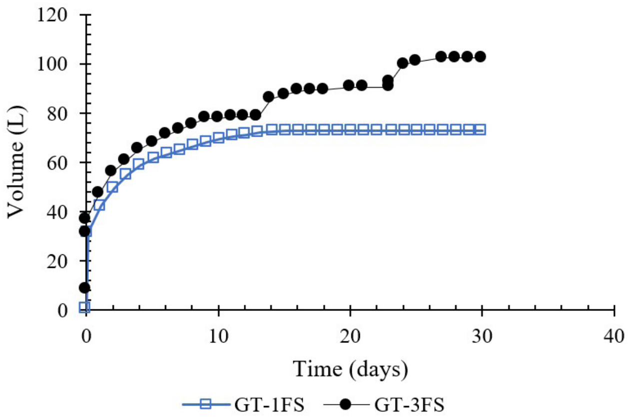

Figure 3. Accumulated volume of water drained during the tests.

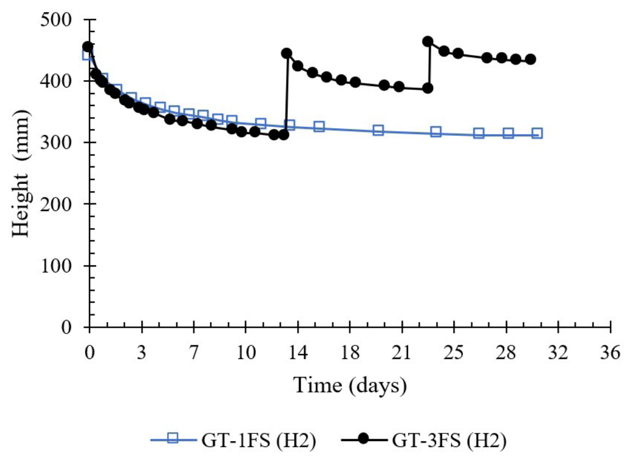

Figure 4. Variation of tube height with time.

$$S_t = \frac{\left(\frac{1}{1-\Delta V_t}\right)\left(\frac{S_0}{1-S_o}\right)}{1+\left(\frac{1}{1-\Delta V_t}\right)\left(\frac{S_o}{1-S_o}\right)} \tag{1}$$

Where St is the concentration of solids at time t, ΔV_t is the contained slurry volume reduction over time t and S_0 is the initial concentration of solids.

From the variation of the slurry volume recorded in the test GT-1FS in Figure 5a, it is possible to obtain the variation of the theorical concentration with time using Equation 1, as shown in Figure 5b. There is a gradual reduction in volume as the water drains, consequently leading to an increase in concentration of solids with time. Higher rates of concentration increase were observed in the first 5 days of testing.

According to Yee & Lawson (2012), once the retained volume inside the tube and the solids concentration stabilize, the process starts to be dominated mainly by consolidation, when small changes of volume of drained water, height of the geotextile tube and dewatering rate (Figure 3, 4, 5 and 6, respectively) take place at a much smaller rate.

The recorded volume of effluent from the geotextile tube over time was used to calculate the variation of dewatering rate with time, as shown in Figure 6. The peaks at 14 and 24 days correspond to the start of the 2nd and 3rd filling stages in test GT-3FS test. It can be noticed that in this test, after the first filling stage, the dewatering rate dropped to nearly zero after 13 days, but this time was smaller in the following steps, showing the drainage capacity of the enveloping geotextile was not compromised during the test duration. For test GT-1FS almost zero drainage was observed after approximately 15 days of testing.

3.2 Pore pressures and total stresses

Figure 7 presents the variation of pore pressure at the base of the tube with time. As expected, maximum pore pressures occur at the start of the filling stage in test GT-1FS and GT-3FS. After filling, the pore pressure transducers (P-01, P-02 and P-03, Figure 2) recorded maximum pore pressure values of 3.45 kPa, 2.52 kPa and 3.12 kPa in test GT-1FS (Figure 7a). Afterwards, a continuous reduction of pore pressure with time can be observed. After 4 weeks of testing, the pore pressures varied between 0 to 0.5 kPa, depending on the pore pressure transducer considered.

Maximum values of a 5.5 kPa, 5.28 kPa and 5.98 kPa in test GT-3FS (Figure 7b) were recorded by the pressure transducers P-01, P-02 and P-03 (Figure 2). During each dewatering stage, the pore pressures gradually decreased. After 4 weeks of testing, the pore pressures varied between 0.26 kPa to 0.46 kPa. Initial larger values of pore pressures recorded after tube filling in test GT-3FS in comparison to those in test GT-1FS are likely to be a consequence of the impact of the jet of the inflow slurry on the pressure transducers at the tube base at the early stages of testing. The direction of this inflow slurry jet could not be efficiently controlled at those testing stages.

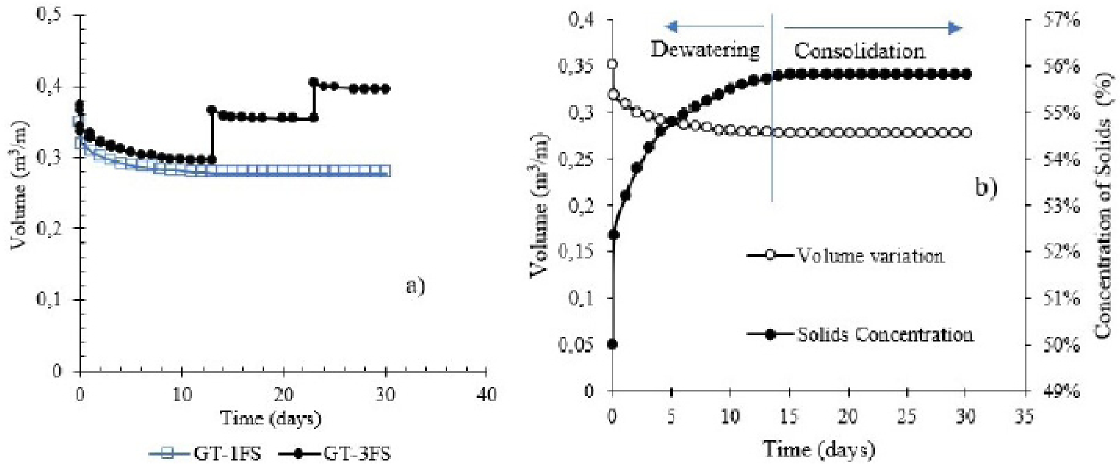

Figure 5. Variation of tube volume and solids concentration with time (a) Volume variation versus time; b) Volume and concentration of solids versus time - GT-1FS.

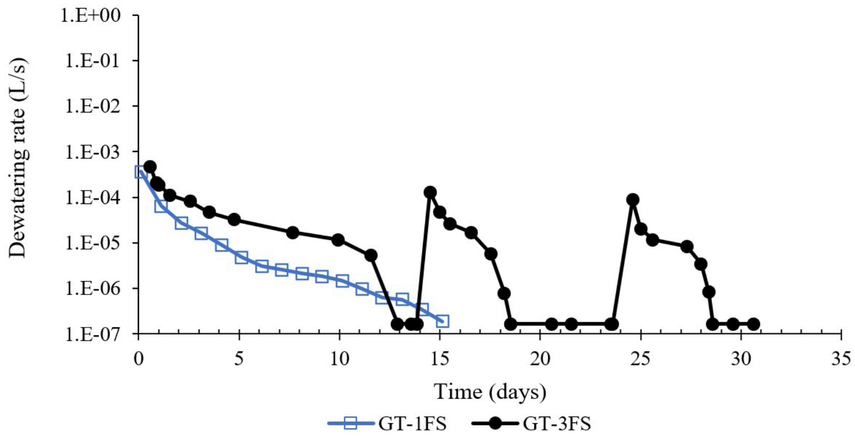

Figure 6. Dewatering rate variation with time.

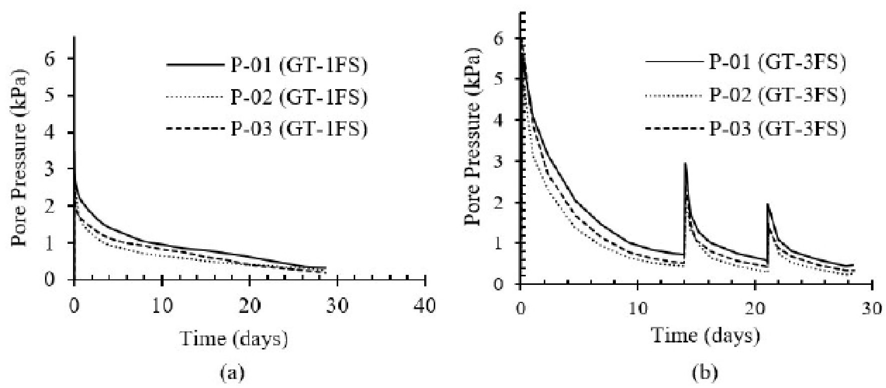

Figure 7. Pore pressure variation with time; a) GT-1FS; b) GT-3SF test.

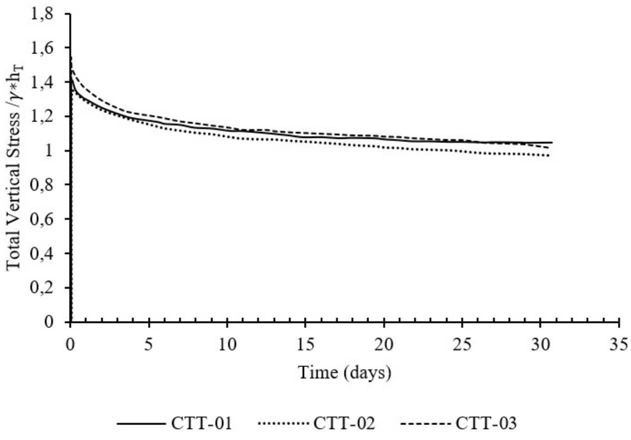

Figure 8. Normalized total pressure at the tube base versus time - test GT-1FS test.

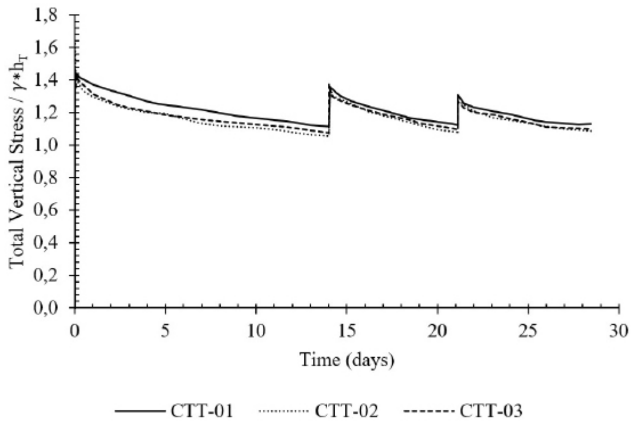

Figure 9. Normalized total pressure at the tube base versus time - GT-3FS.

Figure 8 shows the variation of normalized vertical stress at the tube base with time obtained in test GT-1FS. The total vertical stress at the base was normalized by the product $\gamma.h_T$, where γ is the final unit weight of the soil and h_T is the final tube height. Higher initial vertical stresses are a consequence of the filling process, caused by the impact of the slurry jet on the stress cells. A decrease in normalized total vertical stress due to dewatering can be noted throughout the test until values between 1.05 and 0.97 are reached.

The variation of normalized total vertical stresses at the base of the tube for test GT-3FS is depicted in Figure 9. Similar initial vertical stresses as those observed in test GT-1FS can be noted, followed by reductions with time. In comparison to test GT-1FS, a slight increase in the final vertical stress with the increase in the number of filling stages can be observed due to the slightly greater final soil density at the end of test GT-3FS. In this case, the normalized total vertical stress varied between 1.09 to 1.13 at the end of the last dewatering stage.

3.3 Geotextile strains

Figure 10 shows the variation of geotextile strain along the tube perimeter at the end of tests GT-1FS and GT-3FS, after dewatering stages. The maximum tensile strain was reached at the crown of the tube in both tests decreasing towards the tube base. The strains measured in test GT-3FS were larger than in test GT-1FS along the entire tube perimeter, showing the effect of multiple filling stages on geotextile strain mobilization. As the volume of filling material increased in the tube, so does the geotextile strains.

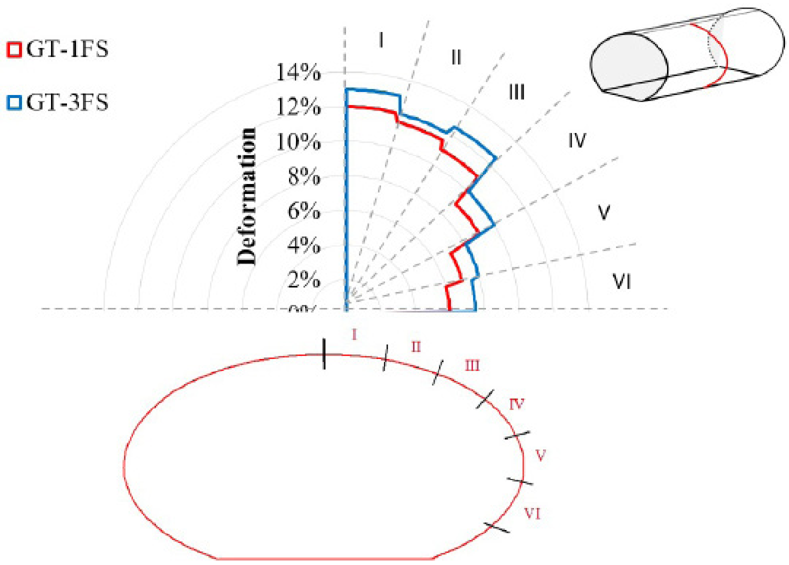

Figure 10. Variation of tensile strain along tube perimeter in tests GT-1FS and GT-3FS.

3.4 Dimensions of the particles that piped through the geotextile.

Figure 11 shows the grain size distribution of the particles (tests without dispersing agent) that piped through the geotextile during the tests, as well as the gradation curve for the particles of the original soil for comparison. This figure shows that the maximum value of the diameter of the particles that piped through the geotextile (taken as d_{95}, which is the particle diameter for which 95% of the remaining particles are smaller) was equal to 0.073 mm in test GT-1FS and 0.093 mm in test GT-3FS, which are values smaller than the filtration opening size of the geotextile (O_{95} = 0.115 mm, Table 2). Thus, the increase in the number of filling stages seems to have caused the piping of coarser material through the geotextile.

It should be pointed out the no flocculating agent was added to the slurry in the current tests and that the geotextile layer is tensioned in this type of application. However, Palmeira et al. (2019) and Palmeira (2020) reported little variation in filtration opening sizes of geotextiles submitted to tension under plane strain conditions.

The total mass of the soil piped through the geotextile was very small, but greater in the case of test GT-3FS (8.51 g against 6.06 g in test GT-1FS). Therefore, despite the small values of piped mass, increasing the number of filling stages resulted in 40.4% increase in piped soil mass. In terms of the total superficial area of the geotextile tube available for particles piping, the values obtained were 3.39 g/m^2 for test GT-3FS and 2.41 g/m^2 for test GT-1FS.

4. Comparisons between predictions and measurements

Predictions of tube volume, tube geometry and geotextile strains were compared to the values measured in the tests. Because the theoretical methods investigated consider a single filling stage in their formulations, emphasis will be given to the comparisons between theoretical predictions and measurements taken in test GT-1FS. In addition, the methods require the knowledge of the pressure (p) employed to fill the tube for the predictions of tube deformations and geotextile tensile forces. In the present study, the average maximum pore pressure measured (3.01 kPa) by the pore pressure transducers during tube filling was adopted in the calculations, since the filling pressure varies during the filling process and the maximum pore pressure value measured would represent more critical filling conditions to the mobilization of strains in the tube.

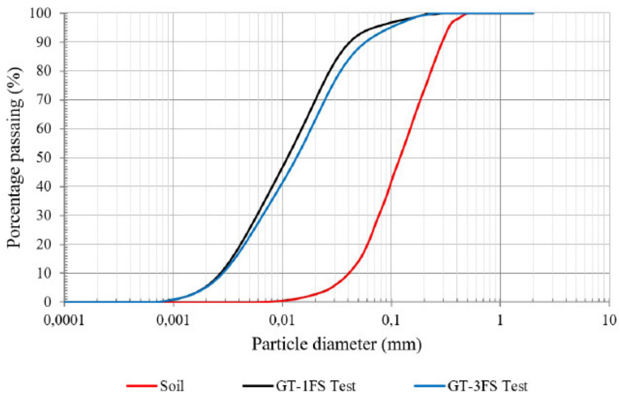

Figure 11. Gradations of the soil particles that piped through the geotextile.

4.1 Tube volume

An empirical relationship which estimates the volume of a geotextile tube as a function of its length, filling height and theoretical diameter was proposed by Yee et al. (2012). According to the authors, satisfactory predictions can be obtained for filling height ratios $h_T/D_T < 0.7$ by the following equation:

$$V_T = L_T D_T^2 \left[\left(\frac{h_T}{D_T} \right)^{0.815} - \left(\frac{h_T}{D_T} \right)^{8.6} \right] \quad (2)$$

Where V_T is the volume of the geotextile tube, L_T is the length of the geotextile tube, h_T is the height of the tube and D_T is the theoretical tube diameter.

The comparison between predicted and measured volume variation with time for test GT-1FS is shown in Figure 12a. Deviations between predicted and measured values can be observed. Equation 2 overpredicted the tube volume by approximately 18% throughout the test. The variation of the geotextile tube volume for test GT-3FS is shown in Figure 12b. In this case, a better agreement between predicted and measured values can be noted, particularly during the last dewatering stage. Up to the 3rd dewatering stage, in average, Equation 2 overpredicted the tube volume by approximately 10% (Figure 12b), but the accuracy of the prediction improved at the end of each dewatering stage.

4.2 Tube geometrical characteristics

The accuracy of available solutions (Guo et al., 2014; Plaut & Suherman, 1998; Lawson, 2008) for the estimate the final shape and dimensions of the tube and the average vertical stress at base were also investigated. Figure 13 shows the comparison between the final cross-section of the tube at the end of the filling stage in test GT-1FS and the prediction by Plaut & Suherman (1998). The method provided an accurate prediction for the tube height (4.5% deviation) and maximum width (5.5% deviation), but underpredicted its tube base width by 20%.

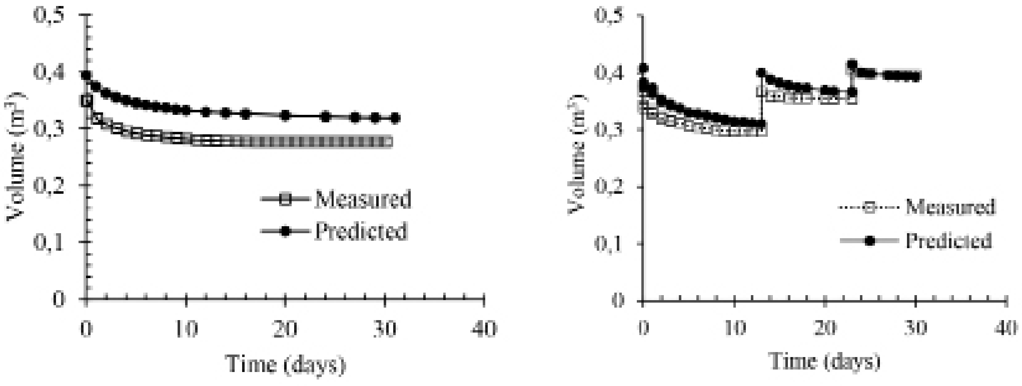

Figure 12. Comparison between predicted and measured volume retained on the geotextile tube (a) Volume variation in test GT-1FS; (b) Volume variation in test GT-3FS.

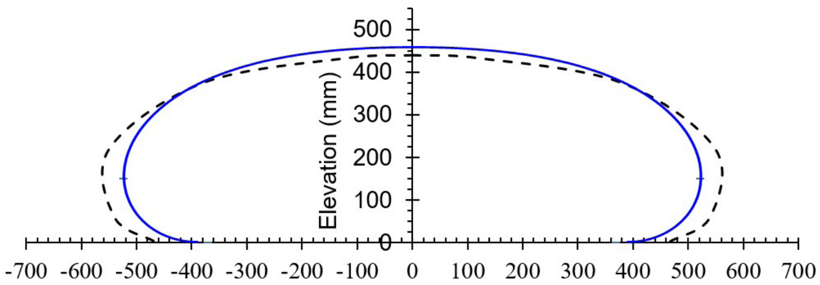

Figure 13. Predicted and measured tube cross-section in test GT-1FS at the end of the filling stage.

Figure 14 presents comparisons between predicted and measured tube height and base width at the end of the filling stage of test GT-1FS. The predictions deviated from the measured values between 4.5% and 29.5%, with the best accuracy being obtained by the predictions by Lawson (2008) and Plaut & Suherman (1998). Guo et al. (2014) over predicted the tube height by 29.5%. All three methods investigated underpredicted the tube base width, with deviations of 13.5% (Lawson), 20.0% (Plaut and Suherman) and 37.3% (Guo et al.).

Comparisons between predicted and measured tube cross-section area, maximum width and the total vertical stress at the base of the tube are depicted in Figure 15. In this figure the vertical stress is normalized by the product of the soil slurry unit weight (13.5 kN/m^3) and the final tube height at the end of the filling stage. The predictions of tube cross-section area deviated from the measurements by 4.7%, 11.6% and 9.3%, for the methods of Guo et al. (2014), Lawson (2008) and Plaut & Suherman (1998), respectively. Regarding predictions of maximum width by Guo et al. (2014), Lawson (2008) and Plaut & Suherman (1998), the deviations from the measured values were 14.5%, 9.1% e 5.5%, respectively.

The predicted values of normalized total vertical stress at the base of the tube compared well with the measurements (Figure 15), with deviations of 2.1% for Lawson (2008) and 2.6% for Plaut & Suherman (1998) methods, respectively.

4.3 Geotextile forces

Table 3 shows maximum and minimum mobilized tensile forces in the tube in tests GT-1FS and GT-3FS. The tensile forces were calculated as the product between the measured tensile strains and the geotextile tensile stiffness (11.5 kN/m, Table 2). Table 3 also presents the predictions of tensile forces by Plaut & Suherman (1998) and Guo et al. (2014) (single filling stage assumed). The mobilized tensile forces in test GT-1FS varied between 0.81 kN/m and 1.49 kN/m after filling (Table 3) depending on the location along the tube perimeter considered. Plaut & Suherman's method predicted a value of 1.26 kN/m for the geotextile tensile force. Thus, the tensile force predicted by that method was closer to the maximum geotextile tensile force measured, but with a deviation of 15.4%. On the other hand, Guo et al. (2014) predicted a tensile force of 1.96 kN/m, which is 31.5% greater than the maximum value measured during the test.

Table 3. Mobilized and predicted geotextile tensile forces at the end of the filling stage and at the end of the test.

Phase	Range	GT-1FS (kN/m)	GT-3FS (kN/m)	Plaut & Suherman (1998) (kN/m)	Guo et al. (2014) (kN/m)
After filling	Maximum	1.49	1.38	1.26	1.96
	Minimum	0.81	0.81		
End of the test	Maximum	1.38	1.49		
	Minimum	0.69	0.86		

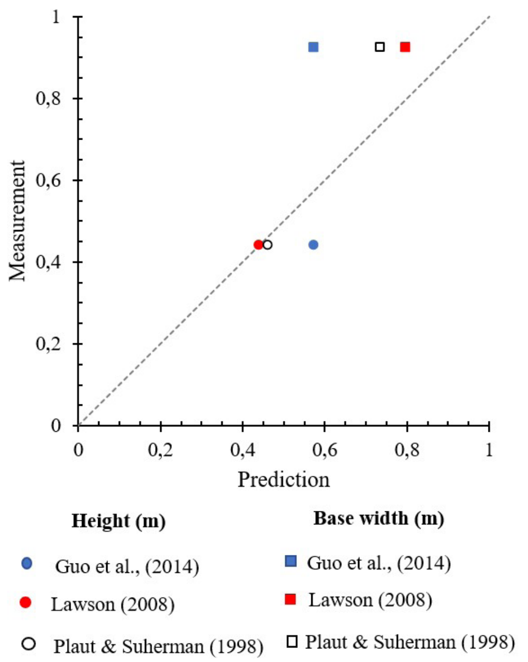

Figure 14. Comparisons between predicted and measured tube dimensions – Test GT-1FS.

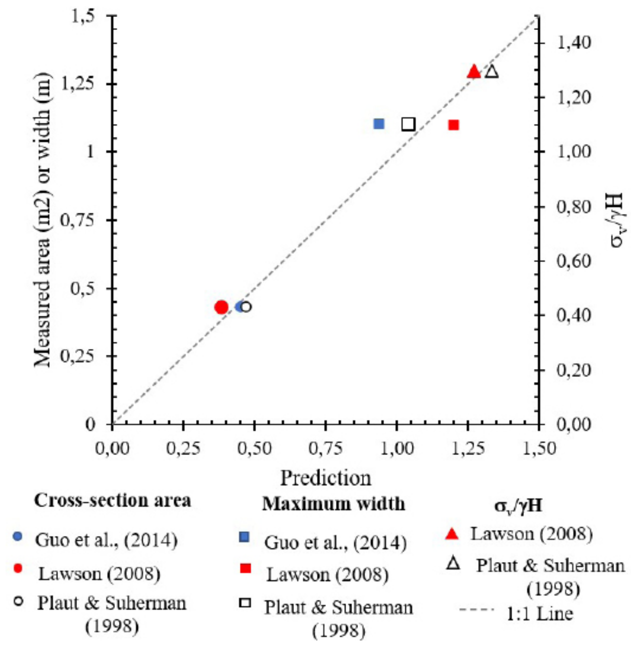

Figure 15. Comparisons between predicted and measured tube dimensions and vertical stresses at the tube base after filling - Test GT-1FS.

5. Conclusions

This work presented an experimental study on the behaviour of geotextile tubes filled with slurry in one and in three filling stages. A large equipment was used to simulate the filling and dewatering stages of the tube and geotechnical instrumentation provided relevant information to understand the tube behaviour. The main conclusions obtained in this study are summarized below.

The use of three filling stages significantly increased the tube final height and volume at the end of the test. Larger geotextile strains were reached in the test with three filling stages, with the maximum strain occurring at the tube crest in both tests. Despite taking much time to fill the tube, the use of multiple filling stages is more efficient regarding final tube height and storage capacity.

The geotextile used was efficient in dewatering the slurry and reducing the pore pressures inside the tube. Particles smaller than the geotextile filtration opening size were capable of piping through the geotextile, but in very small quantities, but larger in size and in quantity in the test with three filling stages.

Regarding comparisons between predictions by methods available in the literature and measurements, deviations ranging from 4.5% to 37.3% between predicted and measured values were observed, depending on the tube parameter and method considered. More accurate predictions were obtained for the tube cross-section area (deviations between 4.7% and 9.3%) and poorer predictions for the tube base width (deviations between 13.5% and 37.3%). Deviations between predicted and measured tube height varied between 4.5% and 29.5%, depending on the method considered. Smaller deviations (2.1% and 2.6%) from the measured values were obtained for the predictions of total vertical stress at the tube base. Deviations of 15.4% and 31.5% were obtained for the predictions of geotextile tensile forces. In general, the relations presented by Lawson (2008) provided the best estimates for the tube behaviour for the conditions of the tests performed.

The results obtained in the study describe herein showed the efficiency of using geotextile tubes for the dewatering of slurries. However, further research in necessary, particularly for the development of methods to predict the behaviour of geotextile tubes subjected to multiple filling stages.

Acknowledgements

The authors would like to thank the following institutions for their help in the research activities described in this paper: The University of Brasília, CNPq- National Council for Scientific and Technological Development, Capes-Brazilian Ministry Education, Federal District Foundation for Research Support-FAPDF and the geosynthetic manufacturer.

Declaration of interest

The authors have no conflicts of interest to declare. All co-authors have observed and affirmed the contents of the paper and there is no financial interest to report.

Authors' contributions

Michael Andrey Vargas Barrantes: conceptualization, visualization, formal analysis, data gathering, data validation & writing. Ennio Marques Palmeira: conceptualization, methodology, visualization, supervision, formal analysis, writing – review & editing. Luis Fernando Martins Ribeiro: conceptualization, supervision, formal analysis, writing – review & editing.

Data availability

All data produced or examined during the current study are included in this article.

List of symbols

h_T	height of the tube (m)
t	time (s)
t_{GT}	geotextile thickness (m)
ASTM	American Society of Testing Materials
CTT	total stress cell
D_n	diameter of the particle for which n% of the remaining particles are smaller (m)
D_T	theoretical tube diameter (m)
J_5	secant tensile stiffness at 5% strain (N/m)
L_T	length of the tube (m)
M_A	geotextile mass per unit area (g/m2)
O_{95}	filtration opening size (m)
P	pore pressure transducer
PET	polyester
S_o	initial concentration of solids (dimensionless)
S_t	concentration of solids (dimensionless)
T_{max}	geotextile tensile strength (N/m)
V_T	volume of the geotextile tube (m3)
Δ_{Vt}	slurry volume reduction (m3)
ε_{max}	maximum geotextile tensile strain (dimensionless)

References

Assinder, P.J., Breytenbach, M., & Wiemers, J. (2016). Utilizing geotextile tubes to extend the life of a Tailings Storage Facility. In: *Proceeding of the First Southern African Geotechnical Conference*, Sun City, South Africa, 5-6 May. Retrieved in October 11, 2022, from https://www.huesker.es/fileadmin/media/Scientific_Revised_Paper/P761_Utilizing_geotextile_tubes_to_extend_the_life_of_a_Tailings_Storage_Facility_.pdf

Bourgès-Gastaud, S., Stoltz, G., Sidjui, F., & Touze-Foltz, N. (2014). Nonwoven geotextiles to filter clayey sludge: an experimental study. *Geotextiles and Geomembranes*, 42(3), 214-223.

Burgos, L.J.F. (2016). *Influência da microestrutura no comportamento mecânico dos solos tropicais naturais e compactados* [Master's dissertation]. Universidade de Brasília.

Cantré, S., & Saathoff, F. (2011). Design parameters for geosynthetic dewatering tubes derived from pressure filtration tests. *Geosynthetics International*, 18(3), 90-103.

Guo, W., Chu, J., Nie, W., & Yan, S. (2014). A simplified method for design of geosynthetic tubes. *Geotextiles and Geomembranes*, 42, 421-427.

Kim, H.J., & Dinoy, P.R. (2021). Two-dimensional consolidation analysis of geotextile tubes filed with fine-grained material. *Geotextiles and Geomembranes*, 49, 1149-1164.

Kim, H.J., Park, T.W., Dinoy, P.R., & Kim, H.S. (2020). Performance and design of modified geotextile tubes during filling and consolidation. *Geosynthetics International*, 28(2), 125-143. http://dx.doi.org/10.1680/jgein.20.00035.

Koerner, G.R., & Koerner, R.M. (2006). Geotextile tube assessment using a hanging bag test. *Geotextiles and Geomembranes*, 24(2), 129-137.

Koh, J. W., Chew, S. H., Chua, K. E., Yim, H. M. A., & Gng, Z. X. (2020). Effect of construction sequence on the performance of geotextile tubes in a containment bund. *International Journal of GEOMATE*, *74*, 1-7.

Lawson, C.R. (2008). Geotextile containment for hydraulic and environmental engineering. *Geosynthetics International*, 15(6), 384-427.

Leshchinsky, D., Leshchinsky, O., Ling, H.I., & Gilbert, P.A. (1996). Geosynthetic tubes for confining pressurized slurry: some design aspects. *Journal of Geotechnical Engineering*, 122(8), 682-690.

Li, Q.Y., Wang, H.D., Ma, G.W., Li, Z.J., Zhou, H.M., & Cui, X. (2016). An experimental study of the mechanical performance of tailings dam geofabriform. *Yantu Lixue*, 37(4), 957-964. [in Chinese]

Liao, K., & Bathia, S. K. (2008). Geotextile tube dewatering: filtration criteria. In *The First Pan American Geosynthetics*

Conference & Exhibition (pp. 506-513). Cancun, Mexico: IFAI.

Maurer, B.W., Gustafson, A.C., Bhatia, S.K., & Palomino, A.M. (2012). Geotextile dewatering of flocculated, fiber reinforced fly-ash slurry. *Fuel*, 97, 411-417.

Moo-Young, H.K., & Tucker, W.R. (2002). Evaluation of vacuum filtration testing for geotextile tubes. *Geotextiles and Geomembranes*, 20, 191-212.

Moo-Young, H.K., Gaffney, D.A., & Mo, X. (2002). Testing procedures to assess the viability of dewatering with geotextile tubes. *Geotextiles and Geomembranes*, 20(5), 289-303.

Muthukumaran, A.E., & Ilamparuthi, K. (2006). Laboratory studies on geotextile filters as used in geotextile tube dewatering. *Geotextiles and Geomembranes*, 24, 210-219.

Newman, P., Hodgson, M., & Rosselot, E. (2004). The disposal of tailings and mine water sludge using geotextile dewatering techniques. *Minerals Engineering*, 17, 115-121.

Palmeira, E.M. (2020). A review on some factors influencing the behavior of nonwoven geotextile filters. *Soil & Rocks*, 43(3), 351-368. http://dx.doi.org/10.28927/SR.433351.

Palmeira, E.M., Melo, D.L.A., & Moraes-Filho, I. (2019). Geotextile filtration opening size under tension and confinement. *Geotextiles and Geomembranes*, 47, 566-576. http://dx.doi.org/10.1016/j.geotexmem.2019.02.004.

Pilarczyk, K.W. (2000). G*eosynthetics and geosystems in hydraulic and coastal engineering* (913 p.). A.A. Balkema Publisher.

Plaut, R. H., & Filz, G. M. (2008). Deformations and tensions in single-layer and stacked geosynthetic tubes. In *The first Pan American Geosynthetics Conference & Exhibition* (pp. 506-513). Cancun, Mexico: IFAI.

Plaut, R.H., & Suherman, S. (1998). Two-dimensional analysis of geosynthetic tubes. *Acta Mechanica*, 129(3-4), 207-218.

Ratnayesuraj, C.R., & Bhatia, S.K. (2018). Testing and analytical modeling of two-dimensional geotextile tube dewatering process. *Geosynthetics International*, 25(2), 132-149.

Satyamurthy, R., & Bhatia, S. K. (2009). Experimental evaluation of geotextile dewatering performance. In *Geosynthetics 2009* (pp. 464-473). pp. 506-513.

Wilke, M., & Cantré, S. (2016). Harbor Maintenance dredging operations-Residual characteristics after treatment by means of geosynthetic dewatering tubes. In *3rd Pan-American conference on geosynthetics, GeoAmericas* (pp. 506-513). Retrieved in October 11, 2022, from https://www.researchgate.net/publication/306916492_Harbour_maintenance_dredging_-_Residual_characteristics_after_treatment_by_means_of_geosynthetic_dewatering_tubes/link/58d12769458515520d581131/download

Wilke, M., Breytenbach, M., Reunanen, J., & Hilla, V. M. (2015). Efficient and environmentally sustainable tailings treatment and storage by geosynthetic dewatering tubes: working principles and Talvivaara case study. In *Proceedings Tailings and Mine Waste* (pp. 506-513). Retrieved in October 11, 2022, from https://open.library.ubc.ca/media/stream/pdf/59368/1.0314229/5.

Yan, S. W., & Chu, J. (2010). Construction of an offshore dike using slurry filled geotextile mats. *Geotextiles and Geomembranes*, *28*, 422-432.

Yang, Y., Wei, Z., Cao, G., Yang, Y., Wang, H., & Zhuang, S. (2019). A case study on utilizing geotextile tubes for tailings dams construction in China. *Geotextiles and Geomembranes*, *47*, 187-192.

Yee, T.W., & Lawson, C.R. (2012). Modelling the geotextile tube dewatering process. *Geosynthetics International*, 19(5), 339-353.

Yee, T.W., Lawson, C.R., Wang, Z.Y., Ding, L., & Liu, Y. (2012). Geotextile tube dewatering of contaminated sediments. Tianjin Eco-City, China. *Geotextiles and Geomembranes*, 31, 39-50.

Zhang, H., Wang, W., Liu, S., Chu, J., Sun, H., Geng, X., & Cai, Y. (2022). Consolidation of sludge dewatering in geotextile tubes under combined fill and vacuum preloading. *Journal of Geotechnical and Geoenvironmental Engineering*, *148*(6), 04022032.

Soils and Rocks

An International Journal of Geotechnical and Geoenvironmental Engineering

www.soilsandrocks.com

ISSN 1980-9743
ISSN-e 2675-5475

Influence of intrinsic variability in anthropic slopes

Cristhian Mendoza[1#], Catalina Lozada[2,3]

Article

Keywords
Anthropic slopes
Monte Carlo simulations
Strength reduction method
Variability of geotechnical parameters

Abstract

Anthropic slopes are common in constructing embankments and earth dams and forming open pit mines and fills, among others. However, these slopes artificially built sometimes could fail due to the variability of the soils, lack of expertise in determining the design parameters, and lack of knowledge of the soil's true behavior and construction methods, among others. To address these problems, physical models were made in a geotechnical centrifuge with similar characteristics to study the effect of variability. Subsequently, Monte Carlo simulations were performed using finite element models (FEM) with random geotechnical parameters for an elastic model with Mohr-Coulomb failure criteria. From these simulations, the influence of geotechnical parameters on the factor of safety and deformations was observed. The results show that the coefficient of variation obtained for the factor of safety was less than the coefficient of variation of the geotechnical parameters taken into account. This means that the coefficient of variation of the factor of safety is not the sum or the average of the coefficients of variation taken in the analysis. However, when the factor of safety is more or less constant, but the coefficient of variation of the parameters increases, the probability of failure may increase. This shows that a slope with a factor of safety greater than one can have a high probability of failure. In addition, low friction angle and low cohesion values tend to present more significant slope crest displacements.

1. Introduction

The construction of artificial slopes is a common practice in practical geotechnics. Some examples of uses are in the construction of embankments, earth dams for mining, earth dams, formation of open pit mines, among others. However, these artificially formed slopes sometimes fail. This could be explained by the intrinsic variability of the soils, lack of expertise in determining the design parameters, lack of knowledge of the true behavior of the soil, inadequate design and construction methods, among others. The research presented here studies the influence of the variation of geotechnical parameters on the behavior of the factor of safety (*FS*) on slopes, trying to understand the possible reasons why one slope fails and another does not, if they were both built using similar materials and following the same construction method.

Studies that have contributed to a better understanding of the variability and sensitivity of the probability of failure for a factor of safety are presented by Lacasse & Nadim (2007), Phoon & Kulhawy (1999) and Tan et al. (2003) . Additionally, Phoon et al. (2006) have experimentally shown that performing many tests can reduce the standard deviation, while Gong et al. (2017) have shown that numerical techniques can optimize site investigation and reduce exploration costs to obtain optimal characterizations.

The effect of variability on slopes has become vitally important in recent years (Jiang et al., 2022). The Strength Reduction Method has been commonly implemented in slope stability and is often preferred over the Limit Equilibrium Methods because assumptions regarding inter-slice forces are not required (Dyson & Tolooiyan, 2019). Zienkiewicz et al. (1975) developed one of the first methods of the Strength Reduction Method (SRM), with a reduction of the shear parameters (cohesion and friction angle). So, slope failure occurs when elements with applied shear stresses exceed the material shear strength, causing excessive distortion. Dyson & Tolooiyan (2018) compared different techniques from Strength Reduction, which showed advantages or disadvantages for different proposals in the literature. Regarding variability geotechnical in slopes, Chok et al. (2015) applied the Local Averaging Subdivision (LAS) technique to incorporate spatial correlation in slope stability. This technique generates random field parameters such as soil weight, elastic modulus, friction angle, cohesion, etc. Dyson & Tolooiyan (2019) conducted a probabilistic slope stability analysis using the Random Finite Element Method (RFEM) combined with processes to determine the level of

[#] Corresponding author. E-mail address: cmendozab@unal.edu.co
[1] Universidad Nacional de Colombia Sede Manizales, Departamento de Ingenierá Civil, Manizales, Colombia.
[2] Pontificia Universidad Javeriana, Departamento de Ingenierá Civil, Bogotá, Colombia.
[3] Escuela Colombiana de Ingeniería Julio Garavito, Departamento de Ingeniería Civil y Ambiental, Bogotá, Colombia.

Submitted on February 9, 2023; Final Acceptance on June 5, 2023; Discussion open until November 30, 2023.
https://doi.org/10.28927/SR.2023.001123

similarity between random fields. The study showed the factor of safety's convergence with less finite element simulation when using the Monte Carlo Method.

The above characteristics create the need to better understand the influence of variability on the factor of safety and the contribution of each geotechnical parameter. This problem is addressed by generating physical models with similar characteristics in a geotechnical centrifuge. This was done starting with a slope with an unstable geometry. Subsequently, Monte Carlo simulations were performed using finite element models (FEM) to introduce the influence of the variability of geotechnical parameters on the factor of safety. This variability was introduced by means of random number generation of the geotechnical parameters. Parameters were generated using two different techniques. The first is when the parameters are not correlated because a parameter should not depend on any variable (Cividini et al., 1983; Lei et al., 2017). With this, it was verified that the calculated factor of safety could capture the behavior of the performed physical models. The second, begins with a slope with an *FS* greater than one, and random numbers are generated when the parameters are correlated because they come from the same test. So, variations in a laboratory test can cause variations in all parameters, for example, the influence of measurement in the test, variations between procedures for the same test, human procedural errors, among others. In both cases, the effect of the intrinsic and epistemic variability of the geotechnical parameters is clear. Finally, the influence of the variability in the deformations was observed, which is a primary variable in the analysis of slope stability. All of the above was performed using an elastoplastic constitutive model with a Mohr Coulomb failure criterion.

The results show that the shear parameters are the most important with the constitutive model used for the FS. The coefficient of variation obtained for the FS was around 20%, this value being lower than the average of the COVs (around 32%) of the parameters, which means the coefficient of variation of the FS is not the sum or average of the COVs of the variables taken into account for the analysis. However, when the factor of safety is close to constant, but the coefficient of variation of the parameters is increased, the probability of failure may increase. In addition, low friction angle and low cohesion values tend to present greater displacements. Thus, better performed shear tests lead to a low standard deviation and a lower probability of failure.

2. Materials and methods

The purpose of this study is to determine the effect of variability on artificial slopes. In a first step, physical models were constructed in the geotechnical centrifuge depicted in Figure 1. This centrifuge is a beam type centrifuge with a ratio to the platform of 610 mm and a maximum acceleration of 200 times the Earth's gravity, supporting a maximum load of 12 kg. Physical models were performed with the centrifuge at one hundred times the Earth's gravity (N = 100) for 6 minutes. The failure zones were obtained for each model, analyzing the images before and after the test in the centrifuge. The magnitude of resultant displacements for the models was obtained using the software GeoPIV_RG (White & Take, 2002; Stanier et al., 2016). Then, numerical models in FEM were performed to compute the factor of safety, the position of the failure surface, and resultant displacements. The failure surface depth and resulting displacements as found in physical and numerical models were compared.

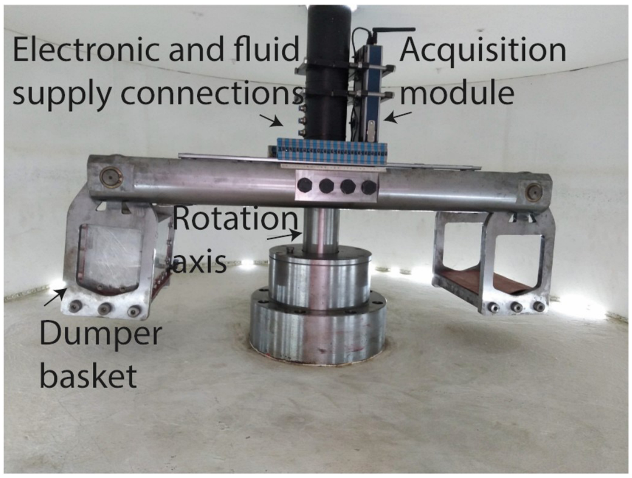

Figure 1. Geotechnical centrifuge at Escuela Colombiana de Ingeniería Julio Garavito.

2.1 Soil properties

Kaolinite clay, prepared using a slurry state with a water content of 1.5 times the liquid limit, was the soil used in the physical model in the geotechnical centrifuge. Then, oedometric consolidation was performed by doubling the applied load until reaching 30 kPa in the automatic consolidation apparatus shown in Figure 2a. As shown in Figure 2b, a sand layer was added at the bottom of the model to obtain double path drainage to accelerate consolidation. Two models were prepared and consolidated identically to obtain the unitary weight in the nearest soil. The characterization tests, consolidated undrained triaxial tests, and oedometric tests were performed to obtain the main parameters and characteristics of the soil. The results of the tests were: classification by the USCS as a high plasticity silt MH, Liquidity limit of 73.34%, Plasticity limit of 45.48%, Shrinkage limit of 33.28%, Specific Gravity of 2.61, Effective cohesion of 5.5 kPa, Effective friction angle of 24 °, Saturated hydraulic conductivity of 1.7 × 10-5 m/s (from the consolidation curve), and Unitary weight of 14.6 kN/m^3.

2.2 Physical models

Two physical models were tested in the geotechnical centrifuge at an acceleration of one hundred times gravity.

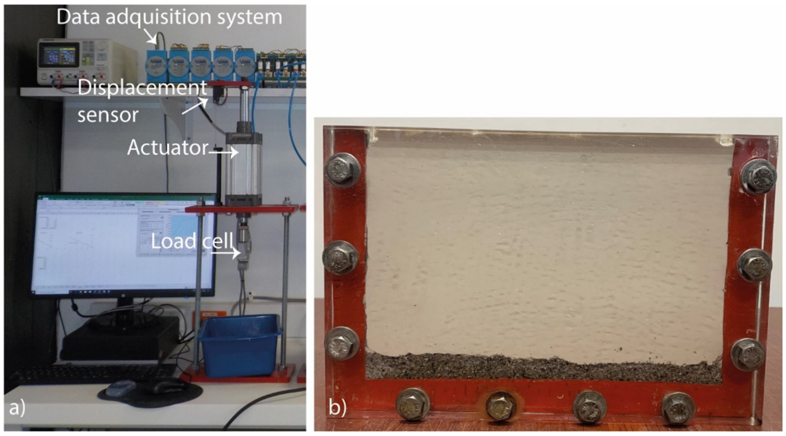

Figure 2. (a) Oedometric consolidometer apparatus for centrifuge models, (b) consolidated soil sample.

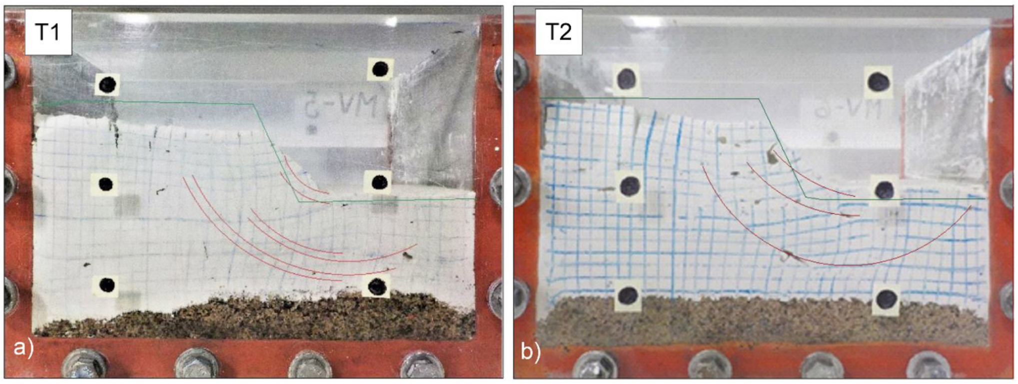

Figure 3. Physical models of slope stability: (a) test T1, (b) test T2.

The models were fabricated with a slope of 67 ° and a height of 3.5 m for the prototype scale. This geometry was obtained by cutting the slope with a wire before the test in the centrifuge (see Figure 2b). The simulated time of the test in the centrifuge for the prototype scale is 42 days. The scaling laws for the centrifuge models at 100 times gravity (N = 100) are shown in Table 1, and the physical models are shown in Figure 3. Multiple sliding surfaces are developed in these models based on Figure 3. In both models, it is observed that the sliding mechanism begins at the toe of the slide, followed by deep sliding failures. An important observation consisted in the differences in the behavior in the displacements for the two models. So, the two models were built in similar conditions, but they presented different failure surfaces. Some of the reasons for these differences include, for example, epistemic variability in the construction of the physical model in consolidation, soil preparation, and soil sample manipulation. These reasons can be extrapolated to the real condition in the field in the construction of artificial slopes.

Table 1. Relevant scaling factors for centrifuge models.

Parameter	Scaling factor	Prototype scale	Model scale
Length H	1/N	7.5 m	7.5 cm
Length B	1/N	4 m	4 cm
Length L	1/N	16 m	16 cm
Time (consolidation)	$1/N^2$	42 days	6 min

3. Implementation of the strength reduction method with randomness

3.1 Constitutive model

The constitutive model used in the present research was elastic with yield criterion of Mohr–Coulomb. The criterion is shown in Equation 1, where the criterion is a function of τ (the shear stress of the soil), c (the cohesion of the soil),

σ_n (the normal stress), and ϕ (the friction angle of the soil). So, Equation 1 shows the increase of shear strength as normal stress increases (or the influence of hydrostatic stress), as shown in Figure 4. In addition, the relationship between stress and strain tensors depends on an elastoplastic tensor (or elastoplastic modulus). This elastoplastic tensor is divided into two-parts. The first part has elastic behavior with the elasticity modulus E and Poisson's ratio μ. The second part works when stress paths reach the yielding criterion in the function of the shearing parameters (c and ϕ).

$$\tau = c + \sigma_n \tan\phi \tag{1}$$

3.2 Strength reduction method (SRM)

To understand slope stability by finite element methods (FEM), the strength reduction finite element method (SRFEM) was implemented in Abaqus 6.21. SRFEM methods have been widely accepted among geotechnical engineers (Dyson & Tolooiyan, 2018). Some advantages of the SRFEM method are that there are no assumptions about the location or shape of the failure surface, similar to the interpretation of the limit state, no assumptions of inter-slice forces, can simulate soils heterogeneously, and show slope displacements. The SRFEM method was presented by Zienkiewicz et al. (1975). Since this work, many other researchers have used the SRFEM method for slope stability, for example, Ugai (1989), Matsui & San (1992), Ugai & Leshchinsky (1995), Dawson et al. (1999), Griffiths & Lane (1999), Yang et al. (2012), Dyson & Tolooiyan (2018), Seyed-Kolbadi et al. (2019) and others. The method consists of adjusting the strength parameters until the slope is unstable. A factor realizes this adjustment, and this factor is the slope factor of safety, as shown below:

$$c = \frac{C_0}{FS} \tag{2}$$

$$\phi = \tan^{-1}\frac{\tan\phi_0}{FS} \tag{3}$$

where c_0 and ϕ_0 are the original cohesion and friction angle provided by soil, and FS is the strength reduction factor to maintain equilibrium. The final strength reduction factor can be obtained in different ways in the function of the definition of slope failure. For example, Dyson & Tolooiyan (2018) showed three criteria. First is the development of plastic zones from the toe to the head of slope. Second is the development of large deformation (defined by the user) in the function of tolerable nodal displacement. The third is the solution non-convergence, often symptomatic of a failure in FEM slope subsidence simulations. Cse (2021) and Tschuchnigg et al. (2015) showed that the successful application of SRM is the criterion for detecting global instability. In general, non-convergence is taken as a criterion for detecting global instability. However, the presence of complicated loads and geometries can prematurely terminate a finite element analysis for nonlinear finite element models. So, non-convergence may not be a suitable criterion for detecting global instability due to numerical or local instabilities.

SRM is not built into the Abaqus program (Dyson & Tolooiyan, 2018). This research used a rule based on the total model plastic dissipated energy ratio to the total model internal strain energy. If this ratio is more significant than 0.2, the model is considered globally unstable. This implementation of SRM is based on the proposal by Cse (2021). It also incorporates the effect of geotechnical variability of parameters for the Monte Carlo method. The automatic calculus of the variability effect into FS slope stability is shown below:

First, it produced an FEM slope model, as shown in Section 3.3.

Second, random parameters were included in FEM simulations, as shown in Section 3.4.

Third, it assumed an interval corresponding from FS stable to FS unstable. Then, iterations were run with reduced cohesion and friction angle to intervals for FS, where FS was the mean value between FS stable and FS unstable. FEM models with reduction parameters were run with a Python script for Abaqus.

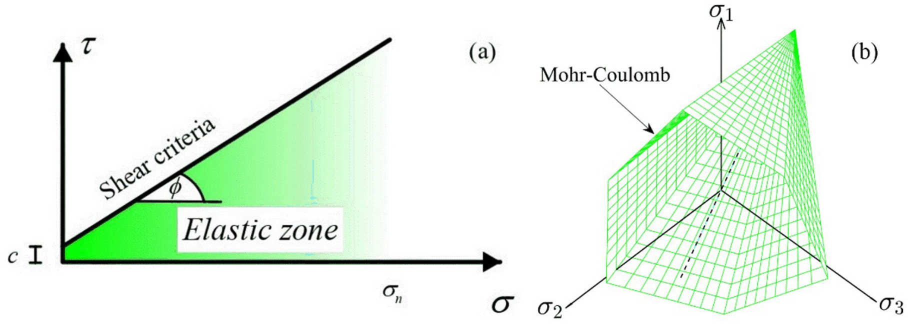

Figure 4. Scheme of the shear criteria to Mohr-Coulomb: (a) *p-q* plane, (b) π-plane [adapted from Helwany (2007)].

Fourth, the global instability criterion was checked. This criterion was a rule based on the ratio of the total plastic dissipated energy of the model to the total internal strain energy of the model, as explained above. It is clear that there are many other criteria to carry out this implementation, including those shown by Tschuchnigg et al. (2015), Dyson & Tolooiyan (2018) and Seyed-Kolbadi et al. (2019).

Fifth, the interval of unstable and stable factor of safety is reduced.

Sixth, the process is performed iteratively until the difference between the unstable and stable factor of safety is less than a specified tolerance ($\Delta FS = 0.01$).

Seventh, the factor of safety obtained from the Monte Carlo simulations are saved in an external file.

On the other hand, implementing the Mohr-Coulomb criterion into the Abaqus program gives rise to the dilation angle, which was not used in this study. The value taken was 0.1.

3.3 FEM models

The ABAQUS version 6.21 was used to generate the finite element model (FEM) of a slope. A two-dimensional model was constructed with plane strain because it presents a good approximation when inside a thick component loaded only in one plane or when an object is constrained in one direction by rigid walls. Thus, the equations only allow the solution in a plane, and the out-of-plane strains are set to zero (Desai & Siriwardane, 1984). Therefore, the plane strain approximation is an excellent approximation to some slopes and centrifuge models, such as those presented in this paper. An FEM model was developed to obtain the factor of safety *FS* and a displacement analyses in the time. The parameterization of the FEM model geometry was a function of the physical model in the centrifuge. The geometry is shown in Figure 3. CPE4P elements were used in the model (plane strain quadrilaterals, two dimensions, four nodes with pore pressure measurement). In addition, the elements concerted near the slope are small in size for a better response as soon as stresses and strains appear. An FEM model was considered saturated and the water table was placed on the ground.

There are two boundary conditions. The first is a fixed condition at the base of the FEM model. This fixed condition does not allow displacements in the x and y directions (See Figure 5). The second involves the lateral rollers in the side edges of the model. This condition does not allow displacements in the x-direction.

Once the geometry of the FEM model is configured, two analyses are performed. The geostatic stresses are induced by the introduction of gravity forces within the FEM model and strength reduction is conducted for *FS*. Another analysis was induced by gravity forces and a simulation of 42 days with consolidation analysis in FEM.

3.4 Create and include random numbers in FEM simulations

To better understand the behavior of artificial slopes, the effect of the variability of the geomechanical properties of the soil was incorporated into the analyses conducted.

This was done through random finite-element analysis using the well-known Monte Carlo method and an elastic model with the yield criterion of Mohr-Coulomb. Random numbers were generated with the statistical parameters shown in Table 2. Mean values of Table 2 were obtained from tests shown in Section 2.1. Statistical values were typical values for fine soils reported by researchers such as Kirby (1991); Phoon & Kulhawy (1999); Griffiths et al. (2005); Papaioannou & Straub (2012); Llano-Serna et al. (2018) and Zevgolis et al. (2018). The influence of variability on soil properties has been published in the past by Lua & Sues (1996); Lump (1970); El-Kadi & Williams (2000); Griffiths & Fenton (2001); Ching et al. (2012); Cai et al. (2017); Al-Bittar et al. (2018); Bolaños & Hurtado (2022), among others. These researchers used normal distributions, lognormal distributions, Monte Carlo analysis, random fields, and other techniques. Thus, the present paper used lognormal distributions to generate each geotechnical parameter for the constitutive model used. Lognormal distributions are

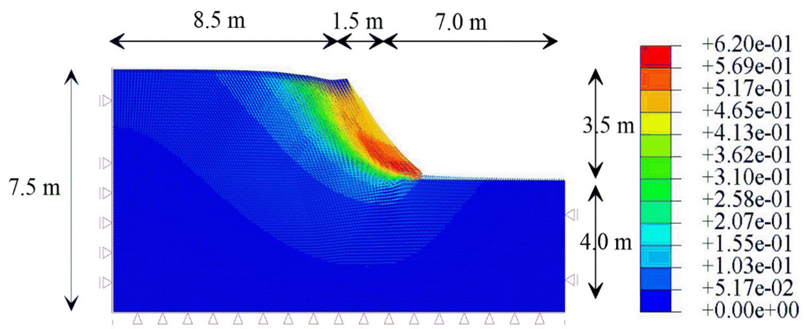

Figure 5. Example of an FEM model for boundary conditions and displacement results in the failure condition.

Table 2. Initial statistical parameters.

Parameter	*E*	μ	*c*	ϕ
Unit.	kPa	-	kPa	°
Mean	7500	0.34	5.5	24
Coefficient of variation	0.5	0.15	0.35	0.3
Standard deviation	3750	0.051	1.75	6.9

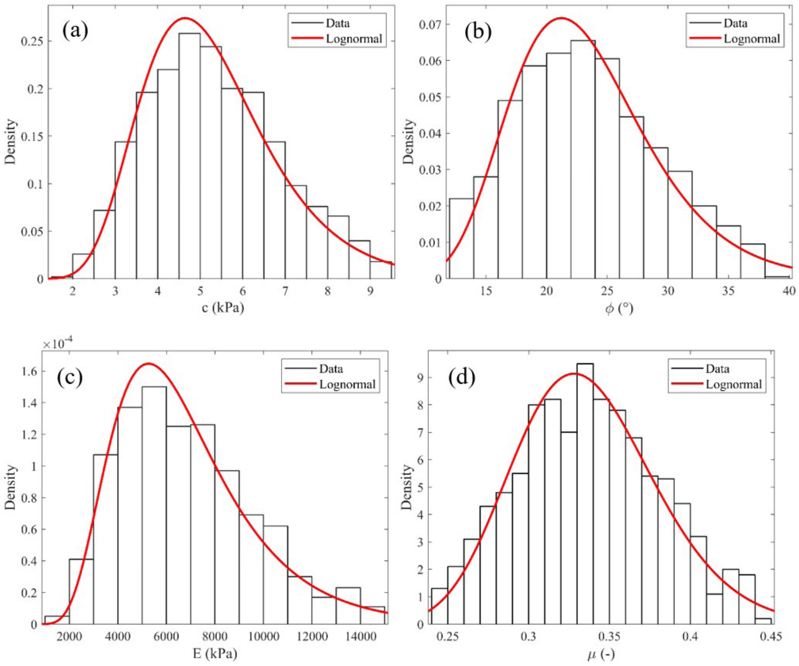

Figure 6. Frequency diagrams and probability distribution function of input variables selected: (a) cohesion, (b) friction angle, (c) elasticity modulus, (d) Poisson's ratio.

well adapted for major geotechnical parameters (Griffiths & Fenton, 2001; Baecher & Christian, 2003).

One thousand random numbers were generated for each geotechnical parameter of the Mohr Coulomb model following a lognormal distribution (see Figure 6). These random parameters were incorporated into the FEM model. The integration was performed by a subroutine in Python and automatically processed because the Abaqus program interacts with Python Script. Subsequently, Monte Carlo simulations were made with geotechnical parameters within an FEM model. This number was used because it stabilized the mean and the standard deviation of *FS*. Then, with the implementation of *FS* shown in Section 3.2, the value of *FS* was obtained for each parameter set used, as shown below in Section 4. Another analysis was the influence of time in displacement for 42 days with transient consolidation. Two analyses were conducted with the same parameter set. Finally, important output variables of the problem FS and displacements were saved in external files. The analyzes in the following sections were based on these external files.

4. Results and discussion

4.1 Displacements fields using PIV

The displacement vectors and the resultant displacements of the physical models were obtained using the Particle Image Velocimetry technique PIV using the GeoPIV_RG software (Stanier et al., 2016). These analyses were performed by comparing two images, the first before the test in the centrifuge and the second after the test in the centrifuge, simulating 42 days for the prototype scale. Figure 7a and 7b show the displacement vectors obtained for all models. This is confirmed when quantifying the displacements obtained in the physical models. The resultant displacements were computed and are shown in Figure 7c and 7d. large displacements were obtained in models with an evident failure mechanism in the slope's body. Indicating lower deformations at greater depths and shifting back movements to the crown of the slope.

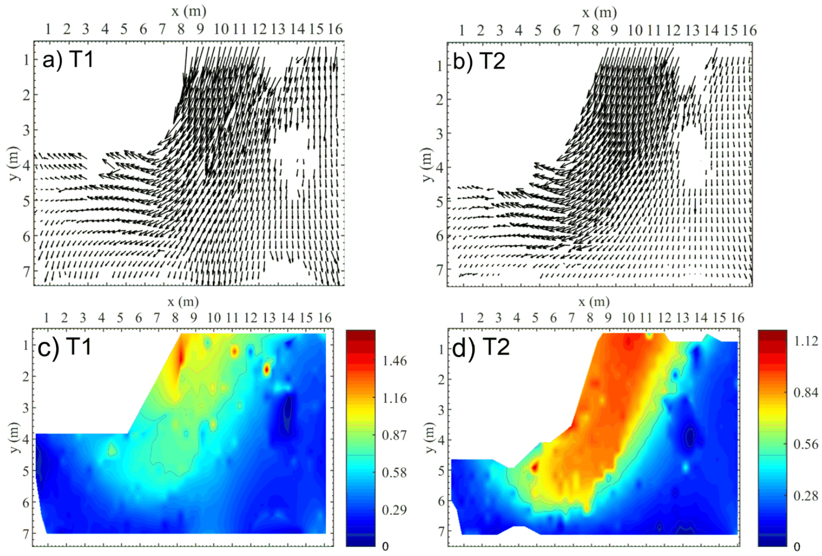

Figure 7. (a) Displacement vectors obtained with GeoPIV_RG of model number one, (b) displacement vectors obtained with GeoPIV_RG of model number two, (c) displacement resultants obtained with GeoPIV_RG of model number one, (d) displacement resultants obtained with GeoPIV_RG of model number two [adapted from Lozada et al. (2022)].

4.2 Main results from random FEM analyses

4.2.1 FS analysis in FEM

The first step was to validate the implementation of the SRM (see Section 3.2). Validation was conducted to compare the implementation of SRM in this study and its implementation in the Plaxis program. The same slope geometry of the physical model (see Section 3.3) was then transferred to Abaqus and Plaxis. However, the initial conditions were changed so that the water table was moved 3 meters below the crest of the slope. The variation of the initial condition was to start with $FS > 1$ because Plaxis does not run to $FS < 1$. It's clear that $FS < 1$ isn't valid (impossible). However, the initial physical model was started from an instability condition (see Figure 2). FS obtained with the implementation of this paper was 1.237 and with Plaxis was 1.221, then the difference between the two was 0.016.

The simulation number for the stabilization of the mean and standard deviation was found based on the validation of the SRM and using the same method proposed by Haldar & Babu (2008), Al-Bittar et al. (2018) and Mendoza & Hurtado (2022) with close to 700 Monte Carlo simulations. The histogram of FS and distributions of cumulative probability of FS were obtained from 1000 simulations, as shown in Figure 8. The statistical values of FS give a mean value of 0.796, a standard deviation of 0.174, and a coefficient of variation of 0.218. In the elastoplastic model with the Mohr-Coulomb rupture criterion, four parameters were varied (E, c, φ, ν) with the coefficient of variations of 0.15 to 0.5 (see Table 2). However, the coefficient of variation of all simulations was 0.218. This value is between the range of COV used. The mean value is less than one, so the results coincide with the experimental tests shown in Figure 2. where the slope used was unstable for this geometric.

All the parameters of the model with the Mohr-Coulomb rupture criterion were varied, E, c, φ, ν with the coefficient of variations from Table 2. So, 700 simulations were conducted, varying each parameter of the model used. This variation was made to show the importance of each parameter in the FS. The important parameters in *FS* are shown in Figure 9 and compared with variations of all parameters. Figure 9 shows that important parameters for *FS* are cohesion and friction angle. The other two parameters ν and E don't change the *FS* value. Table 3 shows the statistical parameters of *FS* with the variation of cohesion, friction angle, and all parameters, where mean values are similar for cohesion and friction angle. However, COV was lower for cohesion.

The important parameters are from rupture criterion (c and ϕ) for *FS*. However, these parameters are statistically correlated because they are from the same test. Nevertheless, this study assumes that the parameters cannot be correlated with other parameters or relations because one of the study's goals was to observe the influence of each parameter on FS for slopes. This assumption was made based on Cividini et al. (1983) and Lei et al. (2017) where the parameter definition is a relation (i.e., a model) that describes a certain physical situation using constants. These constants (or parameters) are often introduced to represent the inherent properties of materials. It is clear that there may be a statistical relationship in parameters, but it was not considered in this paper. Some recently published papers about the dependent parameters are by Brinkgreve (2005) and Bolaños & Hurtado (2022).

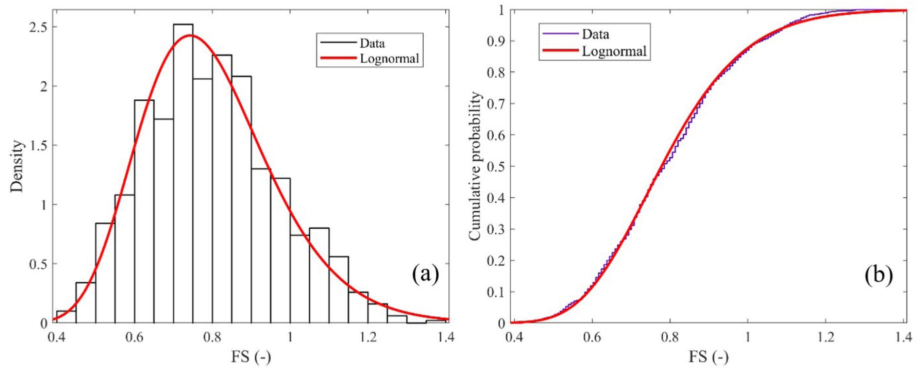

Figure 8. (a) Density curve and histogram of *FS* in the FEM models, (b) distributions of cumulative probability of *FS* in the FEM models.

Table 3. Statistical parameters of *FS* with the variation of cohesion, friction angle, and all parameters.

Parameter	Mean	Standard deviation	Coefficient of variation
c	0.832	0.090	0.108
ϕ	0.840	0.130	0.155
All	0.791	0.166	0.210

Table 4. Statistical parameters of *FS* for each of the combinations from the simulations.

Type	Mean	Standard deviation	Probability of failure (%)
$10\,c + 10\,\phi$	1.230	0.084	0.3148
$20\,c + 20\,\phi$	1.192	0.151	10.0668
$30\,c + 30\,\phi$	1.147	0.202	23.3812
$10\,c + 20\,\phi$	1.209	0.122	4.3224
$10\,c + 30\,\phi$	1.182	0.162	13.0931
$20\,c + 10\,\phi$	1.216	0.123	4.0399
$20\,c + 30\,\phi$	1.168	0.179	17.2956
$30\,c + 10\,\phi$	1.189	0.159	11.8157
$30\,c + 20\,\phi$	1.170	0.146	12.2101

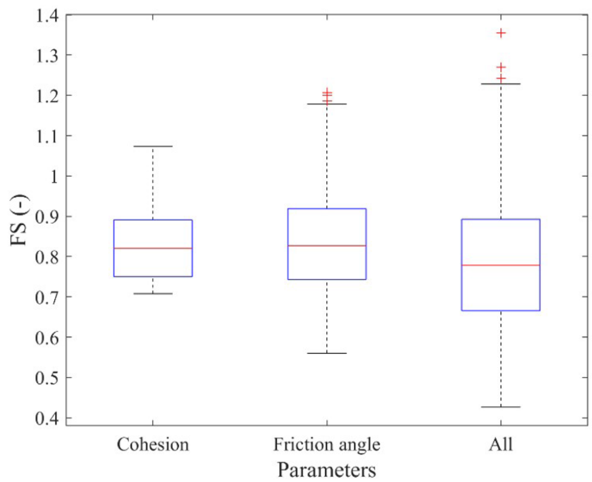

Figure 9. Box-and-whisker plots to *FS* with cohesion, friction angle, and all parameters.

Figure 9 highlights that cohesion and friction angle are important parameters. In addition, the simulations shown in Figure 8 stabilize a mean and a standard deviation of the *FS* near 500 simulations. The cohesion was changed to 11.0 kPa for an FS near 1.2. Then, 500 random numbers were created for cohesion and friction angle parameters. These parameters were built with a COV of 10%, 20%, and 30% to see the influence of the parameters on FS and the probability of failure P_f. Subsequently, the parameters generated with different COVs were combined as follows: 10% cohesion and 10% friction angle, 20% cohesion and 20% friction angle, 30% cohesion and 30% friction angle, 10% cohesion and 20% friction angle, 10% cohesion and 30% friction angle, 20% cohesion and 10% friction angle, 20% cohesion and 30% friction angle, 30% cohesion and 10% friction angle, 30% cohesion and 20% friction angle. In total, 4500 simulations were made. Table 4 shows the main results of the simulations (μ, σ, and P_f).

Figure 10 shows the analysis histograms with equal COVs of 30%, 20%, and 10%. In addition, the curves of a normal distribution are placed. This figure showed that low COVs lead to low standard deviations and almost constant values of *FS*. Then, good characterization tests with calibrated equipment, standardized procedures, and the same measurement systems should lead to low COVs. Also, a standardized construction process is an important factor in reducing standard deviation. These processes lead to a lower probability of failure, as shown in Table 4.

The results from Table 4 are plotted in Figure 11, which shows that the *FS* changes little with the change of the COV. Standard deviation increases as COV increases and mainly with the increase of the COV of cohesion. Thus, a slope with

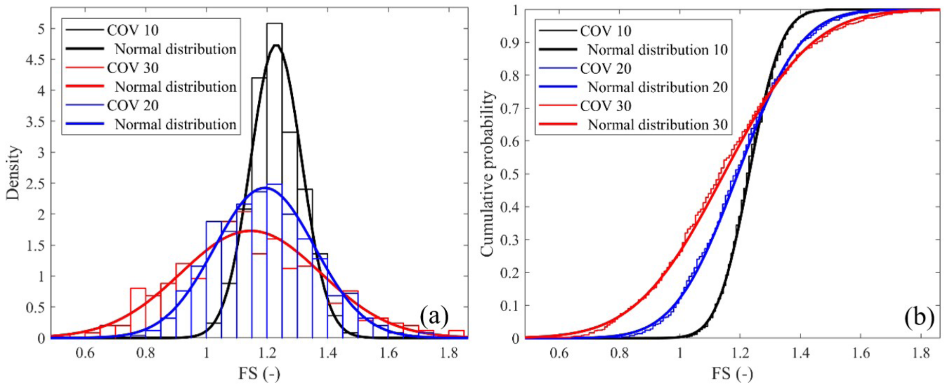

Figure 10. (a) Density curve and histogram of FS for different COVs, (b) distributions of cumulative probability of FS for different COVs.

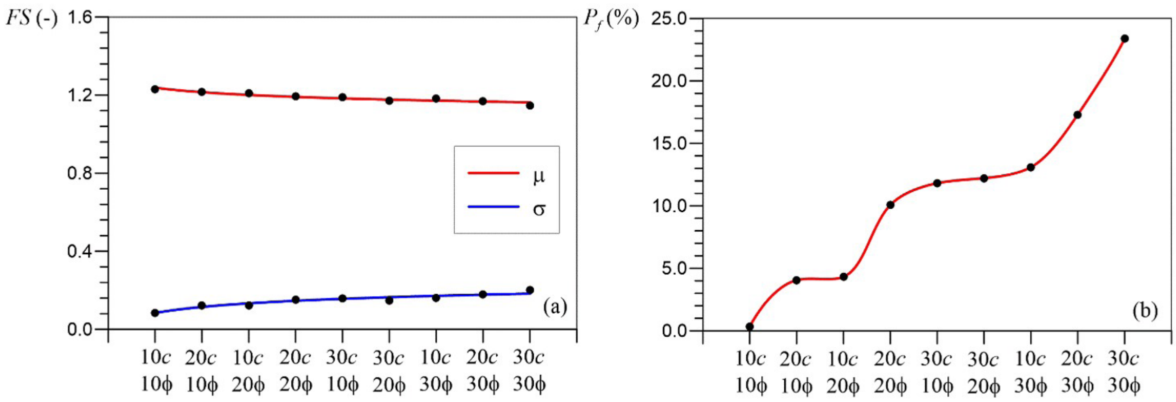

Figure 11. (a) Mean and standard deviation of FS from the simulations for the cases studied, (b) probability of failure for the cases studied.

a nearly constant *FS* can have a higher P_f depending on the increase in the standard deviation of the shear parameters. Nadim & Lacasse (1999) and Lacasse & Nadim (2007) showed that a geotechnical project could have a higher *FS* and a higher probability of failure than a project with a lower *FS* and P_f. Similar results are found in this study. So, a construction process with homogeneous materials and standardized tests can lower the standard deviation, thus lowering the P_f with a constant *FS*. Also, the *FS* methodology does not always guarantee a low probability of failure.

4.2.2 Displacement analysis

A simulated strain analysis for forty-six days was performed as in the simulation in the geotechnical centrifuge. However, the most significant deformation occurred in a few days due to the limitations of the model used, more information can be reviewed in the studies by Soga et al. (2016) and Augarde et al. (2021). This analysis is carried out due to the importance of soil mass displacements in the neighboring structures. Thus, depending on the deformations, the failure of the slope at a certain site may or may not be important. Limit-state models cannot capture this important part of a failure analysis. Figure 12 shows the deformations at the crest of the slope obtained from the Monte Carlo simulations. Figure 12b shows that most deformations are less than 0.2 m. However, depending on the parameters, the displacements of the crest can reach up to two meters. Figure 12c shows that slopes with low friction angle and low cohesion tend to have higher displacements. Regarding the modulus of elasticity, it showed a tendency when there are higher values of the friction angle where there are lower displacements with higher moduli (Figure 12d). However, the displacements presented are not greater than those shown in Figure 12c with respect to low cohesion. In addition, Figure 12c and 12d compare the displacements obtained from the simulations with the displacements obtained from the geotechnical centrifuge tests. This comparison shows that the displacements obtained with the simulations can be similar to those obtained in the centrifuge tests for values close to the parameters obtained experimentally (see Table 2). These results are valid only for the geometry and parameters used in the present research. Furthermore, it is assumed that large crest displacements may indicate large soil mass

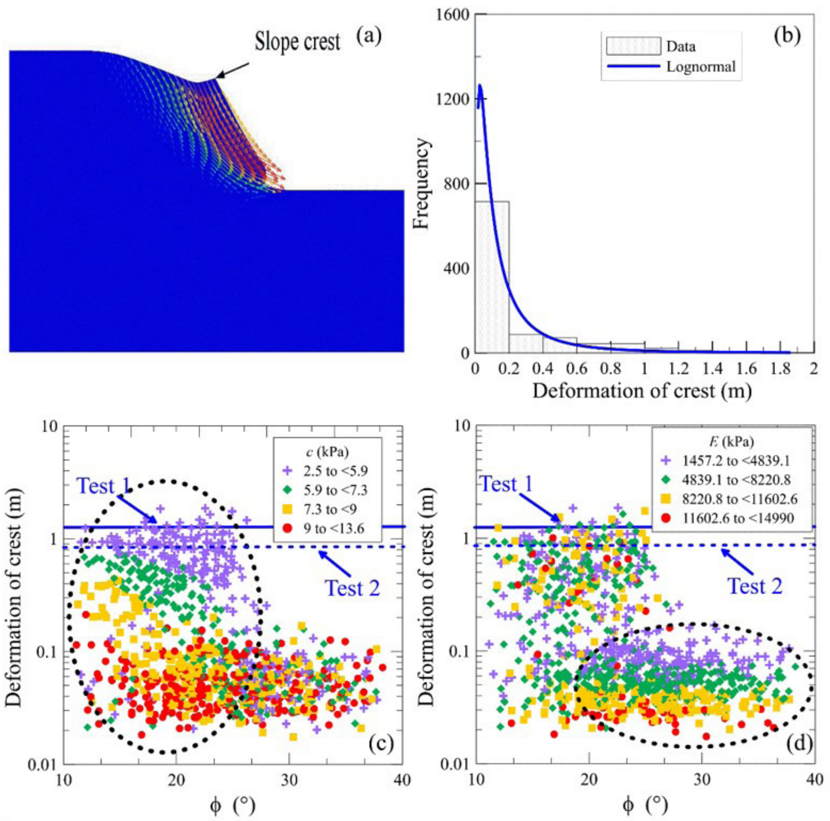

Figure 12. (a) Deformation vectors around of slope, (b) density curve and histogram of crest deformation, (c) and (d) deformation of crest versus variability of parameters.

displacements. A contribution of the present research is that in soil with a low friction angle, it would be essential to know the cohesion value, even if it is low. Therefore, this parameter should be characterized in the best possible way to lower the standard deviation (Phoon et al., 2006).

5. Conclusions

This study presents an innovative procedure to obtain the impact of the geotechnical parameters in the factor of safety and deformation by considering the natural variability of the soil and the variability resulting from the quality of the tests. The following conclusions can be drawn:

- The results of simulations show that the value of the factor of safety is nearly constant with the change of COV in the geotechnical parameters. Standard deviation increases with COV and mainly with the increase of the COV of cohesion. Thus, a slope with a nearly constant *FS* can have a higher P_f depending on the increase in the standard deviation of the shear parameters. Thus, a slope could have a higher *FS* and a higher probability of failure than a similar slope with a lower *FS* and P_f. An *FS* methodology does not always guarantee a low probability of failure. An alternative can be a good characterization of the materials and a standardized construction process to lower the standard deviation, thus reducing the P_f.
- All parameters of the elastoplastic model with the Mohr-Coulomb rupture criterion were varied. The crucial parameters in *FS* are cohesion and friction angle. Displacements of the crest show that slopes with low friction angle and low cohesion tend to present greater displacements. The modulus shows a trend when friction angles are high, but displacements are low.
- The displacements by the FEM simulations are within the limits of the displacements obtained from the geotechnical centrifuge tests. Also, FEM simulations can capture slope stability (factor of safety) in centrifuge tests of slopes. Thus, FEM simulations are a good method to capture the behavior of slopes with the variability of geotechnical parameters.

Acknowledgements

The authors express their gratitude to Universidad Nacional de Colombia, Pontificia Universidad Javeriana and Escuela Colombiana de Ingeniería Julio Garavito in Colombia for their technical and financial support to this paper.

Declaration of interest

The authors have no conflicts of interest to declare. All co-authors have observed and affirmed the contents of the paper and there is no financial interest to report.

Authors' contributions

Cristhian Mendoza: conceptualization, data curation, visualization, writing – original draft. Catalina Lozada: conceptualization, data curation, methodology, supervision, validation, writing – original draft.

Data availability

The datasets produced and analyzed during the present study are available from the corresponding author upon reasonable request.

List of symbols

c	cohesion of the soil
B	width of the models
COV	coefficient of variation
E	elasticity modulus
FEM	finite element models
FS	factor of safety
H	Height of the models
L	Length of the models
LAS	local averaging subdivision
N	length scale in centrifugal model.
P_f	probability of failure
PIV	particle image velocimetry technique
RFEM	random finite element method
SRFEM	strength reduction finite element method
SRM	strength reduction method
μ	Poisson's ratio
σ_n	normal stress
τ	shear stress of the soil
ϕ	friction angle of the soil

References

Al-Bittar, T., Soubra, A.H., & Thajeel, J. (2018). Kriging-based reliability analysis of strip footings resting on spatially varying soils. *Journal of Geotechnical and Geoenvironmental Engineering*, 144(10), 04018071..

Augarde, C.E., Lee, S.J., & Loukidis, D. (2021). Numerical modelling of large deformation problems in geotechnical engineering: a state of-the-art review. *Soils and Foundations*, 61(6), 1718-1735.

Baecher, G., & Christian, J. (2003). *Reliability and statistics in geotechnical engineering*. John Wiley & Sons.

Bolaños, C.C.M., & Hurtado, J.E. (2022). Effects of soil test variability in the bearing capacity of shallow foundations. *Transportation Infrastructure Geotechnology*, 9, 854-873.

Brinkgreve, R.B. (2005). Selection of soil models and parameters for geotechnical engineering application. In J.A. Yamamuro & V.N. Kaliakin (Eds.), *Soil constitutive models: evaluation, selection, and calibration* (pp 69-98). ASCE.

Cai, J.S., Yan, E.C., Yeh, T.C.J., Zha, Y.Y., Liang, Y., Huang, S.Y., Wang, W.K., & Wen, J.C. (2017). Effect of spatial variability of shear strength on reliability of infinite slopes using analytical approach. *Computers and Geotechnics*, 81, 77-86..

Ching, J., Chen, J., Yeh, J., & Phoon, K. (2012). Updating uncertainties in friction angles of clean sands. *Journal of Geotechnical and Geoenvironmental Engineering*, 138(2), 217-229..

Chok, Y.H., Jaksa, M.B., Griffths, D.V., Fenton, G.A., & Kaggwa, W.S. (2015). Probabilistic analysis of a spatially variable c′-φ′ slope. *Australian Geomechanics Journal*, 50, 17-27.

Cividini, A., Maier, G., & Nappi, A. (1983). Parameter estimation of a static geotechnical model using a Bayes' approach. *International Journal of Rock Mechanics and Mining Sciences & Geomechanics Abstracts*, 20(5), 215-226.

Cse, J. (2021). *Fundamentals of geomechanical and geotechnical finite element modeling using Abaqus and Python*. Independently Published.

Dawson, E., Roth, W., & Drescher, A. (1999). Slope stability analysis by strength reduction. *Geotechnique*, 49(6), 835-840.

Desai, C.S., & Siriwardane, H.J. (1984). *Constitutive laws for engineering materials with emphasis on geologic materials*. Prentice-Hall.

Dyson, A.P., & Tolooiyan, A. (2018). Optimisation of strength reduction finite element method codes for slope stability analysis. *Innovative Infrastructure Solutions*, 3, 38. http://dx.doi.org/10.1007/s41062-018-0148-1.

Dyson, A.P., & Tolooiyan, A. (2019). Prediction and classification for finite element slope stability analysis by random field comparison. *Computers and Geotechnics*, 109, 117-129.

El-Kadi, A.I., & Williams, S.A. (2000). Generating two-dimensional fields of autocorrelated, normally distributed parameters by the matrix decomposition technique. *Ground Water*, 38(4), 530-532..

Gong, W., Tien, Y., Juang, C.H., Martin II, J.R., & Luo, Z. (2017). Optimization of site investigation program for improved statistical characterization of geotechnical property based on random field theory. *Bulletin of Engineering Geology and the Environment*, 76, 1021-1035.

Griffiths, D.V., & Fenton, G.A. (2001). Bearing capacity of spatially random soil: the undrained clay Prandtl problem revisited. *Geotechnique*, 51(4), 351-359..

Griffiths, D.V., & Lane, P.A. (1999). Slope stability analysis by finite elements. *Geotechnique*, 49(3), 387-403.

Griffiths, D.V., Fenton, G.A., & Tveten, D.E. (2005). Probabilistic earth pressure analysis by the random finite element method. In G. Barla & M. Barla (Eds.), *Proc. 11th Int. Conf. on Computer Methods and Advances in Geomechanics (IACMAG 05)*, (Vol. 4, pp. 235–249). Bologna: Pátron Editore.

Haldar, S., & Babu, G.S. (2008). Effect of soil spatial variability on the response of laterally loaded pile in undrained clay. *Computers and Geotechnics*, 35(4), 537-547.

Helwany, S. (2007). *Applied soil mechanics with ABAQUS applications* (1st ed.). Wiley.

Jiang, S.H., Huang, J., Griffiths, D.V., & Deng, Z.P. (2022). Advances in reliability and risk analyses of slopes in spatially variable soils: a state-of-the-art review. *Computers and Geotechnics*, 141, 104498.

Kirby, J.M. (1991). Critical-state soil mechanics parameters and their variation for Vertisols in eastern Australia. *Journal of Soil Science*, 42(3), 487-499.

Lacasse, S., & Nadim, F. (2007). Probabilistic geotechnical analyses for offshore facilities. *Georisk*, 1(1), 21-42.

Lei, B., Xu, G., Feng, M., Zou, Y., Van der Heijden, F., Ridder, D.D., & Tax, D.M. (2017). *Classification, parameter estimation and state estimation: an engineering approach using MAT-LAB*. John Wiley & Sons.

Llano-Serna, M.A., Farias, M.M., Pedroso, D.M., Williams, D.J., & Sheng, D. (2018). An assessment of statistically based relationships between critical state parameters. *Geotechnique*, 68(6), 556-560.

Lozada, C., Mendoza, C., & Amortegui, J.V. (2022). Physical and numerical modeling of clayey slopes reinforced with roots. *International Journal of Civil Engineering*, 20, 1115-1128.

Lua, Y.J., & Sues, R.H. (1996). Probabilistic finite-element analysis of airfield pavements. *Transportation Research Record: Journal of the Transportation Research Board*, 1540(1), 29-38.

Lump, P. (1970). The Safety factors and the probability distributions of soil strength. *Canadian Geotechnical Journal*, 7(3), 225-242.

Matsui, T., & San, K.C. (1992). Finite element slope stability analysis by shear strength reduction technique. *Soils and Foundations*, 32, 59-70.

Mendoza, C., & Hurtado, J.E. (2022). The importance of geotechnical random variability in the elastoplastic stress–strain behavior of shallow foundations considering the geological history. *Geotechnical and Geological Engineering*, 40, 3799-3818.

Nadim, F., & Lacasse, S. (May 14, 1999). Probabilistic slope stability evaluation. In Geotechnical division, Hong Kong Institution of Engineers (Ed.), *Proceedings of the 18th Annual Seminar on Geotechnical Risk Management* (pp. 177-186). Hong Kong: Hong Kong Institution of Engineers.

Papaioannou, I., & Straub, D. (2012). Reliability updating in geotechnical engineering including spatial variability of soil. *Computers and Geotechnics*, 42, 44-51.

Phoon, K., & Kulhawy, F.H. (1999). Evaluation of geotechnical property variability. *Canadian Geotechnical Journal*, 36(4), 625-639.

Phoon, K., Nadim, F., Uzielli, M., & Lacasse, S. (2006). Soil variability analysis for geotechnical practice. *Characterisation and Engineering Properties of Natural Soils*, 3, 1653-1752.

Seyed-Kolbadi, S.M., Sadoghi-Yazdi, J., & Hariri-Ardebili, M.A. (2019). An improved strength reduction-based slope stability analysis. *Geosciences*, 9(1), 55. http://dx.doi.org/10.3390/geosciences9010055.

Soga, K., Alonso, E., Yerro, A., Kumar, K., & Bandara, S. (2016). Trends in large-deformation analysis of landslide mass movements with particular emphasis on the material point method. *Geotechnique*, 66(3), 248-273.

Stanier, S.A., Blaber, J., Take, W.A., & White, D.J. (2016). Improved image-based deformation measurement for geotechnical applications. *Canadian Geotechnical Journal*, 53, 727-739. http://dx.doi.org/10.1139/cgj-2015-0253.

Tan, T.S., Phoon, K.K., Hight, D.W., & Leroueil, S. (2003). *Characterisation and engineering properties of natural soils*. A.A. Balkema.

Tschuchnigg, F., Schweiger, H.F., & Sloan, S.W. (2015). Slope stability analysis by means of finite element limit analysis and finite element strength reduction techniques. Part I: numerical studies considering non-associated plasticity. *Computers and Geotechnics*, 70, 169-177.

Ugai, K. (1989). A method of calculation of total safety factor of slope by elasto-plastic FEM. *Soils and Foundations*, 29(2), 190-195.

Ugai, K., & Leshchinsky, D. (1995). Three-dimensional limit equilibrium and finite element analyses: a comparison of results. *Soils and Foundations*, 35(4), 1-7.

White, D.J., & Take, W.A. (2002). *GeoPIV: Particle Image Velocimetry (PIV) software for use in geotechnical testing*. University of Cambridge.

Yang, X., Yang, G., & Yu, T. (2012). Comparison of strength reduction method for slope stability analysis based on ABAQUS FEM and FLAC3D FDM. *Applied Mechanics and Materials*, 170-173, 918-922.

Zevgolis, I.E., Koukouzas, N.C., Roumpos, C., Deliveris, A.V., & Marshall, A.M. (2018) Evaluation of geotechnical property variability: the case of spoil material from surface lignite mines. In: *5th international civil protection conference—SafeKozani 2018*, Kozani, Greece: SafeGreece.

Zienkiewicz, O.C., Humpheson, C., & Lewis, R.W. (1975). Associated and non-associated visco-plasticity and plasticity in soil mechanics. *Geotechnique*, 25, 671-689.

Soils and Rocks
An International Journal of Geotechnical and Geoenvironmental Engineering
www.soilsandrocks.com
ISSN 1980-9743
ISSN-e 2675-5475

Prediction of hydraulic and petrophysical parameters from indirect measurements of electrical resistivity to determine soil-water retention curve – studies in granular soils

Manuelle Santos Góis[1], Katherin Rocio Cano Bezerra da Costa[1], André Luís Brasil Cavalcante[1#]

Article

Keywords
Indirect measures
Hydrogeophysical functions
Electrical resistivity
characteristic curve
Petrophysical relationships
Granular soil

Abstract

The characterization of unsaturated soils using hydromechanical methods is an essential requirement in soil science. However, current laboratory techniques used to obtain soil water retention and unsaturated hydraulic conductivity curves are time-consuming. To address this issue, a method based on indirect measures (electrical resistivity/electrical conductivity) was developed to quantitatively characterize soils. A novel unsaturated semi-empirical hydrogeophysical model of soils was developed by incorporating the hydrodynamic, geophysical, and petrophysical characteristics of soils. The model assumes that the parameters influencing the variation in the volumetric water content with matric suction and electrical resistivity are the same. The electrical resistivity characteristic curve (ERCC) defines a function that correlates environmental variables, electrical resistivity, soil water status, matric suction, hydraulic and petrophysical parameters, and fluid electrical resistivity. Model validation confirmed that the proposed approach can estimate the soil water retention curve (SWRC) via the indirect measures, and the results agreed with the experimental data. This indicates that it is possible to determine the SWRC and unsaturated hydraulic conductivity function of soil using the described approach.

1. Introduction

The characterization and comprehension of Earth's surface dynamics are fundamental in various fields, such as civil engineering. Human activities that modify the soil surface can induce changes in the hydraulic and mechanical properties of materials, reducing the soil's natural infiltration capacity. Such changes influence natural processes, including surface flow, evapotranspiration, groundwater recharge, soil erosion, and contaminants' transport in both surface and groundwater (Fredlund & Rahardjo, 1993; Libardi, 2005; Briaud, 2013; Camapum de Carvalho & Gitirana Junior, 2021; Fredlund, 2021; Carbajal et al., 2022). To tackle this issue, several fields, including geotechnical engineering, geology, geophysics, and hydrology, have utilized numerical and conceptual models to approximate the physical phenomenon of near-surface flux (Liu, 2017). Nonetheless, accurately defining the soil water retention curves and unsaturated hydraulic conductivity function poses a critical challenge in hydrogeological modeling.

Numerous publications have employed indirect measures on porous media to comprehend and depict the soil's saturated and unsaturated states. Mualem & Friedman (1991), Lesmes & Friedman (2005), Hinnell et al. (2010), Revil et al. (2012), and Binley et al. (2015) conducted hydrogeophysical investigations to examine the correlation between electrical parameters and hydrogeological properties of saturated and unsaturated media for the prediction of hydraulic parameters.

Shah & Singh (2005) and Hong-jing et al. (2014) established correlations between electrical conductivity/resistivity and degree of saturation/soil volumetric water content. Di Maio et al. (2015) proposed a combined utilization of Archie's law (Archie,1942) and van Genuchten's model (van Genuchten, 1980) to relate electrical resistivity to hydraulic conductivity. Fu et al. (2021b) developed a generalized form of Archie's law that describes the correlation between soil electrical conductivity and volumetric water content. Doussan & Ruy (2009), Piegari & Di Maio (2013), Mawer et al. (2015), Niu et al. (2015), and Cardoso & Dias (2017) conducted studies for the prediction of unsaturated hydraulic conductivity and matric potential from electrical

[#]Corresponding author. E-mail address: abrasil@unb.br
[1]Universidade de Brasília, Departamento de Engenharia Civil e Ambiental, Brasília, DF, Brasil.

Submitted on December 4, 2022; Final Acceptance on May 26, 2023; Discussion open until November 30, 2023.

https://doi.org/10.28927/SR.2023.013822

conductivity data. Kong et al. (2017), Lu et al. (2020), and Fu et al. (2021a) established functions for the electrical resistivity/electrical conductivity that depend on the volumetric water content and obtained the soil's characteristic curve.

This study presents a novel unsaturated semi-empirical hydrogeophysical model of soils that is based on the hypothesis that the parameters that impact the alteration in the volumetric water content with matric suction and electrical resistivity are the same. These hydrogeophysical functions demonstrate that it is feasible to depict a medium's state through indirect measurements and acquire soil water retention and hydraulic conductivity curves in an unsaturated state.

The validation conducted demonstrates that the proposed hydrogeophysical model can indirectly estimate the water retention curve and unsaturated hydraulic conductivity function of soil using electrical resistivity measurements with low computational and operational cost and in a timely manner.

2. Soils in the unsaturated zone

The vadose zone refers to the region between the ground surface and the water table. In simple terms, subsurface water is distributed in the soil voids, forming the unsaturated zone. Within this region, the surface part of the geological material, which lies between the land's surface and the top of the aquifer, has pores filled with both liquid and gaseous water. However, the capillary fringe immediately above the water table is predominantly saturated. In these soils, the impact of pore pressure is negative and determined by the cumulative effects of thermal, gravitational, kinetic, pressure, pneumatic, matric, and osmotic potentials. Among these factors, osmotic and matric suction play critical roles in determining the hydromechanical properties of unsaturated soils.

The suction effect is physically equivalent to an external pressure that influences the stress state of a material, resulting in an increase in soil strength as suction rises (Fredlund & Rahardjo, 1993; Cavalcante & Mascarenhas, 2021). Matric suction, which depends on capillarity's physical phenomenon, is determined by the degree of soil saturation and the void structure within the soil, which is the main factor responsible for negative pore pressure. Hence, the water state in the soil, as determined by infiltration and percolation, substantially contributes to matric suction. Understanding and enhancing current techniques for determining the volumetric water content-to-suction ratio are crucial, as the relationship between suction and soil processes highlights its significance. The volumetric water content is currently defined using a soil water retention curve (SWRC), and the hydraulic conductivity-suction ratio is established based on the unsaturated hydraulic conductivity function (Fredlund & Rahardjo, 1993; Sheng et al., 2008; Cho, 2016; Crawford et al., 2019; Chou & Wang, 2021; Albuquerque et al., 2022).

2.1 Unsaturated flow constitutive model

Richards equation (Richards, 1931) is commonly utilized in soil science for modeling unsaturated flow. However, the nonlinearity of the constitutive relationships between hydraulic conductivity-suction and volumetric water content-suction hinders analytical solutions to the problem. To address this issue, researchers, such as Brooks & Corey (1964), van Genuchten (1980), and Fredlund & Xing (1994), have attempted to consolidate some of the constitutive models to enable numerical solutions to the partial differential equation for unsaturated flow. Meanwhile, other studies have presented analytical solutions limited to specific cases, such as stationary flow under simplified hydraulic conditions, which leads to a loss of the porous medium's transient approach to the flow problem (Lai & Ogden, 2015; Zhang et al., 2016).

To accurately model transient unsaturated flow, Cavalcante et al. (2019) presented one-, two-, and three-dimensional analytical solutions based on the theory developed by Cavalcante & Zornberg (2017). These authors developed a series of analytical solutions to the problem of transient one-dimensional unsaturated flow, making the following assumptions: (i) volumetric changes of unsaturated soils in the presence of flow are ignored; (ii) soil porosity remains constant in any wetting or drying cycle; (iii) the volumetric water content is an independent variable. Consequently, it is possible to transform the Richards equation into a one-dimensional flow in the z-direction:

$$\frac{\partial\theta}{\partial t}=\frac{\partial}{\partial z}\left(\frac{k_z(\theta)}{g\rho_w}\frac{\partial\psi}{\partial\theta}\frac{\partial\theta}{\partial z}\right)-\frac{\partial k_z(\theta)}{\partial z} \tag{1}$$

where θ = the volumetric soil water content (L^3L^{-3}), t = the time (T); ψ = the soil suction ($ML^{-1}T^{-2}$); g = the acceleration due to gravity (LT^{-2}); ρ_w = the water density (ML^{-1}); $k_z(\theta)$ = the unsaturated hydraulic conductivity function in terms of the volumetric water content in the z-direction (LT^{-1}), and $\partial\psi/\partial\theta$ = the variation in the matric suction concerning the volumetric water content.

Cavalcante & Zornberg (2017) established the constitutive models that physically represent the soil water retention curve and unsaturated hydraulic conductivity function to derive the analytical solutions for the one-dimensional unsaturated flow equation. These models consider a uniform pore distribution that corresponds to the soil macro-porosity of tropical regions. The models provide a clear and concise definition of the physical behaviors of the correlated properties:

$$\theta(\psi)=\theta_r+(\theta_s-\theta_r)\cdot\exp(-|\psi|\cdot\delta) \tag{2}$$

where θ_s = the volumetric soil water content in the saturated state (L^3L^{-3}); θ_r = the volumetric soil water content in the residual state (L^3L^{-3}); ($\theta_s - \theta_r$) = the maximum soil wetting capacity (L^3L^{-3}); and δ = the hydraulic adjustment parameter ($M^{-1}LT^2$). The unsaturated hydraulic conductivity function describes the rate at which fluid seeps through an unsaturated porous medium, as given by:

$$k(\psi) = k_{sat} \cdot \exp\left(-|\psi| \cdot \delta\right) \quad (3)$$

where k_{sat} = the saturated hydraulic conductivity of the soil (LT^{-1}). In unsaturated soils, the unsaturated hydraulic conductivity is contingent upon the pore structure and size, the volume of water present in the medium, and the saturation history. Hence, soils with larger voids (i.e., granular material) are more prone to moisture reduction under pressure application, resulting in significant reductions in hydraulic conductivity, which directly influences the hydromechanical behavior.

The hydraulic adjustment parameter δ refers to the initial angular coefficient of the curves determined by the constitutive model. It is directly affected by the maximum soil wetting capacity and the saturated hydraulic conductivity. Costa & Cavalcante (2020) established an analytical correlation between the air-entry and the δ parameter, expressed as:

$$\psi_{air} = \frac{\exp\left(1 - \exp(1)\right)}{\delta} \quad (4)$$

where ψ_{air} = the air-entry soil suction ($ML^{-1}T^{-2}$).

Hence, by knowing the δ parameter, it is feasible to ascertain the air-entry soil suction value and thereby estimate the magnitude of the capillary zone in the porous medium.

2.2 Electrical properties of near-surface soils

Geophysical properties or attributes have emerged as potent tools for characterizing the environment in diverse research domains, such as geology, archaeology, oceanography, engineering, and agronomy. For instance, electrical attributes are utilized to identify hydrocarbon-producing wells, underground water, contamination, and building foundations. Based on petrophysical relationships, these attributes enable rapid and indirect characterization of the environment from physical, mechanical, and hydraulic standpoints (Telford et al., 1990; Hubbard & Rubin, 2005; Glover, 2015).

Soil electrical attributes can be measured using electronic, dielectric, or electrolytic techniques. Electromagnetically, soil can be viewed as heterogeneous composites of conductive and/or dielectric solid particles surrounded by aqueous electrolytes in varying proportions. Thus, the electrical properties of soil depend on the mineral composition and texture of the solid matrix, which encompasses properties such as structure, void ratio, salt and fluid concentration, temperature, and pore-space geometry, along with the volumetric water content in the voids (Keller & Frischknecht, 1966; Rhoades et al., 1976; Keller, 1988; Telford et al., 1990; Butler, 2005; Friedman, 2005; Lima, 2014). These properties also influence the mechanical and hydraulic traits of soils.

Archie (1942) developed empirical laws that establish connections between the electrical resistivity of rock, its porosity, the resistivity of the water that saturates its pores, and the degree of saturation of the pore space.

The two laws formulated by Archie can be merged into a single equation (Glover, 2015), as given by:

$$ER = ER_w n^{-m} S_w^{-p} \quad (5)$$

where ER = the electrical resistivity of an unsaturated sample ($ML^3T^{-1}Q^{-2}$); ER_w = the fluid electrical resistivity ($ML^3T^{-1}Q^{-2}$), n = the porosity, which is the ratio of the volume of voids to the total volume (non-dimensional), m = the cementation exponent (non-dimensional), p = the saturation exponent (non-dimensional), S_w = the degree of saturation (non-dimensional).

Several empirical equations and physical models have been suggested in the literature to estimate the electrical resistivity of soil mixtures as a function of the degree of saturation or volumetric water content. For low-specific-surface soils (with negligible surface conductivity), such as clean sands, Archie's law is widely employed. However, it is essential to note that Archie's law is applicable only when the liquid phase is continuous, in the funicular state, and it is inadequate when the lithology consists of minerals, usually shales, that provide a substantial surface conductance.

Various studies have employed these empirical relationships to establish a law for unsaturated porous environments, relating the volumetric water content, fluid electrical conductivity, petrophysical parameters, and the electrical conductivity of an unsaturated medium (Glover et al., 2000; Santamarina et al., 2001; Rinaldi & Cuestas, 2002; Shah & Singh, 2005; Ewing & Hunt, 2006; Glover, 2010; Kibria & Hossain, 2012; Glover, 2015; Singha et al., 2014; Datsios et al., 2017). Glover (2015) has proposed the following relationship:

$$ER = \tau \cdot n^{-m} \cdot ER_w \cdot S_w^{-p} \quad (6)$$

where τ = the tortuosity, which is related to the path length of the current flow (non-dimensional).

Equation 6 can be alternatively written in terms of electrical conductivity (inverse of electrical resistivity), as follows:

$$EC = EC_w \cdot \left(\tau \cdot n^{-m} \cdot S_w^{-p}\right)^{-1} \quad (7)$$

where EC_w = the fluid electrical conductivity ($M^{-1}L^{-3}T\,Q^2$).

Hence, Equation 6 can be rephrased and expressed in terms of the soil's volumetric water content, as follows:

$$\theta\left(ER\right)=\left(\frac{ER}{\tau\cdot n^{-m+p}\cdot ER_w}\right)^{-1/p} \tag{8}$$

In granular soils, which are the subject of this study, the electrical conductivity or resistivity of a soil sample is mainly influenced by the fluid's nature, the proportion of voids in the sample, the particle distribution, the salt concentration in the fluid, and the degree of saturation. Hence, it is feasible to illustrate how the electrical resistivity varies as a function of the volumetric water content of the soil. This study aims to establish a hydrogeophysical model based on indirect electrical measurements to characterize a soil's hydraulic and petrophysical environment.

3. Unsaturated semi-empirical hydrogeophysical model of soils

The hydrogeophysical model of soils proposed in this study builds upon the hydrogeomechanical model developed by Cavalcante & Zornberg (2017) and the empirical relationship between the volumetric water content and electrical resistivity. The model operates under the assumption that the parameters influencing the variations in the volumetric water content with both matric suction and electrical resistivity are equivalent. By combining Equations 2 and 8, the model establishes a function that correlates several environmental variables, such as electrical resistivity, soil water content, matric suction, hydraulic and petrophysical parameters, and the electrical resistivity of the fluid within a porous medium. It can be written as:

$$ER\left(\psi\right)=\frac{\tau\cdot n^{-m+p}\cdot ER_w}{\left(\theta_r+\left(\theta_s-\theta_r\right)\cdot\exp\left(-\left|\psi\right|\cdot\delta\right)\right)^{p}} \tag{9}$$

Equation 9 represents a semi-analytical constitutive model for the Electrical Resistivity Characteristic Curve (*ERCC*) as a function of the soil's electrical and hydraulic characteristics, as well as petrophysical parameters (τ, n, m, and *p*). When setting ψ to zero, the starting point of the *ERCC* is obtained, which includes contributions from θ_s, ER_w, and petrophysical parameters, i.e., $ER(0) = \tau.n^{-M+P}.\theta_s^{-P}.ER_w$. In Equation 9, the slope, $\partial ER(\psi)/\partial\psi$, approaches zero as $ER(\psi)$ approaches its residual and saturated states.

The characteristic curves for hydraulic and hydrogeophysical parameters (Figure 1) exhibit a correspondence between the residual and saturated states and the air-entry point. At low levels of matric suction, indicating a higher water content in the system, the electrical resistivity values are lower (Figure 1). As the matric suction increases, corresponding to the air-entry point of 0.28 kPa (determined using Equation 4 for δ = 0.65 kPa^{-1}), the electrical resistivity begins to increase while the water content in the system decreases to the interstitial volumetric water content state (Figure 1).

The hydrogeophysical function for unsaturated hydraulic conductivity as a function of the electrical resistivity was determined using Equations 2, 3, and 8, and is expressed as follows:

$$k_{us}\left(ER\right)=\begin{cases} k_{sat}, \\ \text{if } ER<ER_w\cdot\theta_s^{-p}\cdot\tau\cdot n^{-m+p} \\ \dfrac{k_{sat}}{\theta_s-\theta_r}\left(\left(\dfrac{ER}{\tau\cdot n^{-m+p}\cdot ER_w}\right)^{-1/p}-\theta_r\right), \\ \text{if } ER\geq ER_w\cdot\theta_s^{-p}\cdot\tau\cdot n^{-m+p}\end{cases} \tag{10}$$

Equation 10 describes the unsaturated hydraulic conductivity as a function of electrical resistivity and dependent on hydraulic and petrophysical parameters. If the electrical resistivity (*ER*) is less than $ER_w.\theta_s^{-P}.\tau.n^{-M+P}$, then $k_{US}(ER) = k_{sat}$, indicating a high volumetric water content and thus low soil resistivity. However, if *ER* is greater than or equal to $ER_w.\theta_s^{-P}.\tau.n^{-M+P}$, the unsaturated hydraulic conductivity decreases with increasing electrical resistivity.

At higher levels of electrical resistivity (*ER* > 220.38 Ω·m), there is a noticeable reduction in unsaturated hydraulic conductivity, and it remains constant after reaching 1000 Ω·m (Figure 2).

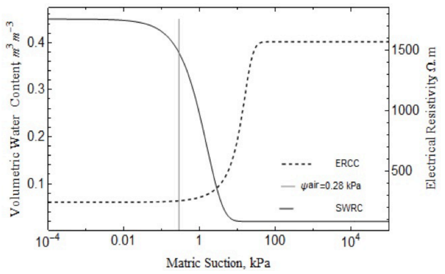

Figure 1. SWRC and ERCC characteristic curves for a sandy soil with parameters: θ_r = 0.02 m³.m⁻³, θ_s = 0.45 m³.m⁻³, δ = 0.65 kPa^{-1} (ψ_{air} = 0.28 kPa), *m* = 1.80, *ERw* = 30.30 Ω.m, τ = 1.50, *n* = 0.40, and *p* = 0.60.

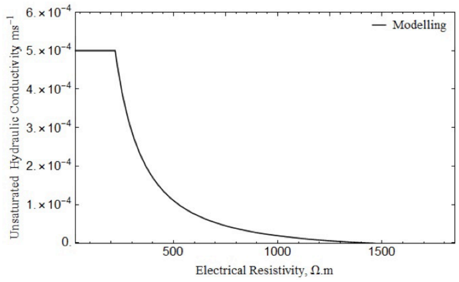

Figure 2. k_{us} *(ER)* function for a sandy soil with parameters: k_{sat} = 5.00 × 10^{-4} m·s^{-1}, θ_r = 0.02 m³·m⁻³, θ_s = 0.45 m³·m⁻³, *m* = 1.80, ER_w = 30.30 Ω·m, τ = 1.50, *n* = 0.40, and *p* = 0.60.

To investigate the impact of the parameters on the hydrogeophysical model, six scenarios (Table 1) were constructed using the parameters from Figure 1 and Figure 2. The sensitivity of the models to changes in the hydraulic and petrophysical parameters (θ_r, θ_s, δ, m, p, and τ) was then analyzed.

4. Model validation for granular soils – sandy

The model's validation was performed using two granular soils with distinct electrical conductivity values. The first dataset consists of medium sand from this study, while the second dataset was obtained from Tuli & Hopmans (2003) and refers to fine sand.

The steps taken to validate the model involved: (1) collecting laboratory data on volumetric water content and electrical resistivity with identification of the saturated, intermediate, and dry regions. (2) Determining the petrophysical parameters (m, p, and τ) through non-linear fitting of the $ER(\theta)$ function. (3) Determining the hydraulic parameter (δ) through minimization of the objective function. (4) Application – Determining the soil-water retention curve (SWRC) and unsaturated hydraulic conductivity function (k_{us}).

4.1 Case Study 1 - Soil with high electrical resistivity

The proposed hydrogeophysical model was verified using a granular material obtained from a civil construction project. The geotechnical classification and geoelectric (electrical resistivity) analysis values of the material were used in the model validation (Table 2). The classification was conducted following the guidelines of the American Society for Testing and Materials (ASTM) and the Brazilian Association of Technical Standards (ABNT).

Table 1. Result of the sensitivity analysis of the hydraulic and petrophysical parameters for the ERCC and $k_{us}(ER)$ functions.

Index	Modeled Scenarios	Analyzed Parameter	ERCC (Equation 9)	$k_{us}(ER)$ (Equation 10)
1	Increased soil residual volumetric water content	θ_r	Decrease in ER values for matric suctions greater than 10 kPa	Decrease in k_{us} for *ER* less than 1400 Ω.m
2	Increased soil saturated volumetric water content	θ_s	Decrease in *ER* values for matric suctions below 1 kPa	Decrease in k_{us} for ER less than 500 Ω.m
3	Increase in the wetting capacity of the soil and the matric suction value corresponding to the air-entry	δ	Decrease in ar-entry point, and increase of the value of *ER* in this points	-
4	Increased interconnectivity between soil particles	m	Increase in *ER* values for all analyzed matric suction interval	Increase in k_{us} for ER great than 500 Ω.m
5	Increased degree of saturation	p	Increase in the *ER* values for matric suctions above the air-entry point and changes in air-entry values	Increase in k_{us} values for all modeled resistivity range
6	Increased soil tortuosity	τ	Increase in the *ER* values for all analyzed matric suction range	Increase of more than one order of magnitude of k_{us} values for *ER* less than 1000 Ω.m

Table 2. Geotechnical and geoelectric characterization of the Soil 1.

Informations/Data		Value
Case Study		Soil 1
Origin of soil		Brazil - Civil construction
Number of samples analyzed		6
Soil texture	Sand	1.00
	Silt	-
	Clay	-
Specific mass, ($kg.m^{-3}$)		1550
Porosity-n, (adm)		0.44
Saturated permeability-k_{sat}, ($m.s^{-1}$)		2.40×10^{-4}
Fluid electrical conductivity-EC_w, ($S.m^{-1}$)		4.28×10^{-3}
Fluid electrical resistivity-ER_w, (Ω.m)		232.56
Volumetric Water Content, ($m^3.m^{-3}$)	θ_r	0.01
	θ_s	0.44

The relationship between the volumetric water content and matric suction (Table 3) was determined through a pressure plate test conducted in a Richards chamber that was equipped with a Pressure Plate Extractor 1500 F2 (Soilmoisture Equipment Corp®), following the procedures outlined in Dane & Topp (2002). The test assumed that the sample volume remained constant throughout.

A temperature-controlled room at 21 °C was used to assemble a geoelectric box for measuring the electrical potential (in volts). The granular material was packed into an acrylic box with dimensions of 0.20 m × 0.08 m × 0.80 m and a thickness of 0.40×10^{-2} m. The box was then connected in series to an adjustable direct current (DC) source (0 V-30 V/0 A-3 A/PS-4000, Icel®) with two multimeters. One multimeter was used to measure the potential difference, while the other measured the electric current being injected into the system. Silver electrodes with a sodium chloride coating, 0.25×10^{-1} m long and spaced at 0.64×10^{-1} m, were used to prevent electrode polarization problems under low-frequency conditions, following the recommendation of Telford et al. (1990).

The potential difference was measured using the Wenner acquisition geometry with a geometric factor of 0.41 m. For each electrical potential measurement, three soil samples were collected, and the gravimetric water content was determined following the guidelines of ASTM (2010) and ABNT (2016). Then, the electrical resistivity values were calculated for each volumetric water content value (Figure 3).

Table 3. Experimentally determined average values of the volumetric water content and matric suction determined in a pressure chamber (Soil 1).

ψ (kPa)	θ ($m^3 \cdot m^{-3}$)
P_{atm}	0.44
2	0.08
4	0.06
6	0.05
8	0.05
10	0.05
14	0.04
20	0.04
30	0.03
40	0.04
60	0.03
80	0.03
100	0.03
150	0.03
200	0.02
300	0.03
350	0.02
600	0.02
1000	0.01
1500	0.02

The experimentally determined average values of the volumetric water content indicated three distinct regions as the electrical resistivity increased: the saturated, intermediate, and dry regions, which corresponded to electrical resistivities of 665.53 Ω·m ≤ ER ≤ 734.64 Ω·m, 920.88 Ω·m ≤ ER ≤ 1909.11 Ω·m, and 1909.11 Ω·m ≤ ER < 2296.13 Ω·m, respectively (Figure 3).

The experimental data obtained in the laboratory (Figure 3) were fitted to the non-linear model (Equation 8) to obtain the petrophysical parameters *m, p,* and τ, which are responsible for the interconnectivity between soil particles, the degree of saturation, and tortuosity of the soil, respectively.

In the region where the volumetric water content equals the saturated water content (θ_s) and the electrical resistivity is lower than $ER_w.\theta_s^{-p}.\tau.n^{-M+P}$, which corresponds to 553.88 Ω·m – the saturated region, the expected physical behavior of low electrical resistivities associated with the volumetric water content is observed. However, for 553.88 Ω·m ≤ ER ≤ 1300 Ω·m, an abrupt decrease in the volumetric water content is noted, and it approaches the residual when ER ≥ 2300 Ω·m (Figure 4).

The $k_{us}(ER)$ function displays the maximum values of unsaturated hydraulic conductivity (approximately 2.40×10^{-4} ms^{-1}) linked with the electrical resistivity when ER is less than or equal to 553.88 Ω·m, which represents

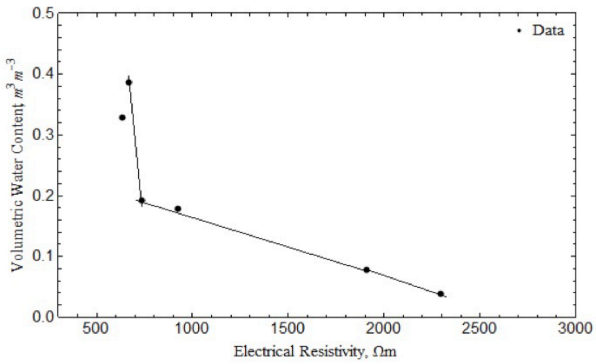

Figure 3. Theoretical piecewise linear relationship between volumetric water content and electrical resistivity for Soil 1

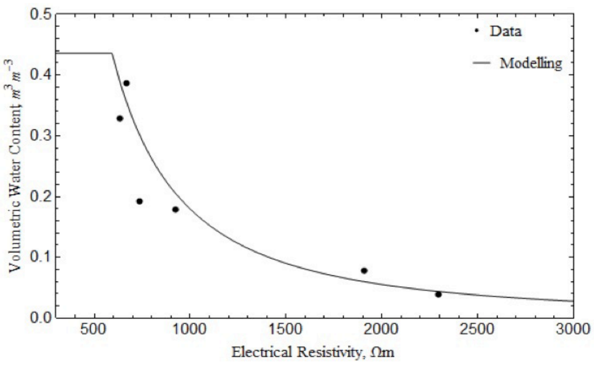

Figure 4. Adjustment of the θ(ER) function applied to soil data resulting in m = 1.00, p = 0.59, and τ = 1.11 (Soil 1).

the soil at the saturation region (Figure 5). In the case of 553.88 Ω·m ≤ ER ≤ 2000 Ω·m, there is a significant variation in the unsaturated hydraulic conductivity associated with the unsaturated soil. When ER is greater than or equal to 2000 Ω·m, the unsaturated hydraulic conductivity remains almost constant, which indicates dry soil.

To determine the hydraulic parameter (δ) that affects the wetting ability of the soil, an inverse problem formulation was employed. In this case, the aim was to minimize a function to find the value of δ that best represents the medium, and subsequently, determine the SWRC and the unsaturated hydraulic conductivity function.

The inverse problem was solved by using an objective function that quantifies the difference between the laboratory measurements and the values calculated using Equation 9. The objective function is defined as follows:

$$OF\left(ER\right)=\left(ER_M-ER_C\right)^2 \tag{11}$$

where ER_M = the experimentally measured electrical resistivity; and ER_C = the computed values for each value of parameter δ. The goal is to estimate the values of the parameters that best represent the soil condition by minimizing this function. It is assumed that all parameters in Equation 9, except δ, are constant based on the available information.

An algorithm was implemented to solve this objective function, where $ER(\psi)$ is computed for each value of δ. These computed values are subtracted from the corresponding experimentally measured values and the difference is squared. The estimated value with the smallest squared residual is then chosen (Equation 11).

A range of less than 10 kPa was examined to minimize the objective function. The selected points (Table 4) represent a range of intermediate electrical resistivity with low matric suction and a range of high resistivity with varying matric suction.

The $ER(\psi)$ function for each point exhibits a region of minimal points that correspond to different values of δ. A point where the quadratic residue is minimum is identified (Figure 6), and it is observed that Point 1 has the smallest quadratic residue. Therefore, the optimal parameter value of δ that best represents this sandy soil with the given geotechnical characteristics is 0.46 kPa^{-1}.

With the value of δ, it is possible to construct the soil water retention curve (SWRC) (Figure 7a) and unsaturated hydraulic conductivity curve (Figure 7b) of soil 1 with the identification of the air-entry point (ψ_{air} = 0.39 kPa) calculated by Equation 4. The data obtained from the pressure plate tests are displayed in Table 3.

The SWRC (Figure 7a) exhibits agreement with the experimental data, indicating the feasibility of obtaining SWRC through indirect measurements of the studied Soil 1.

The accuracy of the proposed hydrogeophysical model in predicting the soil water retention curve and unsaturated hydraulic conductivity curve of soil through electrical resistivity measurements is demonstrated by the good agreement between the model predictions and the experimental values of volumetric water content and electrical potential obtained using pressure plate tests and a geoelectrical box.

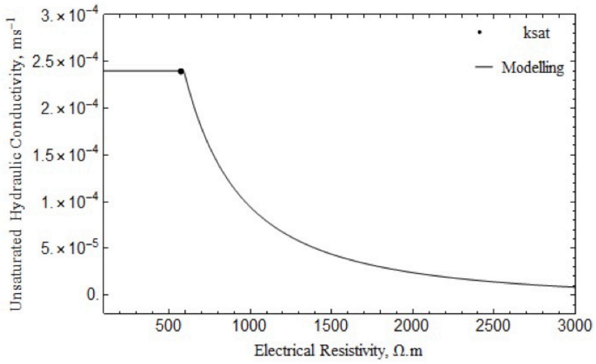

Figure 5. $k_{us}(ER)$ function curve for Soil 1 with parameters m = 1, p = 0.59, and τ = 1.11.

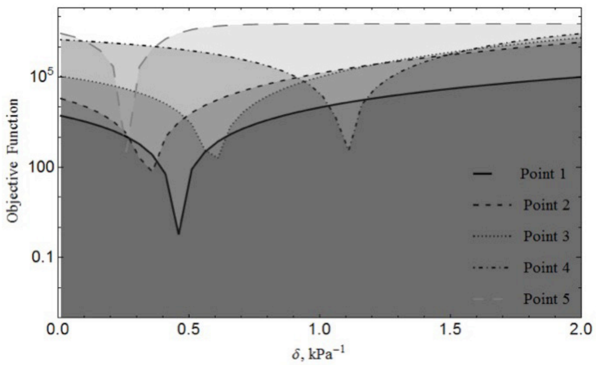

Figure 6. Minimization of the *ER(ψ)* function for Points 1 to 5 – soil 1.

Table 4. Points used in the minimization process and the corresponding values of δ_{min} for Soil 1.

Point	ψ (kPa)	ER_M (Ω·m)	δ_{min} (kPa^{-1})
1	0.45	665.53	0.46
2	1.11	734.64	0.36
3	1.33	920.88	0.61
4	2.00	1909.11	1.11
5	10.00	2296.13	0.26

Table 5. Geotechnical and geoelectric characterization of the Soil 2 (modified from Tuli & Hopmans, 2003).

Informations/Data		Value
Case Study		Soil 2
Origin of soil		USA - Osa Flaco
Number of samples analyzed		20
Soil texture	Sand	1.00
	Silt	-
	Clay	-
Specific mass, (kg.m^{-3})		1550
Porosity-n, (adm)		0.41
Saturated permeability-k_{sat}, (m.s^{-1})		1.13×10^{-5}
Fluid electrical conductivity-EC_w, (S.m^{-1})		2.50×10^{-1}
Fluid electrical resistivity-ER_w, (Ω.m)		4
Volumetric Water Content, (m^3.m^{-3})	θ_r	0.07
	θ_s	0.41

Table 6. Experimentally obtained average values of the volumetric water content and matric suction using the multistep outflow method for Soil 2 (modified from Tuli & Hopmans, 2003).

ψ (kPa)	θ (m^3·m^{-3})
0.01	0.41
0.72	0.38
0.63	0.37
0.74	0.34
0.81	0.34
0.83	0.31
1.04	0.30
1.04	0.28
0.93	0.28
1.17	0.23
1.17	0.21
1.46	0.16
1.46	0.15
1.89	0.11
2.00	0.10
6.34	0.08

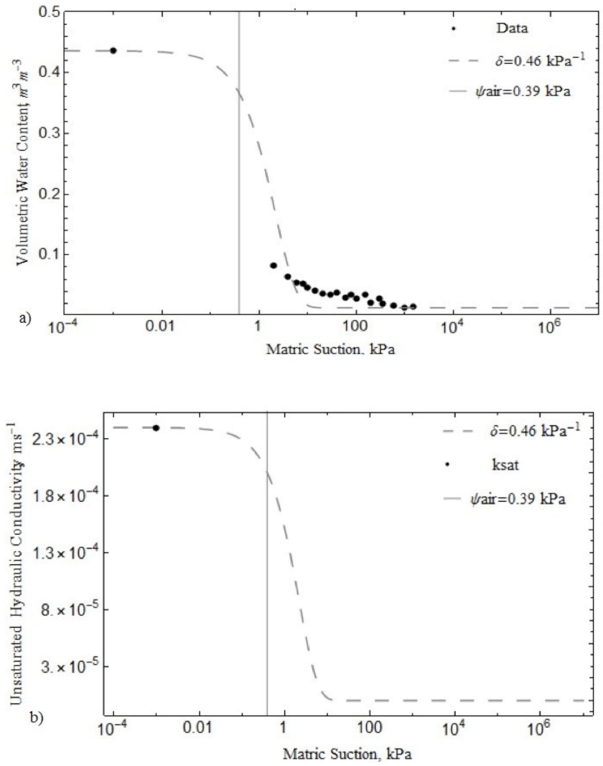

Figure 7. (a) SWRC and (b) unsaturated hydraulic conductivity function for the value of δ obtained by minimization (Soil 1).

4.2 Case Study 2 – Soil with low electrical resistivity

Tuli & Hopmans (2003) investigated the correlation between various transport coefficients and pore geometrical properties, and measured the hydraulic and electrical conductivity of Oso Flaco sand (Table 5) at different levels of saturation for four fluid conductivities. For this study, the data of the saturated samples using a $CaCl_2$ solution (electrical conductivity 2.5×10^{-1} S.m^{-1}) were utilized.

The soil samples were packed uniformly into brass columns (6.00×10^{-2} m high and 8.25×10^{-2} m inner diameter) with a wet strength fast flow filter paper glued at the bottom. The filter paper was soaked in $CaCl_2$ solution, which was maintained about 0.01 m below the rims of the columns. The filter paper was then removed, and the saturated soil samples were assembled in Tempe Pressure Cells to estimate the soil-water retention curve (Table 6) and unsaturated hydraulic conductivity function using the multistep outflow method, as described by Tuli & Hopmans (2003).

A miniature tensiometer and a two-rod TDR mini probe were vertically inserted into the center of each soil sample after assembly of the Tempe pressure cells. The samples were then resaturated with the solution through the bottom porous membrane assembly and allowed to equilibrate with the applied pressure. Electrical conductivity values were determined using the Time Domain Reflectometry (TDR) method, as described by Tuli & Hopmans (2003).

TDR is a technique that uses the propagation of electromagnetic waves to indirectly measure moisture content by correlating it with the electric and dielectric properties of geomaterials. The travel time is associated with the charge storage capacity of the soil and the volumetric water content. TDR measurements involve transmitting an impulse and observing the response within a certain time interval.

The Time Domain Reflectometer (TDR) measures the round-trip time of an electromagnetic wave that is reflected by the medium being tested. It then converts this time into a distance unit and displays the information as a waveform. The time interval between these reflections can be used to calculate the velocity of the electromagnetic wave in the medium. Additionally, TDR waveform measurements can be transformed into electrical conductivity using algorithms. Tuli & Hopmans (2003) utilized a Tektronix 1502B metallic cable-tester and WinTDR99 software to analyze the waveforms.

Using the data from Tuli & Hopmans (2003), it was feasible to distinguish four distinct regions based on electrical resistivity ranges: saturated, intermediate 1, intermediate 2 and dry. These regions correspond to resistivity ranges of 11.11 Ω·m ≤ ER ≤ 39.23 Ω·m, 39.23 Ω·m < ER ≤ 86.73, 86.73 Ω·m < ER ≤ 95.96 Ω·m, and 95.96 Ω·m < ER < 125.28 Ω·m, respectively (Figure 8).

By employing the same methodology presented in Case Study 1, it was feasible to determine the petrophysical parameters m, p, and τ, and consequently, simulate the performance of the θ(ER) and $k_{us}(ER)$ functions.

In Figure 9, the saturated region, where θ(ER) = 44.33%, corresponds to electrical resistivity values ranging from 11.11 Ω·m to 31.32 Ω·m. An abrupt decline in the volumetric water content occurs when the electrical resistivity ranges from 31.32 Ω·m to 100 Ω·m. Conversely, for electrical resistivity values greater than 150 Ω·m, the volumetric water content approaches the residual level.

Figure 10 displays the maximum values of unsaturated hydraulic conductivity (approximately 1.13×10^{-5} m.s^{-1}), which are linked to electrical resistivity values of ER ≤ 31.32 Ω·m, corresponding to the saturation region of the soil. In the unsaturated soil region, significant variability in the unsaturated hydraulic conductivity is evident for 31.32 Ω·m ≤ ER ≤ 100 Ω·m. As for ER values greater than or equal to 100 Ω·m, the unsaturated hydraulic conductivity drops to its minimum level, indicating dry soil conditions.

By applying the same methodology employed in Case Study 1, the hydraulic parameter δ was ascertained by minimizing the objective function (Equation 11). Various scenarios of electrical resistivity and pressure were considered for the data points chosen within the range of less than 10 kPa (see Table 7).

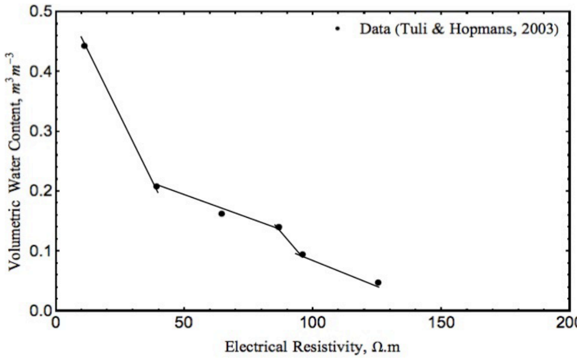

Figure 8. Theoretical piecewise linear relationship between volumetric water content and electrical resistivity for Soil 2.

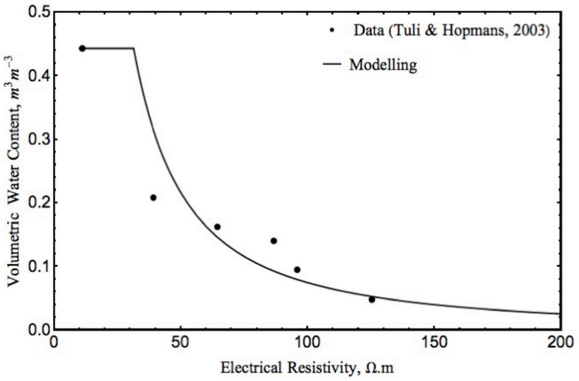

Figure 9. Adjustment of the θ(ER) function applied to soil data resulting in m = 1.79, p = 0.65, and τ = 1.67 (Soil 2).

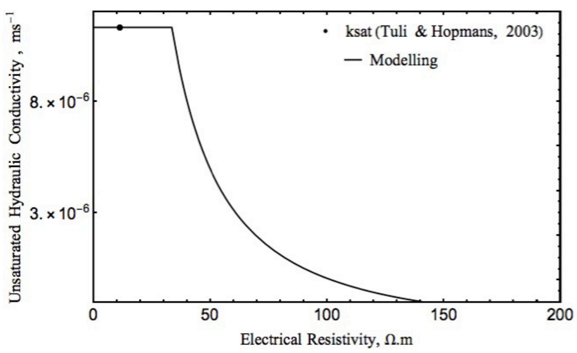

Figure 10. $k_{us}(ER)$ function curve for Soil 2 with parameters m=1.79, p=0.65, and τ=1.67.

Figure 11 shows a cluster of points where the quadratic residue varies according to different values of δ, with one point exhibiting the lowest quadratic residue. These findings suggest that Point 4 yields the minimum quadratic residue, implying that the most suitable δ parameter for this sandy soil with its respective geotechnical features is 0.56 kPa^{-1}.

Table 7. Points used in the minimization process and the corresponding values of δmin – Soil 2 (modified from Tuli & Hopmans, 2003).

Point	ψ (kPa)	ER_M (Ω·m)	δ_{min} (kPa^{-1})
1	0.001	11.11	*
2	1	39.22	0.31
3	2	64.43	0.76
4	5	86.73	0.56
5	6.5	95.96	0.61

* not found.

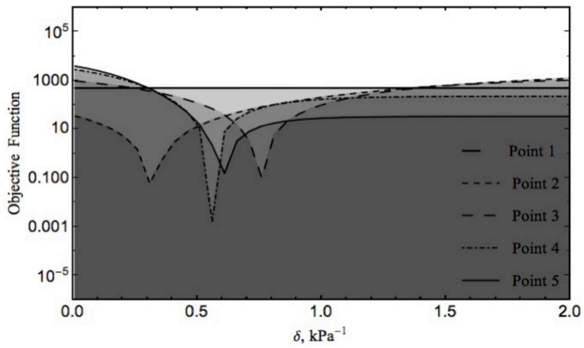

Figure 11. Minimization of the ER(ψ) function for Points 1 to 5 (Soil 2).

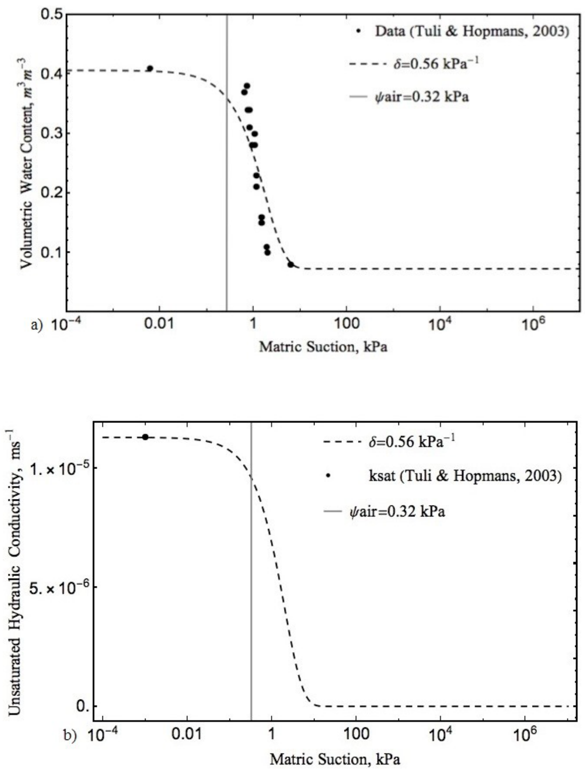

Figure 12. (a) SWRC and (b) unsaturated hydraulic conductivity function for the value of δ obtained by minimization Soil 2.

By using the δ value obtained, it is feasible to generate the SWRC (Figure 12a) and the unsaturated hydraulic conductivity curve (Figure 12b) for Soil 2. Additionally, the air-entry point (ψ_{air} = 0.32 kPa), determined using Equation 4, can be identified.

The outcomes illustrated in Figures 12a and 12b for Soil 2 demonstrate a consistent agreement with the findings obtained for Soil 1. Therefore, it is feasible to represent the SWRC and unsaturated hydraulic conductivity function using indirect measurements. The hydrogeophysical model proposed in this study was validated by TDR measurements for soil with low electrical resistivity.

5. Conclusion

A semi-analytical unsaturated hydrogeophysical constitutive model was formulated, which integrates aspects of geotechnics, hydrogeology, petrophysics, and geophysics. The purpose of this model is to enhance hydrogeological characterization and soil matrix monitoring. The model enables indirect estimation of soil water retention and unsaturated hydraulic conductivity curves by using direct current electrical resistivity measurements (as applied in this study) and TDR measurements (based on literature data from Tuli & Hopmans (2003)). The model is founded on the integration of hydromechanical and petrophysical models, thereby providing a means of describing soil hydrogeophysical characteristics that are crucial to civil engineering projects.

The estimation of the *ERCC* and unsaturated hydraulic conductivity as a function of electrical resistivity has significant practical applications. The effectiveness of the proposed model was verified through examination of a granular material characterized from geotechnical, geophysical, and hydrodynamic perspectives. Using direct measurements and minimizing the objective function, the hydraulic and petrophysical parameters governing the soil-water retention and unsaturated hydraulic conductivity curves as a function of matric suction were ascertained. Remarkably, the model outputs exhibited good agreement with experimental data.

The laboratory experiments conducted in Case Studies 1 and 2 utilized low-cost instrumentation and TDR, respectively, and yielded satisfactory outcomes, thus proving the practical feasibility of these methods for monitoring the state of soils over extensive spatial and temporal scales. Moreover, indirect measurement of soil properties can facilitate high-density spatial sampling of soils and the ability to rapidly and indirectly determine soil conditions, while being more cost-effective compared to direct measurement methods.

The petrophysical parameters determined for the soils provide insight into their physical conditions. For Case Study 1 (medium sand), the hydraulic parameter value is lower compared to that in Case Study 2, resulting in different air-entry values. In contrast, for Case Study 2 (fine sand), the parameters governing the degree of cementation and tortuosity are higher than those in Case Study 1.

The findings of this study may prove valuable to researchers involved in geoscience/geophysics, civil engineering/geotechnology, and agronomy, as they can benefit greatly from the ability to rapidly and indirectly determine soil conditions based on either the SWRC or unsaturated hydraulic conductivity function.

Readers intending to utilize this model should take note that the theoretical framework was based on simplifications regarding water distribution in the soil, the absence of clay in the soil, and fixed values of void ratio, porosity, and specific mass. Therefore, the model may need to be adjusted for soils containing clay or demonstrating significant surface conduction. Also, to broaden the scope of the model, additional laboratory tests are recommended to validate its applicability.

Acknowledgements

This study was financed in part by the Coordination for the Improvement of Higher Education Personnel (CAPES - Finance Code 001). The authors also acknowledge the support of the National Council for Scientific and Technological Development (CNPq - Grant 305484/2020-6), the Foundation for Research Support of the Federal District (FAPDF - Grant 00193.00000920/2021-12), the National Electric Energy Agency (ANEEL) and its R&D partners Neoenergia/CEB Distribuição S.A. (AINOA: A System to Monitor Internal Pathologies in Earth and Rockfill Dams Based on Artificial Intelligence and Internet-of-Things: A Case study of the Paranoá Dam-Grant number PD-05160- 1904/2019, contract CEBD782/2019), the EMBRAPA Instrumentação (Acordo de Cooperação, DOU nº 240, 22 de dezembro de 2022) and the University of Brasília, including the Laboratory of the Physics and Chemistry of Soils of the School of Agronomy, the Laboratory of Applied Geophysics, and the Laboratory of Geochemistry of the Institute of Geosciences.

Declaration of interest

The authors have no conflict of interest regarding the matter included in this paper. All co-authors have observed and affirmed the contents of the paper and there is no financial interest to report.

Authors' contributions

Manuelle Santos Góis: conceptualization, methodology, formal analysis, writing – original draft, Writing – review & editing, Investigation. Katherin Rocio Cano Bezerra da Costa: methodology, formal analysis, writing – original draft, writing – review & editing, Investigation. André Luís Brasil Cavalcante: conceptualization, formal analysis, writing – original draft, writing – review & editing, Investigation.

Data availability

All data produced or examined in the course of the current study are included in this article.

List of symbols

g	Gravitational acceleration
k_{sat}	Saturated hydraulic conductivity of the soil
$k_z(\theta)$	Function of the unsaturated hydraulic conductivity in terms of the volumetric water content in the z-direction
m	Cementation exponent
n	Porosity
p	Saturation exponent
t	Time
z	Direction
DC	Direct current
EC	Electrical conductivity
EC_w	Fluid electrical conductivity
ER	Electrical resistivity
ERC	Computed values electrical resistivity
$ERCC$	Electrical Resistivity Characteristic Curve
ERM	Experimentally measured electrical resistivity
ER_w	Fluid electrical resistivity
S_w	Fractional water saturation
$SWRC$	Soil Water Retention Curve
TDR	Time Domain Reflectometry
δ	Hydraulic adjustment parameter
θ	Volumetric soil water content
θ_r	Volumetric soil water content in the residual state
$\theta_s - \theta_r$	Maximum soil wetting capacity
θ_s	Volumetric soil water content in the saturated state
ρ_w	Water density
τ	Tortuosity
ψ	Soil suction
ψ_{air}	Air-entry soil suction
$\partial\psi/\partial\theta$	Variation in the matric suction in relation to the volumetric water content

References

ABNT NBR 6457. (2016). *Amostras de Solo — Preparação para Ensaios de Compactação e Ensaios de Caracterização*. ABNT - Associação Brasileira de Normas Técnicas, Rio de Janeiro, RJ.

Albuquerque, E.A.C., Borges, L.P.D.F., Cavalcante, A.L.B., & Machado, S.L. (2022). Prediction of soil water retention curve based on physical characterization parameters using machine learning. *Soils and Rocks*, 45(3), e2022000222. http://dx.doi.org/10.28927/SR.2022.000222.

Archie, G.E. (1942). The electrical resistivity log as an aid in determining some reservoir characteristics. *Transactions of the AIME*, 146(1), 54-62. https://doi.org/10.2118/942054-G.

ASTM D2216-19. (2010). *Standard Test Methods for Laboratory Determination of Water (Moisture) Content of Soil and Rock by Mass*. ASTM International, West Conshohocken, PA. https://doi.org/10.1520/D2216-19.

Binley, A., Hubbard, S.S., Huisman, J.A., Revil, A., Robinson, D.A., Singha, K., & Slater, L.D. (2015). The emergence of hydrogeophysics for improved understanding of subsurface processes over multiple scales. *Water Resources Research*, 51(6), 3837-3866. http://dx.doi.org/10.1002/2015WR017016.

Briaud, J.L. (2013). *Geotechnical engineering: unsaturated and saturated soils*. John Wiley & Sons. https://doi.org/10.1002/9781118686195.

Brooks, R.H., & Corey, A.T. (1964). *Hydraulic properties of porous media* (Hydrology Papers, No. 3). Colorado State University.

Butler, D.K. (2005). *Near-surface geophysics* (SEG investigations in geophysics series, No. 13). Society of Exploration Geophysicists. https://doi.org/10.1190/1.9781560801719.

Camapum de Carvalho, J., & Gitirana Junior, G.D.F. (2021). Unsaturated soils in the context of tropical soils. *Soils and Rocks*, 44, 1-25. http://dx.doi.org/10.28927/SR.2021.068121.

Carbajal, E.J., Diniz, M.D.S., Rodriguez-Pacheco, R.L., & Cavalcante, A.L.B. (2022). Contaminant transport model in transient and unsaturated conditions applied to laboratory column test with tailings. *Soils and Rocks*, 45, e2022076021. http://dx.doi.org/10.28927/SR.2022.076021.

Cardoso, R., & Dias, A.S. (2017). Study of the electrical resistivity of compacted kaolin based on water potential. *Engineering Geology*, 226, 1-11. http://dx.doi.org/10.1016/j.enggeo.2017.04.007.

Cavalcante, A.L.B., & Mascarenhas, P.V.S. (2021). Efficient approach in modeling the shear strength of unsaturated soil using soil water retention curve. *Acta Geotechnica*, 16, 3177-3186. http://dx.doi.org/10.1007/s11440-021-01144-6.

Cavalcante, A.L.B., & Zornberg, J.G. (2017). Efficient approach to solving transient unsaturated flow problems. I: analytical solutions. *International Journal of Geomechanics*, 17(7), 04017013-1-04017013-17. http://dx.doi.org/10.1061/(ASCE)GM.1943-5622.0000875.

Cavalcante, A.L.B., Borges, L.P.D.F., & Zornberg, J.G. (2019). New 3D analytical solution for modeling transient unsaturated flow due to wetting and drying. *International Journal of Geomechanics*, 19(7), 04019077. http://dx.doi.org/10.1061/(ASCE)GM.1943-5622.0001461.

Cho, S.E. (2016). Stability analysis of unsaturated soil slopes considering water-air flow caused by rainfall infiltration. *Engineering Geology*, 211, 184-197. http://dx.doi.org/10.1016/j.enggeo.2016.07.008.

Chou, Y., & Wang, L. (2021). Soil-water characteristic curve and permeability coefficient prediction model for unsaturated loess considering freeze-thaw and dry-wet. *Soils and Rocks*, 44(1), e2021058320. http://dx.doi.org/10.28927/SR.2021.058320.

Costa, M.B.A.D., & Cavalcante, A.L.B. (2020). Novel approach to determine soil–water retention surface. *International Journal of Geomechanics*, 20(6), 04020054-1-04020054-9. http://dx.doi.org/10.1061/(ASCE)GM.1943-5622.0001684.

Crawford, M.M., Bryson, L.S., Woolery, E.W., & Wang, Z. (2019). Long-term landslide monitoring using soil-water relationships and electrical data to estimate suction stress. *Engineering Geology*, 251, 146-157. http://dx.doi.org/10.1016/j.enggeo.2019.02.015.

Dane, J.H., & Topp, G.C. (2002). *Methods of soil analysis, Part 4 physical methods*. Soil Science Society of America, Inc. https://doi.org/10.2136/sssabookser5.4.

Datsios, Z.G., Mikropoulos, P.N., & Karakousis, I. (2017). Laboratory characterization and modeling of DC electrical resistivity of sandy soil with variable water resistivity and content. *IEEE Transactions on Dielectrics and Electrical Insulation*, 24(5), 3063-3072. http://dx.doi.org/10.1109/TDEI.2017.006583.

Di Maio, R., Piegari, E., Todero, G., & Fabbrocino, S. (2015). A combined use of Archie and van Genuchten models for predicting hydraulic conductivity of unsaturated pyroclastic soils. *Journal of Applied Geophysics*, 112, 249-255. http://dx.doi.org/10.1016/j.jappgeo.2014.12.002.

Doussan, C., & Ruy, S. (2009). Prediction of unsaturated soil hydraulic conductivity with electrical conductivity. *Water Resources Research*, 45(10), W10408. http://dx.doi.org/10.1029/2008WR007309.

Ewing, R.P., & Hunt, A.G. (2006). Dependence of the electrical conductivity on saturation in real porous media. *Vadose Zone Journal*, 5(2), 731-741. http://dx.doi.org/10.2136/vzj2005.0107.

Fredlund, D.G. (2021). Myths and misconceptions related to unsaturated soil mechanics. *Soils and Rocks*, 44(3), e2021062521. http://dx.doi.org/10.28927/SR.2021.062521.

Fredlund, D.G., & Rahardjo, H. (1993). *Soil mechanics for unsaturated soils*. John Wiley & Sons. https://doi.org/10.1002/9780470172759.

Fredlund, D.G., & Xing, A. (1994). Equations for the soil-water characteristic curve. *Canadian Geotechnical Journal*, 31(4), 521-532. http://dx.doi.org/10.1139/t94-061.

Friedman, S.P. (2005). Soil properties influencing apparent electrical conductivity: a review. *Computers and Electronics in Agriculture*, 46(1-3), 45-70. http://dx.doi.org/10.1016/j.compag.2004.11.001.

Fu, Y., Horton, R., & Heitman, J.L. (2021a). Estimation of soil water retention curves from soil bulk electrical conductivity and water content measurements. *Soil & Tillage Research*, 209, http://dx.doi.org/10.1016/j.still.2021.104948.

Fu, Y., Horton, R., Ren, T., & Heitman, J.L. (2021b). A general form of Archie's model for estimating bulk soil electrical conductivity. *Journal of Hydrology (Amsterdam)*, 597, http://dx.doi.org/10.1016/j.jhydrol.2021.126160.

Glover, P.W.J. (2010). A generalized Archie's law for n phases. *Geophysics*, 75(6), E247-E265.

Glover, P.W.J. (2015). 11.04–geophysical properties of the near surface earth: electrical properties. In G. Schubert (Ed.), *Treatise on geophysics* (Vol. 11, pp. 89-137). https://doi.org/10.1016/B978-0-444-53802-4.00189-5.

Glover, P.W.J., Hole, M.J., & Pous, J. (2000). A modified Archie's law for two conducting phases. *Earth and Planetary Science Letters*, 180(3-4), 369-383. http://dx.doi.org/10.1016/S0012-821X(00)00168-0.

Hinnell, A.C., Ferré, T.P.A., Vrugt, J.A., Huisman, J.A., Moysey, S., Rings, J., & Kowalsky, M.B. (2010). Improved extraction of hydrologic information from geophysical data through coupled hydrogeophysical inversion. *Water Resources Research*, 46(4), http://dx.doi.org/10.1029/2008WR007060.

Hong-jing, J., Shun-qun, L., & Lin, L. (2014). The relationship between the electrical resistivity and saturation of unsaturated soil. *The Electronic Journal of Geotechnical Engineering*, 19, 3739-3746.

Hubbard, S.S., & Rubin, Y. (2005). Introduction to hydrogeophysics. In Y. Rubin & S.S. Hubbard (Eds.), *Hydrogeophysics. Water Science and Technology Library* (pp. 3-21). Springer. https://doi.org/10.1007/1-4020-3102-5_1.

Keller, G.V. (1988). 2. Rock and mineral properties. In M.N. Nabighian (Ed.), *Electromagnetic methods in applied geophysics* (pp. 13-52). Society of Exploration Geophysicists. https://doi.org/10.1190/1.9781560802631.ch2.

Keller, G.V., & Frischknecht, F.C. (1966). *Electrical methods in geophysical prospecting*. Pergamon Press.

Kibria, G., & Hossain, M.S. (2012). Investigation of geotechnical parameters affecting electrical resistivity of compacted clays. *Journal of Geotechnical and Geoenvironmental Engineering*, 138(12), 1520-1529. http://dx.doi.org/10.1061/(ASCE)GT.1943-5606.0000722.

Kong, L.W., Sayem, H.M., Zhang, X.W., & Yin, S. (2017). Relationship between electrical resistivity and matric suction of compacted granite residual soil. In *Proceedings of the PanAm unsaturated soils 2017: swell-shrink and tropical soils* (pp. 430-439). ASCE. https://doi.org/10.1061/9780784481707.043.

Lai, W., & Ogden, F.L. (2015). A mass-conservative finite volume predictor–corrector solution of the 1D Richards' equation. *Journal of Hydrology (Amsterdam)*, 523, 119-127. http://dx.doi.org/10.1016/j.jhydrol.2015.01.053.

Lesmes, D.P., & Friedman, S.P. (2005). Relationships between the electrical and hydrogeological properties of rocks and soils. In Y. Rubin & S. S. Hubbard (Eds.), Hydrogeophysics (pp. 87-128). Water Science and Technology Library. https://doi.org/10.1007/1-4020-3102-5_4.

Libardi, P.L. (2005). *Dinâmica da água no solo* (Vol. 61). Edusp.

Lima, O.A.L. (2014). *Propriedades físicas das rochas–bases da geofísica aplicada*. Sociedade Brasileira de Geofísica.

Liu, H.H. (2017). Theory and applications of transport in porous media. In S. Majid Hassanizadeh & J. Bear (Eds.), *Fluid flow in the subsurface. History, generalization and applications of physical laws* (Vol. 28). Springer.

Lu, D., Wang, H., Huang, D., Li, D., & Sun, Y. (2020). Measurement and estimation of water retention curves using electrical resistivity data in porous media. *Journal of Hydrologic Engineering*, 25(6), http://dx.doi.org/10.1061/(ASCE)HE.1943-5584.0001925.

Mawer, C., Knight, R., & Kitanidis, P.K. (2015). Relating relative hydraulic and electrical conductivity in the unsaturated zone. *Water Resources Research*, 51(1), 599-618. http://dx.doi.org/10.1002/2014WR015658.

Mualem, Y., & Friedman, S.P. (1991). Theoretical prediction of electrical conductivity in saturated and unsaturated soil. *Water Resources Research*, 27(10), 2771-2777. http://dx.doi.org/10.1029/91WR01095.

Niu, Q., Fratta, D., & Wang, Y.H. (2015). The use of electrical conductivity measurements in the prediction of hydraulic conductivity of unsaturated soils. *Journal of Hydrology (Amsterdam)*, 522, 475-487. http://dx.doi.org/10.1016/j.jhydrol.2014.12.055.

Piegari, E., & Di Maio, R. (2013). Estimating soil suction from electrical resistivity. *Natural Hazards and Earth System Sciences*, 13(9), 2369-2379. http://dx.doi.org/10.5194/nhess-13-2369-2013.

Revil, A., Karaoulis, M., Johnson, T., & Kemna, A. (2012). Review: some low-frequency electrical methods for subsurface characterization and monitoring in hydrogeology. *Hydrogeology Journal*, 20(4), 617-658. http://dx.doi.org/10.1007/s10040-011-0819-x.

Rhoades, J.D., Raats, P.A.C., & Prather, R.J. (1976). Effects of liquid-phase electrical conductivity, water content, and surface conductivity on bulk soil electrical conductivity. *Soil Science Society of America Journal*, 40(5), 651-655. http://dx.doi.org/10.2136/sssaj1976.03615995004000050017x.

Richards, L.A. (1931). Capillary conduction of liquids through porous mediums. *Physics*, 1(5), 318-333. http://dx.doi.org/10.1063/1.1745010.

Rinaldi, V.A., & Cuestas, G.A. (2002). Ohmic conductivity of a compacted silty clay. *Journal of Geotechnical and Geoenvironmental Engineering*, 128(10), 824-835. http://dx.doi.org/10.1061/(ASCE)1090-0241(2002)128:10(824).

Santamarina, J.C., Klein, A., & Fam, M.A. (2001). Soils and waves: particulate materials behavior, characterization and process monitoring. *Journal of Soils and Sediments*, 1(2), 130. http://dx.doi.org/10.1007/BF02987719.

Shah, P.H., & Singh, D.N. (2005). Generalized Archie's law for estimation of soil electrical conductivity. *Journal of ASTM International*, 2(5), 1-20. http://dx.doi.org/10.1520/JAI13087.

Sheng, D., Gens, A., Fredlund, D.G., & Sloan, S.W. (2008). Unsaturated soils: from constitutive modelling to numerical algorithms. *Computers and Geotechnics*, 35(6), 810-824. http://dx.doi.org/10.1016/j.compgeo.2008.08.011.

Singha, K., Day-Lewis, F.D., Johnson, T., & Slater, L.D. (2014). Advances in interpretation of subsurface processes with time-lapse electrical imaging. *Hydrological Processes*, 29(6), 1549-1576. http://dx.doi.org/10.1002/hyp.10280.

Telford, W.M., Geldart, L.P., & Sheriff, R.E. (1990). *Applied geophysics*. Cambridge University Press. https://doi.org/10.1017/CBO9781139167932.

Tuli, A., & Hopmans, J.W. (2003). Effect of degree of fluid saturation on transport coefficients in disturbed soils. *European Journal of Soil Science*, 55(1), 147-164. http://dx.doi.org/10.1046/j.1365-2389.2002.00493.x-i1.

van Genuchten, M.T. (1980). A closed-form equation for predicting the hydraulic conductivity of unsaturated soils. *Soil Science Society of America Journal*, 44(5), 892-898. http://dx.doi.org/10.2136/sssaj1980.03615995004400050002x.

Zhang, Z., Wang, W., Yeh, T.C.J., Chen, L., Wang, Z., Duan, L., An, K., & Gong, C. (2016). Finite analytic method based on mixed-form Richards' equation for simulating water flow in vadose zone. *Journal of Hydrology (Amsterdam)*, 537, 146-156. http://dx.doi.org/10.1016/j.jhydrol.2016.03.035.

TECHNICAL NOTES

Soils and Rocks
An International Journal of Geotechnical and Geoenvironmental Engineering
www.soilsandrocks.com
ISSN 1980-9743
ISSN-e 2675-5475

Dosage method for unconfined strength and fatigue life of fiber-reinforced cement-treated sand

Hernando da Rocha Borges[1], Marina Paula Secco[1], Giovani Jordi Bruschi[1#], Lucas Festugato[1]

Technical Note

Keywords
Polypropylene fibers
Portland cement
Soil-cement
Fatigue life
Rational dosage methodology

Abstract
Fiber-reinforcement has been reported as an effective and cost-attractive technique to improve the mechanical behavior of cemented soils. However, the dosage methodologies for these mixtures are still limited, especially regarding dynamic loading. The objective of this research was to analyze the dynamic response and strength behavior of fiber-reinforced cement-treated sand. In this sense, fatigue life, unconfined compressive strength, and split tensile strength tests were conducted. Results indicated that the mechanical behavior of the soil-cement mixtures was governed by fiber content, cement content and void ratio. The presence of fibers, the increase in cement content and the decrease in void ratio improved the overall mechanical behavior of all specimens. The porosity/cement content index resulted in a viable dosage method to predict both the monotonic and cyclic behavior of the mixtures. Lastly, the statistical analysis of variance corroborated the experimentally observed findings.

1. Introduction

Fiber-reinforcement and Portland cement stabilization have been widely utilized to improve the engineering properties of soils structures, such as embankments (Bieliatynskyi et al., 2021; Zhao et al., 2021) and subgrade stabilization for footings (Nasr, 2014), pavements (Li et al., 2022; Ozturk & Ozyurt, 2022), earth dams (Sangma & Tripura, 2020), and barriers for landfills and containment pounds (Mukherjee & Kumar Mishra, 2021). Cement addition increases strength and stiffness of the soils (Bruschi et al., 2022; Bruschi, Santos, Ferrazzo, et al., 2023; Queiróz et al., 2022; Quiñónez Samaniego et al., 2021); however, it also increases brittleness, leading the enhanced soil to fail in a brittle way (Consoli et al., 2007, 2021a). On the other hand, fiber addition increases the ductility and durability of the reinforced soil without compromising the strength of the composite (Festugato et al., 2017). The addition of fibers to cemented soils has been reported as an effective and cost attractive technique to increase the mechanical characteristics such as strength, ductility, and post-rupture bearing capacity (Chen et al., 2015; Consoli et al., 2009a, 2009b, 2011a). Even though fiber-reinforcement has been proved effective, dosage methodologies for these mixtures are still limited.

Consoli et al. (2010) created the first rational dosage methodology for fiber-reinforced cemented soil, considering the porosity/cement content ratio (η/C_{iv}), as an appropriate parameter to evaluate the unconfined compressive strength (q_u). Later, Consoli et al. (2013) quantified the influence of the amount of cement, the porosity and the porosity/cement ratio in the assessment on tensile strength (q_t) and compressive strength (q_u) of fiber-reinforced artificially cemented sand, as well as in the changes of q_t/q_u relationships and particular increases in q_t and q_u due to fiber insertion. Festugato et al. (2017) studied a dosage methodology based on the tensile and compressive strength of fiber-reinforced cemented soils, considering the fiber length. Authors indicated that the length of the filaments and the porosity/cement ratio are key parameters in the evaluation of the tensile strength and the compressive strength of the mixture studied. For each fiber length, there is a linear proportionality between the tensile and compressive strength, being independent of the porosity/cement ratio. As a consequence, rational dosing methodologies can be centered on tensile or compression tests on reinforced or unreinforced samples.

Despite these extensive findings, most of the experimental work regarding the mechanical behavior of fiber-reinforced cemented soils and their dosage methodologies entails exclusively the analysis of these composites under monotonic/static loading. The porosity/cement content ratio (η/C_{iv}) dosage framework has recently started to be investigated for mixtures under dynamic loading. Festugato et al. (2021) studied mixtures of unreinforced cemented sand and showed such ratio was able to assess resilient modulus and fatigue life. Piuzzi et al. (2021) observed the porosity/cement ratio could be used for the assessment of asphalt concrete mixtures mechanical behavior under cyclic loading.

[1]Universidade Federal do Rio Grande do Sul, Programa de Pós-graduação em Engenharia Civil, Porto Alegre, RS, Brasil.
[#]Corresponding author. E-mail address: gio.bruschi@gmail.com

Submitted on June 29, 2022; Final Acceptance on April 27, 2023; Discussion open until November 30, 2023.

https://doi.org/10.28927/SR.2023.007322

However, the use of η/Civ has not yet been investigated for the study of fiber reinforced cement mixtures behavior under not monotonic loading. Dynamic loading is especially important on pavement design, reinforcement of areas susceptible to earthquakes, foundations of coastal structures, and even wind turbines. Pavements design, for instance, usually considers the fatigue life of the subgrade constituent materials. Fatigue is the process of localized progressive permanent structural change which occurs in a point of the material subjected to stresses of variable amplitude, below the ultimate strength of the material, that causes cracks that lead to failure after a certain number of cycles (ASTM, 2013).

In this sense, the objective of this research was to analyze dynamic response and strength behavior of fiber-reinforced cement-treated sand. To that extent, fatigue life, unconfined compressive strength, and split tensile strength tests were conducted on fiber-reinforced and non-reinforced cemented mixtures. In addition, all results were correlated with the porosity/cement content index to create a rational dosage methodology for the stabilized mixtures.

2. Materials and methods

2.1 Materials

The soil utilized in this research was a clean sand, known as Osorio sand (*OS*). The material was collected nearby Porto Alegre, in southern Brazil. *OS* was classified as a poorly graded sand (*SP*) in accordance with the Unified Soil Classification System (*USCS*) (ASTM, 2020) with a specific weight of grains of 2.65 g/cm^3 [D854 (ASTM, 2014)]. This sand is composed of approximately 99.5% quartz (Consoli et al., 2009a). For the cementing agent, high initial strength Portland cement (type III) was utilized, with a specific weight of grains of 3.15 g/cm^3. This cement was selected considering its high capacity of generating considerable strength over short periods of time. Regarding the fiber-reinforcement, monofilament polypropylene fibers were applied. These fibers presented average dimensions of 50 mm length and 0.1 mm diameter, with a specific weight of grains of 0.91 g/cm^3, elastic modulus of 3 GPa, tensile strength of 120 MPa, and strain failure of 80%. The materials physical properties are summarized in Table 1, while Figure 1 shows the grain size distribution.

2.2 Molding and curing procedures

For unconfined compressive strength and split tensile strength tests, triplicates of specimens of 10 cm diameter and 20 cm in height were utilized. As for fatigue life tests, duplicates of cylindrical specimens of 10 cm in diameter and 5 cm in height were applied. The cement addition was 1, 2, 3, 5, and 7%, in accordance with the indications of the Portland Cement Association (PCA, 1992) and previous studies (Consoli et al., 2020; Consoli & Tomasi, 2018). The fiber addition was 0.5% for all samples. Previous studies shown the increase of fiber content improves materials mechanical behavior up to a limit, from which mixing and compaction processes become not effective and reinforcement benefits are negatively affected. For the studied polypropylene fibers, considering mixture preparation and compaction, an optimum value of 0.5% observed (e.g. Festugato et al., 2018, 2021). To explore a wide range of porosities and its effect on the mechanical properties, three void ratios were also selected (0.64, 0.70, and 0.78) based on Proctor compaction tests under standard energy (ASTM, 2021). All specimens were molded with the 9% optimum moisture content from the compaction tests. The fiber reinforced compacted cemented soil specimens were prepared by hand-mixing, in this order, dry soil, cement, water and polypropylene fibers. It was found important to add water prior the addition of fibers to prevent their floating. The quantity of fibers for each mixture was calculated by the mass of dry soil plus cement.

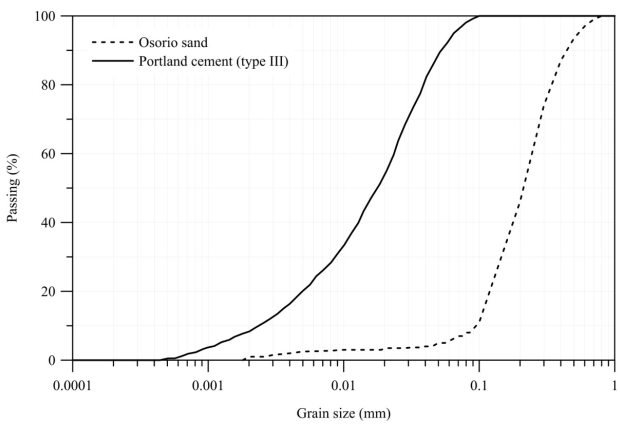

Figure 1. Grain size distribution.

Table 1. Materials physical properties.

Properties	Osorio Sand	Portland cement	Polypropylene fiber
Mineralogy	Quartz	-	-
Specific unit weight of grains (g.cm^{-3})	2.65	3.15	0.91
Medium sand (%)	33	-	-
Fine sand (%)	67	-	-
USCS classification (ASTM, 2020)	SP	-	-

Visual and microscope examination of exhumed specimens showed the mixtures to be satisfactorily uniform. The molding procedures followed the undercompaction method proposed by Ladd (1978). After confection specimens were measured and stored at 23 ± 2°C and 95 ± 2% controlled moisture for 7 days curing. The acceptance criteria were as follows: degree of compaction between 99% and 101%; water content within 0.5% of the target value; diameter within 0.5 mm of the target value; and height within 1 mm of the target value. Figure 2 depicts the aspect of a prepared specimen after fatigue life testing.

2.3 Unconfined compressive strength (*qu*)

Unconfined compression strength (*qu*) tests were conducted in accordance with the procedures of ASTM D2166 (ASTM, 2016), with an automatic loading machine (50 kN load capacity and 1.14mm/min displacement rate).

2.4 Split tensile strength (*qt*)

Split tensile strength tests (*qt*) tests were conducted in accordance with the procedures of ASTM D6931 (ASTM, 2017); performed in an automatic loading machine with a maximum load capacity of 50 kN, with a ring of 10 kN load capacity and resolution of 0.005 kN.

2.5 Fatigue life (*Nf*)

Fatigue life tests were conducted in accordance with the procedures of BS EN 12697-24 (BSI, 2016). The cyclic load (haversine-shaped pulse of 2 Hz) was applied with a pneumatic load machine. The magnitude of the applied load was 90% of the specimens' tensile strength. A 10 kN loading cell with a resolution of 0.0001 kN was employed to measure the applied load. In addition, two linear variable differential transformers (*LVDT*) located on the opposite side of the specimens, were responsible to measure radial displacements with a resolution of 0.001 mm.

2.6 Porosity/cement content index (η/Civ)

Resilient modulus, split tensile strength, and durability results were also expressed in function of the porosity/cement index proposed by Consoli et al. (2007) and defined by Equations 1 and 2.

$$\eta = 100 - 100\left\{\left[\frac{\gamma_d}{\frac{OS}{100}+\frac{F}{100}}\right]\left[\frac{\frac{OS}{100}}{\gamma_{s_{OS}}}+\frac{\frac{F}{100}}{\gamma_{s_F}}\right]\right\} \tag{1}$$

$$Civ = \frac{V_C}{V} = \frac{m_C / \gamma_{s_C}}{V} \tag{2}$$

Porosity (η) is a function of the dry unit weight (γ_d) and unit weight of solids (γs_{OS} and γs_F) of the Osorio sand (*OS*) and the fibers (*F*). The cement content (*Civ*) results from the volume occupied by Portland cement (*PC)* divided by the total volume of the sample. This index allows the unification of all experiments in a single relation, resulting in a rational dosage methodology for cemented soil mixtures. However, such equations are valid for the cemented mixtures studied herein and are only functional if the boundary conditions of the applied variables are ensured.

3. Results and discussion

3.1 Unconfined compressive strength (*qu*)

The unconfined compressive strength results are presented in Figure 3. The data was presented as a function of the porosity/cement content index (η/Civ).

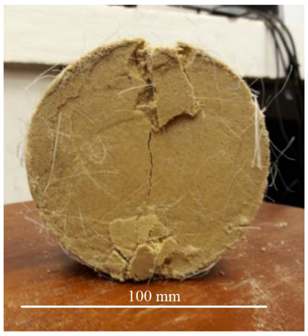

Figure 2. Typical aspect of tested specimen.

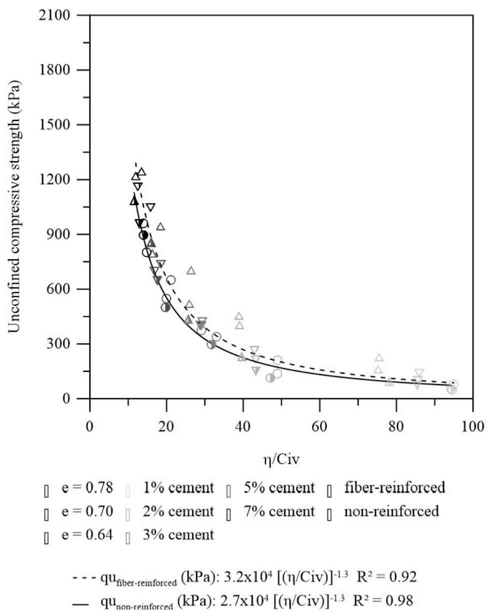

Figure 3. Unconfined compressive strength.

For all studied combinations, the increase in cement content and decrease in porosity (lower η/Civ values) resulted in higher *qu*. Cement content presented a considerable effect on *qu*, for both unreinforced and fiber-reinforced specimens. The increase in cement content (1% to 2% and latter to 3%, 5% and 7%) also increased the hydrated products of the mixture, contributing to the further development of a stiffer soil-cement matrix and, consequently, an increase in strength (Consoli et al., 2007, 2011b; Festugato et al., 2018); a small addition of cement was enough to generate significant gains in strength. Regarding the porosity effect, the reduction in mixtures void ratio resulted in an increase in the rate of *qu* gain with cement content (Carvalho Queiróz et al., 2022; Pereira dos Santos et al., 2022; Queiróz et al., 2022). At lower porosities the contact area between particles is enlarged, enhancing the interlocking phenomenon and friction mobilization resulting in an increase in strength, and so the effectiveness of the cement and the fibers is greater (Festugato et al., 2017). This physical-chemical phenomenon has also been evidenced in different cemented geotechnical materials (Bruschi et al., 2021; Carvalho Queiróz et al., 2022; Pereira dos Santos et al., 2022; Quiñónez Samaniego et al., 2021; Silva et al., 2022; Tonini de Araújo et al., 2021; Bruschi et al., 2023).

When comparing non-reinforced and fiber-reinforced specimens, the average *qu* of reinforced specimens was 18% higher than non-reinforced ones, indicating that fiber addition contributed for strength development. Consoli et al. (2009b) claim that the efficiency of fiber reinforcement is governed by several factors, such as: fiber content, orientation, geometry, mechanical characteristics, and properties of the soil such as grading, mineralogy, and grain shape. Fiber reinforcement in cemented soils is only effective when the fiber length is large when compared to the grain size of the soil (Michalowski, 2008; Michalowski & Čermák, 2003). Furthermore, Festugato et al. (2017) indicated that an increase of fiber reinforcement length directly improves the strength of cemented soils.

Fair correlations were identified between the η/Civ index and *qu*, as shown by Equations 3 and 4. For the non-reinforced mixtures the determination coefficient (R^2) was 0.98, while for the reinforced ones the coefficient was 0.92. This suggests that through these equations it becomes possible to predict the *qu* of the fiber-reinforced cement-treated mixtures over a wide range of porosities and cement contents, avoiding unnecessary testing on practical soil-cement applications. Furthermore, this index has also been shown to work on the prediction of *qu* in different fiber-reinforced cemented soils (Consoli et al., 2011a, 2017a; Mazhar & GuhaRay, 2021).

Unreinforced cemented mixture:

$$qu\ (\text{kPa}) = 2.7\times10^4\left[\left(\eta/_{\text{Civ}}\right)\right]^{-1.3} \tag{3}$$

Fiber-reinforced cemented mixture:

$$qu\ (\text{kPa}) = 3.2\times10^4\left[\left(\eta/_{\text{Civ}}\right)\right]^{-1.3} \tag{4}$$

3.2 Split tensile strength (*qt*)

Results of split tensile strength tests are presented in Figure 4. Once again, the data was expressed in function of the porosity/cement content index *(η/Civ)*.

As in the case of the compressive strength results, the decrease in the porosity/cement content index led to an increase in split tensile strength. The mechanism by which the reduction in porosity influences the soil-cement strength is again related to the existence of a larger contact area between particles of the cemented mixture, enhancing the interlocking phenomenon. As for the cement content, its increase enhances the cementitious reactions happening on the mixtures, contributing for strength development (Piuzzi et al., 2021).

The average *qt* of reinforced specimens was 20% higher than non-reinforced ones, indicating that fiber addition also contributed for split tensile strength development. Fiber-reinforcement seems to be more efficient for tensile strength than for compressive strength; similar findings were presented by Festugato et al. (2017), while studying the compressive and tensile strength of fiber-reinforced soils.

Adequate correlations between split tensile strength and η/Civ index were shown for all studied combinations. The determination coefficients (R^2) were 0.94 and 0.92 for the unreinforced and fiber-reinforced specimens, respectively, indicating the viability of the η/Civ index on the prediction of the split tensile strength for the analyzed conditions.

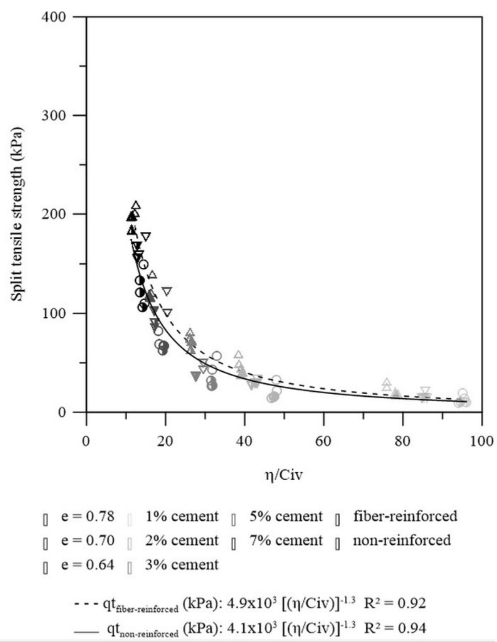

Figure 4. Split tensile strength.

This viability has also been proven for other cemented geotechnical materials (Consoli et al., 2016, 2017b, 2018, 2021b; Piuzzi et al., 2021).

Unreinforced cemented mixture:

$$qt\ (\text{kPa}) = 4.1\times10^{3}\left[\left(\eta/_{\text{Civ}}\right)\right]^{-1.3} \tag{5}$$

Fiber-reinforced cemented mixture:

$$qt\ (\text{kPa}) = 4.9\times10^{3}\left[\left(\eta/_{\text{Civ}}\right)\right]^{-1.3} \tag{6}$$

3.3 Fatigue life (*Nf*)

Fatigue life results are presented in Figure 5 also expressed in function of the porosity/cement content index *(η/Civ)*.

Analogous to the behavior evidenced for split tensile and compressive strength, a reduction in porosity and increase in cement content led to the improvement of fatigue life for both fiber-reinforced and non-reinforced specimens. This behavior is attributed to the greater friction mobilization and higher contact area between particles, as the porosity decreases and cement content increases. Similar trends have also been reported for fatigue life studies (Consoli et al., 2021c; Piuzzi et al., 2021).

Regarding the effect of fiber reinforcement, non-reinforced specimens resulted in average *Nf* values 78% lower than fiber reinforced ones. The cement addition increases strength of soil; however, it also increases brittleness, which leads to brittle-like failure. In opposition, fiber addition increases the ductility of the cemented soil, without considerably compromising its strength. In the case of this research, fiber addition enhanced the bridging effect between particles, playing a critical role in the initiation and extension of cracks. This effect can be related to the hydrophilic characteristics and surface roughness of the fibers (Consoli et al., 2012; Festugato et al., 2017). The inclusion of fibers was able to mitigate internal stresses in distinctive orientations, contributing for a more distributed stress field, thus avoiding local fractures.

Satisfactory correlations were identified for both non-reinforced and fiber reinforced specimens and the η/Civ index. For both the non-reinforced and fiber reinforced specimens, R^2 was 0.9. The elevated R^2 indicate the viability of the index in also predicting *Nf* of the cemented mixtures, providing a rational dosage methodology for a wide range of porosities and cement contents.

Unreinforced cemented mixture:

$$Nf\ (\text{cycle}) = 8.1\times10^{5}\left[\left(\eta/_{\text{Civ}}\right)\right]^{-1.9} \tag{7}$$

Fiber-reinforced cemented mixture:

$$Nf\ (\text{cycle}) = 5.1\times10^{6}\left[\left(\eta/_{\text{Civ}}\right)\right]^{-1.9} \tag{8}$$

3.4 Statistical analysis

Unconfined compressive strength, split tensile strength and fatigue life results were statistically analyzed with an analysis of variance (*ANOVA*). This analysis included three main factors (fiber content, cement content, and void ratio) and their second-order interactions. *ANOVA* results are illustrated through Pareto charts (Figure 6) and main effects plots (Figure 7). The significance of the analysis is shown in the Pareto charts; the horizontal bars portray the magnitude of the studied effects while the dotted vertical line is associated with the significance level (95% confidence) of the analysis. Values exceeding the vertical line represent factors that have significant effects over the mechanical behavior. As for the main effects charts (Figure 7), the dotted line represents the mean result of the tests.

For unconfined compressive strength tests, the Pareto charts (Figure 6) show that all main factors (*B*, *C*, and *A*) were statistically significant, while their second-order interactions showed no influence on the response variable. As for split tensile strength tests, only the main factors (*B*, *C*, and *A*) and the second order interaction *BC* (cement content and void ratio) were statistically significant. Finally, for fatigue life tests all main factors (*A*, *B*, and *C*) and their second-order interactions (*AB*, *AC*, and *BC*) presented a significant influence. As for the main effects (Figure 7) an increase on fiber and cement content and decrease in void ratio resulted in a positive effect for all tests (compressive strength, split tensile strength and fatigue life).

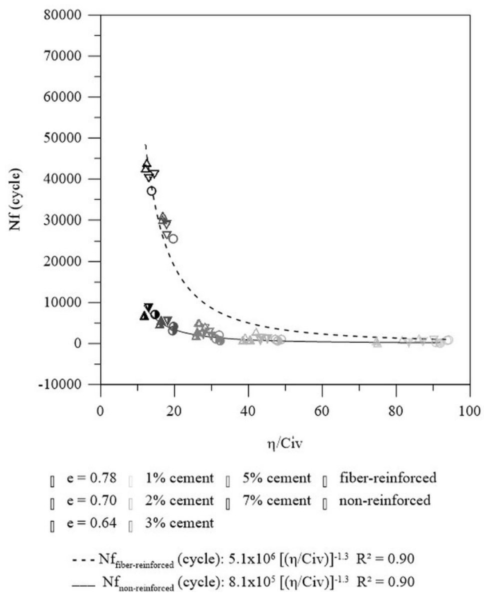

Figure 5. Fatigue life.

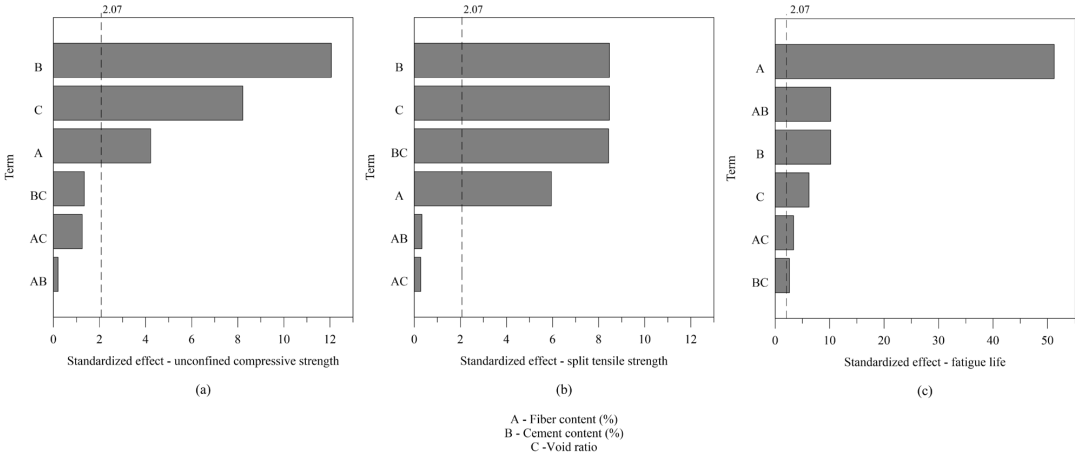

Figure 6. Pareto charts: (a) unconfined compressive strength; (b) split tensile strength; (c) fatigue life.

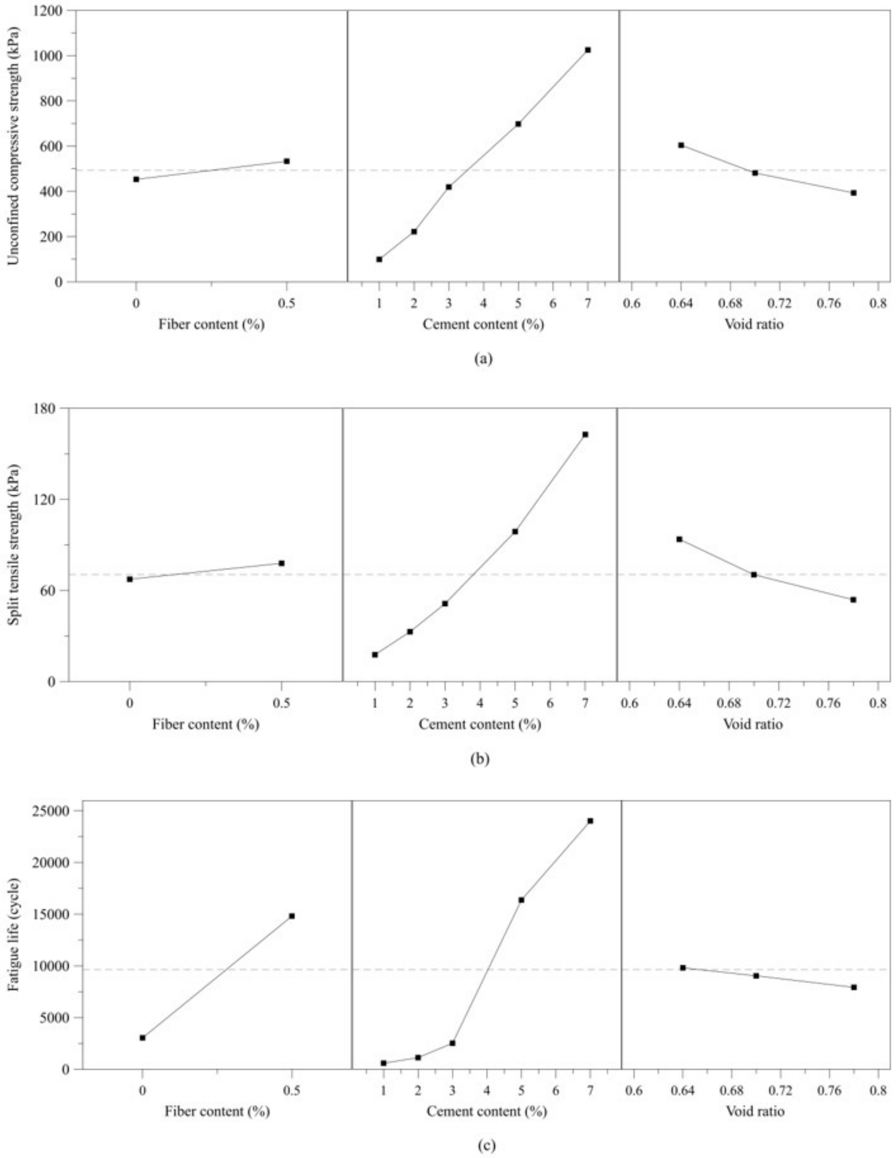

Figure 7. Main effect plots: (a) unconfined compressive strength; (b) split tensile strength; (c) fatigue life.

The statistical analysis corroborates the mechanical results, in which *qu*, *qt*, and *Nf* were governed by fiber content, cement content, and void ratio. It is important to highlight that, fiber content was the main factor that presented the most influence over fatigue life results, once again corroborating the presented results.

4. Conclusions

This study investigated the fatigue life and strength behavior of fiber-reinforced cement-treated sand. In addition, a rational dosage methodology (porosity/cement content index) was also investigated. Based on the findings of this study, for the studied materials and conditions (polypropylene fiber reinforced fine sand cemented with type III Portland cement under unconfined monotonic and cyclic loading), the following conclusions can be disclosed:

a) Fiber-reinforcement improved the mechanical behavior of both monotonic (unconfined compressive strength and split tensile strength) and dynamic loading (fatigue life) tests. This improvement was more pronounced for the fatigue life tests, considering that fiber addition enhanced the bridging effect between particles, playing a critical role in the initiation and extension of cracks;

b) Statistical analysis showed that the mechanical behavior of the fiber-reinforced cemented sand was governed by fiber content, cement content and void ratio of the mixtures. An increase in fiber and cement content and decrease in void ratio resulted in a positive effect while a decrease in void ratio on fatigue life, unconfined compressive strength and split tensile strength;

c) The porosity/cement content index (η/Civ) was shown to be an appropriate parameter to evaluate the stabilization of fiber-reinforced cemented sand in terms of fatigue life, unconfined compressive strength and split tensile strength. The provided equations allow the selection of the best combination of void ratio and cement content for a wide range of options, replacing trial and error experiments with a rational dosage methodology for both monotonic and dynamic loading.

Acknowledgements

Authors wish to express their gratitude to the Brazilian Research Council CNPq for supporting the research group (grants # 307289/2018-4 and 402572/2021-1).

Declaration of interest

The authors have no conflicts of interest to declare. All co-authors have observed and affirmed the contents of the paper and there is no financial interest to report.

Authors' contributions

Hernando da Rocha Borges: conceptualization, data curation, visualization, writing – original draft. Marina Paula Secco: conceptualization, data curation, methodology, validation, writing – original draft. Giovani Jordi Bruschi: conceptualization, data curation, methodology, validation, writing – original draft. Lucas Festugato: supervision, validation, writing – review & editing. The authors above kindly granted the permission of using parts of their publications in this template.

Data availability

All data produced or examined in the course of the current study are included in this article.

List of symbols

qt	split tensile strength
qu	unconfined compressive strength
Civ	cement content
F	fibers
LVDT	linear variable differential transformer
OS	Osorio Sand
PC	Portland cement
PCA	Portland cement association
SP	poorly graded sand
γ_d	dry unit weight
γs_F	unit weight of solids fibers
γs_{OS}	unit weight of solids Osorio sand
η	Porosity
η/Civ	porosity/cement content ratio

References

ASTM D2166/D2166M. (2016). *Standard Test Method for Unconfined Compressive Strength of Cohesive Soil*. ASTM International, West Conshohocken, PA. https://doi.org/10.1520/D2166.

ASTM D2487. (2020). *Standard Practice for Classification of Soils for Engineering Purposes (Unified Soil Classification System)*. ASTM International, West Conshohocken, PA. https://doi.org/10.1520/D2487-17E01.

ASTM D6931. (2017). *Standard Test Method for Indirect Tensile (IDT) Strength of Bituminous Mixtures*. ASTM International, West Conshohocken, PA. https://doi.org/10.1520/D6931-12.2.

ASTM D698-12. (2021). *Standard Test Methods for Laboratory Compaction Characteristics of Soil Using Standard Effort (12 400 Ft-lbf/ft3 (600 KN-m/m3))*. ASTM International, West Conshohocken, PA. https://doi.org/10.1520/D0698-12E02.

ASTM D854. (2014). *Standard Test Methods for Specific Gravity of Soil Solids by Water Pycnometer*. ASTM International, West Conshohocken, PA. https://doi.org/10.1520/D0854-14.

ASTM E1823-13. (2013). *Standard Terminology Relating to Fatigue and Fracture Testing*. ASTM International, West Conshohocken, PA. https://doi.org/10.1520/E1823-21.

Bieliatynskyi, A., Krayushkina, K., Breskich, V., & Lunyakov, M. (2021). Basalt fiber geomats – modern material for reinforcing the motor road embankment slopes. *Transportation Research Procedia*, 54, 744-757. http://dx.doi.org/10.1016/j.trpro.2021.02.128.

Bruschi, G.J., Santos, C.P., de Araújo, M.T., Ferrazzo, S.T., Marques, S., & Consoli, N.C. (2021). Green stabilization of bauxite tailings: a mechanical study on alkali-activated materials. *Journal of Materials in Civil Engineering*, 33(11), 1-25. http://dx.doi.org/10.1061/(ASCE)MT.1943-5533.0003949.

Bruschi, G.J., Santos, C.P., Ferrazzo, S.T., Araújo, M.T., & Consoli, N.C. (2023). Parameters controlling loss of mass and stiffness degradation of 'green' stabilized bauxite tailings. *Proceedings of the Institution of Civil Engineers - Geotechnical Engineering*, 176(3), 306-314. https://doi.org/10.1680/jgeen.21.00119.

Bruschi, G.J., Santos, C.P., Levandoski, W.M.K., Ferrazzo, S.T., Korf, E.P., Saldanha, R.B., & Consoli, N.C. (2022). Leaching assessment of cemented bauxite tailings through wetting and drying cycles of durability test. *Environmental Science and Pollution Research International*, 29, 59247-59262. http://dx.doi.org/10.1007/s11356-022-20031-5.

BSI EN 12697-25. (2016). *Bituminous mixtures — test methods*. British Standards Institution, London, United Kingdom. https://doi.org/10.3403/30288544U.

Carvalho Queiróz, L., Dias Miguel, G., Jordi Bruschi, G., & Deluan Sampaio de Lima, M. (2022). Macro–micro characterization of green stabilized alkali-activated sand. *Geotechnical and Geological Engineering*, 40, 3763-3778. http://dx.doi.org/10.1007/s10706-022-02130-9.

Chen, M., Shen, S.-L., Arulrajah, A., Wu, H.-N., Hou, D.-W., & Xu, Y.-S. (2015). Laboratory evaluation on the effectiveness of polypropylene fibers on the strength of fiber-reinforced and cement-stabilized Shanghai soft clay. *Geotextiles and Geomembranes*, 43(6), 515-523. http://dx.doi.org/10.1016/j.geotexmem.2015.05.004.

Consoli, N.C., & Tomasi, L.F. (2018). The impact of dry unit weight and cement content on the durability of sand–cement blends. *Proceedings of the Institution of Civil Engineers - Ground Improvement*, 171(2), 96-102. http://dx.doi.org/10.1680/jgrim.17.00034.

Consoli, N.C., Arcari Bassani, M.A., & Festugato, L. (2010). Effect of fiber-reinforcement on the strength of cemented soils. *Geotextiles and Geomembranes*, 28(4), 344-351. http://dx.doi.org/10.1016/j.geotexmem.2010.01.005.

Consoli, N.C., Carretta, M.S., Leon, H.B., Schneider, M.E.B., Reginato, N.C., & Carraro, J.A.H. (2020). Behaviour of cement-stabilised silty sands subjected to harsh environmental conditions. *Proceedings of the Institution of Civil Engineers -. Geotechnical Engineering*, 173(1), 40-48. http://dx.doi.org/10.1680/jgeen.18.00243.

Consoli, N.C., Festugato, L., & Heineck, K.S. (2009a). Strain-hardening behaviour of fibre-reinforced sand in view of filament geometry. *Geosynthetics International*, 16(2), 109-115. http://dx.doi.org/10.1680/gein.2009.16.2.109.

Consoli, N.C., Vendruscolo, M.A., Fonini, A., & Rosa, F.D. (2009b). Fiber reinforcement effects on sand considering a wide cementation range. *Geotextiles and Geomembranes*, 27(3), 196-203. http://dx.doi.org/10.1016/j.geotexmem.2008.11.005.

Consoli, N.C., Festugato, L., Miguel, G.D., & Scheuermann Filho, H.C. (2021a). Swelling prediction for green stabilized fiber-reinforced sulfate-rich dispersive soils. *Geosynthetics International*, 28(4), 391-401. http://dx.doi.org/10.1680/jgein.20.00050.

Consoli, N.C., Festugato, L., Miguel, G.D., Moreira, E.B., & Scheuermann Filho, H.C. (2021b). Fatigue life of green stabilized fiber-reinforced sulfate-rich dispersive soil. *Journal of Materials in Civil Engineering*, 33(9), 04021249. http://dx.doi.org/10.1061/(ASCE)MT.1943-5533.0003842.

Consoli, N.C., Tebechrani Neto, A., Correa, B.R.S., Quiñónez Samaniego, R.A., & Cristelo, N. (2021c). Durability evaluation of reclaimed asphalt pavement, ground glass and carbide lime blends based on unconfined compression tests. *Transportation Geotechnics*, 27, 100461. http://dx.doi.org/10.1016/j.trgeo.2020.100461.

Consoli, N.C., Foppa, D., Festugato, L., & Heineck, K.S. (2007). Key parameters for strength control of artificially cemented soils. *Journal of Geotechnical and Geoenvironmental Engineering*, 133(2), 197-205. http://dx.doi.org/10.1061/(ASCE)1090-0241(2007)133:2(197).

Consoli, N.C., Moraes, R.R., & Festugato, L. (2011a). Split tensile strength of monofilament polypropylene fiber-reinforced cemented sandy soils. *Geosynthetics International*, 18(2), 57-62. http://dx.doi.org/10.1680/gein.2011.18.2.57.

Consoli, N.C., Zortéa, F., Souza, M., & Festugato, L. (2011b). Studies on the dosage of fiber-reinforced cemented soils. *Journal of Materials in Civil Engineering*, 23(12), 1624-1632. http://dx.doi.org/10.1061/(ASCE)MT.1943-5533.0000343.

Consoli, N.C., Moraes, R.R., & Festugato, L. (2013). Parameters controlling tensile and compressive strength of fiber-reinforced cemented soil. *Journal of Materials in Civil Engineering*, 25(10), 1568-1573. http://dx.doi.org/10.1061/(ASCE)MT.1943-5533.0000555.

Consoli, N.C., Nierwinski, H.P., Peccin da Silva, A., & Sosnoski, J. (2017a). Durability and strength of fiber-reinforced compacted gold tailings-cement blends. *Geotextiles and Geomembranes*, 45(2), 98-102. http://dx.doi.org/10.1016/j.geotexmem.2017.01.001.

Consoli, N.C., Quiñónez, R.A., González, L.E., & López, R.A. (2017b). Influence of molding moisture content and porosity/cement index on stiffness, strength, and failure envelopes of artificially cemented fine-grained soils. *Journal of Materials in Civil Engineering*, 29(5), 04016277. http://dx.doi.org/10.1061/(ASCE)MT.1943-5533.0001819.

Consoli, N.C., Pasche, E., Specht, L.P., & Tanski, M. (2018). Key parameters controlling dynamic modulus of crushed reclaimed asphalt paving–powdered rock–Portland cement blends. *Road Materials and Pavement Design*, 19(8), 1716-1733. http://dx.doi.org/10.1080/14680629.2017.1345779.

Consoli, N.C., Ruver, C.A., Girardello, V., Festugato, L., & Thomé, A. (2012). Effect of polypropylene fibers on the uplift behavior of model footings embedded in sand. *Geosynthetics International*, 19(1), 79-84. http://dx.doi.org/10.1680/gein.2012.19.1.79.

Consoli, N.C., Samaniego, R.A.Q., & Villalba, N.M.K. (2016). Durability, strength, and stiffness of dispersive clay–lime blends. *Journal of Materials in Civil Engineering*, 28(11), 04016124. http://dx.doi.org/10.1061/(ASCE)MT.1943-5533.0001632.

Festugato, L., Menger, E., Benezra, F., Kipper, E.A., & Consoli, N.C. (2017). Fibre-reinforced cemented soils compressive and tensile strength assessment as a function of filament length. *Geotextiles and Geomembranes*, 45(1), 77-82. http://dx.doi.org/10.1016/j.geotexmem.2016.09.001.

Festugato, L., Peccin da Silva, A., Diambra, A., Consoli, N.C., & Ibraim, E. (2018). Modelling tensile/compressive strength ratio of fibre reinforced cemented soils. *Geotextiles and Geomembranes*, 46(2), 155-165. http://dx.doi.org/10.1016/j.geotexmem.2017.11.003.

Festugato, L., Venson, G.I., & Consoli, N.C. (2021). Parameters controlling cyclic behaviour of cement-treated sand. *Transportation Geotechnics*, 27, 100488. http://dx.doi.org/10.1016/j.trgeo.2020.100488.

Ladd, R.S. (1978). Preparing test specimens using undercompaction. *Geotechnical Testing Journal*, 1(1), 16-23. http://dx.doi.org/10.1520/GTJ10364J.

Li, Y., Hao, P., & Li, N. (2022). Preparation and properties of a novel rejuvenator-loaded fiber for asphalt pavement. *Construction & Building Materials*, 324, 126687. http://dx.doi.org/10.1016/j.conbuildmat.2022.126687.

Mazhar, S., & GuhaRay, A. (2021). Stabilization of expansive clay by fibre-reinforced alkali-activated binder: an experimental investigation and prediction modelling. *International Journal of Geotechnical Engineering*, 15(8), 977-993. http://dx.doi.org/10.1080/19386362.2020.1775358.

Michalowski, R.L. (2008). Limit analysis with anisotropic fibre-reinforced soil. *Geotechnique*, 58(6), 489-501. http://dx.doi.org/10.1680/geot.2007.00055.

Michalowski, R.L., & Čermák, J. (2003). Triaxial compression of sand reinforced with fibers. *Journal of Geotechnical and Geoenvironmental Engineering*, 129(2), 125-136. http://dx.doi.org/10.1061/(ASCE)1090-0241(2003)129:2(125).

Mukherjee, K., & Kumar Mishra, A. (2021). Recycled waste tire fiber as a sustainable reinforcement in compacted sand–bentonite mixture for landfill application. *Journal of Cleaner Production*, 329, 129691. http://dx.doi.org/10.1016/j.jclepro.2021.129691.

Nasr, A.M. (2014). Behavior of strip footing on fiber-reinforced cemented sand adjacent to sheet pile wall. *Geotextiles and Geomembranes*, 42(6), 599-610. http://dx.doi.org/10.1016/j.geotexmem.2014.10.004.

Ozturk, O., & Ozyurt, N. (2022). Sustainability and cost-effectiveness of steel and polypropylene fiber reinforced concrete pavement mixtures. *Journal of Cleaner Production*, 363(03), 132582. http://dx.doi.org/10.1016/j.jclepro.2022.132582.

Pereira dos Santos, C., Bruschi, G.J., Mattos, J.R.G., & Consoli, N.C. (2022). Stabilization of gold mining tailings with alkali-activated carbide lime and sugarcane bagasse ash. *Transportation Geotechnics*, 32, 100704. https://doi.org/10.1016/j.trgeo.2021.100704.

Piuzzi, G.P., Scheuermann Filho, H.C., Villena Del Carpio, J.A., & Consoli, N.C. (2021). The effects of porosity, asphalt content and fiberglass incorporation on the tensile strength and resilient modulus of asphalt concrete blends. *Geotextiles and Geomembranes*, 49(3), 864-870. http://dx.doi.org/10.1016/j.geotexmem.2021.01.002.

Portland Cement Association – PCA. (1992). *Soil-cement construction handbook*. PCA.

Queiróz, L.C., Batista, L.L.S., Souza, L.M.P., Lima, M.D., Danieli, S., Bruschi, G.J., & Bergmann, C.P. (2022). Alkali-activated system of carbide lime and rice husk for granular soil stabilization. *Proceedings of the Institution of Civil Engineers - Ground Improvement*, 1-37. Ahead of print. https://doi.org/10.1680/jgrim.21.00048.

Quiñónez Samaniego, R.A., Scheuermann Filho, H.C., de Araújo, M.T., Bruschi, G.J., Festugato, L., & Consoli, N.C. (2021). Key parameters controlling strength and resilient modulus of a stabilised dispersive soil. *Road Materials and Pavement Design*, 24(1), 279-294. http://dx.doi.org/10.1080/14680629.2021.2013937.

Sangma, S., & Tripura, D.D. (2020). Experimental study on shrinkage behaviour of earth walling materials with fibers and stabilizer for cob building. *Construction & Building Materials*, 256, 119449. http://dx.doi.org/10.1016/j.conbuildmat.2020.119449.

Silva, A., Festugato, L., Daronco, J.V.L., & Menger, E.S. (2022). Mechanical response of a sand, reclaimed-asphalt pavement, and Portland cement mixture. *Journal of Materials in Civil Engineering*, 34(9), 520-533. http://dx.doi.org/10.1061/(ASCE)MT.1943-5533.0004361.

Tonini de Araújo, M., Tonatto Ferrazzo, S., Bruschi, G.J., & Cesar Consoli, N. (2021). Mechanical and environmental performance of eggshell lime for expansive soils improvement. *Transportation Geotechnics*, 31(2), 100681. http://dx.doi.org/10.1016/j.trgeo.2021.100681.

Zhao, Y., Yang, Y., Ling, X., Gong, W., Li, G., & Su, L. (2021). Dynamic behavior of natural sand soils and fiber reinforced soils in heavy-haul railway embankment under multistage cyclic loading. *Transportation Geotechnics*, 28, 100507. https://doi.org/10.1016/j.trgeo.2020.100507.

Soils and Rocks
An International Journal of Geotechnical and Geoenvironmental Engineering
www.soilsandrocks.com
ISSN 1980-9743
ISSN-e 2675-5475

Load capacity evaluation of different typologies of short and small diameter piles

Gustavo Corbellini Masutti[1], Patricia Rodrigues Falcão[2], Magnos Baroni[2#],
Rinaldo José Pinheiro Barbosa[2], Tiago de Jesus Souza[3,4]

Technical Note

Keywords
Unsaturated soils
Static load test
Small diameter piles
Loading capacity

Abstract

It is common to observe residences with a high number of pathologies related to differential settlements in the municipality of Cruz Alta, Rio Grande do Sul, Brazil. Motivated by this perspective the first Geotechnical Engineering Experimental Field was implemented in the municipality. Standard penetration test and cone penetration test was conducted to characterize the subsoil and execute 17 excavated piles: nine compression piles and eight reaction piles. This technical note presents and discusses the results of the geotechnical load capacity obtained with the static load test in three different pile conditions: conventional piles, floating piles, and reinforced piles by inserting a crushed stone layer compacted at the bottom of the drilling. The piles evaluated have a length of 3 m and a diameter of 30 cm. The piles are immersed in a layer of unsaturated laterite soil. Conventional piles are extensively executed in the municipality due to the limited equipment of the companies offering this service. In summary, the piles presented low bearing capacity, however, the reinforced piles proved to be a viable alternative in terms of increased resistance. The conventional piles presented low load capacity and significant settlements. The insertion of the reinforcement at the tip of the pile resulted in a resistance gain in the range of 31%. The study of floating piles was important to understand the behavior of the pile base. This technical note will enable the geotechnical understanding for future researchers or designers who will work with this soil condition in the state of Rio Grande do Sul, Brazil.

1. Introduction

The behavior of piles in unsaturated soils subjected to axial loading has been the subject of field research, physical models, and numerical simulations (Stewart et al., 2011; Vanapalli & Taylan, 2012; Liu & Vanapalli, 2021; Wu & Vanapalli, 2022). In tropical climatic regions, it is commonly the occurrence of unsaturated soils directly influenced by mineralogical and drainage conditions (Camapum de Carvalho & Gitirana Junior, 2021). This condition denotes the importance of the study of foundations in unsaturated soils.

Studies have demonstrated the importance of foundation studies in unsaturated soils in Brazil (Rebolledo et al., 2019; Pereira et al., 2019; Monteiro et al., 2021; Chaves et al., 2022). In the Brazilian geotechnical practice, two are the ABNT standards that regulate the execution of the pile load tests: NBR 12131 (ABNT, 2006) and NBR 6122 (ABNT, 2010). The first specifies the types of tests and the executive procedures and the second defines the number of load tests to be performed. NBR 6122 (ABNT, 2010) specifies that the load tests must be carried out on the first piles on site to validate the length prediction procedures or adapt them according to the results of these load tests.

Customs and practices for pile execution in the Cruz Alta municipality, is to execute small diameter and short length excavated piles due to its ease of execution compared to superficial foundations. However, there are cracks in buildings that are the result of improperly dimensioned foundations. From this perspective, the first geotechnical engineering experimental field was implemented at the University of Cruz Alta, whose objective is to explain the behavior of piles submitted to axial compression through static load tests. Nine excavated piles with a diameter of 0.30 m and a length of 3.00 m, were designed and tested under compression on site. Eight piles with a length of 6.00 m and a diameter of 0.30 m were executed for the reaction system.

#Corresponding author. E-mail address: magnos.baroni@gmail.com
[1]Universidade de Cruz Alta, Departamento de Engenharia Civil, Cruz Alta, RS, Brasil.
[2]Universidade Federal de Santa Maria, Programa de Pós-graduação em Engenharia Civil, Santa Maria, RS, Brasil.
[3]Instituto Tecnológico de Aeronáutica, São José dos Campos, SP, Brasil.
[4]Solotechnique Consultoria e Engenharia Geotécnica, Jundiaí, SP, Brasil.

Submitted on May 5, 2022; Final Acceptance on May 18, 2023; Discussion open until November 30, 2023.
https://doi.org/10.28927/SR.2023.004722

In this context, static load tests (*SLT*) were conducted with slow loading, in three concrete piles, as per the usual practice, resisting by the side and tip friction. It is important to note that *SLT* can be methodologically presented in several stages: test preparation, test equipment control, in-situ pile test on the construction site, analysis, and decision making. Three floating piles, executed with expanded polystyrene discs at the tip, were later dissolved. Finally, to increase the cutting-edge strength of the analyzed system, the other piles included a layer of compacted crushed stone and subsequent concreting at the base of the foundation. Add to the results two cone penetration tests (*CPT*), and four standard penetration tests (*SPT*) without water circulation were conducted for the subsoil investigation, and deformed samples were removed from a depth of 2.00 m for physical characterization tests.

2. Materials and methods

2.1 Characterization of the geotechnical engineering experimental field

Nine short (3 m) and small diameter (0.30 m) excavated piles were executed in the experimental field (Figure 1a). The distribution of piles in the plan and work after execution is presented in Figure 1b. As shown in Figure 1c, the piles were separated into three distinct typologies, namely: conventional piles, reinforced piles, and floating piles. Additionally, eight reaction piles with a length of 6.00 m and a diameter of 0.30 m were executed. The three conventional piles are characterized by lateral friction and tip resistance. The type corresponding to the three reinforced piles has the differential of a layer of crushed gravel at the bottom of the perforation with a thickness of 0.30 m. The floating piles aimed to evaluate the magnitude of the resistance by lateral friction. The constructive methodology of the flotation piles consisted of introducing four expanded polystyrene discs at the bottom of the perforation, which were dissolved before conducting the load tests. The discs had a diameter of 0.30 m and a thickness of 0.08 m each, totaling 0.32 m in height. It is important to highlight that the pile was exhumed after the load test, and the correct functioning of the executive process was verified (Figure 1d).

2.2 Soil characterization

Figure 2 presents the results obtained from the *SPT* and *CPT* tests. The local subsoil was characterized using four *SPT* tests without water circulation to determine the subsoil profile, tactile-visual identification of the different layers, and penetration resistance index (N_{SPT}).

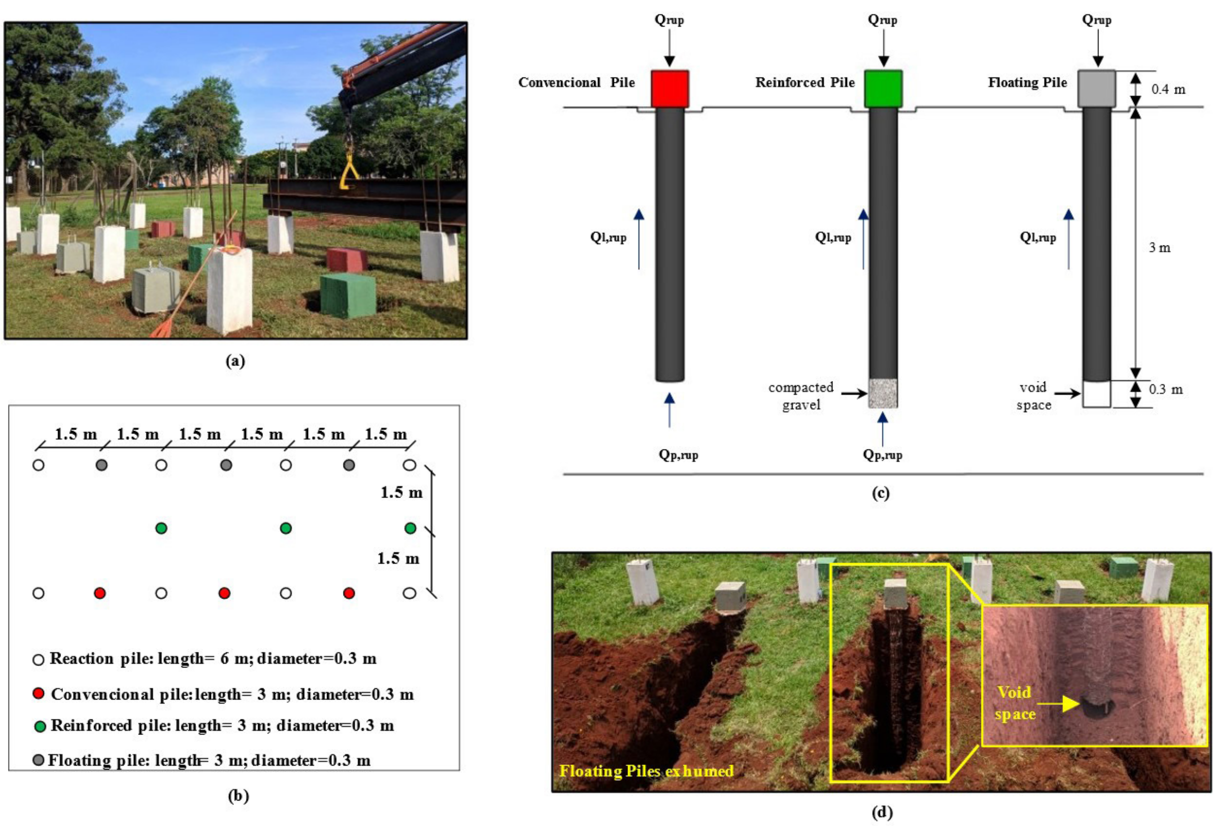

Figure 1. (a) piles executed; (b) arrangement of piles; (c) characteristics of structural elements and (d) exhumed floating pile.

The *SPT* tests were performed in the light of NBR 6484 (ABNT, 2001). *SPT*-01 was executed up to 30 m in depth. The others (*SPT*-02, *SPT*-03, and *SPT*-04) were interrupted at 6.00 m since this was the depth of interest for the research, twice the length of the piles. The water table level is at a depth of 14.50 m from the ground level; confirming that the piles are embedded in unsaturated soil. The soil is composed of a layer of red-colored silty clay with increasing compactness along the depth. The geotechnical profile of the site presents low resistance to penetration, indicating a soil with low support capacity depending on the imposed demand. With the *CPT* results, a soil classification along depth was performed using Robertson's (2010) proposal. Indicating that the soil profile is composed of clay, mixed sands, and sand. Being different from that obtained by the *SPT* test, this fact may be linked to the fact that the methodology for interpreting the *CPT* is not based on tropical soils. Note that the clay layer presents relatively low cone strength values (3 to 5 MPa) and low friction sleeve (6 to 40 kPa). The sand layer is characterized by the opposite pattern to the clay, with high values of cone strength and friction sleeve.

Table 1 presents the soil characterization and classification results for the 2 m depth. The ratio between the plasticity index and the fraction smaller than 0.002 mm results in a colloidal activity index of 0.27. Indicating that the clay is inactive, corroborating with the results of X-ray diffraction that indicated the presence of the kaolinite mineral that does not present expansive characteristics. The soil was classified using the *MCT* (Miniature Compaction Tropical) methodology developed for tropical soils by Nogami & Villibor (1995). The results indicate that the soil belongs to the class of clayey soils with lateritic behavior (*LG'*). Through the Unified Soil Classification System (*USCS*) the soil belongs to the ML group, silt with low compressibility.

Table 1. Soil characteristic at a depth of 2 m.

Parameters	Value
X-ray diffraction	kaolinite and gibbsite
Liquid Limit (%)	49
Plastic Limit (%)	32
Plasticity Index- PI (%)	17
Real specific weight of the grains (kN/m^3)	27.96
Natural specific weight (kN/m^3)	15.16
Void index	1.41
% gravel (>2.0mm)	0
% coarse sand (0.6 – 2.0 mm)	1
% average sand (0.2 – 0.6 mm)	11
% fine sand (0.06 – 0.2 mm)	11
% silt (2 μm – 0.06 mm)	15
% clay (%< 2 μm)	62
Brazilian MCT	LG'
USCS	ML

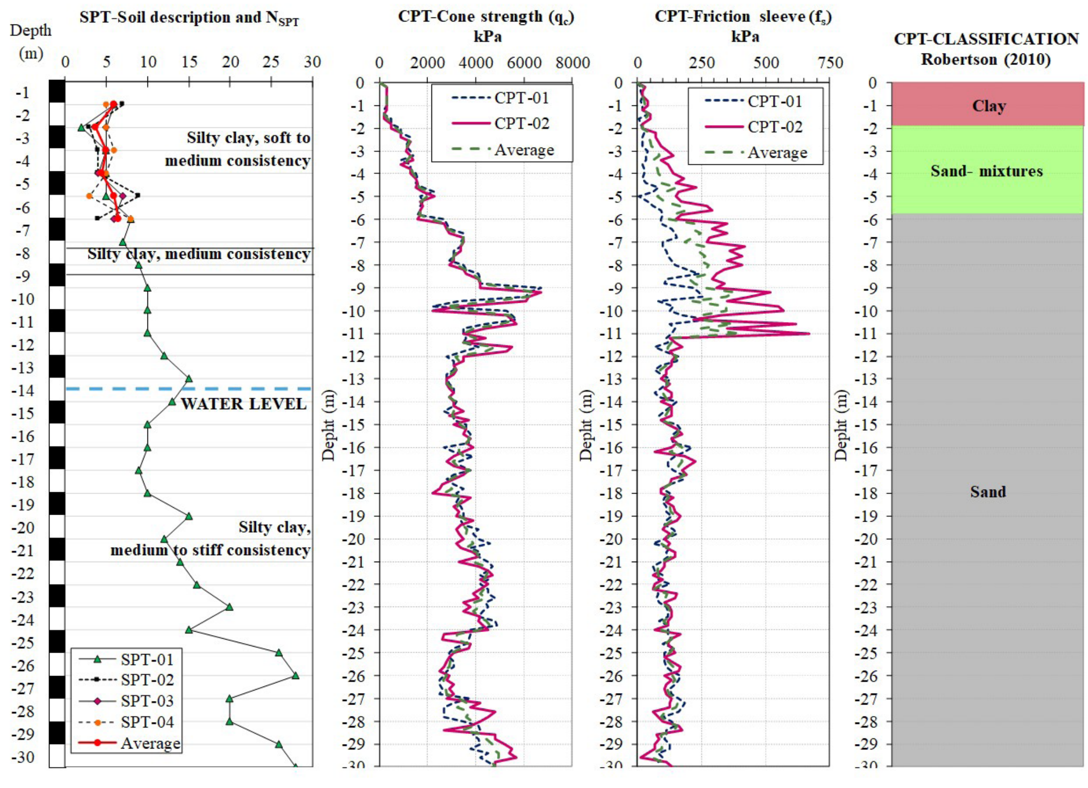

Figure 2. Analysis of the typical subsoil profile by *SPT* and *CPT* tests.

3. Analysis and results

Figure 3 shows the results from the *SLT* for the conventional (*C*), reinforced (*R*), and floating piles (*F*). For conventional piles the load increments were estimated according to the recommendations of NBR 12131 (ABNT, 2006), therefore, the stages conducted were of 30 kN. When the first test was conducted on the *C-1* pile, the load test ended with a maximum load of 75 kN, at which the strain readings did not stabilize, indicating a potential rupture. For this element, the average settlement was 21.04 mm. After the preliminary experience with the stages adopted for the *C-1* pile, the load increments for the other piles in this group were reduced to 10 kN to analyze the highest number of experimental data. However, in conventional piles, the settlements did not stabilize for the last load stage applied, characterizing the conventional failure of the pile. It can be observed that in the unloading section there was no elastic recovery, which is another indication that the resistive capacity reached its limit. This typology showed a discrepancy of around 37.5% for the maximum load capacity achieved in the test. Despite the proximity of the structural elements, a variation in soil characteristics may have occurred, which would justify the higher strength observed for pile *C-3*. The *SLT* was conducted up to the 105 kN stage for the reinforced piles, with settlements in the range of 2.6 to 4.4% of the pile diameter. When comparing the reinforced pile with the conventional pile (*C-1* and *C-2*) the average strength gain is 31%. For the floating piles, the *SLT* was conducted until settlements 1.5 to 1.9% of the pile diameter, where a load capacity of 83 kN was obtained for *F-1* and *F-2* and 67.5 kN for *F-3*. The floating piles present settlements 89 to 93% lower than those obtained for the conventional piles. It is estimated that by applying the load stages a kind of compaction occurs at the pile toe, reducing the void index and consequently increasing the degree of saturation. This increase can reduce the suction in the region justifying the high magnitude settlements observed in conventional piles.

Figure 4 shows the results obtained in *SLT* using different methods. The data suggests proximity between the experimental results and those obtained by the methods of van der Veen (1953) and Van der Venn modified by Aoki (1976). The results should be considered that the *SLT* was taken to small stiffness values, indicating conventional pile failure. In line with this hypothesis, the good fit obtained with the methods of van der Veen (1953) and Van der Venn modified by Aoki (1976) indicates a poorly defined curve with failure load values close to those obtained experimentally. This premise agrees with Décourt and Niyama's (1994) suggestion that the Van der Veen method is only applicable to piles where the load test is taken to 2/3 of the failure load and in displacement piles. The application of the Stiffness method (Décourt, 1998, 2008) made it possible to infer that the insertion of a crushed stone layer increased the ultimate strength promoting a higher bearing capacity.

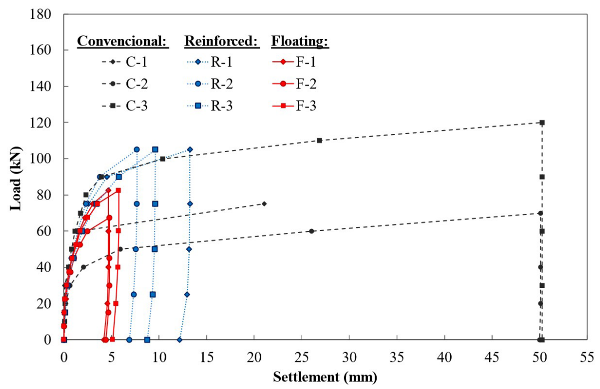

Figure 3. Settlement versus load curve.

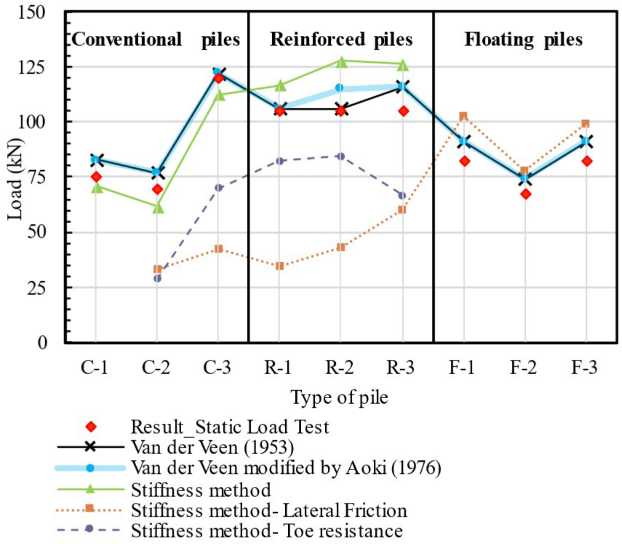

Figure 4. Comparison between the extrapolation methods.

It is estimated that the lower experimental results obtained for conventional piles by the stiffness method come from the consideration that the settlement that leads the pile to conventional rupture corresponds to 0.1 of the element diameters. Evaluating the results of the floating piles it is estimated that the Stiffness method is underestimating the load capacity results by lateral friction. Another fact that corroborates that the tip is being overestimated is that the excavated piles are short and inserted in porous soil with little resistance.

4. Conclusion

This Technical Note presents the results of the compressive behavior of short and small diameter excavated piles. The granulometric characterization tests demonstrate that the soil surrounding the pile is a silty-sandy clay. The low N_{SPT} values in the first meters support the theory that these results are typical of lateritic soils.

The results of the *SPT* tests show significant dispersion, even though they are all conducted in the same location. It is emphasized that the load capacity in pile compression can be evaluated from theoretical-empirical equations, where it is possible to discriminate the base component and the component by lateral friction. The appeal of this technical note is to work in the light of field measured data (static load tests).

Regarding the load versus settlement curves, the *C* piles presented a high dispersion from the *C-3* pile, which presented load approximately 50 kN higher than the others. The study of *F* piles indicates the remarkable relevance of lateral friction resistance in the load capacity of foundations by excavated piles, even if these are short and with a small diameter. This premise corroborates the statement of Kulhawy (1991), where the author indicates that peak strength is responsible for only approximately 5 to 20% of the load capacity of excavated piles. The load results do not show dispersion for the three *R* piles, as they all reached 105 kN as measured maximum strength. The compaction of 0.30 m of crushed stone at the bottom of the perforation contributed to the increase in strength of the *R* piles. This typology had a load capacity 35.50% higher than the results obtained by floating piles and 18.90% higher when compared to conventional piles. Reinforced piles are a simple, affordable, and efficient form to increase the strength of short piles due to the ease of execution. The method of van der Veen (1953) and Van der Veen modified by Aoki (1976) proved inadequate in load tests approaching rupture. The Stiffness method made it possible to evaluate lateral friction and tip resistance separately. Evaluating the *SLS* obtained for the floating piles it is verified that the Stiffness method may be underestimating the lateral friction.

Declaration of interest

The authors have no conflicts of interest to declare. All co-authors have observed and affirmed the contents of the paper and there is no financial interest to report.

Authors' contributions

Gustavo Corbellini Masutti: conceptualization, data curation, visualization, writing – original draft. Patricia Rodrigues Falcão: conceptualization, data curation, methodology, supervision, validation, writing – original draft. Magnos Baroni: formal analysis, funding acquisition, investigation, methodology, project administration, supervision, validation, writing – original draft. Rinaldo José Pinheiro Barbosa: supervision, validation, data curation, writing – reviewing & editing. Tiago de Jesus Souza: methodology, data curation, supervision, validation, writing – reviewing & editing.

Data availability

The datasets produced and analyzed during the current study are available upon reasonable request to the corresponding author.

List of symbols

C	conventional Piles
CPT	cone penetration test
F	floating piles
LG'	clayey soils with lateritic behavior
MCT	Miniature Compaction Tropical
N_{SPT}	penetration resistance index
$Q_{p,rup}$	load transfer by the toe
$Q_{l,rup}$	load transfer by the friction
Q_{rup}	applied load at the top of the pile.
R	reinforced piles
SLT	static load test
SPT	standard penetration test
USCS	Unified Soil Classification System

References

ABNT NBR 6484 (2001). *Soil - Simple reconnaissance drilling with SPT reconnaissance drilling with SPT – test method*. ABNT - Associação Brasileira de Normas Técnicas, Rio de Janeiro, RJ (in Portuguese).

ABNT NBR 12131 (2006). *Piles - static load test - testing method*. ABNT - Associação Brasileira de Normas Técnicas, Rio de Janeiro, RJ (in Portuguese).

ABNT NBR 6122 (2010). *Design and execution of foundations*. ABNT - Associação Brasileira de Normas Técnicas, Rio de Janeiro, RJ (in Portuguese).

Camapum de Carvalho, J., & Gitirana Junior, G.F.N. (2021). Unsaturated soils in the context of tropical soils. *Soils and Rocks*, 44(3), e2021068121. http://dx.doi.org/10.28927/SR.2021.068121.

Chaves, C.P., Silva, J.D.J.C., Cunha, R.P., & Cavalcante, A.L.B. (2022). Laboratory experimental and numerical thermal response tests in thermal piles prototypes in tropical soil. *Soils and Rocks*, 45(1), 1-13. http://dx.doi.org/10.28927/SR.2022.078921.

Décourt, L. (1998). Foundation failure and safety coefficients in light of the stiffness concept. In: *Proceedings of the XI Brazilian Congress of Soil Mechanics and Geotechnical Engineering* (Vol. 3, pp. 1599-1606). São Paulo: ABMS - Brazilian Association of Soil Mechanics (in Portuguese).

Décourt, L. (2008). Load tests on piles can tell you much more than they have been saying. In *Proceedings of the VI Seminar on Engineering of Special Foundations and Geotechnics* (vol. 1, pp. 221-245). São Paulo: ABMS - Brazilian Association of Soil Mechanics. (in Portuguese).

Décourt, L., & Niyama, S. (1994). Predicted and measured behavior of displacement piles in residual soil. In *Proceedings of the XIII ICSMFE* (Vol. 2, pp. 477-486). New Delhi.

Kulhawy, F.H. (1991). *Drilled shaft foundations* (pp. 537-552). Foundation Engineering Handbook.

Liu, Y., & Vanapalli, S.K. (2021). Mechanical behavior of a floating model pile in unsaturated expansive soil associated with water infiltration: laboratory investigations and numerical simulations. *Soil and Foundation*, 61(4), 929-943. http://dx.doi.org/10.1016/j.sandf.2021.06.004.

Monteiro, F.F., Cunha, R.P., de Aguiar, M.F.P., & Silva, C.M. (2021). Settlement of bored piles with expander body system in lateritic soils. *REM - International Engineering Journal*, 74(3), 309-318. http://dx.doi.org/10.1590/0370-44672020740057.

Nogami, J.S., & Villibor, D.F. (1995). *Low-cost paving with lateritic soils* (240 p.). Editora Villibor. (in Portuguese).

Pereira, M.S., de Hollanda Cavalcanti Tsuha, C., Vilar, O.M., Schiavon, J.A., Tibana, S., Saboya, F., & Dias, D. (2019). Performance evaluation of a collapsible soil reinforced with compacted lateritic soil columns. *Journal of Geotechnical and Geoenvironmental Engineering*, 145(9), 04019055. http://dx.doi.org/10.1061/(asce)gt.1943-5606.0002093.

Rebolledo, J.F.R., León, R.F.P., & Camapum De Carvalho, J. (2019). Performance evaluation of rigid inclusion foundations in the reduction of settlements. *Soils and Rocks*, 42(3), 265-279. http://dx.doi.org/10.28927/sr.423265.

Robertson, P.K. (2010). Soil Behaviour Type from the CPT: an update. In *Proceedings of the 2nd International Symposium on Cone Penetration Testing*, Huntington Beach.

Stewart, W.P., Cunha, R.P., & Mota, N.M.B. (2011). Settlement of floating bored piles in brasilia porous clay. *Soils and Rocks*, 34(2), 153-159.

van der Veen, C. (1953). The bearing capacity of a pile. In *Proceedings of the 3rd International Conference on Soil Mechanics and Foundation Engineering* (Vol. 2, pp. 84-90). London: ISSMGE - International Society for Soil Mechanics.

Vanapalli, S.K., & Taylan, Z.N. (2012). Design of single piles using the mechanics of unsaturated soils. *International Journal of GEOMATE*, 2(1), 197-204. Retrieved in May 5, 2022, from https://www.researchgate.net/publication/286091954

Wu, X., & Vanapalli, S.K. (2022). Three-dimensional modeling of the mechanical behavior of a single pile in unsaturated expansive soils during infiltration. *Computers and Geotechnics*, 145, 104696. http://dx.doi.org/10.1016/j.compgeo.2022.104696.

CASE STUDIES

Soils and Rocks
An International Journal of Geotechnical and Geoenvironmental Engineering
www.soilsandrocks.com
ISSN 1980-9743
ISSN-e 2675-5475

A dig into the past: the first tieback wall

Alberto Ortigao[1#], Paulo Henrique Dias[2], Hélio Brito[3], Marnio Camacho[4]

Case Study

Keywords
Tieback wall
Ground anchors
Tiebacks
Wedge method

Abstract
This is an investigative work by the authors, all of them former students and employees at Tecnosolo Ltd, the company founded by our late Professor Costa Nunes, to find and photograph the first tieback wall designed and built in 1957 by Tecnoloso under Prof Costa Nunes' guidance.

1. Introduction

This is a story of digging into the past, which the Authors embarked on and eventually had a successful outcome on 26 June 2023.

In the late 60's the first three Authors were undergraduate students at the Federal University of Rio de Janeiro, while the fourth Author, 10 years senior, was a practising geotechnical engineer working at Tecnosolo SA. This company was founded in the early 50s by the late Engineer and Professor Costa-Nunes (1917-1990) – researcher and pioneer in ground anchors.

In his classes, Costa Nunes (Figure 1) talked about the first tieback wall built in 1957. He mentioned it was built at the site of an old 19th-century hospital named "Beneficiência Portuguesa" in the city centre of Rio de Janeiro, and 1958 in Germany.

Weatherby (1982) and Hunt & Costa Nunes (1978) reported that permanently tied-back walls have been the most common method of slope retention in Brazil since 1957. After 1958 tiebacks found their way into Europe in Germany (Jelinek & Ostermayer, 1966; Jelinek & Ostermayer, 1967) and later in Switzerland, England, and France (Ranke & Ostermayer, 1968; Dupeuble & Brulois, 1969; Descoeudres, 1969; Littlejohn, 1980).

The first permanent soil tiebacks in the United States took place in 1961 (Jones & Kerkhoff, 1961).

The Authors were engineers and colleagues at Tecnosolo since the early 70s and recently realized that no photographs of this early wall survived. This is the story of a quest to find this wall.

Figure 1. Professor Costa Nunes.

2. A quest to find a wall

The first Author contacted several old colleagues from Tecnosolo, but only the second Author, aka PH, knew exactly the wall location, as he had visited the site long ago. The other Authors shared information about this first wall.

Today it is located between an old and the recent hospital building (Figure 2 and Figure 3) and it is difficult to access, hidden between two buildings (Figure 4).

Corresponding author. E-mail address: ortigao@terratekinc.com
[1] Terratek, Rio de Janeiro, RJ, Brasil.
[2] Seel, Rio de Janeiro, RJ, Brasil.
[3] Consultor independente, Rio de Janeiro, RJ, Brasil.
[4] Pesquisador independente, Belo Horizonte, MG, Brasil.

Submitted on June 20, 2023; Final Acceptance on June 21, 2023; Discussion open until November 30, 2023.
https://doi.org/10.28927/SR.2023.007423

Figure 2. Site view, foreground: the old Beneficiência Portuguesa Hospital, at the back of the Gloria D'Or Hospital in Rio de Janeiro city centre.

Figure 3. 19th Hospital (foreground) and the new hospital building (background).

3. Eureka

On 26 June 2023, the first (AO) and the second (PH) Authors visited the site. It did not take long for PH to find it hidden between two buildings (Figure 4). Eureka!

After conversations with the hospital management, permission was granted for this visit (Figure 5).

4. Description

Figure 6 presents the 6 m high and some 50 m long wall sketches. Hunt & Costa Nunes (1978) described this innovative construction method taken from the top (Figure 7), replacing gravity walls which demanded a lot more excavation volume to be built.

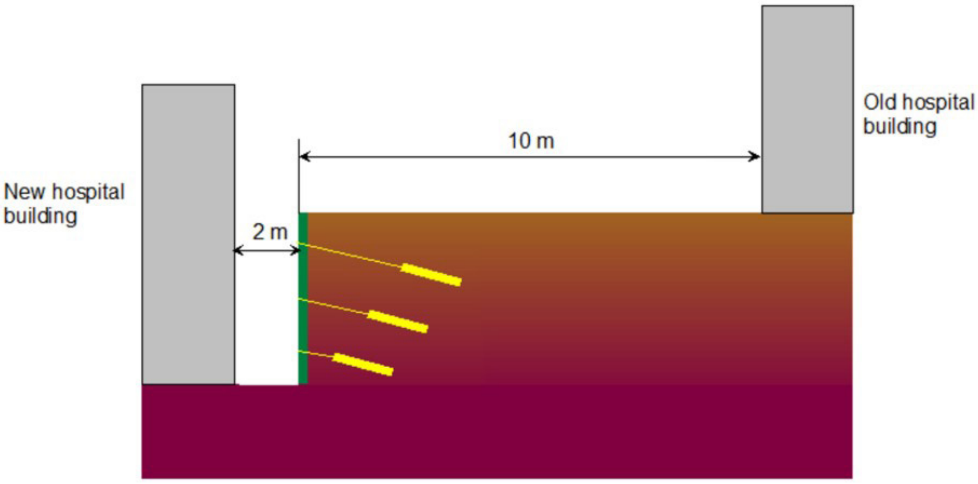

Figure 4. Sketch of the tieback wall location, squeezed into the new hospital building.

Figure 5. Evidence of this “archaeological” digging, left A Ortigao, right PH Dias.

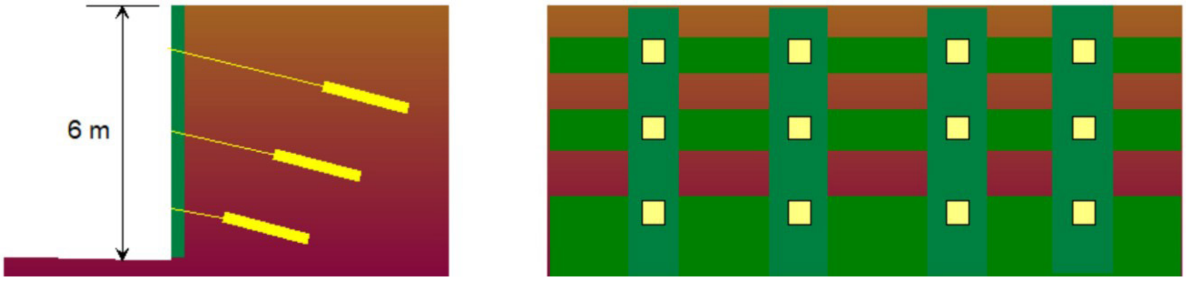

Figure 6. Tieback wall sketch.

Figure 7. Tieback wall pictures.

Professor Costa Nunes once told in his classes that he designed the upper part of the wall with a concrete grid, given the high cohesion of this residual soil. Nevertheless, he changed his design of later walls and used a concrete slab, replacing the grid. "Concrete grid only for rock slopes", he said.

The Authors found that the ground anchors were 20 mm in diameter, certainly CA-50 steel-grade, which became available a few years before. All anchors were tested to 90% of the steel yield load (170 kN), then reduced to the working load of about 100 kN.

5. Design method

It took a few years for Prof Costa Nunes to publish a paper on the design method of anchored walls, which he did in 1963 (Costa Nunes & Velloso, 1963). They devised a wedge method (Figure 8) and equations which were used in Brazil for the design of thousands of anchored walls, until the advent of computers and limit equilibrium specialized software.

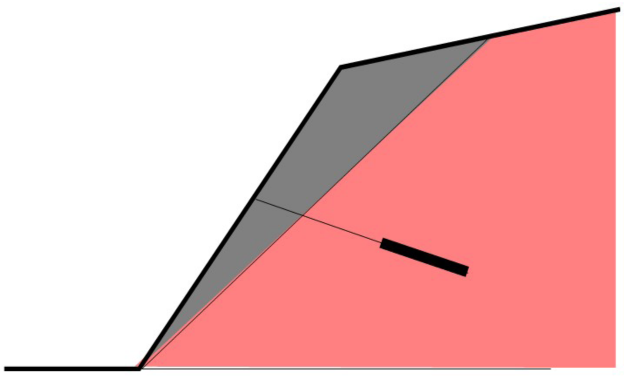

Figure 8. Wedge method (Costa Nunes & Velloso, 1963).

6. Corrosion

Corrosion protection was certainly not an issue in this first tieback wall. Nonetheless, the corrosion level seems quite small (Figure 9), given its 60 years of ageing.

Figure 9. Corrosion is underway.

It was the first of its kind, followed by a series of developments which included corrosion protection, and higher load reduction factors, among others, thanks to Prof Costa-Nunes' ingenuity.

The Authors are very pleased to re-discover this geotechnical engineering milestone and to remember our mentor, the late Prof Costa-Nunes.

Declaration of interest

The authors have no conflict of interest regarding the matter included in this paper. All co-authors have observed and affirmed the contents of the paper and there is no financial interest to report.

Authors' contributions

Alberto Ortigao: writing, reviewing and editing. Paulo Henrique Dias: methodology. Hélio Brito: validation. Marnio Camacho: validation.

Data availability

All data produced or examined in the course of the current study are included in this article.

References

Costa Nunes, A.J., & Velloso, D.A. (1963). Estabilização de taludes em capas residuais de origem granito-gnaissica. In Associação Brasileira de Mecânica dos Solos (Org.), *Proceedings of the Second Panamerican Conference on Soil Mechanics and Foundation Engineering* (pp. 383-394). São Paulo: ABMS (in Portuguese).

Descoeudres, J. (1969). Permanent anchors in rock and soils. In Sociedad Mexicana de Mecanica (Org.), *Proceedings of the Seventh International Conference on Soil Mechanics and Foundation Engineering* (pp. 195-197). London: ISSMGE.

Dupeuble, P., & Brulois, J. (1969). Measurements and observations on the behaviour of anchorages in soils. In Sociedad Mexicana de Mecanica (Org.), *Proceedings of the Seventh International Conference on Soil Mechanics and Foundation Engineering* (pp. 147-155). London: ISSMGE.

Hunt, R.E., & Costa Nunes, A.J. (1978). Retaining walls: taking it from the top. *Civil Engineering*, 48(5), 73-75.

Jelinek, R., & Ostermayer, H. (1966). *Verankerung von Baugruben Umschließungen. Vortrage der Baugrundtagung München*. Deutsche Gesellschaft für Erde und Grundbau.

Jelinek, R., & Ostermayer, H. (1967). Zur berechnung von fangdämmen und verankerten stutz wanden. *Die Bautechnik*, 44.

Jones, N., & Kerkhoff, G. (1961). Belled caissons anchor walls as Michigan remodels an expressway. *Engineering News-Record*, (May 11), 28-31.

Littlejohn, G. (1980). Design estimation of the ultimate load-holding capacity of ground anchors. *Ground Engineering*, 13(8), 25-39.

Ranke, A., & Ostermayer, H. (1968). Beitrag zur Stabilitätsuntersuchung mehrfach verankerter Baugruben Umschließungen. *Bautechnik*, 45(10), 341-350.

Weatherby, D.E. (1982). *Tiebacks: executive summary*. Federal Highway Administration. Report no. FHWA/RD-82/04 7.

Soils and Rocks

An International Journal of Geotechnical and Geoenvironmental Engineering

www.soilsandrocks.com

ISSN 1980-9743
ISSN-e 2675-5475

Integrated use of georadar, electrical resistivity, and SPT for site characterization and water content estimative

Érdeson Soares Farias[1], Sandro Lemos Machado[1#], Heraldo Luiz Giacheti[2], Alexsandro Guerra Cerqueira[3]

Case Study

Keywords
In situ tests
Site characterization
GPR
ERT
SPT
Coupled surveys

Abstract

Geophysical methods are potent tools for geotechnical site characterization in a non-destructive way. They improve the extrapolation of punctual data from direct survey methods, allowing a fast and cost-effective evaluation of large areas. Ground Penetrating Radar (GPR) and DC electrical resistivity (ER) are the most requested methods for geotechnical and geoenvironmental applications. Their use, however, is usually uncoupled, with no sharing of information from one method to another to improve data interpretation. This case study illustrates the development of protocols and scripts in R© programming language for ER and GPR data analysis with Standard Penetration Tests (SPT) data to produce more accurate information on subsurface conditions concerning lithology, water content, and groundwater table (GWT) position. The SPT data were used to associate resistivity ranges with different soil lithologies and GPR pulse velocities for estimating the soil water content. Estimated water content values aided in interpreting ER data and locating the groundwater table. The contacts between layers in the radargrams allowed the refinement of the ER model, rendering 3D volumes for each soil layer in situ.

1. Introduction

Geotechnical and geoenvironmental applications use the Ground Penetrating Radar (GPR) and electrical resistivity geophysical investigation methods intensively. They provide the possibility of extrapolating punctual geotechnical surveys, allowing a better and less expensive subsurface characterization (Cosenza et al., 2006). GPR is a non-destructive subsurface investigation method based on the propagation and reflection of electromagnetic pulses. It has proven to be a high-resolution, time and cost-efficient subsurface imaging method for geotechnical applications. GPR, however, presents limitations in the case of high-conductivity soils because of their elevated electrical conductivity, which causes GPR's signal attenuation. GPR's most common geotechnical applications are related to the subsurface location of buried structures such as pipes, galleries, and tanks and detection of different soil layer interfaces (Souza & Gandolfo, 2012). The reflections caused by an object crossing the radargram plane will form a hyperbola (Davis & Annan, 1989), a function of the velocity of propagation of the electromagnetic pulse (V), as illustrated in Equation 1:

$$V = \frac{2\sqrt{x^2 + z^2}}{t} \tag{1}$$

where x is the horizontal distance between the antenna's center and the object's center, z is its depth, and t is the two-way travel time. The value of V is a function of the electromagnetic properties of the propagation medium, and it can be estimated using an expression derived from Maxwell's equation (Equation 2):

$$V = \frac{C}{\sqrt{\frac{\mu\varepsilon}{2}\left[\sqrt{1+\left(\frac{\sigma}{\omega\varepsilon}\right)^2}+1\right]}} \tag{2}$$

where C is the light propagation in vacuum (3.10^8 m/s), σ is the medium electrical conductivity (S/m), ω is the angular frequency (rad/s), μ ($\mu = 4\pi \times 10^{-7}$ T m/A in vacuum, μ_o) is the magnetic permeability, and ε is the electric permittivity ($\varepsilon = 8.854$ $C^2/N\,m^2$ in a vacuum, ε_o) (Topp & Davis, 1981; Topp et al., 1980). Most minerals and fluids present values of μ close to μ_o. However, values of ε can vary widely in soils due to the soil water content. Furthermore, for the pulse

#Corresponding author. E-mail address: smachado@ufba.br
[1]Universidade Federal da Bahia, Departamento de Ciência e Materiais, Salvador, BA, Brasil.
[2]Universidade Estadual Paulista "Júlio de Mesquita Filho", Escola de Engenharia, Bauru, SP, Brasil.
[3]Universidade Federal da Bahia, Departamento de Geofísica, Salvador, BA, Brasil.

Submitted on June 10, 2022; Final Acceptance on May 18, 2023; Discussion open until November 30, 2023.
https://doi.org/10.28927/SR.2023.006422

frequencies used by GPR (0.02 to 2.5 GHz), the medium conductivity has a minor influence on the pulse propagation velocity, which can be approximated by Equation 3 (Davis & Annan, 1989):

$$V = \frac{C}{\sqrt{\varepsilon_r}} \tag{3}$$

where $\varepsilon_r = \varepsilon/\varepsilon_o$ is the relative dielectric constant of the medium.

Table 1 illustrates typical values of relative dielectric constant, electrical conductivity, and propagation velocity for different materials. As observed, water content significantly influences the pulse propagation velocity because of its high dielectric constant ($\varepsilon_r = 80$).

The interval velocity between two reflectors (V_{int}) can be calculated using Equation 4, proposed by Dix (1955), where V_n and V_{n-1} are the average velocities from the soil surface to the top of reflectors n and n-1 and, respectively, and t_n and t_{n-1} are the corresponding two-way travel times.

$$V_{\text{int}} = \sqrt{\frac{V_n^2 t_n - V_{n-1}^2 t_{n-1}}{t_n - t_{n-1}}} \tag{4}$$

Several studies related the soil water content with the propagation velocity of an electromagnetic pulse. The first contributions to this subject used the Time Domain Reflectometry (TDR) technique (Conciani et al., 1996; Topp & Davis, 1981; Topp et al., 1980). Similar concepts can be applied to GPR (Amparo et al., 2007; Botelho et al., 2003; Machado et al., 2006), although the position of the reflectors has yet to be discovered, contrary to TDR. Equation 5 was proposed (Botelho et al., 2003) based on the Wyllie equation for the elastic wave velocity of propagation (Wyllie et al., 1958) to estimate the gravimetric water content (w) in unsaturated soils. In this equation, ε_{rw} and ε_{rs} are the relative dielectric constants for water and soil solid particles, e is the soil void ratio, and G is the solid particles' relative density. According to the authors, for practical purposes, values of $\varepsilon_{rw} = 80$ and $\varepsilon_{rs} = 4.2$ (the relative dielectric constant for quartz) can be assumed for most cases.

$$w = \frac{\frac{C(e+1)}{V_{\text{int}}} - \sqrt{\varepsilon_{rs}} - e}{G\left(\sqrt{\varepsilon_{rw}} - 1\right)} \tag{5}$$

Grain size distribution, mineralogy, porosity, and water content/salinity are the main parameters controlling the soil's electrical resistivity (ρ). Furthermore, the soil cation exchange capacity (CEC) can indicate the mobility of the ions around soil particles. These ions facilitate the electrical current flow through the soil. Soil clay content and the predominance of 2:1 minerals such as bentonite and montmorillonite increase CEC (Nguyen, 2014). Thus, coarser soils present higher resistivity than silty and clayey soils. Electrical resistivity tomography (ERT) provides continuous 2D images of the subsoil, making it possible to analyze the ρ variations laterally and with depth (Souza & Gandolfo, 2012). The analysis of the resistivity sections allows for identifying the resistivity anomalies due to different lithologies and water contents or contaminant plumes in the subsurface (Sass et al., 2008).

Although demanding the injection of higher current intensities due to its low signal to noise ratio, the dipole-dipole arrangement allows rapid data acquisition and enables studying the lateral resistivity variations at different depths. In such an arrangement, the current (AB) and the potential (MN) dipoles are placed/aligned on the ground surface. The distance between the electrodes is kept constant and equal to a. The data acquisition starts with a minimum distance $x = 1\,a$ between the pairs AB, and MN and the following measurements are performed by displacing the pairs of electrodes at multiples of a (Souza & Gandolfo, 2012). Although providing continuous 2D and even 3D images of the subsoil, ERT resolution is a function of the distance a, and its use for high-resolution images is time-consuming. According to Zorzi & Rigoti (2011), the depth investigation can vary from AN/4 to AN/10. Furthermore, soil resistivity is a function of its water content, varying along the year according to the dry/rainy seasons. Using ERT associated with GPR offers a possibility to overcome these drawbacks.

In recent years, there has been an increase in the simultaneous use of GPR and ERT in site investigations,

Table 1. Typical values of ε_r, σ and V for different materials (Davis & Annan, 1989).

Material	ε_r (-)	σ (mS/m)	V (m/ns)
Air	1	0	0.300
Water	80	0.01	0.033
Dry sand	3-5	0.01	0.150
Saturated sand	20-30	0.1-1	0.060
Limestone	4-8	0.5-2	0.120
Shale	5-15	1-100	0.090
Silt	5-30	1-100	0.070
Clay	5-40	2-100	0.060
Granite	4-60	0.01-1	0.130

although such use has been limited to geotechnical applications. The purpose of site investigations varies depending on its objective, ranging from soil characterization and layer interface delimitation (Evangelista et al., 2017); to geological studies in unsaturated karst zones (Carrière et al., 2013), assessment of the thickness of talus layers in the European Alps (Sass et al., 2008), and stratigraphical characterization of Quaternary sediments layers (Pellicer & Gibson, 2011). In such works, GPR data is used to better define the interface between layers or as an additional tool in delineating high attenuation (or high conductivity) zones detected by ERT surveys. The use of GPR data to estimate moisture content and assist in interpreting ERT data is scarce. No publications with such characteristics were found in the literature by the authors. This case study uses SPT, GPR, and ERT for site characterization, including the water content estimation and definition of groundwater table position. SPT and GPR data are used to improve the ERT 2D sections, and the results of the modified ERT sections are used to construct a 3D stratigraphical model.

2. Study site

The study site is located at the countryside (thorp of Água Branca, 12°35’39.8”S; 38°26’06.2”W) of the city of São Sebastião do Passé, Bahia, Brazil, about 68 km from the capital of Bahia. The local geology is dominated by the Todos os Santos sedimentary Bay, formed from the evolution of the crustal stretching, which caused the fragmentation of the Gondwana supercontinent in the Mesozoic era (Lima, 1999).

Sediments of the São Sebastião and Barreira Formations and Quaternary deposits predominate in the study area (Figure 1). The São Sebastião Formation is a fluvial deposit lithologically composed of fine to coarse sandstones interspersed with silty clay layers. The typical composition of the clayey layers presents kaolinite and illite with a considerable amount of iron oxides (Souza et al., 2004).

Due to its high effective porosity and hydraulic conductivity, this formation is one of the most important underground water reserves of Todos os Santos Bay (Alves, 2015; Lima, 1999). The Barreira Formation is formed by fine sand and kaolinitic silty clay fractions with crossbedding and plane-parallel lamination. Its thickness ranges from 30 m to 40 m (Ghignone, 1979). The alluvial Quaternary sediments occur in shallower depths in valleys, floodplains, and the coast (Barbosa & Dominguez, 1996). Lithologically, they are poorly graded sandy sediments usually rich in organic matter. According to Lima (1999), the Reconcavo aquifer system, composed of the São Sebastião, Marizal, and Barreiras Formations, has a water reserve estimation of approximately five hundred billion cubic meters and is used to attend villages, cities, and industrial facilities.

3. In-situ site investigation campaign

The investigation campaign (Figure 2) used five SPTs boreholes excavated down to 15 m depth (ABNT, 2020), three ERT, and two GPR sections (Farias, 2021). Investigation line 3 was positioned close to SPT boreholes. SPT results (Figure 3) were used to interpret the ERT data and define the electrical resistivity ranges in the ERT sections. Unfortunately, the SPT performed tests could not detect groundwater table. The cisterns provided the only evidence concerning the groundwater table position in some residences’ backyards during the rainy season.

ERT surveys used a Syscal Pro resistivity meter (Iris Instruments®) with ten channels and an internal transmitter with 250 W and 2000 Vpp, allowing the injection of a maximum current of 2.5 A into the soil. The integrated transmitter/ receptor unities enable setting automatic reading scales

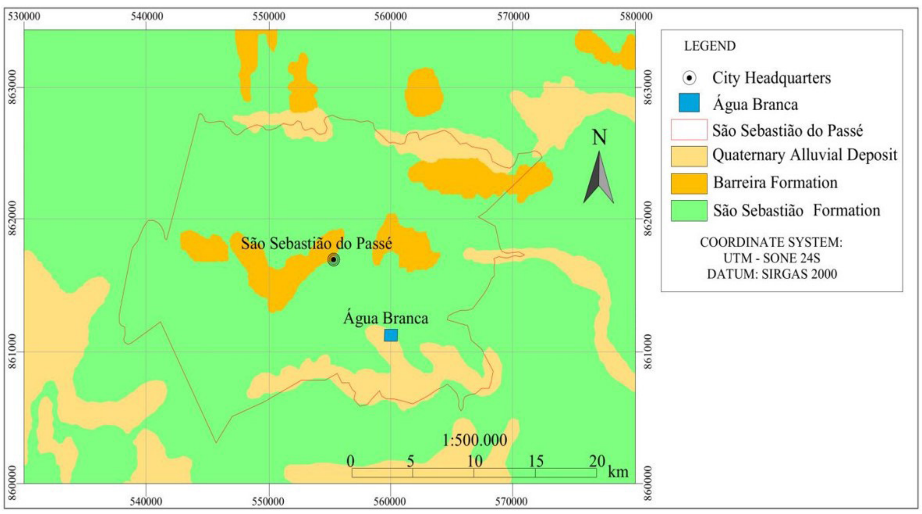

Figure 1. Lithology of the study site. Modified from Souza et al. (2004).

Figure 2. In situ tests carried out at the study site.

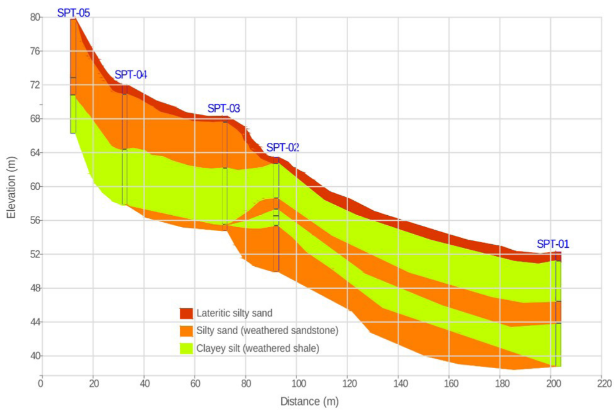

Figure 3. Associated soil profile obtained from SPT data. Adopted sobrelevation: 3.5.

and simultaneous measurements of apparent resistivity and chargeability. An inter-electrode spacing of a = 10 m was adopted (see Figure 4a). This value was adopted, aiming for a balance between ERT resolution and survey feasibility. The authors suggest a value of a = 5 m for better integration with GPR and SPT results for shallower investigations. A saline solution was used to improve the electrode/soil electrical conductivity. ERT surveys followed ABNT (2011).

The three ERT sections (ERT1, ERT2, and ERT3) had lengths of 270 m, 220 m, and 270 m, respectively. The experimental procedure initially positioned the two dipoles AB and MN in the first four electrodes and, while keeping the current dipole (AB) fixed, moving the potential dipole (MN) until a distance between the dipoles of 8a. The procedure was then resumed by positioning the dipoles at electrodes 2 to 5 (offset from the last initial position of 1 a), and the procedure was repeated until the last possible position.

The ERT apparent resistivity was inverted using ZondRes2d© software. The inversion process adopted a maximum depth of 45 m and ten iterations. Based on the obtained results from ERT and SPT, the following correspondence between local lithology and electrical resistivity was assumed for the study area: Clayey silt (weathered shale): ρ < 80 Ωm; Silty sand (weathered sandstone): 80 Ωm ≤ ρ < 180 Ωm and Lateritic silty sand ρ ≥ 180 Ωm. Although shale layers, especially if saturated, usually present resistivity values less than 20 Ωm, in this case, the material is described as clayey silt with a considerable amount of fine sand. Similarly, the silty sand (weathered sandstone) layer has a significant amount of clay, which is likely responsible for its relatively low electrical resistivity values. The 2D ERT sections were georeferenced using a R© (2020) programming language script developed for this study, the local topography, and the location of the survey points. Similar procedures were adopted for GPR

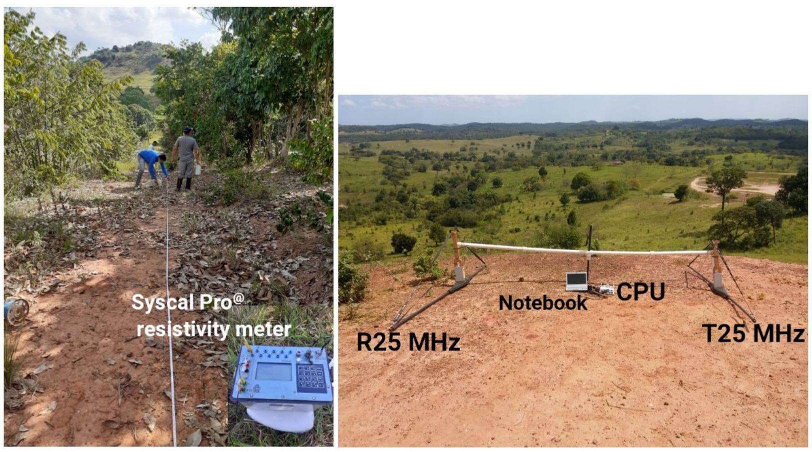

a) b)

Figure 4. Field activities. a) ERT and b) GPR.

data, in this case, using a different script. The GPR surveys used Mala Geoscience© equipment consisting of central unity (CUII), odometer, 25 MHz antennas, and laptop (see Figure 4b). A constant offset of 4 m between the antennas and a step distance of 0.5 m were adopted. The time window was 800 ns, corresponding to an investigation depth of about 40 m, if a V = 10 cm/ns is initially assumed for the soil. These values follow those usually suggested in the technical literature (Davis & Annan, 1989). The GPR data were processed using a R© (2020) script and the RGPR Libraries (Huber & Hans, 2018) with the following filter sequence: time zero correction -> dewow -> bandpass filter -> power time. The obtained radargrams were analyzed, and the existent reflection hyperbolas were fitted using Equation 1. This procedure enabled the creation of a velocity field for each radargram, which was used to convert travel time to depth (or elevation). Radargrams were then geo-referenced using the developed scripts.

The R© (2020) scripts developed for this study allows GPR and ERT data to be superimposed for better comparison and the 3D interpolation of the field data. The interpolated data can be used to construct 3D interactive images to visualize the investigation campaign results better. Fitted hyperbolas were also used to calculate the interval velocities according to Equation 4 and then estimate soil water content (Equation 5). In this case, values of G = 2.70 and e = 0.81 were assumed based on the data from undisturbed samples.

4. Results and analysis

Figure 5 presents the resistivity contours for section ERT3 jointly with the lithology data from SPT. There is a fair agreement between interpolated resistivity and soil lithology. However, the distinction between the clayey silt (weathered shale) and silty sand (weathered sandstone) layers was only sometimes satisfactory. These discrepancies are influenced by groundwater table position (SPT and ERT were performed in different periods) and the similar texture of the layers, besides ERT resolution, around 5 m. Individual bore log details can be found in Farias (2021).

Figure 6a presents data from the GPR2 radargram after filtering. Figure 6b shows some adjusted hyperbola and possible layer interfaces. The radargrams' hyperboles are valuable information often neglected in GPR surveys. They allow underground water content estimations using the TDR principles as previously discussed. Furthermore, the indicated layer interfaces help separate the different soil layers, adding resolution to the ERT surveys. Depth (z) and mean pulse velocity (V) are also indicated in Figure 6b (Equation 1). Figure 6c highlights high attenuation zones and crossbedding, which are coherent with the layering pattern observed in some SPT samples and with the findings of Lima (1999) concerning the Barreira Formation. High attenuation zones (loss of GPR return signal) in radargrams indicate the presence of high plasticity soils, which absorb most of the electrical-magnetic pulse energy due to their high electrical conductivity.

The high attenuation zones shown in Figure 6c were used with the estimated soil water contents to indicate the occurrence of the saturated shale layer. Equation 5 provided w estimations from V_{int}, which were calculated using the values of V presented in Figure 6b (Equation 4). Higher values of V are observed on the left side of the radargram (Figure 6b), indicating less saturated soil for shallower depths in this region. Figure 7 presents soil water content contours for GPR2 and indicates the probable position of the groundwater table. The soil was considered saturated for pulse velocities $V_{int} \leq 6.0$ cm/ns, corresponding to $w > 25\%$. This value follows the average value of void ratio of the collected specimens in the field (Farias, 2021). A sharp transition in the w values is noted on the left side of Figure 7, probably related to the occurrence of the sandstone (higher hydraulic conductivity) layer on the top of the shale layer. Therefore, rainwater is expected to infiltrate through sandstone and accumulate in the layers' interface. The groundwater table position obtained from GPR's surveys was coherent with the field observations performed in some cisterns located in the area during the rainy season.

Figure 8a presents the overlapping of ERT2 and GPR2 data. There is a good agreement between the high

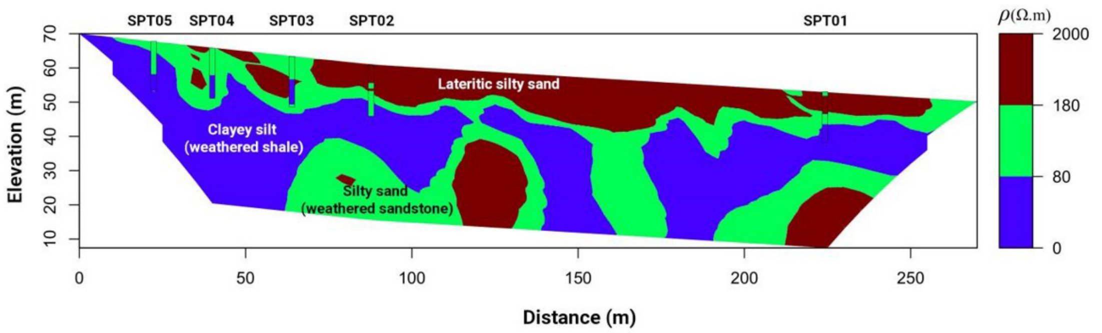

Figure 5. ERT3 inverted section and SPT.

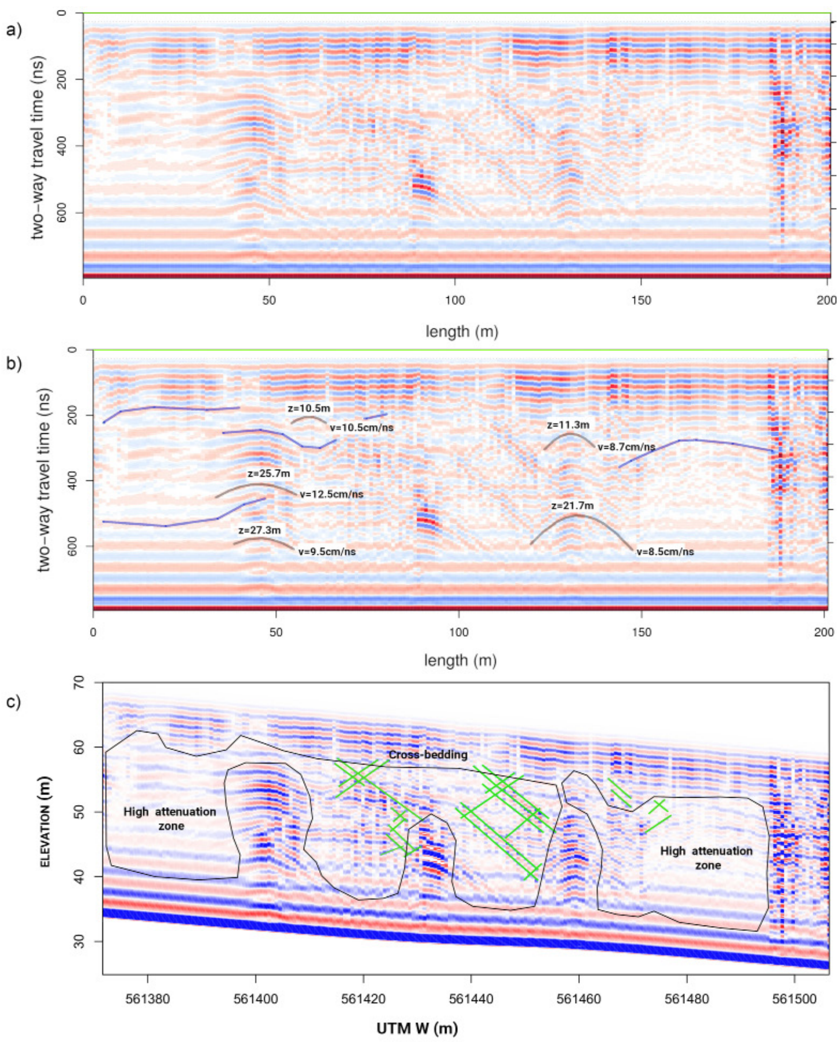

Figure 6. GPR2 radargram a) radargram after filtering sequence b) hyperbola fitting and c) crossbedding attenuation zones.

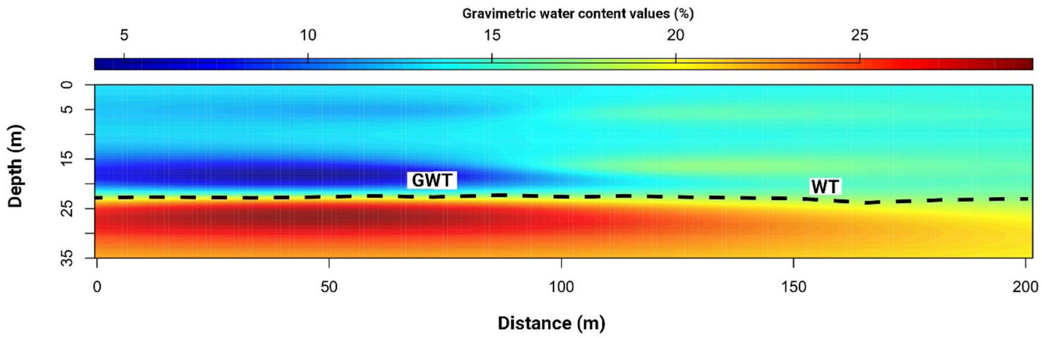

Figure 7. Contours of estimated water content values for GPR2 section.

attenuation zones in GPR2 and the occurrence of the weathered shale layer indicated in ERT2.

The hyperbolas identified in the radargram appear to be related to the high-resistivity zones detected in the lower part of Figure 8a. Due to their position at great depths and below the water table, these data indicate that it is possible that it is a different lithology than the shallower high-resistivity layer (silty lateritic sand). Figure 8b presents the modified ERT2 section after the coupled analysis of the SPTs, electrical resistivity, and GPR campaigns. Figure 9a presents the overlapping of ERT1 and GPR1 data. In this case, the high attenuation zones extend beyond the areas initially marked

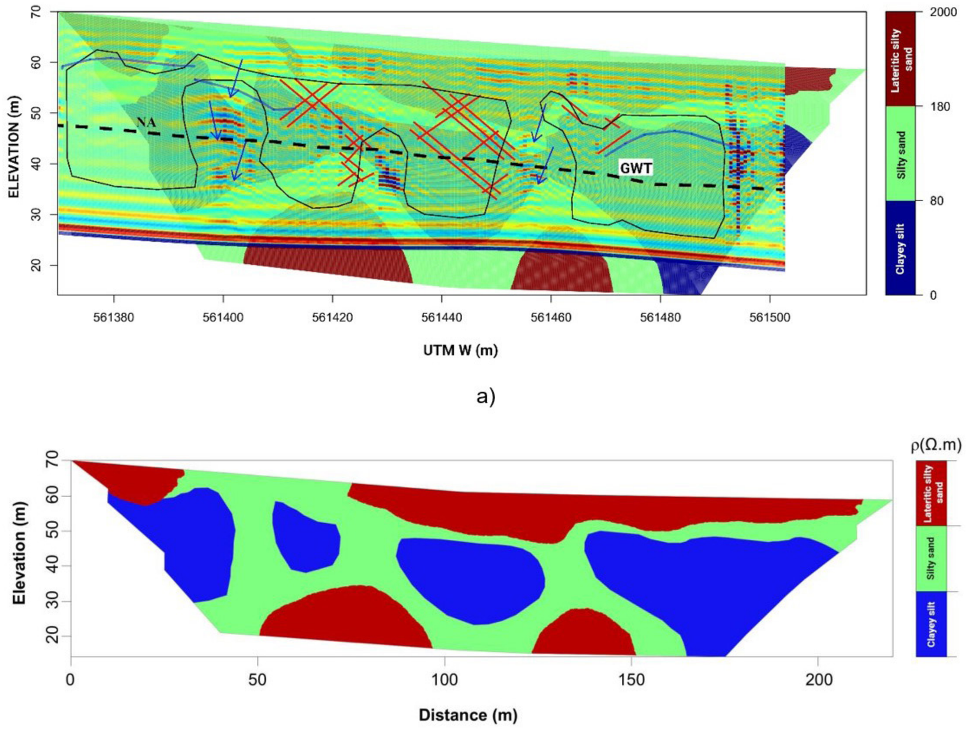

b)

Figure 8. a) ERT2 and GPR2 results overlapped and b) reinterpreted ERT2 section.

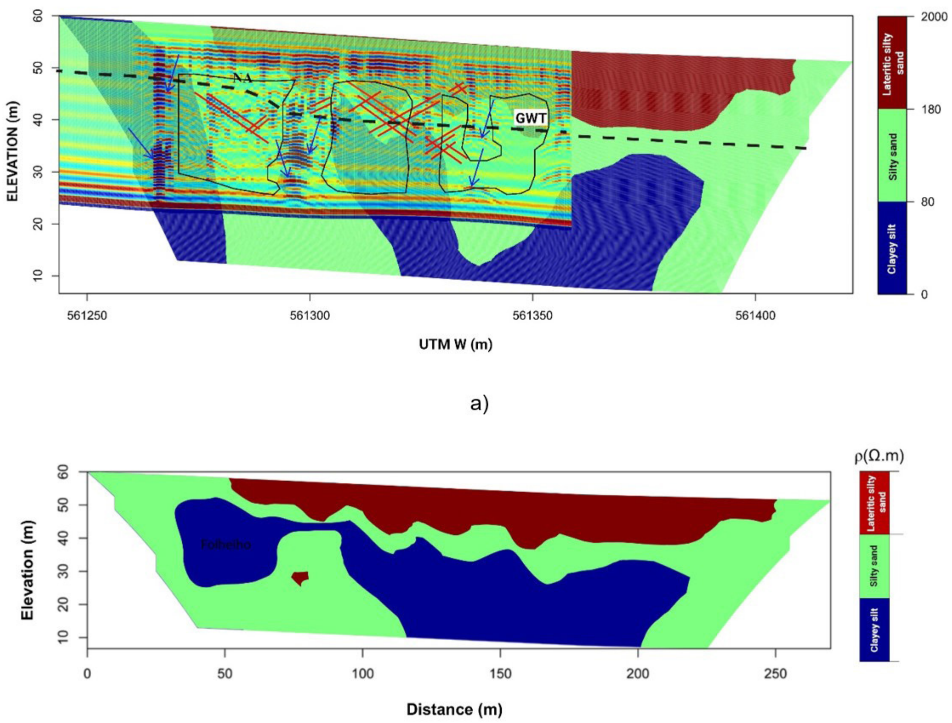

b)

Figure 9. a) ERT1 and GPR1 results overlapped and b) reinterpreted ERT1 section.

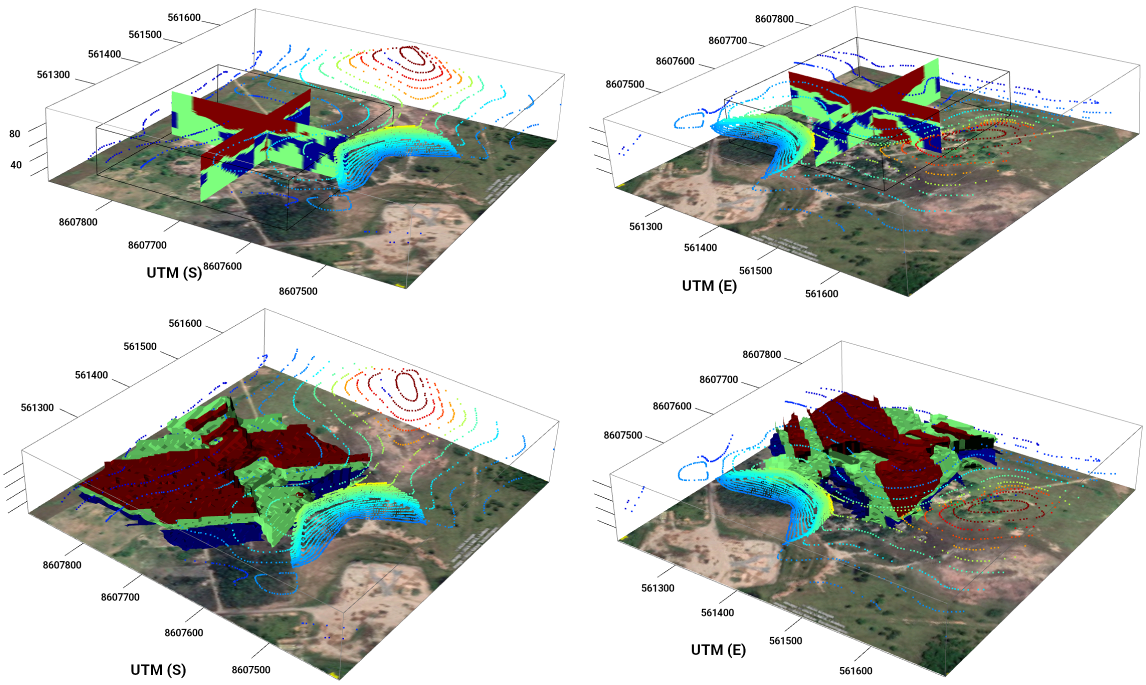

Figure 10. Typical sections of the elaborated 3D model.

as the weathered shale layer, motivating the changes in the ERT interpretation, as indicated in Figure 9b.

Figure 10 shows some sections of the 3D model obtained by interpolating the electrical resistivity values. Downloading the following links provide interactive versions of the Figure 10: Sections 3D (Machado, 2023a) and Surfaces 3D (Machado, 2023b).

5. Conclusion

Results from different direct and indirect investigation methods are presented and discussed to highlight how they can be used in a coupled manner for better characterization of subsurface conditions. The GPR data provided valuable information concerning the high conductance zones and aided in delimitating the contacts between the different layers in the field. In addition, the pulse propagation velocities obtained from hyperbola fitting were fundamental in correcting the radargram depth, also making it possible to estimate the soil moisture distribution and groundwater table location. The estimated moisture content values provided valuable information to interpret the ERT data since water can widely change ER values for a given soil formation. The SPT provided the basis for sketching the subsurface model, correlating the data from direct and indirect methods, and providing the information for ERT ranges definition. The developed activities in this case study may contribute to better site characterization, aggregating data from different sources, and analyzing the results in a coupled and interactive manner. The investigation procedures reduce doubts about the geotechnical characteristics of the subsurface soil layers. Detection of the layer interface is improved, in addition to providing estimates of soil water content that helps define the groundwater table location.

Acknowledgements

The authors would like to thank the Research Center on Geophysics and Geology of the Federal University of Bahia who provided the electro resistivity meter used in the paper.

Declaration of interest

The authors have no conflicts of interest to declare. All co-authors have observed and affirmed the contents of the paper and there is no financial interest to report.

Authors’ contributions

Érdeson Soares Farias: data curation, visualization, methodology, writing – original draft. Sandro Lemos Machado: methodology, supervision, writing – original draft. Heraldo Luiz Giacheti: writing – review and editing. Alexsandro Guerra Cerqueira: writing – review and editing.

Data availability

All data, models, or code that support the findings of this study are available from the corresponding author upon reasonable request.

List of symbols

a	distance between the electrodes
e	void ratio
t	two-way travel time
t_n	two-way travel time to reflector n
t_{n-1}	two-way travel time to reflector n-1
w	gravimetric humidity
x	horizontal distance between the antennas center to the center of the object
z	depth
A, B, M, and N	letters assigned to electrodes in ER methods
C	velocity of propagation of light in a vacuum
CEC	cation exchange capacity
ER	electrical resistivity
ERT	electrical resistivity tomography
G	specific density
GWT	groundwater water table
GPR	ground penetrating radar
SPT	standard penetration test
TDR	time domain reflectometry
V	velocity of propagation of the electromagnetic pulse
V_n	average velocity from the soil surface to the top of reflector n
V_{n-1}	average velocity from the soil surface to the top of reflector n-1
V_{int}	interval velocity
ε	electric permittivity
ε_0	electric permittivity of vacuum
ε_r	relative dielectric constant
ε_{rs}	relative dielectric constant for soil solid particles
ε_{rw}	relative dielectric constant for water
μ	magnetic permeability
μ_0	magnetic permeability in vacuum
ρ	electrical resistivity
σ	electrical conductivity
ω	angular frequency

References

ABNT NBR 15935. (2011). *Investigações ambientais — aplicação de métodos geofísicos*. ABNT - Associação Brasileira de Normas Técnicas, Rio de Janeiro, RJ (in Portuguese).

ABNT NBR 6484. (2020). *Solo - sondagens de simples reconhecimento com SPT - método de ensaio*. ABNT - Associação Brasileira de Normas Técnicas, Rio de Janeiro, RJ (in Portuguese).

Alves, J.E. (2015). *Estudos hidrogeoquímico comparativo entre os membros da Formação São Sebastião, Recôncavo Norte – BA* [Master's dissertation, Federal University of Bahia]. Federal University of Bahia repository (in Portuguese). Retrieved in May 18, 2023, from https://repositorio.ufba.br/handle/ri/21557

Amparo, N.S., Machado, S.L., Botelho, M.A.B., & Dourado, T.C. (November 1-3, 2007). Uso de GPR como uma ferramenta não intrusiva para levantamento de perfis de umidade de campo. In Associação Brasileira de Mecânica dos Solos e Engenharia Geotécnica (Org.), *VI Simpósio Brasileiro de Solos Não Saturados* (Vol. 1, pp. 229-236). São Paulo, Brazil: Associação Brasileira de Mecânica dos Solos e Engenharia Geotécnica (in Portuguese).

Barbosa, J.S.F., & Dominguez, J.M.L. (1996). *Mapa geológico do Estado da Bahia: texto explicativo*. Salvador: SICM (in Portuguese).

Botelho, M.A.B., Machado, S.L., Dourado, T.C., & Amparo, N.S. (September 14-18, 2003). Experimentos laboratoriais com GPR (1GHz) em corpos arenosos para analisar a influência da água e de hidrocarbonetos na sua velocidade de propagação. In Brazilian Geophysical Society (Org.), *8th International Congress of the Brazilian Geophysical Society* (pp. 1-6). Rio de Janeiro, Brazil: Brazilian Geophysical Society (in Portuguese). https://doi.org/10.3997/2214-4609-pdb.168.arq_1021.

Carrière, S.D., Chalikakis, K., Sénéchal, G., Danquigny, C. & Emblanch, C. (2013). Combining electrical resistivity tomography and ground penetrating radar to study geological structuring of karst unsaturated zone. *Journal of Applied Geophysics*, 94, 31-41. http://dx.doi.org/10.1016/j.jappgeo.2013.03.014.

Conciani, W., Herrmann, P.S.P., Machado, S.L., & Soares, M.M. (1996). O uso da técnica de reflectometria no domínio do tempo (TDR) para determinação da umidade do solo in situ. *Solos e Rochas*, 19, 189-199 (in Portuguese).

Cosenza, P., Marmet, E., Rejiba, F., Cui, Y.J., & Tabbagh, A. (2006). Correlations between geotechnical and electrical data: a case study at Garchy in France. *Journal of Applied Geophysics*, 60, 165-178. http://dx.doi.org/10.1016/j.jappgeo.2006.02.003.

Davis, J.L., & Annan, A.P. (1989). Ground penetrating radar for high resolution mapping of soil and rock stratigraphy. *Geophysical Prospecting*, 37(5), 531-551. http://dx.doi.org/10.1111/j.1365-2478.1989.tb02221.x.

Dix, C.H. (1955). Seismic velocities from surface measurements. *Geophysics*, 20, 68-86. http://dx.doi.org/10.1190/1.1438126.

Evangelista, L., Silva, F., D'Onofrio, A., Di Fiore, V., Silvestri, F., Santolo, A.S., Cavuoto, G., Punzo, M., & Tarallo, D. (2017). Application of ERT and GPR geophysical testing to the subsoil characterization of cultural heritage sites in Napoli (Italy). *Measurement*, 104, 326-335. http://dx.doi.org/10.1016/j.measurement.2016.07.042.

Farias, E.S. (2021). *Integração de técnicas GPR e eletrorresistividade para investigação do subsolo com foco na aplicação em geotecnia e meio ambiente* [Master's dissertation, Federal University of Bahia]. Federal University of Bahia Repository (in Portuguese). Retrieved in May 18, 2023, from http://www.geoamb.eng.ufba.br/site/sites/default/files/dissertations/erdeson_disserta_final_menor.pdf

Ghignone, J. (1979). Geologia dos sedimentos fenerozóicos do Estado da Bahia. In H.A.V. Inda (Ed.), *Geologia e recursos minerais do estado da Bahia: textos básicos* (Vol. 1, pp. 23-117). Salvador: Secretaria de Minas e Energia do Estado da Bahia (in Portuguese).

Huber, E., & Hans, G. (June 18-21, 2018). RGPR — an open-source package to process and visualize GPR data. In Institute of Electrical and Electronics Engineers (Org.), *17th International Conference on Ground Penetrating Radar (GPR)* (pp. 1-4). New York, United States: IEEE. https://doi.org/10.1109/ICGPR.2018.8441658.

Lima, O.A.L. (1999). *Caracterização hidráulica e padrões de poluição no aquífero Recôncavo na Região de Camaçari - Dias D'Avila* [Unpublished full professor thesis]. Universidade Federal da Bahia (in Portuguese).

Machado, S.L., Botelho, M.A.B., Amparo, N.S., & Dourado, T.C. (June 26-30, 2006). The use of the Ground Penetrating Radar, GPR in environmental non intrusive diagnostic and monitoring tasks. In H.R. Thomas (Ed.), *5th ICEG Environmental Geotechnics: Opportunities, Challenges and Responsibilities for Environmental Geotechnics* (Vol. 1, pp. 549-556). London, United Kingdom: Institute of Civil Engineers.

Machado, S.L. (2023a). Retrieved in June 14, 2023, from https://drive.google.com/file/d/1lhm60DdZfb_2m8m68In5hpS3Lu8IWPA5/view

Machado, S.L. (2023b). Retrieved in June 14, 2023, from https://drive.google.com/file/d/1KEX7VLRfdtnhNRwSjXKoweWBhyuwqYbz/view

Nguyen, S.T. (2014). Micromechanical approach for electrical resistivity and conductivity of sandstone. *Journal of Applied Geophysics*, 111, 135-140. http://dx.doi.org/10.1016/j.jappgeo.2014.10.001.

Pellicer, X.M., & Gibson, P. (2011). Electrical resistivity and Ground Penetrating Radar for the characterisation of the internal architecture of Quaternary sediments in the Midlands of Ireland. *Journal of Applied Geophysics*, 75(4), 638-647. http://dx.doi.org/10.1016/j.jappgeo.2011.09.019.

Sass, O., Bell, R., & Glade, T. (2008). Comparison of GPR, 2-D resistivity and traditional techniques for the subsurface exploration of the Öschingen landslide, Swabian Alb (Germany). *Geomorphology*, 93, 89-103. http://dx.doi.org/10.1016/j.geomorph.2006.12.019.

Souza, J.D., Melo, R.C., & Kosin, M. (2004). Mapa geológico do Estado da Bahia. In CPRM (Org.), *Repositório Institucional de Geociências*. Retrieved in May 18, 2023, from https://rigeo.cprm.gov.br/handle/doc/8665 (in Portuguese).

Souza, L.A., & Gandolfo, O.C.B. (2012). Métodos geofísicos em geotecnia e geologia ambiental. *Revista Brasileira de Geologia de Engenharia e Ambiental*, 2, 9-27 (in Portuguese). Retrieved in May 18, 2023, from https://www.abge.org.br/downloads/revistas/metodos.pdf

Topp, G.C., & Davis, J.L. (1981). Detecting infiltration of water through soil cracks by time-domain reflectometry. *Geoderma*, 26, 13-23. http://dx.doi.org/10.1016/0016-7061(81)90073-2.

Topp, G.C., Davis, J.L., & Annan, A.P. (1980). Electromagnetic determination of soil water content: measurements in coaxial transmission lines. *Water Resources Research*, 16(3), 574-582. http://dx.doi.org/10.1029/WR016i003p00574.

Wyllie, M.R.J., Gregory, A.R., & Gardner, G.H.F. (1958). An experimental investigation of factors affecting elastic wave velocities in porous media. *Geophysics*, 23, 459-493. http://dx.doi.org/10.1190/1.1438493.

Zorzi, R. R. & Rigoti, A (2011). Aplicação de métodos geoelétricos para monitoramento da barragem de concreto da UHE Gov. José Richa. *Boletim Paranaense de Geociências*, 64-65, 48-58 (in Portuguese). http://dx.doi.org/10.5380/geo.v65i0.10481.

REVIEW ARTICLES

Soils and Rocks
An International Journal of Geotechnical and Geoenvironmental Engineering
www.soilsandrocks.com
ISSN 1980-9743
ISSN-e 2675-5475

Systematic literature review and mapping of the prediction of pile capacities

Sofia Leão Carvalho[1,2#], Mauricio Martines Sales[2], André Luís Brasil Cavalcante[3]

Review Article

Keywords
ANN
Regression
Pile bearing capacity
Pile foundation
Systematic review

Abstract

Predicting the pile's load capacity is one of the first steps of foundation engineering design. In geotechnical engineering, there are different ways of predicting soil resistance, which is one of the main parameters. The pile load test is the most accurate method to predict bearing capacity in foundations, as it is the most accurate due to the nature of the experiment. On the other hand, it is an expensive test, and time-consuming. Over the years, semi-empirical methods have played an important role in this matter. Initially, many proposed methods were based on linear regressions. Those are still mainly used, but recently the use of a new method has gained popularity in Geotechnics: Artificial Neural Network. Over the past few decades, Machine Learning has proven to be a very promising technique in the field, due to the complexity and variability of material and properties of soils. Considering that, this work has reviewed and mapped the literature of the main papers published in journals over the last decades. The aim of this paper was to determine the main methods used and lacks that can be fulfilled in future research. Among the results, the bibliometric and protocol aiming questions such as types of piles, tests, statistic methods, and characteristics inherent to the data, indicated a lack of works in helical piles and instrumented pile load tests results, dividing point and shaft resistance.

1. Introduction

Estimating the bearing capacity of piles is an important step of foundation design and one of the best ways to get to know this capacity is through the execution of pile load tests. Despite the accuracy of this test, it is not always used in small or medium constructions due to its high cost. In such cases, semi-empirical methods are a very important tool for predicting pile load in the foundation design process.

Semi-empirical methods, such as Aoki & Velloso (1975) and Décourt & Quaresma (1978), were created comparing the prediction of bearing capacities obtained from pile load tests against other tests, which are easier to implement but more difficult to interpret, such as Standard Penetration Test (SPT), Cone Penetration Test (CPT) or Pile Driving Analyser (PDA). Besides, most of these methods might have limited information regarding imprecisions in the mobilization of the load by the pile, regarding the diameter and the regionalization of the data used (Schnaid & Odebrecht, 2012). These imprecisions in the prediction of load are caused by mostly on the share of mobilization between shaft and point of the piles.

In the meantime, other modern methods using artificial intelligence have become more popular and offer more precise predictions (Moayedi et al., 2020a). Artificial Neural Network, or ANN, and Machine Learning are artificial intelligence approaches that are popular in many fields, but not very popular among design engineers because they do not provide analytic equations that those are used to working with (Hanandeh et al., 2020).

Machine Learning based methods have become more common in the literature because of their improved precision compared to other methods, and the ability to be continually improved by introducing new data in the training set. On the other hand, models like ANN are considered by many "black-boxes". According to Shahin et al. (2009), this happens due to the little transparency of the methods and the fact that these methods do not explicitly explain the underlying physical process. This happens since all knowledge from ANN learning is stored in the weights, which are very difficult to interpret, due to the complex structure of the model.

[#]Corresponding author. E-mail address: sofia.leao@ufca.edu.br
[1]Universidade Federal do Cariri, Centro de Ciência e Tecnologia, Juazeiro do Norte, CE, Brasil.
[2]Universidade Federal de Goiás, Escola de Engenharia Civil e Ambiental, Goiânia, GO, Brasil.
[3]Universidade de Brasília, Departamento de Engenharia Civil e Ambiental, Brasilia, DF, Brasil.

Submitted on November 18, 2022; Final Acceptance on March 19, 2023; Discussion open until November 30, 2023.
https://doi.org/10.28927/SR.2023.011922

Nevertheless, Tarawneh & Imam (2014), for example, compared a Multiple Linear Regression (MLR) to an ANN model for the prediction of bearing capacity in time. They used a database of 169 piles of different types of section and material. The analysis of the ANN was more precise with an R^2 of 0,94 against 0,841 from the MLR model. Amâncio et al. (2022) conducted a successful comparison of a multilayer perceptron-based ANN model with Aoki & Velloso (1975) and Décourt & Quaresma (1978) methods, demonstrating improved accuracy in predicting tip and shaft resistance in 95 instrumented piles. Similarly, Gomes et al. (2021) employed machine learning models to estimate the bearing capacity of 165 precast concrete piles based on SPT results, surpassing the performance of Décourt & Quaresma (1978) method. The random forest technique exhibited the best performance, with RMSE values below 710, compared to Décourt & Quaresma (1978) RMSE value of 900.

According to Yong et al. (2020), there are two main divisions in the methods of Machine Learning. The first is Neuro-based Predictive Machine Learning (NPML), to which ANN belongs, and the second is Evolutionary Predictive Machine Learning (EPML), which contains Genetic Programming (GP), a powerful algorithm that provides a mathematic model, in the form of a regression. However, EPML models are generally more precise because regressions use functions pre-determined for modeling. Some examples of GP are linear-GP (LGP), Gene Expression Programming (GEP), and Simulated Annealing-GP (SA-GP).(Yong et al., 2020)

In this work, the main aim of the systematic review is to determine the main methods used and lacks that can be fulfilled in future research. The use of a protocol of research shows the main papers that have been published about bearing capacity in piles, compiling important information about the methods used, the data that have been applied.

The methodology presents the criteria of research, exclusion, and inclusion of papers within the string in the citation database search. The results of the bibliometric show information about the papers published, such as authors, publications over the years, and main journals of publication. At last, it was possible to also know some aspects of the research established by a protocol that will guide future works.

2. Methodology

In this work, a literature mapping was performed based on the search of two important abstract and citation databases: Web of Science (WOF), from Clarivate Analytics, and Scopus (SCP), from Elsevier. For both these databases, the string used was (Regression OR neural network) AND (bearing OR load) AND capacity AND piles. The systematic review was then conducted in three phases: planning the research guidelines based on a protocol; the proper search and selection of works of interest according to inclusion and exclusion criteria; and the extraction of information from the papers to understand the subject under investigation.

The Population, Intervention, Comparison, Outcomes, and Context (PICOC) methodology was used for to conduct the selection process. The description and application of each of the terms is provided in Table 1.

The collection of the papers is shown in Figure 1 and is divided into identification, selection, and eligibility. In the WOF database, 210 published works while in the SCP database 156 published works were returned, for a total of 366 publications, including theses, papers published in conferences, book chapters, and journal articles. As the aim of this work was to analyze only papers published in journals in English, the selection was reduced to 241 works that met these criteria.

Continuing the down-selection, all the duplicated documents were excluded (a total of 17 articles) and, following the flowchart, a selection criterion was applied to the titles, abstracts, and keywords. For this step, the criteria established by the PICOC protocol were applied. Hence, all publications whose subject was related to horizontal load, dynamic load, shallow foundations, and any other geotechnical field were excluded. This resulted in a final selection of 162 papers to pass to the eligibility phase.

During the eligibility phase, in which the complete reading of the papers is completed resulting in a further reduction of eligible papers to 80. In the process, some information about the bibliometrics and the methods and criteria of the papers were extracted. In the bibliometric research, the following information from the publications was collected:

Table 1. Description of the PICOC components of this systematic review.

Acronym	Definition	Description and application
P	population	Papers in English published in Journals on the WOF and SCP databases, that present any methods among linear regressions and neural networks for the prediction of pile bearing capacity.
I	intervention	Here, the criteria for inclusion or exclusion were defined. The papers under analysis should include both or any of linear regression or neural network, it should include only piles with application of vertical load only (dynamic and horizontal load excluded)
C	comparison	Not applicable.
O	outcomes	It was expected to obtain results regarding the main tests and types of piles that have been used, database size, and statistic parameters used to determine the accuracy of the methods.
C	context	To better understand the main application of the statistical methods to predict the bearing capacity of piles, and to outline decisions for future works.

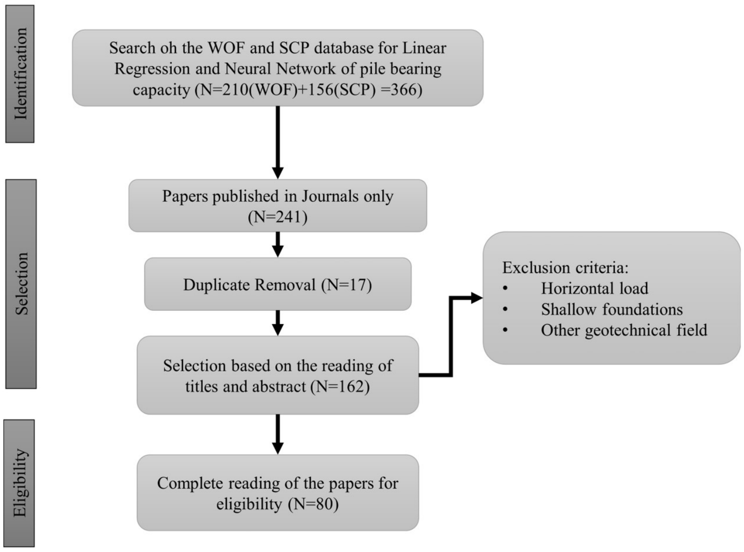

Figure 1. Flowchart of selection of papers for reading.

- Main journals of publication;
- Number of publications per year;
- Main authors and their countries;
- Main keywords used in the publications.

In line with the PICOC methodology, the following questions regarding the methods used in each publication were addressed:

- Main methods used by the authors to predict the bearing capacity, among linear regression methods and Neuro network methods;
- Most used statistic methods;
- Geotechnical tests used to generate the methods and types of piles used;
- Size of the database split between training and testing;
- Use instrumented pile load tests in the methods.

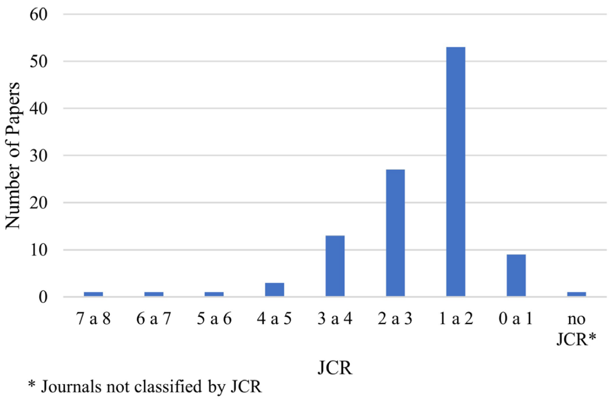

Figure 2. Papers per impact factor JCR.

3. Results

The search on the database platforms, WOS and SCP, happened on May 12th of 2021. 366 papers were collected from both platforms, from which only 241 were published in journals. From this analysis, after sorting (reading of titles, abstracts, and keywords) and removing duplicates, 80 papers were eligible to be read and analyzed. The results are presented as bibliometric results and protocol results.

3.1 Bibliometric

All 80 papers were published in English in journals that are listed in Table 2. Figure 2 shows the latest ranking by the Journal Citation Reports (JCR) from 2021 grouped. Among the journals, the best JCR factor was 7.963 from Engineering with Computers, with a total of 11 publications (13.75%), and 51,25% scored over 3.0. A total of 21 publications did not have a JCR factor, which represents 26.25% of the publications listed in this paper.

Figure 3 shows the distribution of these publications against time. In the search, there was no exclusion criterion related to the year of publications. The first eligible publication is from 1995, and the year that registered the largest number of eligible publications up to the date of the search (May 12th, 2021) was the year 2020, with 19 publications. The year 2021 was omitted from the figure as the data for this year was incomplete at the time of the search. Publications were rare between the years 1998 and 2009, with only 4 publications, and 90% of publications were made after 2009.

Bearing capacity semi-empirical prediction methods have been used for some decades. Even though prediction methods are quite known and used for a long time, methods based on machine learning are still a novelty in geotechnical engineering as also highlighted in the review by Moayedi et al. (2020a). Nejad et al.(2009), Baziar et al. (2015), and Nejad &

Table 2. Journal and papers published.

Journal	Number	Papers
Acta Geotechnica	1	Haque & Abu-Farsakh (2019)
Advances in Civil Engineering	1	Prayogo & Susanto (2018)
Applied Sciences (Switzerland)	1	Armaghani et al. (2020)
Applied Sciences-Basel	1	Pham et al. (2020a)
Arabian Journal for Science and Engineering	1	Momeni et al. (2020)
Arabian Journal of Geosciences	1	Mosallanezhad & Moayedi (2017)
Artificial Intelligence for Engineering Design, Analysis and Manufacturing: Aiedam	1	Harandizadeh (2020)
Canadian Geotechnical Journal	1	Shahin (2010); Shahin & Jaksa (2006)
Computers And Geotechnics	7	Ardalan et al. (2009); Chan et al. (1995); Kordjazi et al. (2014); Lee & Lee (1996); Nejad et al. (2009); Nejad & Jaksa (2017); Pal & Deswal (2010)
Earth Sciences Research Journal	1	Momeni et al. (2015)
Electronic Journal of Geotechnical Engineering	1	Dantas Neto et al. (2014)
Engineering Applications of Artificial Intelligence	3	Alkroosh & Nikraz (2012); Ismail et al. (2013); Ismail & Jeng (2011)
Engineering With Computers	11	Benali et al. (2021); Chen et al. (2020); Harandizadeh et al. (2021); Liu et al. (2020); Luo et al. (2021); Moayedi & Armaghani (2018); Moayedi et al. (2020b, 2021); Shaik et al. (2019); Wang et al. (2020); Yong et al. (2020)
European Journal of Environmental and Civil Engineering	1	Jebur et al. (2021)
Frontiers Of Structural and Civil Engineering	1	Singh et al. (2019)
Geomechanics And Geoengineering	1	Shahin (2015)
Georisk-Assessment and Management of Risk for Engineered Systems and Geohazards	1	(Zhang et al. (2021)
Geotechnical and Geological Engineering	8	Alzo'ubi & Ibrahim (2019); Das & Dey (2018); Ghorbani et al. (2018); Jebur et al. (2018b); Kardani et al. (2020); Kumar & Samui (2019); Samui (2012); Yamin et al. (2018)
International Journal of Geomate	1	Hanandeh et al. (2020)
International Journal of Geomechanics	3	Borthakur & Dey (2020); Moayedi & Hayati (2018); Shahin (2014)
International Journal of Geotechnical Engineering	3	Mohanty et al. (2018); Samui (2011); Suman et al. (2016)
Iranian Journal of Science And Technology - Transactions Of Civil Engineering	1	Harandizadeh & Toufigh (2020)
Journal Of Civil Engineering and Management	1	Benali et al. (2017)
Journal Of Computing in Civil Engineering	1	Teh et al. (1997)
Journal Of Geotechnical and Geoenvironmental Engineering	3	Kiefa (1998); Moayedi & Hayati (2019b); Pal & Deswal (2008); Zhang et al. (2006)
Journal Of Geotechnical Engineering	1	Goh (1996)
Journal Of Zhejiang University-Science A	1	Lu et al. (2020)
Ksce Journal of Civil Engineering	3	Baziar et al. (2015); Milad et al. (2015); Tarawneh & Imam (2014)
Marine Georesources and Geotechnology	1	Park & Cho (2010)
Measurement	3	Jebur et al. (2019); Momeni et al. (2014); Sun et al. (2020)
Neural Computing and Applications	3	Moayedi & Hayati (2019b); Moayedi & Rezaei (2019); Singh & Walia (2017)
Plos One	1	Pham et al. (2020b)
Processes	1	Kumar et al. (2021)
Sensors	1	Bui et al. (2019)
Ships And Offshore Structures	2	Ebrahimian & Movahed (2017); Jebur et al. (2018a)
Soft Computing	2	Dehghanbanadaki et al. (2021); Harandizadeh et al. (2019)
Soils And Foundations	1	Shahin (2014)
Transportation Geotechnics	1	Alzabeebee & Chapman (2020)
Vietnam Journal of Earth Sciences	1	Nguyen et al. (2020)

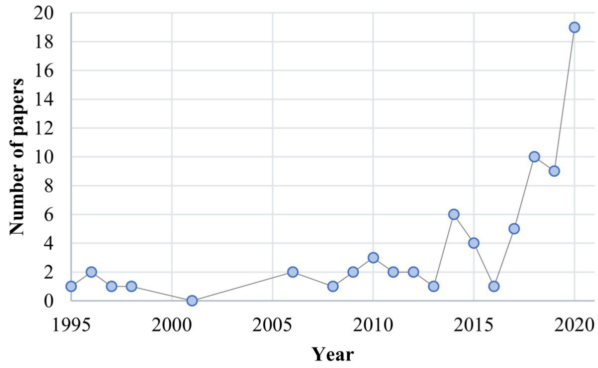

Figure 3. Distribution of papers per year.

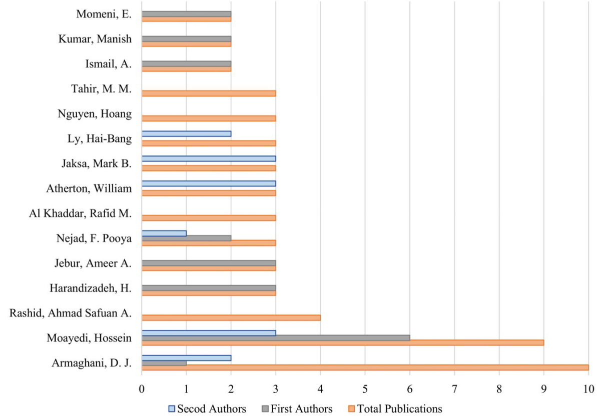

Figure 5. Main authors publishing as first authors, second authors, and total publications.

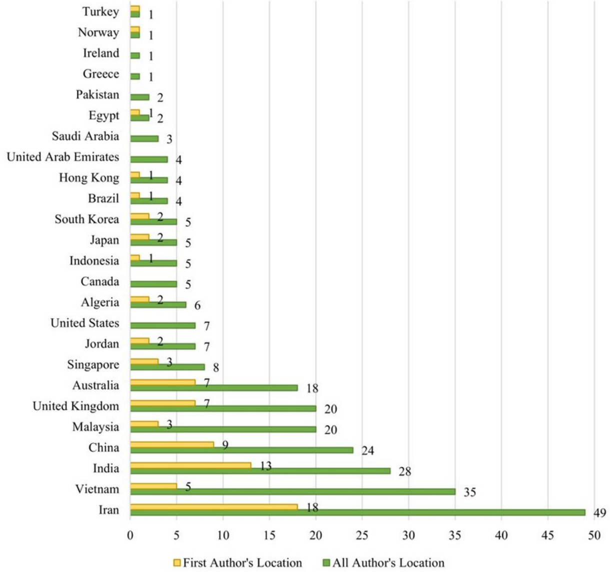

Figure 4. Distribution of authors and first authors per country.

Table 3. Main keywords as they appear in the paper.

Keywords	Number
Artificial neural network	15
Bearing capacity	8
ANN	8
Pile	6
ANFIS	7
Pile bearing capacity	7
Neural networks	6
Driven piles	5
Pile foundation	5
Sandy soil	4
Cone penetration test	4
Driven pile	4
Ultimate bearing capacity	3
Cone penetration test (CPT)	3
CPT	3

Jaksa (2017) have compared their methods to other methods such as Poulos & Davis (1980).

Publications were also sorted using the authors' location at the time of publication and the data is presented in Figure 4. Author country rankings are shown using only the first author as well as using all authors. In both cases, the top country is Iran. Making up the rest of the top seven in both cases includes Vietnam, India, China, Malaysia, the United Kingdom, and Australia.

Figure 5 shows the main 15 publishing authors, among which the first and second authors are included. The first 5 authors that have mostly published papers were Armaghani, D.J, Moayedi, H, Rashid, A.S.A, Harandizadeh, H, and Jebur, A.A.

The keywords used by the authors in the papers were variable, with up to 244 different expressions. The fifteen most recurrent are shown in Table 3, and in Table 4 those words that were lookalike, shown both in the acronym or expanded forms or with the main word in common, such as the types of the "pile", were grouped. Despite the use of many different methods, algorithms, and methods, the words ANN, "Artificial Neural Network" and "neuro networks" are still preferred as keywords.

Table 4. Main keywords grouped in recurrence.

Keywords	Number
Pile	83
Capacity	45
Artificial neural network (ANN)	43
Regression	16
Cone Penetration Test (CPT)	12
Artificial Intelligence (AI)	3

3.2 Protocol of search

The protocol search sought to answer important questions on the types of piles studied, the size of the databases used, the methods used, and how they are validated with statistical parameters. The database size is of major importance because it can help the decision-making of future research on how to collect and analyze this database. A large database can improve predictions but is very laborious to generate. On the other hand, a small database may be easier to establish but can lead to poor variance and big errors. According to Jebur et al. (2018a), the ideal size of database in ANN depends on the individual number of entrance parameters, composed mostly by information over the pile geometry, soil resistance, and type, and can be described by:

$$N \geq 50 + 8.I \tag{1}$$

where, N is the database size, and I is the individual number of entrance parameters.

In statistical learning, the correlation of data is transcribed in a function f that represents systematic correlation between one or more inputs, also known as independent variables, and output, or dependent, variables (James et al, 2013). Statistical learning methods, in which regressions and Machine Learning methods are included, use such approach to estimate f.

The observations called training data is a partition exclusively used to train or teach the method that finds and calibrates f. The other set of data is the testing data, which is used to confirm f.

Figure 6 shows the boxplot of both data sizes and how their division between training and test partitions is made in the papers. The average size of data, in Figure 6a, used by the authors is 304 while the median is 80. Some works used data sizes bigger than 200 units, and 4 of them did not say the size at all. Further, four studies used dataset sizes well outside the norm, of 1300, 2314, 4072, and 6437 (Baziar et al, 2015;Alzo'ubi & Ibrahim, 2019; Pham et al., 2020a; Zhang et al., 2021), and were omitted from the diagram for a better visualization of the boxplot.

In Figure 6b, the split between training and test partitions of the databases is shown. The average percentage used as training data is, according to the reviewed papers, 74%, and the median is 75%, while the average distribution for the testing set is 25% and a median of 20%.

Shahin (2010) highlights that just like empirical models, ANNs perform better using interpolation than extrapolation and so, within the training data should be included the extremes of it. The author also says that once the input and output data are selected, all variables should be normalized to vary between 0 and 1. This elimination of scales and dimensions allows the algorithm to pay equal attention to all variables during training.

Among the papers, some included different proportions between training and testing share to understand the influence of this factor on the prediction results (Das & Dey, 2018; Harandizadeh et al., 2019; Nejad et al., 2009; Nejad & Jaksa, 2017). From all the 80 papers, only 9 included a validation partition, separate from the test and training set, containing between 15 and 20% of the samples (Alzabeebee & Chapman, 2020; Benali et al., 2017; Ebrahimian & Movahed, 2017; Hanandeh et al., 2020; Jebur et al., 2018a, 2019; Milad et al., 2015; Moayedi & Hayati, 2019a).

The most used types of piles are presented in Table 5, and it shows that 57 out of 80 papers (71.25%) used driven

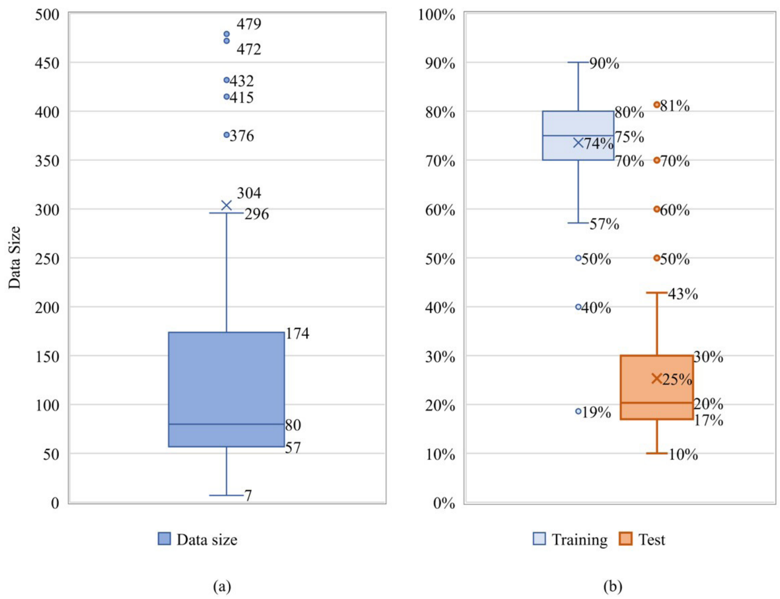

Figure 6. Boxplot: (a) database size used by the authors; (b) Training and Test share of the database.

Table 5. Types of piles analyzed in the papers.

Piles	Count
Driven Pile	57
Bored Piles	13
Non determined	5
Helical Piles	3
Drilled shafts	3
Piles Embedded	2
Belled Piles	1
Cast-in-site piles	1
Eco-friendly raft-pile system	1
Jacked Pile	1
Micropiles	1
Screw Piles in Laboratory	1
Small group of anchors	1
Socket Piles	1
Stone Columns	1

Table 6. Methods used as they were named in the papers.

Methods and Acronyms	Complete Names	Number
ANN	Artificial Neural Network	26
BP	Back-Propagation	17
ANFIS	Adaptive-Neuro-Fuzzy Inference System	13
GaP	Gaussian Process	9
Regression		9
LM	Levenberg-Marquardt	8
GA	Genetic Algorithm	7
PSO	Particle Swarm Optimization	7
SVM	Support Vector Machine	6
Random Forest	Random Forest	4
Hybrid models		4
MARS	Multivariate Adaptive Regression Spline	4
GMDH	Group Method of Data Handling	4
RNN	Recurrent Neural Networks	3
ICA-ANN	Imperialism Competitive Algorithm	3
GRNN	General Regression Neural Network	3
Kernel functions		3
FFNN	Feedforward Neural Network	2
GeP	Genetic Programming	1
GEP	Gene Expression Programming Technique	1
HON	High-Order Neural Network	1
ST-LSSVM	Self-Tuning Least Squares Support Vector Machine	1
RBNN	Radial Basis Functions Neural Networks	1
RGP-SVM	Regularized Generalized Proximal SVM	1
t-SVM	Twin SVM	1
FPNN	Fuzzy Polynomial Neural Network	1
Neuro fuzzy		1
TLBO	Teaching-Learning-Based Optimization Algorithm	1
EPR	Evolutionary Polynomial Regression	1
RVM	Relevance Vector Machine	1
MLP	Multilayer Percepton Artificial Neural Network	1
GSA	Gravitational Search Algorithm	1
SOS	Symbiotic Organisms Search	1
Fireflies		1
Cuckoo Search		1
Bacterial Foraging		1
MPMR	Minimax Probability Machine Regression	1
ENN	Emotional Neural Network	1
LSMT deep learning technique	Long Short-Term Memory	1

piles of different sections (pipe with open and closed ending, octagonal, square) and different materials (concrete, steel, and timber). The second most cited type of pile is the bored piles (16.25%), and helical piles, which are commonly used over the world, are represented by only 3.75% of piles in the papers. In the Table 6 papers that used chamber load test were omitted, since they do not represent a type of pile.

The data extracted from a geotechnical test are shown in Table 7 and the most used is CPT, representing 17% of the papers. Unfortunately, 21% of the papers do not specify exactly what tests were used. Of the specified test, the second most used is SPT (15%), followed by laboratory chamber load test (12%) and PDA (11%), which is commonly used in driven piles, as it can be obtained during the installation of the pile. In only 7 papers the pile capacity has been measured by dividing the contribution of the shaft and the tip of piles (Haque & Abu-Farsakh, 2019; Kiefa, 1998; Lu et al., 2020; Samui, 2012; Teh et al., 1997; Yamin et al., 2018; Zhang et al., 2006).

The methods that were used in the works are shown in Table 6. Regressions and MARS are mentioned in 13 different works. All the other names represent an algorithm of Machine Learning, which makes clear that most recent research is based on these methods. Most methods are described by the authors as ANNs (26 times), whilst Back Propagation, Adaptive Neuro-Fuzzy Inference Systems, Gaussian Process and Levenberg-Marquardt are mentioned a combined total of 47 times. Many studies use optimization algorithms, with some authors referring to their approach as a hybrid method, since optimization is an auxiliary tool to reach the global minimum.

Finally, the statistical parameters were analyzed, to evaluate the efficiency of the methods used and allow comparisons when needed. In this matter, there were significant differences in the statistical parameters used by the authors, and the main ones are listed in Table 8 and the main 10 used in Figure 7. The most used parameter that appears in 61% of the papers is the Root-Mean-Square Deviation, followed by the coefficient of Determination, R^2, with 54% and the correlation coefficient, R, in 32% of the use in papers. In many

Table 7. Geotechnical test used in the methods by the authors.

Tests	Count	%
Not specified	22	21%
CPT	18	17%
SPT	16	15%
Laboratory load test	13	12%
PDA	12	11%
Soil Characterization	6	6%
HSDT	5	5%
CAPWAY	4	4%
Stress wave data	2	2%
Flap number	2	2%
CPTu	1	1%
SLT	1	1%
CRP	1	1%
Pullout Capacity	1	1%
Piezocone penetration test (PCPT)	1	1%

Table 8. Main Statistical parameters used in the works.

Symbol	Meaning	Number
RMSE	Root-Mean-Square Deviation	51
R^2	Coefficient Of Determination	45
R	Correlation coefficient	27
MAE	Mean Absolute Error	20
VAF	Variance Account Factor	13
MSE	Mean Squared Error	7
σ	Standard Deviation	6
Mean	Mean	5
R	Correlation Coefficient	5
MAPE	Mean Absolute Percentage Error	4
ANOVA	Analysis of Variance	4
AAE	Absolute Average Error	3
A20	Error Under 20%	2
SE	Standard Error	2
MPE	Mean Percentage Error	1
COV	Covariance	1
Others	Others	19

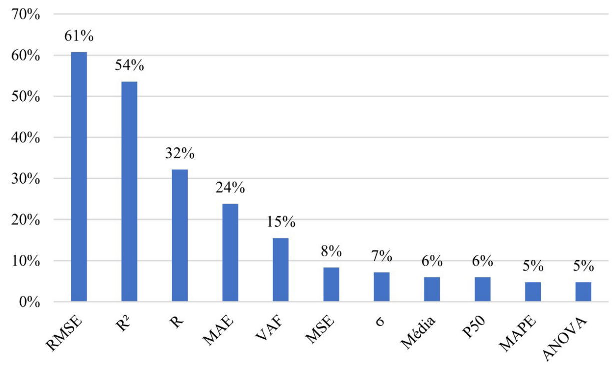

Figure 7. The 10 main statistical parameters used in the papers and their usage percentage.

papers, more than 5 parameters are used and, in this case, a ranking of the performance of each is used, to assist in the evaluation of the methods compared.

4. Conclusion

This systematic literature review and mapping have shown that Machine Learning has become predominant in the prediction of pile bearing capacity over the last 25 years and has surpassed the most traditional regression-based methods both in number and performance.

The protocol assisted to know the type of piles that are studied, the geotechnical tests that have been used, the size of the database the authors have collected and their share among training and testing, and the main statistical tools along with statistical parameters.

The mapping of literature enabled a better understanding of the main publications over the years, the most relevant authors, and journals, as well as the main keywords used by the authors.

In comparison to other methods, ANN has shown to be a very efficient tool when compared to classic empirical methods that are consolidated. ANNs have performed better, and, in most cases, results are much closer to the bearing capacities measured by pile load tests. The main algorithms used were Backpropagation, ANFIS, Gaussian Process and Levenberg-Marquardt. The most recent papers included meta-heuristics algorithms as well, in a hybrid approach.

Regarding the database, the average size used by authors was 304 and the median of 80 piles, while the average share between training and testing data were respectively 74% and 25%.

This work showed also that the main type of pile that has been investigated is driven piles, corresponding to almost 63% of the papers, along with the main tests being CPT and PDA accordingly. This might be justified because of the availability of data since to better perform such methods, a big database is expected to be used. Helical piles, on the other hand, are one of the most used piles in the world, and according to this research, were represented by only 4% of these papers, which shows an opportunity for new research. Besides, only seven of the papers mentioned that the pile capacity was measured by dividing the shaft and the point resistance.

Acknowledgements

This research was supported by the Brazilian sponsorship organizations CNPq, CAPES and FAPEG. We thank Prof. Marcus A. Siqueira Campos for his assistance with the methodology used on the systematic literature review.

Declaration of interest

The authors have no conflicts of interest to declare.

Authors' contributions

Sofia Leão Carvalho: conceptualization, data curation, methodology, writing – original draft. Mauricio Martines Sales: methodology, writing – review & editing, supervision. André Luís Brasil Cavalcante: writing – review & editing, supervision.

Data availability

The data that support the findings of this study are available upon request to interested parties. Please contact the corresponding author for further information on data availability.

References

Alkroosh, I., & Nikraz, H. (2012). Predicting axial capacity of driven piles in cohesive soils using intelligent computing. *Engineering Applications of Artificial Intelligence*, 25(3), 618-627. http://dx.doi.org/10.1016/j.engappai.2011.08.009.

Alzabeebee, S., & Chapman, D.N. (2020). Evolutionary computing to determine the skin friction capacity of piles embedded in clay and evaluation of the available analytical methods. *Transportation Geotechnics*, 24, 100372. http://dx.doi.org/10.1016/j.trgeo.2020.100372.

Alzo'ubi, A.K., & Ibrahim, F. (2019). Predicting Loading–unloading pile static load test curves by using artificial neural networks. *Geotechnical and Geological Engineering*, 37(3), 1311-1330. http://dx.doi.org/10.1007/s10706-018-0687-4.

Amâncio, L.B., Neto, S.A.D., & Cunha, R.P. (2022). Estimative of shaft and tip bearing capacities of single plies using multilayer perceptrons. *Soils and Rocks*, 45(3), e2022077821. https://doi.org/10.28927/SR.2022.077821.

Aoki, N., & Velloso, D. A. (1975). An approximate method to estimate the bearing capacity of piles. In *Proceedings of the 5th Pan-American Conference on Soil Mechanics and Foundation Engineering* (pp. 367-376), Buenos Aires.

Ardalan, H., Eslami, A., & Nariman-Zadeh, N. (2009). Piles shaft capacity from CPT and CPTu data by polynomial neural networks and genetic algorithms. *Computers and Geotechnics*, 36(4), 616-625. http://dx.doi.org/10.1016/j.compgeo.2008.09.003.

Armaghani, D.J., Asteris, P.G., Fatemi, S.A., Hasanipanah, M.M., Tarinejad, R., Rashid, A.S.A., & van Huynh, V. (2020). On the use of neuro-swarm system to forecast the pile settlement. *Applied Sciences*, 10(6), 1904. http://dx.doi.org/10.3390/app10061904.

Baziar, M.H., Saeedi Azizkandi, A., & Kashkooli, A. (2015). Prediction of pile settlement based on cone penetration test results: an ANN approach. *KSCE Journal of Civil Engineering*, 19(1), 98-106. http://dx.doi.org/10.1007/s12205-012-0628-3.

Benali, A., Boukhatem, B., Hussien, M.N., Nechnech, A., & Karray, M. (2017). Prediction of axial capacity of piles driven in non-cohesive soils based on neural networks approach. *Journal of Civil Engineering and Management*, 23(3), 393-408. http://dx.doi.org/10.3846/13923730.2016.1144643.

Benali, A., Hachama, M., Bounif, A., Nechnech, A., & Karray, M. (2021). A TLBO-optimized artificial neural network for modeling axial capacity of pile foundations. *Engineering with Computers*, 37(1), 675-684. http://dx.doi.org/10.1007/s00366-019-00847-5.

Borthakur, N., & Dey, A.K. (2020). Evaluation of group capacity of micropile in soft clayey soil from experimental analysis using SVM-based prediction model. *International Journal of Geomechanics*, 20(3), 04020008. http://dx.doi.org/10.1061/(ASCE)GM.1943-5622.0001606.

Bui, D.T., Moayedi, H., Abdullahi, M.M., Rashid, A.S.A., & Nguyen, H. (2019). Prediction of pullout behavior of belled piles through various machine learning modelling techniques. *Sensors*, 19(17), 3678. http://dx.doi.org/10.3390/s19173678.

Chan, W.T., Chow, Y.K., & Liu, L.F. (1995). Neural network: an alternative to pile driving formulas. *Computers and Geotechnics*, 17(2), 135-156. http://dx.doi.org/10.1016/0266-352X(95)93866-H.

Chen, W., Sarir, P., Bui, X.-N.N., Nguyen, H., Tahir, M.M., Armaghani, D.J., & Armaghani, D.J. (2020). Neuro-genetic, neuro-imperialism and genetic programing models in predicting ultimate bearing capacity of pile. *Engineering with Computers*, 36(3), 1101-1115. http://dx.doi.org/10.1007/s00366-019-00752-x.

Dantas Neto, S.A., Silveira, M.V., Amâncio, L.B., & dos Anjos, G.J.M. (2014). Pile settlement modeling with multilayer perceptrons. *The Electronic Journal of Geotechnical Engineering*, 19, 4517-4528.

Das, M., & Dey, A.K. (2018). Prediction of Bearing Capacity of Stone Columns Placed in Soft Clay Using ANN Model. *Geotechnical and Geological Engineering*, 36(3), 1845-1861. http://dx.doi.org/10.1007/s10706-017-0436-0.

Décourt, L., & Quaresma, A.R. (1978). Capacidade de carga de estacas a partir de valores de SPT. *Congresso Brasileiro de Mecânica dos Solos e Engenharia de Fundações*, 6, 45-53.

Dehghanbanadaki, A., Khari, M., Amiri, S.T., & Armaghani, D.J. (2021). Estimation of ultimate bearing capacity of driven piles in c-φ soil using MLP-GWO and ANFIS-GWO models: a comparative study. *Soft Computing*, 25(5), 4103-4119. http://dx.doi.org/10.1007/s00500-020-05435-0.

Ebrahimian, B., & Movahed, V. (2017). Application of an evolutionary-based approach in evaluating pile bearing capacity using CPT results. *Ships and Offshore Structures*, 12(7), 937-953. http://dx.doi.org/10.1080/17445302.2015.1116243.

Ghorbani, B., Sadrossadat, E., Bazaz, J.B., & Oskooei, P.R. (2018). Numerical ANFIS-based formulation for prediction of the ultimate axial load bearing capacity of piles through CPT data. *Geotechnical and Geological Engineering*, 36(4), 2057-2076. http://dx.doi.org/10.1007/s10706-018-0445-7.

Goh, A.T.C. (1996). Pile driving records reanalyzed using neural networks. *Journal of Geotechnical Engineering*, 122(6), 492-495. http://dx.doi.org/10.1061/(ASCE)0733-9410(1996)122:6(492).

Gomes, Y.F., Verri, F.A.N., & Ribeiro, D.B. (2021). Use of machine learning techniques for predicting bearing capacity of piles. *Soils and Rocks*, 44(4), e2021074921. https://doi.org/10.28927/SR.2021.074921.

Hanandeh, S., Alabdullah, S.F., Aldahwi, S., Obaidat, A., & Alqaseer, H. (2020). Development of a constitutive model for evaluation of bearing capacity from CPT and theoretical analysis using ANN techniques. *International Journal of GEOMATE*, 19(74), 229-235. http://dx.doi.org/10.21660/2020.74.36965.

Haque, M.N., & Abu-Farsakh, M.Y. (2019). Development of analytical models to estimate the increase in pile capacity with time (pile setup) from soil properties. *Acta Geotechnica*, 14(3), 881-905. http://dx.doi.org/10.1007/s11440-018-0654-5.

Harandizadeh, H. (2020). Developing a new hybrid soft computing technique in predicting ultimate pile bearing capacity using cone penetration test data. *Artificial Intelligence for Engineering Design, Analysis and Manufacturing*, 34(1), 114-126. http://dx.doi.org/10.1017/S0890060420000025.

Harandizadeh, H., Jahed Armaghani, D., & Khari, M. (2021). A new development of ANFIS-GMDH optimized by PSO to predict pile bearing capacity based on experimental datasets. *Engineering with Computers*, 37(1), 685-700. http://dx.doi.org/10.1007/s00366-019-00849-3.

Harandizadeh, H., Toufigh, M.M., & Toufigh, V. (2019). Application of improved ANFIS approaches to estimate bearing capacity of piles. *Soft Computing*, 23(19), 9537-9549. http://dx.doi.org/10.1007/s00500-018-3517-y.

Harandizadeh, H., & Toufigh, V. (2020). Application of developed new artificial intelligence approaches in civil engineering for ultimate pile bearing capacity prediction in soil based on experimental datasets. *Civil Engineering*, 44(Suppl. 1), 545-559. http://dx.doi.org/10.1007/s40996-019-00332-5.

Ismail, A., & Jeng, D.S. (2011). Modelling load-settlement behaviour of piles using high-order neural network (HON-PILE model). *Engineering Applications of Artificial Intelligence*, 24(5), 813-821. http://dx.doi.org/10.1016/j.engappai.2011.02.008.

Ismail, A., Jeng, D.S.-S., & Zhang, L.L. (2013). An optimised product-unit neural network with a novel PSO-BP hybrid training algorithm: applications to load-deformation analysis of axially loaded piles. *Engineering Applications of Artificial Intelligence*, 26(10), 2305-2314. http://dx.doi.org/10.1016/j.engappai.2013.04.007.

James, G.J., Witten, D., Hastie, T., & Tibshirani, R. (2013). *An introduction to statistical learning: with applications in R.* New York: Springer.

Jebur, A.A., Atherton, W., & Al Khaddar, R.M. (2018a). Feasibility of an evolutionary artificial intelligence (AI) scheme for modelling of load settlement response of concrete piles embedded in cohesionless soil. *Ships and Offshore Structures*, 13(7), 705-718. http://dx.doi.org/10.1080/17445302.2018.1447746.

Jebur, A.A., Atherton, W., Al Khaddar, R.M., & Loffill, E. (2018b). Settlement prediction of model piles embedded in sandy soil using the Levenberg-Marquardt (LM) training algorithm. *Geotechnical and Geological Engineering*, 36(5), 2893-2906. http://dx.doi.org/10.1007/s10706-018-0511-1.

Jebur, A.A., Atherton, W., Al Khaddar, R.M., & Aljanabi, K.R. (2019). Performance analysis of an evolutionary LM algorithm to model the load-settlement response of steel piles embedded in sandy soil. *Measurement*, 140, 622-635. http://dx.doi.org/10.1016/j.measurement.2019.03.043.

Jebur, A.A., Atherton, W., Al Khaddar, R.M., & Loffill, E. (2021). Artificial neural network (ANN) approach for modelling of pile settlement of open-ended steel piles subjected to compression load. *European Journal of Environmental and Civil Engineering*, 25(3), 429-451. http://dx.doi.org/10.1080/19648189.2018.1531269.

Kardani, N., Zhou, A., Nazem, M., & Shen, S.L. (2020). Estimation of bearing capacity of piles in cohesionless soil using optimised machine learning approaches. *Geotechnical and Geological Engineering*, 38(2), 2271-2291. http://dx.doi.org/10.1007/s10706-019-01085-8.

Kiefa, M.A.A. (1998). General regression neural networks for driven piles in cohesionless soils. *Journal of Geotechnical and Geoenvironmental Engineering*, 124(12), 1177-1185. http://dx.doi.org/10.1061/(ASCE)1090-0241(1998)124:12(1177).

Kordjazi, A., Nejad, F.P., & Jaksa, M.B. (2014). Prediction of ultimate axial load-carrying capacity of piles using a support vector machine based on CPT data. *Computers and Geotechnics*, 55, 91-102. http://dx.doi.org/10.1016/j.compgeo.2013.08.001.

Kumar, M., Bardhan, A., Samui, P., Hu, J.W., & Kaloop, M.R. (2021). Reliability analysis of pile foundation using soft computing techniques: a comparative study. *Processes*, 9(3), 486. http://dx.doi.org/10.3390/pr9030486.

Kumar, M., & Samui, P. (2019). Reliability analysis of pile foundation using ELM and MARS. *Geotechnical and Geological Engineering*, 37(4), 3447-3457. http://dx.doi.org/10.1007/s10706-018-00777-x.

Lee, I.M., & Lee, J.H. (1996). Prediction of pile bearing capacity using artificial neural networks. *Computers and Geotechnics*, 18(3), 189-200. http://dx.doi.org/10.1016/0266-352X(95)00027-8.

Liu, L., Moayedi, H., Rashid, A.S.A., Rahman, S.S.A., & Nguyen, H. (2020). Optimizing an ANN model with genetic algorithm (GA) predicting load-settlement behaviours of eco-friendly raft-pile foundation (ERP) system. *Engineering with Computers*, 36(1), 421-433. http://dx.doi.org/10.1007/s00366-019-00767-4.

Lu, S., Zhang, N., Shen, S., Zhou, A., & Li, H. (2020). A deep-learning method for evaluating shaft resistance of the cast-in-site pile on reclaimed ground using field data. *Journal of Zhejiang University. Science A*, 21(6), 496-508. http://dx.doi.org/10.1631/jzus.A1900544.

Luo, Z., Hasanipanah, M., Amnieh, H.B., Brindhadevi, K., & Tahir, M.M. (2021). GA-SVR: a novel hybrid data-driven model to simulate vertical load capacity of driven piles. *Engineering with Computers*, 37(2), 823-831. http://dx.doi.org/10.1007/s00366-019-00858-2.

Milad, F., Kamal, T., Nader, H., & Erman, O.E. (2015). New method for predicting the ultimate bearing capacity of driven piles by using Flap number. *KSCE Journal of Civil Engineering*, 19(3), 611-620. http://dx.doi.org/10.1007/s12205-013-0315-z.

Moayedi, H., & Armaghani, D.J. (2018). Optimizing an ANN model with ICA for estimating bearing capacity of driven pile in cohesionless soil. *Engineering with Computers*, 34(2), 347-356. http://dx.doi.org/10.1007/s00366-017-0545-7.

Moayedi, H., & Hayati, S. (2018). Applicability of a CPT-Based Neural Network Solution in Predicting Load-Settlement Responses of Bored Pile. *International Journal of Geomechanics*, 18(6), 06018009. http://dx.doi.org/10.1061/(ASCE)GM.1943-5622.0001125.

Moayedi, H., & Hayati, S. (2019a). Artificial intelligence design charts for predicting friction capacity of driven pile in clay. *Neural Computing & Applications*, 31(11), 7429-7445. http://dx.doi.org/10.1007/s00521-018-3555-5.

Moayedi, H., & Hayati, S. (2019b). Artificial intelligence design charts for predicting friction capacity of driven pile in clay. *Neural Computing & Applications*, 31(11), 7429-7445. http://dx.doi.org/10.1007/s00521-018-3555-5.

Moayedi, H., Mosallanezhad, M., Rashid, A.S.A., Jusoh, W.A.W., & Muazu, M.A. (2020a). A systematic review and meta-analysis of artificial neural network application in geotechnical engineering: theory and applications. *Neural Computing & Applications*, 32(2), 495-518. http://dx.doi.org/10.1007/s00521-019-04109-9.

Moayedi, H., Raftari, M., Sharifi, A., Jusoh, W.A.W., & Rashid, A.S.A. (2020b). Optimization of ANFIS with GA and PSO estimating α ratio in driven piles. *Engineering with Computers*, 36(1), 227-238. http://dx.doi.org/10.1007/s00366-018-00694-w.

Moayedi, H., Mu'azu, M.A., & Foong, L.K. (2021). Swarm-based analysis through social behavior of grey wolf optimization and genetic programming to predict friction capacity of driven piles. *Engineering with Computers*, 37(2), 1277-1293. http://dx.doi.org/10.1007/s00366-019-00885-z.

Moayedi, H., & Rezaei, A. (2019). An artificial neural network approach for under-reamed piles subjected to uplift forces in dry sand. *Neural Computing & Applications*, 31(2), 327-336. http://dx.doi.org/10.1007/s00521-017-2990-z.

Mohanty, R., Suman, S., & Das, S.K. (2018). Prediction of vertical pile capacity of driven pile in cohesionless soil using artificial intelligence techniques. *International Journal of Geotechnical Engineering*, 12(2), 209-216. http://dx.doi.org/10.1080/19386362.2016.1269043.

Momeni, E., Dowlatshahi, M.B., Omidinasab, F., Maizir, H., & Armaghani, D.J. (2020). Gaussian process regression technique to estimate the pile bearing capacity. *Arabian Journal for Science and Engineering*, 45(10), 8255-8267. http://dx.doi.org/10.1007/s13369-020-04683-4.

Momeni, E., Nazir, R., Armaghani, D.J., & Maizir, H. (2014). Prediction of pile bearing capacity using a hybrid genetic algorithm-based ANN. *Measurement*, 57, 122-131. http://dx.doi.org/10.1016/j.measurement.2014.08.007.

Momeni, E., Nazir, R., Armaghani, D.J., & Maizir, H. (2015). Application of artificial neural network for predicting shaft and tip resistances of concrete Piles. *Earth Sciences Research Journal*, 19(1), 85-93. http://dx.doi.org/10.15446/esrj.v19n1.38712.

Mosallanezhad, M., & Moayedi, H. (2017). Developing hybrid artificial neural network model for predicting uplift resistance of screw piles. *Arabian Journal of Geosciences*, 10(22), 479. http://dx.doi.org/10.1007/s12517-017-3285-5.

Nejad, F.P., & Jaksa, M.B. (2017). Load-settlement behavior modeling of single piles using artificial neural networks and CPT data. *Computers and Geotechnics*, 89, 9-21. http://dx.doi.org/10.1016/j.compgeo.2017.04.003.

Nejad, F.P., Jaksa, M.B., Kakhi, M., & McCabe, B.A. (2009). Prediction of pile settlement using artificial neural networks based on standard penetration test data. *Computers and Geotechnics*, 36(7), 1125-1133. http://dx.doi.org/10.1016/j.compgeo.2009.04.003.

Nguyen, T.-A., Ly, H.-B., Jaafari, A., & Pham, T.B. (2020). Estimation of friction capacity of driven piles in clay using artificial Neural Network. *Vietnam Journal of Earth Sciences*, 42(3), 265-275. http://dx.doi.org/10.15625/0866-7187/42/3/15182.

Pal, M., & Deswal, S. (2008). Modeling pile capacity using support vector machines and generalized regression neural network. *Journal of Geotechnical and Geoenvironmental Engineering*, 134(7), 1021-1024. http://dx.doi.org/10.1061/(ASCE)1090-0241(2008)134:7(1021).

Pal, M., & Deswal, S. (2010). Modelling pile capacity using Gaussian process regression. *Computers and Geotechnics*, 37(7–8), 942-947. http://dx.doi.org/10.1016/j.compgeo.2010.07.012.

Park, H.I., & Cho, C.W. (2010). Neural network model for predicting the resistance of driven piles. *Marine*

Georesources and Geotechnology, 28(4), 324-344. http://dx.doi.org/10.1080/1064119X.2010.514232.

Pham, T.A., Ly, H.-B., Tran, V.Q., Giap, L.V., Vu, H.-L.T., & Duong, H.-A.T. (2020a). Prediction of pile axial bearing capacity using artificial neural network and random forest. *Applied Sciences*, 10(5), 1871. http://dx.doi.org/10.3390/app10051871.

Pham, T.A., Tran, V.Q., Vu, H.-L.T.L.T., & Ly, H.-B.B. (2020b). Design deep neural network architecture using a genetic algorithm for estimation of pile bearing capacity. *PLoS One*, 15(12), e0243030. http://dx.doi.org/10.1371/journal.pone.0243030.

Poulos, H.G.H.G., & Davis, E.H.E.H. (1980). *Pile foundation analysis and design*. New York: Wiley.

Prayogo, D., & Susanto, Y.T.T. (2018). Optimizing the prediction accuracy of friction capacity of driven piles in cohesive soil using a novel self-tuning least squares support vector machine. *Advances in Civil Engineering*, 2018, 1-9. http://dx.doi.org/10.1155/2018/6490169.

Samui, P. (2011). Prediction of pile bearing capacity using support vector machine. *International Journal of Geotechnical Engineering*, 5(1), 95-102. http://dx.doi.org/10.3328/IJGE.2011.05.01.95-102.

Samui, P. (2012). Application of relevance vector machine for prediction of ultimate capacity of driven piles in cohesionless soils. *Geotechnical and Geological Engineering*, 30(5), 1261-1270. http://dx.doi.org/10.1007/s10706-012-9539-9.

Schnaid, F., & Odebrecht, E. (2012). *Ensaios de campo e suas aplicações à engenharia de fundações* (2ª ed.). São Paulo: Oficina de Textos.

Shahin, M.A., Jaksa, M.B., & Maier, H.R. (2009). Recent advances and future challenges for artificial neural systems in geotechnical engineering applications. *Advances in Artificial Neural Systems*, 2009, 1-9. http://dx.doi.org/10.1155/2009/308239.

Shahin, M.A. (2010). Intelligent computing for modeling axial capacity of pile foundations. *Canadian Geotechnical Journal*, 47(2), 230-243. http://dx.doi.org/10.1139/T09-094.

Shahin, M.A. (2014). Load-settlement modeling of axially loaded steel driven piles using CPT-based recurrent neural networks. *Soil and Foundation*, 54(3), 515-522. http://dx.doi.org/10.1016/j.sandf.2014.04.015.

Shahin, M.A. (2015). Use of evolutionary computing for modelling some complex problems in geotechnical engineering. *Geomechanics and Geoengineering*, 10(2), 109-125. http://dx.doi.org/10.1080/17486025.2014.921333.

Shahin, M.A., & Jaksa, M.B. (2006). Pullout capacity of small ground anchors by direct cone penetration test methods and neural networks. *Canadian Geotechnical Journal*, 43(6), 626-637. http://dx.doi.org/10.1139/t06-029.

Shaik, S., Krishna, K.S.R., Abbas, M., Ahmed, M., & Mavaluru, D. (2019). Applying several soft computing techniques for prediction of bearing capacity of driven piles. *Engineering with Computers*, 35(4), 1463-1474. http://dx.doi.org/10.1007/s00366-018-0674-7.

Singh, G., & Walia, B.S. (2017). Performance evaluation of nature-inspired algorithms for the design of bored pile foundation by artificial neural networks. *Neural Computing & Applications*, 28(1), 289-298. http://dx.doi.org/10.1007/s00521-016-2345-1.

Singh, T., Pal, M., & Arora, V.K. (2019). Modeling oblique load carrying capacity of batter pile groups using neural network, random forest regression and M5 model tree. *Frontiers of Structural and Civil Engineering*, 13(3), 674-685. http://dx.doi.org/10.1007/s11709-018-0505-3.

Suman, S., Das, S.K., & Mohanty, R. (2016). Prediction of friction capacity of driven piles in clay using artificial intelligence techniques. *International Journal of Geotechnical Engineering*, 10(5), 469-475. http://dx.doi.org/10.1080/19386362.2016.1169009.

Sun, G., Hasanipanah, M., Amnieh, H.B., & Foong, L.K. (2020). Feasibility of indirect measurement of bearing capacity of driven piles based on a computational intelligence technique. *Measurement*, 156, 107577. http://dx.doi.org/10.1016/j.measurement.2020.107577.

Tarawneh, B., & Imam, R. (2014). Regression versus artificial neural networks: predicting pile setup from empirical data. *KSCE Journal of Civil Engineering*, 18(4), 1018-1027. http://dx.doi.org/10.1007/s12205-014-0072-7.

Teh, C.I., Wong, K.S., Goh, A.T.C., & Jaritngam, S. (1997). Prediction of Pile Capacity Using Neural Networks. *Journal of Computing in Civil Engineering*, 11(2), 129-138. http://dx.doi.org/10.1061/(ASCE)0887-3801(1997)11:2(129).

Wang, B., Moayedi, H., Nguyen, H., Foong, L.K., & Rashid, A.S.A. (2020). Feasibility of a novel predictive technique based on artificial neural network optimized with particle swarm optimization estimating pullout bearing capacity of helical piles. *Engineering with Computers*, 36(4), 1315-1324. http://dx.doi.org/10.1007/s00366-019-00764-7.

Yamin, M., Khan, Z., El Naggar, H., & Al Hai, N. (2018). Nonlinear regression analysis for side resistance of socketed piles in rock formations of Dubai area. *Geotechnical and Geological Engineering*, 36(6), 3857-3869. http://dx.doi.org/10.1007/s10706-018-0577-9.

Yong, W., Zhou, J., Jahed Armaghani, D., Tahir, M.M., Tarinejad, R., Pham, B.T., & van Huynh, V. (2020). A new hybrid simulated annealing-based genetic programming technique to predict the ultimate bearing capacity of piles. *Engineering with Computers*, 37(3), 2111-2127. http://dx.doi.org/10.1007/s00366-019-00932-9.

Zhang, L.M., Ng, C.W.W., Chan, F., & Pang, H.W. (2006). Termination criteria for jacked pile construction and load transfer in weathered soils. *Journal of Geotechnical and Geoenvironmental Engineering*, 132(7), 819-829. http://dx.doi.org/10.1061/(ASCE)1090-0241(2006)132:7(819).

Zhang, W., Wu, C., Li, Y., Wang, L., & Samui, P. (2021). Assessment of pile drivability using random forest regression and multivariate adaptive regression splines. *Georisk-Assessment and Management of Risk for Engineered Systems and Geohazards*, 15(1), 27-40. http://dx.doi.org/10.1080/17499518.2019.1674340.

Soils and Rocks

An International Journal of Geotechnical and Geoenvironmental Engineering

www.soilsandrocks.com

ISSN 1980-9743
ISSN-e 2675-5475

The hydraulic conductivity of fuel permeated geosynthetic clay liners: a bibliometric study

Julia Favretto[1#], Adeli Beatriz Braun[1], Márcio Felipe Floss[2], Pedro Domingos Marques Prietto[1]

Review Article

Keywords
Soil contamination
Hydraulic barriers
Bentonite geocomposites
Database
Bibliometric indicators

Abstract

The use of geosynthetic clay liners (GCLs) as a hydraulic barrier for contaminants containment has proved to be an efficient alternative for the soil and groundwater protection. This geocomposite can be used in engineering systems to contain accidental spills and leaks of fuel in distribution centers, reservoirs and resulting from transport, where the geosynthetic acts as a protection against subsoil contamination. However, there is a concern about the behavior of GCLs in the face of these contaminants about possible changes in their properties, in order to compromise the retention capacity and permeability of the material. In this regard, the present work aimed to carry out a systemic and bibliometric study of publications related to the hydraulic conductivity of GCLs after contact with some type of fuel, available in the Scopus database (Elsevier) and Web of Science (Clarivate). The primary data selected directly from the databases were analyzed, making it possible to filter the publications that made up the bibliographic portfolio of the research, resulting in 14 selected documents, which were synthesized, and the main points were highlighted. From the bibliographic portfolio, bibliometric indexes of scientific production were created, as well as the temporal distribution of publications, authors, countries, and scientific journals that most contribute to the theme and the terms most evidenced in the documents. The panorama observed through bibliometrics was that it is a very recent theme, which still has a lack of scientific production, revealing itself as a promising area for the development of research.

1. Introduction

Environmental protection in infrastructure facilities has been receiving greater concern over time with respect to the main problems such as the intrusion of toxic contaminants in the subsurface soil and groundwater. The low hydraulic conductivity of bentonite geocomposites encouraged its use in several civil engineering to flow containment applications, such as hydraulic barriers in waste disposal, landfill bottom and cover systems, ponds, canals, reservoirs, whose first associated function was to control the water percolation (Petrov et al., 1997; Viana et al., 2011).

Geocomposites of bentonite or geosynthetic clay liners (GCLs) are industrialized products, consisting of a bentonite layer chemically or mechanically bonded to geotextiles and/or geomembranes (Lake & Rowe, 2000; Bouazza, 2002; Bouazza & Vangpaisal, 2007). The low permeability of GCLs is due to the high swelling capacity of the bentonite present in the compound.

Effective barriers against the advective transport of both liquids and gases can be achieved with the use of GCLs. In the absence of any other materials, the permeant flow is controlled by the permeability of the GCL with respect to that fluid (Rowe, 2020). The hydraulic conductivity k of GCLs is normally in the range of (1 to 5) x 10^{-11} m/s when permeated with water (Koerner, 2012). Bouazza (2002) presents compiled results from various sources of laboratory tests conducted on GCLs, that indicate values of hydraulic conductivity with respect to water varying between 2 x 10^{-12} m/s and 2 x 10^{-10} m/s, depending on applied confining stress.

The GCLs can also be used in secondary containment barriers for chemicals, as part of a composite containment system in applications to contain accidental fuel spills, caused by leaks in underground reservoirs, spills and accidents during the exploration, refinement, transport, and storage operations of oil and its derivatives, in order to provide short-term barrier to prevent site contamination (Rowe et al., 2004; Mukunoki et al., 2005; Rowe et al., 2006; Rowe et al., 2008; Hosney & Rowe, 2014; McWatters et al., 2016; McWatters et al., 2020).

[#]Corresponding author. E-mail address: juliafavretto@hotmail.com
[1]Universidade de Passo Fundo, Passo Fundo, RS, Brasil.
[2]Instituto de Ciências Agronômicas, Passo Fundo, RS, Brasil.

Submitted on November 23, 2022; Final Acceptance on April 18, 2023; Discussion open until November 30, 2023.
https://doi.org/10.28927/SR.2023.012222

When GCLs is applied to contain liquids other than water, its hydraulic performance can potentially be affected in some cases due to the chemistry of the permeant fluid and bentonite. To ensure good performance of the GCLs as a barrier, the compatibility between the bentonite and the expected pollutant liquid should be verified (Mazzieri et al., 2000) and it is necessary sufficient hydration of the bentonite with water before contact with contaminants (Mazzieri et al., 2000; Rowe et al., 2005a; Rowe et al., 2005b; Rowe et al., 2007).

Research on the performance of GCLs has made considerable progress in recent decades (e.g., Hewitt & Daniel, 1997; LaGatta et al., 1997; Bouazza, 2002; Bouazza et al., 2006; Touze-Foltz et al., 2006; Meer & Benson, 2007; Rowe, 2012; Bradshaw & Benson, 2013; Rowe, 2014; Rowe et al., 2016; Bouazza et al., 2017; Rowe et al., 2019; Wang et al., 2019; Carnero-Guzman et al., 2021; Rowe & AbdelRazek, 2021). However, to-date there has been very little research relating to the use of GCLs in fuel containment barriers, as already noted by Rowe et al. (2008) years ago with respect to GCLs in contact with hydrocarbons.

This study employs a quantitative-descriptive bibliometric approach to locate and analyze existing studies on the use of GCLs in fuel containment barriers and their interaction with contaminants, with a focus on changes in permeability and hydraulic conductivity. Two of the most widely used databases in the field are Scopus and the Web of Science (WoS). Scopus is the largest database of abstracts and citations of literature, scientific journals, books, and peer-reviewed scholarly works. The Web of Science (WoS), on the other hand, is a bibliographic reference database that contains information about scientific production from 1945 onwards (Scopus, 2022; Web of Science, 2022).

Bibliometrics is a tool that expands knowledge on the subject presented and is characterized by a search with pre-defined criteria, minimizing implicit tendencies of the researcher and enabling the direction of new research with greater precision (Macedo et al., 2010). This type of research, in addition to allowing the collection of data from primary sources, also allows the collection of secondary data through the elaboration of a bibliographic portfolio, which represents the perception and delimitation of the authors regarding the relevance and representativeness of the studies according to with the interests of the research and the topic addressed (Braun et al., 2019).

The objective of this article is to address a significant research gap related to the hydraulic conductivity of geosynthetic clay liners after exposure to fuel. Through a thematic synthesis of the main studies in this area and an examination of publication patterns (including temporal distribution, authors, countries, and scientific journals that contribute most to the topic) it is expected to identify gaps in the literature and provide guidance for future research.

2. Materials and methods

The methodology of this study involved a systematic and bibliometric research using qualitative and quantitative approaches, which was based on the studies of Braun et al. (2019) and Visentin et al. (2020).

2.1 Database and research delimitation

This research was conducted using two prominent scientific databases, Scopus (Elsevier) and Web of Science (Clarivate), selected for their extensive coverage of scientific publications and their ability to provide reliable citation data. No restrictions were placed on the types of documents, type of access and areas of knowledge that publish on the subject. Therefore, this review encompasses a broad range of materials, including scientific articles, reviews, books and book chapters, conference proceedings, contributions to edited volumes and working papers.

The analysis time considered in the research was until the year 2022, when the last query in the databases was performed. The initial year of the research was not specified, to verify the entire scientific contribution related to the topic. The language selected for research in both databases was English. In Scopus, the search was carried out using as a criterion that the combinations of the selected keywords were found in the "title, abstract and keywords" of the publications. In WoS, the keyword search criterion was in the "topic" of the publications, which corresponds to the "title, abstract, author's keywords and keywords plus", the latter consisting of words or phrases created or extracted from the titles of cited articles and retrieved by searching the topic field.

2.2 Selection and composition of the bibliographic portfolio

Initially, the keywords for the research were defined, being: "hydraulic conductivity", "permeability", "GCL", "geosynthetic clay liners", "fuel", "oil", "petroleum", "hydrocarbons", "diesel", "biodiesel", "gasoline" and "ethanol".

For the combination of words, the Boolean operators "AND" and "OR" were used. The use of the AND operator is necessary when you want all the terms used to appear in publications, while the OR operator indicates that at least one of the terms must appear in the document. In the case of a term or expression, operators (" ") were also used in order to represent a single word in the search.

The systemic search of primary data (raw) in both databases, Scopus and WoS, considering the previously defined boundaries, included 54 documents, 34 of which were found in the Scopus database and 20 in the WoS. These publications were stored in the Bibliometrix/R software, which allows for the initial filtering of the publications; assists in coding and managing data and ideas, visually modeling and generating reports through Biblioshiny, a web interface to Bibliometrix, which facilitates data analysis; and allows extracting the main information from each publication.

The filtering process used in this study consisted of reading the entire text of each publication. First, duplicate publications (14 in total) were excluded, followed by those that were unavailable for full download (3 in total, indexed in Scopus). Additionally, 15 publications were excluded due to their incompatibility with the study theme, indexed in Scopus, and 6 more were excluded from WoS. Finally, 2 publications that were redundant and incompatible with the study theme, indexed in both databases, were also excluded. Thus, a total of 40 publications were excluded, and the bibliographic portfolio was reduced to 14 publications, which correspond to specific works on the hydraulic conductivity of GCLs permeated with some type of combustible fluid. Figure 1 presents the synthesis of the process of treatment of the primary results for the construction of the work portfolio.

When comparing the initial results of the research, there is a greater difference in the number of publications indexed in each database. However, after a more careful analysis, it is seen that this difference significantly reduces the composition of the portfolio, so that the difference of articles exclusively indexed is reduced to only 2 articles, which are indexed in Scopus, against none exclusively indexed in WoS. The other articles that make up the group are found in both databases.

In the end, 14 articles were part of the set of publications related to the theme, also called the bibliographic research portfolio (Petrov et al., 1997; Mazzieri et al., 2000; Rowe et al., 2004; Mukunoki et al., 2005; Rowe et al., 2005a; Rowe et al., 2005b; Rowe et al., 2006; Rowe et al., 2007; Rowe et al., 2008; Sari & Chai, 2013; Hosney & Rowe, 2014; Gitipour et al., 2015; McWatters et al., 2016; McWatters et al., 2020).

With the portfolio defined, the analysis of the selected works began and the elaboration of indicators, such as number of publications per year, authors, countries and journals that contribute most with publications on this topic. And finally, each article was analyzed individually, and comparisons were made to detect higher order themes within the literature and thus compose a synthesis regarding the theme.

3. Analysis and results

3.1 Temporal distribution of scientific production of primary data

The distribution referring to the temporal cut of the data of the first phase of the research, where 54 publications were found (34 in Scopus and 20 in WoS), is represented in Figure 2. The temporal distribution of the works found is situated in a period of 24 years, starting in 1997 until 2021.

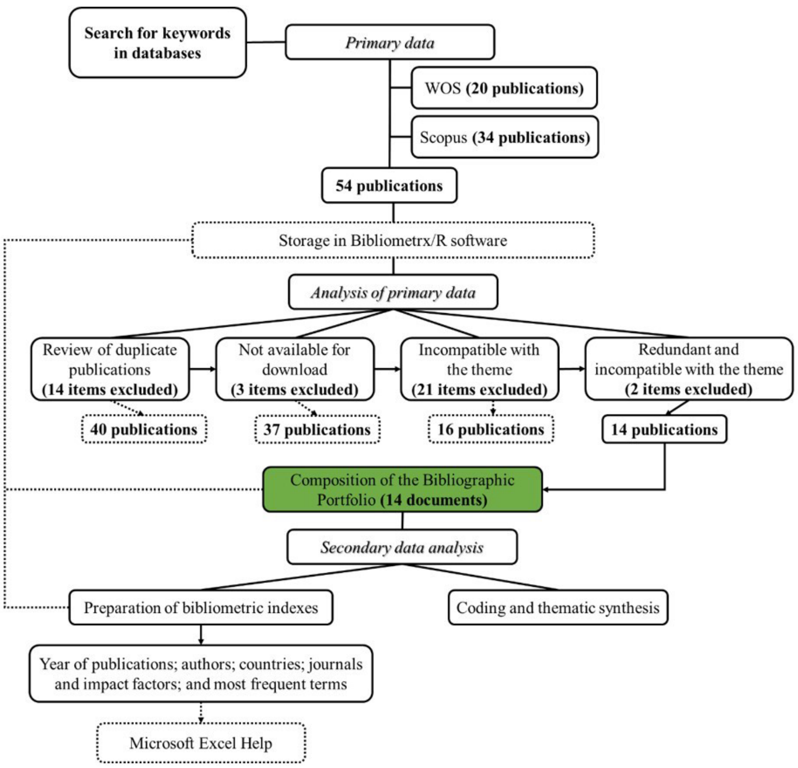

Figure 1. Scheme of the bibliographic portfolio construction process.

It was observed that the first research on the subject began in mid-1997. However, clearly in the following years there were no publications, and these were resumed with greater frequency only from 2004 onwards. There was no gradual growth, there were always oscillations in the number of annual publications, with the peak being reached in 2016, and the last publication in 2021.

3.2 Temporal distribution of scientific production of secondary data

This item presents the evolution of scientific production only of publications related to the subject of study, which make up the bibliographic portfolio (14 articles) and from which subsequent analyses are presented. The temporal distribution of these works is situated in a period of 12 years, as can be seen in Figure 3.

The more specific theme was already present in the first publications by Petrov et al. (1997). However, from this first publication there were no major developments, since the number of annual publications and the accumulated frequency remained constant, except for the year 2005, which peaked in publications directly related to the theme. Another important finding is related to the last publication specific to the theme that occurred in 2020 by McWatters et al. (2020), approximately two years from the date of this research, which shows that studies are evolving quite slowly, with extended periods without publication.

Therefore, the scientific production related to the evaluation of the hydraulic conductivity of the GCL material when in contact with fuels still lacks research, seen by the low number of publications over the years. In view of this and the fact that it is a very recent theme, the scenario, in addition to being relevant, is promising for the development of new works in this area.

3.3 Authors with the greatest contribution to the topic

Based on the 14 selected publications, it was possible to identify the authors with more publications on the subject. In total, 33 different authors were responsible for the publications, and of these, 10 authors have two or more publications.

Highlight is given to researcher Ronald Kerry Rowe, professor and researcher at Queen's University, (Kingston, Canada), which has the largest number of published research in the area and is one of the leaders in research on GCL. Rowe is a renowned researcher in geoenvironmental engineering, considered one of the pioneers in research on waste barrier systems. In a broad search in Scopus databases, searching documents where only the words "GCL" or "geosynthetic clay liners" appear in the title, abstract or keywords, Rowe appears first in terms of the number of publications, with a total of 98 articles, distributed in the period from 1997 to 2021. The same search, when performed in the WoS database searching for "topic", resulted in a total of 110 articles, distributed in the period from 1997 to 2021.

Of the 14 analyzed works that made up the bibliographic portfolio, Rowe contributed in 11 works, which represents 79% of the portfolio. In second place is Toshifumi Mukunoki with participation in 7 published articles, equivalent to 50% of the total, followed by Richard J. Bathurst with 6 articles, 43% of the total and by Paul Hurst, who collaborated in 4 articles, 29% of the total. Six authors participated in 2 publications, each representing 14.3% of the total. The other authors (23 remaining) contributed to only 1 publication, or 7.14% of the total.

In Figure 4, generated by the Biblioshiny interface of the Bibliometrix/R software, it is possible to better observe the distribution networks of publications among the 10 main authors highlighted. The authors are divided into two large groups that publish on the subject, with Rowe as the highlight. The greater the thickness of the branch, the greater the number of publications together between the authors. The largest collaboration network is between Rowe, Bathurst, Mukunoki and Hansen. Group 1 can be considered as the main research group on the topic addressed.

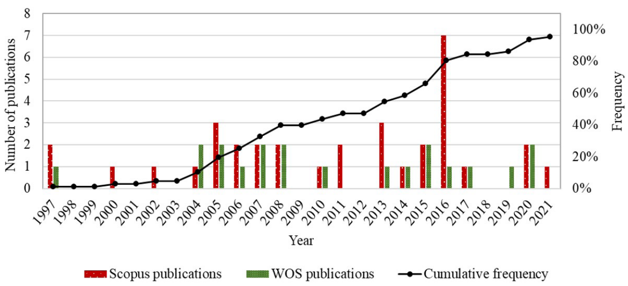

Figure 2. Time evolution of total publications in Scopus and WOS databases.

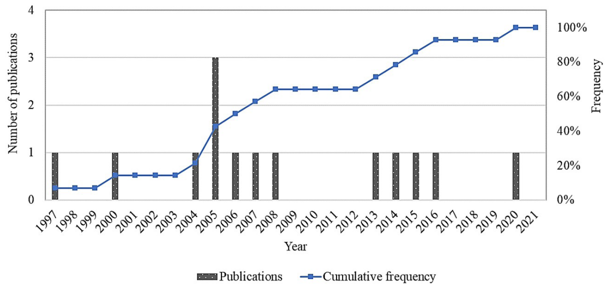

Figure 3. Temporal distribution of scientific production of secondary data.

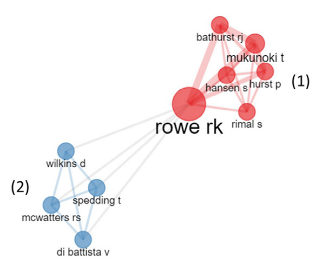

Figure 4. Network collaboration between the main authors with (1) the highest number of publications on the topic; and (2) the lowest number of publications on the topic.

3.4 Countries that publish the most on the topic

An analysis of the countries that have publications on the subject was carried out and a total of 5 countries involved in the research were verified. The emphasis is given to Canada, which has 11 of the 14 publications representing the portfolio, which corresponds to 79% of the total publications. Followed by Japan with 4 publications, Australia with 2, Belgium, Iran and Italy with 1 publication each. Figure 5 represents the geographic distribution of the analyzed studies.

Exploring the articles, it was observed two significant research groups composed of institutions from more than one country. One of them resulted from the co-authors union from institutions in Canada and Japan, and the other was formed by the relations between institutions in Canada and Australia. In this regard, it was noticed that 50% of the articles that have more than one author were developed in partnership with foreign institutions.

Canada had the highest number of publications involving GCLs and permeation with fuels. Some important studies were developed in Canada by one of these groups, specifically in the Canadian radar region on Brevoort Island, located in northern Canada, because of a cleanup program initiated in the summer of 2001 by the Canadian Department of National Defence in consequence of spills and fuel leaks at the site (Rowe et al., 2004; Rowe et al., 2005b; Rowe et al., 2007; Mukunoki et al., 2005; Bathurst et al., 2006; Hosney & Rowe, 2014).

As part of the cleanup program, the alternative built to control the contamination plume was a subsurface geosynthetic composite barrier wall, composed of needle-punched and non-woven GCL with sodium bentonite, HDPE geomembrane, protection layer with needle-punched geotextile and local filling material, constructed during the summer of 2001 (Li et al., 2002; Bathurst et al., 2006).

With regards to the other group of researchers from different countries, Tin et al. (2009) report that several stations in Antarctica have soils contaminated with hydrocarbons due to fuel spills over the years. The strategy developed to remediate the contaminated soil with hydrocarbons was through the construction of biopiles, composed of GCL, HDPE geomembrane and geotextiles, installed over 2011-2013 (McWatters et al., 2016; McWatters et al., 2020).

3.5 Journals where scientific research has been published

The articles that comprise the portfolio of work were distributed in seven journals (not counting the three publications in congresses, conferences and symposia), as shown in Figure 6. The journals "Geotextiles and Geomembranes" and "Journal of Geotechnical and Geoenvironmental Engineering" had featured, with 3 publications each. The other journals - "Géotechnique", "International Journal of Environmental Research", "Canadian Geotechnical Journal", "Geosynthetics International", and "Journal of ASTM International" - contributed with only 1 article each.

Analyzing the two journals with the highest number of publications, "Geotextiles and Geomembranes" is a journal indexed by Elsevier, aimed at disseminating information among researchers, designers, users and manufacturers of geosynthetic materials. By providing a growing base of information, the journal raises general awareness, stimulates further research and assists in the establishment of codes and regulations. The "Journal of Geotechnical and Geoenvironmental Engineering" is a journal indexed by the ASCE Library and covers research in the field of geotechnical engineering practice.

Another indicator analyzed and represented in Figure 6 was the impact factor (IF) of the mentioned journals, based on the most recent year available (2021). This factor corresponds to a measure of evaluation of journals and is based on citations received, considering publications for the same period, normally one year. Clarivate annually publishes the Journal Citation Report (JCR) with journal impact factor values.

In this case, it is possible to verify that one of the journals - "Geotextiles and Geomembranes" - with the highest number of publications also has a higher impact factor (FI = 5.839). The other journal that also presented the highest number of publications - "Journal of Geotechnical and Geoenvironmental Engineering" exhibited only the fourth highest impact factor (FI = 2.032), with a value very close to the journals that presented only one publication. The journal "Géotechnique", which, despite having only one publication, has the second highest impact factor (FI = 5.070) and the "International Journal of Environmental Research" with the third highest impact factor (FI = 3.160).

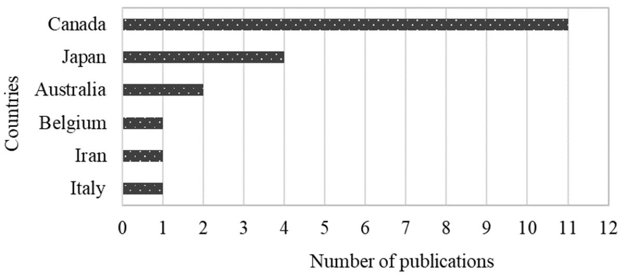

Figure 5. List of countries with publications on the subject.

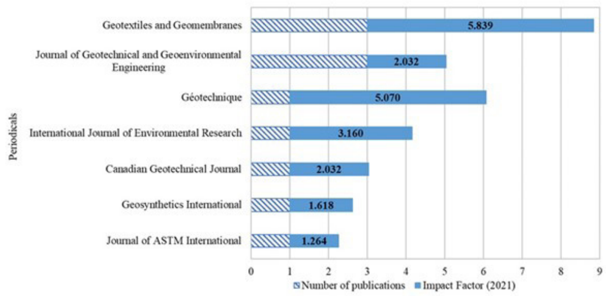

Figure 6. Periodicals with publications on the subject and the respective impact factors.

3.6 Frequency of terms

Determining the frequency of words used in publications is one of the ways to analyze the set of works that make up the bibliographic portfolio, and it can be given through the construction of a word cloud, as illustrated in Figure 7a. The cloud presents the most used terms in the scientific texts under study, and the font size of the word is proportional to the frequency with which they appear.

To assess the relationships between the most frequently identified terms, a thematic map was made, as shown in Figure 7b, which ramifies the terms by similarity and groups them according to their relationships in the texts. Figure 7 was generated with the help of the Biblioshiny interface of the Bibliometrix/R software.

It is observed that the highlight of the cloud is the word "GCL" and its similar ones. The cloud was built with 1-term words/expressions, so the expression "geosynthetic clay liners" is being considered by the word "GCL", for example. The word "GCL" had approximately 73 counts, representing 14% of the total of the 30 most frequent words. Then we have the words that make up the expression "hydraulic conductivity", which together represent 15% of the total, with "hydraulic" and "conductivity" having 43 and 37 counts each, respectively. The emphasis of these words is justified by the fact that they represent the keywords used in the research in the databases.

Next come the words "jet" and "water", each representing 5% of the total frequency. The word "jet" is in evidence because it is the nomenclature of a type of diesel, common in the Canadian arctic regions, where most of the studies were carried out, and the word "water" is quite frequent due to its use as a reference liquid in permeability tests. The same justification given for the word "jet" can also be associated with the expression "freeze and thaw cycles" (composed of the words "cycles" and the expression "freeze_thaw") which, due to the arctic climate where the GCL was exposed and tested, these cycles were considered in the studies. In addition to these two terms, each representing 4% of the total frequency, the words "geomembrane", "specimens" and "fuel" are also found in this range. The other words follow less frequently (less than 20 counts in the publications).

From the thematic map, it is possible to observe the grouping of words into three large niches (Figure 7b). Group 1 includes words that represent basic, emerging themes, with a degree of central relevance, especially the terms "gcl", "hydraulic" and "clay". Group 2 represents the motor themes, with emphasis on the words "conductivity", "liner" and "jet", presenting a degree of development and relevance. Group 3, on the other hand, combines the terms that present more niche themes, with a low-density degree of development, especially the words "performance", "conditions" and "hydrocarbons".

In general, it is possible to highlight that the elaboration of the word cloud and the thematic map complements what was previously observed, about most of the works on containment barriers for fuels with GCL being concentrated on a specific research group, seen by the highlight observed in words and expressions related to climate issues and type of fuel, typical of the places where the research was carried out.

3.7 Thematic synthesis

The bibliometric research carried out on the evaluation of the hydraulic conductivity of protective barriers for fuels with GCL revealed that it is a topic of interest to a limited group of researchers. The indices pointed to several studies on the hydraulic behavior of GCL in containment barriers for the spills of Jet A-1 diesel, a common fuel in the Canadian arctic regions. As the work was concentrated in these extreme climate regions, the freezing and thawing cycles of the geosynthetic were also objectives of these studies.

Petrov et al. (1997) examined the hydraulic conductivity of hydrated GCLs permeated with different concentrations of water and ethanol solutions. Mazzieri et al. (2000) also evaluated the hydraulic conductivity of GCLs with various ethanol solutions in water, performing tests on hydrated and unhydrated GCLs.

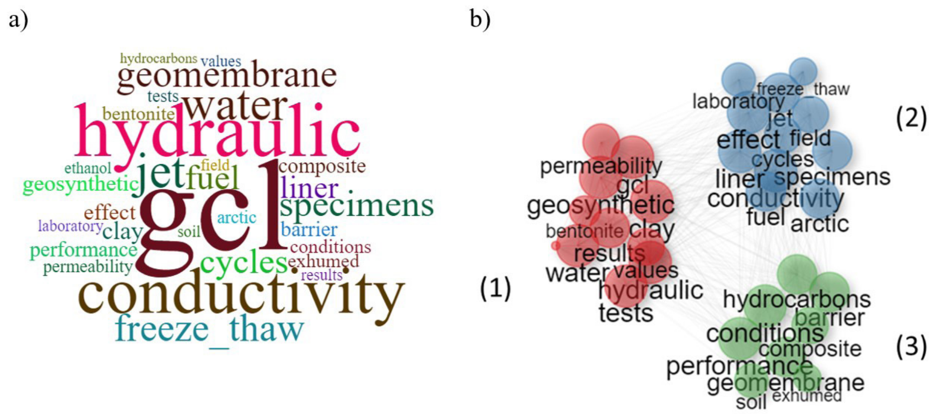

Figure 7. Frequency of the most used words in publications (a) and their interrelationships (b) through clusters of (1) basic, emerging, and central relevant terms; (2) driving terms; and (3) low-density terms.

Sari & Chai (2013) investigated self-healing capacity of GCLs with respect to different liquids permeation, including ethanol, considering circular induced damages. Rowe et al. (2004), Mukunoki et al. (2005), Rowe et al. (2006) and Rowe et al. (2008) presented results on the performance of GCLs used in temporary containment barriers for fuel spills of Jet A-1, considering the freeze and thaw cycles in laboratory investigation and exhumation of samples in different periods of exposition in the field. Rowe et al. (2005a), Rowe et al. (2005b) and Rowe et al. (2007) studied the hydraulic behavior of GCLs in the laboratory with respect to jet fuel A-1 for saturated and unsaturated conditions, also considering temperature variations. Hosney & Rowe (2014) conducted research on the hydraulic conductivity of samples extracted from the field over 10 years, exposed to arctic diesel contact, at different depths. Gitipour et al. (2015) performed permeability tests on bentonites sandwiched between geotextiles, which simulate a sample of GCL, with respect to permeation of water and crude oil. McWatters et al. (2016) and McWatters et al. (2020) evaluated the hydraulic performance of biopiles developed to contain and remediate soil contaminated by hydrocarbons and leachate in Antarctica.

A decade ago, Rowe et al. (2008) found that little attention had been paid to permeability studies of GCLs with hydrocarbons. Through the portfolio of the present research, it is observed that there has been no significant growth in the number of publications related to the theme over the years, until today.

The Table 1 presents the synthesis of the main data from these articles obtained on hydraulic conductivity of GCLs permeated with fuels, published over the years.

Table 1. Results from published research on hydraulic conductivity of GCLs in contact with fuels.

Reference	Main Points		Permeameter type	Hydraulic conductivity *k* (distilled/de-aired/de-ionized water / *tap water*)			Hydraulic conductivity *k* (fuel)			
	General	Specifics		Freeze-thaw cycles (n); *Exposure time*	*k* Virgin (m/s) [σ' (kPa)]	*k* Exhumed (m/s) [σ' (kPa)]	Fuel type	Freeze-thaw cycles (n); *Exposure time*	*k* Virgin (m/s) [σ' (kPa)]	*k* Exhumed (m/s) [σ' (kPa)]
Petrov et al., 1997	Ethanol/water mixtures		Fixed-WP		6.0 x 10^{-11} [4]		100% ethanol		2.0 x 10^{-9} [35]	
					1.3 x 10^{-11} [35]		75% ethanol		4.1 x 10^{-11} [35]	
					7.5 x 10^{-12} [114]		50% ethanol		6.0 x 10^{-12} [35]	
					1.6 x 10^{-11} [35]		25% ethanol		7.3 x 10^{-12} [35]	
Mazzieri et al., 2000	Ethanol/water mixtures	Water-hydrated GCL	FWP		1.0 x 10^{-11} [50]		100% ethanol		1.0 x 10^{-10} [50]	
		Ethanol-hydrated GCL					100% ethanol		5.5 x 10^{-8} [50]	
							75% ethanol		5.5 x 10^{-8} [50]	
							50% ethanol		3.5 x 10^{-10} [50]	
							25% ethanol		3.0 x 10^{-11} [50]	
Rowe et al., 2004	Canadian Arctic; Hydrocarbon spill	Freeze-thaw cycles	FWP	0	8.3 x 10^{-11} [1.4]		Jet Fuel A-1	0	4.3 x 10^{-12} [14]	
					4.0 x 10^{-11} [14]					
				5	6.3 x 10^{-11} [1.4]			6	8.7 x 10^{-12} [14]	
					2.9 x 10^{-11} [14]					
				12	4.3 x 10^{-11} [1.4]			12	2.7 x 10^{-10} [14]	
					2.3 x 10^{-11} [14]					
				1 year		4.0 x 10^{-11} [1.4]		13	5.6 x 10^{-12} [14]	
						2.0 x 10^{-11} [14]				
Mukunoki et al., 2005	Canadian Arctic; Hydrocarbon spill	Freeze-thaw cycles	RWP	0	2.0 x 10^{-11} [14]		Jet Fuel A-1	0	2.0 x 10^{-11} [14]	
				5	2.0 x 10^{-11} [14]			5	8.0 x 10^{-11} [14]	
				3 years		7.1 x 10^{-12} [14]		*3 years*		3.6 x 10^{-11} [14]
Rowe et al., 2005a	Canadian Arctic; Laboratory investigation	5°C	Fixed-WP		1.0 x 10^{-11} [14]		Jet Fuel A-1		4.1 x 10^{-11} [14]	
		5°C; w_c=60%							1.6 x 10^{-9} [14]	
		5°C; w_c=90%							1.7 x 10^{-9} [14]	
		5°C; w_c=120%							1.2 x 10^{-9} [14]	
		-5°C; w_c=60%							1.3 x 10^{-9} [14]	
		-5°C; w_c=90%							0.4 x 10^{-9} [14]	
		-5°C; w_c=120%							0.4 x 10^{-9} [14]	
		-5°C							< 1.3 x 10^{-12} [14]	
		5°C; 1 freeze							4.1 x 10^{-10} [14]	
		0 < T < 20°C; S_r=77%							≤ 3.0 x 10^{-10} [14]	
		0 > T > -20°C; S_r=70%							≤ 2.5 x 10^{-10} [14]	

FWP – flexible wall permeameter; RWP – rigid wall permeameter; Fixed-WP – fixed-wall permeameter; n – quantity of freeze-thaw cycles; w_c – moisture content; S_r – saturation degree; GCL – geosynthetic clay liner; GTX – geotextile; k – hydraulic conductivity; σ' – effective confining stress.

Table 1. Continued...

Reference	Main Points		Permeameter type	Hydraulic conductivity *k* (distilled/de-aired/de-ionized water / *tap water*)			Hydraulic conductivity *k* (fuel)			
	General	Specifics		Freeze-thaw cycles (n); *Exposure time*	*k* Virgin (m/s) [σ' (kPa)]	*k* Exhumed (m/s) [σ' (kPa)]	Fuel type	Freeze-thaw cycles (n); *Exposure time*	*k* Virgin (m/s) [σ' (kPa)]	*k* Exhumed (m/s) [σ' (kPa)]
Rowe et al., 2006	Canadian Arctic; Hydrocarbon spill		RWP	0	2.0 x 10^{-11} [15]		Jet Fuel A-1	0	2.0 x 10^{-11} [15]	
				5	2.0 x 10^{-11} [15]			5	8.0 x 10^{-11} [15]	
				12	2.6 x 10^{-11} [15]			12	1.5 x 10^{-10} [15]	
				1 year		1.2 x 10^{-11} [15]		*1 year*		7.1 x 10^{-11} [15]
				3 years		0.7 x 10^{-11} [15]		*3 years*		5.3 x 10^{-11} [15]
Rowe et al., 2005b;	Canadian Arctic; Laboratory investigation		RWP	0	2.0 x 10^{-11} [14]		Jet Fuel A-1	0	2.0 x 10^{-11} [14]	
				5	2.0 x 10^{-11} [14]			5	8.0 x 10^{-11} [14]	
			FWP	0	3.4 x 10^{-11} [14]			0	4.0 x 10^{-11} [14]	
				12	3.4 x 10^{-11} [14]			12	6.0 x 10^{-11} [14]	
Rowe et al., 2007		20°C; S_r=60%	RWP						1.6 x 10^{-8} [14]	
		5°C; S_r=60%							1.6 x 10^{-9} [14]	
		-5°C; S_r=60%							2.4 x 10^{-10} [14]	
		-20°C; S_r=60%							2.8 x 10^{-11} [14]	
		20°C; S_r=90%							3.4 x 10^{-10} [14]	
		5°C; S_r=90%							1.4 x 10^{-9} [14]	
		-5°C; S_r=90%							9.0 x 10^{-11} [14]	
		-20°C; S_r=90%							1.8 x 10^{-11} [14]	
Rowe et al., 2008	Canadian Arctic; Hydrocarbon spill	Contrast with Rowe et al. (2006)	FWP	0	3.3 x 10^{-11} [13]		Jet Fuel A-1	0	< 7.8 x 10^{-11} [23-41]	
				5	4.3 x 10^{-11} [13]			5	< 2.6 x 10^{-11} [17-20]	
				12	3.1 x 10^{-11} [13]			12	< 7.9 x 10^{-11} [20-30]	
				50	5.3 x 10^{-11} [13]			50	< 1.5 x 10^{-10} [17-27]	
				100	3.6 x 10^{-11} [13]			100	< 3.4 x 10^{-10} [13-20]	
				3 years		2.3 x 10^{-11} [13]		*3 years*		< 3.3 x 10^{-11} [17-27]
Hosney & Rowe, 2014	Canadian Arctic;Hydrocarbon spill		FWP		*3.8 x 10^{-11} [15]*		Jet Fuel A-1		6.2 x 10^{-12} [15]	
		Trench; Depth: 0.8 m		*1 year*		*2.6 x 10^{-11} [15]*		*1 year*		3.3 x 10^{-12} [15]
		Trench; Depth: 0.8 m		*4 years*		*4.0 x 10^{-11} [15]*		*4 years*		2.7 x 10^{-11} [15]
		Frame; Depth: 1.5-2.3 m		*6 years*		*3.1 x 10^{-10} [15]*		*6 years*		1.4 x 10^{-9} [15]
		Frame; Depth: 0-0.5 m		*7 years*		*3.0 x 10^{-11} [15]*		*7 years*		3.5 x 10^{-11} [15]
		Frame; Depth: 0.8-1.3 m		*10 years*		*3.9 x 10^{-10} [15]*		*10 years*		3.2 x 10^{-10} [15]
Gitipour et al., 2015		Simulated GCL; GTX + Bentonite + GTX	RWP		9.6 x 10^{-13}		Crude oil		1.2 x 10^{-8}	
					-				-	
McWatters et al., 2016	Antarctica; Biopiles; Hydrocarbon spill	w_c=13%	FWP		*4.0 x 10^{-11} [13]*					
		w_c=162%		*3 years*		*3.1 x 10^{-11} [13]*				
		w_c=22%		*3 years*		*3.0 x 10^{-11} [13]*				
McWatters et al., 2020	Antarctica; Biopiles; Hydrocarbon spill	w_c=12%	FWP		*1.5 x 10^{-11} [13]*					
		w_c=10%		*4 years*		*3.6 x 10^{-11} [13]*				
		w_c=200%		*4 years*		*3.9 x 10^{-11} [13]*				

FWP – flexible wall permeameter; RWP – rigid wall permeameter; Fixed-WP – fixed-wall permeameter; n – quantity of freeze-thaw cycles; w_c – moisture content; S_r – saturation degree; GCL – geosynthetic clay liner; GTX – geotextile; k – hydraulic conductivity; σ' – effective confining stress.

4. Conclusion

The present research aimed to evaluate the scientific production on the hydraulic conductivity of GCL in contact with fuels through a quantitative and descriptive analysis. The study provided an overview of the publications, authors, countries, and journals that published the most on the subject. The analyzed databases, Scopus and Web of Science, presented similar consistency and bibliographic coverage regarding the theme, since most of the articles were found in both bases, proving to be efficient research tools.

The bibliometric review identified that the scientific production on the subject is limited to a small number of articles, with a total of 14 articles forming the bibliographic portfolio. Through a critical analysis of these studies, several knowledge gaps and opportunities for future research were identified. The main contributions of this review study, including the synthesis of key results and the identification of general trends in the research area, are of great importance to the scientific community. Additionally, the bibliometric indicators obtained in this study indicate that this is a promising area for further research, given the limited scientific production found on the topic.

As already mentioned, GCL can be used as an hydraulic barrier in places where there is movement and distribution of fuels, in storage tanks and to contain some type of accidental spillage, to avoid contact and percolation of fuel towards the subsoil and groundwater waters. Therefore, it is important to pay attention to the development of research in the area aimed at clarifying the behavior of the hydraulic conductivity of GCL in contact with fuels, ensuring the efficiency of the barrier.

The collected data show that the number of publications related to the studied topic did not increase significantly over the years. Most studies were conducted by the same research group, indicating that more researchers should be encouraged to explore this area.

The study achieved its objective of expanding readers' knowledge about the scientific collection related to the use of GCL in fuel hydraulic containment systems, as well as the hydraulic conductivity of the geosynthetic in contact with these contaminants. Through the collected data, the study established indicators that allow the researcher to select and analyze existing publications, directing their future research in order to contribute to the scientific development of the area.

Acknowledgements

The authors desire to express their gratitude to CNPq (Grant n. 314643/2020-6), to the Graduate Program in Civil and Environmental Engineering of the University of Passo Fundo, and to the Geotechnical Laboratory of the Technological Center for Civil, Environmental Engineering and Architecture, at the same university, which enabled the development of practical experiments to compare the information collected in the respective study.

Declaration of interest

The authors have no conflicts of interest to declare. All co-authors have observed and affirmed the contents of the paper and there is no financial interest to report.

Authors' contributions

Julia Favretto: project administration, supervision, conceptualization, data curation, investigation, validation, visualization, writing – original draft. Adeli Beatriz Braun: conceptualization, data curation, investigation, methodology, visualization, writing – original draft. Márcio Felipe Floss: formal analysis, supervision, validation. Pedro Domingos Marques Prietto: formal analysis, supervision, validation.

Data availability

All data produced or examined in the course of the current study are included in this article.

References

Bathurst, R.J., Rowe, R.K., Zeeb, B., & Reimer, K. (2006). A geocomposite barrier for hydrocarbon containment in the Arctic. *International Journal of Geoengineering Case Histories*, 1(1), 18-34.

Bouazza, A. (2002). Geosynthetic clay liners. *Geotextiles and Geomembranes*, 20(1), 3-17. http://dx.doi.org/10.1016/S0266-1144(01)00025-5.

Bouazza, A., & Vangpaisal, T. (2007). Gas permeability of GCLs: effect of poor distribution of needle punched fibres. *Geosynthetics International*, 14(4), 248-252. http://dx.doi.org/10.1680/gein.2007.14.4.248.

Bouazza, A., Rouf, M.A., Singh, R.M., Rowe, R.K., & Gates, W.P. (2017). Gas advection-diffusion in geosynthetic clay liners with powder and granular bentonites. *Geosynthetics International*, 24(6), 607-614. http://dx.doi.org/10.1680/jgein.17.00027.

Bouazza, A., Vangpaisal, T., & Jefferis, S. (2006). Effect of wet-dry cycles and cation exchange on gas permeability of geosynthetics clay liners. *Journal of Geotechnical and Geoenvironmental Engineering*, 132(8), 1011-1018. http://dx.doi.org/10.1061/(ASCE)1090-0241(2006)132:8(1011).

Bradshaw, S.L., & Benson, C.H. (2013). Effect of municipal solid waste leachate on hydraulic conductivity and exchange complex of geosynthetic clay liners. *Journal of Geotechnical and Geoenvironmental Engineering*, 140(4), 04013038. http://dx.doi.org/10.1061/(ASCE)GT.1943-5606.0001050.

Braun, A.B., Trentin, A.W.S., Visentin, C., & Thomé, A. (2019). Sustainable remediation through the risk management perspective and stakeholder involvement: a systematic and bibliometric view of the literature. *Environmental Pollution*, 255, 113221. http://dx.doi.org/10.1016/j.envpol.2019.113221.

Carnero-Guzman, G.G., Bouazza, A., Gates, W.P., Rowe, R.K., & McWatters, R. (2021). Hydration/dehydration behavior of geosynthetic clay liners in the Antarctic environment. *Geotextiles and Geomembranes*, 49(1), 196-209. http://dx.doi.org/10.1016/j.geotexmem.2020.10.020.

Gitipour, S., Hosseinpour, M.A., Heidarzadeh, N., Yousefi, P., & Fathollahi, A. (2015). Application of modified clays in geosynthetic clay liners for containment of petroleum contaminated sites. *International Journal of Environmental Research*, 9(1), 317-322. http://dx.doi.org/10.22059/IJER.2015.903.

Hewitt, R.D., & Daniel, D.E. (1997). Hydraulic conductivity of geosynthetic clay liners after freeze-thaw. *Journal of Geotechnical and Geoenvironmental Engineering*, 123(4), 305-313. http://dx.doi.org/10.1061/(ASCE)1090-0241(1997)123:4(305).

Hosney, M.S., & Rowe, R.K. (2014). Performance of GCL after 10 years in service in the Arctic. *Journal of Geotechnical and Geoenvironmental Engineering*, 140(10), 04014056. http://dx.doi.org/10.1061/(ASCE)GT.1943-5606.0001160.

Koerner, R.M. (2012). *Designing with geosynthetics* (6th ed., Vol. 2). Bloomington: Xlibris Corporation.

LaGatta, M.D., Boardman, B.T., Cooley, B.H., & Daniel, D.E. (1997). Geosynthetic clay liners subjected to differential settlement. *Journal of Geotechnical and Geoenvironmental Engineering*, 123(5), 402-410. http://dx.doi.org/10.1061/(ASCE)1090-0241(1997)123:5(402).

Lake, C.B., & Rowe, R.K. (2000). Swelling characteristics of needlepunched thermally treated geosynthetic clay liners. *Geotextiles and Geomembranes*, 18(2), 77-101. http://dx.doi.org/10.1016/S0266-1144(99)00022-9.

Li, H.M., Bathurst, R.J., & Rowe, R.K. (2002). Use of GCLs to control migration of hydrocarbons in severe environmental conditions. In H. Zanzinger, R.M. Koerner & E. Gartung (Eds.), *Clay geosynthetic barriers* (pp. 187-198). London: CRC Press. https://doi.org/10.1201/9781003078777-22.

Macedo, M., Botelho, L.L.R., & Duarte, M.A.T. (2010). Revisão bibliométrica sobre a produção científica em aprendizagem gerencial. *Gestão e Sociedade*, 4(8), 619-639. http://dx.doi.org/10.21171/ges.v4i8.999.

Mazzieri, F., Pasqualini, E., & Van Impe, W.F. (November 19-24, 2000). Compatibility of GCLs with organic solutions. In International Society for Rock Mechanics (Ed.), *ISRM International Symposium* (pp. ISRM-IS-2000-001). Lisbon: International Society for Rock Mechanics.

McWatters, R.S., Rowe, R.K., Battista, V., Sfiligoj, B., Wilkins, D., & Spedding, T. (2020). Exhumation and performance of an Antarctic composite barrier system after 4 years exposure. *Canadian Geotechnical Journal*, 57(8), 1130-1152. http://dx.doi.org/10.1139/cgj-2018-0715.

McWatters, R.S., Rowe, R.K., Wilkins, D., Spedding, T., Jones, D., Wise, L., Mets, J., Terry, D., Hince, G., Gates, W.P., Di Battista, V., Shoaib, M., Bouazza, A., & Snape, I. (2016). Geosynthetics in Antarctica: performance of a composite barrier system to contain hydrocarbon-contaminated soil after three years in the field. *Geotextiles and Geomembranes*, 44(5), 673-685. http://dx.doi.org/10.1016/j.geotexmem.2016.06.001.

Meer, S.R., & Benson, C.H. (2007). Hydraulic conductivity of geosynthetic clay liners exhumed from landfill final covers. *Journal of Geotechnical and Geoenvironmental Engineering*, 133(5), 550-563. http://dx.doi.org/10.1061/(ASCE)1090-0241(2007)133:5(550).

Mukunoki, T., Rowe, R.K., Hurst, P., & Bathurst, R.J. (2005). Application of geosynthetic barrier wall to containment of hydrocarbons in the Arctic. In Organizing Committee of the 16th International Conference on Soil Mechanics and Geotechnical Engineering (Ed.), *Proceedings of the 16th International Conference on Soil Mechanics and Geotechnical Engineering: Geotechnology in Harmony with the Global Environment* (pp. 2415-2418). Amsterdam, The Netherlands: IOS Press. https://doi.org/10.3233/978-1-61499-656-9-2415.

Petrov, R.J., Rowe, R.K., & Quigley, R.M. (1997). Selected factors influencing GCL hydraulic conductivity. *Journal of Geotechnical and Geoenvironmental Engineering*, 123(8), 683-695. http://dx.doi.org/10.1061/(ASCE)1090-0241(1997)123:8(683).

Rowe, R.K. (2012). Short and long-term leakage through composite liners. The 7th Arthur Casagrande Lecture. *Canadian Geotechnical Journal*, 49, 141-169. http://dx.doi.org/10.1139/t11-09.

Rowe, R.K. (2014). Performance of GCLs in liners for landfill and mining applications. *Environmental Geotechnics*, 1(1), 3-21. http://dx.doi.org/10.1680/envgeo.13.00031.

Rowe, R.K. (2020). Geosynthetic clay liners: perceptions and misconceptions. *Geotextiles and Geomembranes*, 48(2), 137-156. http://dx.doi.org/10.1016/j.geotexmem.2019.11.012.

Rowe, R.K., & AbdelRazek, A.Y. (2021). Performance of multicomponent GCLs in high salinity impoundment applications. *Geotextiles and Geomembranes*, 49(2), 358-368. http://dx.doi.org/10.1016/j.geotexmem.2020.10.007.

Rowe, R.K., Brachman, R.W.I., Take, W.A., Rentz, A., & Ashe, L.E. (2016). Field and laboratory observations of down-slope bentonite migration in exposed composite liners. *Geotextiles and Geomembranes*, 44(5), 686-706. http://dx.doi.org/10.1016/j.geotexmem.2016.05.004.

Rowe, R.K., Garcia, J.D., Brachman, R.W.I., & Hosney, M.S. (2019). Hydraulic and chemical performance of geosynthetic clay liners isothermally hydrated from silty sand subgrade. *Geotextiles and Geomembranes*, 47(6), 740-754. http://dx.doi.org/10.1016/j.geotexmem.2019.103486.

Rowe, R.K., Hurst, P., & Mukunoki, T. (2005a). Permeating partially hydrated GCLs with jet fuel at temperatures from -20 °C and 20 °C. *Geosynthetics International*, 12(6), 333-343. http://dx.doi.org/10.1680/gein.2005.12.6.333.

Rowe, R.K., Mukunoki, T., & Bathurst, R.J. (2006). Compatibility with Jet A-1 of a GCL subjected to freeze thaw cycles. *Journal of Geotechnical and Geoenvironmental Engineering*, 132(12), 1526-1537. http://dx.doi.org/10.1061/(ASCE)1090-0241(2006)132:12(1526).

Rowe, R.K., Mukunoki, T., & Bathurst, R.J. (2008). Hydraulic conductivity to Jet-Al of GCLs after up to 100 freeze-thaw cycles. *Geotechnique*, 58(6), 503-511. http://dx.doi.org/10.1680/geot.2008.58.6.503.

Rowe, R.K., Mukunoki, T., Bathurst, R.J., Rimal, S., Hurst, P., & Hansen, S. (January 24-26, 2005b). The performance of a composite liner for retaining hydrocarbons under extreme environmental conditions. In M. Gabr, J. J. Bowders, D. Elton & J. G. Zornberg (Eds.), *Geo-Frontiers Congress 2005* (pp. 2795-2811). Reston, USA: American Society of Civil Engineers. https://doi.org/10.1061/40787(166)16.

Rowe, R.K., Mukunoki, T., Bathurst, R.J., Rimal, S., Hurst, P., & Hansen, S. (2007). Performance of a geocomposite liner for containing Jet A-1 spill in an extreme environment. *Geotextiles and Geomembranes*, 25(2), 68-77. http://dx.doi.org/10.1016/j.geotexmem.2006.10.003.

Rowe, R.K., Mukunoki, T., Li, M.H., & Bathurst, R.J. (2004). Effect of freeze-thaw on the permeation of arctic diesel through a GCL. In R.E. Mackey & K.P. von Maubeuge (Eds.), *Advances in geosynthetic clay liner technology* (pp. 134-146). West Conshohocken: ASTM International. http://dx.doi.org/10.1520/STP12203S.

Sari, K., & Chai, J. (2013). Self healing capacity of geosynthetic clay liners and influencing factors. *Geotextiles and Geomembranes*, 41, 64-71. http://dx.doi.org/10.1016/j.geotexmem.2013.08.006.

Scopus. (2022). *Quick reference guide*. Retrieved in 2022, August 16, from https://www.scopus.com/

Tin, T., Fleming, Z.L., Hughes, K.A., Ainley, D.G., Convey, P., Moreno, C.A., Pfeiffer, S., Scott, J., & Snape, I. (2009). Impacts of local human activities on the Antarctic environment. *Antarctic Science*, 21, 3-33. http://dx.doi.org/10.1017/S0954102009001722.

Touze-Foltz, N., Duquennoi, C., & Gaget, E. (2006). Hydraulic and mechanical behavior of GCLs in contact with leachate as part of a composite liner. *Geotextiles and Geomembranes*, 24, 188-197. http://dx.doi.org/10.1016/j.geotexmem.2006.01.004.

Viana, P.M.F., Palmeira, E.M., & Viana, H.N.L. (2011). Evaluation on the use of alternative materials in geosynthetic clay liners. *Soils and Rocks*, 34(1), 65-77. http://dx.doi.org/10.28927/SR.341065.

Visentin, C., Trentin, A.W.S., Braun, A.B., & Thomé, A. (2020). Life cycle sustainability assessment: a systematic literature review through the application perspective, indicators, and methodologies. *Journal of Cleaner Production*, 270, 122509. http://dx.doi.org/10.1016/j.jclepro.2020.122509.

Wang, B., Xu, J., Chen, B., Dong, X., & Dou, T. (2019). Hydraulic conductivity of geosynthetic clay liners to inorganic waste leachate. *Applied Clay Science*, 168, 244-248. http://dx.doi.org/10.1016/j.clay.2018.11.021.

Web of Science. (2022). *Quick reference guide*. Retrieved in 2022, August 16, from https://clarivate.com/webofsciencegroup/

The Best Solution!

***Tecnilab Portugal, S.A.** will provide you with answers to your Geotechnical engineering needs.*

Tecnilab Portugal, S.A. is a professional Geotechnical engineering company and has a lot of experience as a professional group that mainly engages in measurement engineering in dam, subway(Metro), harbor, power plant, soft ground and structure construction.

WE ARE THE DISTRIBUTOR OF PORTUGAL OF ACE INSTRUMENT CO., LTD. IN KOREA.

ACE INSTRUMENT CO., LTD. is a company that obtains worldwide reputation for supplying high precision, high reliability products in all Geotechnical instruments, data logger and in-situ test equipments. Independently developed automatic monitoring system can be used anywhere in the world, including buildings, bridges, ground and any constructions.

Data Acquisition System & Web Monitoring Program

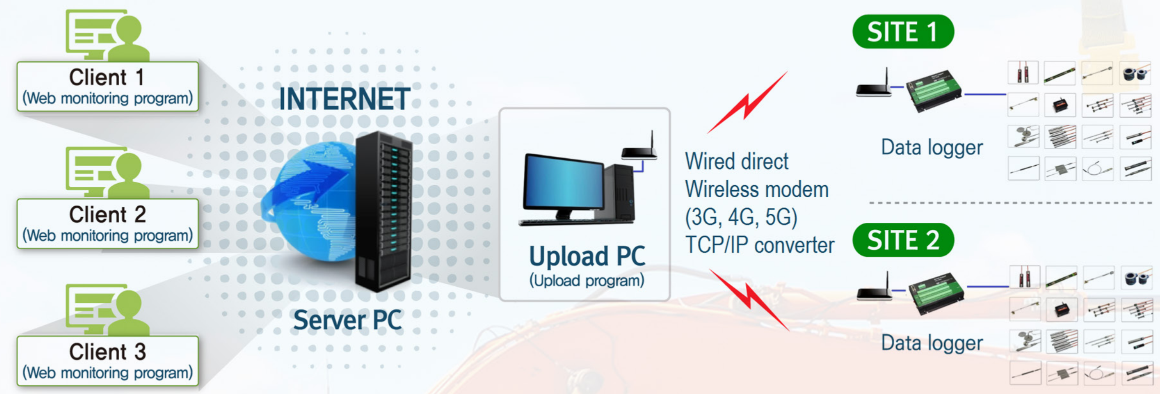

Sales company

Tecnilab Portugal, S.A.
A: Rua Gregorio Lopes, Lote 1512B 1449-041 Lisboa Portugal
T: +351 217 220 870 F: +351 217 264 550
www.tecnilab.pt

Manufacturer

ACE INSTRUMENT CO., LTD.
The first value in Geotechnical & Structural Instrumentation
A: 9, Dangjung-ro 27 beon-gil, Gunpo-si, Gyeonggi-do, Korea
T: +82 31 459 8753-7 F: +82 31 459 8758 E: acens@naver.com
www.aceinstrument.com

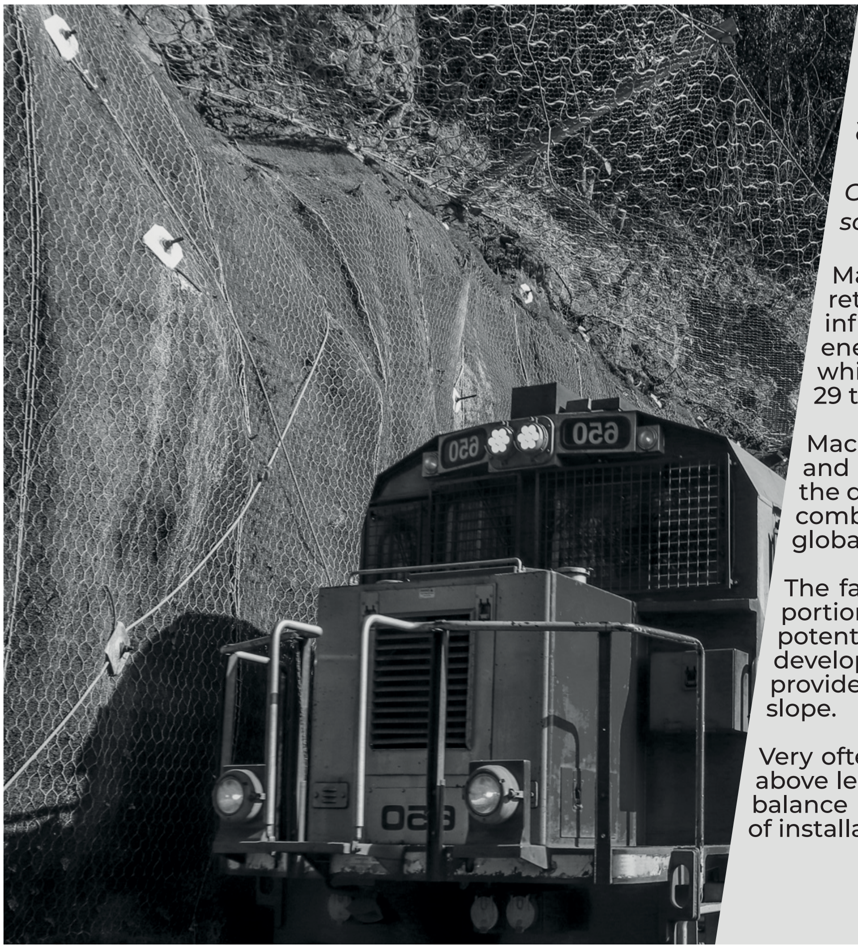


JET SJ
The Ground is our Challenge
MAIN ACTIVITY AREAS
Consultancy, Supervision and Training
· Earth Retaining Structures
· Special Foundations
· Ground Improvement
· Foundations Strengthening and Underpinning
· Façades Retention
· Tunnels and Underground Structures
· Slope Stability
· Geological and Geotechnical Investigation
· Demolition
www.jetsj.com
Tool Plazas P2 and P3
Santa Catarina, Brazil
Mining Shaft
Kamsar, Guiné
Lisbon Municipality Central Library and Archive
Lisboa, Portugal
Solar Santana Building
Lisboa, Portugal
Main Office
Rua Julieta Ferrão, 12 - Office 1501
1600-131 LISBOA, Portugal
Phone.: [+351] 210 505 150 / 51
Email: info@jetsj.com
www.linkedin.com/company/jetsj-geotecnia-lda/

Parque Oriente, Bloco 4, EN10
2699-501 Bobadela LRS
Tel. 21 995 80 00
Fax. 21 995 80 01
e.mail: mail@geocontrole.pt
www.geocontrole.pt


DF+
TRANSFORMATIVE ENGINEERING, MANAGEMENT, AND INNOVATION DELIVERING RESULTS
DF+ IS AN INTEGRATED ENGINEERING CONSULTING FIRM WITH OVER 25 YEARS OF EXPERIENCE IN THE SECTORS OF MINING, INFRASTRUCTURE, AGRIBUSINESS, AND INDUSTRIAL.
WE DEVELOP PROJECTS BASED ON CONSOLIDATED TECHNICAL SOLUTIONS THAT ENCOMPASS THE STATE OF THE ART IN DIGITAL ENGINEERING.
in
AV. BARÃO HOMEM DE MELO, 4554 - 5th floor
ESTORIL, BELO HORIZONTE/MG
+55 31 2519-1001
dfmais.eng.br
comercial@dfmais.eng.br
DF+ ENGENHARIA

Guide for Authors

Soils and Rocks is an international scientific journal published by the Brazilian Association for Soil Mechanics and Geotechnical Engineering (ABMS) and by the Portuguese Geotechnical Society (SPG). The aim of the journal is to publish original papers on all branches of Geotechnical Engineering. Each manuscript is subjected to a single-blind peer-review process. The journal's policy of screening for plagiarism includes the use of a plagiarism checker on all submitted manuscripts.

Soils and Rocks embraces the international Open Science program and is striving to meet all the recommendations. However, at this moment, the journal is not yet accepting preprints and open data, and has not adopted open peer reviews.

Soils and Rocks provides a manuscript template available at the journal's website.

1. Category of papers

Submissions are classified into one of the following categories:

Article – an extensive and conclusive dissertation about a geotechnical topic, presenting original findings.
Technical Note – presents a study of smaller scope or results of ongoing studies, comprising partial results and/or particular aspects of the investigation.
Case Study – report innovative ways to solve problems associated with design and construction of geotechnical projects. It also presents studies of the performance of existing structures.
Review Article – a summary of the State-of-the-Art or State-of-the-Practice on a particular subject or issue and represents an overview of recent developments.
Discussion – specific discussions about published papers.

Authors are responsible for selecting the correct category when submitting their manuscript. However, the manuscript category may be altered based on the recommendation of the Editorial Board. Authors are also requested to state the category of paper in their Cover Letter.

When submitting a manuscript for review, the authors should indicate the category of the manuscript, and is also understood that they:

a) assume full responsibility for the contents and accuracy of the information in the paper;
b) assure that the paper has not been previously published, and is not being submitted to any other journal for publication.

2. Paper length

Full-length manuscripts (Article, Case Study) should be between 4,000 and 8,000 words. Review articles should have up to 10,000 words. Technical Notes have a word count limit of 3,500 words. Discussions have a word count limit of 1,000 words. These word count limits exclude the title page, notation list (e.g., symbols, abbreviations), captions of tables and figures, acknowledgments and references. Each single column and double column figure or table is considered as equivalent to 150 and 300 words, respectively.

3. Scientific style

The manuscripts should be written in UK or US English, in the third person and all spelling should be checked in accordance with a major English Dictionary. The manuscript should be able to be readily understood by a Civil Engineer and avoid colloquialisms. Unless essential to the comprehension of the manuscript, direct reference to the names of persons, organizations, products or services is not allowed. Flattery or derogatory remarks about any person or organization should not be included.

The author(s) of Discussion Papers should refer to himself (herself/themselves) as the reader(s) and to the author(s) of the paper as the author(s).

The International System (SI) units must be used. The symbols are recommended to be in accordance with Lexicon in 14 Languages, ISSMFE (2013) and the ISRM List of Symbols. Use italics for single letters that denote mathematical constants, variables, and unknown quantities, either in tables or in the text.

4. Submission requirements and contents

A submission implies that the following conditions are met:

- the authors assume full responsibility for the contents and accuracy of the information presented in the paper;
- the manuscript contents have not been published previously, except as a lecture or academic thesis;
- the manuscript is not under consideration for publication elsewhere;
- the manuscript is approved by all authors;
- the manuscript is approved by the necessary authorities, when applicable, such as ethics committees and institutions that may hold intellectual property on contents presented in the manuscript;
- the authors have obtained authorization from the copyright holder for any reproduced material;
- the authors are aware that the manuscript will be subjected to plagiarism check.

The author(s) must upload two digital files of the manuscript to the Soils and Rocks submission system. The size limit for each submission file is 20 MB. The manuscript should be submitted in docx format (Word 2007 or higher) or doc format (for older Word versions). An additional PDF format file of the manuscript is also required upon submission. Currently, the journal is not accepting manuscripts prepared using LaTeX.

The following documents are required as minimum for submission:

- cover letter;
- manuscript with figures and tables embedded in the text (doc or docx format);

manuscript with figures and tables embedded in the text for revision (PDF format);
- permission for re-use of previously published material when applicable, unless the author/owner has made explicit that the image is freely available.

4.1 Cover letter

The cover letter should include: manuscript title, submission type, authorship information, statement of key findings and work novelty, and related previous publications if applicable.

4.2 Title page

The title page is the first page of the manuscript and must include:

- A concise and informative title of the paper. Avoid abbreviations, acronyms or formulae. Discussion Papers should contain the title of the paper under discussion. Only the first letter of the first word should be capitalized.
- Full name(s) of the author(s). The first name(s) should not be abbreviated. The authors are allowed to abbreviate middle name(s).
- The corresponding author should be identified by a pound sign # beside his/her and in a footnote.
- The affiliation(s) of the author(s), should follow the format: Institution, (Department), City, (State), Country.
- Affiliation address and e-mail must appear below each author's name.
- The 16-digit ORCID of the author(s) – mandatory
- Main text word count (excluding abstract and references) and the number of figures and tables

4.3 Permissions

Figures, tables or text passages previously published elsewhere may be reproduced under permission from the copyright owner(s) for both the print and online format. The authors are required to provide evidence that such permission has been granted at the moment of paper submission.

4.4 Declaration of interest

Authors are required to disclose conflicting interests that could inappropriately bias their work. For that end, a section entitled "Declaration of interest" should be included following any acknowledgments and prior to the "Authors' contributions" section. In case of the absence of conflicting interests, the authors should still include a declaration of interest.

4.5 Authors' contributions

Authors are required to include an author statement outlining their individual contributions to the paper according to the CASRAI CRediT roles (as per https://casrai.org/credit). The minimum requirements of contribution to the work for recognition of authorship are: a) Participate actively in the discussion of results; b) Review and approval of the final version of the manuscript. A section entitled "Authors' contributions" should be included after the declaration of interest section, and should be formatted with author's name and CRediT role(s), according to the example:

Samuel Zheng: conceptualization, methodology, validation. Olivia Prakash: data curation, writing - original draft preparation. Fatima Wang: investigation, validation. Kwame Bankole: supervision. Sun Qi: writing - reviewing and editing.

Do not include credit items that do not follow the Taxonomy established by CASRAI CRediT roles.

The authors' contributions section should be omitted in manuscripts that have a single author.

5. Plagiarism checking

Submitted papers are expected to contain at least 50 % new content and the remaining 50 % should not be verbatim to previously published work.

All manuscripts are screened for similarities. Currently, the Editorial Board uses the plagiarism checker Plagius (www.plagius.com) to compare submitted papers to already published works. Manuscripts will be rejected if more than 20 % of content matches previously published work, including self-plagiarism. The decision to reject will be under the Editors' discretion if the percentage is between 10 % and 20 %.

IMPORTANT OBSERVATION: Mendeley software plug-in (suggested in this guide) for MS-Word can be used to include the references in the manuscript. This plug-in uses a field code that sometimes includes automatically both title and abstract of the reference. Unfortunately, the similarity software adopted by the Journal (Plagius) recognizes the title and abstract as an actual written text by the field code of the reference and consequently increases considerably the percentage of similarity. Please do make sure to remove the abstract (if existing) inside Mendeley section where the adopted reference is included. This issue has mistakenly caused biased results in the past. The Editorial Board of the journal is now aware of this tendentious feature.

6. Formatting instructions

The text must be presented in a single column, using ISO A4 page size, left, right, top, and bottom margins of 25 mm, Times New Roman 12 font, and line spacing of 1.5. All lines and pages should be numbered.

The text should avoid unnecessary italic and bold words and letters, as well as too many acronyms. Authors should avoid to capitalize words and whenever possible to use tables with distinct font size and style of the regular text.

Figures, tables and equations should be numbered in the sequence that they are mentioned in the text.

Abstract

Please provide an abstract between 150 and 250 words in length. Abbreviations or acronyms should be avoided. The abstract should state briefly the purpose of the work, the main results and major conclusions or key findings.

Keywords

A minimum of three and a maximum of six keywords must be included after the abstract. The keywords must represent the content of the paper. Keywords offer an opportunity to include synonyms for terms that are frequently referred to in the literature using more than one term. Adequate keywords maximize the visibility of your published paper.

Examples:

Poor keywords – piles; dams; numerical modeling; laboratory testing

Better keywords – friction piles; concrete-faced rockfill dams; material point method; bender element test

List of symbols

A list of symbols and definitions used in the text must be included before the References section. Any mathematical constant, variable or unknown quantity should appear in italics.

6.1 Citations

References to other published sources must be made in the text by the last name(s) of the author(s), followed by the year of publication. Examples:

- Narrative citation: […] while Silva & Pereira (1987) observed that resistance depended on soil density
- Parenthetical citation: It was observed that resistance depended on soil density (Silva & Pereira, 1987).

In the case of three or more authors, the reduced format must be used, e.g.: Silva et al. (1982) or (Silva et al., 1982). Do not italicize "et al."

Two or more citations belonging to the same author(s) and published in the same year are to be distinguished with small letters, e.g.: (Silva, 1975a, b, c.).

Standards must be cited in the text by the initials of the entity and the year of publication, e.g.: ABNT (1996), ASTM (2003).

6.2 References

A customized style for the Mendeley software is available and may be downloaded from this link.

Full references must be listed alphabetically at the end of the text by the first author's last name. Several references belonging to the same author must be cited chronologically.

Some formatting examples are presented here:

Journal Article

Bishop, A.W., & Blight, G.E. (1963). Some aspects of effective stress in saturated and partly saturated soils. *Géotechnique*, 13(2), 177-197. https://doi.org/10.1680/geot.1963.13.3.177

Castellanza, R., & Nova, R. (2004). Oedometric tests on artificially weathered carbonatic soft rocks. *Journal of Geotechnical and Geoenvironmental Engineering*, 130(7), 728-739. https://doi.org/10.1061/(ASCE)1090-0241(2004)130:7(728)

Fletcher, G. (1965). Standard penetration test: its uses and abuses. Journal of the Soil Mechanics Foundation Division, 91, 67-75.

Indraratna, B., Kumara, C., Zhu S-P., Sloan, S. (2015). Mathematical modeling and experimental verification of fluid flow through deformable rough rock joints. *International Journal of Geomechanics*, 15(4): 04014065-1-04014065-11. https://doi.org/10.1061/(ASCE)GM.1943-5622.0000413

Garnier, J., Gaudin, C., Springman, S.M., Culligan, P.J., Goodings, D., Konig, D., ... & Thorel, L. (2007). Catalogue of scaling laws and similitude questions in geotechnical centrifuge modelling. *International Journal of Physical Modelling in Geotechnics*, 7(3), 01-23. https://doi.org/10.1680/ijpmg.2007.070301

Bicalho, K.V., Gramelich, J.C., & Santos, C.L.C. (2014). Comparação entre os valores de limite de liquidez obtidos pelo método de Casagrande e cone para solos argilosos brasileiros. *Comunicações Geológicas*, 101(3), 1097-1099 (in Portuguese).

Book

Lambe, T.W., & Whitman, R.V. (1979). *Soil Mechanics, SI version*. John Wiley & Sons.

Das, B.M. (2012). *Fundamentos de Engenharia Geotécnica*. Cengage Learning (in Portuguese).

Head, K.H. (2006). *Manual of Soil Laboratory Testing - Volume 1*: Soil Classification and Compaction Tests. Whittles Publishing.

Bhering, S.B., Santos, H.G., Manzatto, C.V., Bognola, I., Fasolo, P.J., Carvalho, A.P., ... & Curcio, G.R. (2007). *Mapa de solos do estado do Paraná*. Embrapa (in Portuguese).

Book Section

Yerro, A., & Rohe, A. (2019). Fundamentals of the Material Point Method. In *The Material Point Method for Geotechnical Engineering* (pp. 23-55). CRC Press. https://doi.org/10.1201/9780429028090

Sharma, H.D., Dukes, M.T., & Olsen, D.M. (1990). Field measurements of dynamic moduli and Poisson´s ratios of refuse and underlying soils at a landfill site. In *Geotechnics of Waste Fills - Theory and Practice* (pp. 57-70). ASTM International. https://doi.org/10.1520/STP1070-EB

Cavalcante, A.L.B., Borges, L.P.F., & Camapum de Carvalho, J. (2015). Tomografias computadorizadas e análises numéricas aplicadas à caracterização da estrutura porosa de solos não saturados. In *Solos Não Saturados no Contexto Geotécnico* (pp. 531-553). ABMS (in Portuguese).

Proceedings

Jamiolkowski, M.; Ladd, C.C.; Germaine, J.T., & Lancellotta, R. (1985). New developments in field and laboratory testing of soils. *Proc. 11th International Conference on Soil Mechanics and Foundation Engineering,* San Francisco, August 1985. Vol. 1, Balkema, 57-153.

Massey, J.B., Irfan, T.Y. & Cipullo, A. (1989). The characterization of granitic saprolitic soils. *Proc. 12th International Conference on Soil Mechanics and Foundation Engineering*, Rio de Janeiro. Vol. 6, Publications Committee of XII ICSMFE, 533-542.

Indraratna, B., Oliveira D.A.F., & Jayanathan, M. (2008b). Revised shear strength model for infilled rock joints considering overconsolidation effect. *Proc. 1st Southern Hemisphere International Rock Mechanics Symposium*, Perth. ACG, 16-19.

Barreto, T.M., Repsold, L.L., & Casagrande, M.D.T. (2018). Melhoramento de solos arenosos com polímeros. *Proc. 19º Congresso Brasileiro de Mecânica dos Solos e Engenharia Geotécnica*, Salvador. Vol. 2, ABMS, CBMR, ISRM & SPG, 1-11 (in Portuguese).

Thesis

Lee, K.L. (1965). *Triaxial compressive strength of saturated sands under seismic loading conditions* [Unpublished doctoral dissertation]. University of California at Berkeley.

Chow, F.C. (1997). *Investigations into the behaviour of displacement pile for offshore foundations* [Doctoral thesis, Imperial College London]. Imperial College London's repository. https://spiral.imperial.ac.uk/handle/10044/1/7894

Araki, M.S. (1997). *Aspectos relativos às propriedades dos solos porosos colapsíveis do Distrito Federal* [Unpublished master's dissertation]. University of Brasília (in Portuguese).

Sotomayor, J.M.G. (2018). *Evaluation of drained and non-drained mechanical behavior of iron and gold mine tailings reinforced with polypropylene fibers* [Doctoral thesis, Pontifical Catholic University of Rio de Janeiro]. Pontifical Catholic University of Rio de Janeiro's repository (in Portuguese). https://doi.org/10.17771/PUCRio.acad.36102*

* *official title in English should be used when available in the document.*

Report

ASTM D7928-17. (2017). Standard Test Method for Particle-Size Distribution (Gradation) of Fine-Grained Soils Using the Sedimentation (Hydrometer) Analysis. *ASTM International, West Conshohocken, PA.* https://doi.org/10.1520/D7928-17

ABNT NBR 10005. (2004). Procedure for obtention leaching extract of solid wastes. *ABNT - Associação Brasileira de Normas Técnicas*, Rio de Janeiro, RJ (in Portuguese).

DNIT. (2010). Pavimentação - Base de solo-cimento - Especificação de serviço DNIT 143. *DNIT -Departamento Nacional de Infraestrutura de Transportes*, Rio de Janeiro, RJ (in Portuguese).

USACE (1970). Engineering and Design: Stability of Earth and Rock-Fill Dams, Engineering Manual 1110-2-1902. Corps of Engineers, Washington, D.C.

Web Page

Soils and Rocks. (2020). *Guide for Authors*. Soils and Rocks. Retrieved in September 16, 2020, from http://www.soilsandrocks.com/

6.3 Artworks and illustrations

Each figure should be submitted as a high-resolution image, according to the following mandatory requirements:

- Figures must be created as a TIFF file format using LZW compression with minimum resolution of 500 dpi.
- Size the figures according to their final intended size. Single-column figures should have a width of up to 82 mm. Double-column figures should have a maximum width of 170 mm.
- Use Times New Roman for figure lettering. Use lettering sized 8-10 pt. for the final figure size.
- Lines should have 0.5 pt. minimum width in drawings.
- Titles or captions should not be included inside the figure itself.

Figures must be embedded in the text near the position where they are first cited. Cite figures in the manuscript in consecutive numerical order. Denote figure parts by lowercase letters (a, b, c, etc.). Please include a reference citation at the end of the figure caption for previously published material. Authorization from the copyright holder must be provided upon submission for any reproduced material.

Figure captions must be placed below the figure and start with the term "Figure" followed by the figure number and a period. Example:

Figure 1. Shear strength envelope.

Do not abbreviate "Figure" when making cross-references to figures.

All figures are published in color for the electronic version of the journal; however, the print version uses grayscale. Please format figures so that they are adequate even when printed in grayscale.

Accessibility: Please make sure that all figures have descriptive captions (text-to-speech software or a text-to-Braille hardware could be used by blind users). Prefer using patterns (e.g., different symbols for dispersion plot) rather than (or in addition to) colors for conveying information (then the visual elements can be distinguished by colorblind users). Any figure lettering should have a contrast ratio of at least 4.5:1

Improving the color accessibility for the printed version and for colorblind readers: Authors are encouraged to use color figures because they will be published in their original form in the online version. However, authors must consider the need to make their color figures accessible for reviewers and readers that are colorblind. As a general rule of thumb, authors should avoid using red and green simultaneously. Red should be replaced by magenta, vermillion, or orange. Green should be replaced by an off-green color, such as blue-green. Authors should prioritize the use of black, gray, and varying tones of blue and yellow.

These rules of thumb serve as general orientations, but authors must consider that there are multiple types of color blindness, affecting the perception of different colors. Ideally, authors should make use of the following resources: 1) for more information on how to prepare color figures, visit https://jfly.uni-koeln.de/; 2) a freeware software available at http://www.vischeck.com/ is offered by Vischeck, to show how your figures would be perceived by the colorblind.

6.4 Tables

Tables should be presented as a MS Word table with data inserted consistently in separate cells. Place tables in the text near the position where they are first cited. Tables should be numbered consecutively using Arabic numerals and have a caption consisting of the table number and a brief title. Tables should always be cited in the text. Any previously published material should be identified by giving the original source as a reference at the end of the table caption. Additional comments can be placed as footnotes, indicated by superscript lower-case letters.

When applicable, the units should come right below the corresponding column heading. Horizontal lines should be used at the top and bottom of the table and to separate the headings row. Vertical lines should not be used.

Table captions must be placed above the table and start with the term "Table" followed by the table number and a period. Example:

Table 1. Soil properties.

Do not abbreviate "Table" when making cross-references to tables. Sample:

Table 1. Soil properties

Parameter	Symbol	Value
Specific gravity of the sand particles	G_s	2.64
Maximum dry density (Mg/m^3)	$\rho_{d(max)}$	1.554
Minimum dry density (Mg/m^3)	$\rho_{d(min)}$	1.186
Average grain-size (mm)	d_{50}	0.17
Coefficient of uniformity	C_u	1.97

6.5 Mathematical equations

Equations must be submitted as editable text, created using MathType or the built-in equation editor in MS Word. All variables must be presented in italics.

Equations must appear isolated in a single line of the text. Numbers identifying equations must be flushed with the right margin. International System (SI) units must be used. The definitions of the symbols used in the equations must appear in the List of Symbols.

Do not abbreviate "Equation" when making cross-references to an equation.